Collège Doctoral des Sciences de l'Université de Liège

Laboratoire de Pétrologie et Géochimie des roches ignées

PhD presented by BILLON Melvyn

Defended: 16th of January 2026

A dissertation submitted in fulfillment of the requirements for the degree of Doctor of Philosophy of the University of Liège

Speciality: Volcanology, Experimental Petrology

Crystallization kinetics of Plagioclase and application to timescale of crystal mush storage

Advisor: Prof. Jacqueline Vander Auwera

Jury members:

Prof. Frédéric Hatert: Université de Liège, Liège, President of the jury

Prof. Jacqueline Vander Auwera: Université de Liège, Liège, Advisor

Prof. Bernard Charlier: Université de Liège, Liège, Jury secretary

Prof. Olivier Namur: KULeuven, Leuven

Prof. François Faure: Université de Lorraine, CRPG, Nancy

Prof. Marian Holness: University of Cambridge, Cambridge

Dr. Juliana Troch: Faculty of Georesources and Material Sciences, Aachen

« Le succès n'est pas la clé du bonheur. Le bonheur est la clé du succès. Si vous aimez ce que vous faites, vous réussirez. »

Albert Schweitzer

Abstract

Over the last decades, igneous petrology has shifted from large, melt-dominated magma chambers to interconnected dykes and sills dominated by crystal mushes. This change has stimulated interest in magmatic timescales, critical for understanding volcanic processes and hazards. Timescales from shallow differentiation to magma ascent can be estimated using various techniques: isotopic dating, diffusion chronometry, thermal modeling, or textural analyses such as Crystal Size Distributions (CSDs). When accessory phases like zircon are absent or diffusion chronometry is hindered by melt inclusions, CSD analyses combined with experimentally constrained growth rates may provide a valuable alternative for estimating storage durations. In these cases, the CSD method offers a quantitative link between texture and time. The slope of the ln(N)–L linear relationship constrains the growth rate (G) and residence time (t), and any departure from linearity can indicate late-stage processes such as mixing, coarsening, or recharge.

This thesis evaluates the potential of textural methods to constrain magmatic timescales by combining two complementary approaches (experimental and natural) using a natural basaltic andesite representative of arc magmatism, and by applying these constraints to natural samples from three Chilean volcanoes (Osorno, Calbuco, and Villarrica). A first part of the experimental study focuses on quantifying plagioclase growth kinetics at low undercoolings relevant to hypabyssal storage, while a second investigates how the solidification path and thermal pre-treatment (superheating and nucleation suppression) influence nucleation mode and crystal habit. Both sets of experiments were conducted at atmospheric pressure (1 atm) in the vertical furnace at ULiège, under Ni–NiO buffering and controlled thermal conditions. A natural basaltic andesite from Osorno was used as the starting material. Together, these experiments provide robust constraints on plagioclase growth rates, which can be applied to the analysis of natural crystal size distributions (CSDs).

In the first part of the experimental study, charges were equilibrated 15 °C above the liquidus for 24 h, then cooled at rates of 1, 3, or 9 °C/h and quenched between 1175 and 1000 °C. Plagioclase nucleation (J) and growth (G) rates show similar trends, peaking near the liquidus and rapidly decreasing during cooling, with minor Fe–Ti oxides and pyroxene crystallizing at lower temperatures. At the slowest cooling rates, G remains nearly constant, and microtextures evolve from euhedral tabular/prismatic forms (1–3 °C/h) to hopper and

swallowtail morphologies at 9 °C/h, marking a transition from interface- to diffusion-limited growth. Measured growth rates range from ~10^{-7} cm·s^{-1} (9 °C/h) to ~10^{-9} cm·s^{-1} (1 °C/h), stabilizing after ~20 h. In the second experimental series, thermal history and particularly the degree of initial superheating was found to strongly influence nucleation mode, and crystal habit. Three sets of atmospheric-pressure experiments were performed using the same crystal-poor, anhydrous basaltic andesitic starting material, containing plagioclase fragments: (1) isothermal runs across super- and sub-liquidus conditions, (2) continuous cooling from super-liquidus temperatures, and (3) cooling followed by isothermal holds. To assess the role of superheating, equivalent experiments were repeated with a crystal-free melt preheated to 1450 °C. Isothermal runs produced numerous small, homogeneous crystals by spontaneous nucleation, whereas continuous cooling promoted both nucleation and growth, yielding euhedral to dendritic plagioclase as cooling rate increased. Enhanced superheating, which suppresses nucleation, generated fewer but larger dendritic crystals, similar to those from the fastest seeded cooling runs. These results highlight the strong control of thermal pre-treatment on nucleation efficiency, crystal habit, and growth dynamics. Although experimental boundaries can trigger early crystallization, most nucleation occurred on heterogeneities such as gas bubbles or impurities, suggesting that homogeneous and heterogeneous nucleation may be indistinguishable at nano- to micrometric scales.

Finally, experimentally constrained plagioclase growth rates were combined with Crystal Size Distribution (CSD) analyses of 19 volcanic samples from Osorno, Calbuco, and Villarrica, three major active stratovolcanoes of the Chilean subduction arc, to estimate crystal residence times in mush-dominated arc systems. These volcanoes, lacking accessory phases and displaying widespread sieve-textured plagioclase, limit the use of conventional U-series or diffusion chronometry, which require suitable minerals such as zircon and well-preserved zoning. CSD-based analyses, grounded in experimental growth kinetics, provide a complementary approach, allowing the study of the various steps of crystallization, whereas zonation is mainly used to constrain the timescales of magma mixing or transport during the final ascent. Estimated plagioclase crystallization durations range from a few days to roughly three years, depending on cooling conditions and assumed growth rates (10^{-12}–10^{-8} cm·s^{-1}), with a minimum experimental growth rate of ~10^{-9} cm·s^{-1}, corresponding to the slowest cooling rates. Different crystal populations record distinct stages of magmatic evolution: macrocrystals reflect solidification in the main reservoir; microphenocrysts capture residence times in intermediate-level reservoirs (~1 kbar) prior to eruption, critical for hazard assessment; and

microlites record magma ascent timescales, typically from hours to days. These short timescales, much shorter than those inferred from diffusion modeling or U-series disequilibria, indicate that different chronometers record distinct stages of magmatic evolution. Overall, the results highlight the sensitivity of CSD analysis to short-lived crystallization events and its value as a complementary tool to geochemical chronometers, providing refined insights into magma residence and crystal growth in arc volcanic systems.

Résumé

Au cours des dernières décennies, le concept de réservoir magmatique a connu une refonte majeure, passant de grandes chambres magmatiques dominées par le liquide magmatique, à un enchevêtrement complexe de dykes et sills interconnectés, dominé par des mushs cristallins. Cette évolution majeure s'est accompagnée d'un intérêt croissant pour l'estimation des échelles de temps magmatiques (depuis la différenciation en profondeur jusqu'à l'ascension du magma), essentielles à la compréhension des processus volcaniques et des risques qui y sont associés. Ces échelles de temps peuvent être évaluées à l'aide de diverses techniques, telles que la datation isotopique, la chronométrie par diffusion, la modélisation thermique ou encore les analyses texturales, notamment la distribution de tailles de cristaux (*CSD*, Crystal Size Distributions). Cette dernière, lorsqu'elle est couplée à des taux de croissance déterminés expérimentalement, constitue une alternative particulièrement utile en cas d'absence de phases accessoires comme le zircon, ou lorsque la chronométrie par diffusion est rendue difficile par la présence d'inclusions vitreuses. Son utilisation dans des systèmes ouverts, tels que les chambres magmatiques, à l'état stationnaire, permet d'estimer le temps de résidence (t) ou le taux de croissance (G) des cristaux grâce à la relation linéaire entre le logarithme de la densité de cristaux, $\ln(N)$, et leur taille (L), dont la pente correspond à $-1/(G\mathbf{t})$. Associés à des données géochimiques, les déviations par rapport à cette tendance linéaire peuvent refléter l'intervention de processus tardifs tels que le mélange de deux magmas (magma mixing), le grossissement textural, ou le réapprovisionnement magmatique.

Cette thèse a pour objectif d'évaluer le potentiel des techniques texturales, telle que la méthode CSD, pour contraindre les échelles de temps magmatiques, en combinant deux approches complémentaires, expérimentale et naturelle. L'approche expérimentale, menée sur

une andésite basaltique naturelle représentative du magmatisme d'arc, visait à déterminer expérimentalement les taux de croissance en fonction de divers chemins de solidification, puis à appliquer ces résultats à des échantillons naturels provenant de trois volcans chiliens (Osorno, Calbuco et Villarrica) afin de contraindre les temps de résidence du magma dans ces systèmes. Afin d'évaluer l'impact du chemin de cristallisation sur les taux de croissance estimés à partir du plagioclase, deux sous-études expérimentales ont été réalisées. La première se concentrait sur la quantification de la cinétique de croissance du plagioclase à faibles sous-refroidissements, pertinents pour le stockage hypabyssal, tandis que la seconde examinait l'influence du chemin de solidification et du prétraitement thermique (surchauffe et suppression de la nucléation) sur le mode de nucléation et la microtexture des cristaux. Ces deux séries d'expériences ont été effectuées à pression atmosphérique (1 atm), sous tampon Ni–NiO, dans un four vertical à l'Université de Liège, offrant des conditions thermiques parfaitement contrôlées. Un échantillon naturel d'andésite basaltique provenant du volcan Osorno a été utilisé comme matériel de départ. Ensemble, ces expériences fournissent des contraintes robustes sur les vitesses de croissance du plagioclase, applicables à l'analyse des distributions naturelles de tailles de cristaux (CSD).

Dans la première partie de cette étude expérimentale, les échantillons ont été mis en équilibre 15 °C au-dessus du liquidus pendant 24 h, puis refroidis à 1, 3 ou 9 °C/h et trempés à diverses températures entre 1175 et 1000 °C. Les vitesses de nucléation (*J*) et de croissance (*G*) du plagioclase montrent des tendances similaires, atteignant un maximum près du liquidus et diminuant rapidement au cours du refroidissement, avec de faibles quantités d'oxydes Fe–Ti et de pyroxène cristallisant à des températures plus basses. Aux vitesses de refroidissement les plus lentes, *G* reste presque constant, et les microtextures évoluent de formes tabulaires ou prismatiques euédriques (1–3 °C/h) vers des morphologies en creux (*hopper*) et en queue d'hirondelle (swallowtail) à 9 °C/h, marquant la transition d'une croissance contrôlée par l'attachement des atomes à l'interface cristalline vers une croissance limitée par diffusion. Les vitesses de croissance mesurées varient d'environ 10^{-7} cm·s^{-1} (9 °C/h) à ~10^{-9} cm·s^{-1} (1 °C/h), et se stabilisent après environ 20 h.

Dans la seconde série expérimentale, l'histoire thermique, et en particulier le degré de surchauffe initiale, s'est révélée jouer un rôle majeur sur le mode de nucléation et la microtexture cristalline. Trois ensembles d'expériences à pression atmosphérique ont été réalisés sur le matériau basaltique andésitique initial : (1) des expériences isothermes couvrant

des conditions supra- et sub-liquidus, (2) des refroidissements continus à des vitesses comprises entre 1 et 125 °C/h à partir de températures supra-liquidus situées de 15 à 55 °C au-dessus du liquidus, et (3) des refroidissements suivis de paliers isothermes. Afin d'évaluer l'effet de la surchauffe, des expériences équivalentes ont été répétées avec un liquide initial préchauffé à 1450 °C et dépourvu de cristaux. Les expériences isothermes produisent de nombreux petits cristaux homogènes par nucléation spontanée, tandis qu'un refroidissement continu favorise à la fois la nucléation et la croissance, générant des plagioclases euédriques à dendritiques à mesure que la vitesse de refroidissement augmente. En présence d'une surchauffe accrue, un nombre réduit de cristaux, mais de plus grande taille et dendritiques, est observé, suggérant une inhibition de la nucléation. Ces cristaux sont comparables à ceux obtenus lors des expériences de refroidissement rapide avec germes. Ces résultats mettent en évidence le rôle prépondérant du prétraitement thermique sur l'efficacité de la nucléation, la microtexture cristalline et la dynamique de croissance. Bien que certaines conditions expérimentales puissent induire une cristallisation précoce, la majorité des nucléations se produit sur des hétérogénéités telles que des bulles de gaz ou des impuretés, suggérant que la distinction entre nucléation homogène et hétérogène reste souvent difficile à l'échelle nano- à micrométrique.

Les vitesses de croissance déterminées expérimentalement sur les cristaux de plagioclase ont été combinées aux analyses CSD de 19 échantillons volcaniques provenant de trois stratovolcans actifs de l'arc de subduction chilien (Osorno, Calbuco et Villarrica) afin d'estimer les temps de résidence cristallins. Ces volcans, dépourvus de phases accessoires et présentant un plagioclase à texture criblée (sieve texture), limitent l'utilisation des chronomètres conventionnels, tels que les séries de l'uranium ou la chronométrie par diffusion, qui nécessitent des minéraux appropriés et une texture cristalline préservée. Les analyses CSD, basées sur des cinétiques de croissance expérimentales, offrent une approche complémentaire pour étudier les différentes étapes de la cristallisation, tandis que la zonation des cristaux est surtout utilisée pour contraindre les temps de mélange ou de transport magmatique lors de l'ascension finale. Les durées de cristallisation estimées varient de quelques jours à environ trois ans, selon les conditions de refroidissement et les vitesses de croissance considérées (10^{-8}–10^{-12} cm·s^{-1}), la vitesse expérimentale minimale (~10^{-9} cm·s^{-1}) correspondant aux taux de refroidissement les plus lents. Les différentes populations de cristaux enregistrent des stades distincts de l'évolution magmatique : les macrocristaux reflètent la solidification dans le réservoir principal ; les microphénocristaux correspondent à des temps de résidence dans des réservoirs intermédiaires (~1 kbar) avant l'éruption, essentiels pour l'évaluation des risques ; et

les microlites documentent l'ascension finale du magma, sur des durées de quelques heures à quelques jours. Ces durées, bien plus courtes que celles déduites par diffusion ou par les séries de l'uranium, indiquent que chaque type de chronomètre enregistre des stades différents de l'évolution magmatique. Dans l'ensemble, ces résultats soulignent la sensibilité de l'analyse CSD aux épisodes de cristallisation de courte durée et sa valeur comme outil complémentaire aux chronomètres géochimiques, offrant une compréhension plus fine du stockage magmatique et de la croissance cristalline dans les systèmes volcaniques d'arc.

Remerciements

Mes remerciements vont tout d'abord au **Prof. Jacqueline Vander Auwera**, sans qui ce projet de thèse n'aurait pas été possible, et qui m'a apporté aide, soutien et précieux conseils chaque fois que j'en avais besoin. Je remercie également le **Fonds National de la Recherche Scientifique** (*FNRS*) qui a financé ce projet durant quatre années.

Je souhaite également exprimer une reconnaissance toute particulière aux **Prof. Bernard Charlier** et **Olivier Namur**. Bien qu'ils n'aient pas été mes encadrants directs, ils m'ont fortement guidé, soutenu et transmis leur passion pour la pétrologie expérimentale. Je les remercie pour leurs nombreux conseils, leur disponibilité lors des moments difficiles, ainsi que pour les excellents souvenirs, qu'il s'agisse des barbecues au B20 ou des diverses conférences (notamment l'EMPG 2025). Un remerciement particulier au **Prof. Olivier Namur** pour son accueil à de nombreuses reprises au sein de la KULeuven. Encore désolé pour le fil de platine !

Je remercie également les membres du jury (**Prof. Frédéric Hatert**, pour avoir accepté d'en assurer la présidence ; **Prof. François Faure ; Prof. Marian Holness ;** ainsi que le **Prof. Juliana Troch**) pour la lecture de ce manuscrit, qui leur a certainement demandé un temps considérable.

Quelques mots personnels:

- **Au Prof. François Faure**, pour m'avoir fait découvrir la volcanologie et la pétrologie il y a plus de cinq ans à l'ENSG Nancy. Sans lui, je ne serais peut-être pas en thèse aujourd'hui.
- **À la Prof. Juliana Troch**, pour nos discussions enrichissantes et la découverte de son laboratoire de pétrologie expérimentale au sein de l'Université de Aachen.
- **À la Prof. Marian Holness**, pour son accueil lors de mon séjour à l'Université de Cambridge. Un séjour court mais mémorable.

Je remercie également le **Prof. Eduardo Morgado** pour son accueil lors de notre séjour au Chili, ainsi qu'une partie du personnel de l'Université de Cambridge : **Prof. John McLennan** (pour ses cours auxquels j'ai eu la chance d'assister), **Iris Buisman** (pour son aide avec le SEM)

et, surtout : **Francesca Butler**, **Kate Greenaway**, **Josh Turner**, **Julian Pal** (que j'ai eu plaisir à revoir à Aachen), **Harriet**, **Oscar**, **Lara** et **Megan**. Merci pour les soirées quiz au bar, et à **Harriet**, **Francesca**, **Kate** et **Julian** pour nos expéditions au musée de Géologie. Ce séjour restera un très beau souvenir.

Mes remerciements vont aussi à **Robert Dennen** pour ses diverses corrections et éditions concernant les diverses publications, ainsi qu'à **Roman Klinghardt** et au **Dr Alexandre Fadel** pour leur aide lors des analyses SEM, EPMA et EBSD.

Merci à toute l'équipe du B20 : **Olivier Bolle** (et nos moments de rire au Chili il y a déjà deux ans), **Prof. Anne-Christine Da Silva**, **Prof. Damien Pas**, **Nicolas**, **Raphaël**, **Hadrien**, **Merry**, **Laurie**, **Paul**, **Tonin**, **Fabrizio**, **Aliou**, **Marien**, **Michiel**, **Dhouha**, **Imen**, **Jarno**, **Isaline**, **Manon**, **Tianqi**, **Wenmei**, **Mélina** et **Laura**; et à l'équipe du B18, en particulier **Joëlle** et **Mariella** pour leur aide administrative, ainsi que les bons moments partagés à midi ou autour d'un café. Merci aussi à **Valentine**, **Marina**, **Maxime**, **Amine**, **Florent**, **Martin**, **Prof. Valentin Fischer**, **Prof. Nathalie Fagel**, **Philippe**, **Melvin**, **Antoine**, **Romain**, **Francesco** et **Raphaël**.

Quelques mentions spéciales:

- À **Fabrizio**, mon collègue Italien préféré, pour les moments mémorables à l'EMPG ;
- À **Aliou** et **Michiel**, mes compagnons du week-end ;
- À **Martin Blavier**, **Isaline**, **Marina** et **Manon**, collègues et amis formidables, pour leur soutien et tous les instants partagés, que ce soit au café ou restaurant. Merci à **Marina** pour sa présence lors d'un moment difficile, et à **Martin** pour son aide lors du déménagement (désolé encore pour le matelas et la machine à laver ! ahah) ;
- À **Laurie Llado**, une amie fidèle, qui a toujours été présente. Merci pour nos discussions café, les salons du vin et les voyages partagés.
- A **Joëlle** pour son soutien et son aide importante.

Merci également à mes collègues de Leuven : **Kat**, **Eason**, **Saffy**, **Sander**, **Thomas**, **Ephrem**, **Nanxing**, **Shuchang** et **Soetkin**.

Je n'oublie pas mes amis de longue date et plus récents : **Steph**, **Esther**, **Sami** (qui m'accompagne depuis le lycée), ainsi que mes camarades de l'ENSG (**Anaïs**, **Orphée**, **Loann**, **Vanina**, **Eva**, **Mathilde**, **Valentin**, **Rémi** et **Laura**) pour les soirées pizza et nos rendez-vous

du vendredi à la FNAC. Sans oublier **David** et **Cynthia**, **Gilles**, **Odile**, **Alex** et **Jess** pour leurs encouragements.

Enfin, un immense merci à ma famille (mes parents et grands-parents) pour leur soutien indéfectible tout au long de ma scolarité. Sans vous, rien de tout cela n'aurait été possible. Merci aussi à mes « bébés »: **Angy**, **Vasco** et **Silver** pour la joie qu'ils m'ont apportée ; sans oublier ma compagne **Camilla**, pour sa présence et son aide précieuse, particulièrement durant ces derniers mois de thèse.

Acknowledgments

My first acknowledgements are dedicated to **Prof. Jacqueline Vander Auwera**, for her guidance, support, and invaluable advice throughout this project. I am also grateful to the National Fund for Scientific Research (FNRS) for funding this project over the past four years.

I would like to extend special thanks to **Prof. Bernard Charlier** and **Olivier Namur**. Although they were not my direct supervisors, they provided essential guidance, encouragement, and shared their passion for experimental petrology. Thank you for your thoughtful advice, your support during challenging moments, and all the memorable experiences, whether at B20 barbecues or at conferences (especially EMPG 2025). I am also grateful to **Olivier Namur** for welcoming me to KU Leuven on several occasions. Apologies again for the platinum wire incident!

I sincerely thank the members of my thesis jury for dedicating time to review this manuscript:

- **Prof. Frédéric Hatert**, for kindly agreeing to chair the jury;
- **Prof. François Faure** (CRPG Nancy, France);
- **Prof. Marian Holness** (University of Cambridge, UK);
- **Prof. Juliana Troch** (RWTH Aachen University, Germany).

A few personal acknowledgments:

- To **Prof. François Faure**, for introducing me to volcanology and petrology over five years ago at ENSG Nancy. Without his inspiration, I might not be pursuing a PhD today.

- To **Prof. Juliana Troch**, for our enriching discussions and the opportunity to explore her experimental petrology laboratory at RWTH Aachen.
- To **Prof. Marian Holness**, for her warm welcome during my stay at the University of Cambridge. A short but unforgettable experience.

I am also grateful to **Prof. Eduardo Morgado** for hosting us in Chile, as well as to many colleagues at the University of Cambridge: **Prof. John McLennan** (for his lectures), **Iris Buisman** (for assistance with SEM), and especially **Francesca Butler**, **Kate Greenaway**, **Josh Turner**, **Julian Pal** (whom I had the pleasure of seeing again in Aachen), **Harriet**, **Oscar**, **Lara**, and **Megan**. Thank you for the quiz nights at the pub, and to **Harriet**, **Francesca**, **Kate**, and **Julian** for our trips to the Geology Museum. This stay remains a cherished memory.

My thanks also go to **Robert Dennen** for his careful corrections and edits concerning publications, and to **Roman Klinghardt** and **Dr. Alexandre Fadel** for their help with SEM, EPMA, and EBSD analyses.

A huge thank you to the entire B20 team: **Olivier Bolle** (and our laughter in Chile two years ago), **Prof. Anne-Christine Da Silva**, **Prof. Damien Pas**, **Nicolas**, **Raphaël**, **Hadrien**, **Merry**, **Laurie**, **Paul**, **Tonin**, **Fabrizio**, **Aliou**, **Marien**, **Michiel**, **Dhouha**, **Imen**, **Jarno**, **Isaline**, **Manon**, **Tianqi**, **Wenmei**, and **Mélina**; and to the B18 team, especially **Joëlle** and **Mariella**, for administrative support and for the enjoyable moments shared over lunch or coffee. Thanks also to **Valentine**, **Marina**, **Maxime**, **Amine**, **Florent**, **Martin**, **Prof. Valentin Fischer**, **Prof. Nathalie Fagel**, **Philippe**, **Melvin**, **Antoine**, **Romain**, **Francesco**, and **Raphaël**.

Special mentions:

- To **Fabrizio**, my favorite Italian, for the unforgettable moments at EMPG;
- To **Aliou** and **Michiel**, my weekend companions;
- To **Martin Blavier**, **Isaline**, **Marina**, and **Manon**, wonderful colleagues and friends, for their support and all the shared moments, whether at coffee breaks or meals. Special thanks to **Marina** for being there during a difficult moment, and to Martin for helping with the move (sorry again for the mattress and washing machine!);
- To **Laurie Llado**, a loyal friend, always present. Thank you for our coffee chats, wine fairs, and shared trips.
- To **Joëlle** for her support and valuable help.

Thanks also to my colleagues in Leuven: **Kat**, **Eason**, **Saffy**, **Sander**, **Thomas**, **Ephrem**, **Nanxing**, **Shuchang**, and **Soetkin**.

I would also like to acknowledge my longtime and newer friends: **Steph**, **Esther**, **Sami** (who has supported me since high school), and my ENSG peers (**Anaïs**, **Orphée**, **Loann**, **Vanina**, **Eva**, **Mathilde**, **Valentin**, **Rémi**, and **Laura**) for pizza nights and our Friday gatherings at FNAC. I also thank **David** and **Cynthia**, **Gilles**, **Odile**, **Alex**, and **Jess** for their encouragement.

Finally, my heartfelt gratitude goes to my family (my parents and grandparents) for their unwavering support throughout my education. Without you, none of this would have been possible. Thanks also to my "babies," **Angy**, **Vasco**, and **Silver**, for the joy they bring me; and to my partner **Camilla**, for her presence and invaluable support, especially during the final months of my PhD.

Table of contents

Chapter 1

General Introduction

Introduction

Magmatism refers to the suite of processes involved in the generation, transport, storage, solidification, and eventual eruption of magma (the combination of silicate liquid, crystalline phases, and exsolved fluids; *Cooper and Kent 2025*) within the planets of the solar system, and more specifically within Earth's lithosphere. It also includes the crystallization of eruptive products both in volcanic rocks at the surface and in plutonic rocks at depth. Magmatism plays a fundamental role in the planet's thermal and chemical evolution, contributing to crustal differentiation and the formation of new igneous rocks.

Volcanism and volcanic systems represent only the surface expression of terrestrial and extraterrestrial magmatic activity, driven by plate tectonics and planetary heat loss (*Humphreys et al. 2025*). Volcanism is characterized by a variety of eruptive processes, including the emission of lavas, pyroclastic materials, and gases through volcanic conduits connected to deeper magmatic systems. More than 500 active volcanoes are currently present on Earth (**Figure I-1**; *Siebert et al. 2015*), with around 50 erupting each year (*Siebert et al. 2015*). These eruptions, and more particularly the most explosive and violent (e.g. Tambora eruption in 1815 which killed more than 90 000 people; *Stothers 1984*), constitute a major economic and societal risk for the surrounding population (*Petrelli and Zellmer 2021*). An important example is Naples (Italy), an important European economic center, whose the population lives near various magmatic systems, such as the Vesuvio volcano at the East of Naples (famous for the major eruption in 79 ap J.C, with the destruction of Pompéi and Herculanum), and the Campi Phlegrei volcanic system at the west part of the Naples region, whose the important caldeira (**Figure I-2**) testifies to the largest Mediterranean eruption during the Quaternary (called Campanian ignimbrite eruption), about 40,000 years ago, with an eruption of some 100 to 300 km^3 of trachytic magma (*Association Volcanologique Européenne, website*).

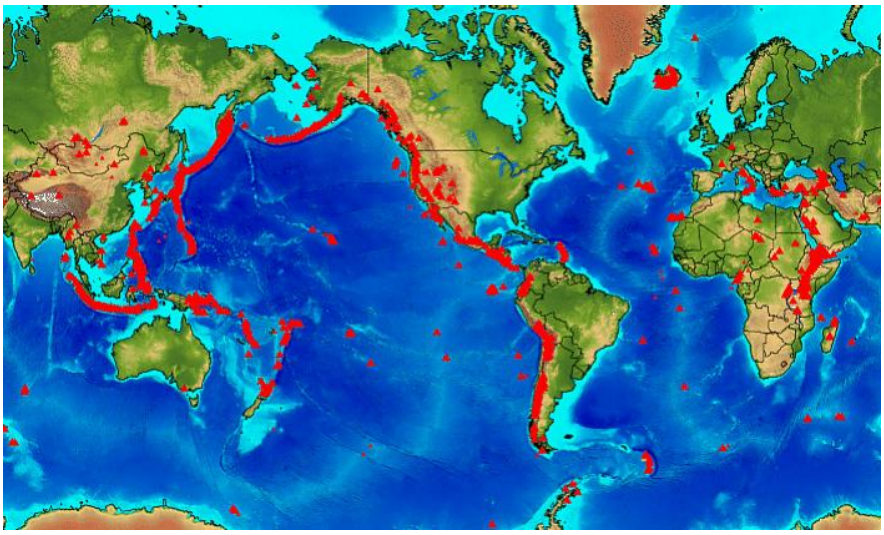

***Figure I-1**: Map showing the global distribution of volcanoes (data from the European Space Agency, website)*

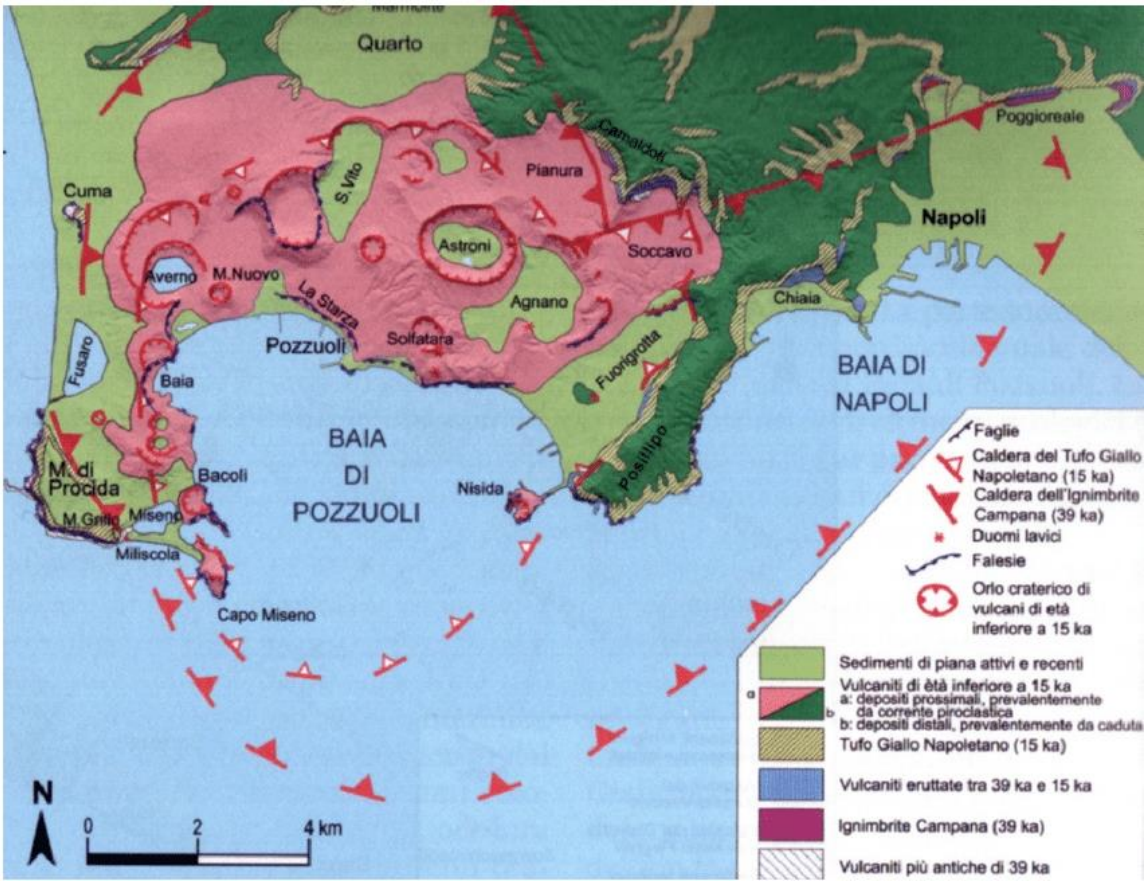

***Figure I-2**: Schematic geological map of the Campi Flegrei caldera (from Orsi et al. 1996)*

A clear understanding of processes operating within the crust beneath active volcanoes, as well as the structure and temporal evolution, is therefore crucial for providing effective hazard-reduction strategies (e.g. *Marsh 1981*; *Petrelli and Zellmer 2021*; *Cooper and Kent*

2025). The magmatic systems are globally organized around one or more transient storage zones known as magma reservoirs (or magma chambers), corresponding to volumes of partially molten material located at various depths within the crust (**Figure I-3**). These reservoirs are known to be the sites of magma evolution, where several processes such as fractional crystallization, magma mixing, and crustal assimilation occur. Eruptions correspond to a remobilization of this magma within the transcrustal system (*Bachmann et al. 2002*; *Humphreys 2025*; *Cooper and Kent 2025*). Despite the eruptive products preserved at the surface, the internal dynamics remain difficult to observe directly. However, some investigations through geophysical, geochemical, petrological, and experimental studies have been carried out to improve our understanding of these systems. The present study is situated within this context, focusing on the crystallization processes that occur during the progressive cooling of magma stored in such reservoirs, and on the timescales corresponding in these reservoirs.

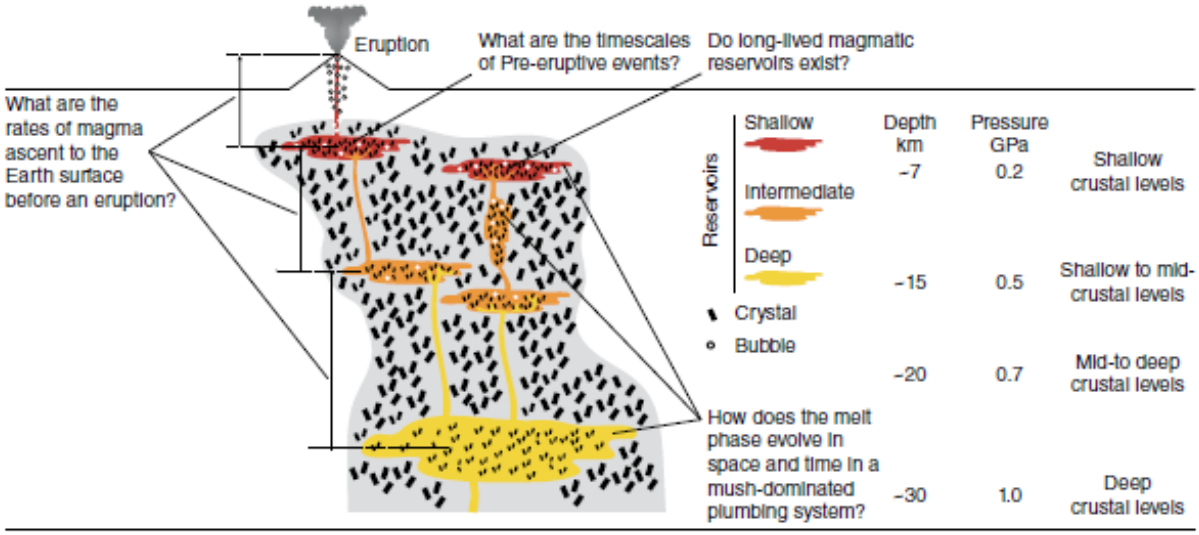

***Figure I-3**: Simplified view of an intracrustal mush-dominated volcanic plumbing system (from Petrelli and Zellmer 2021)*

The concept of magmatic chamber

Each volcanic structure (e.g., caldeira, shield or stratovolcano) is underlain by one or more crustal magma reservoirs (up to more than 20 Km; *Pritchard and Simons 2004*), partially or totally molten and recharged by deeper magmatic sources. Depending on the magmatic system, these reservoirs occur at depths of a few kilometres to more than 20 km (**Figure I-3**). These reservoirs act as transient storage zones where magma accumulates and evolves before

ascending to the surface through vertical channels. During eruptions, the formation or reactivation of fractures temporarily connects the reservoir to the surface, shifting the system from a closed to a more open configuration, and allowing the magma to ascent. Remnants of these conduits, such as solidified **necks**, can be sometimes observed at the surface.

While some volcanoes such as Stromboli (Italy), Kilauea (Hawaii), or also Nyiragongo (Africa) are marked by a continuous activity (*Simkin and Siebert 2000*; *Siebert et al. 2010*; *Molendijk et al. 2024*); most are not permanent open systems (without magma influx and outflux). They are supplied by new, fluid-driven fractures for each eruption (*Guomundsson 2012*), or remain open only for limited periods (from 10 to several thousand years), a brief interval compared to the 10^5–10^6 year lifespan of such edifices.

The behaviour of volcanic systems, although complex, is key to understanding eruption styles (explosive/effusive), as well as the large textural and geochemical diversity of volcanic rocks. The magma chamber concept, still debated today, raises questions about the dynamics controlling the development of these systems (*Tatsumi and Kogiso 2003*; *Bergantz et al. 2015*), their crystallization histories (*Reubi and Blundy 2009*), and the associated timescales (*Annen et al. 2015*; *Cooper and Kent 2014*). The shape, size, and physical state of magma bodies are fundamental parameters (*Bachmann and Huber 2016*; *Zellmer and Annen 2008*) influencing processes such as magma mixing and mingling (interaction of compositionally distinct magmas; *Montagna et al. 2015*).

This section briefly reviews the historical development of the magma chamber concept, the main mechanisms operating within these reservoirs, and the fundamental role of magmatic timescale evolution.

History of the concept

Shape of the plumbing system

Before the advent of geophysical data, studies of magmatic reservoirs relied primarily on plutons, corresponding to ancient and fully crystallized magma chambers exposed by erosion (*Marsh 2015*). The earliest model, also called “big tank” model (*Glazner et al. 2004*), considered magma chambers like a large, long-lived, and spherical magma chamber dominated by phenocryst-poor magma (melt-dominated) (**Figure I-4a**; *Pitcher 1979*; *Oldenburg et al. 1989*). This model, rooted in petrological and geochemical studies (*Smith 1979*; *Hildreth 1981*; *Crisp and Spera 1987*) since *Bowen’s pioneering work (1947)*, considered magma as a

Newtonian fluid convecting via buoyancy-driven flow controlled by cooling-induced density variations (*Petrelli et al. 2016*). Crystallization and differentiation were assumed to occur slowly as the system cooled (*Annen et al. 2015*). Such models did not consider complex reservoir geometry or variable magma fluxes but remain a common starting point for many numerical simulations (**Figure I-4b**; *Montagna et al. 2015*).

Plutons were traditionally viewed as closed magma batches that solidified during ascent from deep crustal levels (20–40 km) to shallower depths (0–10 km), becoming isolated from their source (*Paterson et al. 2011*). Studies of granitic plutons in continental crust led to the batholithic concept, in which large crustal domains are constructed from multiple magma bodies emplaced over long timescales (*Petford and Clemens 2000*). Early models associated the emplacement of these bodies with Hot-Stokes diapirism (*Pitcher 1979*; *Bateman and Marsh 1984*), a mechanism that is now considered unrealistic for the mid- and upper crust (*Zellmer and Annen 2008*).

Recent geophysical and geochronological data have revealed that magma bodies exhibit a wide range of shapes, sizes, and degrees of connectivity, inconsistent with emplacement in a single rapid intrusion event (*Marsh 2015*; *Annen 2009*; *Annen et al. 2015*) (**Figure I-4c-d**). Unlike sills and dykes formed by discrete injections, batholiths, assembled from hundreds of closely spaced plutons, represent long-lived, mobile magma systems in which magma at the margins can spread laterally while new injections ascend from below (**Figure I-4c**).

Sills and dykes represent the most common shapes of magma bodies near large-scale fault zones. Sills correspond to laterally extensive magma bodies with low aspect ratios (e.g., the Socorro magma body; *Brocher 1981a, b*) whereas dykes are vertically oriented, elongated intrusions that cut across stratigraphy (*Farris et al. 2006*; *Menand 2008*). Sills commonly act as temporary storage levels, while dykes form the principal conduits connecting different crustal levels (**Figure I-3**). This dyke emplacement model is supported by numerous studies on granitic plutons (*Clemens and Mawer 1992*; *Clemens et al. 1997*). Another emplacement mechanism, viscoelastic diapirism, defined as the upwelling of mobile material through or into overlying rocks (*Van den Eeckhout et al. 1986*), has been proposed for certain felsic plutons (*Farris et al. 2006*; *Žák and Paterson 2006*).

Observations from Popocatépetl volcano show that networks of interconnected sills and dykes can collectively mimic the geometry of a large reservoir (*Martin-Del Pozzo et al. 2008*). Most intrusive bodies exhibit tabular morphologies (*Petford and Clemens 2000*), and the overall plumbing system can often be described as a vertically interconnected, transcrustal mush column.

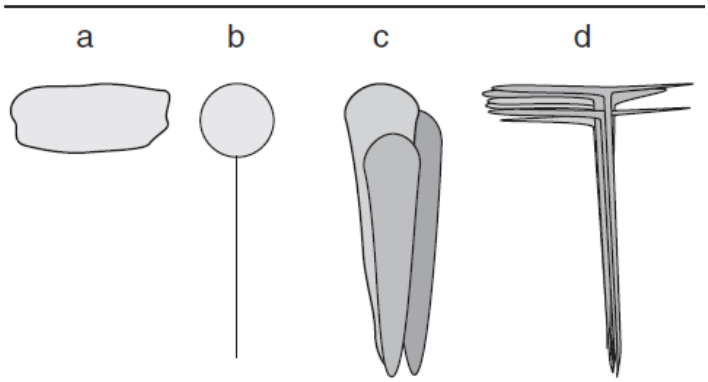

***Figure I-4**: Conceptual models of igneous bodies (taken from Annen et al. 2015). (a) First "big tank" model with a large long-lived and melt dominated magma reservoir (Pitcher 1979; Oldenburg et al. 1989). No assumption was done concerning the crustal emplacement and shape of the chamber, or also on the existence of a thermal gradient. (b) Simple spherical model often used as the starting point in some analytical and numerical studies (Montagna et al. 2015). (c) A vertically elongated igneous intrusion with deep roots (diapir; Paterson et al. 2011). (d) interconnected dykes and sills, in which magma ascends through vertically oriented dykes that penetrate the strata until reaching a lithological boundary, where it spreads into laterally extensive sills that are subparallel to the host layers.*

Magma reservoir evolution

Cold/Warm storage paradigm

Sparks and Cashman (2017) defined magma as a partially molten rock, composed of an eruptible melt containing a certain amount of suspended crystals and volatiles. The transition from eruptible magma to a mush occurs when the particle volume fraction reaches ~ 0.55 – 0.65, resulting to a dramatic increase in relative viscosity, by 6 to 7 orders of magnitude (**Figure I-5**). This limit, called "**packing limit**" depends on several parameters, including the particle size distribution, particle shape, and also strain rate (**Figure I-5**). Below this critical value, magma forms a rigid but porous crystal framework where the melt and gases can move independently (*Zellmer and Annen 2008*).

Because some volcanic rocks, such as basalts and rhyolites, are particularly crystal-poor compared with basaltic andesites, early models conceived magmatic systems as being dominated by liquid melt (melt-dominated systems; e.g., *Hildreth 1981*; *McBirney 1993*; *Irvine et al. 1998*), with mush-rich zones restricted to reservoir margins. This concept, consistent with a shallow, long-lived, spherical pool of largely molten magma (*Cashman et al. 2017*), remained the dominant paradigm for over a century. Cooling at the contact with colder crustal wall rocks

rapidly forms a crystal-rich solidification front, isolating the melt-dominated core from the surrounding rock.

More recently, this view has been refined through the "**cold versus warm storage**" paradigm (*Cooper and Kent 2025*), which emphasizes that magmatic systems oscillate between long-lived, predominantly cold and crystalline states, and short-lived, warm, melt-rich conditions capable of generating eruptions. Here, "cold" refers to crystal-mush, and "warm" to melt-dominated magma.

Constraints on Thermal Conditions

Recent geophysical (e.g., tomographic, seismic velocity, gravity and magnetic data), geochemical, and geochronological studies indicate that magmatic systems in the upper ~10 km of the crust are commonly dominated by crystal-rich bodies, or crystal mushes (< 15% silicate melt; *Miller and Wark 2008*; *Paulatto et al. 2022*; *Humphreys et al. 2025*). This applies across a range of geological contexts, from subduction systems to mid-ocean ridges and ocean islands, and reflects the relatively low temperatures of the mid- to upper crust, supporting the transient nature of melt-dominated bodies. Long-term storage of crystal-poor, high-temperature magma therefore requires periodic rejuvenation through injections of hotter magma (*Cooper and Kent 2025*). Such repeated replenishment occurs in some persistently active volcanic systems (e.g., Etna, Stromboli, Villarrica) but is unlikely to characterize all volcanoes throughout their life histories.

Crystal mush bodies can be described as super-solidus rocks containing an interconnected melt within a crystal framework, whose physical and chemical properties (such as temperature, melt composition, and density), as well as their mobility and eruptibility, are strongly controlled by the crystal fraction (**Figure I-5**; e.g., *Glazner et al. 2004*; *Annen et al. 2006*; *Sparks et al. 2019*; *Humphreys et al. 2025*). In this view, crystal mush and magma thus occupy different positions along a liquid–solid continuum. Due to their rheological properties, particularly their high viscosity (>10^6 Pa·s; *Gottsmann et al. 2009*), mush zones cannot erupt in their entirety. Although factors such as local crystal shape, surface roughness, bubble fraction, strain rate, and melt composition can influence the particle fraction at lock-up (*Gottsmann et al. 2009*; *Bergantz et al. 2017*; *Cooper and Kent 2025*), it is generally accepted that only melt-rich portions with particle volume fractions below ~0.50–0.60 (*Marsh 1981*; *Gottsmann et al. 2009*), either extracted by compaction or generated by remelting of the crystal framework (*Marsh 2015*), are mobile and eruptible (i.e. when reservoir overpressure exceeds lithostatic pressure and the magma viscosity remains sufficiently low). These domains form ephemeral

melt pockets within the mush and may entrain crystal aggregates (glomerocrysts; *Bachmann and Huber 2016*; *Cashman et al. 2017*).

This crystal-mush model is also consistent with the **Daly Gap** (the scarcity of intermediate rock compositions at the surface) and with observations from several magmatic systems. For example, beneath Osorno volcano (*Bechon et al. 2022*), progressive crystal accumulation from basalt to basaltic andesite greatly increases magma viscosity and restricts eruptibility. The presence of crystal-poor basaltic andesite suggests that melt-extraction processes reduce viscosity and facilitate magma ascent in the shallow crust.

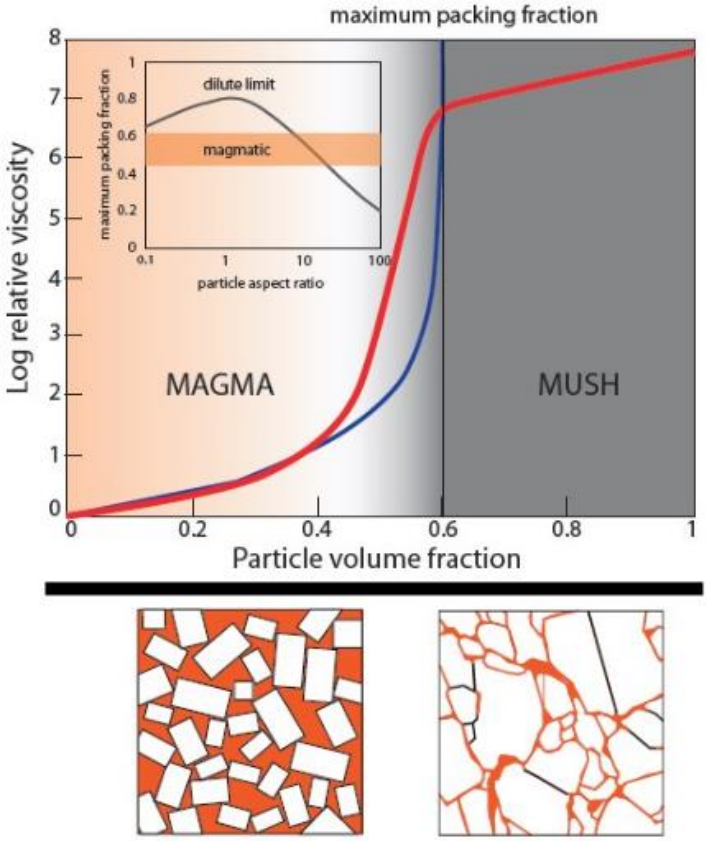

***Figure I-5**: Diagram illustrating the evolution of relative viscosity as a function of crystal content (from Cashman 2017). The vertical line at 0.6 (orange band in the inset) indicates the maximum packing limit, marking the transition from a porous crystal framework (bottom left) to a non-eruptible crystal framework (bottom right) within the 'mush' zone. The dilute curve in the inset represents the theoretical maximum packing limit as a function of crystal aspect ratio (long/minor axis). The blue and red curves correspond to the classical Einstein–Roscoe model (Marsh 1981) and the modification by Costa et al. (2009), respectively.*

Processes occurring within plumbing systems

Processes occurring within magmatic plumbing systems, including crustal magma transfer, storage, and differentiation, are highly complex (*Marsh 2004*). Various parameters, such as the shape, size, and age of the system, as well as magma crystallinity and the nature of the wall rock, determine the characteristics of the eruptive products (*Zellmer and Annen 2008*). Examples from systems such as Coso volcanic field, Santorini, Mount St. Helens, and Kīlauea indicate that magmatic systems often evolve through the frequent transport of small magma batches (*Bacon et al. 1981*; *Hildreth 1981*), rather than through the injection of large magma volumes stored for long periods. Evidence includes repeated injections, short-lived reservoirs, and successive mixing of small magma batches, with rejuvenation processes reactivating the mush system and enabling its chemical and thermal evolution.

Two critical parameters, intrusion frequency and melt segregation, less well understood, coupled with tectonic settings, control not only the thermal structure of the crust but also the amount and composition of magma transported through magmatic plumbing systems (*Zellmer and Annen 2008*).

Solidification front and crystallization

The dynamics of crystallization in magma reservoirs play a fundamental role in magma evolution. Most crystallization occurs over a temperature range of approximately 200 °C, between the liquidus and solidus. Several major minerals crystallize within the first 20–50 °C below the liquidus, strongly influencing the chemical evolution of the magma during a significant part of cooling (*Bowen 1915*). Minerals nucleate at distinct stages (discontinuous series), consuming specific melt components, while pre-existing minerals such as plagioclase may evolve continuously in composition (continuous series) (**Figure I-6**). Consequently, the residual melt progressively evolves from mafic to more silicic compositions (**Figure I-6**). This general sequence of fractional crystallization, called Bowen's series, directly controls the development of solidification fronts and is strongly influenced by volatile content, itself linked to the geodynamic context.

Numerous experimental studies have explored in detail the crystallization sequences of a wide range of silicate liquids. The cooling process depends on both the melt volume and the geometry of the intrusion (*Cashman et al. 2017*). Several processes, such as conduction (in small intrusions), mixing with cooler stored melts, assimilation of partially molten wall rocks, or interaction with hydrothermal systems, can increase the cooling rate of large intrusions. At

the opposite, a high crystallinity fraction tends to suppress convection, A detailed discussion of crystallization kinetics is provided in the section "*Crystallization kinetic processes*".

The **solidification front** can be seen as the spatial expression of the crystallization sequence. As magma cools, minerals crystallize in the sequence defined by Bowen, creating a progression from fully liquid at the hottest inner edges (liquidus) to fully solid at the cooler outer edges (solidus) (*Marsh 2015*). Because the density and viscosity of the residual liquid depend on temperature and composition, they also strongly depend on fractional crystallization. In other words, the sequence of mineral formation in Bowen's series manifests physically as distinct zones within the solidifying magma. These zones are commonly divided as follows (**Figure I-6**):

- **Suspension zone**: Closest to newly injected magma, between the hottest and trailing edges (~25 % crystallinity). Magma is fluid and mobile, containing small, sparse crystals. Early-crystallizing minerals from Bowen's series begin to appear here.
- **Capture front**: Characterized by a bulk viscosity increase of roughly an order of magnitude (~30 – 40 % crystallinity), inhibiting crystal settling. Minerals forming according to Bowen's discontinuous series are increasingly trapped within the magma.
- **Mush zone**: Extends from the bottom of the capture front to the top at the critical crystallinity (~50 – 55 %). The residual melt is trapped in an interconnected crystal network, limiting mobility to percolation. Continuous compositional changes in minerals such as plagioclase continue as defined in Bowen's continuous series. Rejuvenation processes, triggered by injections of new magma batches, can locally reactivate the mush, promoting further chemical and thermal evolution.
- **Rigid crust**: Crystallinity exceeds 60 – 70%, reaching the solidus at 100 %. Crystals form a strong interlocking network (dilatant solid), and viscosity becomes extremely high, preventing magma transport without fracturing. This final stage reflects the culmination of the Bowen sequence in a fully solidified framework.

The entire evolution of magma, whether transported or stored within a reservoir, is thus controlled by the interplay between Bowen's crystallization sequence and the development of the solidification front. However, the characteristics of the solidification front depend on magma type. In plagioclase-rich basalts or basaltic andesites, a robust three-dimensional crystal network can form at only 25 – 30 % crystallinity (*Philpotts et al. 1998*). This is typical of high-alumina island-arc basalts, where crystallinity reaches 40 – 50 %, approaching the dilatancy threshold. In such cases, eruption is mainly possible through violent explosive events.

The initial crystal content strongly controls differentiation in the solidification front (detailed below; *Marsh 2015*). Magmas with phenocrysts experience enhanced segregation: margin crystals are captured by the solidification front, while larger crystals settle to the bottom. Pre-existing crystals act as nucleation sites, accelerating local crystallization and enhancing fractionation compared with initially crystal-free magmas. This explains compositional differences between margins and interiors, reflecting magma transport dynamics, as observed in Shonkin Sag (Montana), Kīlauea Iki (Hawai'i), and the Basement Sill (Antarctica). Crystal-free zones of the magma (**Figure I-6**), crystallize entirely after emplacement, during a late-stage crystallization process. In these zones, crystal growth proceeds slowly, nucleation is highly sensitive to cooling rates, and limited fractionation results in a more homogeneous overall composition. Examples of such late-crystallizing systems include the Peneplain Sill (Scotland) and the Sudbury Igneous Complex (Canada).

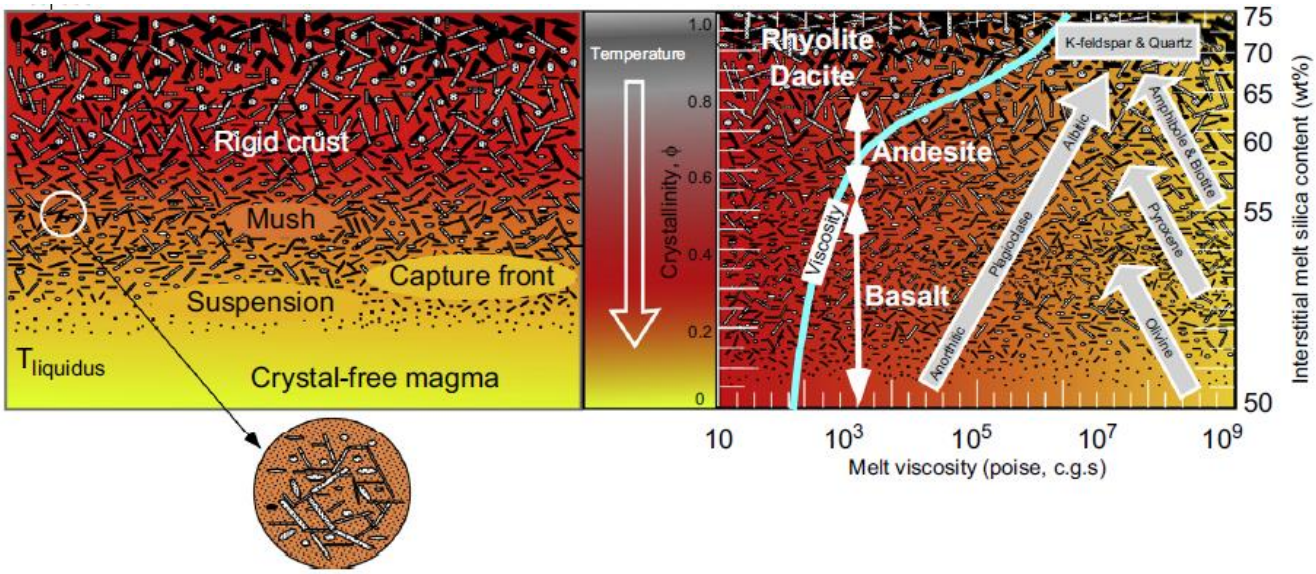

Figure I-6: *Left part: Schematic representation of the solidification front (Marsh 2015). Temperature decreases from the liquidus at the bottom, where new magma is injected, to the solidus at the top. Inset: crystal framework at ~30% crystallinity. Right: Bowen's reaction series. As crystallization proceeds, viscosity rises with new phase nucleation, and the residual melt becomes increasingly silica-rich (see righ axis), evolving from basaltic to dacitic/rhyolitic.*

Differenciation processes

Differentiation of magmas refers to all processes that modify the composition of primary magma after its formation. These changes in melt chemistry can lead to elemental enrichment necessary for the formation of mineral resources such as rare earth elements (*Larsen and*

Sørensen 1987), platinum group elements (*Nielsen et al. 2015*), or copper (*Buret et al. 2016*). Evolved intermediate and silicic magmas can form either through partial melting of the lower crust (*Rapp and Watson 1995*; *Sisson et al. 2005*) or via differentiation of mafic magmas in shallow reservoirs, where stagnation promotes solidification fronts and crystal frameworks (*Grove et al. 1997*; *Pichavant et al. 2002*). Both mechanisms may operate simultaneously in large, deep magmatic reservoirs within deep crustal hot zones (>20 km depth; *Annen and Sparks 2002*; *Annen et al. 2006*).

Magma chemical evolution depends on crystallization location and crystal-melt separation mode (*Jaupart and Tait 1995*). *Bowen (1915)* first demonstrated that fractionated crystallization drives chemical evolution. At low crystallinity (<50%), segregation occurs via settling, floating, mush compaction, or convection (*Marsh 2015*; *Humphreys et al. 2025*). At high crystallinity (>50%), residual melt is trapped within a rigid crystal framework, requiring physical processes to liberate it:

- **Solidification front instability:** When the solidification front grows denser than the underlying melt, it can become gravitationally unstable. Once sufficiently thick, the front cracks, allowing interstitial melt to infiltrate and accumulate as silicic lenses, often 2–3 m thick and 40 – 50 m long.
- **Mush flow fractionation:** In highly crystallized magmas (mush), the intrusion of new magma can extract fractionated melt and incorporate older crystals, promoting differentiated eruptions. This process mainly occurs in reactivated fissures of large volcanoes and can produce primitive, olivine-rich basalts. Its effectiveness depends on the size of the crystal network and magma viscosity, and it is especially significant in extensive, long-lived magmatic systems.
- **Silicic melt segregation:** Silicic segregations are a common consequence of basaltic solidification (*Marsh 2015*). Highly viscous and immiscible with basalt, these pockets persist even if the host body is remelted. During wholesale reprocessing of basaltic crust, as in Iceland, they accumulate into eruptible rhyolite volumes, explaining the basalt–rhyolite bimodality and scarcity of intermediate lavas. Eruptions such as Askja 1875 and rhyolites at Torfajökull demonstrate crystal-poor magmas containing debris from the original crystalline framework, a process favored by progressive crustal remelting along active fissures.
- **Compaction:** The weight of a solidifying crystal network deforms the mush and expels interstitial melt, especially in large or deep chambers. This process is enhanced by

recharge of crystal-rich magma, promoting additional melt extraction (*McKenzie 1984*; *Pec et al. 2015*).

High temperatures and low melt viscosities in the lower crust favor compaction-driven segregation and reactive flow, allowing evolved melts enriched in volatiles and incompatible elements to migrate upwards (*Edmonds et al. 2016*). Episodic destabilization of melt lenses and convective return of dense cumulates explain mid-crustal compositional changes and magma storage (*Paterson et al. 2011*; *Jagoutz and Schmidt 2012*; *Kiser et al. 2016*). Recharge of upper-crustal chambers from deeper melts transports volatiles and crystals, which can trigger melting, crystallization, degassing, hydrothermal activity, or phreatic eruptions (*Sparks et al. 1977*; *Christopher et al. 2015*).

In addition to these physical processes, chemical differentiation may also occur through ***MASH* processes** at the crust-mantle interface. *Hildreth and Moorbath (1988)* identified four key mechanisms:

- **Mixing:** Interaction between different magmas.
- **Assimilation:** Incorporation of crustal material into the magma.
- **Storage:** Magma stagnation in reservoirs allows thermal and chemical exchanges.
- **Homogenization:** Convection reduces local variations in temperature and composition.

Together, these physical and chemical processes drive the evolution of magmas, explaining the diversity of eruptive products observed in natural volcanic systems.

Dynamics occurring during the magma transport

The dynamics of magma transport from its mantle source to its final emplacement in the crust or at the surface occur within the complex magmatic architecture described above, which defines the pathways along which magma migrates. The rate of magma generation in the mantle exerts the primary control on these transport processes. Comparisons between eruptive style, surface heat flux, and plate convergence rates in different volcanic arcs demonstrate that this mantle supply rate governs how magma migrates through the crust (*Zellmer and Annen 2008*). A higher supply rate increases the volume of magma accumulated in the deep crustal “hot zone” (*Annen et al. 2006*) and influences the chemical composition, viscosity, and physical properties

of the magma and its eruptive products. Depending on composition and ascent mechanism, magma can rise through the crust over timescales ranging from days to years (*Petford 2003*; *Annen et al. 2006*).

Within crustal magma reservoirs, slowly cooled magma typically retains a crystal-poor component that is transported upward through vertically extensive mush columns, spanning from 5 km up to more than 20 km, depending on the system type (*Marsh 2015*). These columns occur in both mafic and felsic systems, but in mafic settings they are weaker, cooler, and more spatially restricted (*Marsh 2015*). Such vertically continuous mush zones provide a key pathway linking deep magma generation to shallower storage and eventual eruption.

During magma ascent, the dominant process is volatile loss (degassing), caused by decompression (*Burgisser and Degruyter 2015*). Gas forms bubbles, gradually turning the magma into a foam that promotes crystal growth and raises its viscosity (*Toramaru 2025*). Degassing in shallow reservoirs affects melt, gas, and crystals alike, producing a spectrum of eruptive products, from effusive degassed lavas to highly fragmented gas–particle mixtures that erupt explosively as towering columns.

Volatiles (mainly CO_2, H_2O, SO_2, with minor H_2S, CO, HCl, HF; *Symonds et al. 1994*; *Carroll and Holloway 1994*), typically present at a few weight percent, strongly influence magma dynamics. When dissolved, they lower melt viscosity; once exsolved, they enhance buoyancy and govern ascent style (*Blundy et al. 2010*; *Wallace and Edmonds 2011*; *Christopher et al. 2015*). Their solubility is pressure-dependent (*Burgisser and Degruyter 2015*), linking volatile exsolution to eruption style. Volatile contents are commonly assessed by analyzing melt inclusions trapped in crystals. Water, in particular, controls bubble nucleation, growth, coalescence, and collapse. As H_2O decreases, liquidus temperatures rise, generating undercooling or oversaturation (*Cashman and Blundy 2000*) whenever magma temperature falls below the liquidus corresponding to surface solubility conditions (1 atm). Bubble nucleation depends on temperature, oversaturation, surface tension, volatile content, and decompression rate (*Rutherford 2008*): faster ascent promotes abundant bubble formation. Volatile diffusion, mainly of water, governs bubble growth, while crystallinity further modifies rheology. Crystals may nucleate on bubble walls, or vice versa, depending on mineral surface tension (*Burgisser and Degruyter 2015*). Together, crystals and bubbles exert a primary control on magma behavior.

In melt–crystal–fluid systems, the geometry of the volatile phase is strongly controlled by crystallinity (*Oppenheimer et al. 2015*). Ascending volatiles can disrupt the crystalline framework and trigger eruptions of crystal-rich magma. At crystallinities of ~50 – 60%,

concentration of the volatile phase into narrow channels can greatly enhance segregation efficiency. At very high crystallinities (>> 60%), gas overpressure can fracture and brecciate the mush. Thus, the efficiency and style of volatile extraction evolve as the magma cools and crystallizes.

Geophysical observations, including ground deformation measurements and direct eruption monitoring, further show that magma pathways evolve with system maturity and magma viscosity. Andesitic magmas commonly ascend through focused, nearly cylindrical conduits, whereas more silicic, rhyolitic magmas often associated with caldera formation, are transported through ring dykes (*Zellmer and Annen 2008*). These contrasting geometries reflect differences in rheology and the degree of crustal interaction during ascent. At deeper crustal levels, felsic magmas are often emplaced as plutons. As discussed above, classical buoyancy-driven diapirism (*Pitcher 1979*; *Bateman and Marsh 1984*) is not feasible in the mid- to upper crust due to mechanical and thermal limits. A more realistic mechanism is viscoelastic diapirism, involving downward host-rock displacement, brittle deformation, stoping, incremental emplacement, and tectonic controls (*Van den Eeckhout et al. 1986*; *Miller and Patterson 1999*). This process highlights how magma transport dynamically shifts from dyke-fed ascent in the upper crust to diapiric emplacement in deeper levels, depending on magma composition, viscosity, and the tectonic regime.

Numerical models further support such complex transport behavior. *Annen (2009)* modeled the formation of large magma chambers through episodic sill accretion with variable magma fluxes over time. More advanced models have incorporated non-Newtonian rheology, chaotic advection (*Petrelli et al. 2016*), and volatile exsolution (*Petrelli et al. 2018*). Earlier work (*Oldenburg et al. 1989*; *Montagna et al. 2015*) emphasized upper-crustal emplacement (<10 km), accounting for shallow earthquakes, deformation, and gas emissions (*Sparks and Cashman 2017*), but do not capture the full diversity of magmatic systems. For instance, eruptions at Soufrière Hills and Mount St. Helens involve magmatic sources distributed between 5 and 30 km depth (*Blundy et al. 2008*; *Christopher et al. 2015a, b*). Phenocryst geobarometry confirms the existence of transcrustal magmatic systems extending into the middle and lower crust (*Putirka 2017*), where shallow reservoirs represent only a small component of the overall plumbing architecture (*Sparks and Cashman 2017*).

Influence of the crustal thermal maturity

The rejuvenation efficiency in crustal mush systems is governed by several factors, including the thermal and textural maturity of the crust, regional tectonics, and the structure and composition of the crystal framework and interstitial melt. The crustal thermal state, which reflects the balance between heat supplied by mantle-derived magmas (*Boulanger and France 2023*) and heat lost through conduction and hydrothermal circulation, is a key parameter. It depends primarily on crustal thickness, mantle melt flux, and the regional tectonic environment. Warmer crust, particularly in regions of thickened continental crust (*Farner and Lee 2017*), cools more slowly, allowing crystal mushes to persist for longer periods and to undergo processes such as melt extraction, compaction, and reactive flow. Because the thermal state of the crust evolves over the lifetime of a volcanic system (**Figure I-7**; *Annen et al. 2006*; *Humphreys et al. 2025*), the efficiency of mush processes, and thus of rejuvenation, varies accordingly.

In thermally immature systems (**Figure I-7a**), rapid cooling produces short-lived and poorly equilibrated mushes that limit melt extraction, assimilation, and viscous compaction, making it difficult for large reservoirs to develop (*Jackson et al. 2018*). In contrast, thermally mature systems (**Figure I-7b**) maintain elevated temperatures for extended periods, allowing mushes to develop connected melt networks and more equilibrated textures. Such conditions promote efficient rejuvenation, melt differentiation, reactive flow, and crustal assimilation (Jackson et al. 2018). During waning stages, reduced heat input diminishes the potential for rejuvenation, and residual mushes or cumulates may instead be remobilized (**Figure I-7c;** *Wark et al. 1990*). In these long-lived mush systems (0.1–10 Myr), repeated episodes of heating, resorption and recrystallization drive the development of more mature crystal textures, with a more equant crystal shape approaching Wulff equilibrium (*Cooper and Kent 2014*).

Regional tectonics and melt properties (e.g., composition, volatile content) further modulate rejuvenation (*Humphreys et al. 2025*): extension enhances melt extraction and mush remobilization, while compression restricts ascent; water-rich melts segregate more readily, whereas dry melts crystallize rapidly and impede mush mobility.

Overall, the evolving thermal and textural state of the crust, combined with tectonic regime and melt composition, exerts primary control on the timescales and efficiency of rejuvenation in magmatic systems.

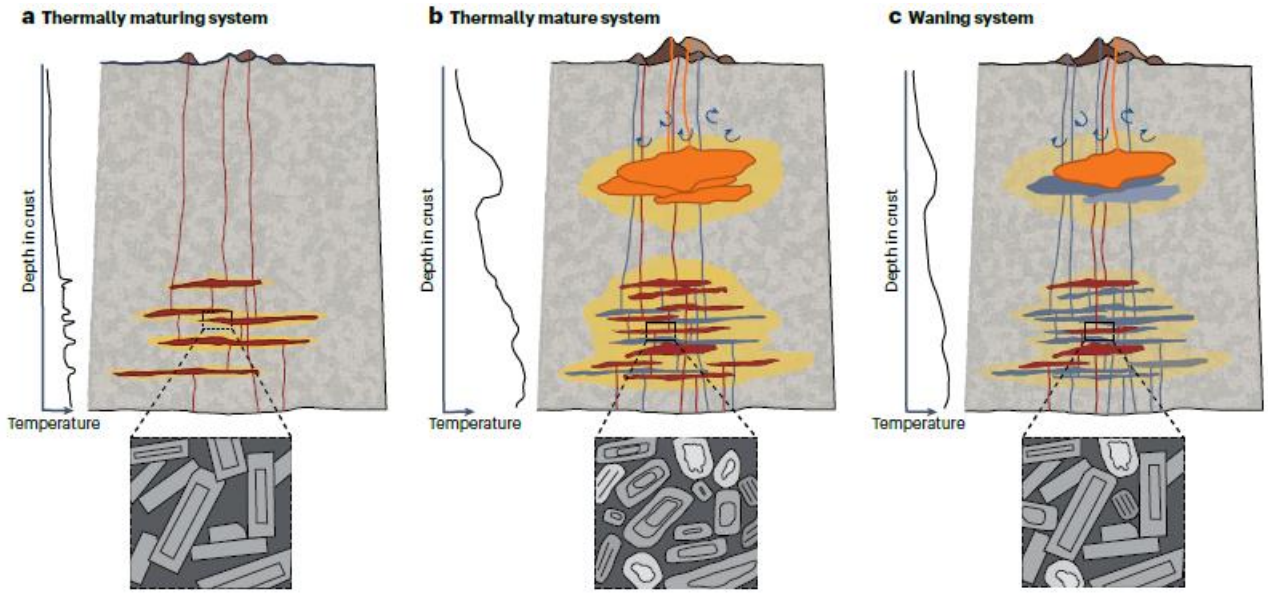

***Figure I-7**: Schematic view of the crustal thermal maturity (from Humphreys et al. 2025). In a thermally maturing system (**a**), key features include a schematic temperature profile (left axis), developing mush textures (inset), vertical dykes (in red), and horizontal sills (dark red). In a thermally mature system (**b**), evolved magma (orange) is emplaced at mid- to upper-crustal levels. Thick margins correspond to cooler boundaries, and curved blue arrows indicate hydrothermal circulation. Older inactive intrusions are shown in blue-grey. In a waning system (**c**), crustal temperatures increase and become less localized during maturation, promoting widespread mush formation, partial melting, and crustal assimilation (yellow). Crystal textures evolve from unequilibrated in maturing systems to more equilibrated and equant/tabular after repeated intrusion, resorption, rejuvenation, and recrystallization. Individual intrusions cool rapidly in immature systems but can persist longer as the system matures. A waning system returns to a more localized heat distribution and lower ambient temperatures, while retaining some complex crystals and high assimilation rates.*

The crucial importance of time parameter

Petrelli and Zellmer (2021) highlighted a strong increase in studies on magmatic timescales between 1980 and 2018, rising from fewer than five per year to over fifty after 2015. Understanding the timing and dynamics of magmatic processes within the crust is essential for evaluating volcanic hazards. Timescale estimates span a wide range of processes, from magma differentiation and transfer to shallow reservoirs (*Turekian and Holland 2013*) to storage (*Reid 2003*; *Cooper and Kent 2014*) and ascent rates (*Rutherford 2008*; *Burgisser and Degruyter 2015*).

The choice of method depends on the process under investigation. Approaches include isotopic-dating techniques, chemical-diffusion geospeedometers, Crystal Size Distribution (*CSD*) method, melt-inclusion chronometers, thermal modeling, mechanical models of magma ascent, and modeling of the volatile phase (*Petrelli and Zellmer 2021*). The following sections provide a brief overview of these techniques.

Isotope dating techniques

Various dating methods are used depending on the timescales of interest: either eruption ages or pre-eruptive processes (*Petrelli and Zellmer 2021*). The main difference lies in the temperature at which isotopes begin to record time, known as the closure temperature. For eruption ages, this temperature is much lower than the magma temperature, so the isotopic clock only starts during the rapid cooling caused by the eruption. For pre-eruptive processes, the closure temperature is at or near magmatic temperatures, allowing these processes to be dated if the eruption age is known or can be determined.

Dating eruption ages

The isotope pairs used to constrain eruption ages are generally:

- **K–Ar and Ar–Ar:** These methods are based on the decay of the natural potassium isotope ^{40}K to ^{40}Ar (*Kelley 2002*). In the K–Ar method, potassium is measured directly, while the Ar–Ar method provides higher precision by measuring potassium after the conversion of ^{39}K to ^{39}Ar. Dating young eruptions (< 20 ka) remains difficult due to the long half-life of ^{40}K, except in very potassic rocks. As with any isotopic method, the system must remain closed: argon loss leads to ages that are too young, whereas excess of argon from deeper magmas or old crustal xenoliths produces ages that are too old.
- **Rb–Sr:** This method relies on the decay of ^{87}Rb to ^{87}Sr (half-life: 4.88×10^{10} years) and is widely used for dating ancient eruptions. Due to its relatively low closure temperature, it is mainly applicable for eruption ages. Its long half-life limits high-precision dating, but it is suitable for very old volcanic rocks.
- **(U–Th)/He:** This technique uses the decay of ^{238}U, ^{235}U, ^{232}Th, and ^{147}Sm to ^{4}He (*Farley 2002*; *Schmitt 2011*; *Farley and Stockli 2019*) and is applied to U- and Th-bearing minerals such as apatite and zircon. With closure temperatures ranging from 50 to 200

°C, it can date rapid cooling events, rock exhumation, and landscape evolution (*House et al. 1998*; *Shuster et al. 2005*; *Farley et al. 2002*; *Schmitt et al. 2006, 2010*). Although not yet widely used, (U–Th)/He dating has also been applied to young magmatic eruptions (< 1.5 Ma; *Danisik et al., 2017*).

Pre-eruptive processes

Uranium-series dating relies on the decay of ^{232}Th, ^{238}U, and ^{235}U to their respective lead isotopes (^{208}Pb, ^{206}Pb, ^{207}Pb) (*Bourdon et al. 2003*; *Cooper 2015, 2019*; *Cooper and Reid 2008*) and can also use intermediate daughter isotopes in disequilibrium dating. These methods are mainly applied to accessory minerals such as zircon (*Charlier and Zellmer 2000*), monazite (*Parrish 1990*), and titanite (*Frost et al. 2000*), which have high closure temperatures (e.g., >900°C for zircon; *Lee et al. 1997*), allowing determination of pre-eruptive crystallization ages. A key requirement is that the system remains closed to isotope loss or gain. Monitoring the ^{234}U/^{238}U activity ratio helps detect interaction with fluids, which can compromise age estimates. Recent studies have shown that groundmasses in equilibrium can carry crystals in disequilibrium, highlighting the need for caution when interpreting U-series ages.

U-series disequilibrium dating is widely used to study magmatic systems, providing estimates of magma degassing (*Turner et al. 2013*), mixing events (*Ruprecht and Cooper 2012*), cooling rates, residence times in magma reservoirs (*Bourdon et al. 2000*; *Cooper and Kent 2014*), magma genesis (*Avanzinelli et al. 2007*), evolution, and ascent (*Zellmer et al. 2005*), as well as petrogenetic processes at mid-ocean ridges (*Goldstein et al. 1993*; *Rubin et al. 2005*).

Chemical-diffusion chronometry

Chemical diffusion is a time-dependent process commonly used to estimate rates and timescales of magmatic processes (*Costa et al. 2008, 2020*; *Costa and Morgan 2010*). It relies on analyzing chemical heterogeneities in crystals and glasses, which gradually evolve toward equilibrium at rates controlled by diffusion coefficients. By measuring these heterogeneities and using appropriate diffusion coefficients, timescales can be determined through Fick's second law of diffusion:

$$\frac{\partial C}{\partial t} = D \times \frac{\partial^2 C}{\partial x^2} \quad (1)$$

With C the concentration of the diffusing element, t the time, D the diffusion coefficient (depending on the temperature and material), and x the spatial coordinates along which the diffusion profile is measured.

Focusing on Fick's second law, several studies have estimated timescales of open-system processes in magmatic reservoirs (*Costa et al. 2003, 2008*; *Turner and Costa 2007*), as well as magma cooling rates (*Dohmen et al. 2018*) and ascent rates (*Lloyd et al. 2016*). These geospeedometers have also been applied to melt embayments, where volatile diffusion during magma ascent constrains decompression timescales (*Humphreys et al. 2008*; *Myers et al., 2018*).

Crystal-melt reactions

Reactions between phenocrysts and magma, triggered by decompression, or heating (*De Angelis et al. 2015*) during ascent can be used to estimate magma ascent rates (*Browne and Gardner 2006*). Alteration of hydrous minerals such as amphibole or biotite forms reaction rims whose kinetics depend on multiple parameters (composition, temperature, viscosity), making theoretical constraints difficult but experimentally achievable. Experimental calibrations across various systems (e.g. basaltic to rhyolitic, and kimberlitic,) allow ascent rate estimates (*Rutherford and Devine 2003*). The experimental determination of crystal growth rates, in turn, is essential for the derivation of crystal residence times in magmatic systems through other methods, such as the crystal-size-distribution (CSD) technique (see below).

Textural methods

Chronometers based on textural methods such as Melt-inclusion textural analyses, Microlite number density (MNT), and Crystal Size Distribution (CSD) provide direct constraints on magmatic crystallization rates and timescales by analyzing crystals themselves. These techniques constrain the relative durations of magmatic processes, regardless of the rock's or event's absolute age (*Costa et al. 2020*). Melt-inclusion textural analyses use three-dimensional imaging of quartz-hosted melt inclusions to quantify faceting times, providing estimates of crystal growth rates and magma residence durations (*Beddoe-Stephens et al. 1983*; *Pamukcu et al. 2015*). This approach relies on the progressive change of melt inclusions from rounded to fully faceted shapes as diffusion drives them toward equilibrium.

Microlite number density (MND) water-exsolution-rate meter constrains volatile exsolution rates from decompression-induced microlite crystallization, under the assumption that it is equivalent to cooling-induced crystallization (*Toramaru et al. 2008*). This method uses microlites in effusive or pyroclastic rocks to quantify crystallization dynamics linked to degassing.

Crystal-Size-Distribution (CSD) analysis relates crystal population density to crystal size to infer nucleation and growth rates as well as crystal residence times (*Marsh 1988, 1998*; *Cashman 1988*; *Higgins 2000*). In CSD plots, the zero-size intercept reflects nucleation density, while the slope constrains the product of crystal growth rate and residence time. Determine one parameter requires knowledge of the other. A detailed description of this method is provided in the Methods chapter.

Modeling approaches

Magmatic timescales can be constrained using several complementary modeling-based approaches. Concentration variance decay models the reduction of compositional heterogeneities during magma mixing to estimate the time between magma intrusion and eruption (*Perugini et al. 2015*; *Laeger et al. 2019*). Thermal numerical modeling simulates heat exchange between magmas and host rocks, from static formulations to fully dynamic models that track chemical evolution, crystals, and volatiles, providing insights into the evolution, dynamics, and lifetimes of volcanic plumbing systems (*Blundy and Annen 2016*; *Petrelli et al. 2016, 2018*).

Mechanical modeling of the volatile phase focuses on bubble behavior (H_2O, CO_2, S, Cl, F) to infer magma ascent rates and eruptive styles through numerical, experimental, and analogue approaches (*Toramaru, 2006*; *Wallace et al. 2015*; *Edmonds and Wallace 2017*). Mechanical modeling of magma ascent constrains melt-migration and magma ascent velocities at scales ranging from grain-scale porous flow to crustal-scale dike propagation, diapirism, and vein networks, and has been applied to study magmatic waves, reactive flow, shear-band formation, mid-ocean ridge melt migration, and mantle xenoliths (*Rutherford 2008*; *O'Neill and Spiegelman 2010*). Together, these modeling approaches provide a robust framework to quantify the rates and timescales of magma mixing, ascent, and evolution in volcanic systems.

Seismic data

Because seismicity requires stressed, brittle rock, it does not always accompany magma migration, particularly in aseismic regions. However, earthquake studies beneath volcanic systems can provide valuable constraints on magma ascent rates (*Rutherford 2008*). The first applications of this approach were by *Blot (1972)*, who analyzed mantle-depth earthquakes beneath the New Hebrides volcanoes, and by *Fedotov et al. (1983)*, who tracked crustal earthquakes immediately prior to the Great Tolbachik Fissure eruption in Kamchatka.

Limitations and Challenges in Estimating Magma Timescales

The reliability of timescale and rate estimates depends on both analytical precision and modeling assumptions. **Figure I-8** summarizes the range of timescales that can be constrained depending on the dating method. For example, at Mount St. Helens, isotopic data show that plagioclase crystals grew over thousands of years (*Cooper and Reid 2003*), whereas zircon crystals record magmatic activity tens or hundreds of thousands of years before the 1980 eruption (*Claiborne et al. 2010*). Diffusion timescales for magma assembly, however, are on the order of months to years (*Saunders et al. 2012*), consistent with observed pre-eruptive unrest.

Direct methods, such as radiometric dating (K–Ar, Ar–Ar, U-series), provide highly precise ages (*Schoene et al. 2013*; *Schaltegger et al. 2015*) but are limited to processes $\geq 10^3$ years. Indirect methods, including diffusion chronometry, crystal size distribution (CSD) analysis, and thermal modeling, cover a broader temporal range from hours to geological timescales but depend strongly on kinetic parameters and boundary conditions (*Costa et al. 2008*; *Marsh 1998*; *Higgins 2002*). Combining multiple techniques provides the most robust constraints. Recent studies integrating textural analyses, diffusion, and thermo-mechanical modeling reveal both long-term magma storage (thousands of years) and rapid ascent (days to months) before eruptions (*Arzilli et al. 2016*; *Ruth et al. 2018*; *Petrelli et al. 2018*).

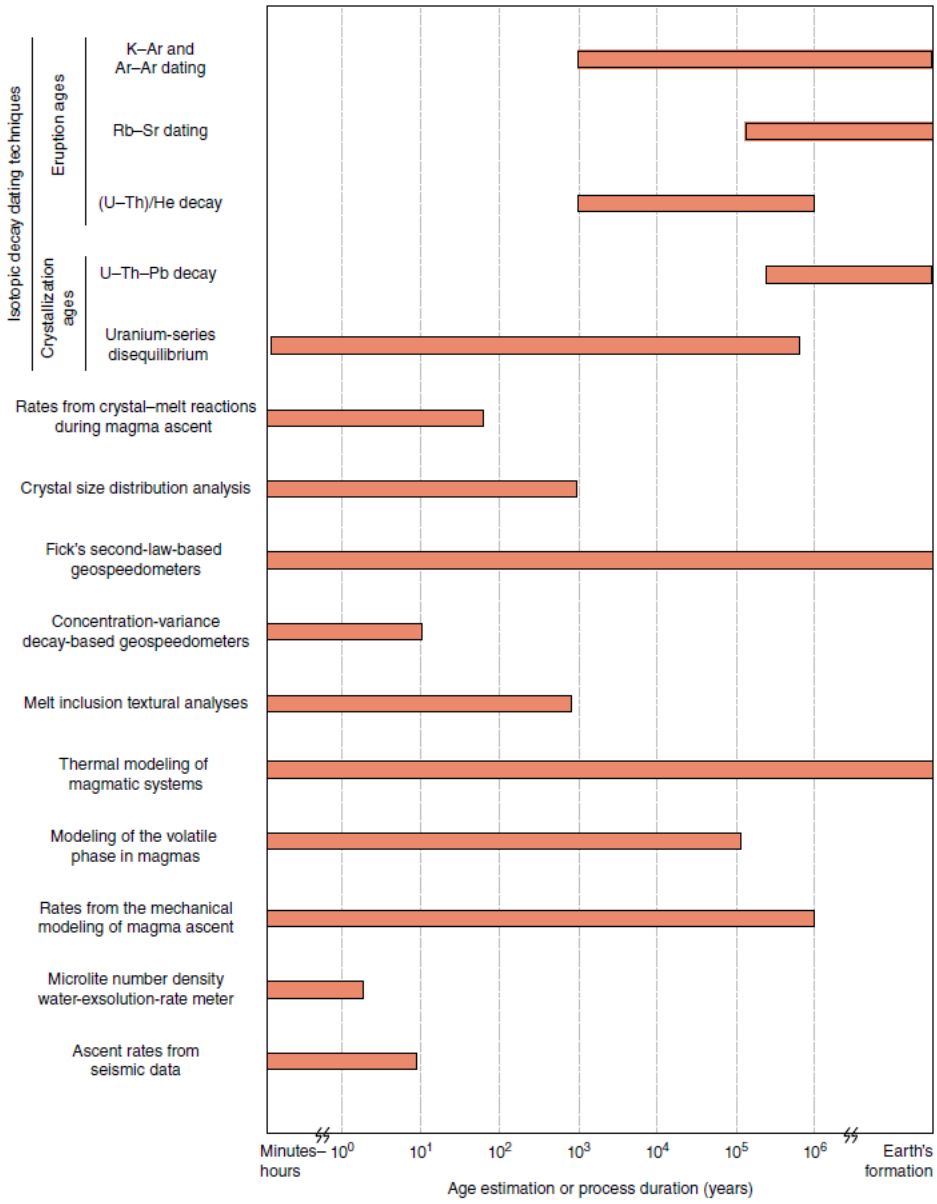

***Figure I-8**: Timescales estimated through the analytical methods and modeling approaches reported. Taken from Petrelli and Zellmer 2021 (Modified from Turner and Costa 2007).*

Crystallization kinetic processes: nucleation and growth

A key aspect of magma evolution is the crystallization kinetics of silicate melts, occurring over a temperature range of ~200 °C (*Marsh 2015*). Crystal sizes in magmatic bodies typically range from hundreds of micrometers to centimeters, though pegmatites can host crystals several meters long (*Simmons and Webber 2008*). Even isolated crystals tend to cluster, contributing to the diverse textures observed in igneous rocks.

Volcanic rocks commonly contain phenocrysts, groundmass phases, and occasionally nanolites (<1 μm; formed during late-stage cooling or surface oxidation; *Yoshida et al. 2023*).

Phenocrysts record growth during deep storage, while groundmass and nanolites form during rapid ascent and quenching.

This section focuses on nucleation and growth, the primary processes controlling crystal formation and textural evolution. Both are highly sensitive to physicochemical conditions such as temperature, pressure, and oxygen fugacity, which evolve along the crystallization pathway.

The theory of nucleation

Nucleation refers to the formation of stable crystal embryos that possess the chemical and physical properties of macroscopic crystals, arising from random fluctuations in a homogeneous melt below the liquidus temperature (*Dowty 1980*). Nucleation controls the final number of crystals in a rock (*Swanson 1977*) and indirectly influences crystal size, as well as the mechanical properties and texture of the rock. A distinction is made between primary nucleation, in which the first crystals of a crystalline phase are directly formed from the initial melt, and secondary nucleation, in which pre-existing crystals act as seeds through mechanisms such as crystal motion or inter-crystal contact. Micro-attrition processes, including mechanical breakage or shear between crystals larger than 10 µm, also correspond to secondary nucleation, facilitating further nucleation at lower temperatures (*Cui and Myerson 2014*).

Notion of critical radius

The classical nucleation theory (*CNT*) originally based on the thermodynamic observations from *Gibbs (1875, 1878)* of heterogeneous systems, is replaced by a model system of two homogeneous phases (parent and nucleus). The *CNT* was developed by *Volmer and Weber (1926)* and *Becker and Doring (1935)* to explain the primary nucleation, in a perfectly homogeneous liquid (without pre-existing substrates). This theory is based on the continuous appearance and disappearance of clusters of atoms called “homophase fluctuations”, due to melts fluctuations below the liquidus temperature. It supposes the same formation probability of critical nucleus in any point of the liquid volume. *CNT* assumes that clusters grow by addition of several individual atoms until they become observable (ten to hundreds or thousands of atoms; *Teng 2013*). A cluster becomes stable and grow into a macroscopic crystal only if its radius exceeds the critical radius size (r^*), beyond which the volumetric bulk free energy gain (ΔG_V) from phase change overcomes the interfacial energy cost (σ) associated to the crystal–melt boundary (**Figure I-9**; *Dowty 1980*; *Kirkpatrick 1981*; *Hammer 2008*). Considering cluster

as spherical, the total Gibbs free energy associated to the thermodynamic barrier (ΔG^*) required to have the properties of a macroscopic object (r > r*) is expressed as

$$\Delta G^* = \left(\frac{4}{3}\right)\pi(r^*)^3\Delta G_V + 4\pi(r^*)^2\sigma \quad (1)$$

With ΔG_V refering to the free energy in reaction, which becomes negative when the crystallization of a new phase occurs; σ which corresponds to the interface free energy when a crystal forms. This last term is always positive and destabilize the cluster formation (*Kirkpatrick 1981*; *Fokin et al. 2006*).

As explained by *Dowty (1980)*, the critical radius is obtained when ΔG^* passes through a maximum. By derivating the *equation 1*, $r^* = \frac{-2\sigma}{\Delta G_V}$. The total Gibbs free energy (ΔG^*) reaches a positive maximum at the critical cluster radius (r); once the cluster exceeds r*, growth becomes spontaneous as ΔG* decreases with increasing size. Only the largest clusters (whose size is larger than the critical size) grow spontaneously because the ΔG^* decreases as they grow. According to *Volmer and Weber 1926*, once the critical size is reached, the cluster will grow rapidly without decreasing in size.

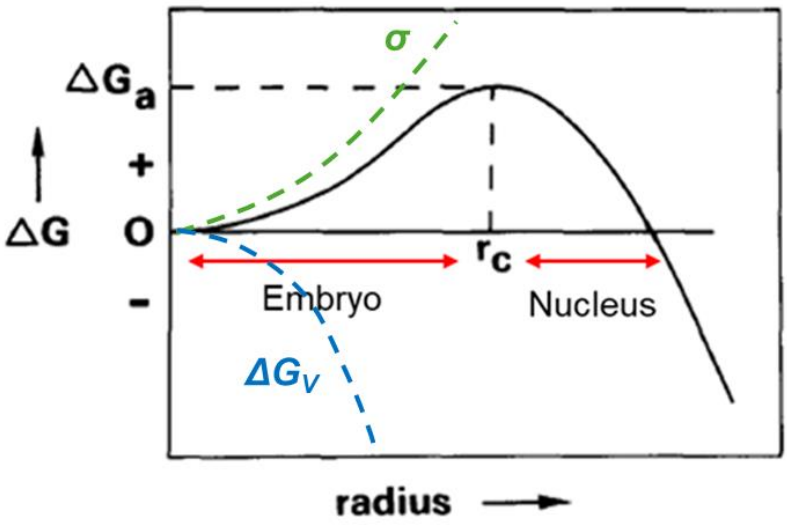

***Figure I-9**: Gibbs free energy (G*) as a function of spherical embryo size (Equation 1; Dowty 1980). Embryo larger than the critical radius, r, are expected to grow spontaneously (nucleus), as this reduces the system's free energy. The two main contributions: volumetric bulk free energy (ΔG_V) and interfacial energy cost (σ), are shown in blue and green, respectively.*

Dependence on temperature

The formation of nuclei clusters is dependent on the temperature and duration. At the critical radius, ΔG^* reaches a maximum value corresponding to the activation energy (ΔG_a) required for the embryo to develop into a critical nucleus capable of stable growth (*Dowty 1980*):

$$\Delta G^* = \Delta G_a = \frac{16\pi\sigma^3}{3\Delta G_V^2} \quad (2)$$

The temperature dependence of nuclei clusters (n_r) is linked to the Gibbs free energy required to form a crystal nucleus of size r from the melt (ΔG_a); and is governed by the Arrhenius law (obeying to the Boltzmann equation; *Turnbull 1956*):

$$n_r = n_0 exp(\frac{-\Delta G_a}{kT}) \quad (3)$$

where n_0 the total number of clusters, k the Boltzmann's constant, and T the system temperature in Kelvin. The nuclei critical size, and so the nucleation is very sensitive to the temperature, and undercooling[1] (driving force of crystallization, basically defined as: $-\Delta T = T_{liq} - T$; *Kirkpatrick 1981*). The decrease of the temperatures (increase of the undercooling) leads to an increase of the negative value of ΔG_V, reducing the critical radius size and leading to a rapid increase in the nucleation. Following the *CNT* theory, the nucleation is supposed to be minimally near the liquidus, due to the maximum value of the critical size at this point. Numerous experimental studies observed a random nucleation at subliquidus temperatures (*Gibb 1974*; *Sato 1995*; *Billon et al. 2025*). *Porter and Easterling (2009)* explained this sensitivity of the subliquidus nucleation to the magnitude (temperature and duration) of the initial overheating heat treatment. An increase of the temperature above the liquidus leads to a melt depolymerization, decreasing the number of nuclei clusters. Thus, in numerous experimental studies where the cooling rate following the initial superheated magnitude is sufficiently fast, the resulting nucleation will be delayed or inhibited at the subliquidus temperature (*Donaldson 1979*; *Corrigan 1982*; *Vetere et al. 2013*). *Lofgren et al. (1978)* shown in contrary that nucleation occurs very rapidly when samples are cooled just below the liquidus, in absence of any overheating step. *Porter and Easterling (2009)* suggested that the overheating

[1] *See* ***BOX 1***

effect is all the greater, as its magnitude is important. A fact rejected by *Tsuchiyama (1983)*, and *First et al. (2020)*, who suggested that after a certain amount of overheating, the effect will be similar on the nucleation. This observation will be discussed in **Chapter IV**.

However, as explained by *Swanson (1977)*, nucleation is dependent of the mobility of atoms and molecules in the melts. This transport factor is dependent of the diffusion coefficient, which drops significantly when the temperature decreases (*Towers and Chipman 1957*). The nucleation will follow a bell-shaped curve, passing through a maximum at a certain amount of undercooling, before to decrease at very high degree of undercooling, due to the strong decrease of the diffusion coefficient values. The reduction of crystallizing components, as well as the decrease of diffusion coefficient, re-increase the critical radius size, leading to a decrease in the nucleation rate.

Steady state Nucleation

The nucleation rate (J) corresponds to the product of the density/concentration of critical nuclei (linked to the free energy of activation ΔG_J), and the rate at which atoms attach to them (dependent on the melt diffusivity D) (*Dowty 1980*; *Kirkpatrick 1981*). At the "steady-state", the nucleation rate (J; $m^{-3}.s^{-1}$) corresponding to the formation of spherical critical nuclei, as a function of the Temperature (T; in kelvin) is expressed as (*James 1985*):

$$J = \frac{N_V * k_B \times T}{h} \times exp\left(\frac{\Delta G_J - \Delta G^*}{RT}\right) \quad (4)$$

with k_B and h the Boltzmann and Planck's constant respectively, and N_v the volume number density of atoms of the reactant phase. ΔG_J corresponds to the nucleation activation energy linked to the atom's attachment to the nucleus (similar to E_J; *Burkhard 2005*; *Billon et al. 2025*); referring to the barrier including the transport of components through the melt.

BOX 1

The undercooling concept (*Kirkpatrick 1981*) is defined by the difference between the saturation temperature of the phase considered in the liquid, and the temperature of the system. It is used to link the temporal evolution of nucleation and growth, in function of the environmental conditions such as the temperature, pressure, and liquid composition. ne of its complexities is linked to the fact that the saturation temperature decreases during crystallization as the liquid composition evolves, thereby reducing the undercooling (*Mollo and Hammer 2017*).

Some variations of this concept are used in function of the experimental parameter considered. The term nominal undercooling ($-\Delta T_n = T_{sat,\ bulk} - T_{quench}$; *Faure et al. 2003*; *Faure and Tissandier 2014*), often used for cooling runs, refer to a differential of the temperature between the saturation temperature of the bulk composition ($T_{sat,\ bulk}$), and the final temperature at the quench moment (T_{quench}). Contrary to the actual or « real » undercooling which decreases during the crystallization, the nominal undercooling remains fix and independent of any change of the melt composition. It provides some indications regarding the evolution of the "real" undercooling but does not allow for any precise quantification.

Homogeneous vs. Heterogeneous

Nucleation is generally divided into two main types: homogeneous nucleation (a stochastic process resulting from random thermal fluctuations in the melt) and heterogeneous nucleation (which occurs at preferential sites such as pre-existing crystals, surface particles or defects, or Pt holder), often more favorable by reducing the activation energy of nucleation. In the most extreme case, if the growth rate is sufficient fast, the final texture could be due only to a primary heterogeneous nucleation (without effect of the homogeneous nucleation; Turnball 1950). This suggestion does not take into account the secondary nucleation that could affect the formation of new crystals when the crystallization rate is sufficient. The formation of a critical cluster (ΔG^*) in these two processes can be related by the general equation (*Schmelzer 2003*; *Fokin et al. 2006*):

$$\Delta G^*_{het} = \Delta G^*_{hom} \times \varphi(\theta) \quad (5)$$

With θ is the contact angle between the surface upon which nucleation occurs and the nucleating phase (*Hammer 2008; Rusiecka et al. 2020*). $\varphi(\theta)$ can be expressed as (*Fokin et al. 2006*):

$$\varphi(\theta) = \frac{1}{2} - \frac{3}{4}\cos(\theta) + \frac{1}{4}cos^3(\theta) \quad (6)$$

φ is a dimensionless parameter ranging from 0 to 1, representing the various conditions that promote heterogeneous nucleation. In the case of homogeneous nucleation, $\varphi(\theta) = 1$. However, homogeneous nucleation often presents in the case of metals and alloys (*Hammer 2008*) is quite rare in silicate melt, where the heterogeneous nucleation is favored. According to *Lofgren et al. (2006)*, homogeneous nucleation typically occurs during the final stages of crystallization, under conditions of strong undercooling ($T/T_L < 0.6$, corresponding to 705 °C in our case).

Toramaru (2025) used a quantitative method based to the relation between the crystal/bubble number density, and the cooling/decompression rate to determine the dynamic of the nucleation:

$$N_{crys/bubble} \approx \frac{dT}{dt}^{\varepsilon_T} \quad (7)$$

$$N_{crys/bubble} \approx \frac{dP}{dt}^{\varepsilon_P} \quad (8)$$

With $\boldsymbol{\varepsilon}$, the cooling/decompression rate exponent. Similar equation can be obtained using the decompression rate. Plotting the $\log(N_{crys/bubble})$ in function of the log $(\frac{dT}{dt})$ or log $(\frac{dP}{dt})$, the slope value gives a measure of $\boldsymbol{\varepsilon}$**.** In the case of a perfectly homogeneous, or heterogeneous system, $\boldsymbol{\varepsilon}$ has a value of 3/2 or -1 respectively. Some experimental (*Walker et al. 1976*; *Billon et al. in review*) and natural (*Wallace et al. 2020*; *Bonechi et al. 2024*) studies found a range of values between these two extremes, depending on the cooling or decompression rate. *Toramaru and Kichise (2023)* demonstrated that $\boldsymbol{\varepsilon}$ value depends on the intensity of the heterogeneous nucleation (abundance of preferential nucleation sites, and probably of their repartition). This method discussed by *Toramaru (2025)* for the impact of the dynamic of nucleation to the microlith and bubbles number density is also employed in our study concerning the impact of nucleation on the plagioclase texture (**Chapter IV**).

The time dependence of the nucleation

The second important aspect as mentioned above corresponds to the time-dependent nucleation. This phenomenon called "*transient nucleation*" occurs because nucleation does not start immediately at a given temperature (*Hammer 2008*). A relaxation duration is necessary for the melt to restructure and reorganize to establish a "steady-state" cluster distribution (*Fokin et al. 2006*; *Hammer 2008*). The studies of *Fenn (1977)*, and *Swanson (1977)* observed both a nucleation delay up to 144h, depending on the temperature considered, but also on the initial composition of the system. A subliquidus temperature will favor a longer nucleation delay. The nucleation delay refers to the duration between when the temperature decreases below the liquidus, and the onset of the nucleation. At a small undercooling degree for example, because the critical nucleus radius is larger, the steady state cluster distribution needs more time to be reached, and the nucleation delay is higher, explaining the observations of *Fenn (1977)* and *Swanson (1977)*.

The modelling of the nucleation incubation time ($\boldsymbol{\tau}$) could provide important information of the timescales of crystallization from the melt, but also to the capacity of the liquid to remain vitreous (*Rusiecka et al. 2020*). It can be estimated as follows (*Kashchiev 1969*; *James 1985*; *Slezov and Schmelzer 2002*; *Fokin et al. 2006*):

$$\tau = \frac{16h}{\pi} \times \frac{\sigma}{\Delta G_V^2 a^4} \times \exp\left(\frac{\Delta G_J}{k_B T}\right) \quad (9)$$

With $\boldsymbol{a}$ the structural unit size. In the case of heterogeneous nucleation, the nucleation delay is adjusted to consider the effect of pre-existing substract surfaces:

$$\tau_{het} = \tau \times \varphi(\theta)^{\frac{1}{3}} \quad (10)$$

Heterogeneous nucleation on a pre-existing surface lead to lowering of the surface free energy, reducing the nucleation delay.

Implication of other parameters

Nucleation is not governed by temperature alone but by any factor that modifies the energetic barrier to forming new crystals or provides favorable sites for their formation. The melt structure influences this barrier directly (*Toshiyama et al. 1991*), while volatile content

(particularly H_2O) reduces both thermodynamic and kinetic barriers, enhancing nucleation and shortening induction times (*Hammer 2004*). The strong effect of water on the crystal–melt interfacial energy (σ) led to the development of the Diffuse Interface Theory (*DIT*), developed for hydrous silicate melts (*Hammer and Rutherford 2002*).

The nature and preparation of starting material also affect nucleation by suppressing or promoting heterogeneous sites. Synthetic charges prepared from reagent oxides or carbonates (*Pupier et al. 2008*) and overheated natural rocks (*Vetere et al. 2013*; *Vona and Romano 2013*) are often used to homogenize melts and remove bubbles or crystal fragments. These effects are discussed in more detail in **Chapter IV**. Nevertheless, experiments using crystal-bearing starting materials (*Shea and Hammer 2013*) or a limited superheating ($+\Delta T$ = 15 °C; *Billon et al. 2025*) commonly yield higher nucleation rates than fully synthetic or strongly superheating charges (**Figure I-10b and c**) and promote overgrowth rims around pre-existing seeds (**Figure I-10a**). Dynamic conditions such as stirring can also accelerate crystallization by enhancing nucleation and growth rates by one to two orders of magnitude compared with static experiments (*Vona and Romano 2013*; *Vetere et al. 2024*).

Overall, these observations highlight that nucleation can be enhanced either by lowering the energy barrier (e.g., via melt structure, volatile content, or shear) or by providing heterogeneous nucleation sites (e.g., crystal fragments, bubbles), both of which strongly modulate crystallization kinetics.

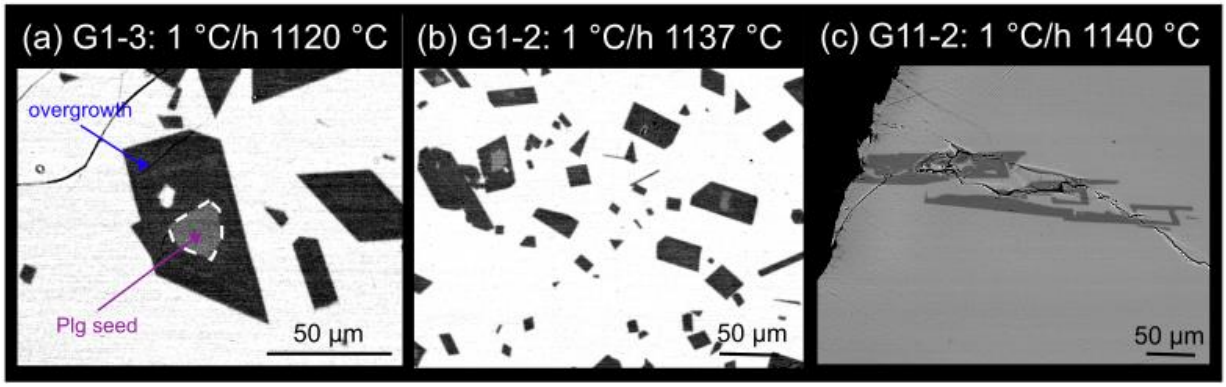

***Figure I-10**: Effect of initial superheating on seed-bearing runs cooled at 1 °C/h (quenched at 1120 °C for a, 1137–1140 °C for b and c). (a) Overgrowth rims around pre-existing plagioclase fragments. (b) Crystal cargo following an initial superheating of 15 °C above the liquidus (see Chapter 3), characterized by a wide range of crystal sizes and morphologies. (c) Crystallization of a few large dendritic crystals after an initial overheating of 35 °C above the liquidus (see **Chapter IV**).*

Limitation of the CNT

The understanding on the nucleation dynamic, as well as the determination of the nucleation rate are both difficult to constrain. As mentioned by *Fokin et al. (2006)*, the critical nuclei, due to their size, are impossible to optically define. Only the growing crystals are observable, leading to a potential underestimation of the number density of critical nuclei; whose some are dissolved. From this CNT theory, one of the first experimental method to measure the nucleation rate was defined by *James (1974, 1985)*. To summarize, the initial material of desired composition is sufficiently heated to obtain a glass material, and glass pieces obtained are reheated during a known time at a nucleation temperature (T_1 far below the supposed liquidus temperature). At the end, this same sample is reheated at a temperature T_2 ($T_2 > T_1$) to allow a sufficient growth step, leading to visible crystals. The classical estimation consists simply to evaluate the crystal number density (N_V), in function of the time (t):

$$J = \frac{dN_V}{dt} \times \frac{1}{1-f} \quad (11)$$

with *f* corresponding to the percentage of crystallization (corrected to the porosity).

The largest crystals, supposed to nucleate first, are the only to be considered (*Kirkpatrick 1977*). Plotting the crystal number density in function of the time, the slope corresponding to $\frac{dN}{dt}$ gives an estimation of the nucleation. However, one of the main problems of the *James (1974)* method is to suppose that the nucleation and growth process are separated in term of temperature (nucleation supposed to be inefficient at growth temperature). This depends in fact to the used undercooling value. Moreover, this classical estimation, currently only rarely used experimentally, needs isothermal conditions with various durations, and is not really adapted to cooling/decompression experiments. The textural evolution is note directly followed. Alternative method such as the Crystal Size Distribution (*CSD*) method, or also the batch method, in which an average *J* value is obtained by the ratio between N_v (of the sample considered) and the duration *t* (generally the experimental duration until the quench of the sample). As we will see after, the CSD method has also limitations, and the batch method proposed here is generally only used on experimental samples because an estimation of the timescale is necessary.

Concerning the nucleation delay, the classical model of nucleation (*CNT*) is particularly reliable for simple Li and Na-metasilicate melts (with congruent melting points; *Lasaga 1998*; *Fokin et al. 2006*). However, its use does not accurately reproduce the nucleation process in

natural multicomponent structures such magma silicate systems (*Rusiecka et al. 2020*), especially under dynamic regimes involving temperature variations.

The theory of crystal growth

Crystal growth, in addition to governing crystal shape, is a necessary step to increase the cluster sizes and directly measure the nucleation rate. In a multicomponent system such as silicate melt, three parameters govern crystal growth: (1) the reactions at the crystal/melt interface corresponding to the atom attachment on the crystal surface, divided itself in continuous and layer growth as a function of the mechanism of the atom attachment (*Dowty 1980*; *Sunagawa 1981*; *Cabane et al. 2005*); (2) the diffusion of components in the melt (~100 years/cm in natural magma body; *Marsh 2015*), and (3) the transfer of the latent crystallization heat from the crystal surface (*Kirkpatrick 1975*; *Dowty 1980*; *Cashman 1990*). It is important to note that each of these three mechanisms can control the growth process.

Similarly to nucleation, the growth process is intimately linked to the undercooling and supersaturation (see **Box 2**). Even if it can play a role in each of these 3 mechanisms (*Tiller 1963, 1977*), it is possible with some assumptions to obtain simplified equations. Generally, we consider that the interface kinetics is the dominant mechanism at low undercooling, while the growth becomes diffusion-limited at higher undercooling (*Dowty 1980*, *Kirkpatrick 1981*). Compared to the diffusion coefficient which are very small (10^{-2} – 10^{-3} cm^2/s), the thermal diffusivity in silicate melt is several order larger; so the heat transfer cannot really impact the growth process.

BOX 2

Crystallization processes are generally defined as a function of the undercooling (see BOX 1 and supersaturation, defined as the difference between the actual concentration of one element, and its concentration at the equilibrium (Kirkpatrick 1981).

In a multicomponent system as the magmatic melt, a direct estimation of the supersaturation is very difficult, and even impossible. The undercooling as the advantage to be well defined, so it will be use preferentially. However, when we consider the "actual" undercooling, the liquidus temperature considered is not the liquidus of the bulk composition and evolves with the melt composition.

Interface-growth control

The interface-growth control occurs when the diffusion of elements at the crystal/melt interface is very fast. In this case, crystal growth is controlled by the rate of attachment of atoms to the crystal surface (*Dowty 1980*; *Kirkpatrick 1981*). In the interface growth controlled (the dominant growth mechanism for many igneous rocks), growth rate corresponds to the rate at which atoms/molecules attach (R_a) and detach (R_d):

$$R_a = v \times \exp\left(\frac{-\Delta G'}{RT}\right) \quad (12)$$

$$R_d = v \times \exp\left(\frac{-(\Delta G_c + \Delta G')}{RT}\right) \quad (13)$$

With v the atomic vibration frequency, $\Delta G'$ the activation energy for atoms attachment (defined in the section concerning the theory of nucleation), and ΔG_c the chemical driving force (crystalline barrier reflecting the cohesion of the network).

The total growth rate (G) corresponding to the difference between these two rates can be defined as:

$$G = f \times a_0 \times v \times \exp\left(\frac{-\Delta G'}{RT}\right) \times \left[1 - \exp\left(\frac{-\Delta G_c}{RT}\right]\right. \quad (14)$$

As explained by *Kirkpatrick (1981)*, at high temperature, ΔG_c is negligible compared to $\Delta G'$ which is temperature dependent. In such case, the second exponential term approaches 1, and the equation can be simplified as follows:

$$G = f \times a_0 \times v \times \exp\left(\frac{-\Delta G'}{RT}\right) \quad (15)$$

where f is the fraction of available sites for attachment, and $\boldsymbol{a_0}$ the thickness of the various added layers. Regrouping the terms f, v and a_0 in a general constant G_0, the growth rate can be linearly represented as a function of $\Delta G'$ (*Burkhard 2005*; *Billon et al. 2025*):

$$\ln(G) = \ln(G_0) - \frac{\Delta G'}{R} \times \frac{1}{T} \quad (16)$$

With $ln(G_0)$ the intercept, $\frac{\Delta G'}{R}$ the slope, and $\frac{1}{T}$ the abscisse.

The interface growth mechanism can itself lead to various growth models: continuous growth and layer-spreading growth, depending on the number of attachment sites (as a function of undercooling), and of the surface roughness (*Kirkpatrick 1981*; *Sunagawa 1981*). In the continuous growth model, which corresponds to a relatively fast mechanism (with f =1), the crystal surface is considered rough, and all sites are available for atomic attachment. This type of growth is the principal mechanism for metals. In the layer-spreading growth, except at some steps where the atoms will be attached, the surface is considered as flat; and the growth occurs by ***surface nucleation*** (where atoms attach preferentially on crystal surface edges), or ***screw dislocation*** (the emerging of a screw dislocation on the crystal surface forms a spiral-shaped on it). For these 2 types of growth, f (fraction of available sites) varies in function of the undercooling/supersaturation, defining the passage from one type of growth to the other. *Gilmer (1977)* showed that layer-spreading growth evolves from screw-dislocation-dominated at low undercooling to surface-nucleation-dominated as undercooling increases. A comparative image of a crystal growing by screw dislocation, and surface nucleation is provided in **Figure I-11**.

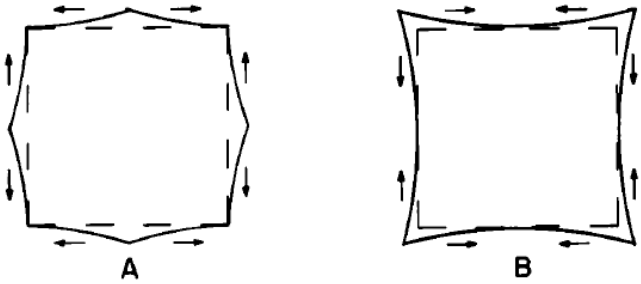

Figure I-11*: Schematic (exaggerated) view from Kirkpatrick (1981) illustrating plagioclase growth mechanisms: (A) screw dislocation-controlled growth at small undercooling, and (B) surface nucleation-controlled growth at large undercooling.*

Diffusion growth control

In a one component system, only the interface growth control occurs. However, in the case of a multicomponent system, if the mobility (diffusion) of the element is slower than the atom attachment, the growth process will be ***diffusion limited***. This is generally the case at a larger undercooling degree. The growth case, in this case, can be written like this (*Christian 1965*; *Dowty 1980*; *Kirkpatrick 1981*):

$$G = k \times (\frac{D}{t})^{1/2} \quad (17)$$

where k is a constant correction term, t the time, and D the diffusion coefficient of the elements in melt.

Crystal shape variation

As discussed above, although two main growth mechanisms dominate depending on the degree of undercooling, further subdivisions exist, adding complexity to the overall picture. Critically, both the growth mechanism and undercooling jointly control the resulting crystal morphology, as illustrated in **Figure I-12**, showing the evolution of olivine habits as a function of temperature and cooling rate. Since crystal shape can serve as a proxy for undercooling, we summarize here how crystal morphologies evolve with increasing undercooling and the associated growth mechanisms, progressing toward disequilibrium conditions. A summary table is provided at the end (**Table I-1**).

Interface-controlled growth, which occurs when element mobility in the melt is high, typically produces well-faceted, euhedral crystals. According to *Gilmer and Jackson (1977)*, several stages can be identified within this regime. At very low undercooling, stable planar growth dominates, often facilitated by screw dislocation processes. As undercooling increases, instabilities develop at the interface, leading to the appearance of edge protuberances (**Figure I-12**). This transition marks the onset of surface nucleation and continuous growth mechanisms, progressively leading to skeletal morphologies (**Figure I-12**). These intermediate forms may resemble early diffusion-limited growth, as they produce similar skeletal-like shapes. At high undercooling, reduced diffusivity in the melt leads to diffusion-controlled growth, resulting in strong disequilibrium textures such as skeletal and dendritic morphologies (*Sunagawa 1981*). An intermediate growth regime, incorporating both melt diffusion and interfacial reaction, was proposed by *Mangler et al. (2023)*, based on the formulation of *Kitayama (1998)*. In this framework, both growth processes are rate-limiting, allowing different growth modes to coexist along distinct crystallographic axes and leading to anisotropic growth that influences the resulting mineral shape (*Mangler et al. 2023*; *Lindoo et al. 2025*).

Traditionally, linear regressions of crystal size versus the square root of time have been used to distinguish between diffusion- and interface-controlled growth. However, as noted by *Kirkpatrick (1975)*, steady-state diffusion may produce similar trends, making the identification of the dominant growth mechanism inherently challenging.

supersaturation/undercooling (ΔT)	Type of growth	Kinetics control	Crystal shape
Small	spiral/screw dislocation	interface-contolled	Euhedral, well-faceted
	Surface nucleation	interface (sometimes mix)	Euhedral, with edge irregularities
	Continuous growth	Mix (interface and diffusion)	Sub-euhedral, skeletal
Large	Diffusion	diffusion-controlled	skeletal/dendritic

***Table I-1**: Summary of crystal shapes and growth types (spiral/screw dislocation, surface nucleation, and continuous growth) associated with each kinetic control (interface- and/or diffusion-controlled) as a function of undercooling.*

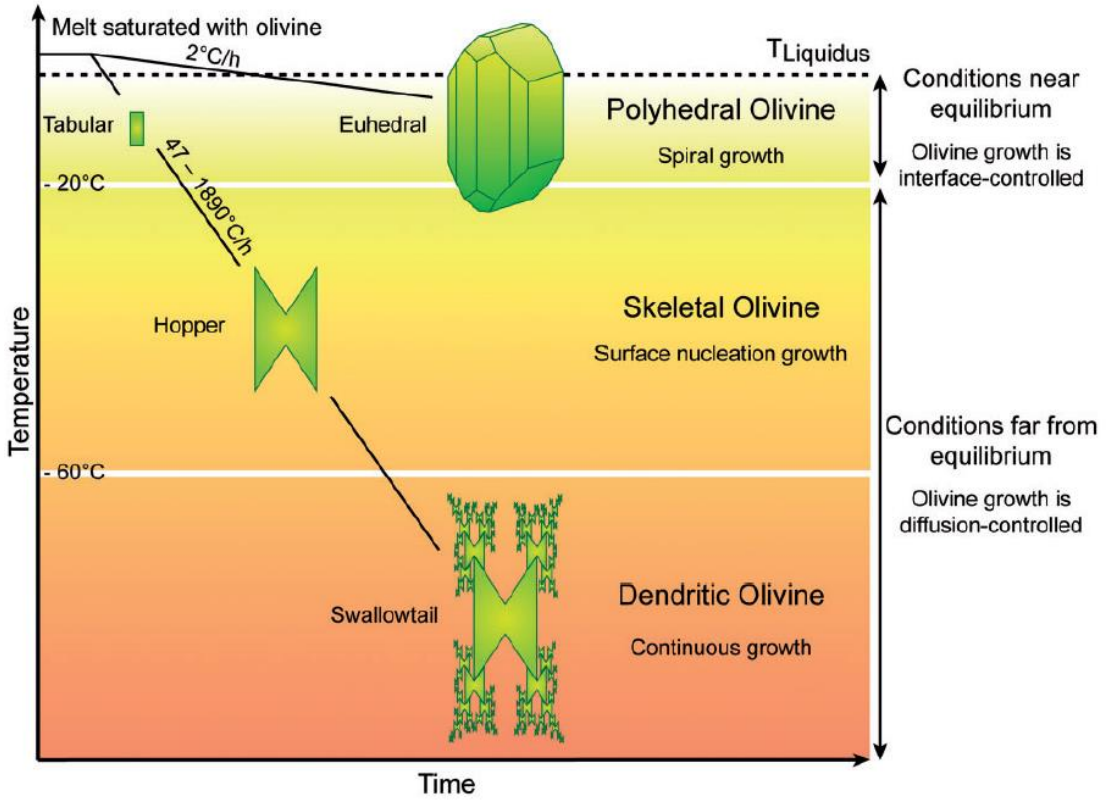

***Figure I-12**: Evolution of olivine habits as a function of cooling rate and nominal undercooling ($-\Delta T = T_{liq} - T_{quench}$), after Welsch et al. (2013). As the degree of undercooling increases, olivine habit evolves from euhedral to dendritic (swallowtail), consistent with the classic model of Sunagawa (1981). Polyhedral (euhedral) olivine grows by interface-controlled spiral growth at low undercooling ($-\Delta T$ < 20 °C) and cooling rates less than 47 °C/h. Skeletal olivine forms by diffusion-controlled surface-nucleation growth at moderate undercooling ($-\Delta T$ = 20–60 °C) and cooling rates between 47 and 1890 °C/h, producing hollow faces. Dendritic olivine develops by diffusion-controlled continuous growth at high undercooling ($-\Delta T$ > 60 °C).*

Experimental investigation of crystallization

Analytical techniques applied to natural magmas provide essential information on magmatic processes. Experimental petrology, by reproducing natural crystallization conditions under controlled parameters (pressure, temperature, redox state, and initial composition; *Rutherford 1993*) and crystallization pathways, offers a powerful complementary approach to reconstruct magmatic processes, including phenocryst stability fields and magma storage conditions. Data from natural samples, such as fO_2, equilibrium temperatures of coexisting crystalline phases, and volatile contents (H_2O, CO_2), guide experimental designs and help reduce the number of trial conditions required to reproduce natural assemblages.

Combining natural observations with experiments provides a more comprehensive understanding of magma evolution and timescales, yielding key parameters such as crystal growth rates, which are critical for accurate timescale estimations. Some limitations must nevertheless be considered: experimental systems are generally simpler than natural magmas, they often fail to achieve complete equilibrium, and sample volumes are far smaller than those of real magmatic reservoirs (*Edgar 1973*).

We summarize here the fundamental experimental parameters that must be considered (initial material, controlled variables, and types of experiments), as well as the relevance of using plagioclase to experimentally investigate crystallization kinetics.

Experimental parameters

Experimental runs investigating crystallization kinetics (nucleation and growth) require precise control of several parameters, including the nature and composition of the starting material, pressure, temperature, fO_2 conditions, and the experimental setup. Each of these factors influences nucleation and crystal growth, determining the resulting crystal habit and the types of crystalline phases formed.

Nature and composition of the starting material

The nature and composition of the starting material strongly control crystallization behavior in experimental studies. Two main types are used: synthetic and natural. Synthetic compositions, typically prepared by mixing high-purity oxide powders to reproduce natural targets (*Pupier et al. 2008*; *Saracino et al. 2025*), are generally free of impurities and allow precise control over crystallizing phases. They can also cover a broad range of compositions, from terrestrial (Pupier et al. 2008) to extraterrestrial systems (Saracino et al. 2025), explaining

their frequent use. Natural samples (lavas, pyroclasts) better reflect magmatic conditions, incorporating volatiles and crystal fragments (*Lesher et al. 1999*; *Hammer and Rutherford 2002*), but are often more difficult to work with. To homogenize them, many studies apply an initial superheating step to remove nucleation sites (bubbles; crystal fragments) and produce homogeneous glass (*Vona and Romano 2013*; *Vetere et al. 2013, 2024*), whereas others preserve bubbles and crystal fragments to allow both nucleation and growth (*Couch et al. 2003*; *Billon et al. 2025*).

The bulk composition, especially volatiles (H_2O, CO_2, Cl, S) governs which crystalline phases form. For plagioclase, water decreases the liquidus temperature, favoring crystal growth over nucleation and increasing anorthite content (*Heckmann et al. 2023*). Alkali content (e.g., Na_2O) must also be monitored, as alkalis volatilize above ~900 °C (*Edgar 1973*), particularly during long-duration runs, which could also affect the crystallization kinetic and raise the liquidus temperature (*First et al. 2020*).

Experimental conditions

The sequence of phase crystallization is controlled by temperature (*T*), pressure (*P*), and oxygen fugacity (fO_2), with chemical composition and crystal habit being particularly sensitive to *T* and *P* variations. In systems containing both silicates and oxides, fO_2 influences not only the order of crystallizing phases but also the differentiation path of the liquid and the phase compositions (*Shea and Hammer 2013*).

Temperature and pressure effects are typically studied through distinct solidification pathways: (1) isothermal or isobaric runs, with dwell times before a final quench (*Nabelek et al. 1978*); (2) single-step cooling or decompression, involving an almost instantaneous drop to the final conditions (*Couch et al. 2003*; *Shea and Hammer 2013*); (3) multiple-step runs, with evenly spaced cooling or decompression increments (*Martel and Schmidt 2003*); and (4) continuous runs, where T and P change steadily (*Pupier et al., 2008*; *Brugger and Hammer 2010a, b*; *Billon et al. 2025*). Variations may include initial superheating or final dwell steps (*Nabelek et al. 1978*; *Pupier et al. 2008*). All runs end with a rapid quench (from 100 to more than 1000 °C/h) to preserve the system's final state (*Hammer 2008*).

The chosen pathway strongly affects the final microtexture, including liquid and solid composition and crystal habit. Because T and P conditions depend on the starting composition and system setup, crystallization is often described in terms of undercooling, the difference between the phase saturation temperature and the system temperature (*Kirkpatrick 1981*). In

single-step experiments, real undercooling is directly calculated ($-\Delta T = T_{liq} - T_f$). In dynamic or continuous runs, real undercooling is difficult to quantify; changes in cooling rates only provide a relative measure, with faster rates corresponding to higher undercooling. To simplify, nominal undercooling ($-\Delta T_n$) is defined as the difference between the starting liquidus temperature and the final run temperature (*Faure et al. 2003*; *Faure and Tissandier 2014*). In decompression experiments at constant T, effective undercooling (ΔT_{eff}) is defined as the difference between the liquidus at the starting pressure and the system temperature at the final pressure (*Hammer and Rutherford 2002*).

Type of experiments

Depending on the research objective, different experimental approaches are employed:

- Experiments at atmospheric pressure (1 atm); performed in a simple vertical or horizontal furnace under dry conditions. These experiments are particularly suited to investigating processes occurring at very low pressure (shallow depths), near-surface environments without volatiles, and for initial liquidus determinations. This is the experimental approach adopted in the present study and described in detail in the following chapter.
- Experiments at moderate pressure (up to ~10 kbar): Conducted under hydrated conditions, these experiments are used to study the genesis of plutonic and metamorphic rocks and to investigate differentiation processes of volcanic magmas within the crust and uppermost mantle. High-pressure vessel (HPV) furnaces (see **Chapter II**) are a typical example of the equipment used.
- High-pressure experiments (> 10 kbar); using devices such as piston-cylinder presses (up to ~50 kbar and ~2000 °C; *Boyd and England 1960*) or multi-anvil presses (up to ~200 kbar; *Hall 1958*; *Bradley 1969*). Although not detailed in this manuscript, such experiments are essential for studying high-grade metamorphism, deep mantle and transition-zone processes, and planetary interiors.

The sample holder depends on the experimental setup: Pt or Rh wire is commonly used in 1 atm furnaces, whereas Au or Au–Pd capsules are employed in hydrated experiments using HPV furnace or piston-cylinder techniques. The choice of holder plays an essential role in crystallization kinetics, notably affecting nucleation behavior, with preferential nucleation sometimes occurring on Pt wire (*Billon et al. 2025*). In capsule-based experiments, a temperature gradient often develops, leading to heterogeneous textures within a single sample.

in such configurations, the sample volume and geometry become critical parameters impacting thermal gradients and resulting crystal assemblages.

Significance of plagioclase

Plagioclase ($NaAlSi_3O_8$ - $CaAl_2Si_2O_8$) is a triclinic tectosilicate feldspar forming a complete solid solution between albite (sodic end-member) and anorthite (calcic end-member). Owing to the higher abundance of calcium relative to potassium in the crust, plagioclase is the most common feldspar mineral. The series is subdivided by albite (Ab) and anorthite (An) contents: albite (90–100% Ab), oligoclase (70–90% Ab), andesine (50–70% Ab), labradorite (30–50% Ab), bytownite (10–30% Ab) and anorthite (0–10% Ab).

Plagioclase is widespread in magmatic environments such as subduction zones, ocean islands, mid-ocean ridges and intrusive complexes (*Cullen et al. 1989*; *Cashman and Blundy 2013*; *Drignon et al. 2018*; *Bechon et al. 2022*). Because Ca–Al and Na–Si interdiffusion is extremely slow, its original textures are well preserved over long timescales, providing robust records of crystallization processes (*Grove et al. 1984*; *Bennett et al. 2019*). Plagioclase usually exhibits a simple prismatic habit (rectangular in 2D, parallelepipedal in 3D), which facilitates quantitative textural studies (*Higgins 2000*). Both crystal shape and composition reflect nucleation and growth conditions, controlled by variations in temperature, pressure and melt composition (*Pupier et al. 2008*; *Brugger and Hammer 2010a*; *Bennett et al. 2019*; *Billon et al. 2025*). Increasing undercooling promotes a morphological transition from tabular to skeletal and dendritic forms (*Lofgren 1974*), with higher anorthite contents typically found in tabular or resorbed cores compared to acicular or skeletal crystals (*Bennett et al. 2019*). These features make plagioclase an excellent recorder of crystallization conditions and magma evolution.

Target area and goal of the study

Interest and particularities of subduction zones

General presentation

Among the different geodynamical environments where magma is generated: mid-ocean ridges, hotspots, or also continental rifts; subduction zones represent a key setting. Subduction-related magmatism contributes roughly 15% (0.4–0.6 km^3/yr) of the global magma production (*Crisp 1984*). They host the majority of the world's active and hazardous volcanoes (Mt Pelée,

Mt St Helens, Krakatau, Tambora; responsible of some historical eruptions), which develop at convergent margins where an old and cold oceanic plate descends beneath either an oceanic or continental plate (**Figure I-13 and Figure I-14**; *Turner et al. 2000*; *Ducea et al. 2015*). Volcanic chains in these regions are typically arranged in linear or arcuate patterns, 25 to 150 km wide, and parallel to the trench. Andesite is the volumetrically dominant magma type erupted in these settings, accounting for about 61% of subaerial volcanoes worldwide (*Gill 1981*). Since the continental crust has an overall andesitic composition, subduction zones were originally considered the primary site of continental crust generation (*Taylor and McLennan 1981*), a view that is no longer supported. Andesites are no longer regarded as primary magmas, but rather as products of differentiation from basaltic parental magmas (derived from peridotite partial melting; *Grove and Kinzler 1986*) combined with crustal processes.

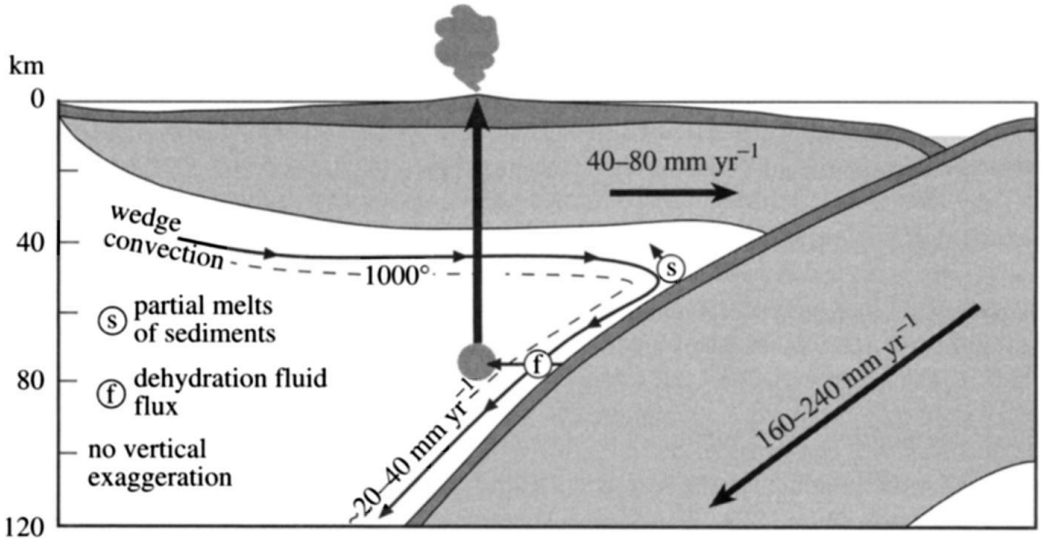

***Figure I-13**: Scaled cross-section of the Tonga–Kermadec subduction zone illustrating the inferred mantle wedge dynamics and fluid fluxes (modified from Turner and Hawkesworth 1997; Turner et al. 2000).*

Examples of subduction zones include the Andes in South America, the Gangdese arc south of Tibet, and the Caledonian arc of the Appalachians in the eastern United States. When the overriding plate is continental, the subduction system is referred to as a continental arc (e.g., the Andean arc), whereas when the overriding plate is oceanic, it forms an island arc (e.g., the Mariana arc). Continental arcs are (e.g. the Andean arc) typically more tectonically complex and long-lived than island arcs (*Ducea et al. 2015*), producing rocks with higher silica content due to several processes such as fractional crystallization, crustal assimilation, and remelting of preexisting mafic rocks.

The upper plate can display different tectonic regimes; compressional, extensional, or neutral, which define the overall subduction setting (*Ducea et al. 2015*). In an extensional regime (**Figure I-14a**), the crust is relatively thin (~30 km), and sedimentary basins can develop anywhere from the backarc to the forearc region. In continental systems, examples include the Japan and Aegean Seas, associated respectively with the Japanese and Hellenic arcs. Volcanism related to this type of arc generally develops across more subdued uplands.

In contrast, under a compressional regime (**Figure I-14b**), volcanism mainly occurs along elevated regions. The upper plate undergoes significant crustal and lithospheric thickening, with crustal thickness reaching up to ~70 km. Extensive backarc plateaus may form in such contexts (**Figure I-14b**), such as the Altiplano–Puna plateau in the Central Andes, or the Mesozoic–Cenozoic plateaus of western North America (*Chamberlain et al. 2012*). Moreover, large fold-and-thrust belts develop on the inboard side of the arc, as material is transported from the continental interior toward the core of the orogen.

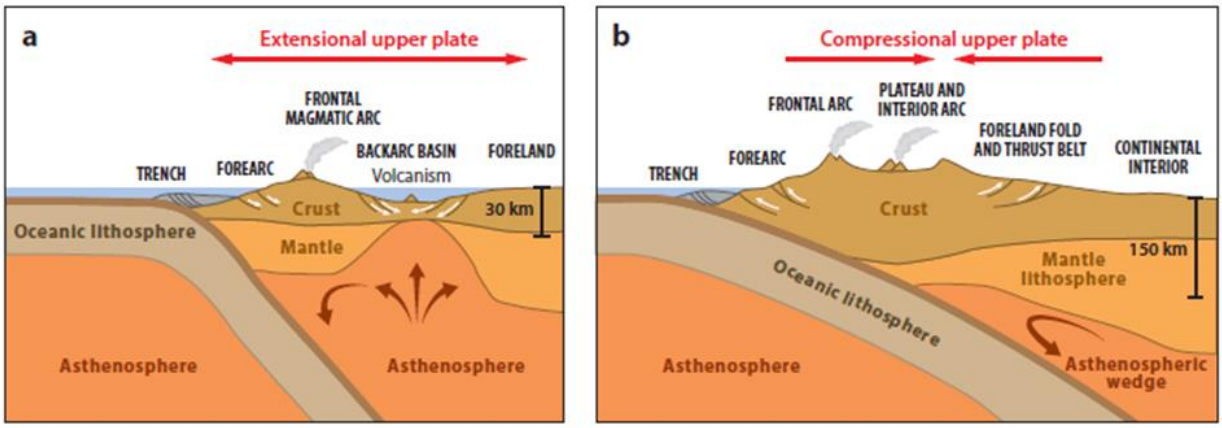

***Figure I-14**: Schematic cross-section of a continental subduction system illustrating its two end-member regimes (taken from Ducea et al. 2015): (a) extensional and (b) compressional.*

Subducted components

As shown by incompatible trace-element diagrams, subduction-related magmas display a distinctive geochemical signature, with enrichment in large-ion lithophile elements (LILEs) relative to high-field-strength elements (HFSEs) (**Figure I-15**; *Gill 1981*; *Hawkesworth et al., 1997*). This pattern reflects contributions from multiple slab-derived components, which can be distinguished using geochemical tracers:

- Altered oceanic crust and slab-derived fluids: Experimental studies demonstrate that the LILE/HFSE ratio reflects the mobility of these elements in fluids released from the

subducting slab. The highest LILE/HFSE ratios, commonly associated with the lowest $^{87}Sr/^{86}Sr$ and $^{206}Pb/^{204}Pb$ values, are interpreted as a signature of fluids derived from altered oceanic crust (*Miller et al. 1994*; Turner et al. 1996). U-series disequilibria further support this, as U and Ra are highly mobile in oxidizing slab-derived fluids, whereas Th and Pa remain relatively immobile (*Brenan et al. 1995*; *Keppler 1996*). The addition of U to the mantle wedge results in elevated U/Th ratios in arc magmas. These ratios are largely unaffected by partial melting, crystal fractionation, or crustal contamination, making U–Th isotopes a reliable tool for dating fluid-transfer events (e.g., in Papua New Guinea or Santorini; *Gill et al. 1993*; *Zellmer et al. 2000*).

- Subducted sediments: In contrast, the presence of 10Be, negative Ce anomalies, elevated Th/Ce, and $^{143}Nd/^{144}Nd$ ratios indicate contributions from subducted sediments (e.g. *Morris et al. 1990*). This is exemplified by the Mariana Arc, where fractionated U/Th ratios record sediment transfer from the subducting plate around 350 kyr ago (*Elliott et al. 1997*). Excess ^{226}Ra in arc lavas, correlated with Ba/Th and low $^{87}Sr/^{86}Sr$, also reflects a mantle signature resulting from fluid addition influenced by sediments (e.g. *Turner and Hawkesworth 1997*). Although ^{226}Ra records very recent fluid additions over a few thousand years, it is continuously replenished from decay of residual ^{230}Th in the slab, so Ra and U-Th isotopes together provide complementary constraints on both the timing and composition of slab-derived contributions (*Turner et al. 2000*).

***Figure I-15* (see below)**: *Example of a primitive mantle–normalized trace element diagram for a basalt (SiO_2 = 51.7%) from the Rumble seamounts, southern Kermadec island arc (after Turner et al. 1997; square symbols). The model involves a 15% partial melt of fertile peridotite with 0.5% sediment addition (solid line without symbols), reproducing Th, REE, Zr, Hf, and Ti contents. Overestimated Ta and Nb indicate sediment input as a partial melt formed in the presence of residual rutile, while enrichments in Rb, Ba, U, K, Pb, and Sr reflect fluid addition to the mantle source (shaded areas).*

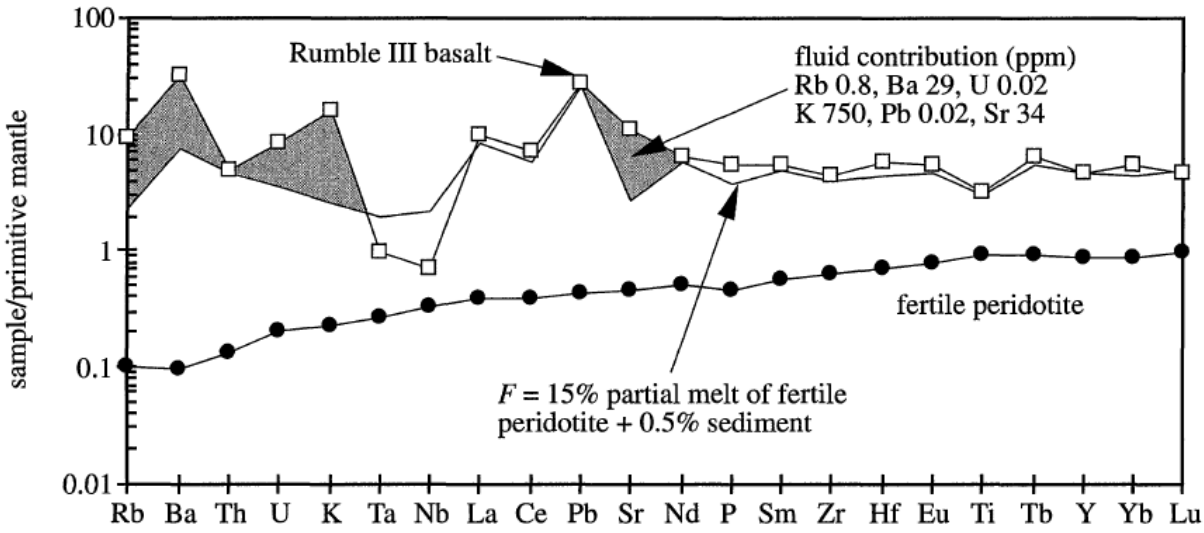

These observations led to the development of three-component models that distinguish the respective roles of the mantle wedge, slab-derived fluids, and subducted sediments in arc magmatism (**Figure I-13**; *Turner et al. 1996*; *Hawkesworth et al. 1997*).

Melt generation in volcanic arcs

Magmatism in subduction zones is primarily driven by dehydration reactions within the subducting oceanic slab, which releases hydrous components as temperature and pressure increase with depth (**Figure I-13**; *Gill 1981*; *Turner and Hawkesworth 1997*; *Turner et al. 2000*). These volatiles form a water-rich flux that accumulates in the overlying mantle lherzolites, lowering the mantle solidus and triggering partial melting of mantle peridotites, generating basaltic magmas (*Gaetani and Grove 1998*). The degree of melting depends on temperature, pressure, water content, and local mantle composition. This process depletes source rocks in incompatible elements and produces hydrous calc-alkaline magmas, with a wide range of silica (~45 to >75 wt.% SiO_2) and higher volatile concentrations than magmas from hotspots or mid-ocean ridges. Such magmas are commonly associated with high-pressure metamorphism in subduction environments.

High eruptive temperatures exceeding the hydrous peridotite solidus, along with the presence of some essentially anhydrous arc magmas, have been used by *Sisson and Bronto (1998)* for example to question the classical hydrous fluxing model. However, some geochemical and isotopic evidence points to a potential contribution from decompression

melting in some arc lavas linked to fluid addition (*Plank and Langmuir 1988*; *Pearce and Parkinson 1993*).

Slab-derived fluids strongly influence the chemical signature of arc magmas. U-series disequilibria (U-Th-Pa-Ra) provides a powerful tool to trace fractionation processes and the role of slab fluids. In oxidizing conditions, U and Ra are highly mobile, whereas Th and Pa remain relatively immobile (*Brenan et al. 1995*; *Keppler 1996*). Consequently, fluids released by slab dehydration enrich the mantle wedge in U. High U/Th ratios in arc lavas are thus interpreted as reflecting fluid addition, since crustal contamination would instead lower this ratio. Lavas with the strongest fluid signatures, characterized by high ($^{238}U/^{230}Th$), elevated Ba/Th, and Ra excesses suggest that amphibole is consumed during melting, and they record both recent and older fluid inputs. Combined U-Th and Ra isotopes therefore provide complementary constraints on the timing and nature of slab-derived fluids (*Turner et al. 2000*). The U/Th and Th/Ra fractionation implies fluid release from the subducting plate via hydraulic fracturing under highly oxidized conditions (*Davies 1999*).

Impact of subducted elements

Some evidence indicates that partial melting in subduction zones is primarily controlled by hydrous fluxing. Fluid transfer is inferred to occur rapidly, likely through hydraulic fracturing, emphasizing the central role of slab-derived volatiles in triggering mantle melting. The extent of melting increases with the amount of water introduced into the mantle source (e.g. *Stolper and Newman 1994*), and U-series data show that the flux of slab-derived fluids (^{238}U–^{230}Th disequilibria) is strongly dependent on subduction rate (e.g. *Gill 1981*; *Jarrard 1986*). Rapid subduction is associated with shorter transfer times for U addition, whereas sediments, though not directly responsible for melting, can significantly prolong transfer times. In some cases, sediments may also contribute to the fluid component, as suggested by thermal and geochemical models. For instance, *Turner and Hawkesworth (1997)* estimated transfer times of 2–4 Myr for Louisville volcaniclastic sediments in the northern Tonga arc, requiring shallow incorporation (<40 km), partial decoupling of mantle wedge convection, and wedge temperatures several hundred degrees higher than those predicted by classical thermal models (*Davies and Stevenson 1992*).

Associated volcanism

Active arcs are dominated by large volcanic complexes, mainly stratovolcanoes and calderas, which reflect the highly explosive character of arc magmatism due to its enrichment in volatiles. These edifices grow over millions of years through alternating lava flows and pyroclastic deposits, producing steep, tall volcanoes that are prone to structural instability and erosion. In the Andes, for example, stratovolcanoes can reach elevations of up to 3 - 4 km above the surrounding terrain (Osorno: 2.6 km; Calbuco: 2.0 km; Villarrica: 2.8 km), posing significant hazards to nearby populations. Eruptions typically alternate between rhyolitic–dacitic ash-flow tuffs and basaltic-andesitic to andesitic lava flows (*Ducea et al. 2015*), and central edifices are often accompanied by secondary cones, such as the dacitic cones documented in the Osorno region (*Bechon et al. 2022*).

Despite extensive studies on volcanoes such as Mt. St. Helens (*Cashman 1988*; *Volpe and Hammond 1991*), Santorini (*Zellmer et al. 2000*), Etna (*Armienti et al. 1994*), and Villarrica (*Cortés et al. 2024*), no clear correlation has been established between magma (crystal) residence time and eruptive periodicity. Andesitic eruptions typically recur on timescales of tens to hundreds of years, largely independent of magma residence times. Instead, eruptive frequency appears controlled by processes such as degassing (*Jaupart 1996*), crystallization-induced volatile overpressure (*Tait et al. 1989*), vapour exsolution (*Wittington et al. 1999*), or recharge of magma chambers by fresh mafic inputs (*Sparks et al. 1977*). Consequently, eruptive timescales are generally shorter than those resolvable with ^{226}Ra–^{230}Th measurements, while studies using shorter-lived isotopes such as ^{210}Pb (22 years) or ^{228}Ra (6 years) indicate residence times of decades for some andesitic magmas (*Pyle 1992*). In more evolved subduction-zone systems, andesites progressively differentiate over time, often culminating in dacitic eruptions, which may require several thousand years to develop from basaltic-andesite parental magmas (*Gill 1981*).

In contrast, extinct arcs are typically eroded down to their plutonic roots, providing rare access to the intrusive portions of arc crust that are otherwise hidden beneath active volcanoes. Despite the large volumes of erupted continental arc magmas, most magma solidifies at depth as plutonic bodies rather than reaching the surface. This is reflected in the low volcanic-to-plutonic volume ratios, typically between 1:2 and 1:20 (*Paterson et al. 2011*), indicating that arc magmatism predominantly contributes to crustal construction beneath the volcanic cover.

The Central Southern Volcanic Zone of Chile (CSVZ)

The Andean arc, one major subduction zone, results from the subduction of the Nazca and Antarctic plates beneath the South American plate (*Dewey and Lamb 1992*). The slightly oblique convergence of the Nazca plate (~26° at 40°S, 66 mm/yr) has generated the Liquiñe–Ofqui Fault Zone (LOFZ), a 1,200 km-long dextral strike-slip fault accommodating transpression between ~38°S and ~47°S (*Cembrano and Lara 2009*; *Pérez-Flores et al. 2016*). The Andean arc is subdivided into four sectors (North, Central, Southern, and Austral) separated by volcanic gaps (*Stern 2004*).

The Southern Volcanic Zone (SVZ; **Figure I-16**) itself is divided into four segments (NSVZ, TSVZ, CSVZ, SSVZ) based on tectonic and geochemical criteria (*López-Escobar et al. 1995*; *Stern et al. 2007*). The Central SVZ (CSVZ, 37–42°S), which is the focus of this study, is bounded to the north by the southern termination of the LOFZ. It hosts some of the most active volcanoes of the arc and includes the Lake Region, an important touristic area near 41°S and 73°W. This area contains several major stratovolcanoes, including Villarrica, Calbuco, and Osorno, which rise directly above glacial lakes and some touristic cities (e.g. Puerto Montt, Valdivia, and Pucon; **Figure I-16**). Villarrica is characterized by persistent open-vent degassing and strombolian to subplinian explosions (*Gurioli et al. 2008*), Calbuco by recurrent subplinian eruptions and dome-building phases, with its last eruption in 2015 (*Namur et al. 2020*; *Mixon et al. 2021*), and Osorno by dominantly effusive to mildly explosive activity (*Bechon et al. 2022*). Petrological data indicate similar basaltic parent magmas with 1–2 wt.% H_2O at Villarrica, Osorno, and La Picada, and up to ~3 wt.% H_2O at Calbuco, with the main magma storage located at ~2 kbar (*Stern 2007*; *Vander Auwera et al. 2021*).

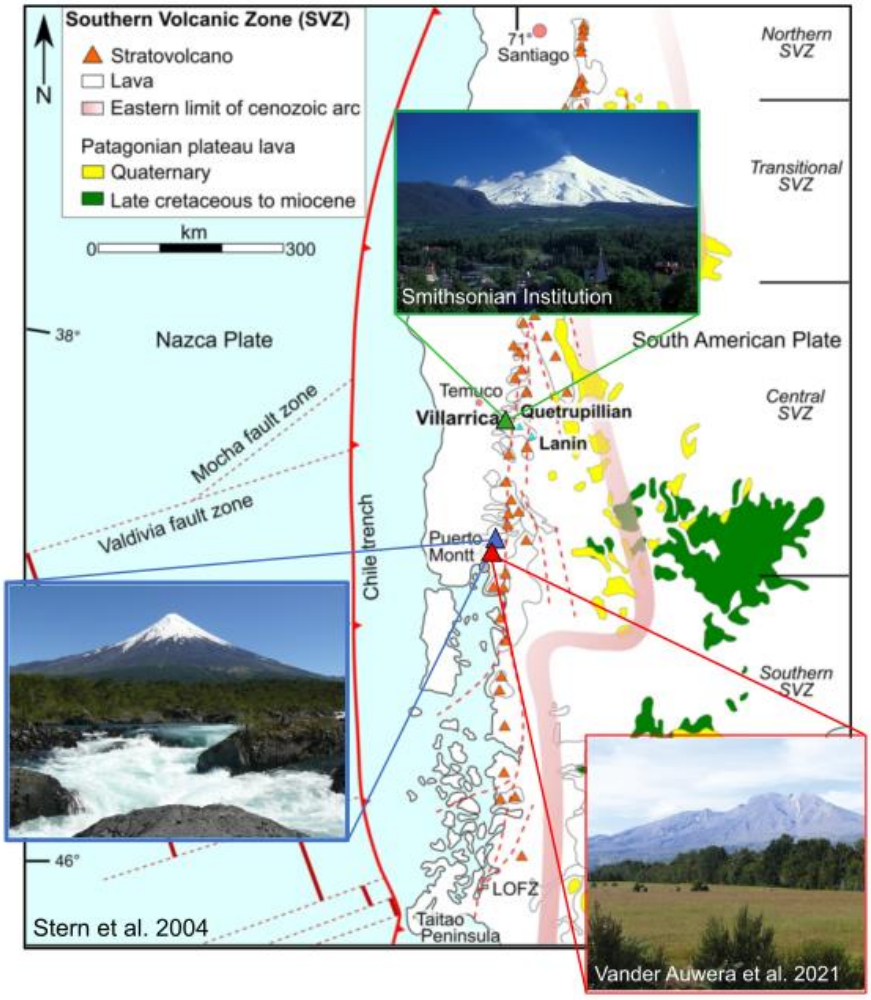

***Figure I-16**: Map of the Southern Volcanic Zone (SVZ) of the Andean arc (modified after Stern et al. 2004). Photographs of the studied volcanoes (Osorno, Calbuco, Villarrica) are also provided.*

Goal of the study and general overview

The aim of this thesis is to investigate pre-eruptive magmatic timescales using a textural approach based on Crystal Size Distribution (CSD) analysis. Geochemical methods such as U-series dating (e.g. *Bourdon et al. 2003*; *Cooper 2015*; *Schmitt 2011*) or diffusion chronometry (e.g. *Costa et al. 2008*, *2020*) have shown that magma ascent from shallow reservoirs is generally rapid, whereas deeper or mush-rich reservoirs can store magma over much longer periods (from decades to tens of thousands of years; *Cooper and Reid 2008*, *Reubi et al. 2017*). However, these techniques require well-preserved crystals, which is not always the case. When zircon is absent or feldspars are overprinted by abundant melt inclusions, textural approaches become essential. In this context, CSD, combined with experimentally constrained plagioclase

growth rates, offers an alternative way to estimate storage durations when geochemical chronometers cannot be applied.

The thesis brings together experimental work and applications to natural systems. **Chapter II** presents the analytical and experimental methods used throughout the study, including high-temperature crystallization experiments, image segmentation procedures, and the CSD technique. **Chapter III**, written as a manuscript published in *Contributions to Mineralogy and Petrology* (https://doi.org/10.1007/s00410-025-02213-9), investigates plagioclase nucleation and growth at low cooling rates and compares several approaches used to calculate growth and nucleation rates. **Chapter IV**, submitted to the same journal, examines the effect of thermal history (cooling rate, degrees of superheating, and isothermal holds) on nucleation behaviour, textural evolution, and plagioclase crystal habits.

These experimental constraints are then applied to natural samples in **Chapter V**, which uses the experimentally derived growth rates to estimate magma residence times beneath three active volcanoes of the Southern Andes: Osorno volcano, Calbuco volcano, and Villarrica volcano. The residence times obtained from CSD are compared with results from other approaches such as U-series disequilibria and diffusion chronometry, in order to evaluate the contribution and limitations of textural methods in arc magmatic systems. **Chapter VI** concludes by summarizing the main findings from the experimental and natural parts of the thesis.

References

Annen C (2009) From plutons to magma chambers: Thermal constraints on the accumulation of eruptible silicic magma in the upper crust. Earth and Planetary Science Letters 284:409–416. https://doi.org/10.1016/j.epsl.2009.05.006

Annen C, Sparks RSJ (2002) Effects of repetitive emplacement of basaltic intrusions on thermal evolution and melt generation in the crust. Earth and Planetary Science Letters 203:937-955. https://doi.org/10.1016/S0012-821X(02)00929-9

Annen C, Blundy JD, Sparks RSJ (2006) The Genesis of Intermediate and Silicic Magmas in Deep Crustal Hot Zones. Journal of Petrology 47:505–539. https://doi.org/10.1093/petrology/egi084

Annen C, Blundy JD, Leuthold J, Sparks RSJ (2015a). Construction and evolution of igneous bodies: Towards an integrated perspective of crustal magmatism. Lithos 230:206–221. https://doi.org/10.1016/j.lithos.2015.05.008

Annen C, Blundy JD, Leuthold J, Sparks RSJ (2015b) Construction and evolution of igneous bodies: Towards an integrated perspective of crustal magmatism. Lithos 230:206–221. https://doi.org/10.1016/j.lithos.2015.05.008

Association Volcanologique Européenne (n.d.) Campi Flegrei. Website of the Association Volcanologique Européenne. Available at: https://lave-volcans.com/lave_gp/index.php?action=072&ar=5

Avanzinelli R, Elliott T, Tommasini S, Conticelli S (2007) Constraints on the Genesis of Potassium-rich Italian Volcanic Rocks from U/Th Disequilibrium. Journal of Petrology 49:195–223. https://doi.org/10.1093/petrology/egm076

Bachmann O, Dungan MA, Lipman PW (2002) The Fish Canyon magma body, San Juan volcanic field, Colorado: rejuvenation and eruption of an upper-crustal batholith. J. Petrol. 43:1469–503. https://doi.org/10.1093/petrology/43.8.1469

Bachmann O, Huber C (2016) Silicic magma reservoirs in the Earth's crust. American Mineralogist 101(11):2377–2404. https://doi.org/10.2138/am-2016-5675

Bateman R, Marsh BD (1984). On the mechanics of igneous diapirism, stoping, and zone-melting. American Journal of Science, 284(8), 979-984. https://doi.org/10.2475/ajs.284.8.979

Bechon T, Billon M, Namur O, et al (2022) Petrology of the magmatic system beneath Osorno volcano (Central Southern Volcanic Zone, Chile). Lithos 426–427:106777. https://doi.org/10.1016/j.lithos.2022.106777

Becker R, Döring W (1935) Kinetische behandlung der keimbildung in übersättigten dämpfen. Annalen der physik, 416(8):719-752.

Beddoe-Stephens B, Aspden JA, Shepherd TJ (1983) Glass inclusions and melt compositions of the Toba Tuffs, northern Sumatra. Contributions to Mineralogy and Petrology, 83(3):278-287.

Bennett EN, Lissenberg CJ, Cashman KV (2019) The significance of plagioclase textures in mid-ocean ridge basalt (Gakkel Ridge, Arctic Ocean). Contrib Mineral Petrol 174:49. https://doi.org/10.1007/s00410-019-1587-1

Bergantz GW, Schleicher JM, Burgisser A (2017) On the kinematics and dynamics of crystal-rich systems, J. Geophys. Res. Solid Earth, 122:6131–6159. https://doi.org/10.1002/2017JB014218.

Billon M, Vander Auwera J, Namur O, et al (2025) Plagioclase crystal size distributions, growth and nucleation rates in an anhydrous arc basaltic andesite. Contrib Mineral Petrol 180:26. https://doi.org/10.1007/s00410-025-02213-9

Blundy J, Cashman KV, Berlo K (2008) Evolving Magma Storage Conditions Beneath Mount St. Helens Inferred from Chemical Variations in Melt Inclusions from the 1980–1986 and Current (2004–2006) Eruptions. USGS Professional Paper, 1750: 755-790.

Blundy J, Cashman KV, Rust A, Witham F (2010) A case for CO2-rich arc magmas. Earth and Planetary Science Letters 290:289–301. https://doi.org/10.1016/j.epsl.2009.12.013

Blundy JD, Annen CJ (2016) Crustal Magmatic Systems from the Perspective of Heat Transfer. ELEMENTS 12:115–120. https://doi.org/10.2113/gselements.12.2.115

Bonechi B, Polacci M, Arzilli F, et al. (2024) Magma residence time, ascent rate and eruptive style of the November ash-laden activity during the 2021 Tajogaite eruption (La Palma, Spain). Volcanica 7:51–65. https://doi.org/10.30909/vol.07.01.5165

Boulanger M, France L (2023) Cumulate formation and melt extraction from mush dominated magma reservoirs: the melt flush process exemplified at mid-ocean ridges. Journal of Petrology 64(2), egad005. https://doi.org/10.1093/petrology/egad005

Bourdon B, Wörner G, Zindler A (2000) U-series evidence for crustal involvement and magma residence times in the petrogenesis of Parinacota volcano, Chile. Contributions to Mineralogy and Petrology 139:458–469. https://doi.org/10.1007/s004100000150

Bourdon B, Turner S, Henderson GM, Lundstrom CC (2003) Introduction to U-series. Geochemistry Reviews in Mineralogy and Geochemistry Vol. 52. *Geochemical Society-Mineralogical Society of America, Washington, DC (1–21 pp.)*.

Bowen NL (1915) Crystallization-differentiation in silicate liquids. American Journal of Science S4-39(230): 175-191. https://doi.org/10.2475/ajs.s4-39.230.175

Bowen NL (1947) MAGMAS. GSA Bulletin 58(4):263-280. https://doi.org/10.1130/0016-7606(1947)58[263:M]2.0.CO;2

Boyd FR, England JL (1960). Apparatus for Phase-Equilibrium Measurements at Pressures up to 50 Kilobars and Temperatures up to 1750°C. Journal of Geophysical Research, 65(2):741-748

Bradley CC (1969). High Pressure Methods in Solid State Research. Springer New York, NY. https://doi.org/10.1007/978-1-4899-5877-8

Brenan JM, Shaw HF, Ryerson FJ, Phinney DL (1995) Mineral-aqueous fluid partitioning of trace elements at 900°C and 2.0 GPa: Constraints on the trace element chemistry of mantle and deep crustal fluids. Geochimica et Cosmochimica Acta 59:3331–3350. https://doi.org/10.1016/0016-7037(95)00215-L

Brocher TM (1981a) Shallow velocity structure of the Rio Grande Rift north of Socorro, New Mexico: A reinterpretation. Journal of Geophysical Research 86:4960–4970. https://doi.org/10.1029/JB086iB06p04960

Brocher TM (1981b) Geometry and physical properties of the Socorro, New Mexico, magma bodies. Journal of Geophysical research 86:9420–9432. https://doi.org/10.1029/JB086iB10p09420

Browne B, Gardner J (2006) The influence of magma ascent path on the texture, mineralogy, and formation of hornblende reaction rims. Earth and Planetary Science Letters 246:161–176. https://doi.org/10.1016/j.epsl.2006.05.006

Brugger CR, Hammer JE (2010a) Crystallization Kinetics in Continuous Decompression Experiments: Implications for Interpreting Natural Magma Ascent Processes. Journal of Petrology 51:1941–1965. https://doi.org/10.1093/petrology/egq044

Brugger CR, Hammer JE (2010b) Crystal size distribution analysis of plagioclase in experimentally decompressed hydrous rhyodacite magma. Earth and Planetary Science Letters 300:246–254. https://doi.org/10.1016/j.epsl.2010.09.046

Burgisser A, Degruyter W (2015) Magma Ascent and Degassing at Shallow Levels. In: The Encyclopedia of Volcanoes. Elsevier, pp 225–236

Burkhard DJM (2005) Nucleation and growth rates of pyroxene, plagioclase, and Fe-Ti oxides in basalt under atmospheric conditions. European Journal of Mineralogy 17:675–686. https://doi.org/10.1127/0935-1221/2005/0017-0675

Cabane H, Laporte D, Provost A (2005) An experimental study of Ostwald ripening of olivine and plagioclase in silicate melts: implications for the growth and size of crystals in magmas. Contributions to Mineralogy and Petrology 150:37–53. https://doi.org/10.1007/s00410-005-0002-2

Carroll MR, Holloway JR (eds 1994). Reviews in Mineralogy: Volatiles in Magmas. Mineralogical Society of America.

Cashman K, Blundy J (2013) Petrological cannibalism: the chemical and textural consequences of incremental magma body growth. Contributions to Mineralogy and Petrology 166:703–729. https://doi.org/10.1007/s00410-013-0895-0

Cashman K, Blundy J (2000) Degassing and crystallization of ascending andesite and dacite. Philosophical Transactions of the Royal Society of London Series A: Mathematical, Physical and Engineering Sciences 358:1487–1513. https://doi.org/10.1098/rsta.2000.0600

Cashman KV (1988) Crystallization of Mount St. Helens 1980-1986 dacite: A quantitative textural approach. Bulletin of Volcanology 50:194–209. https://doi.org/10.1007/BF01079682

Cashman KV (1990) Textural constraints on the kinetics of crystallization of igneous rocks. Reviews in Mineralogy and Geochemistry 24(1):259-314.

Cashman KV, Sparks RSJ, Blundy JD (2017) Vertically extensive and unstable magmatic systems: A unified view of igneous processes. Science 355:eaag3055. https://doi.org/10.1126/science.aag3055

Cembrano J, Lara L (2009) The link between volcanism and tectonics in the southern volcanic zone of the Chilean Andes: A review. Tectonophysics 471:96–113. https://doi.org/10.1016/j.tecto.2009.02.038

Chamberlain CP, Mix HT, Mulch A, et al (2012) The Cenozoic climatic and topographic evolution of the western North American Cordillera. American Journal of Science 312:213–262. https://doi.org/10.2475/02.2012.05

Charlier B, Zellmer G (2000) Some remarks on U–Th mineral ages from igneous rocks with prolonged crystallisation histories. Earth and Planetary Science Letters 183:457–469. https://doi.org/10.1016/S0012-821X(00)00298-3

Christian JW (1965) The Theory of Transformations in Metals and Alloys. Pergamon Press, Oxford.

Christopher TE, Blundy J, Cashman K, et al (2015) Crustal-scale degassing due to magma system destabilization and magma-gas decoupling at Soufrière Hills Volcano, Montserrat. Geochemistry, Geophysics, Geosystems 16:2797–2811. https://doi.org/10.1002/2015GC005791

Clemens JD, Mawer CK (1992). Granitic magma transport by fracture propagation. Tectonophysics, 204, 339–360. https://doi.org/10.1016/0040-1951(92)90316-X

Clemens JD, Petford N, Mawer CK (1997). Ascent mechanisms of granitic magmas: causes and consequences. In: Holness MB (ed.) Deformation enhanced Fluid Transport in the Earth's Crust and Mantle. Chapman & Hall, London, 145–172.

Cooper KM (2015) Timescales of crustal magma reservoir processes: insights from U-series crystal ages. Geological Society, London, Special Publications 422:141–174. https://doi.org/10.1144/SP422.7

Cooper KM (2019). Time scales and temperatures of crystal storage in magma reservoirs: Implications for magma reservoir dynamics. Philosophical Transactions of the Royal Society A Mathematical, Physical and Engineering Sciences, 377(2139):. https://doi.org/10.1098/rsta.2018.0009

Cooper KM, Reid MR (2008) Uranium-series Crystal Ages. Reviews in Mineralogy and Geochemistry 69:479–544. https://doi.org/10.2138/rmg.2008.69.13

Cooper KM, Kent AJR (2014) Rapid remobilization of magmatic crystals kept in cold storage. Nature 506:480–483. https://doi.org/10.1038/nature12991

Cooper KM, Kent AJR (2025) Petrological Constraints on the Thermal History of Magma Storage in the Crust. Annual Review of Earth and Planetary Sciences 54. https://doi.org/10.1146/annurev-earth-032524-113641

Corrigan GM (1982) Supercooling and the crystallization of plagioclase, olivine, and clinopyroxene from basaltic magmas. Mineral mag 46:31–42. https://doi.org/10.1180/minmag.1982.046.338.06

Costa F, Chakraborty S, Dohmen R (2003) Diffusion coupling between trace and major elements and a model for calculation of magma residence times using plagioclase. Geochimica et Cosmochimica Acta 67:2189–2200. https://doi.org/10.1016/S0016-7037(02)01345-5

Costa F, Dohmen R, Chakraborty S (2008) Time Scales of Magmatic Processes from Modeling the Zoning Patterns of Crystals. Reviews in Mineralogy and Geochemistry 69:545–594. https://doi.org/10.2138/rmg.2008.69.14

Costa A, Caricchi L, Bagdassarov N (2009) A model for the rheology of particle-bearing suspensions and partially molten rocks. Geochemistry, Geophysics, Geosystems, 10(3). https://doi.org/10.1029/2008GC002138

Costa F, Morgan D (2010). Time Constraints from Chemical Equilibration in Magmatic Crystals ,In Dosseto A, Turner SP, Van Orman JA (Eds.), Timescales of magmatic processes: From core to atmosphere (pp. 125–159). Chichester, UK: J. Wiley & Sons. https://doi:10.1002/9781444328509

Costa F, Shea T, Ubide T (2020) Diffusion chronometry and the timescales of magmatic processes. Nat Rev Earth Environ 1:201–214. https://doi.org/10.1038/s43017-020-0038-x

Couch S, Sparks RSJ, Carroll MR (2003) The Kinetics of Degassing-Induced Crystallization at Soufriere Hills Volcano, Montserrat. 44(8):1477-1502. https://doi.org/10.1093/petrology/44.8.1477

Crisp JA (1984) Rates of magma emplacement and volcanic output. Journal of Volcanology and Geothermal Research 20:177–211. https://doi.org/10.1016/0377-0273(84)90039-8

Crisp JA, Spera FJ (1987). Pyroclastic flows and lavas of the Mogan and Fataga formations, Tejeda Volcano, Gran Canaria, Canary Islands: mineral chemistry, intensive parameters, and magma chamber evolution. Contributions to Mineralogy and Petrology, 96(4), 503-518.

Cui Y, Myerson AS (2014) Experimental Evaluation of Contact Secondary Nucleation Mechanisms. Crystal Growth & Design 14:5152–5157. https://doi.org/10.1021/cg500861f

Cullen A, Vicenzi E, McBirney AR (1989) Plagioclase-ultraphyric basalts of the galapagos archipelago. Journal of Volcanology and Geothermal Research 37:325–337. https://doi.org/10.1016/0377-0273(89)90087-5

Danišík M, Schmitt AK, Stockli DF, et al (2017) Application of combined U-Th-disequilibrium/U-Pb and (U-Th)/He zircon dating to tephrochronology. Quaternary Geochronology 40:23–32. https://doi.org/10.1016/j.quageo.2016.07.005

Davies JH, Stevenson DJ (1992) Physical model of source region of subduction zone volcanics. J Geophys Res 97:2037–2070. https://doi.org/10.1029/91JB02571

De Angelis SH, Larsen J, Coombs M, et al (2015) Amphibole reaction rims as a record of pre-eruptive magmatic heating: An experimental approach. Earth and Planetary Science Letters 426:235–245. https://doi.org/10.1016/j.epsl.2015.06.051

Dewey JF, Lamb SH (1992) Active tectonics of the Andes. Tectonophysics 205:79–95. https://doi.org/10.1016/0040-1951(92)90419-7

Dohmen R, Faak K, Blundy JD (2017) Chronometry and Speedometry of Magmatic Processes using Chemical Diffusion in Olivine, Plagioclase and Pyroxenes. Reviews in Mineralogy and Geochemistry 83:535–575. https://doi.org/10.2138/rmg.2017.83.16

Donaldson CH (1979) An experimental investigation of the delay in nucleation of olivine in Mafic Magmas. Contr Mineral and Petrol 69:21–32. https://doi.org/10.1007/BF00375191

Dowty E (1980) Chapter 10. Crystal Growth and Nucleation Theory and the Numerical Simulation of Igneous Crystallization. In: Physics of Magmatic Processes. Princeton University Press, pp 419–486

Drignon M, Nielsen R, Tepley F, Kotash A (2018). Tracking the Mantle Origins of Mid-Ocean Ridge Basalts Using Plagioclase-Hosted Melt Inclusions. In Twenty-eighth Annual Goldschmidt Conference (p. 604).

Ducea MN, Saleeby JB, Bergantz G (2015) The Architecture, Chemistry, and Evolution of Continental Magmatic Arcs. Annual Review Earth and Planetary Sciences 43:299–331. https://doi.org/10.1146/annurev-earth-060614-105049

Edgar AD (1973) Experimental Petrology- Basic Principles and Techniques. Oxford University Press, New York

Edmonds M, Wallace PJ (2017) Volatiles and Exsolved Vapor in Volcanic Systems. ELEMENTS 13:29–34. https://doi.org/10.2113/gselements.13.1.29

Elliott T, Plank T, Zindler A, et al (1997) Element transport from slab to volcanic front at the Mariana arc. J Geophys Res 102:14991–15019. https://doi.org/10.1029/97JB00788

European Space Agency (n.d.) Eduspace – Natural Disasters. Available at: https://www.esa.int/SPECIALS/Eduspace_Disasters_FR/SEMC8M0T1PG_0.html

Farley KA (2002) (U-Th)/He Dating: Techniques, Calibrations, and Applications. Reviews in Mineralogy and Geochemistry 47:819–844. https://doi.org/10.2138/rmg.2002.47.18

Farley KA, Stockli DF (2002) (U-Th)/He Dating of Phosphates: Apatite, Monazite, and Xenotime. Reviews in Mineralogy and Geochemistry 48:559–577. https://doi.org/10.2138/rmg.2002.48.15

Farner MJ, Lee CTA (2017). Effects of crustal thickness on magmatic differentiation in subduction zone volcanism: a global study. Earth and Planetary Science Letters 470: 96–107. https://doi.org/10.1016/j.epsl.2017.04.025

Farris DW, Haeussler P, Friedman R, et al (2006) Emplacement of the Kodiak batholith and slab-window migration. Geological Society of America Bulletin 118:1360–1376. https://doi.org/10.1130/B25718.1

Faure F, Tissandier L (2014) Contrasted Liquid Lines of Descent Revealed by Olivine-hosted Melt Inclusions and the External Magma. Journal of Petrology 55:1779–1798. https://doi.org/10.1093/petrology/egu041

Faure F, Trolliard G, Nicollet C, Montel J-M (2003) A developmental model of olivine morphology as a function of the cooling rate and the degree of undercooling. Contributions to Mineralogy and Petrology 145:251–263. https://doi.org/10.1007/s00410-003-0449-y

First EC, Leonhardi TC, Hammer JE (2020) Effects of superheating magnitude on olivine growth. Contributions to Mineralogy and Petrology 175:13. https://doi.org/10.1007/s00410-019-1638-7

Fokin VM, Zanotto ED, Yuritsyn NS, Schmelzer JWP (2006) Homogeneous crystal nucleation in silicate glasses: A 40 years perspective. Journal of Non-Crystalline Solids 352:2681–2714. https://doi.org/10.1016/j.jnoncrysol.2006.02.074

Gaetani GA, Grove TL (1998) The influence of water on melting of mantle peridotite. Contributions to Mineralogy and Petrology 131(4):323-346. https://doi.org/10.1007/s004100050396

Gibb FGF (1974) Supercooling and the crystallization of plagioclase from a basaltic magma. Mineral mag 39:641–653. https://doi.org/10.1180/minmag.1974.039.306.02

Gill JB (1981) Orogenic Andesites and Plate Tectonics. Springer, Berlin, 390. https://doi.org/10.1007/978-3-642-68012-0

Gilmer GH (1977) Computer simulation of crystal growth. Journal of Crystal growth 42:3-10. https://doi.org/10.1016/0022-0248(77)90170-1

Glazner AF, Bartley JM, Coleman DS, Gray W, Taylor RZ (2004) Are plutons assembled over millions of years by amalgamation from small magma chambers? GSA Today 14:4–11. https://doi.org/10.17615/nspy-zk53

Goldstein SJ, Murrell MT, Williams RW (1993) 231Pa and230Th chronology of mid-ocean ridge basalts. Earth and Planetary Science Letters 115:151–159. https://doi.org/10.1016/0012-821X(93)90219-Y

Gottsmann JH, Lavallee Y, Marti J, Aguirre-Diaz GJ (2009). Magma-tectonic interaction and the eruption of silicic batholiths. Earth and Planetary Science letters 284: 426-434. https://doi.org/10.1016/j.epsl.2009.05.008

Grant SL (2000) Union member receives Nation's Premier Award for Young Scientists. EoS Transactions 81:531–531. https://doi.org/10.1029/EO081i045p00531

Grove TL, Baker MB, Kinzler RJ (1984) Coupled CaAl-NaSi diffusion in plagioclase feldspar: Experiments and applications to cooling rate speedometry. Geochimica et Cosmochimica Acta 48:2113–2121. https://doi.org/10.1016/0016-7037(84)90391-0

Grove TL, Kinzler RJ (1986). Petrogenesis of andesites. Annual Review of Earth and Planetary Sciences 14:417-454. https://doi.org/10.1146/annurev.ea.14.050186.002221

Grove TL, Donnelly-Nolan JM, Housh T (1997) Magmatic processes that generated the rhyolite of Glass Mountain, Medicine Lake volcano, N. California. Contributions to Mineralogy and Petrology 127:205–223. https://doi.org/10.1007/s004100050276

Guðmundsson MT (2012). The 2010 eruption of Eyjafjallajökull, Iceland. In McGraw-Hill Yearbook of Science & Technology 2012 (pp. 282-284)

Gurioli L, Harris AJL, Houghton BF, et al (2008) Textural and geophysical characterization of explosive basaltic activity at Villarrica volcano. Journal of Geophysical Research 113(B8). https://doi.org/10.1029/2007JB005328

Hall HT (1958). Some high-pressure, high-temperature apparatus design considerations – Equipment for use at 100000 atmospheres and 3000°C. Rev. Sci. Instrum, 29(4):267 – 275.

Hammer JE (2004) Crystal nucleation in hydrous rhyolite: Experimental data applied to classical theory. American Mineralogist 89:1673–1679. https://doi.org/10.2138/am-2004-11-1212

Hammer JE (2008) Experimental Studies of the Kinetics and Energetics of Magma Crystallization. Reviews in Mineralogy and Geochemistry 69:9–59. https://doi.org/10.2138/rmg.2008.69.2

Hammer JE, Rutherford MJ (2002) An experimental study of the kinetics of decompression-induced crystallization in silicic melt. J Geophys Res 107(B1). https://doi.org/10.1029/2001JB000281

Hawkesworth CJ, Turner SP, McDermott F, et al (1997) U-Th Isotopes in Arc Magmas: Implications for Element Transfer from the Subducted Crust. Science 276:551–555. https://doi.org/10.1126/science.276.5312.551

Heckmann P, Iacono-Marziano G, Strmić Palinkaš S (2023) An experimental study of the effect of water and chlorine on plagioclase nucleation and growth in mafic magmas: application to mafic pegmatites. Eur J Mineral 35:1111–1124. https://doi.org/10.5194/ejm-35-1111-2023

Higgins MD (2000) Measurement of crystal size distributions. American Mineralogist 85:1105–1116. https://doi.org/10.2138/am-2000-8-901

Hildreth W (1981). Gradients in silicic magma chambers: implications for lithospheric magmatism. J. Geophys. Res. 86(B11):10153–10192. https://doi.org/10.1029/JB086iB11p10153

Hildreth W, Moorbath S (1988). Crustal contributions to arc magmatism in the Andes of Central Chile. Contributions to mineralogy and petrology, 98(4), 455-489.

House MA, Wernicke BP, Farley KA (1998) Dating topography of the Sierra Nevada, California, using apatite (U–Th)/He ages. Nature 396:66–69. https://doi.org/10.1038/23926

Humphreys MCS, Menand T, Blundy JD, Klimm K (2008) Magma ascent rates in explosive eruptions: Constraints from H2O diffusion in melt inclusions. Earth and Planetary Science Letters 270:25–40. https://doi.org/10.1016/j.epsl.2008.02.041

Humphreys MCS, Namur O, Bohrson WA, Bouilhol P, Cooper GF, et al. (2025). Crystal mush processes and crustal magmatism. Nat. Rev. Earth Environ. 6:401–16. https://doi.org/10.1038/s43017-025-00682-x

Irvine TN, Andersen JC, Brooks CK (1998) Included blocks (and blocks within blocks) in the Skaergaard intrusion: Geologic relations and the origins of rhythmic modally graded layers. GSA Bulletin 110:1398–1447. https://doi.org/10.1130/0016-7606(1998)110%3C1398:IBABWB%3E2.3.CO;2

Jackson M, Blundy J, Spark R (2018). Chemical differentiation, cold storage and remobilization of magma in the Earth's crust. Nature 564: 405–409. https://doi.org/10.1038/s41586-018-0746-2

Jagoutz O, Schmidt MW (2012) The formation and bulk composition of modern juvenile continental crust: The Kohistan arc. Chemical Geology 298–299:79–96. https://doi.org/10.1016/j.chemgeo.2011.10.022

James PF (1974). Kinetics of crystal nucleation in lithium silicate glasses. Phys Chem Glasses 15:95-105

James PF (1985) Kinetics of crystal nucleation in silicate glasses. Journal of Non-Crystalline Solids 73:517–540. https://doi.org/10.1016/0022-3093(85)90372-2

Jarrard RD (1986) Relations among subduction parameters. Reviews of Geophysics 24:217–284. https://doi.org/10.1029/RG024i002p00217

Jaupart C, Tait S (1995) Dynamics of differentiation in magma reservoirs. J Geophys Res 100:17615–17636. https://doi.org/10.1029/95JB01239

Kashchiev D (1969) Solution of the non-steady state problem in nucleation kinetics. Surface Science 14:209–220. https://doi.org/10.1016/0039-6028(69)90055-7

Kelley S (2002) K-Ar and Ar-Ar Dating. Reviews in Mineralogy and Geochemistry 47:785–818. https://doi.org/10.2138/rmg.2002.47.17

Keppler H (1996). Constraints from partitioning experiments on the composition of subduction-zone fluids. Nature, 380(6571), 237-240. https://doi.org/10.1038/380237a0

Kirkpatrick RJ (1977) Nucleation and growth of plagioclase, Makaopuhi and Alae lava lakes, Kilauea Volcano, Hawaii. Geol Soc America Bull 88:78. https://doi.org/10.1130/0016-7606(1977)88<78:NAGOPM>2.0.CO;2

Kiser E, Palomeras I, Levander A, et al (2016) Magma reservoirs from the upper crust to the Moho inferred from high-resolution Vp and Vs models beneath Mount St. Helens, Washington State, USA. Geology 44:411–414. https://doi.org/10.1130/G37591.1

Kitayama M, Hirao K, Toriyama M, Kanzaki S (1998) Modeling and simulation of grain growth in Si_3N_4—I. Anisotropic Ostwald ripening. Acta Materiala 46(18):6541-6550. https://doi.org/10.1016/S1359-6454(98)00290-0

Kirkpatrick RJ (1975) Crystal Growth from the Melt: A Review. American Mineralogist 60:798-814.

Laeger K, Petrelli M, Morgavi D, et al (2019) Pre-eruptive conditions and triggering mechanism of the ~ 16 ka Santa Bárbara explosive eruption of Sete Cidades Volcano (São Miguel, Azores). Contrib Mineral Petrol 174:11. https://doi.org/10.1007/s00410-019-1545-y

Larsen HC, Duncan RA, Allan JF, Brooks K (eds) (1999) Proceedings of the Ocean Drilling Program, 163 Scientific Results. Ocean Drilling Program. https://doi.org/10.2973/odp.proc.sr.163.1999

Lasaga AC (1998). Kinetic theory in the earth sciences. Princeton university press. http://www.jstor.org/stable/j.ctt7zvgxm.

Lindoo A, Humphreys MCS, Gordon C et al. (2025). Linking crystal shape and dynamic undercooling: a new framework for inferring magmatic crystallization histories. Contributions to Mineralogy and Petrology 180:92. https://doi.org/10.1007/s00410-025-02278-6

Lloyd AS, Ferriss E, Ruprecht P, et al (2016) An Assessment of Clinopyroxene as a Recorder of Magmatic Water and Magma Ascent Rate. J Petrology 57:1865–1886. https://doi.org/10.1093/petrology/egw058

Lofgren GE, Huss GR, Wasserburg GJ (2006) An experimental study of trace-element partitioning between Ti-Al-clinopyroxene and melt: Equilibrium and kinetic effects including sector zoning. American Mineralogist 91:1596–1606. https://doi.org/10.2138/am.2006.2108

López-Escobar L, Cembrano J, Moreno H Geochemistry and tectonics of the Chilean 80uthern Andes basaltic Quaternary volcanism (37-46°8)

Mangler MF, Humphreys MCS, Geifman E, et al (2023) Melt Diffusion-Moderated Crystal Growth and its Effect on Euhedral Crystal Shapes. Journal of Petrology 64:egad054. https://doi.org/10.1093/petrology/egad054

Marsh BD (1981). On the crystallinity, probability of occurrence, and rheology of lava and magma. Contrib. Mineral. Petrol. 78, 85–98. https://doi.org/10.1007/BF00371146

Marsh BD (1998) On the Interpretation of Crystal Size Distributions in Magmatic Systems. Journal of Petrology 39(4):553-599. https://doi.org/10.1093/petroj/39.4.553

Marsh BD (1988) Crystal size distribution (CSD) in rocks and the kinetics and dynamics of crystallization: I. Theory. Contr Mineral and Petrol 99:277–291. https://doi.org/10.1007/BF00375362

Marsh BD (2004) A magmatic mush column rosetta stone: The McMurdo Dry Valleys of Antarctica. EoS Transactions 85:497–502. https://doi.org/10.1029/2004EO470001

Marsh BD (2015) Chapter 8 - Magma Chambers. In: The Encyclopedia of Volcanoes. Elsevier, pp 185–201. https://doi.org/10.1016/B978-0-12-385938-9.00008-0

Martel C, Schmidt BC (2003) Decompression experiments as an insight into ascent rates of silicic magmas. Contrib Mineral Petrol 144:397–415. https://doi.org/10.1007/s00410-002-0404-3

Martin-Del Pozzo AL, Cifuentes G, Gonzalez E, et al. (2008). Magnetic signatures associated with magma ascent and stagnation at Popocatepetl volcano, Mexico, during 2006. Geological Society London 304: 117-131. https://doi.org/10.1144/SP304.6

McBirney AR (1993). Igneous Petrology, second ed. Jones and Bartlett Pubs., Boston, MA. 508 p.

McKenzie D (1984) The Generation and Compaction of Partially Molten Rock. Journal of Petrology 25:713–765. https://doi.org/10.1093/petrology/25.3.713

Menand T (2008) The mechanics and dynamics of sills in layered elastic rocks and their implications for the growth of laccoliths and other igneous complexes. Earth and Planetary Science Letters 267:93–99. https://doi.org/10.1016/j.epsl.2007.11.043

Miller CF, Wark DA (2008) SUPERVOLCANOES AND THEIR EXPLOSIVE SUPERERUPTIONS. Elements 4:11–15. https://doi.org/10.2113/GSELEMENTS.4.1.11

Miller DM, Goldstein SL; Langmuir CH (1994). Cerium/lead and lead isotope ratios inarc magmas and the enrichment of lead in the continents. Nature 368, 514-520. https://doi.org/ 10.1038/368514a0

Miller RB, Paterson SR (1999) In defense of magmatic diapirs. Journal of Structural Geology 21:1161–1173. https://doi.org/10.1016/S0191-8141(99)00033-4

Mixon EE, Singer BS, Jicha BR, Ramirez A (2021) Calbuco, a monotonous andesitic high-flux volcano in the Southern Andes, Chile. Journal of Volcanology and Geothermal Research 416:107279. https://doi.org/10.1016/j.jvolgeores.2021.107279

Molendijk SM, Namur O, Kamate Kaleghetso E, Mason PR, Smets B, Vander Auwera J, Neave DA (2024). Plumbing system architecture and differentiation processes of the Nyiragongo Volcano, DR Congo. Journal of Petrology, 65(1), egad088. https://doi.org/10.1093/petrology/egad088

Mollo S, Hammer JE (2017) Dynamic crystallization in magmas. In: Heinrich W, Abart R (eds) Mineral reaction kinetics: Microstructures, textures, chemical and isotopic signatures, 1st edn. Mineralogical Society of Great Britain & Ireland, pp 378–418

Montagna CP, Papale P, Longo A (2015) Timescales of mingling in shallow magmatic reservoirs. SP 422:131–140. https://doi.org/10.1144/SP422.6

Morris J, Leeman W, Tera F (1990). The subducted component in island arc lavas: constraints from Be isotopes and B–Be systematics. Nature 344, 31–36. https://doi.org/10.1038/344031a0

Myers ML, Wallace PJ, Wilson CJN, et al (2018) Ascent rates of rhyolitic magma at the onset of three caldera-forming eruptions. American Mineralogist 103:952–965. https://doi.org/10.2138/am-2018-6225

Nabelek PI (1978) Nucleation and growth of plagioclase and the development of textures in a high-alumina basaltic melt. In Lunar and Planetary Science Conference, 9th, Houston, Tex. p.725-741

Namur O, Montalbano S, Bolle O, Vander Auwera J (2020) Petrology of the April 2015 Eruption of Calbuco Volcano, Southern Chile. Journal of Petrology 61:egaa084. https://doi.org/10.1093/petrology/egaa084

Oldenburg CM, Spera FJ, Yuen DA, Sewell G (1989) Dynamic mixing in magma bodies: Theory, simulations, and implications. J Geophys Res 94:9215–9236. https://doi.org/10.1029/JB094iB07p09215

O'Neill C, Spiegelman M (2010). Formulations for simulating the multiscale physics of magma ascent. In A. Dosseto, S. P. Turner, J. A. Van Orman (Eds.), Timescales of magmatic processes: From core to atmosphere (pp. 87–101). Chichester, UK: J. Wiley & Sons. https://doi:10.1002/9781444328509.ch4

Orsi G, De Vita S, Di Vito M (1996) The restless, resurgent Campi Flegrei nested caldera (Italy): constraints on its evolution and configuration. Journal of Volcanology and Geothermal Research 74:179–214. https://doi.org/10.1016/S0377-0273(96)00063-7

Pamukcu AS, Gualda GAR, Bégué F, Gravley DM (2015) Melt inclusion shapes: Timekeepers of short-lived giant magma bodies. Geology 43:947–950. https://doi.org/10.1130/G37021.1

Parrish RR (1990a) U–Pb dating of monazite and its application to geological problems. Can J Earth Sci 27:1431–1450. https://doi.org/10.1139/e90-152

Parrish RR (1990b) U–Pb dating of monazite and its application to geological problems. Can J Earth Sci 27:1431–1450. https://doi.org/10.1139/e90-152

Paterson SR, Okaya D, Memeti V, et al (2011) Magma addition and flux calculations of incrementally constructed magma chambers in continental margin arcs: Combined field, geochronologic, and thermal modeling studies. Geosphere 7:1439–1468. https://doi.org/10.1130/GES00696.1

Paulatto M, Hooft EE, Chrapkiewicz K et al. (2022). Advances in seismic imaging of magma and crystal mushes. Front. Earth Sci. 10. https://doi.org/10.3389/feart.2022.970131

Pearce JA, Parkinson IJ (1993) Trace element models for mantle melting: application to volcanic arc petrogenesis. SP 76:373–403. https://doi.org/10.1144/GSL.SP.1993.076.01.19

Pec M, Holtzman BK, Zimmerman M, Kohlstedt DL (2015) Reaction infiltration instabilities in experiments on partially molten mantle rocks. Geology 43:575–578. https://doi.org/10.1130/G36611.1

Pérez-Flores P, Cembrano J, Sánchez-Alfaro P, et al (2016) Tectonics, magmatism and paleo-fluid distribution in a strike-slip setting: Insights from the northern termination of the Liquiñe–Ofqui fault System, Chile. Tectonophysics 680:192–210. https://doi.org/10.1016/j.tecto.2016.05.016

Perugini D, De Campos CP, Petrelli M, et al (2015) Quantifying magma mixing with the Shannon entropy: Application to simulations and experiments. Lithos 236–237:299–310. https://doi.org/10.1016/j.lithos.2015.09.008

Petford N (2003) Rheology of Granitic Magmas During Ascent and Emplacement. Annu Rev Earth Planet Sci 31:399–427. https://doi.org/10.1146/annurev.earth.31.100901.141352

Petford N, Clemens JD (2000) Granites are not diapiric! Geology Today 16:180–184. https://doi.org/10.1111/j.1365-2451.2000.00008.x

Petrelli M, El Omari K, Le Guer Y, Perugini D (2016) Effects of chaotic advection on the timescales of cooling and crystallization of magma bodies at mid crustal levels. Geochem Geophys Geosyst 17:425–441. https://doi.org/10.1002/2015GC006109

Petrelli M, El Omari K, Spina L, et al (2018) Timescales of water accumulation in magmas and implications for short warning times of explosive eruptions. Nat Commun 9:770. https://doi.org/10.1038/s41467-018-02987-6

Petrelli M, Zellmer GF (2021) Rates and Timescales of Magma Transfer, Storage, Emplacement, and Eruption. In: Vetere F (ed) Geophysical Monograph Series, 1st edn. Wiley, pp 1–41. https://doi.org/ 10.1002/9781119521143.ch1

Philpotts AR, Shi J, Brustman C (1998) Role of plagioclase crystal chains in the differentiation of partly crystallized basaltic magma. Nature 395:343–346. https://doi.org/10.1038/26404

Pichavant M, Martel C, Bourdier J, Scaillet B (2002) Physical conditions, structure, and dynamics of a zoned magma chamber: Mount Pelée (Martinique, Lesser Antilles Arc). J Geophys Res 107:. https://doi.org/10.1029/2001JB000315

Pitcher WS (1979) The nature, ascent and emplacement of granitic magmas. JGS 136:627–662. https://doi.org/10.1144/gsjgs.136.6.0627

Plank T, Langmuir CH (1988) An evaluation of the global variations in the major element chemistry of arc basalts. Earth and Planetary Science Letters 90:349–370. https://doi.org/10.1016/0012-821X(88)90135-5

Porter DA, Easterling KE (2009). Phase transformations in metals and alloys (Revised Reprint) (3rd ed.). CRC press. https://doi.org/10.1201/9781439883570

Pritchard ME, Simons M (2004) An InSAR-based survey of volcanic deformation in the central Andes. Geochem Geophys Geosyst 5:2003GC000610. https://doi.org/10.1029/2003GC000610

Pupier E, Duchene S, Toplis MJ (2008) Experimental quantification of plagioclase crystal size distribution during cooling of a basaltic liquid. Contrib Mineral Petrol 155:555–570. https://doi.org/10.1007/s00410-007-0258-9

Putirka KD (2017) Down the Crater: Where Magmas are Stored and Why They Erupt. ELEMENTS 13:11–16. https://doi.org/10.2113/gselements.13.1.11

Pyle DM (1992) The volume and residence time of magma beneath active volcanoes determined by decay-series disequilibria methods. Earth and Planetary Science Letters 112:61–73. https://doi.org/10.1016/0012-821X(92)90007-I

Rapp RP, Watson EB (1995) Dehydration Melting of Metabasalt at 8–32 kbar: Implications for Continental Growth and Crust-Mantle Recycling. Journal of Petrology 36:891–931. https://doi.org/10.1093/petrology/36.4.891

Reid MR (2003). Timescales of Magma Transfer and Storage in the Crust, Treatise on Geochemistry. In The crust, Treatise on geochemistry (Vol. *3*–9, pp. 1–27). https://doi.org/10.1016/B0-08043751-6/03022-X

Reubi O, Blundy J (2009) A dearth of intermediate melts at subduction zone volcanoes and the petrogenesis of arc andesites. Nature 461:1269–1273. https://doi.org/10.1038/nature08510

Reubi O, Scott SR, Sims KWW (2017) Evidence of Young Crystal Ages in Andesitic Magmas from a Hyperactive Arc Volcano—Volcan de Colima, Mexico. Journal of Petrology 58:261–276. https://doi.org/10.1093/petrology/egx015

Ruprecht P, Cooper KM (2012) Integrating the Uranium-Series and Elemental Diffusion Geochronometers in Mixed Magmas from Volcán Quizapu, Central Chile. Journal of Petrology 53:841–871. https://doi.org/10.1093/petrology/egs001

Rusiecka MK, Bilodeau M, Baker DR (2020) Quantification of nucleation delay in magmatic systems: experimental and theoretical approach. Contrib Mineral Petrol 175:47. https://doi.org/10.1007/s00410-020-01682-4

Rutherford MJ (2008a) Magma Ascent Rates. Reviews in Mineralogy and Geochemistry 69:241–271. https://doi.org/10.2138/rmg.2008.69.7

Rutherford MJ (2008b) Magma Ascent Rates. Reviews in Mineralogy and Geochemistry 69:241–271. https://doi.org/10.2138/rmg.2008.69.7

Rutherford MJ (1993) Experimental petrology applied to volcanic processes. EoS Transactions 74:49–55. https://doi.org/10.1029/93EO00142

Rutherford MJ, Devine JD (2003) Magmatic Conditions and Magma Ascent as Indicated by Hornblende Phase Equilibria and Reactions in the 1995±2002 SoufrieÁ re Hills Magma. 44:

Saracino F, Charlier B, Zhang Y, et al (2025) The role of sulfur on the liquidus temperature and olivine-orthopyroxene equilibria in highly reduced magmas. Chemical Geology 683:122777. https://doi.org/10.1016/j.chemgeo.2025.122777

Sato H (1995) Textural difference between pahoehoe and aa lavas of Izu-Oshima volcano, Japan — an experimental study on population density of plagioclase. Journal of Volcanology and Geothermal Research 66:101–113. https://doi.org/10.1016/0377-0273(94)00055-L

Schmitt AK (2011) Uranium Series Accessory Crystal Dating of Magmatic Processes. Annu Rev Earth Planet Sci 39:321–349. https://doi.org/10.1146/annurev-earth-040610-133330

Schmitt AK, Stockli DF, Hausback BP (2006) Eruption and magma crystallization ages of Las Tres Vírgenes (Baja California) constrained by combined 230Th/238U and (U–Th)/He dating of zircon. Journal of Volcanology and Geothermal Research 158:281–295. https://doi.org/10.1016/j.jvolgeores.2006.07.005

Schmitt AK, Stockli DF, Niedermann S, et al (2010) Eruption ages of Las Tres Vírgenes volcano (Baja California): A tale of two helium isotopes. Quaternary Geochronology 5:503–511. https://doi.org/10.1016/j.quageo.2010.02.004

Shea T, Hammer JE (2013) Kinetics of cooling- and decompression-induced crystallization in hydrous mafic-intermediate magmas. Journal of Volcanology and Geothermal Research 260:127–145. https://doi.org/10.1016/j.jvolgeores.2013.04.018

Shuster DL, Vasconcelos PM, Heim JA, Farley KA (2005) Weathering geochronology by (U-Th)/He dating of goethite. Geochimica et Cosmochimica Acta 69:659–673. https://doi.org/10.1016/j.gca.2004.07.028

Siebert L, Simkin T, Kimberly P. (2010). Volcanoes of the World. Univ of California Press.

Siebert L, Cottrell E, Venzke E, Andrews B (2015) Earth's Volcanoes and Their Eruptions: An Overview. In: The Encyclopedia of Volcanoes. Elsevier, pp 239–255

Simmons WmBS, Webber KL (2008) Pegmatite genesis: state of the art. ejm 20:421–438. https://doi.org/10.1127/0935-1221/2008/0020-1833

Sisson TW, Ratajeski K, Hankins WB, Glazner AF (2005) Voluminous granitic magmas from common basaltic sources. Contrib Mineral Petrol 148:635–661. https://doi.org/10.1007/s00410-004-0632-9

Slezov VV, Schmelzer J (2002) Kinetics of formation of a phase with an arbitrary stoichiometric composition in a multicomponent solid solution. Phys Rev E 65:031506. https://doi.org/10.1103/PhysRevE.65.031506

Smith RL (1979) Ash-flow magmatism. In: Chapin CE, Elston WE (eds) Ash-Flow Tuffs. Geological Society of America, pp 5–28. https://doi.org/10.1130/SPE180-p5

Sparks RSJ, Pinkerton H, Macdonald R (1977) The transport of xenoliths in magmas. Earth and Planetary Science Letters 35:234–238. https://doi.org/10.1016/0012-821X(77)90126-1

Sparks RSJ, Cashman KV (2017) Dynamic Magma Systems: Implications for Forecasting Volcanic Activity. ELEMENTS 13:35–40. https://doi.org/10.2113/gselements.13.1.35

Sparks RSJ, Annen C, Blundy JD, Cashman KV, Rust AC, Jackson MD (2019). Formation and dynamics of magma reservoirs. Philos. Trans. R. Soc. A 377(2139), 20180019. https://doi.org/10.1098/rsta.2018.0019

Stern CR (2004) Active Andean volcanism: its geologic and tectonic setting. Rev geol Chile 31:. https://doi.org/10.4067/S0716-02082004000200001

Stern CR, Moreno H, López-Escobar L, et al (2007) Chilean volcanoes. In: Moreno T, Gibbons W (eds) The Geology of Chile, First. The Geological Society of London, pp 147–178. https://doi.org/ https://doi.org/10.1144/GOCH

Stolper E, Newman S (1994) The role of water in the petrogenesis of Mariana trough magmas. Earth and Planetary Science Letters 121:293–325. https://doi.org/10.1016/0012-821X(94)90074-4

Stothers RB (1984) The Great Tambora Eruption in 1815 and Its Aftermath. SCIENCE 224 (4654):1191-1198. https://doi.org/10.1126/science.224.4654.1191

Sunagawa I (1981) Characteristics of crystal growth in nature as seen from the morphology of mineral crystals. bulmi 104:81–87. https://doi.org/10.3406/bulmi.1981.7438

Swanson SE (1977) Relation of nucleation and crystal-growth rate to the development of granitic textures. American Mineralogist 62(9-10):966-978.

Symonds RB, Rose WI, Bluth GJS, Gerlach TM (1994) Chapter 1. Volcanic-gas studies: Methods, results, and applications. Mineralogical Society of America, 30, 1-66.

Tait S, Jaupart C, Vergniolle S (1989) Pressure, gas content and eruption periodicity of a shallow, crystallising magma chamber. Earth and Planetary Science Letters 92:107–123. https://doi.org/10.1016/0012-821X(89)90025-3

Tatsumi Y, Kogiso T (2003) The subduction factory: its role in the evolution of the Earth's crust and mantle. SP 219:55–80. https://doi.org/10.1144/GSL.SP.2003.219.01.03

Taylor S, McLennan S The Composition and Evolution of the Continental Crust. In Planetary Crusts: Their Composition, Origin and Evolution. Cambridge Planetary Science.301:324

Teng HH (2013) How Ions and Molecules Organize to Form Crystals. Elements 9:189–194. https://doi.org/10.2113/gselements.9.3.189

Tiller WA (1963). Principles of solidification. In The Art and Science of Growing Crystals, J. J. Gilman, (ed.), John Wiley, New York.

Tiller WA (1977). On the cross-pollination of crystallization ideas between metallurgy and geology. Physics and chemistry of minerals 2:125-151. https://doi.org/10.1007/BF00307528

Toramaru A (2006) BND (bubble number density) decompression rate meter for explosive volcanic eruptions. Journal of Volcanology and Geothermal Research 154:303–316. https://doi.org/10.1016/j.jvolgeores.2006.03.027

Toramaru A (2025) The theoretical basis for textural indices of eruption dynamics: review and new conceptual models. Earth Planets Space 77:27. https://doi.org/10.1186/s40623-025-02146-4

Toramaru A, Kichise T (2023) A New Model of Crystallization in Magmas: Impact of Pre-Exponential Factor of Crystal Nucleation Rate on Cooling Rate Exponent and Log-Linear Crystal Size Distribution. JGR Solid Earth 128:e2023JB026481. https://doi.org/10.1029/2023JB026481

Toramaru A, Noguchi S, Oyoshihara S, Tsune A (2008) MND(microlite number density) water exsolution rate meter. Journal of Volcanology and Geothermal Research 175:156–167. https://doi.org/10.1016/j.jvolgeores.2008.03.035

Towers H, Chipman J (1957) Diffusion of Calcium and Silicon in a Lime-Alumina-Silica Slag. JOM 9:769–773. https://doi.org/10.1007/BF03377932

Tsuchiyama A (1983) Crystallization kinetics in the system $CaMgSi_2O_6$-$CaAl_2Si_2O_8$: the delay in nucleation of diopside and anorthite. American Mineralogist 68:687-698.

Turekian KK, Holland HD (2013) Treatise on geochemistry, second edition, Elsevier.

Turner MB, Reagan MK, Turner SP, et al (2013) Timescales of magma degassing — Insights from U-series disequilibria, Mount Cameroon, West Africa. Journal of Volcanology and Geothermal Research 262:38–46. https://doi.org/10.1016/j.jvolgeores.2013.06.003

Turner S, Hawkesworth C, Van Calsteren P, et al (1996) U-series isotopes and destructive plate margin magma genesis in the Lesser Antilles. Earth and Planetary Science Letters 142:191–207. https://doi.org/10.1016/0012-821X(96)00078-7

Turner S, Hawkesworth C (1997) Constraints on flux rates and mantle dynamics beneath island arcs from Tonga–Kermadec lava geochemistry. Nature 389:568–573. https://doi.org/10.1038/39257

Turner S, Hawkesworth C, Rogers N, et al. (1997) ^{238}U-^{230}Th disequilibria, magma petrogenesis, and flux rates beneath the depleted Tonga-Kermadec island arc. Geochimica et Cosmochimica Acta 61(22):4855-4884. https://doi.org/10.1016/S0016-7037(97)00281-0

Turner S, Costa F (2007) Measuring Timescales of Magmatic Evolution. Elements 3:267–272. https://doi.org/10.2113/gselements.3.4.267

Van Den Eeckhout B, Grocott J, Vissers R (1986). On the role of diapirism in the segregation, ascent and final emplacement of granitoid magmas discussion. Tectonophysics, 127, 161–166.

Vander Auwera J, Montalbano S, Namur O, et al (2021) The petrology of a hazardous volcano: Calbuco (Central Southern Volcanic Zone, Chile). Contrib Mineral Petrol 176:46. https://doi.org/10.1007/s00410-021-01803-7

Vetere F, Iezzi G, Behrens H, et al (2013) Intrinsic solidification behaviour of basaltic to rhyolitic melts: A cooling rate experimental study. Chemical Geology 354:233–242. https://doi.org/10.1016/j.chemgeo.2013.06.007

Vetere F, Merseburger S, Pisello A, et al (2024) The role of deformation on the early crystallization and rheology of basaltic liquids. Earth and Planetary Science Letters 644:118934. https://doi.org/10.1016/j.epsl.2024.118934

Volmer M, Weber A (1926). Keimbildung in übersättigten Gebilden. Zeitschrift für physikalische Chemie, 119(1), 277-301.

Volpe AM, Hammond PE (1991) 238U230Th226Ra disequilibria in young Mount St. Helens rocks: time constraint for magma formation and crystallization. Earth and Planetary Science Letters 107:475–486. https://doi.org/10.1016/0012-821X(91)90094-X

Vona A, Romano C (2013) The effects of undercooling and deformation rates on the crystallization kinetics of Stromboli and Etna basalts. Contrib Mineral Petrol 166:491–509. https://doi.org/10.1007/s00410-013-0887-0

Walker D, Kirkpatrick RJ, Longhi J, Hays JF (1976) Crystallization history of lunar picritic basalt sample 12002: Phase-equilibria and cooling-rate studies. Geol Soc America Bull 87:646. https://doi.org/10.1130/0016-7606(1976)87<646:CHOLPB>2.0.CO;2

Wallace PJ, Edmonds M (2011) The Sulfur Budget in Magmas: Evidence from Melt Inclusions, Submarine Glasses, and Volcanic Gas Emissions. Reviews in Mineralogy and Geochemistry 73:215–246. https://doi.org/10.2138/rmg.2011.73.8

Wallace PJ, Plank T, Edmonds M, Hauri EH (2015). Volatiles in magmas. In The encyclopedia of volcanoes (pp. 163-183). Academic Press.

Wark, D., Kempter, K. & McDowell, F. Evolution of waning, subduction-related magmatism, northern Sierra Madre Occidental, Mexico. Geol. Soc. Am. Bull. 102: 1555–1564. https://doi.org/10.1130/0016-7606(1990)102%3C1555:EOWSRM%3E2.3.CO;2

Welsch B, Faure F, Famin V, et al (2013) Dendritic Crystallization: A Single Process for all the Textures of Olivine in Basalts? Journal of Petrology 54:539–574. https://doi.org/10.1093/petrology/egs077

Whittington CS, Park Y-R, Brophy JG (1999) Sector-zoned augite megacrysts in Aleutian high alumina basalts: implications for the conditions of basalt crystallization and the generation of calc-alkaline series magmas. Contributions to Mineralogy and Petrology 135:277–290. https://doi.org/10.1007/s004100050512

Yoshida K, Miyake A, Okumura SH, et al (2023) Oxidation-induced nanolite crystallization triggered the 2021 eruption of Fukutoku-Oka-no-Ba, Japan. Sci Rep 13:7117. https://doi.org/10.1038/s41598-023-34301-w

Žák J, Paterson SR (2006) Roof and walls of the Red Mountain Creek pluton, eastern Sierra Nevada, California (USA): implications for process zones during pluton emplacement. Journal of Structural Geology 28:575–587. https://doi.org/10.1016/j.jsg.2005.12.017

Zellmer G, Turner S, Hawkesworth C (2000) Timescales of destructive plate margin magmatism: new insights from Santorini, Aegean volcanic arc. Earth and Planetary Science Letters 174:265–281. https://doi.org/10.1016/S0012-821X(99)00266-6

Zellmer GF, Annen C (2008) An introduction to magma dynamics. SP 304:1–13. https://doi.org/10.1144/SP304.1

Zellmer GF, Annen C, Charlier BLA, et al (2005) Magma evolution and ascent at volcanic arcs: constraining petrogenetic processes through rates and chronologies. Journal of Volcanology and Geothermal Research 140:171–191. https://doi.org/10.1016/j.jvolgeores.2004.07.020

Chapter II

Methodology

Introduction

Most metamorphic and magmatic processes occur under pressure–temperature conditions and over timescales that prevent direct observation. Experimental petrology provides a controlled framework to reproduce these conditions by controlling pressure, temperature, and oxygen fugacity, in order to investigate the mechanisms governing rock formation. It therefore provides a necessary complement to natural petrology.

Depending on the objectives, experiments can be characterized using 3D/4D techniques, which allow complete visualization of the crystal cargo, or by indirect 2D observations on polished sections. These approaches enable the extraction of key textural parameters such as crystal number density, size, and shape, which are essential for constraining crystallization processes including nucleation and growth rates, clustering, and melt-inclusion entrapment.

Although crystallization parameters have been extensively studied in basaltic (e.g., *Kirkpatrick 1977*; *Cashman 1993*; *Lesher et al. 1999*; *Pupier et al. 2008*) and, to a lesser extent, in dacitic compositions (*Brugger and Hammer 2010a, b*), fewer datasets exist for intermediate basaltic-andesitic to andesitic compositions, which are typical of subduction-zone magmatism (*Shea and Hammer 2013*; *Vetere et al. 2021*). Recent growth-rate determinations for basaltic-andesitic melts (*Billon et al. 2025*; *Billon et al., in review*) now allow comparison with previously reported basaltic (10^{-9}–10^{-6} cm·s^{-1}) and dacitic (10^{-11}–10^{-8} cm·s^{-1}) values.

This chapter is dedicated to presenting experimental procedures and analytical techniques, including BSE images segmentation, the CSD method, EDS and WDS analyses, and EBSD techniques. A detailed description of the 1-atmosphere furnace used in **Chapters III** and **IV** is also provided. Some details from the subsequent chapters are repeated here for clarity and further explanation.

Experimental Procedure

Anhydrous experiments at 1 atmosphere

The 80 experiments in this study were performed using the 1-atm GERO gas-mixture vertical furnace at the University of Liège (ULiège) under Ni–NiO buffer conditions. Experiments at atmospheric pressure are classified as “dry” and are particularly suited for investigating the formation of volcanic rocks and those crystallizing under shallow crustal conditions. In several studies, such experiments are also employed as an initial step before using hydrated or higher-pressure conditions.

Presentation of the ULiege vertical furnace

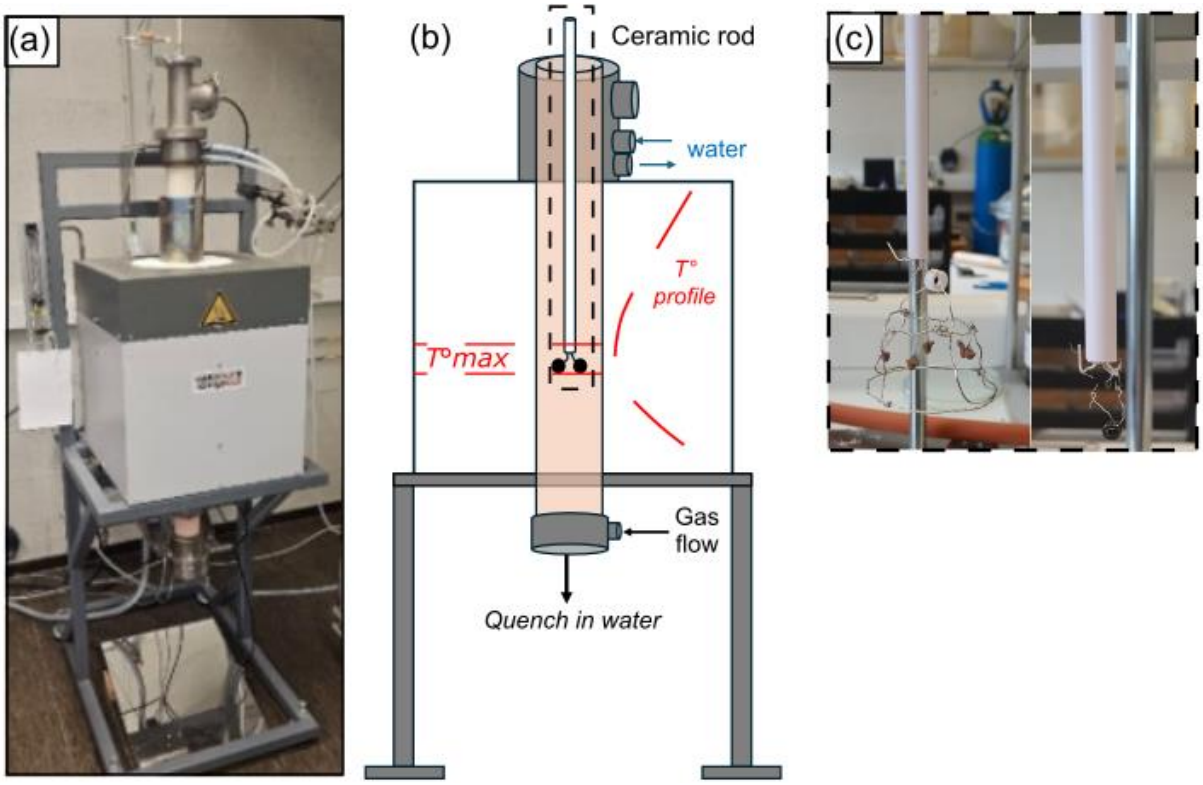

***Figure II-1**: Image and schematic representation of the 1-atm furnace in the experimental laboratory of the University of Liège (a and b). The temperature profile and the position of the maximum temperature are also shown (b). (c) Ceramic rod with several aliquots of starting material on the left (grouped with a platinum holder), and the final quenched glass on the right (black spherical run).*

This type of quenching furnace consists of a "ceramic tube" vertical box furnace where an alumina/mullite ceramic tube runs through the entire furnace from top to bottom (**Figure II-1a and b**). Heating is provided by U-shaped resistances. The global concept of this method was initially described by *Faust (1936)* and *Schairer (1959)*. A multiple-bore ceramic rod containing samples and thermocouple is introduced from the top (**Figure II-1c**). The temperature within the furnace is measured with an S-type ($Pt_{90}Rh_{10}$-Pt: 0 to 1450 °C; *Roeser 1941*) thermocouple attached to the bottom end of the ceramic rode, approximately 1cm above the suspension. The thermocouple was originally calibrated by measuring melting points of pure *Ag* and *Au,* which have melting temperatures of 960.8 and 1062.6 °C. An additional monitor near the furnace allows control of the internal temperature and programming of various cooling paths. In agreement with the oxygen fugacity conditions relevant to the plumbing systems of the three volcanoes studied (*Morgado et al. 2015*; *Vander Auwera et al. 2021*; *Bechon et al. 2022*), all experiments were performed in a controlled atmosphere close to the Ni–NiO buffer, achieved using a constant CO–CO_2 gas mixture. Various sample holders can be used, such as

sealed inert capsules, open crucibles, or also suspended wire loops in our case. Experiments are quenched by dropping them into a cold-water bath, or only by removing them out of the furnace. Because our samples are very small (2D sections of 2 – 3 millimeters), quenching in water or in air has a similar effect (*Xu and Zhang 2002*).

Preliminary calibrations

Calibration in temperature

Although this method is relatively easy to implement, two major issues can arise. First, the furnace is subject to a thermal gradient along the ceramic tube, which can affect crystal growth experiments by inducing temperature variations, particularly in centimetre-scale samples. It is therefore necessary to determine the extent of the hot-spot region corresponding to an isothermal zone. This is achieved by setting a fixed temperature in the furnace and measuring the temperature at different heights using a thermocouple attached to the ceramic rod. In our case, the hot spot extends over approximately 5 cm (see **Figure II-2a**). *Biggar and O'Hara (1969)* reported that the hot-spot position may shift during the lifetime of a furnace, requiring periodic verification. The second major issue concerns the divergence between the temperature indicated by the furnace controller and the temperature measured inside the furnace. A calibration curve (**Figure II-2b**) was established by measuring these differences at nominal temperatures ranging from 800 °C to 1400 °C. The deviation was found to increase linearly with temperature.

***Figure II-2 (see below)**: Temperature calibration inside the furnace. (a) Determination of the hot-spot position (constant temperature over several centimetres). (b) Calibration regression line showing the deviation between the temperature setpoint and the temperature actually measured. Note that the deviation increases from about 7 °C at 1000–1050 °C to 23–27 °C between 1300 and 1400 °C.*

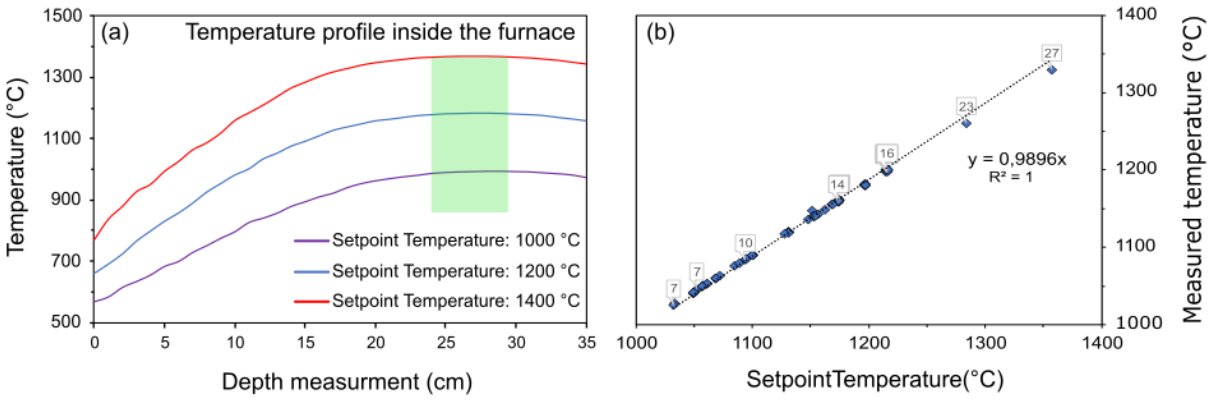

fO_2 calibration

The fO_2 calibration at the Ni-NiO buffer was performed using a zirconia probe. The zirconia (ZrO_2) probe operates according to the Nernst equation, which relates its electromotive force (E, in volts) to the oxygen fugacity difference between two gases (reference gas vs. experimental gas):

$$E = \frac{R \times T}{4 \times F} \times \ln\left(\frac{fO_2^{ref}}{fO_2^{exp}}\right) \quad (1)$$

where R is the universal gas constant (8.314 J mol^{-1} K^{-1}), T is the temperature (K), and F is the Faraday constant (96 485 C mol^{-1}). The reference gas in this setup is air (fO_2 = 0.21 bar). **Figure II-3** shows the evolution of the measured emf at different gas flow rates (100, 150, 200, 250, and 300 cm^3/min). Although the Ni–NiO buffer is often assumed to correspond to FMQ + 1, its position shifts slightly with temperature. At 1200 °C, our calibration temperature, a log fO_2 value of about −7.73 (Ni-NiO = QFM + 0.68; $fO_2 = 10^{-7.7}$) is expected for the Ni–NiO buffer (**Figure II-3**; *O'Neill and Pownceby 1993*). A gas flow rate of 200 cm^3/min was chosen as a compromise to limit gas consumption (especially CO_2) while minimizing the deviation between the measured and theoretical log fO_2 values (**Table II-1**).

Log fO_2 FMQ (Oneill)	-8,41	**Ni-NiO = QFM + 0.68**		
Température (°C)	1200	(1473,15 K)		
Flow (cm^3/min)	emf (mV)	logfO_2	ΔFMQ	différence
100	476,7	-7,2	1,21	0,53
150	481	-7,25	1,16	0,48
200	**482**	**-7,27**	**1,14**	**0,46**
300	484,8	-7,31	1,1	0,42
350	485	-7,31	1,1	0,42

Table II-1 *: Summary of the EMF values, along with log fO_2 and ΔQFM, as a function of the CO–CO_2 gas flow rate. The selected value (200 cm^3/min) is highlighted in red.*

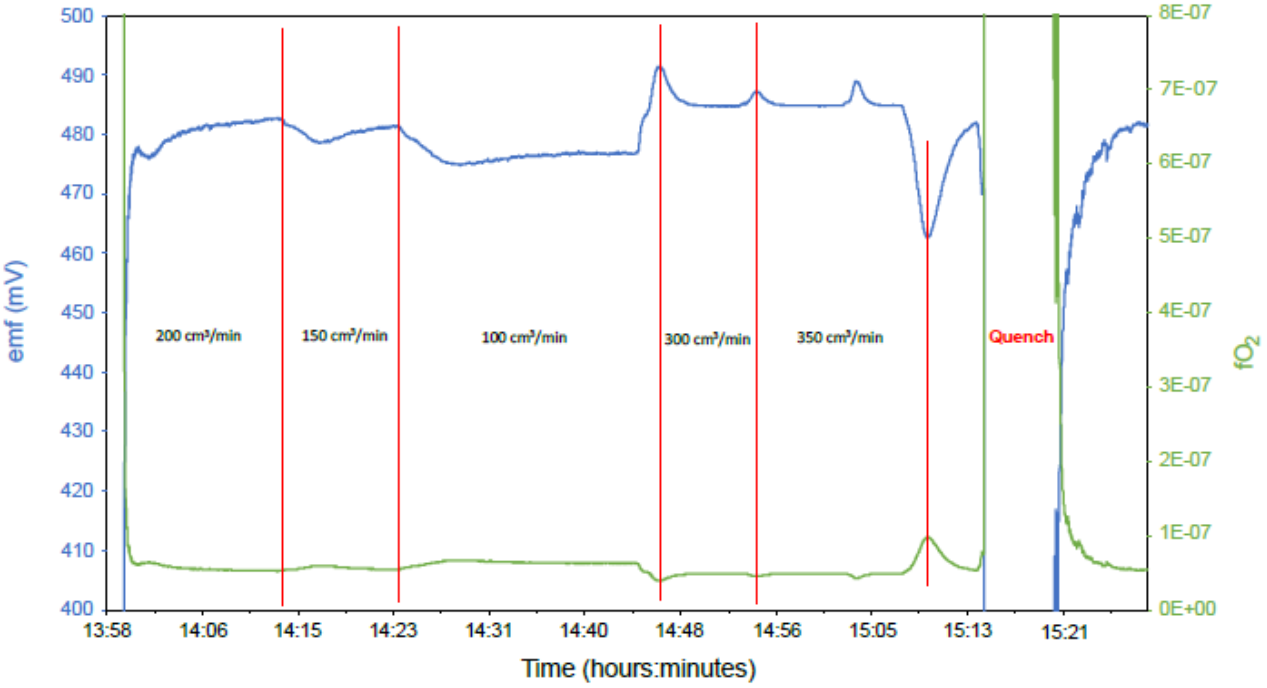

Figure II-3*: Evolution of the electromotive force (emf) and fO_2 associated in function of the gas flow rate (cm^3/min) and time.*

A final issue concerns the fO_2 evolution with temperature and time, which makes it difficult to adjust during overnight runs. As shown in **Table II-2**, the change in fO_2 with temperature results in a relative difference of up to 0.087 between 1190 °C, corresponding to the starting temperature of many runs in this study, and the lowest quenching temperature at 1000 °C (ΔQFM = 0.68 and 0.767 at 1190 and 1000 °C, respectively). This evolution, and its regulation via the CO/CO_2 gas flow, remain minimal and require only a 2 cm^3/min adjustment

(**Table II-2**). Considering the different cooling rates used (1, 3, 9, 25, 125 °C/h), we conclude that it does not pose any issue.

Température (°C)	ΔQFM	($\Delta QFM_{T°C}$ - $\Delta QFM_{1190°C}$)	fO2	log(fO_2)	CO[a]	CO_2[a]
1190	0,68		1,4E-08	-7,85	4,31	195,69
1180	0,684	0,004	1,1E-08	-7,96	4,2	195,8
1170	0,6925	0,0125	8,4E-09	-8,08	4,07	195,93
1160	0,6985	0,0185	6,4E-09	-8,19	3,96	196,04
1150	0,704	0,024	4,9E-09	-8,31	3,85	196,15
1140	0,709	0,029	3,7E-09	-8,43	3,74	196,26
1130	0,713	0,033	2,8E-09	-8,56	3,63	196,37
1120	0,718	0,038	2,1E-09	-8,68	3,53	196,47
1110	0,724	0,044	1,6E-09	-8,81	3,42	196,58
1100	0,728	0,048	1,2E-09	-8,94	3,32	196,68
1050	0,743	0,063	2,5E-10	-9,61	2,86	197,14
1000	0,767	0,087	4,7E-11	-10,33	2,4	197,6

[a]: *gas flow in cm^3/min*

***Table II-2**: Evolution of fO_2 and gas flow (in cm^3/min) as a function of temperature. Under Ni–NiO conditions, the major component remains CO_2 (from 97% to 99% of the total gas flow at 1190 and 1000 °C, respectively).*

Selection and preparation of the starting material

Selection of the starting composition

The samples from our three volcanoes (Osorno, Calbuco, and Villarrica) exhibit a wide range of chemical compositions, from basalts (the most primitive rocks) to dacites (more evolved; see **Chapter V**). This chemical diversity is reflected in the nature and abundance of crystals, including olivine, plagioclase, and pyroxene. Basaltic andesites (52–57 wt.% SiO_2) and andesites (57–63 wt.% SiO_2), corresponding to intermediate compositions, are common compositions in arc magmas (*Reubi and Blundy 2009*; *Kent et al. 2010*; *Bechon et al. 2022*).

Simulations at 1 atm and Ni–NiO/FMQ oxygen fugacity were performed using *Rhyolite-MELTS v. 1.2.0* (*Gualda et al. 2012*) to model mineral saturation temperatures, particularly for plagioclase, across a range of basaltic-andesitic compositions (

Table *II-3*). The plagioclase saturation temperature varies considerably among samples, from 1175 °C to above 1200 °C.

These variations can be partially attributed to differences in CaO and Na_2O concentrations: a higher CaO relative to Na_2O (i.e., an increase in CaO / [CaO + Na_2O]) tends to raise the plagioclase saturation temperature. Conversely, other elements such as MgO or FeO(t) tend to lower the saturation temperature, helping to explain the observed variations.

The starting composition for all our experiments was selected to achieve a moderate plagioclase saturation temperature while also considering the phenocryst content. *OS36* was chosen as the experimental starting material because it combines a moderate saturation temperature with a low crystal content (9 % crystals, including only 2 % plagioclase macrocrysts >300 µm), facilitating partial dissolution of pre-existing crystals without requiring excessively high temperatures. Moreover, its composition is representative of basaltic-andesitic magmas typical of the volcanic arc under study, ensuring that the experimental conditions remain relevant to natural systems.

Compo (wt. %)	**OS36**	**OS78**	**OS07**	**OS142**	**OS13**	**CL01**	**CL15**
SiO_2	56.94	55.81	55.59	58.05	54.66	55.51	55.93
TiO_2	1.30	1.18	1.16	1.02	1.42	0.75	0.92
Al_2O_3	16.27	17.78	17.23	17.70	16.22	18.96	19.07
Fe_2O_3	10.63	9.40	9.97	9.35	11.46	7.29	8.00
Cr_2O_3	0.00	0.00	0.00	0.00	0.00	0.00	0.00
MnO	0.18	0.16	0.16	0.16	0.18	0.13	0.14
MgO	2.79	2.93	3.37	2.82	3.76	3.85	3.49
NiO	0.00	0.00	0.00	0.00	0.00	0.00	0.00
CaO	6.39	7.72	7.98	6.83	7.74	8.55	7.69
Na_2O	4.32	3.97	3.51	3.96	3.44	3.49	3.83
K_2O	0.91	0.81	0.83	0.87	0.87	0.85	0.68
P_2O_5	0.26	0.24	0.21	0.23	0.24	0.2	0.14
H_2O	0.00	0.00	0.00	0.00	0.00	0.00	0.00
Total	*99.99*	*100*	*100.01*	*100.99*	*99.99*	*99.58*	*99.89*
Ca/(Ca+Na)	*0.60*	*0.66*	*0.69*	*0.63*	*0.69*	*0.71*	*0.67*
$T_{sat,\ Plg}$ (°C)	1175	> 1200	1195	1185	1180	> 1200	> 1200

***Table II-3**: Summary of the chemical compositions of various basaltic-andesitic samples and the corresponding plagioclase saturation temperatures for each sample (estimated using MELTS v. 1.2.0; Gualda et al. 2012). Red values refer to the selected sample (OS36).*

Preparation of the starting material

The procedure is described in **Chapters III** (*Billon et al. 2025*) and **IV**, but it is reiterated here for convenience. To prepare the starting glasses, the rock sample was first crushed with a hammer and then ground to a fine powder in an agate mortar using a Fritsch Pulverisette planetary mill (*Bechon et al. 2022*). The resulting fine, homogeneous powder was pressed into pellets (1–3 mm in diameter) and mounted on 0.2-mm-diameter Pt wire loops (**Figure II-1c**). Since initial substrates (microscopic gas bubbles or pre-existing crystal fragments) can significantly influence nucleation processes, they were either partially heated at 1190 °C for 24 hours ($+\Delta T$ = 15 °C; sufficient to preserve a minimal amount of plagioclase fragments) or fully dissolved by heating at 1450 °C for 2 hours to obtain a crystal-free glass (OS36*), depending on the experimental conditions. Pt wire loops were previously equilibrated with material of the same composition as the experimental charge, at the target temperature and oxygen fugacity (Ni + $1/2O_2$ = NiO equilibrium, NiNiO) for 24 hours to minimize iron loss during the experiments (*Grove 1981*; *Pupier et al. 2008*). Before each experiment, the assemblage was heated in a muffle furnace for 10–15 minutes to sinter the powder (**Figure II-1c**).

Crystallization path

As suggested by *Pupier et al. (2008)*, to focus on plagioclase crystals and simplify their segmentation and separation, experiments were designed to limit crystallization to 40-50% (see G 3-5 and 3-6 runs in ***Supplementary file II-1***). The plagioclase liquidus temperature and crystallization evolution were modeled using Rhyolite-MELTS v.1.2.0 (*Gualda et al. 2012*) and estimated to be around 1175 °C (

Table *II-3*). This model was tested during isothermal experiments maintained at various temperatures from 1200 to 1150 °C for 24 hours; using OS36* powder (see **Chapter III**; *Billon et al. 2025*). Most of our experiments correspond to cooling crystallization paths divided into 3 stages:

- An initial incubation time: 24 hours at various positions relative to the liquidus temperature.
- A cooling ramp at various rates: 1, 3, 9, 25 and 125 °C/h for OS36, and 1, 9, 25 and 125 °C/h for OS36*. Samples were quenched at various crystallization temperatures ranging from 1175 to 1000 °C.

- Additional potential isothermal steps at the final temperature to study maturation processes and relaxation time.

To investigate the influence of parameters such as overheating degree ($+\Delta T$), and also relaxation time on nucleation and growth processes, modifications were applied to these stages (more explanation are provided in **Chapter IV**). In addition to the files associated with the different chapters, a summary of the experimental runs and the BSE images corresponding to the various experiments are provided in the ***Supplementary File II-1***.

Hydrated experiments

This subsection on hydrated experiments is dedicated to the construction and calibration of the High-Pressure Vessel (*HPV*) furnace. It provides a comprehensive overview of the different components and procedures, including the determination of the hotspot position and temperature calibration. A brief description of the impact of pressure and water on plagioclase crystallization, modeled using Rhyolite-MELTS software, is also included

Rhyolite MELTS modeling

Pressure and water content are key parameters that significantly influence crystallization. Water content directly affects plagioclase formation, especially its anorthite content. Rhyolite-MELTS models were run at pressures of 500 bar, 1 kbar, 1.5 kbar, 2 kbar, 5 kbar, and 10 kbar (an extreme value). The influence of water content was also modeled over a range from 0.5 to 3 wt% H_2O, corresponding to the estimated water content at the depth of the magma chamber beneath the volcanoes of interest (*Namur et al. 2020*; *Vander Auwera et al. 2021*; *Bechon et al. 2022*; *Cortés et al. 2024*): Osorno (1 – 1.5 wt% H_2O), Calbuco (3 – 4.5 wt% H_2O).

According to models established using *MELTS v.1.2.0* (*Gualda et al. 2012*), the main crystalline phases affected by pressure are clinopyroxene, oxides, and quartz (**Table II-4**). Up to 2 kbar, the saturation temperature of plagioclase, as well as its anorthite content, are not significantly impacted (**Table II-4**). Indeed, the estimated anorthite content remains comparable to both the *MELTS* predictions and the experimental measurements obtained at 1 atm under dry conditions (≈59 mol% An at the liquidus). At pressures above 5 kbar, both the liquidus temperature of plagioclase and its anorthite content are more significantly affected. The anorthite content decreases, while the liquidus temperature generally increases above 1200

°C (**Table II-4**). At 10 kbar, the liquidus temperature drops to around 1200 °C and the anorthite content decreases to approximately 40 mol% An.

In contrast to pressure, water content strongly influences plagioclase crystallization. With ~2–3 wt.% H_2O, the plagioclase saturation temperature decreases substantially, reaching ~1080–1050 °C, while the anorthite content increases to 65–69 mol% An (**Table II-4**). Increasing water content also lowers the liquidus temperature of clinopyroxene. Additionally, hydrous conditions promote crystallization of phases such as orthopyroxene, whereas minerals like quartz and apatite tend to disappear as water content increases.

		T_{sat} (°C)						
	An (mol. %)	Plagioclase	Cpx	Opx	Oxides	Spinel	Quartz	whitlockite/Apatite
500 bars	57	1170	1130		950	1120	980	
1 Kbar	57	1180	1120/1130		960	1120	990	
1,5 Kbars	55	1180	1130/1140		930	1120	1000	
2 Kbars	54	1180	1150		980	1120	1010	
5 Kbars	50	> 1200	1190		1020	1130	1060	
10 Kbars	40	> 1200	> 1200		1140	1130	1110	1200
2 Kbars_0,5%wt H_2O	57	1150	1120		930	1110	910	910
2K bars_1%wt H_2O	59	1120	990	1090	900	1100		
2 Kbars_1,5%wt H_2O	62	1100	960	1060	900	1090		
2 Kbars_2%wt H_2O	65	1080	940	1040	900	1090		
2 Kbars_2,5%wt H_2O	66	1060	920	1030	900	1090		
2 Kbars_3%wt H_2O	69	1050	900	1020		1090		

***Table II-4**: Saturation temperatures of various minerals in OS36 at different pressures and water contents. The anorthite content corresponding to the newly nucleated plagioclase crystals is also indicated.*

HPV furnace construction (KULeuven)

The term HPV furnace here refers to a Carbolite GERO vertical furnace with a U-shaped heating resistor system, equipped with a metal-alloy test tube with a pressure seal. This setup can reach high pressures (commonly up to 5kbar) at relatively low temperatures (around 750 °C), or lower pressures (around 2–3 kbar) at higher temperatures (*Edgar 1973*). The HPV furnace presented here is an externally heated pressure vessel, meaning that the furnace and pressure vessel are separate. Compared to internally heated systems, the maximum achievable

temperature is lower and temperature regulation is more complex; however, maintenance is simpler, and the pressure vessel can be more easily replaced in case of wear.

The KULeuven furnace described here uses a "cold-seal" design (**Figure II-4**). The pressure vessel is a long Tuttle-type vessel (*Tuttle 1948*), with the open end and seal located outside the furnace. Cold-seal vessels allow rapid quenching of high-temperature states by enabling the isobaric, gravity-driven removal of the run product from the temperature hotspot. This is achieved by rotating the furnace/vessel assembly from a horizontal to a vertical position. Unlike the 1-atm gas-mixing furnace, no CO–CO_2 gas flow is connected to the cold-seal furnace, and no control of oxygen fugacity is possible, as it is fixed at the Ni–NiO buffer. To minimize heat loss, insulating wool is placed at both ends of the furnace.

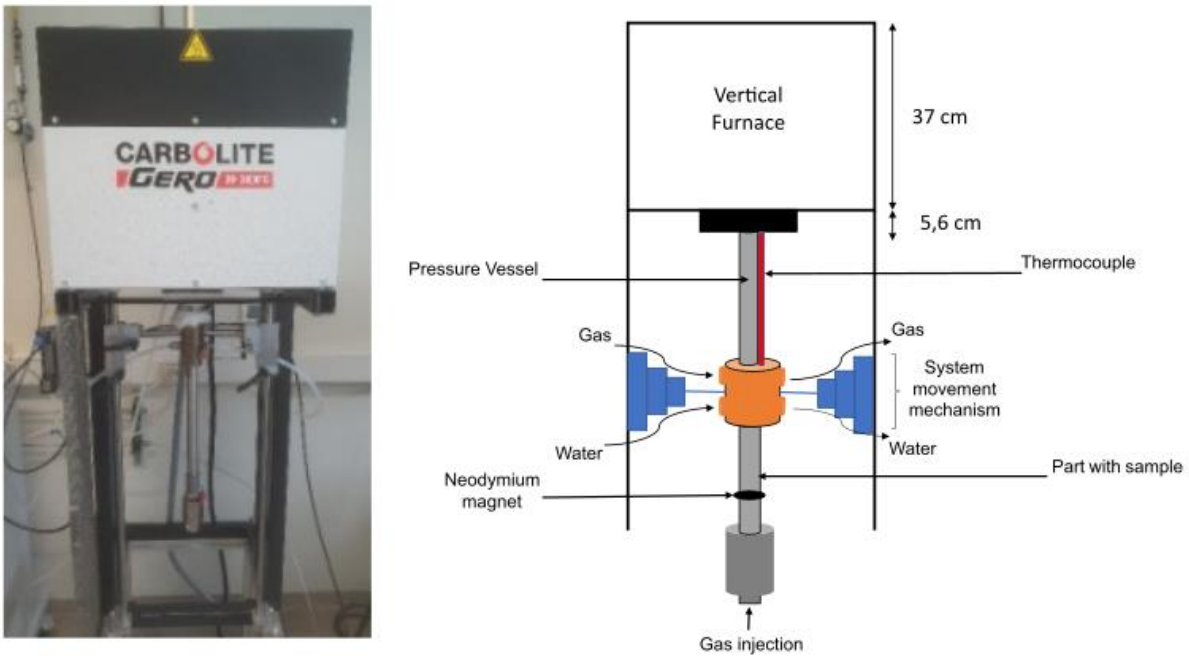

***Figure II-4**: Image and schematic representation of the HVP furnace (KU Leuven) on the left and right, respectively.*

Preparation of the sample and run

In this type of experiment, the starting powder and water are put into a Gold-Paladium (Au-Pd) capsule sealed by a triple junction, which is then placed at the extremity of a thin ceramic rod. To ensure proper support of the capsule, the end of the rod is hollowed out (**Figure II-5**). A platinum (Pt) wire may also be used to secure the capsule to the rod. The ceramic rod (~ 55 cm), equipped with the capsule containing the sample, is then inserted horizontally into

the cold-seal apparatus using the movement mechanism. Pressure is applied via Ar gas injected at the bottom end of the system (**Figure II-4** and **Figure II-6**).

Pressurized vessels are typically preheated for 1 to 2 hours before the start of the experiment to ensure that the target temperature is reached and stabilized. To avoid thermal gradients, the capsule size should not exceed the length of the furnace hot spot and preferably be smaller (~0.5 cm here). *Edgars (1973)* refers to a gold capsule approximately ¾ inch long (~1.9 cm), which can accommodate around 50 mg of silicate starting material along with water.

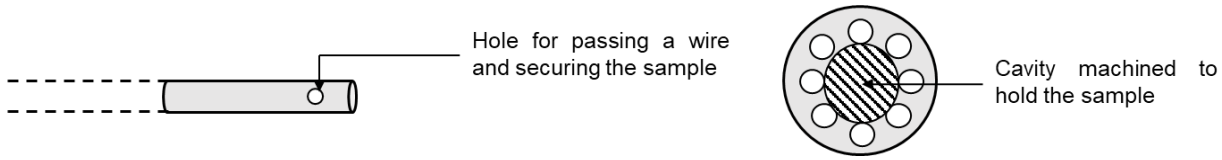

***Figure II-5**: Sample holder mechanism fixing the Au-Pd capsule at the ceramic rod extremity*

Composition of the pressure lining

The pressure lining consists, in its upper segment, of a Tuttle-type MHC pressure vessel made of a molybdenum–hafnium–carbide (Mo–Hf–C) alloy and enclosed within an Inconel tube (Ni > 50 %, Cr 15–23 %, Fe 10–20 %) to prevent oxidation. A water-cooled bronze closure nut connects the pressure vessel to the cold part of the system (**Figure II-6**). Through this closure nut, water and argon gas (Ar) circulate to cool the system and limit oxidation.

The cold segment contains a ceramic rod equipped with a magnet and a back piece at its lower extremity (**Figure II-6**). This assembly is inserted into the cold part of the system. The combination of the back piece and magnet, extending over 3 cm and manipulated by an external neodymium magnet, allows vertical adjustment of the ceramic rod to position the sample at the furnace hot spot. A double copper cone, placed at the center of the closure nut, ensures both leak-tight sealing and proper alignment of the two segments (cold segment and pressure vessel; **Figure II-6**). Teflon tape is applied to both connection points, and a copper gasket at the junction between the cone and the pressure vessel further guarantees gas tightness. Because intense thermal shocks during quenching can lead to cracking of the pressure vessel, its condition must be carefully inspected throughout the experimental series.

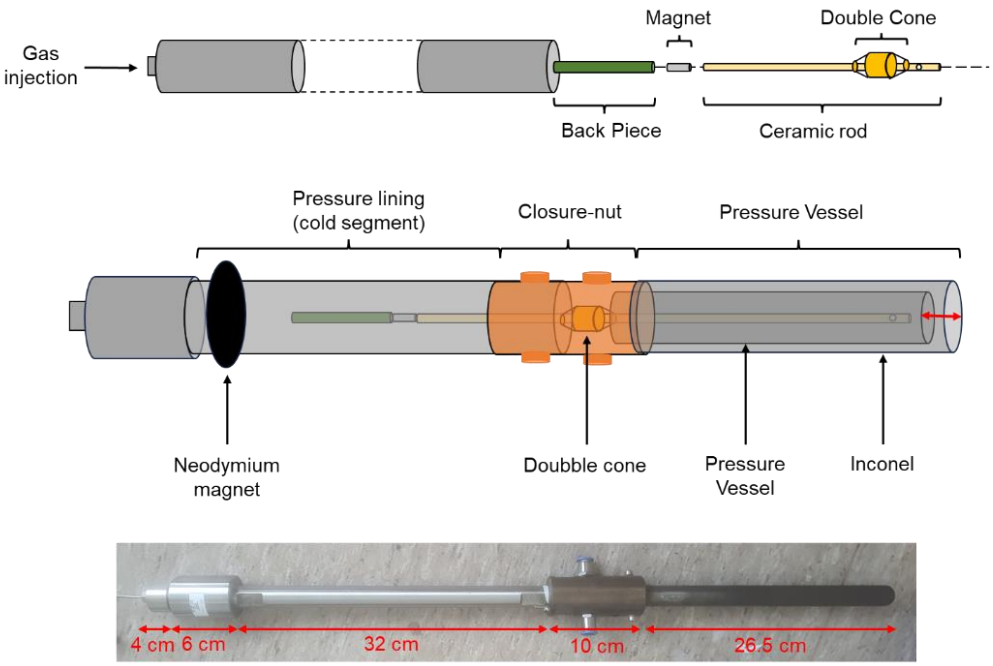

***Figure II-6**: Organization of the pressure lining containing the ceramic rod with the sample capsule (upper schematic representation). During experiments, the upper segment of the pressure lining is positioned inside a pressure vessel enclosed in an Inconel tube, then shifted to the cold segment during quenching (middle schematic representation). Both parts are connected by a bronze closure nut. The bottom image shows the overall assembly.*

Calibration

As with the 1 atm furnace, accurately determining the hot spot within the furnace is a critical preliminary step. The same calibration procedure was employed. A ceramic rod, marked at 1 cm intervals and equipped with an N-type thermocouple, was progressively raised through the furnace, and the temperature at each position was measured using a digital thermometer connected to the thermocouple. This calibration was performed at programmed setpoints from 800 to 1350 °C (set temperatures; ***Supplementary file II-2***). The reference zero point was defined at the base of the furnace. Results indicate that the hot spot is located between 20.5 cm and 22.5 cm from this reference, corresponding to a vertical thickness of approximately 2 cm in the central part of the furnace. In addition, the temperature offset between the programmed setpoint and the measured values was quantified to evaluate the furnace's thermal accuracy and stability.

Inconvenients

If the general method for determining the hot spot is similar to that used in the 1 atm furnace, three major issues must be addressed:

- The correct positioning of the Inconel capsule relative to the hot spot.
- The potential upward shift of the hot spot due to the insertion of the pressure vessel.
- The relative difference between the set temperature, the measured temperature, and the temperature measured inside the pressure vessel (
- **Figure II-7**).

Concerning the first point, the pressure vessel is 28 cm in length (26.5 cm excluding the screw thread) and contains both the ceramic rod and the sample capsule. However, it is not fully drilled along its entire length, as the last 2.55 cm at the closed end remain solid. In addition, a small clearance exists between the pressure vessel and the surrounding Inconel tube. To ensure correct sample positioning, both the pressure vessel and the Inconel tube must be placed approximately 3 cm above the furnace hot spot.

For the second point, the insertion of the cold metallic pressure vessel into the furnace causes the hot spot to shift upward, which makes its precise location unstable during sample insertion. This effect can be mitigated by relying on the previously calibrated hot spot position and accounting for the corresponding temperature offset relative to the programmed setpoint. Without pressure vessel, a temperature difference of approximately 0.93×Setpoint temperature exists between the setpoint temperature and the value measured at the hot spot. When the pressure vessel and Inconel tube are inserted, this discrepancy increases substantially, reaching about 330 °C at a setpoint of 800 °C and 229 °C at 1200 °C. Although this relative difference decreases with increasing temperature, setpoints above 1300 °C are required to fully cover the plagioclase crystallization range at 2 kbar with 1.5–2 wt.% H_2O.

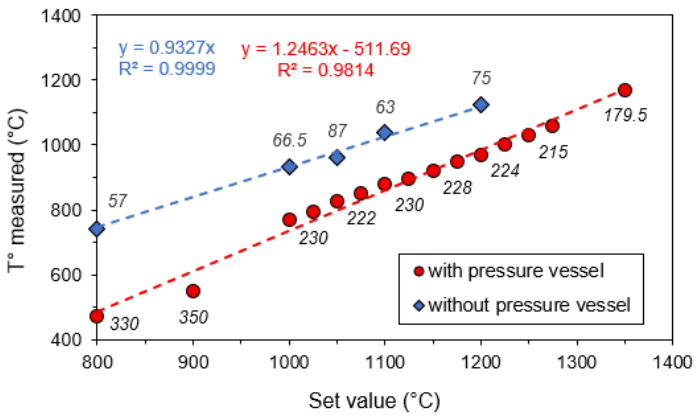

***Figure II-7**: Diagram illustrating the difference between the set and measured temperatures without the pressure vessel (blue) and with the pressure vessel (red). Italic values indicate the difference between imposed and measured temperatures. Note that the addition of the pressure vessel increases this discrepancy from 171 °C at 1350 °C to 330 °C at 800 °C, limiting the range of realizable experimental conditions. A temperature of 1600 °C appears to be necessary to completely eliminate the influence of the pressure vessel on temperature.*

Because the system is almost completely closed once the gas is added (with the pressure vessel entirely inside the furnace), the temperature inside the furnace cannot be easily measured during the experiment. A flexible N-type thermocouple (rated up to ±1250–1300 °C) must be pressed against the Inconel tube to measure the actual surrounding temperature. However, no temperature reading is available from inside the mechanism. A calibration diagram must therefore be established before planning any experiment. In addition, it seems important to verify the effect of the gas (and pressure) on the measured temperature difference.

Segmentation and Textural Quantification

Regardless of the geological context (sedimentary, magmatic, or metamorphic), the term ***texture*** refers to the geometric characteristics and spatial arrangement of a rock's components, including bubbles, grains, crystals, and glass. As outlined by *Higgins (2006)*, several key parameters are commonly quantified:

- Number and size of grains, crystals and porosities
- Shape, circularity and orientations of grains and crystals
- Proportion and relation between the different phases

Quantifying these parameters (often independently; *Cashman and Marsh 1988*) first requires the acquisition of suitable images and the segmentation of the distinct phases present in the sample. Several analytical techniques can be employed, including transmission electron microscopy (TEM), cathodoluminescence, scanning electron microscopy (SEM), thin section analysis under transmitted or reflected light, and X-ray microtomography. The choice of technique depends on factors such as sample size, analytical resolution, and the specific parameters to be extracted.

Each method has its own advantages and limitations, making it essential to carefully select the imaging approach according to the objectives of the study. For instance, X-ray microtomography is widely used for three-dimensional imaging but is often limited by low

phase contrast, due to similar densities between phases, and by segmentation challenges, particularly for small crystals.

This section presents the methodological approaches employed to image, segment, and extract two-dimensional textural parameters from both experimental charges and petrographic thin sections.

Experimental samples

All the procedures detailed here are also used throughout the manuscript and are similar to those described by *Pupier et al. (2008)*. The experimental loads are embedded in epoxy, polished, and imaged using SEM (BSE image; Figure II-8). The small contrast difference between glass and plagioclase crystals makes the use of an optical microscope in reflected light impossible.

As explained by *Pupier (2008)*, the representativeness of the sample in terms of crystal size and number density depends on the section position. Except for samples quenched at the earliest steps of the crystallization, where the largest crystals are found near the Pt-wire (heterogeneous nucleation), the largest crystals are generally found at the center of the sample, while a higher number of crystals (particularly the smallest ones) are positioned around the sample edges, in contact with the Pt-wire. To ensure good representativeness, it is therefore preferable to polish up to the center of the sample. This is particularly important for samples corresponding to the beginning of crystallization, at temperatures where crystals are not yet evenly distributed in terms of size and shape.

Depending on the crystal number density and distribution in the samples, images were taken at various magnifications, ranging from 40× to 160–750×, to capture the entire sample and enhance the level of detail. Depending on the experimental conditions, between 3 and more than 2000 crystals, ranging in size from 2 µm to over 1 mm, were segmented. Since the BSE pixel size was approximately 0.5 µm per side, we could only accurately measure crystals larger than 2 µm. Crystals smaller than 5 µm can also be confused with impurities.

The Weka Segmentation plugin of *Fiji* (*ImageJ*) was initially used to automate the outlining of the different phases (plagioclase, Fe-Ti oxide, and clinopyroxene) after adjusting the image contrast. Subsequently, crystal outlines were verified, and each crystal was manually extracted from the images using *GIMP* software. Resulting images are then binarized, and textural parameters such as the crystal area, circularity or long (l) and short axes (w) of the

outlined crystals were measured using *Fiji* (*Abramoff et al. 2004*). The long and short axis were extracted using the best-fit ellipse method, implemented in Fiji (*Higgins 2000*; **Figure II-8**).

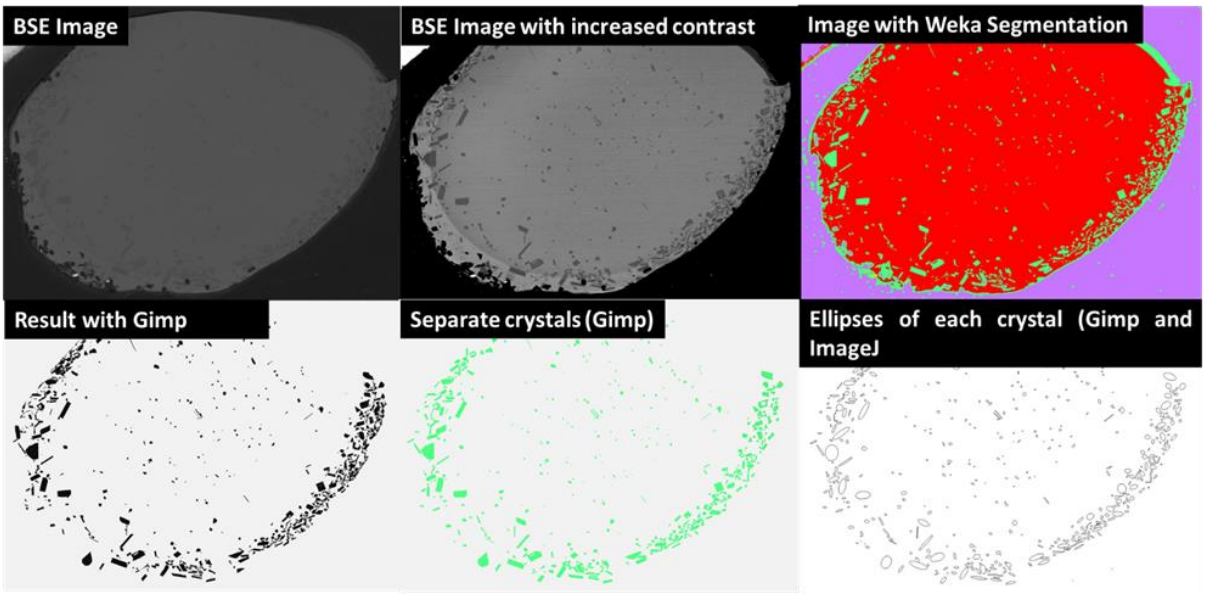

Figure II-8: *Sequence of images illustrating the various steps of image processing, from BSE image acquisition to the final representation of each segmented crystal as an ellipsoid. From left to right: the original BSE image, showing the similar densities of the melt and plagioclase crystals (resulting in similar gray values); contrast enhancement; phase separation using Weka Segmentation in Fiji (deep learning); manual refinement using the freeware GIMP to increase segmentation precision. Each crystal is contoured and separated from its neighbors. The resulting image is then binarized in Fiji, and textural data are extracted, with each crystal represented as an ellipsoid in the final figure.*

Since some of our crystals in the case of a strong initial overheating step exhibited complex dendritic textures, appearing as several fragments in 2D sections depending on the experimental conditions, segmentation was often challenging. Therefore, we decided to use the *EBSD* method (see below for further explanation; **Figure II-9**) to access different crystallographic orientations and facilitate the outlining of each crystal.

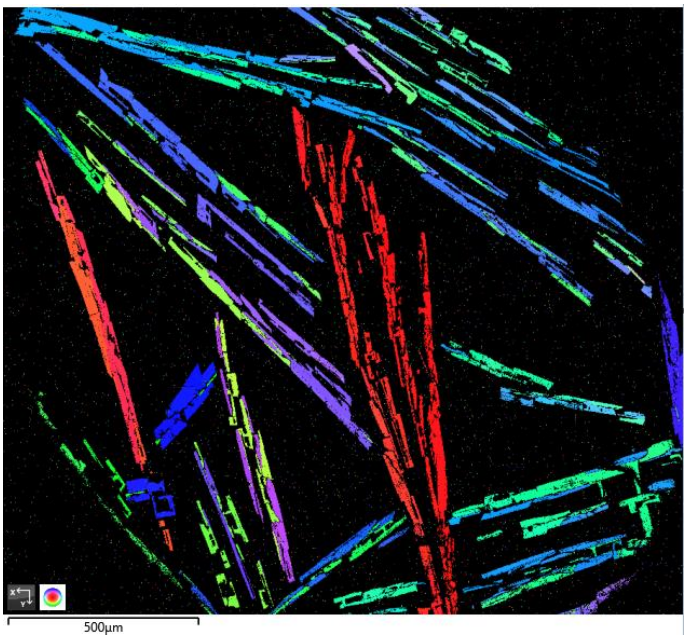

***Figure II-9**: EBSD image showing complex dendritic crystals divided into several segments. Fragments with the same color (e.g., red) indicate parts of a single crystal oriented in the same direction.*

Natural thin sections

Samples selected for textural analysis correspond to basalts, basaltic-andesites, andesites and dacites from 3 Chilean volcanoes: Osorno, Calbuco and Villarrica. These rocks were collected during various field campaigns. As segmentation is a time-consuming process, it is essential to select the most relevant samples based on:

- The alignment of the sample with the differentiation trend
- The possibility of segmentation (countable crystals, distinct gable crystals, ...)
- Plagioclase abundance within the thin sections
- The representativeness of the sample

A similar procedure to that used for experimental loads was applied for the segmentation of thin sections. A complete summary of the entire procedure for extracting textural data is presented in **Figure II-10**. All thin sections observed in transmitted light were digitized using *Mosaic* software and used for segmentation. Since natural crystals display various shades of birefringence, each plagioclase crystal was manually outlined using *GIMP* software. A new *Python* software published in 2024, *MinDet1* (*Toth and Maclennan 2024*), can automate the segmentation of plagioclase in digitized thin sections. This software also attempts to separate

individual plagioclase crystals in complex arrangements such as clusters and syneusis. For more consistency concerning the segmentation method, this software was not used here. However, a comparison between the two methods, in terms of segmentation quality and extracted textural data, could be precious to validate this automated procedure, allowing a significant reduction in processing time.

In total, between 100 and 500 crystals were contoured per thin section. Due to various natural processes, including decompression during ascent and deep magmatic evolution, these samples display a wide range of crystal sizes, from 10–30 µm (likely underestimated in thin section segmentation) to millimeters or even centimeters. BSE images were used to segment microlith populations smaller than 150 µm. Some late-stage processes, such as clustering and syneusis (the close association of multiple growing crystals), complicate the distinction of individual crystals. During segmentation, these composite textures were treated both as single crystals and as separate entities (see **Chapter V**).

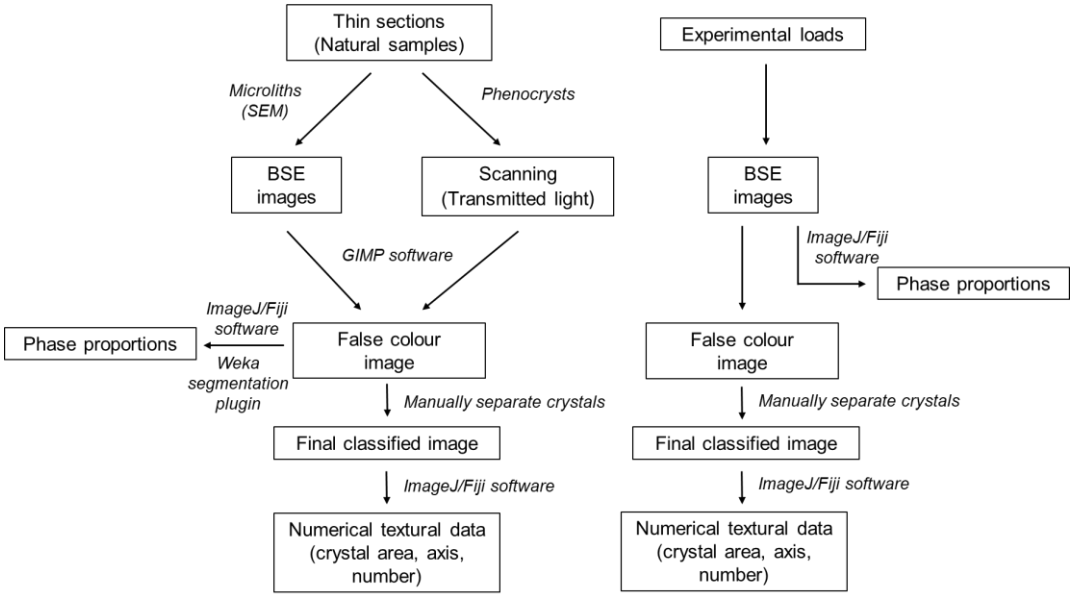

***Figure II-10**: Flow diagram illustrating the steps for extracting textural data from natural thin sections (left) and experimental charges (right).*

Textural parameters

Extraction of 2D data

Regardless of the nature of sample (natural vs. experimental), the phase proportions (φ_V), crystal aspect ratio (minor axis *w* of the crystal / major axis *l* of the crystal), crystal number

density (N_A; determined by point counting) or also crystal size are directly extracted from 2D sections, using the following equations and methods:

$$\varphi_{V_i} = \frac{phase_i\ area}{sample\ area} \quad (2)$$

$$N_A = \frac{number\ of\ crystals}{sample\ area} \quad (3)$$

Two methods were compared to obtain phase proportions: 2D image processing (φ_V) and mass balance (φ_{WDS}) based on the chemical WDS/EDS data. The imaging method assumes that calculated phase proportions correspond to volume proportions (*Delesse 1847*; *Brugger and Hammer 2010b*). For the mass balance method, phase densities were estimated using MELTS, at the temperature of quenching (see ***Supplementary file III-4***). As highlighted by *Vetere et al. (2024)*, the two methods give similar results. The absolute differences estimated by *Billon et al. (2025)* (see **Chapter III**) range between 1% and 4%, with an average difference around 1 and 2%. Due to this good agreement, only phase proportions derived from 2D image analysis ($\boldsymbol{\varphi_V}$) are used in the following chapters.

The 2D crystal size is a fundamental parameter for the growth rate estimation. Depending to the time allowed to the segmentation, several methods can be used. I detail here the 3 most used, with examples of studies each time:

- The **Batch method** (*Brugger and Hammer 2010a, b*; *Shea and Hammer 2013*) corresponds to the simplest and most expedient textural method for a general estimate of particle sizes (S_N). This method, based on crystal counting is directly linked to the φ_{V_i} and N_A parameters, following the equation:

$$S_N = \sqrt{\frac{\varphi_V}{N_A}} \quad (4)$$

  Any consideration of crystallographic axis is provided; and each crystal can be seen as a spherical particle.

- The **segmentation method** (*Shea and Hammer 2013*) allows access to minimum (l_{min}, w_{min}) average (l_{mean}, w_{mean}) and maximum (l_{max}, w_{max}) size values considering the various 2D crystallographic axis (l and w). This method is only based on the quality of the segmentation performed (number of crystals, homogeneous distribution of crystals or not).

- The last method called Crystal Size Distribution (*CSD;* *Burkhard 2002*; *Pupier et al. 2008*) is detailed below. It allows to determine the characteristic crystal size L_c value referring to the mean crystal size of the linear CSD regression line.

The aspect ratio is directly obtained by the ratio between the short (w) and long (l) 2D crystal axis.

Estimation of 3D data

Because crystals imaged by SEM represent only 2D cross-sections of 3D objects (randomly cut), the textural parameters obtained from such sections correspond only to apparent 2D parameters. X-ray tomography (*Schiavi et al. 2009*; *Le Gall et al. 2021*) remains the most reliable method for determining true 3D parameters such as crystal size and shape. Several factors such as low contrast between crystals and glass, limited resolution for small crystals, or very high crystal number densities, may restrict the applicability of this technique. *Duchêne et al. (2008)* proposed a 3D reconstruction method for plagioclase crystals from 2D sections, in which the three-dimensional morphology of 261 crystals was manually reconstructed. A series of polished sections spaced at 20 µm intervals was prepared, and the 3D reconstruction was performed using Gocad software. The main limitation of this approach is a potential underestimation of the number of crystals due to manual segmentation and reconstruction.
A detailed description of the method used to estimate 3D parameters is provided in the following section, which focuses on the Crystal Size Distribution (*CSD*) method.

Nucleation and growth rate

Nucleation and growth rates can be calculated using several methods: (i) Batch method (*Brugger and Hammer 2010a, b*; *Shea and Hammer 2013*) (i) direct calculation based on 2D crystal size value from segmented images (*Shea and Hammer 2013*); (ii) the Crystal Size Distribution method (*Pupier et al. 2008*). All the theory and textural parameters derived from the CSD method are detailed into the following section.

Regarding the first method, in which textural parameters are extracted from segmented images, several equations are used. The nucleation rate (J) is generally calculated with the Batch method:

$$J_{Batch} = \frac{N_V}{t} \quad (5)$$

N_v represents the nucleation density calculated by dividing the crystal number density (N_A) by the 2D mean crystal size (S_N):

$$N_V = \frac{N_A}{S_N} \quad (6)$$

Crystal growth rate values depend on what crystal size parameter is used (l_{min}/w_{min}, l_{mean}/w_{mean}, l_{max}/w_{max}). Values can refer to the minimum (G_{min}), maximum (G_{max}) or also average value (G_{mean}/G_{Batch}), but also to different crystallographic axis ($G_{...,w}$ and $G_{...,l}$). Equations presented here correspond to those used in the following chapters:

$$G_{Bactch} = \frac{S_N}{2t} \quad (7)$$

$$G_{mean,w/l} = \frac{l_{mean}/w_{mean}}{2t} \quad (8)$$

$$G_{max,w/l} = \frac{l_{max}/w_{max}}{2t} \quad (9)$$

An additional equation, not used in our study, is based on the crystal area (*Hammer and Rutherford 2002*; *Pontesilli et al. 2019*), and uses both minor (w) and major (l) crystal axis:

$$G_{area} = \frac{(w \times l)^{1/2}}{2t} \quad (10)$$

The factor 2 in the denominator accounts for the fact that the growth rate is expressed in terms of crystal radius rather than diameter.

The time parameter (***t***) typically refers to the experimental duration. However, as it is discussed in **Chapter IV**, depending on the initial conditions (existence of pre-existing crystal fragments, initial overheating), the effective time for nucleation and growth may differ and must be adjusted accordingly.

The Crystal Size Distribution (CSD) method

Abbreviations

n	Population density of crystals (number per unit of volume per size)
N	Number of crystals per unit of volume
L	Crystal size
V	Volume of the system
t	Crystallizarion time
Open system	
τ	Residence time
G	Growth rate (size/crystallization time)
J	Nucleation rate (number/unit of volume/crystallization time)
n^0	Nucleation density (L = 0)
L_c	Characteristic crystal size (= G×τ)
Close system	
t_c	Characteristic crystallization time
N_0, L_c	Typical crystal number and crystal size
V_0	Initial volume of the system (initial volume of liquid)
J_c, G_c	Characteristic nucleation and growth rates
J_0, G_0	Constants of nucleation and growth rates for t = 0
K_1, K_2	Constants of rate for respectively J and G
a, b	Constants for respectively J(t) and G(t) functions
φ	Crystallinity (or crystal fraction)
L_m	Maximum crystal size

***Table II-5**: Abbreviations used in this section.*

The Crystal Size Distribution Method (*CSD*) is a quantitative textural method used to describe the crystalline population in a sample. It was initially developed by *Randolph and Larson (1971)* in chemical engineering to control the crystal size and determine some textural parameters such as the nucleation density, or nucleation and growth rates in samples crystallizing from industrial crystallizers (**Figure II-11**). *Randolph and Sikdar (1976)* for example demonstrated the use of this technique in the case of a size dependent growth rate. The main strength lies in its ability to transform textural observations into dynamic data that can be exploited from a kinetic perspective.

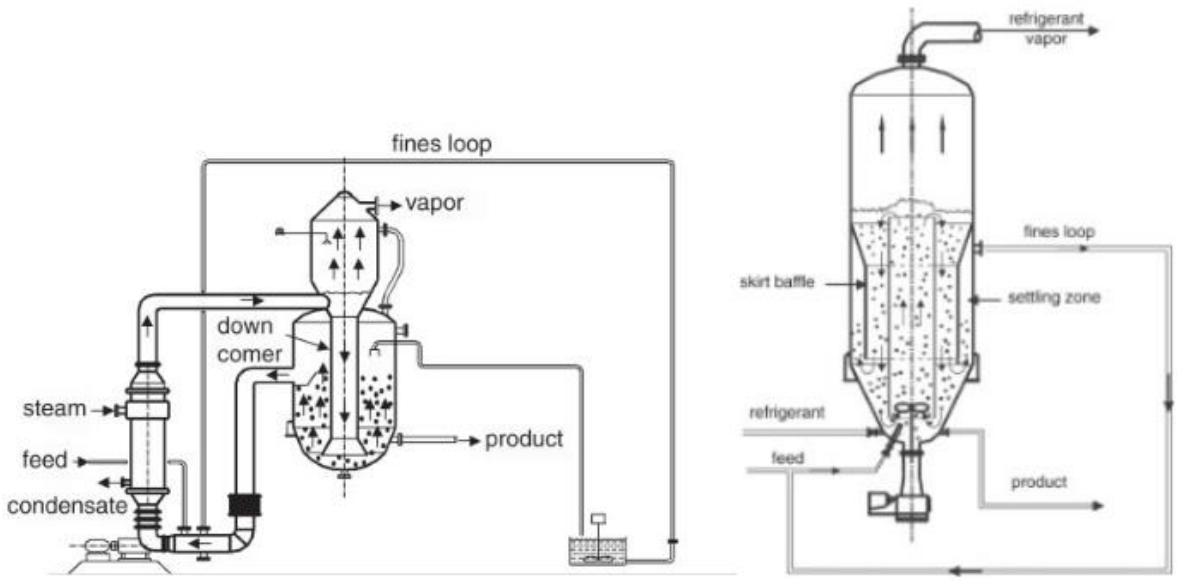

***Figure II-11**: Schematic design of an industrial crystallizer (left) with a zoomed view of the crystallization column (right) (taken from Kramer and Lakerveld 2019).*

The concept and first applications of the Crystal Size Distribution (CSD) method in geological systems were introduced by *Cashman and Marsh (1988)*, *Marsh (1988, 1998)*, *Resmini and Marsh (1995)*, and later refined by *Hammer (2008)* to investigate crystallization kinetics in natural systems. The CSD method allows the conversion of measurements of polygonal cross-sections per unit area into corresponding estimates of crystal number per unit volume, based on both cross-section and crystal size (*Cashman 1986*; *Paterson 1996*). Parameters such as crystal size and crystal number density reflect various physical processes, including nucleation destruction, crystal fractionation, accumulation, and population mixing, affecting different crystal populations (microlites and phenocrysts) as well as vesicularity. Since then, the CSD method has been widely applied in both experimental studies (*Burkhard 2002*; *Pupier et al. 2008*; *Moschini et al. 2023*) and natural systems (*Cashman 1988*; *Higgins and Roberge 2003*; *Namur et al. 2020*; *Cortés et al. 2024*), particularly to quantify crystallization kinetics of major minerals such as olivine, pyroxene, and plagioclase, and to constrain the timescales of magmatic processes, including magma ascent rates and residence times (τ) in magmatic chambers.

CSD theory

The theory of the CSD was initially developed by *Randolph and Larson (1971)* for steady state crystallizers. In this model, CSD is controlled by the initial presence of crystal fragments (seeds) in the crystallizer, the time (t) spent inside, and by the rate at which crystals

nucleate (J) and grow (G) (*Cashman 2020*). The nucleation and growth rate here controlled by supersaturation is directly linked to the crystallization time (t), but not dependent on other parameters such as the temperature (T) or pressure (P). The number of crystals for a given class of size (L) per unit of volume is defined as:

$$n(L) = \frac{dN(L)}{dL} \quad (11)$$

$$N(L) = \int_0^L n(L)dL \quad (12)$$

where $N(L)$ is the number of crystals with a size less than L.

Population balance

Considering 2 crystal populations n_1 and n_2 of different volume V, size L, and growth rate G. Modification of the volume and number density of crystals in a given size range is governed by the rate at which new crystals grow, and by the influx and outflux of crystals from the system: (net accumulation) = (growth input-growth output) + (flux in-flux out)

$$(VG_1n_1) + (Q_in_i\Delta L) = (VG_2n_2) + (Q_0n_0\Delta L) \quad (13)$$

$$\frac{\partial(Vn)}{\partial t} + \frac{\partial(GVn)}{\partial L} = Q_in_i - Q_0n_0 \quad (14)$$

Considering $Q_in_i << Q_0n_0$, and V constant:

$$\frac{\partial(Vn)}{\partial t} + \frac{\partial(GVn)}{\partial L} + Qn = 0 \quad (15)$$

Dividing by the volume V:

$$\frac{\partial(n)}{\partial t} + \frac{\partial(Gn)}{\partial L} + \frac{n}{\tau} = 0 \quad (16)$$

with $\tau = \frac{V}{Q}$ refers to the residence time in the system.

This method was adapted in both igneous and metamorphic rocks systems by *Marsh (1998)* considering 2 extreme cases; the batch/closed (experimental or metamorphic systems) and open systems. However, it is essential to mention that it is extremely rare that natural magmatic systems exhibit CSD perfectly similar to one of these 2 extreme cases.

CSD in open system of constant volume

In the case of a steady-state crystallization model (with n independent of time), as in open magmatic chamber (**Figure II-12a**) supposed continuously reprovisioned (*Marsh 1998*), or in industrial crystallizer (**Figure II-11**), crystal population can be expressed as:

$$\frac{d(Gn)}{dL} = -\frac{n}{\tau} \quad (17)$$

Where $\frac{n}{\tau}$ represents the outflow of a crystal population with a residence time τ in the system (reactor or magmatic chamber), and G corresponds to the mean linear growth rate (*Marsh 1988 1998*). Supposing G independent of the size L, the equation can be written as:

$$n = n^0 \times \exp\left(\frac{-L}{G\tau}\right) \quad (18)$$

or

$$Ln\,(n) = Ln(n^0) - \frac{L}{G\tau} \quad (19)$$

Linear relationship exists between the logarithm of the population density of size L, and that size (**Figure II-12b**), with Ln (n^0) the intercept, and $\frac{-1}{G\tau}$ the negative slope of the regression. The product of the growth rate (G) and residence time (τ) gives the characteristic crystal size (L_c) corresponding to the mean length of the CSD regression line:

$$L_c = G \times \tau = \frac{-1}{slope} = \left({}^{G}/_{J}\right)^{1/4} \quad (20)$$

Mathematically, L_c corresponds to the mode of size-based distribution (*Cashman 2020*). The constant of integration n^0 corresponds to the nuclei population density (L = 0). The knowledge of growth rate (G) and intercept n^0 allow to determine the nucleation rate (J):

$$J = \frac{dN}{dL}|L = 0 \times \frac{dL}{dt} = n^0 G \quad (21)$$

The interdependence between nucleation and growth rates governs the relationship between the number of crystals and their size (**equation 21**; *Shaw 1965*). According to mass balance, high nucleation rates result in many small crystals, whereas low nucleation rates favor the growth of fewer, larger crystals.

In a steady state system with G constant, J is also a constant and has no impact on the CSD slope as long as $J \neq 0$ (*Marsh 1998*). In the case of an infinite residence time τ, J being independent of the slope, the CSD will be horizontal and reflects a batch system. In open systems, crystal size allows to measure the growing time. An increase or a decrease of $G \times \tau$ has a direct impact on the slope.

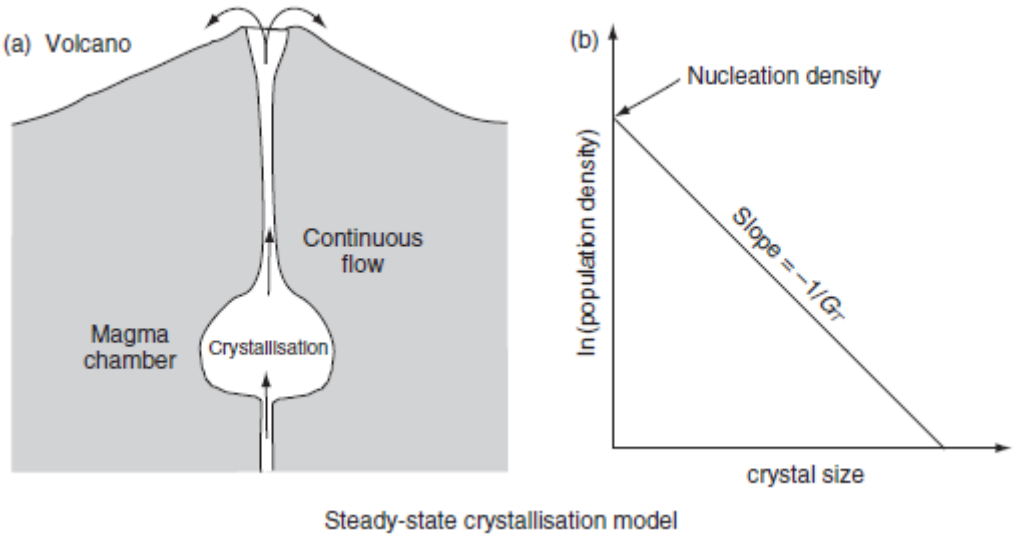

***Figure II-12**: **(a)** Continuously erupting volcano with an open magma chamber, represented as a steady-state reactor model (from Marsh 1988; Higgins 2006). **(b)** Crystal Size Distribution (CSD) associated with magma chamber crystallization, shown as a straight line on a plot of ln(population density) versus crystal size (from Higgins 2006).*

CSD in Batch (closed) system

Formulations presented above correspond to steady-state crystallizing system and are not directly applicable to closed systems such as lava lake (influx = outflux = 0) where magma cools and crystallizes completely (decrease in the volume V in function of time t; *Marsh 1988*; *Cashman and Marsh 1988*; *Higgins 2006*). In a Batch system, the population balance becomes:

$$\frac{\partial(Vn)}{\partial t} + G\frac{\partial(Vn)}{\partial L} = 0 \quad (22)$$

The solution of the equation can be written under the form:

$$\ln\left(\frac{n}{n_0}\right) = \left(-\frac{t}{t_c} + \frac{L}{Gt_c}\right) + \ln\left(\frac{V_0}{V(t)}\right) \quad (23)$$

with $\boldsymbol{t_c}$ the characteristic crystallization time to fully solidified a rock (similar to $\boldsymbol{\tau}$ in open systems), and V_0 the initial volume of crystallization. Because $\frac{V_0}{V(t)}$ can be considered as negligible, the solution becomes (23):

$$\ln\left(\frac{n}{n_0}\right) = -\frac{t}{t_c} + L \times \frac{1}{Gt_c} \quad (24)$$

With t_c the characteristic crystallization time reflecting the crystallization kinetic. The intercept depends both on the absolute time (t), and t_c. However, the intercept variation is mainly governed $\boldsymbol{t}$, while $\boldsymbol{t_c}$ acts as a time scale factor (small and high $\boldsymbol{t_c}$ refers respectively to fast and slow crystallization).

Similarly to steady state in open system, particularly at the earliest steps of the crystallization, the plot $ln\left(\frac{n}{n_0}\right)$ Vs. L takes the form of a linear regression of slope $\frac{-1}{Gt_c}$ (*Marsh 1988*, *1998*). In such a system, the log–linear relationship results from nucleation density increasing exponentially with time, a behaviour consistent with linearly increasing undercooling combined with linear crystal growth (*Higgins 2002b*). Compared to open systems where each CSD have a different intercept (exponential increase in J at constant growth rate G) (**Figure II-13a**), in closed systems, CSD slopes are normalized to the same intercept (exponential increase in G with size L at a constant nucleation rate J; *Cashman and Marsh 1988*) (**Figure II-13b**).

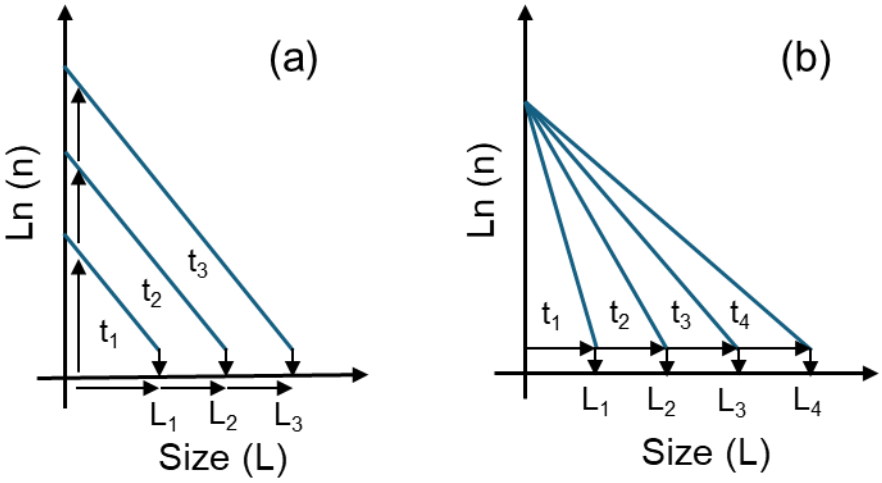

***Figure II-13**: (a) CSD resulting from a constant crystal growth rate combined with an exponential increase in nucleation rate. (b) CSD resulting from an increasing growth rate at a constant nucleation rate (from Marsh 1988).*

Avrami Approach

An alternative way to describe the evolution of the crystal number density *n(t)* is given by the Avrami approach (*Avrami 1939, 1940*), linking *n(t)* to the crystallinity $\varphi(t)$ of a phase in function of time *t*:

$$n(t) = \frac{dN}{dL} = [1 - \varphi(t)]\frac{J(t)}{G(t)} \quad (25)$$

Where the crystallinity evolution can be written as:

$$\varphi = 1 - \exp\left(-\frac{4\pi}{3} \times J_c G_c t^4\right) \quad (26)$$

With J_c and G_c, the characteristic nucleation and growth rates.

The characteristic crystallization time (t_c) is given by the following relations:

$$t_c = C_t (G_c^3 \times J_c)^{-1/4} \quad (27)$$

According to Marsh (1988, 1998), the nucleation *J* and growth *G* rates can be expressed as:

$$J = K_1 \Delta T^a \quad (28)$$

$$J(t) = J_0 \exp\left(\frac{at}{t_c}\right) \quad (29)$$

$$G = K_2 \Delta T^b \quad (30)$$

$$G(t) = G_0 \exp\left(\frac{bt}{t_c}\right) \quad (31)$$

With K_1 and K_2 constant of rate, J_0 and G_0 corresponding to J and G values for t = 0, t_c to the characteristic crystallization time, and a and b corresponding to the kinetics order constant for the nucleation and growth rates respectively. ΔT in (**28**) and (**30**) refers to the undercooling. Combining the **equations 25, 29 and 31,** we obtain:

$$\ln\left(\frac{n\left(t/t_c\right)}{n_0}\right) = \ln\left(1 - \varphi\left(\frac{t}{t_c}\right)\right) + (a - b) \times \left(t/t_c\right) \quad (32)$$

The CSD slope is thus controlled by the difference *(a – b)*. Higher is the difference, corresponding to the difference between the nucleation and growth rates, steepest is the slope. We give here some examples of CSD evolution in function of *a* and *b*:

- If a = b: The CSD is horizontal and reflects only the degree of crystallinity.
- If b = 0: Growth rate (*G*) is constant, and the slope is governed solely by an exponential increase in nucleation rate *J*. CSDs shift upward along the nucleation density axis with a constant slope $\frac{a}{t_c}$, independent of time and crystal size.
- If a = 0: With constant nucleation rate (*J*), CSDs depend only on exponential growth with increasing *L*. This results in a curved CSD, where the y-intercept is governed by the nucleation, and the slope is equal to $\frac{b}{t_c}$. At a constant growth rate (*G*), CSDs become flat.

Because magmatic systems rarely produce flat or positive CSD slopes (i.e., $a < 0$), log–linear CSDs are generally interpreted as reflecting an exponential increase in nucleation rate at constant growth rate G_0, with $a - b$ typically between 6 and 10 and $b = 0$. **Figure II-14**

illustrates the evolution of the CSD as a function of crystallinity ϕ. The maximum crystal size $L_m = G_0 t_c$ increases continuously during crystallization. Below 75% crystallinity, the CSDs remain approximately parallel, indicating a constant slope. Above 75%, curvature appears at the smallest crystal sizes. *Marsh (1998)* proposed that linear CSDs (i.e., $\phi < 50\%$) are characteristic of volcanic rocks. The only other mechanism capable of producing log–linear CSDs under constant nucleation rate is an exponential increase in growth rate with increasing crystal size (*Eberl et al. 1998, 2002*; *Higgins 2006*).

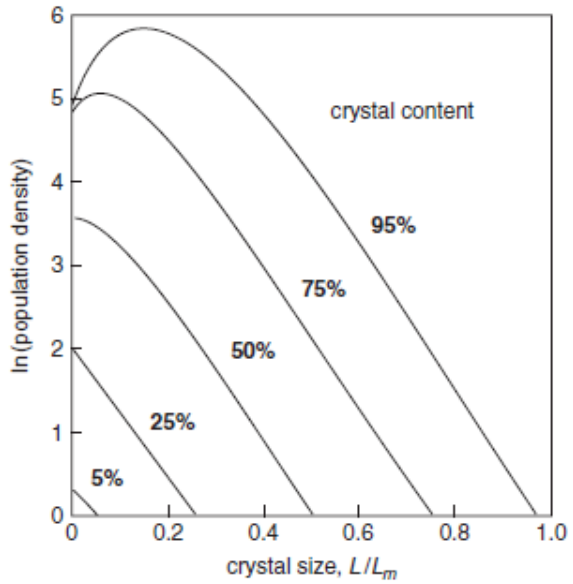

Figure II-14*: The development of the batch crystal size distribution with increasing crystallinity or time for a system where a – b = 8. Notice the CSD curvature after 50% of crystallinity. The slope is generally constant and that the effect of decreasing melt on nucleation becomes prominent beyond ~50% crystallization.*

In summary, the determination of CSD parameters, such as the growth rate G, depends on the type of system (batch or open). In a batch system with constant growth rate, the system's age is related to the size of the largest crystals, L_m, which increases continuously during crystallization (*Marsh 1998*). In contrast, in an open system, Gcan be directly inferred from the CSD slope (slope $= -1/G\tau$) if the actual residence time $\tau$is known. In this case, $L_c = G\tau$ differs from L_m.

Processes modifying CSD

Several physical processes are known to modify the CSD shape (*Pupier 2006*). Based on the studies from *Marsh (1988)*, *Higgins (1998, 1999, 2002)*, or also *Burkhart et al. (1980)*; we will present some examples here:

- **Crystal settling** is a straightforward process in which crystals separate from the melt due to density contrasts, without accounting for particle interactions. *Higgins (2002a and b)* developed a numerical model in which one million olivine and plagioclase spheres, uniformly distributed, sediment in a closed box with nucleation and growth rates set to zero. The CSD evolves progressively (**Figure II-15a**): it is initially linear, then pivots as the largest, densest crystals settle first. When most crystals have sedimented, the distribution shows a relative depletion of the smallest sizes, which remain suspended longer. In its final stage, the CSD takes on a form comparable to that produced by simple compaction, reflecting the complete gravitational sorting of crystals.

- **Textural coarsening** is a late process in which smaller grains dissolve in favor of larger ones (*Marsh 1988*; *Higgins 1998, 1999*). This occurs because small crystals have a higher surface energy per unit volume than large ones. To minimize the system's overall energy, grains below a critical size are dissolved, feeding the growth of larger crystals. The best-studied mechanism is Ostwald ripening, which takes place at constant composition and under isothermal conditions, without any external thermodynamic change. In the Lifshitz-Slyozov-Wagner (LSW) model, grains below a critical size are rapidly dissolved, while larger crystals grow at a decreasing rate that tends toward zero. As a result, CSDs remain superimposed above the critical size, but their intercept gradually decreases over time (**Figure II-15b**). In contrast, the Communication Neighbours (CN) model considers that each crystal interacts only by diffusion with its immediate neighbors, predicting a growth rate that increases exponentially with grain size and leading to a flattening of the CSD (**Figure II-15b**), as observed in some natural systems.

- **Agglomeration** is a mechanism in which crystals adhere to each other, forming clusters that can grow into larger aggregates. The experimental study of Burkhart et al. (1980) on nuclei shows that they tend to agglomerate, producing larger particles. The result is

a kink CSD (**Figure II-15c**) between the smallest particles, and the largest (clusters) corresponding to the second crystal population.

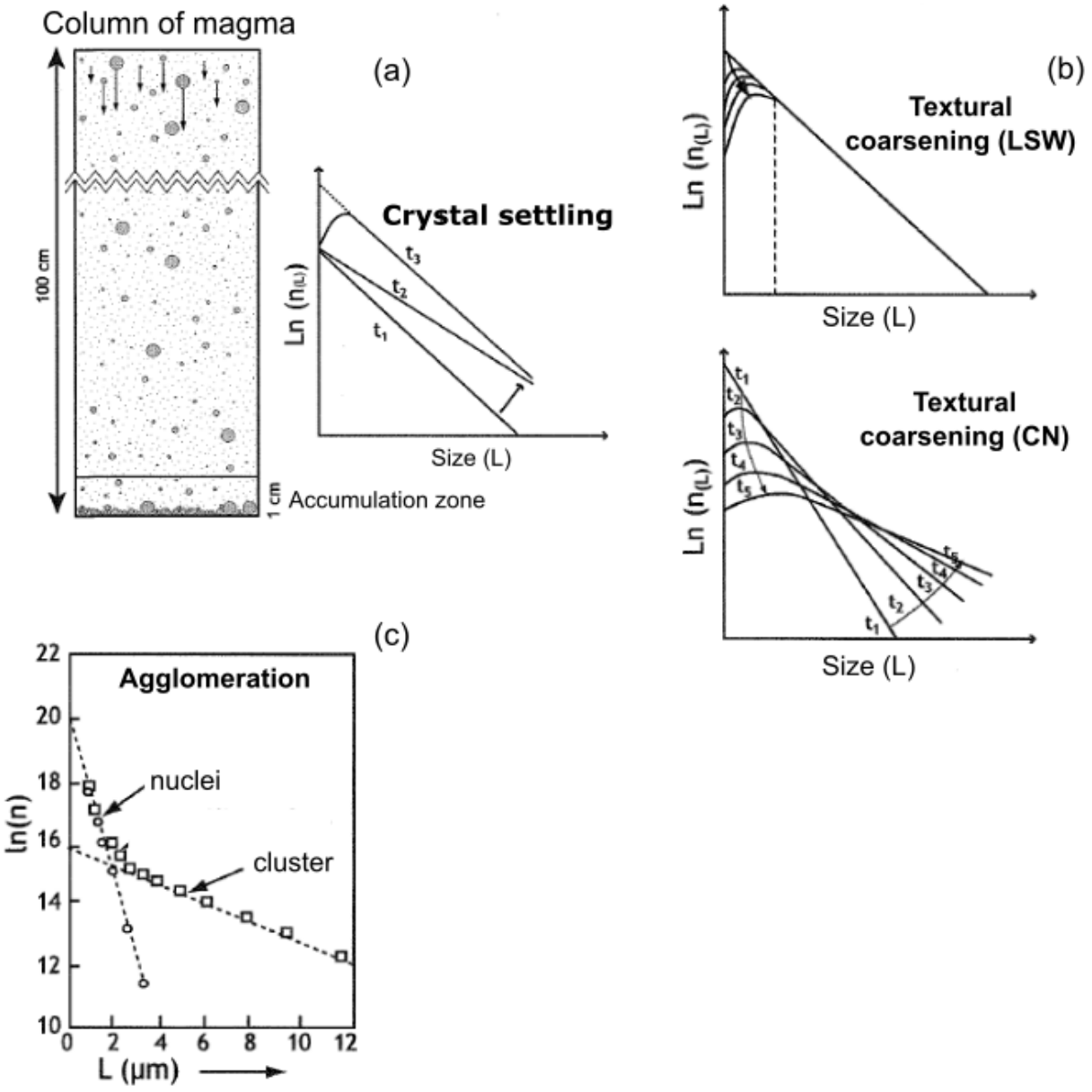

***Figure II-15**: CSD profiles resulting from different physical processes: (a) crystal settling, (b) textural coarsening, (c) agglomeration.*

Challenges linked to CSD construction

The CSD construction involves two main challenges: defining crystal size and converting 2D data into 3D measurements. here is no clear consensus on how to define crystal

size, with different studies using various approaches: the major axis (*Morgan et al. 2007*; *Muir et al. 2012*), the minor axis (*Cashman 1992*; *Pupier et al. 2008*), or the square root of the crystal area ($\sqrt{crystal\ area}$) (*Cashman and McConnell 2005*; *O'Driscoll et al. 2007*; *Namur et al., 2020*). *Cashman (1992)* argued that, for tabular crystals, the apparent 2D crystal width (w) is a more stable and reliable measurement than the apparent crystal length (l).

Passage from 2D to 3D data

Concerning the second challenge related to the passage from 2D data to 3D CSD, the easiest method remains the use of tomography/X-ray microtomography technique allowing direct 3D (*Gualda and Rivers 2006*; *Jerram et al. 2009*) and 4D measurements (*Le Gall et al. 2021*; *Polacci et al. 2018*; *Tripoli et al. 2019*). This method is nevertheless expensive and has limitations such as low contrast differences in the case of phases with similar density. *Duchene et al. 2008* (see above) used an alternative but quite laborious approach with 3D reconstruction using serial sectioning polished sections.

The most used method remains indirect technique based on stereological conversions (*Higgins 2000*) for area to volume correction, and to define real 3D shape. In their paper, *Jaret et al. (2008)* compared the various methods including the area to volume correction alone (the oldest technique), as well as plugins' software such as the CSDcorrection program (*Higgins 2000*). This plugin uses complex algorithm to correct two main problems: the 2D intersection probability effect (where a random section is more likely to intersect larger grains) and the 2D cut section effect (where one crystal can produce sections of different sizes and shapes depending on the orientation).

For a long time, the 2D-3D conversion consisted solely of estimating the volume crystal number density (N_V) by raising the surface density (N_A) to power 3/2 (**Figure II-16**; *Wager 1961*; *Higgins 2000*). An improvement considering the intersection probability effect in non-spherical object was proposed by *Royet (1991)*:

$$N_V(L_{xy}) = \frac{N'_A(L_{xy})}{L_{mean,xy}} \quad (33)$$

With $N_V(L_{xy})$, $N'_A(L_{xy})$ are the number of crystals per unit of volume, and area (corrected to the cut section effect) respectively in the length interval L_x to L_y, and $L_{mean,xy}$ the mean crystal size in this interval (**Figure II-16**).

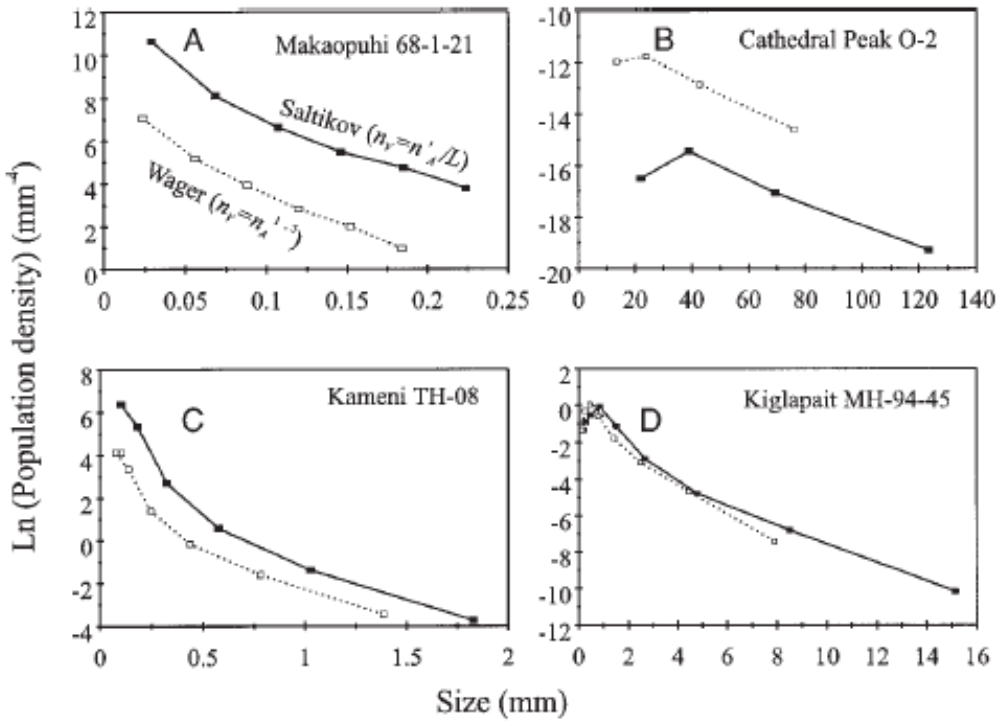

***Figure II-16**: Comparison between the two methods ($N_V = NA^{1/2}$, and = $N_V = \frac{N'_A}{L}$)to convert surface to volume number density (from Higgins 2000)*

Estimation of the 3D crystal habit

The correction of the cutting sections effect allowing the determination of the real crystal size requires knowledges of the 3D crystal shape. The relationship between the 3D crystal shape and the correspondence between 2D measured axes (width ***w***, length ***l***) and the true 3D axes (Short *S*, Intermediate *I*, and Long *L*) is influenced by the rock's fabric (*Higgins 1994*, *2000*). Stereological conversion and intersection probabilities are affected by both lineation and foliation in rocks (**Table II-6**). In the case of massive rock (without preferential crystal alignment), the apparent 2D axis *w* and *l* for parallelepiped object (as plagioclase) correspond to the Short *S* and Intermediate *I* axis respectively.

	Intersection			
Fabric type	Length (*l*)	Width (*w*)	Area	*w*/*l*
Isotropic	I	S	S.I	I/S
Foliated (F), normal	I	S	S.I	I/S
Foliated, parallel	***L***	***I***	***I.L***	***L/I***
Lineated (L), normal	***I***	***S***	***S.I***	***I/S***
Lineated, parallel	L	I	S.L	L/S
F and L, normal	***I***	***S***	***S.I***	***I/S***
F and L, parallel	***L***	***I***	***I.L***	***L/I***

***Table II-6**: Correspondence between 2D intersection length (l) and width (w) and the true 3D crystal dimensions (S, I, L) as a function of rock fabric (isotropic, foliated, or lineated) (from Higgins 2000). S, I, L = Short, Intermediate and Long dimension. Invariant values are in bold italic*

Assuming that all crystal sizes have the same shape, *Higgins (1994)* demonstrated that 3D crystal shape can be estimated from the width (*w*)/length (*l*) crystal distribution. In massive rocks, the mode of the distribution refers to the *S/I* ratio (**Table II-6**). By fixing the 3D short axis (*S*) to 1, the 3D intermediate axis (*I*) can be determined. The *I/L* ratio is then estimated using equations:

$$Skewness = \left(mean\ {}^{w}/_{l} - mode\ {}^{w}/_{l}\right)/standard\ deviation\ {}^{w}/_{l} \quad (34)$$

$${}^{I}/_{L} = Skewness + 0.5 \quad (35)$$

Higgins' equations are based on numerical models in which a parallelepiped object with a defined *S*:*I*:*L* is randomly sectioned over 50 000 times to provide a robust *w/l* distribution. Using the *CSDcorrection* based on this numerical model, it is possible by fitting the observed 2D *w/l* distribution, to estimate the 3D long axis (*L*), provided that the volumetric proportion of plagioclase matches the surfaci proportion estimated in thin sections. Several other tools also offer alternative approaches to estimating 3D crystal habits, such as *CSDslice* (*Morgan and Jerram 2006*) and *ShapeCalc* (*Mangler et al. 2022*) Excel spreadsheets, or *HabitEst3D* Python program (*Li et al. 2022*).

CSDslice, the earliest of these tools, developed by *Morgan and Jerram (2006)*, is still widely used as input for the *CSDcorrection* program. It uses a similar modelling approach, comparing 2D crystal measurements with theoretical 2D shape curves generated from over 10 000 random sections of 703 discrete crystal habits. Depending on the crystal habit (tabular or acicular), between 75 and 250 crystals are typically needed to obtain a robust estimation. *Mangler et al. (2022)* showed that while the *CSDcorrection* and *CSDslice* display similar ***w/l*** distribution for a tabular shape (*w/l* ratio < < 1, where the *w/l* mode well correspond to *S/I*), significant differences appear for a more prismatic/equant 3D shape (*S/I* ~ 1), or with a more spread distribution without clear mode. This lack of clear *w/l* mode is observed in some natural (*Mangler et al. 2022*) and experimental samples (*Duchene et al. 2008*; *Billon et al. 2025*). This lack of a well-defined mode reflects the presence of multiple crystal populations with variable

shapes. The *ShapeCalc* model (*Mangler et al 2022*) is based on similar numerical constructions, using reference *w/l* distributions generated with *CSDcorrection***.** It covers a broader range of crystal habits (from 1:1:1 to 1:20:20), compared to *CSDslice* (1:1:1 to 1:10:10). Estimations with a $R^2 > 0.975$ are considered sufficiently robust. Contrary to *CSDslice* which reports the 5 best estimations (referring on the dominant 3D shape), *ShapeCalc* displays the 100 best-fitting estimations in a Zingg diagram (*I/L* = f(*S/I*)), illustrating shape variability within a same crystal population. **Table II-7** illustrates differences between the CSDslice and ShapeCalc spreadsheets. The *S/I* and *I/L* estimates show relative differences of 12% (±14) and 14% (±90), respectively, between the *CSDslice* and *ShapeCalc* spreadsheets. This indicates that *I/L* values are generally more variable across samples and therefore less robust. A less known program, *HabitEst3D* (Python3 cross-platform; *Li et al. 2022*) also evaluates the crystal shape variability in a same sample, estimating the proportion of each crystal shape, in addition to propose an average 3D crystal habit.

					CSDslice			ShapeCalc		
	Sample	Exp conditions	Type	Crystal number	*S/I*	*I/L*	R^2	*S/I*	*I/L*	R^2
Billon et al. (in review)	G 0-4	ISO 1160 °C	Seed-bearing	455	0,91	0,73	*0,91*	0,77	0,70	*0,998*
Billon et al. (in review)	G 0-10	ISO 1160 °C	1450 °C, 2h	1598	0,31	0,64	*0,84*	0,32	0,39	*0,995*
Billon et al. 2025	G 1-1	1 °C/h, 1165 °C	Seed-bearing	480	0,77	0,29	*0,73*	0,71	0,18	*0,977*
Billon et al. 2025	G 1-4	1 °C/h, 1100 °C	Seed-bearing	2221	0,80	0,69	*0,87*	0,74	0,15	*0,996*
Billon et al. 2025	G 3-3a	9 °C/h, 1120 °C	Seed-bearing	1745	0,71	0,16	*0,52*	0,45	0,34	*0,909*
Billon et al. 2025	G 3-5	9 °C/h, 1050 °C	Seed-bearing	527	0,50	0,20	*0,56*	0,37	0,48	*0,94*
Billon et al. (in review)	G 4-2	25 °C/h, 1100 °C	Seed-bearing	930	0,63	0,20	*0,76*	0,45	0,34	*0,961*
Billon et al. (in review)	G 5-2a1	125 °C/h, 1100 °C	Seed-bearing	1053	0,63	0,14	*0,60*	0,45	0,34	*0,94*
Billon et al. (in review)	G 8-1	9 °C/h, 1050 °C	1450 °C, 2h	129	0,14	0,70	*0,89*	0,12	0,98	*0,993*
Billon et al. (in review)	G 8-2	9 °C/h, 1000 °C	1450 °C, 2h	215	0,17	0,60	*0,90*	0,17	0,46	*0,993*
Billon et al. (in review)	G 9-2	25 °C/h, 1050 °C	1450 °C, 2h	97	0,17	0,60	*0,69*	0,13	0,39	*0,974*
	OS23	Osorno (whole pop)	Basalt	1862	0,53	0,19	*0,70*	0,37	0,48	*0,961*
	OS30	Osorno (whole pop)	B-A	1565	0,63	0,32	*0,77*	0,51	0,35	*0,982*
	OS42	Osorno (whole pop)	Dacite	637	0,25	0,40	*0,56*	0,28	0,53	*0,92*
	CL119	Calbuco (whole pop)	Basalt	1563	1,00	0,10	*0,66*	0,51	0,35	*0,989*
	CL22	Calbuco (whole pop)	B-A	888	0,67	0,75	*0,70*	0,67	0,47	*0,998*
	VR36	Villarrica (whole pop)	B-A	699	0,56	0,18	*0,83*	0,45	0,34	*0,981*
	VR26a	Villarrica (whole pop)	Dacite	501	0,42	0,63	*0,72*	0,40	0,57	*0,993*

Table II-7*: Comparison betwenn 3D shapes (S/I, I/l) estimated by CSDslice (Morgan and Jerram 2006), and ShapeCalc spreadsheet (Mangler et al. 2022). Red values correspond to estimates with an* $R^2 <$ *0.975 in the ShapeCalc spreadsheet.*

Summary, advantages and inconvenients

The Crystal Size Distribution (also called CSD) method is a quantitative technique based on two main textural parameters: the crystal size and crystal number density. Regardless of the type of samples (natural or experimental), the main advantage of the CSD method is its ability to provide a quantitative approach (nucleation and growth rates, crystal residence/ascent time) from qualitative description. In experimental studies where parameters are controlled, this method allows to assess the impact of pressure, temperature, and volatile content for example on the crystal size distribution and crystallization processes (nucleation and growth rates). Compared to certain micro-analytical or isotopic methods used to calculate magmatic timescales, CSD analysis is relatively simple, non-destructive, and based on the examination of optical or BSE images. The CSD method, and its exponential relation between crystal number density and crystal size is based on several key hypothesis:

- Closed system without any exchange
- Continuous, linear growth, independent of crystal size
- Homogeneous nucleation (without intervention of preferential nucleation sites)

Resulting CSDs show a linear regression (*Ln (crystal number density) = f(crystal size)*). However, in most magmatic systems, these assumptions are often contradicted, leading to curved CSDs. Such deviations reflect magmatic processes, including textural maturation, or differences between homogeneous and heterogeneous nucleation. In experimental studies, CSD method has the advantage of providing insights into well-constrained crystallization parameters, such as oxygen fugacity, cooling or decompression rate, overheating effects, initial composition, and volatile content.

However, several limitations must be considered when using this method. First, the accuracy of the CSD is highly dependent on segmentation quality, especially for the smallest crystals. A robust CSD requires a representative sample and a statistically sufficient number of crystals, commonly over 200. Even so, the smallest crystals are often underestimated due to resolution limits. Moreover, software tools like *CSDcorrection*, commonly used to generate CSDs, require the transformation of 2D measurements into 3D data, involving assumptions about crystal shape. These assumptions are often based on simple geometries (e.g., spheres) or rely on a single dominant crystal habit (estimated with tools such as *CSDslice* or *ShapeCalc*), which may be far from reality, especially when multiple crystal populations with varying sizes and morphologies coexist.

CSD interpretation must also be approached with caution as different processes can lead to similar CSD curves. In experimental studies, contrary to open systems where older crystals are removed, curved CSD in closed systems are generated by a modification of the nucleation, rather than variation in growth rate. Another common example is the concave-down curvature commonly observed at small crystal sizes. This observation may result from textural maturation involving the dissolution of small crystals, but also to an underestimation of small crystals due to resolution limitations. These interpretive ambiguities highlight the fact that CSD analysis alone is not always sufficient.

Application for our study

In this study, the use of the CSD method serves a dual purpose: (1) to experimentally constrain nucleation and growth rates at different cooling rates, to compare this method with other textural approaches (**Chapter III**); and (2) to apply this method, combining segmentation of natural samples with experimentally determined growth rates, to constrain magmatic processes. The CSD method is also used qualitatively to track the evolution of nucleation and growth processes under various experimental crystallization conditions (e.g., different cooling rates, degrees of undercooling, and final dwell durations; see **Chapter IV**).

Because it is not straightforward to estimate true 3D population densities from 2D sections, we compared CSDs generated using only the 2D major axis ***l*** (without 3D estimation) to those generated using the CSDCorrections method of *Higgins (2000)* to quantify the associated errors on derived nucleation and growth rates. To plot CSD profiles along the real 3D axis ***L***, the CSDCorrections assumes that all crystals have the same 3D shape. However, it is unlikely that all crystals in a sample have the same shape, particularly when multiple crystal generations coexist.

Here, we considered the 2D major axis (l) and an estimation of the 3D shape of the entire crystal population (i.e. the volumetric aspect ratio S:I:L), simulated using ShapeCalc Excel spreadsheet to simulate L. Plagioclase CSDs were calculated using the 2D major axis, as in several other studies (*Brugger and Hammer 2010a*). All CSD data are provided in ***supplementary file IV-4*** (**Chapter IV**). The total sample area, plagioclase abundance, and vesicularity (often <1%) were calculated using *Fiji* software. 3D CSDs were determined using *Higgins' (2000)* stereological conversion (*CSDCorrections* plugin). The CSDs were created on semi-logarithmic plots of the volumetric crystal density (N_V) normalized by the bin width (bw) vs. the 2D (l) or 3D (L: estimated with the *CSDCorrections* plugin) major axis length.

For each size range i, $N_{V,i} = \frac{N_{A,i}}{S_{n,i}}$ (36)

As noted by *Armienti (2008)*, CSDs depend on the number of size intervals used. Consequently, various size bin widths (*bw*) were compared: log 10; and *bw* = 5, 10, or 20 µm (***Supplementary file III-4***).

Analytical techniques

Scanning Electron Microscope (SEM)

Scanning Electron Microscopy (*SEM*; **Figure II-17a**) is a powerful analytical technique widely used in various fields such as geology (particularly for opaque minerals) and biology (*Smith and Oatley 1955*), to investigate the surface of both organic and inorganic materials at nanometer (nm) to micrometer (µm) scales (*Vernon-Parry et al. 2000*; *Mohamed and Abdullah 2018*; *Herrero et al. 2023*). The concept of SEM originates from the discovery in the 1890s that electrons could be deflected by magnetic fields, which led to the idea of using a high-energy electron beam as a substitute for visible light (*Wells 1974*). The first prototype of a scanning electron microscope was developed in 1933 by the physicists Ernst Ruska and Max Knoll.

Compared to the resolution limits of the human eye (~0.5 mm) and optical microscopy (~2 × 10^{-4} mm; magnification about ×1000), *SEM* offers a significantly higher resolution up to ×1 000 000, making it particularly valuable for detailed surface imaging. SEM can provide information on surface topography, crystalline structure, chemical composition and electrical behavior of the top 1 µm or so of specimen (*Vernon-Parry et al. 2000*). When coupled with Energy Dispersive X-ray Spectroscopy (*EDS*), *SEM* becomes even more powerful, allowing both qualitative and semi-quantitative chemical analysis, which provides rapid elemental information that is often inaccessible with other techniques (*Mohamed and Abdullah 2018*).

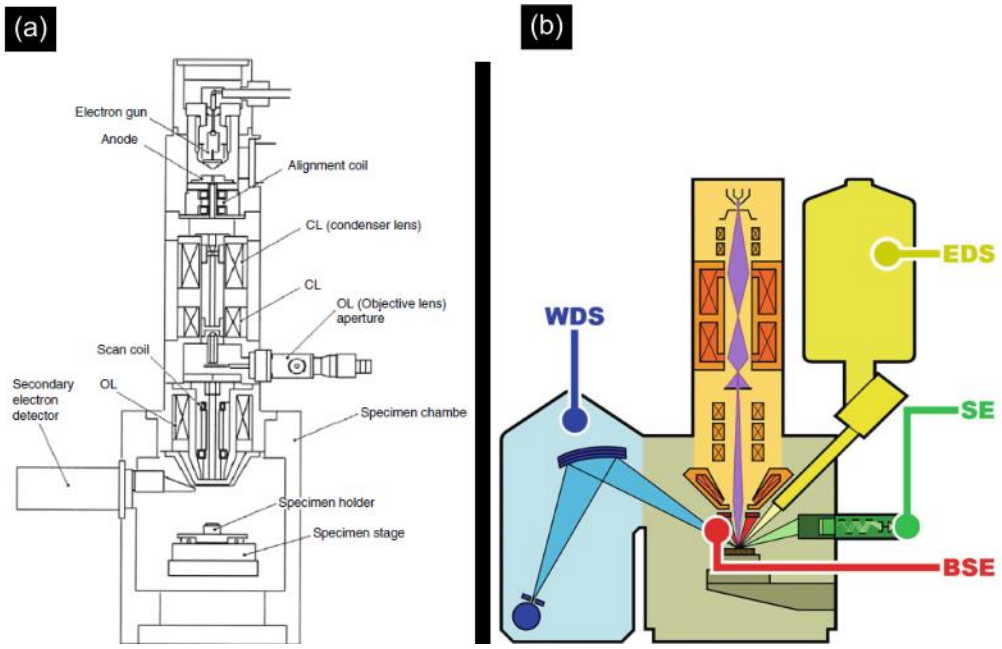

***Figure II-17**: Schematic representation of a Scanning Electron Microscope (SEM). (a) Detailed view of the column components (highlighted in orange in (b)) (from Zhou et al. 2006). (b) Various detectors attached to the SEM (from Frahm 2020): Secondary Electron Detector (SE), Backscattered Electron Detector (BSE), Energy Dispersive Spectroscopy (EDS), and Wavelength Dispersive Spectroscopy (WDS).*

Sample preparation

After embedding in epoxy resin, samples are polished using abrasive papers with progressively finer grain sizes: 22 µm, 8 µm, and 2 µm. This initial polishing is followed using a diamond suspension (~1 µm) to achieve a finer surface polish. For Electron Backscatter Diffraction (*EBSD*) analysis, an additional polishing step using a 1/4 µm diamond suspension or colloidal silica is used to obtain a deformation-free and highly reflective surface. Ultrasonic cleaning can be added after polishing to remove any residual particles or polishing compounds. To ensure optimal X-ray detection during Energy Dispersive Spectroscopy (*EDS*) and Wavelength Dispersive Spectroscopy (*WDS*), a well-polished and perfectly flat surface is essential. Since our samples, comprising both experimental charges and thin sections of natural rocks, are only weakly conductive, a conductive coating (carbon in this study) is applied to prevent any charging and image distorsion. Coating enhances electron conductivity, optimizes backscattered electron (*BSE*) imaging, and helps prevent surface charging artifacts. Such charging effects may otherwise occur in the presence of locally highly conductive phases, such

as oxides or platinum wires, which generate charge imbalances at the microscale. This step is generally not used for semiconductor materials which do not need specific treatment.

Emitted signals

SEM images are the result of the interaction between the sample and the electron beam current. When the incident beam strikes the sample, electrons penetrate the sample for some distance before to be reflect (**Figure II-18**). The contact between the sample and the primary beam electron corresponds to the primary excitation region. The size and shape of this region is directly dependent on the beam electron energy, its incident angle, but also on the atomic number and density of the specimen. Volume and depth increase with accelerating voltage but decrease with an increasing atomic number of the specimen. The use of a high accelerating voltage tends also to decrease the resolution of the surface sample. A good balance is necessary to assure a sufficient depth penetration but also enough surface informations. Various signals can be captured, such as secondary electrons (SE), backscattered electron (BE), or also continuum X rays (**Figure II-17b, and Figure II-18**; *Zhou et al. 2006*; *Vernon-Parry et al. 2000*).

1. ***Secondary Electron (SE) images:*** Secondary electrons are the first signals to be capture, and the most used for sample visualizations. Because of their low energy around 3 – 5 eV (< 50 KeV), they correspond only to the first near-surface layers (few nanometers below the surface). These electrons are used for topographic contrast visualizations, giving very detailed information on the crystal surface and roughness.

2. ***Backscattered Electron (BSE) images:*** Backscattered electrons correspond to the most used signal for sample images. With higher energy (> 50 eV), this signal provides both compositional and surface informations at a slightly deeper layer. The backscattered yield is defined by the percentage of electrons reemitted and depend principally to the atomic number of the element, giving the BSE image contrast. Because elements such as oxides or Pt-wire are quite heavy, they appear are very light compared to other such as quartz, plagioclase or pyroxene.

3. ***Auger electrons and X-rays:*** X-ray signal is used to provide chemical informations. They are generated by atoms when the incident high-energy electrons knock out an

inner-shell electron and an outer-shell electron moves into the empty orbit. This signal is used for EDS measurements (detailed below), giving rapid semi-quantitative analysis.

4. ***Other types***

   i. ***Auger electrons:*** They are emitted from surface atomic layers and provide surface chemical informations, using specific detector and instrument.

   ii. ***Cathodoluminescence (CL)***: This signal corresponds to photos excess energy delivered from materials. CL signal is used to reveal defects degrade from radiative properties; with a resolution between 50 nm and 1 µm.

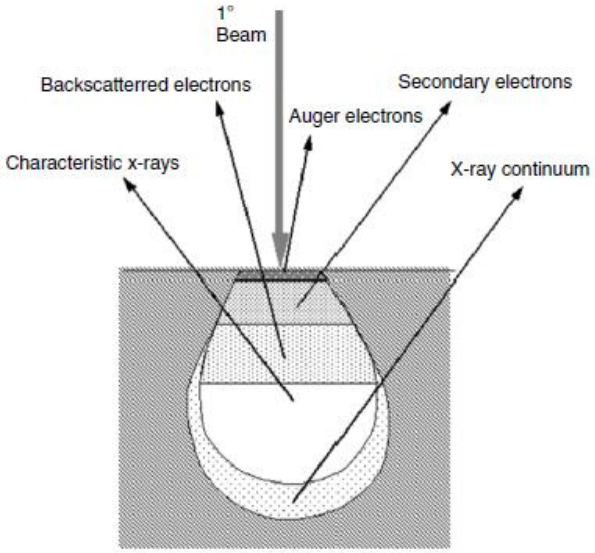

Figure II-18*: Signals generated by electron beam–specimen interactions in SEM and their detection regions (taken from Zhou et al. 2006).*

SEM operation and Configuration

The electron gun, which is on the top of the column, produces the electrons and accelerates them to an energy level up to 30 - 40 keV. Lenses and aperture are used to focus the incident electron beam, to have a high-resolution image. To allow incident electrons to cross without scattering by air, a high vacuum environment is necessary in the specimen chamber. Both mechanical and diffusion are generally used to pump down the atmospheric pressure in the

chamber (Zhou et al. 2006). This section briefly details the different parts of the SEM (**Figure II-17a**):

- **Electron gun**: A source to generate high energy electrons. The most suitable is to provide a stable high energy electron beam current, with a small spot size and the lowest possible energy dispersion. The most common electron gun is the Tungsten hairpin filament (~ 100 µm), heated up to 2500 °C to create electrons by thermal emission (Vernon-Parry et al. 2000; Zhou et al. 2006). An alternative is the LaB_6 filament which produce a stronger electron emission, with a smaller spot size, for the same temperature as the tungsten filament, with also a longer lifetime. However, this last is easily oxidized at high temperature, and a vacuum higher than 10-9 bar is necessary in electron gun chamber (Zhou et al. 2006). Modern SEM use a field emission gun (cold CFE, orthermal field emission TFE) to enhance the current and decrease energy dispersion. A vacuum of 10-13 bar is necessary for this type of source.

- **Electron condenser lenses**: Between two or three electromagnetic condenser lenses in amount of the column are used to magnify or demagnify the incident current and focus it (**Figure II-19**). They consist in two rotational symmetric iron poles, in which a copper winding provide a magnetic field (Zhou et al. 2006). Because incident beam current generally diverges after the mission source (anode plate), condenser lenses allow to electrons to converge in a parallel current, passing through the hole between the two iron pieces. A virtual aperture is generally added on the most modern SEM to limit the beam current and control the size of the focal point (**Figure II-19**).

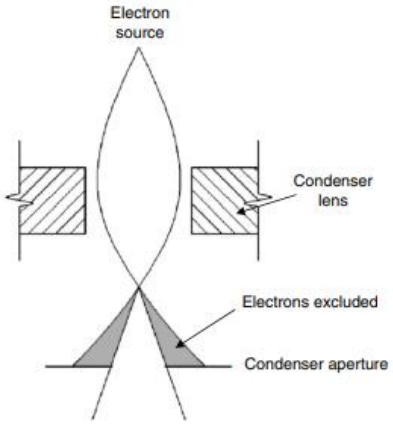

***Figure II-19**: Diagram showing the electron path through the condenser lens and condenser aperture (taken from Zhou et al. 2006). Non-homogeneous or scattered electrons are filtered out by the condenser aperture.*

- **Objective lenses**: They focus the electron current below the condenser aperture, at the bottom of the column. Coupled with a real aperture at the base of the lenses, they focus the incident current into a probe point of the specimen surface, to supply any demagnification. A reduction of the spot size (diameter of the beam current) increases the image resolution. Asymmetric pinhole lens is the most common objective lens but have a quite large lens aberration (**Figure II-20a**). Symmetric lens, the observed specimen is placed inside lens, which reduces the aberration (**Figure II-20b**). However, with this configuration the specimen cannot exceed ~ 5 mm. The Snorckel lens (**Figure II-20c**) corresponding to the last configuration produce a high magnetic field, combining the advantages of the previous lens, but with a larger observed specimen.

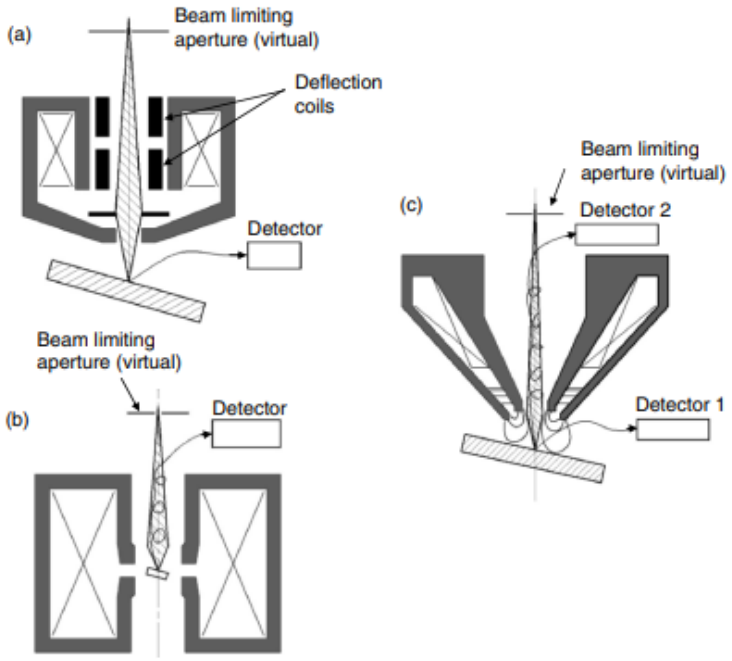

***Figure II-20**: Objective lens configurations (from Zhou et al. 2006): (a) asymmetric pinhole lens, characterized by large lens aberrations; (b) symmetric immersion lens, allowing observation of small specimens with minimal lens aberrations; and (c) snorkel lens, in which the magnetic field.*

- ***Deflection system:*** Lens defects (astigmatism) and contamination on aperture and column can modify the electron beam profile on the sample surface from a circular spot to ellipsoid. The resulting image is in this case deformed in various directions. A series of stigmator coils around lens is used to correct astigmatism and assure a good resolution image.

- **Electron detectors:** The interaction between the surface of the sample and incident beam current produces various types of signals (explained above). These signals are captured by electron detectors such as the BSE detector, ET detector for also secondary electrons, but also energy dispersive X-ray spectrometer (also called EDS detector) and photomultipliers for the cathodoluminescence signal:

    - ✓ *EDS measurements:* Photons corresponding to the lost electron energy are emitted when the incident current interact with the sample surface and captured by an additional EDS detector (*Mohammed and Abdullah 2018*). These photons are specific to chemical elements and correspond to the characteristic X-ray energies. The X-ray dispersive spectrometer measures the X-ray adsorption and converts the X-ray intensity into relative chemical concentration. Quantitative chemical mapping can also be constructed using implemented software such as *Aztec*.

Electron Backscatter Diffraction analysis

The Electron Backscatter Diffraction is a SEM technique providing local microstructural information, and crystalline orientation, down to nanoscale. In a field emission gun SEM, EBSD can provide quantitative analyses on ~ 0.2 µm grains (*Humphreys 2001*). The first commercial system was launched in 1986 by *Oxford Instrument* (*Dingley 2004*). It is based on the original Dingley software and was very elementary. The development of this this method is done by various authors (e.g., *Randle 1992*; *Dingley and Randle 1992*; *Adams 1997*). This technique provides complementary analysis to chemical composition, and can give essential informations on phase identification, distribution, boundary characterization and crystal texture characterization (crystallographic growth in preferential orientation).

The polished sample is titled between 60 and 70 ° to the horizontal. By interacting with the titled sample, the incident current produces diffracted electrons detected with a fluorescent screen. A part of these incident electrons on the atomic lattice planes at different angles (θ) which satisfy the Bragg equation:

$$n\lambda = 2dsin(\theta) \quad (37)$$

With n the diffraction order, λ the electron wavelength, and d the spacing of the diffracting plane.

The diffracted electrons form paired large angles cones corresponding to the diffracting planes, delimited by two right lines on the screen. These characteristic Kikuchi bands (quartz example in **Figure II-21**), specific to each mineral structure, are formed in region where enhanced electron intensity intersect the screen. The pattern imaged by the EBSD detector correspond to a gnomonic projection of the diffracted cone.

When the diffraction diagram is in enough quality, by indexing the Kikuchi bands with the Miller indices (which define the orientation of the crystalline plane) of the diffracting plane, it is possible to know the orientation of the specific analyzed point. Because the crystal orientation is measured at each point, it is possible to refine the crystal shape, orientation and edges (see **Chapter IV**).

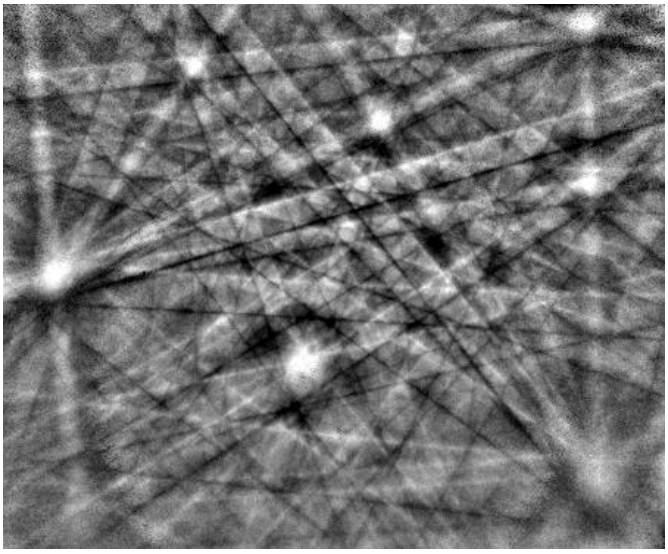

***Figure II-21**: Exemple of quartz (SiO2) Electron Basckattered Diffraction pattern (EBSP) (Taken from the Oxford Instrument website).*

Electron Probe Micro-analysis (EPMA)

The Electron Probe Micro-analysis (EPMA) is a technique used for quantitative chemical analysis at micrometric scale (*Llovet 2019*). As for the SEM, its utilization has a lot of application fields from material sciences to archeology, electronics, or also biology. Its structure and operation is similar to that of the SEM (*Llovet 2019*).

Principle and structure

EPMA globally consists of a column with inside an electron gun, and several electromagnetic lenses used to focus the incident beam on the sample; and several WD spectrometers. As for the SEM, the electron column is maintained at a high vacuum to prevent filament oxidation of the electron gun. WD Spectrometers consist of single crystal Bragg spectrometers operating in reflexion mode, and in semi or fully focusing geometry. WD Spectrometers contain a focusing crystal monochromator, and a gas proportional counter, arranged in a way that diffracted X-ray signal followed the Bragg's law, and only those within a narrow wavelength range are detected by the proportional counter. The wavelength of the X-rays reflected depends on the distance between the crystal and the sample analysed. Electron microprobes can generally have up to 5 WD spectrometers (*Llovet 2019*).

As previously explained, when an incident current beam interacts with the sample, different types of electrons are emitted. In the case of EPMA analysis, signal of interest comes from inelastic interactions, where electron is put to an excited state (a part of the electron energy is adsorbed by atomic electrons). This excited state in valance bands produces a vacancy in the inner shells. After the production of a vacancy by ionization, atom de-excites by the migration of the vacancy to outer shells by a succession of electron transitions (**Figure II-22**). Each transition produces characteristic X-ray and Auger electrons (see above) (*Llovet 2019*). X-ray production is not constant with depth. X-ray energy is directly linked to the energy of the two shells implicated into the transition and is specific to each element (qualitative measurement with EDS).

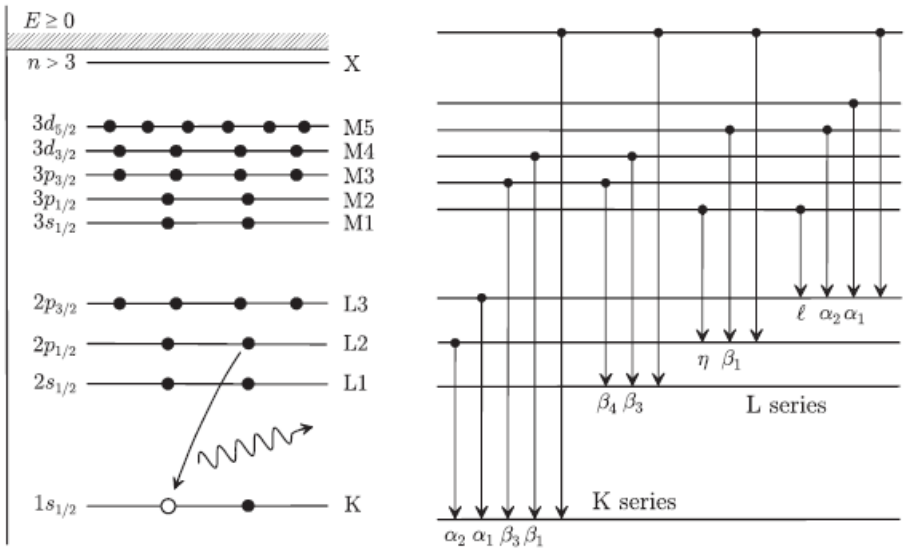

***Figure II-22**: Schematic of inner electron shells (left) and main electronic transitions producing characteristic X-rays (right). Taken from Llovet (2019).*

Quantitative analysis

Quantitative analyses are performed by measuring the ratio of the characteristic X-ray intensity emitted by a sample element, and that from the same element but in a referential material (standard). This ratio called *k-ratio* is corrected to the matrix effects caused by the global composition of the sample. Matrix effect is linked to the atomic number of the matrix (*Z*), potential adsorption (*A*) by other elements, and the secondary fluorescence (*F*) by other elements parasiting the signal. The resulting quantification equation (*Llovet 2019*) can be written like that:

$$k_i = \frac{I_i}{I_i^{std}} = \frac{c_i}{c_i^{std}} \times ZAF \quad (38)$$

with c_i and I_i the weight fraction and background-corrected X-ray intensity of element *i*, respectively. c_i^{std} and I_i^{std} are the weight fraction and background-corrected X-ray intensity of the same element in the standard. The measurements realized in the sample and standard need to be realized in the same operating condition. A well-polished sample, as well as a flat surface perpendicular to the incident current is primordial in these types of measurements. To minimize the matrix error, composition matching standard with the material composition are generally used. These standards are called *primary standards*.

The ZAF correction was replaced by the φ(ρz) method providing more accurate compositions, especially for the light elements. An accuracy of 1 – 2% can be achieved for the major elements. Another way to quantify the results is to use a calibration curve, using also standards with a similar composition to the material measured. X-ray conversion to concentration is in this case is only done by assuming a linear regression between the two. This method is principally used for traces elements, Carbone and Azote.

Operating conditions

EDS/WDS measurements

EDS measurements were realized using the *Quanta-650F FEG-SEM* at Cambridge University (England); and the *Tescan MIRA 4* SEM at KULeuven (Belgium). The EDS analyses were performed using a voltage of 20 KeV, with a beam current of 6-9 nA, and a working distance of 10-15 mm. SEM imaging were done using a 15 KeV voltage, with a working distance of 10-15 mm, and a dwell time of 10 µs.

WDS measurements were them realized with the *CAMECA SX Five Tactics* at the LMV in Clermont-Ferrand (France), the *JEOL JXA-8530F* at the Department of Material Engineering at the KU Leuven (Belgium), and the *JEOL JXA-ISP 100* in Aachen (Germany). The crystal (plagioclase, Fe-Ti oxide and Clinopyroxene) and glass measurements were done using spot, and a defocused beam respectively. Calibration details for WDS analyses are provided below:

The CAMECA SX Five Tactics (Clermont-Ferrand) calibration standards were the same as those of *Bechon et al. (2022)*: wollastonite (Ca, Si), $TiMnO_3$ (Ti, Mn), Al_2O_3 (Al), fayalite (Fe), forsterite (Mg), albite (Na,), Cr_2O_3 (Cr), orthose (K), and NiO (Ni).

Standards used for JEOL JXA-8530F (KULeuven) and JEOL JXA-ISP 100 (Aachen University) are the same used by *Billon et al. (2025)*:

- JEOL JXA-8530F (KULeuven):
    - Obsidian (SiO_2, Al_2O_3, K_2O), apatite (P_2O_5), diopside (CaO), hematite (FeO), jadeite (Na_2O), olivine (MgO), rutile (TiO_2), rhodonite (MnO), chromium oxide (Cr_2O_3), and nickel (NiO) for glasses.
    - Albite (Al_2O_3), diopside (SiO_2), apatite (P_2O_5), hematite (FeO), jadeite (Na_2O), olivine (MgO), obsidian (K_2O), diopside (CaO), rutile (TiO_2), chromium oxide (Cr_2O_3), and rhodonite (MnO) for plagioclase.

- JEOL JXA-ISP 100 (Aachen University):
    - Glass (SiO_2, Al_2O_3, K_2O), jadeite (Na_2O), olivine (MgO), apatite (P_2O_5), diopside (CaO), rutile (TiO_2), hematite (FeO), Mn oxide (MnO), and chromite (Cr_2O_3) for glasses.
    - Plagioclase (SiO_2, Al_2O_3, CaO), jadeite (Na_2O), olivine (MgO), apatite (P_2O_5), orthoclase (K_2O), rutile (TiO_2), hematite (FeO), Mn oxide (MnO), and chromite (Cr_2O_3) for plagioclase.

EDS/WDS data are provided in the various chapters**.** In the case of EDS analysis performed in Leuven, as for WDS data, same secondary standards of plagioclase and glass as used to correct data. The EDS quantitative aspect, in comparison to WDS measurements, is discussed in the **Chapter III**.

EBSD analysis

Electron backscatter diffraction (EBSD) was employed to characterize the complex dendritic textures observed in some experiments (**Chapter IV**). Analyses were carried out on a HITACHI SU5000 field emission scanning electron microscope (FEG-SEM) equipped with a Symmetry EBSD camera at the Université de Lille, France, to assist in image segmentation. The microscope was operated at 20 kV with a beam current of a few nanoamperes and a working distance of 15–20 mm. To obtain a high-quality EBSD signal without applying a carbon coating (which can degrade EBSD quality), a partial vacuum of 30 Pa was used. The samples were tilted 70° towards the EBSD detector. Diffraction patterns were acquired at high acquisition speed with a resolution of 156 × 128 pixels, integrating 2–3 frames per measurement. Prior to EBSD analysis, samples were polished using ¼ µm diamond suspension, followed by final surface preparation with a Fishione Model 1061 ion polisher operated at 5 keV accelerating voltage, 5° milling angle, 50 % beam focus, and continuous rotation of the sample for 5 minutes.

References

Abramoff MD, Kwon YH, Li H, et al. (2004). A spatial truncation approach to the analysis of optical imaging of the retina in humans and cats. 2004 2nd IEEE International Symposium on Biomedical Imaging: Macro to Nano. 2. 1115 - 1118 Vol. 2. https://doi.org/10.1109/ISBI.2004.1398738.

Adams BL (1993) Orientation imaging microscopy: application to the measurement of grain boundary structure. Materials Science and Engineering: A 166:59–66. https://doi.org/10.1016/0921-5093(93)90310-B

Armienti P (2008) Decryption of Igneous Rock Textures: Crystal Size Distribution Tools. Reviews in Mineralogy and Geochemistry 69:623–649. https://doi.org/10.2138/rmg.2008.69.16

Avrami, M. (1939). Kinetics of phase change I. Journal of Chemical Physics 7, 1103-1112.

Avrami, M. (1940). Kinetics of phase change II. Journal of Chemical Physics 8, 212–224.

Bechon T, Billon M, Namur O, et al (2022) Petrology of the magmatic system beneath Osorno volcano (Central Southern Volcanic Zone, Chile). Lithos 426–427:106777. https://doi.org/10.1016/j.lithos.2022.106777

Billon M, Vander Auwera J, Namur O, et al (2025) Plagioclase crystal size distributions, growth and nucleation rates in an anhydrous arc basaltic andesite. Contrib Mineral Petrol 180:26. https://doi.org/10.1007/s00410-025-02213-9

Brugger CR, Hammer JE (2010a) Crystallization Kinetics in Continuous Decompression Experiments: Implications for Interpreting Natural Magma Ascent Processes. Journal of Petrology 51:1941–1965. https://doi.org/10.1093/petrology/egq044

Brugger CR, Hammer JE (2010b) Crystal size distribution analysis of plagioclase in experimentally decompressed hydrous rhyodacite magma. Earth and Planetary Science Letters 300:246–254. https://doi.org/10.1016/j.epsl.2010.09.046

Buret Y, Von Quadt A, Heinrich C, et al. (2016). From a long-lived upper-crustal magma chamber to rapid porphyry copper emplacement: Reading the geochemistry of zircon crystals at Bajo de la Alumbrera (NW Argentina). Earth and Planetary Science letters, 450: 120-131. https://doi.org/10.1016/j.epsl.2016.06.017

Burkhart LE, Hoyt RC, and Oolman T (1980) Control of particle size distribution and agglomeration in continuous precipitations. In G.c. Kuczynski, Ed. Sintering Processes, p. 23-38. Plenum, New York.

Burkhard DJ (2002a) Kinetics of crystallization: example of micro-crystallization in basalt lava. Contrib Mineral Petrol 142:724–737. https://doi.org/10.1007/s00410-001-0321-x

Burkhard DJ (2002b) Kinetics of crystallization: example of micro-crystallization in basalt lava. Contrib Mineral Petrol 142:724–737. https://doi.org/10.1007/s00410-001-0321-x

Cashman KV (1986) Crystal size distributions in igneous and metamorphic rocks. PhD thesis, Johns Hopkins University

Cashman KV (1992) Groundmass crystallization of Mount St. Helens dacite, 1980?1986: a tool for interpreting shallow magmatic processes. Contr Mineral and Petrol 109:431–449. https://doi.org/10.1007/BF00306547

Cashman KV (1993) Relationship between plagioclase crystallization and cooling rate in basaltic melts. Contr Mineral and Petrol 113:126–142. https://doi.org/10.1007/BF00320836

Cashman KV (2020) Crystal Size Distribution (CSD) Analysis of Volcanic Samples: Advances and Challenges. Front Earth Sci 8:291. https://doi.org/10.3389/feart.2020.00291

Cashman KV, Marsh BD (1988) Crystal size distribution (CSD) in rocks and the kinetics and dynamics of crystallization II: Makaopuhi lava lake. Contr Mineral and Petrol 99:292–305. https://doi.org/10.1007/BF00375363

Cashman KV, McConnell SM (2005). Multiple levels of magma storage during the 1980 summer eruptions of Mount St. Helens, WA. Bulletin of Volcanology, 68(1), 57-75.

Cortés JA, Gertisser R, Calder ES (2024) Magma recharge in persistently active basaltic–andesite systems and its geohazards implications: the case of Villarrica volcano, Chile. Int J Earth Sci (Geol Rundsch) 113:1145–1163. https://doi.org/10.1007/s00531-024-02414-w

Delesse MA (1847) Procédé mécanique pour déterminer la composition des roches. Comptes rendus de l'Académie des Sciences (Paris), 25: 544–545.

Dingley DJ, Randle V (1992). Microtexture determination by electron back-scatter diffraction. Journal of materials science, 27(17), 4545-4566.

Duchene S, Pupier E, De Veslud CLC, Toplis MJ (2008) A 3D reconstruction of plagioclase crystals in a synthetic basalt. American Mineralogist 93:893–901. https://doi.org/10.2138/am.2008.2679

Eberl DD, Kile DE, Drits VA (2002) On geological interpretations of crystal size distributions: Constant vs. proportionate growth. American Mineralogist 87:1235–1241. https://doi.org/10.2138/am-2002-8-923

Edgar AD (1973). Experimental Petrology. Basic principles and techniques. Clarendon Press,Oxford, 217 pp

Faust GT (1936). The fusion relations of iron-orthoclase. American Mineralogist: Journal of Earth and Planetary Materials, 21(12), 735-763.

Giuliani L, Iezzi G, Vetere F, et al (2020) Evolution of textures, crystal size distributions and growth rates of plagioclase, clinopyroxene and spinel crystallized at variable cooling rates from a mid-ocean ridge basaltic melt. Earth-Science Reviews 204:103165. https://doi.org/10.1016/j.earscirev.2020.103165

Grove TL (1982) Use of FePt alloys to eliminate the iron loss problem in 1 atmosphere gas mixing experiments: Theoretical and practical considerations. Contr Mineral and Petrol 78:298–304. https://doi.org/10.1007/BF00398924

Gualda GAR, Ghiorso MS, Lemons RV, Carley TL (2012) Rhyolite-MELTS: a Modified Calibration of MELTS Optimized for Silica-rich, Fluid-bearing Magmatic Systems. Journal of Petrology 53:875–890. https://doi.org/10.1093/petrology/egr080

Gualda GAR, Rivers M (2006) Quantitative 3D petrography using x-ray tomography: Application to Bishop Tuff pumice clasts. Journal of Volcanology and Geothermal Research 154:48–62. https://doi.org/10.1016/j.jvolgeores.2005.09.019

Hammer JE (2008) Experimental Studies of the Kinetics and Energetics of Magma Crystallization. Reviews in Mineralogy and Geochemistry 69:9–59. https://doi.org/10.2138/rmg.2008.69.2

Hammer JE, Rutherford MJ (2002a) An experimental study of the kinetics of decompression-induced crystallization in silicic melt. J Geophys Res 107:. https://doi.org/10.1029/2001JB000281

Hammer JE, Rutherford MJ (2002b) An experimental study of the kinetics of decompression-induced crystallization in silicic melt. J Geophys Res 107:. https://doi.org/10.1029/2001JB000281

Herrero YR, Camas KL, Ullah A (2023) Characterization of biobased materials. In: Advanced Applications of Biobased Materials. Elsevier, pp 111–143. https://doi.org/10.1016/B978-0-323-91677-6.00005-2

Higgins MD (1994) Numerical modeling of crystal shapes in thin sections: Estimation of crystal habit and true size. American Mineralogist 79:113-119.

Higgins MD (1998) Origin of Anorthosite by Textural Coarsening: Quantitative Measurements of a Natural Sequence of Textural Development. Journal of Petrology 39:1307-1323. https://doi.org/10.1093/petroj/39.7.1307

Higgins MD (2000) Measurement of crystal size distributions. American Mineralogist 85:1105–1116. https://doi.org/10.2138/am-2000-8-901

Higgins MD (2002a) Closure in crystal size distributions (CSD), verification of CSD calculations, and the significance of CSD fans. American Mineralogist 87:171–175. https://doi.org/10.2138/am-2002-0118

Higgins MD (2002b). A crystal size-distribution study of the Kiglapait layered mafic intrusion, Labrador, Canada: evidence for textural coarsening. Contributions to Mineralogy and Petrology, 114: 314-330. https://doi.org/10.1007/s00410-002-0399-9.

Higgins MD (2006) Quantitative textural measurements in igneous and metamorphic petrology. Cambridge University Press

Higgins MD, Roberge J (2003) Crystal Size Distribution of Plagioclase and Amphibole from Soufrière Hills Volcano, Montserrat: Evidence for Dynamic Crystallization-Textural Coarsening Cycles. Journal of Petrology 44(8):1401-1411. https://doi.org/10.1093/petrology/44.8.1401

Jerram DA, Mock A, Davis GR, et al (2009) 3D crystal size distributions: A case study on quantifying olivine populations in kimberlites. Lithos 112:223–235. https://doi.org/10.1016/j.lithos.2009.05.042

Kent AJR, Darr C, Koleszar AM, et al (2010) Preferential eruption of andesitic magmas through recharge filtering. Nature Geosci 3:631–636. https://doi.org/10.1038/ngeo924

Kirkpatrick RJ (1977) Nucleation and growth of plagioclase, Makaopuhi and Alae lava lakes, Kilauea Volcano, Hawaii. Geol Soc America Bull 88:78. https://doi.org/10.1130/0016-7606(1977)88<78:NAGOPM>2.0.CO;2

Kramer HJ, Lakerveld R, Kong H (2019). Selection and design of industrial crystallizers. Handbook of Industrial Crystallization.

Larsen LM, Sorensen H (1987). The llimaussaq intrusion progressive crystallization and formation of layering in an agpaitic magma. Geol. Soc. Spec. Publ. 30: 473-488. https://doi.org/10.1144/GSL.SP.1987.030.01.23

Larsen HC, Duncan RA, Allan JF, Brooks K (eds) (1999) Proceedings of the Ocean Drilling Program, 163 Scientific Results. Ocean Drilling Program. http://dx.doi.org/10.2973/odp.proc.sr.163.1999

Le Gall N, Arzilli F, La Spina G, et al (2021) In situ quantification of crystallisation kinetics of plagioclase and clinopyroxene in basaltic magma: Implications for lava flow. Earth and Planetary Science Letters 568:117016. https://doi.org/10.1016/j.epsl.2021.117016

Li J, Yang Z-F, Wang Y (2022) HabitEst3D: A User-Friendly Software for Estimating Mixed Crystal Habits from Two-Dimensional Sections in Igneous Rocks. Minerals 12:1001. https://doi.org/10.3390/min12081001

Llovet X (2019) Electron Probe Microanalysis. In: Encyclopedia of Analytical Science (Third Edition, p. 30-38), Academic press, Elsevier. https://doi.org/10.1016/B978-0-12-409547-2.14369-0

Mangler MF, Humphreys MCS, Wadsworth FB, et al (2022) Variation of plagioclase shape with size in intermediate magmas: a window into incipient plagioclase crystallisation. Contrib Mineral Petrol 177:64. https://doi.org/10.1007/s00410-022-01922-9

Marsh BD (1998) On the Interpretation of Crystal Size Distributions in Magmatic Systems. 39:

Mohammed A, Abdullah A (2018). SCANNING ELECTRON MICROSCOPY (SEM): A REVIEW. International Conference on Hydraulics and Pneumatics. https://www.researchgate.net/publication/330168803

Morgado E, Parada MA, Contreras C, Castruccio A, Gutiérrez F, McGee LE (2015) Contrasting records from mantle to surface of Holocene lavas of two nearby arc volcanic complexes: Caburgua-Huelemolle Small Eruptive Centers and Villarrica Volcano, Southern Chile. Journal of Volcanology and Geothermal Research 306:1-16. https://doi.org/10.1016/j.jvolgeores.2015.09.023

Morgan DJ, Jerram DA (2006) On estimating crystal shape for crystal size distribution analysis. Journal of Volcanology and Geothermal Research 154:1–7. https://doi.org/10.1016/j.jvolgeores.2005.09.016

Morgan DJ, Jerram DA, Chertkoff DG, et al (2007) Combining CSD and isotopic microanalysis: Magma supply and mixing processes at Stromboli Volcano, Aeolian Islands, Italy. Earth and Planetary Science Letters 260:419–431. https://doi.org/10.1016/j.epsl.2007.05.037

Moschini P, Mollo S, Pontesilli A, et al (2023) A review of plagioclase growth rate and compositional evolution in mafic alkaline magmas: Guidelines for thermometry, hygrometry, and timescales of magma dynamics at Stromboli and Mt. Etna. Earth-Science Reviews 240:104399. https://doi.org/10.1016/j.earscirev.2023.104399

Muir DD, Blundy JD, Rust AC (2012) Multiphase petrography of volcanic rocks using element maps: a method applied to Mount St. Helens, 1980–2005. Bull Volcanol 74:1101–1120. https://doi.org/10.1007/s00445-012-0586-0

Namur O, Montalbano S, Bolle O, Vander Auwera J (2020) Petrology of the April 2015 Eruption of Calbuco Volcano, Southern Chile. Journal of Petrology 61:egaa084. https://doi.org/10.1093/petrology/egaa084

Nielsen TFD, Andersen JCO, Holness MB, et al. (2015). The Skaergaard PGE and Gold Deposit: the Result of *in situ* Fractionation, Sulphide Saturation, and Magma Chamber-scale Precious Metal Redistribution by Immiscible Fe-rich Melt. Journal of Petrology, 56(8): 1643–1676, https://doi.org/10.1093/petrology/egv049

O'Driscoll B, Donaldson CH, Troll VR, et al (2006) An Origin for Harrisitic and Granular Olivine in the Rum Layered Suite, NW Scotland: a Crystal Size Distribution Study. Journal of Petrology 48:253–270. https://doi.org/10.1093/petrology/egl059

O'Neill HSC, Pownceby MI (1993). Thermodynamic data from redox reactions at high temperatures. I. An experimental and theoretical assessment of the electrochemical method using stabilized zirconia electrolytes, with revised values for the Fe-"FeO", Co-CoO, Ni-NiO and Cu-Cu2O oxygen buffers, and new data for the W-WO2 buffer. Contributions to Mineralogy and Petrology, 114(3), 296-314. https://doi.org/ https://doi.org/10.1007/BF01046533

Orlando AD, Armienti P, Borrini D (2008) Experimental determination of plagioclase and clinopyroxene crystal growth rates in an anhydrous trachybasalt from Mt Etna (Italy). ejm 20:653–664. https://doi.org/10.1127/0935-1221/2008/0020-1841

Oxford Instruments NanoAnalysis (2025) *EBSD.com – Electron Backscatter Diffraction resources*. Available at: https://www.ebsd.com/

Peterson TD (1996). A refined technique for measuring crystal size distributions in thin section. Contributions to Mineralogy and Petrology, 124: 395-405. https://doi.org/10.1007/s004100050199

Polacci M, Arzilli F, La Spina G, et al (2018) Crystallisation in basaltic magmas revealed via in situ 4D synchrotron X-ray microtomography. Sci Rep 8:8377. https://doi.org/10.1038/s41598-018-26644-6

Pupier E, Duchene S, Toplis MJ (2008) Experimental quantification of plagioclase crystal size distribution during cooling of a basaltic liquid. Contrib Mineral Petrol 155:555–570. https://doi.org/10.1007/s00410-007-0258-9

Randle V (1992). Microtexture Determination. Institute of Materials, London

Randolph AD, Larson MA (1971) Theory of particulate processes. Academic Press New York, 251 pp

Randolph AD, Sikdar SK (1976). Creation and Survival of Secondary Crystal Nuciel. The Potassium Sulfate-Water System. Industrial & Engineering Chemistry Fundamentals, 15(1), 64-71

Resmini RG, Marsh BD (1995) Steady-state volcanism, paleoeffusion rates, and magma system volume inferred from plagioclase crystal size distributions in mafic lavas: Dome Mountain, Nevada. Journal of Volcanology and Geothermal Research 68:273–296. https://doi.org/10.1016/0377-0273(95)00003-5

Reubi O, Blundy J (2009) A dearth of intermediate melts at subduction zone volcanoes and the petrogenesis of arc andesites. Nature 461:1269–1273. https://doi.org/10.1038/nature08510

Roeser WF (1941). Thermoelectric thermometry. Temperature, Its Measurement and Control in Science and Industry, 1, 180-205

Royer JP (1991) Stereology: a method for analyzing images. Progress in Neurobiology, 37(5): 433-474. https://doi.org/10.1016/0301-0082(91)90009-P

Schiavi F, Walte N, Keppler H (2009) First in situ observation of crystallization processes in a basaltic-andesitic melt with the moissanite cell. Geology 37:963–966. https://doi.org/10.1130/G30087A.1

Schairer JF (1959). Phase equilibria with particular reference to silicate systems. Butterworths scientific publications, p 117-134.

Shaw HR (1965). Comments on viscosity, crystal settling, and convection in granitic magmas. American Journal of Science 263, 120-152.

Shea T, Hammer JE (2013) Kinetics of cooling- and decompression-induced crystallization in hydrous mafic-intermediate magmas. Journal of Volcanology and Geothermal Research 260:127–145. https://doi.org/10.1016/j.jvolgeores.2013.04.018

Smith KCA, Oatley CW (1955) The scanning electron microscope and its fields of application. Br J Appl Phys 6:391–399. https://doi.org/10.1088/0508-3443/6/11/304

Toth N, Maclennan J (2024) MinDet1: A deep learning-enabled approach for plagioclase textural studies. Volcanica 7:135–151. https://doi.org/10.30909/vol.07.01.135151

Tripoli B, Manga M, Mayeux J, Barnard H (2019) The Effects of Deformation on the Early Crystallization Kinetics of Basaltic Magmas. Front Earth Sci 7:250. https://doi.org/10.3389/feart.2019.00250

Tuttle, OF（1948）: A new hydrothermal quenching apparatus. American Journal of Science, 246, 628-635.

Vander Auwera J, Montalbano S, Namur O, et al (2021) The petrology of a hazardous volcano: Calbuco (Central Southern Volcanic Zone, Chile). Contrib Mineral Petrol 176:46. https://doi.org/10.1007/s00410-021-01803-7

Vernon-Parry KD (2000) Scanning electron microscopy: an introduction. III-Vs Review 13:40–44. https://doi.org/10.1016/S0961-1290(00)80006-X

Vetere F, Merseburger S, Pisello A, et al (2024) The role of deformation on the early crystallization and rheology of basaltic liquids. Earth and Planetary Science Letters 644:118934. https://doi.org/10.1016/j.epsl.2024.118934

Vetere F, Petrelli M, Perugini D, et al (2021) Rheological evolution of eruptible Basaltic-Andesite Magmas under dynamic conditions: The importance of plagioclase growth rates. Journal of Volcanology and Geothermal Research 420:107411. https://doi.org/10.1016/j.jvolgeores.2021.107411

Wager LR (1961) A Note on the Origin of Ophitic Texture in the Chilled Olivine Gabbro of the Skaergaard Intrusion. Geol Mag 98:353–366. https://doi.org/10.1017/S0016756800060829

Wells OC (1974). Resolution of the topographic image in the SEM. Scanning Electron Microsc, 1-8.

Xu Z, Zhang Y (2002) Quench rates in air, water, and liquid nitrogen, and inference of temperature in volcanic eruption columns. Earth and Planetary Science Letters 200:315–330. https://doi.org/10.1016/S0012-821X(02)00656-8

Zhou W, Apkarian RP, Wang ZL, Joy D Fundamentals of Scanning Electron Microscopy. In: Zhou, W., Wang, Z.L. (eds) Scanning Microscopy for Nanotechnology. Springer, New York, NY. https://doi.org/10.1007/978-0-387-39620-0_1

Chapter III

Plagioclase crystal size distributions, growth and nucleation rates in an anhydrous arc basaltic andesite

Published in *Contributions to Mineralogy and Petrology* (*CMP*):
Billon M, Vander Auwera J, Namur O, et al (2025) Plagioclase crystal size distributions, growth and nucleation rates in an anhydrous arc basaltic andesite. Contrib Mineral Petrol 180:26. *https://doi.org/10.1007/s00410-025-02213-9*

Remarks: All the Supplementary files in this Chapter correspond to those submitted and published with Billon et al. (2025).

Abstract

We experimentally investigated plagioclase nucleation and growth in anhydrous arc basaltic andesite at 1 atm and Ni-NiO equilibrium. After equilibration at 1190 °C (15 °C above the liquidus) for 24 h, experiments were cooled at 1, 3, or 9 °C/h and quenched at 1175–1000 °C. New plagioclase grains nucleated near the liquidus, followed by minor amounts of Fe-Ti oxides and pyroxene below 1120 and 1050 °C, respectively. Plagioclase shapes varied from 2D tabular/elongated (1 and 3 °C/h) to hopper and swallowtail textures (9 °C/h), suggesting a transition from interface- to diffusion-controlled growth. Crystal shapes and sizes were correlated, with the smallest and largest having equant/elongated and tabular/bladed 3D shapes, respectively. To identify the most suitable method for inferring storage timescales in natural magmas, we calculated nucleation (J) and growth rates (G) with different methods: G_{max} from the average size of the 10 biggest crystals, G_{mean} from the entire crystal population, J_{batch} and G_{batch} from the number and proportion of plagioclase estimated by point counting, and J_{CSD} and G_{CSD} from the crystal size distribution (CSD). J and G were greatest near the liquidus and decreased during cooling; the decrease was minimal at slow cooling rates, making G nearly constant. G decreased with decreasing cooling rates (from 10^{-7} to 10^{-9} cm/s at 9 and 1 °C/h, respectively), stabilizing after ~20 h of cooling. These variations of G principally resulted from differences in experimental conditions, more than the calculation method considered. Given the uncertainties of CSD theory in closed systems and the size and crystallographic axis-dependence of growth rates, combining G_{mean} and G_{max} appears to be the most effective method for experimentally determining growth rates. However, the batch method (J_{Batch}) still provides a good estimate of J.

Keywords: cooling rate, texture, aspect ratio, 3D shape

Introduction

Magma solidification occurs via crystal nucleation and growth (e.g. *Cashman 1990*) and is recorded as chemical and/or textural changes within crystals. Crystallization timescales are crucial when assessing pre-eruptive dynamics, including magma storage (*Cooper and Kent 2014*) and ascent dynamics (*Humphreys et al. 2008*; *Rutherford 2008*; *Armienti et al. 1994*, 2013). Timescales have been estimated using techniques such as uranium-series disequilibria (*Cooper and Kent 2014*), diffusion relaxation in crystals (*Costa et al. 2008*), and, most commonly, crystal size distributions (CSDs; *Cashman 1993*; *Kent et al. 2010*). This latter approach is particularly useful in the absence of secondary phases used for dating. However, it requires knowledge of crystal growth rates to convert crystal sizes to time.

In many volcanic rocks, plagioclase is the most abundant crystal phase and commonly records magmatic conditions (*T*, *P*, melt H_2O content) because of the slow coupled CaAl-NaSi diffusion (*Grove and Baker 1984*; *Morse 2013*; *Bennett et al. 2019*). Plagioclase crystal habits reflect crystallization kinetics as well as changes of temperature, pressure, and composition (i.e. magma mixing) (*Couch et al. 2001, 2003a, b*; *Hammer and Rutherford 2002*; *Del Gaudio et al. 2010*; *Cassidy et al. 2016*; *Bennett et al. 2019*).

Many experimental investigations have focused on constraining plagioclase crystallization parameters such as the rates of nucleation (*J*), growth (*G*; see **Table III-1** for variable definitions), and chemical equilibration (*Gibb 1974*; *Nabelek et al. 1978*; *Toplis and Carroll 1995*; *Conte et al. 2006*; *Pupier et al. 2008*; *Brugger and Hammer 2010a, b*; *Vetere et al. 2015*; *Shea and Hammer 2013*; *Moschini et al. 2023*). However, aside from the few direct observations of crystal growth rates using *in situ* X-ray tomography experiments in furnaces (e.g. *Le Gall et al. 2021*) or on heating stages (*Schiavi et al. 2009*), *G* and *J* are mostly estimated *post mortem* from polished sections using direct calculations or CSDs.

Basaltic andesites and andesites are very common arc magma compositions (*Reubi and Blundy 2009*; *Kent et al. 2010*). However, most experimental determinations of plagioclase growth rates have been performed on basaltic compositions (e.g. *Kirkpatrick 1977*; *Cashman 1993*; *Lesher et al. 1999*; *Pupier et al. 2008*), with only a few studies devoted to andesites (*Shea and Hammer 2013*; *Vetere et al. 2021*) or dacites (*Hammer and Rutherford 2002*; *Brugger and Hammer 2010a, b*). Available results range from 10^{-9}–10^{-6} cm/s in basalts (e.g. *Lesher et al. 1999*; *Orlando et al. 2008*; *Giuliani et al. 2020*) to 10^{-8}–10^{-7} cm/s in andesites (*Shea and Hammer 2013*; *Vetere et al. 2021*) and 10^{-11}–10^{-8} cm/s in dacites (*Hammer et al. 1999*; *Hammer*

and Rutherford 2002; *Brugger and Hammer 2010a, b*), suggesting that growth rate decreases with increasing melt SiO_2 content.

Nucleation rates have also been estimated in basaltic (*Burkhard 2005*; P*upier et al. 2008*), basaltic andesitic (*Shea and Hammer 2013*), and dacitic compositions (*Hammer and Rutherford 2002*; *Brugger and Hammer 2010a, b*). However, results vary substantially, ranging from 10^{-9} cm^{-3} s^{-1} to 10^{5} cm^{-3} s^{-1}. These variations appear dependent not only on initial composition, but also on the characteristics of the starting material and the specific experimental procedure (e.g. synthetic vs. natural material, with/without superliquidus heating before cooling).

Furthermore, most experimental studies employed rapid cooling rates exceeding 10 °C/h (*Nabelek et al. 1978*; *Conte et al. 2006*; *Iezzi et al. 2008*; *Vetere et al. 2015*; *Giuliani et al. 2020*), which are probably adequate for the cooling of lava flows in contact with the atmosphere. Only a few studies have explored cooling rates slower than 7 °C/h (*Pupier et al. 2008*; *Vetere et al. 2015*; *Giuliani et al. 2020*), although magmas in deep, large reservoirs probably cool much slower than can be experimentally reproduced (*Sunagawa 1977*). For example, core samples from the Kilauea lava lake were interpreted to have cooled at rates of 0.002–0.011 °C/h (*Honour et al. 2019*).

Here, we experimentally determined plagioclase nucleation and growth rates in an anhydrous basaltic andesitic composition as a function of final (quench) temperature (T_f), nominal degree of undercooling ($-\Delta T_n$), and cooling time. Data from 20 new cooling experiments are presented. To best replicate natural conditions, a small density of pre-existing crystals was maintained in the starting material. We used a natural starting composition from Osorno volcano (Southern Volcanic Zone, Chile). To better approximate the gradual cooling of natural magma reservoirs (*Mollo et al. 2012*), we employed slow cooling rates of 1, 3, and 9 °C/h. As modeled by *Mollo et al. (2012)*, this range allows for example to cover the progressive cooling of chilled magmatic intrusions (100-200m thick) from the inner to outer part of the intrusion. We calculated nucleation and growth rates using different methods, then evaluated which method is the most appropriate for calculating storage timescales from textural analyses of volcanic samples.

Abbreviations	
T_{liq}, T_{sat}	Phase-specific liquidus and saturation temperatures, respectively.
T_i, T_f	Initial and final temperatures, respectively.
$-\Delta T$, $-\Delta T_n$,$-\Delta T_{eff}$	True, nominal, and effective degrees of undercooling, respectively.
l, w	2D major and minor axes of each plagioclase crystal, respectively.
L, I, S	3D major, intermediate, and minor axes of each plagioclase crystal, respectively.
Φ_V, Φ_{WDS}	Plagioclase proportions estimated from textural analyses and WDS measurments, respectively.
S_N	Average plagioclase crystal size determined by the batch method.
l_{mean}, w_{mean}	Average 2D size (major and minor axes, respectively) estimated over the section-wide segmented plagioclase population.
$l_{max,avg}$, $w_{max,avg}$	Average 2D maximum sizes estimated from the 10 longest and largest crystals respectively.
N_A, N_V	Areal and volumetric plagioclase crystal densities, respectively.
n_0, l_c	2D initial density and characteristic size determined from the CSD, respectively.
N_0, L_c	3D initial density and characteristic size determined from the CSD, respectively.
J, G	Nucleation and growth rates, respectively.
J_{batch}, $J_{CSD,2D}$, $J_{CSD,3D}$	Nucleation rates determined using batch and 2D and 2D CSD methods, respectively.
J_{mean}	Average nucleation rate (mean of the results using the batch and 2D and 3D CSD methods).
G_{batch}	Growth rates determined by the batch method.
$G_{mean,l}$, $G_{mean,w}$	Average growth rates determined from l_{mean} and w_{mean}, respectively.
$G_{max,l}$, $G_{max,w}$	Maximum growth rates determined from $l_{max,avg}$ and $w_{max,avg}$, respectively.
G_{rim}	Growth rate determined from crystal overgrowths.
$G_{CSD,2D}$, $G_{CSD,3D}$	Growth rates determined using the 2D and 3D CSD methods, respectively.
G_{mean}	Average growth rate.
$t_{cooling/decompression}$	Cooling/decompression time after the initial step.
CR, DP, ISO	Cooling rate, decompression rate, and isothermal experiments, respectively.

Table III-1*: Abbreviations used in this study.*

Methods

Starting material and experimental methodology

Our starting composition was a basaltic andesite (OS36 from *Bechon et al. 2022*) from Osorno volcano (Central Southern Volcanic Zone, Chile) (**Table III-2**). OS36 is crystal-poor (containing only 9% crystals, and 2% plagioclase macrocrysts larger than 300 µm) and bubble-rich (19%) (***Supplementary file III-2***). The sample was crushed with a hammer, then ground to a fine powder in an agate mortar with a Fritsch Pulverisette planetary mill.

To create the starting glasses, an aliquot of the starting powder was prepared as a pellet 1–3 mm in diameter and deposited on a 0.2-mm-diameter Pt wire loop. The Pt wire loops were previously equilibrated with material of the same composition as the experimental charge at the target temperature and oxygen fugacity (Ni + $1/2O_2$ = NiO equilibrium, Ni-NiO) for 24 h to minimize iron loss during the experiments (*Grove 1981*). The assemblage was then heated in a muffle furnace for 10–15 minutes to sinter the powder. All crystallization experiments were conducted at atmospheric pressure (1 atm) in a CARBOLITE GERO vertical furnace (ULiege) at Ni-NiO, close to the estimated oxygen fugacity (approximately QFM+0.8/+1) for storage conditions under Osorno and other volcanoes of the area (*Morgado et al. 2015*; *Vander Auwera et al. 2019*; *Bechon et al. 2022*). Oxygen fugacity was controlled with CO-CO_2 gas. The temperature was measured using a S-type ($Pt_{90}Rh_{10}$-Pt) thermocouple with an accuracy of ±3 °C at the hot spot of the furnace (±4 cm).

Liquidus determination

The liquidus temperature of OS36 was calculated using Rhyolite-MELTS v. 1.2.0 (*Gualda et al. 2012*) to be 1170 °C (1 atm, anhydrous, Ni-NiO). We tested this liquidus estimate using two series of experiments (**Table III-3**): (1) a series of five isothermal experiments run between 1175 °C and 1200 °C for 24 h, and (2) a similar series using a powder previously pre-heated to 1450 °C for 2 h to ensure the complete absence of crystal seeds in the starting material. The first set of experiments showed plagioclase saturation at 1185 ± 5 °C and the complete dissolution of all pre-existing crystals at 1200 °C. In the second set of experiments, we estimated the saturation temperature of plagioclase to be around 1170–1175 °C, indicating that the presence of crystal seeds may lead to plagioclase saturation at a slightly higher temperature.

	Bulk composition	ISO : 24 hours		CR: 9 °C/h					
	OS36[a]	1190°C[b]	1180 °C[b]	1165 °C[b]	1140 °C[b]	1120 °C[b]	1100 °C[b]	1050 °C[c]	1000 °C[c]
SiO_2	56.94	57.65 (1.07)	56.98 (0.20)	58.26 (0.50)	58.67 (0.56)	57.47 (0.79)	59.05 (0.70)	61.05 (1.25)	69.40 (1.34)
TiO_2	1.3	1.28 (0.04)	1.33 (0.09)	1.30 (0.07)	1.50 (0.11)	1.53 (0.07)	1.70 (0.07)	2.33 (0.32)	2.01 (0.42)
Al_2O_3	16.27	16.64 (0.16)	16.09 (0.17)	16.42 (0.18)	14.86 (0.64)	14.92 (0.35)	13.54 (0.26)	14.42 (0.83)	13.66 (1.00)
$FeO_{(t)}$	9.56	9.53 (0.90)	10.24 (0.47)	9.00 (0.31)	10.28 (0.87)	10.78 (0.63)	10.66 (0.80)	10.42 (1.01)	5.54 (0.77)
MnO	0.18	0.19 (0.03)	0.2 (0.03)	0.18 (0.03)	0.21 (0.05)	0.22 (0.03)	0.24 (0.04)	0.25 (0.04)	0.16 (0.03)
MgO	2.79	3.13 (0.15)	3.38 (0.04)	2.80 (0.12)	3.37 (0.25)	3.37 (0.65)	3.77 (0.13)	1.70 (0.14)	0.85 (0.21)
CaO	6.39	6.63 (0.37)	6.47 (0.22)	6.20 (0.20)	5.66 (0.19)	5.78 (0.24)	5.32 (0.21)	5.06 (0.39)	2.98 (0.51)
Na_2O	4.32	4.14 (0.08)	3.91 (0.09)	4.22 (0.10)	4.07 (0.16)	4.03 (0.14)	3.94 (0.18)	2.68 (0.10)	2.62 (0.42)
K_2O	0.91	0.89 (0.06)	0.93 (0.03)	0.97 (0.03)	1.05 (0.04)	1.02 (0.05)	1.11 (0.05)	1.56 (0.11)	2.16 (0.22)
P_2O_5	0.26	0.3 (0.03)	0.27 (0.03)	0.22 (0.05)	0.25 (0.06)	0.28 (0.05)	0.30 (0.08)	0.52 (0.09)	0.63 (0.07)
Total	98.92	100.38	99.79	99.58	99.93	99.56	99.62	99.99	100.01
Type		*Andesitic*	*Andesitic*	*Andesitic*	*Andesitic*	*Andesitic*	*Andesitic*	*Andesitic*	*Dacitic*

	CR: 1 °C/h					CR: 3 °C/h			
	1165[b] °C (Sample 1)	1165[b] °C (Sample 2)	1137[b] °C	1120[b] °C	1100[b] °C	1165[b] °C	1140[b] °C	1120[b] °C	1100[b] °C
SiO_2	57.03 (0.56)	57.99 (0.8)	59.61 (0.50)	58.36 (0.56)	59.08 (0.86)	57.77 (0.56)	57.83 (0.77)	58.42 (0.77)	57.67 (0.32)
TiO_2	1.36 (0.08)	1.31 (0.07)	1.44 (0.06)	1.52 (0.08)	1.68 (0.08)	1.28 (0.06)	1.51 (0.08)	1.57 (0.06)	1.60 (0.07)
Al_2O_3	15.92 (0.18)	16.08 (0.16)	15.13 (0.31)	13.81 (0.16)	13.57 (0.29)	16.39 (0.11)	15.05 (0.22)	14.43 (0.2)	13.14 (0.10)
$FeO_{(t)}$	9.69 (0.46)	9.03 (0.47)	8.87 (0.2)	9.59 (0.47)	10.19 (0.43)	8.83 (0.43)	10.35 (0.48)	10.35 (0.42)	11.09 (0.37)
MnO	0.2 (0.04)	0.19 (0.03)	0.18 (0.04)	0.23 (0.04)	0.22 (0.04)	0.18 (0.04)	0.22 (0.03)	0.21 (0.03)	0.26 (0.06)
MgO	3.17 (0.12)	2.89 (0.14)	3.02 (0.12)	3.77 (0.15)	3.6 (0.21)	2.95 (0.08)	3.39 (0.19)	3.49 (0.12)	4.10 (0.08)
CaO	6.22 (0.18)	5.9 (0.21)	5.17 (0.18)	5.47 (0.17)	5.02 (0.22)	6.13 (0.22)	6.02 (0.21)	5.43 (0.16)	5.53 (0.12)
Na_2O	4.08 (0.07)	4.06 (0.06)	4.38 (0.10)	4.16 (0.2)	4.13 (0.09)	4.18 (0.17)	4.00 (0.11)	3.86 (0.2)	3.82 (0.07)
K_2O	0.88 (0.03)	0.96 (0.05)	1.14 (0.03)	1.05 (0.05)	1.17 (0.05)	0.95 (0.04)	0.97 (0.05)	1.01 (0.04)	1.02 (0.03)
P_2O_5	0.2 (0.05)	0.25 (0.07)	0.21 (0.05)	0.21 (0.04)	0.27 (0.06)	0.24 (0.06)	0.27 (0.04)	0.28 (0.07)	0.30 (0.08)
Total	98.76	98.66	99.14	98.17	98.94	98.88	99.61	99.05	98.53
Type	*Andesitic*	*Andesitic*	*Andesitic*	*Andesitic*	*Andesitic*	*Andesitic*	*Andesitic*	*Andesitic*	*Andesitic*

	Initial Conditions
H_2O (wt. %)	0
P (bar)	1
fO_2	Ni-NiO

***Table III-2**: Chemical compositions of the starting material (OS 36) and the residual liquid at each quench temperature (1190–1000 °C) during cooling at 1, 3 and 9 °C/h. 1σ errors are reported in parentheses.*

Name	Pre-treatment	Cooling rate (°C/h)	T_f (°C)	$-\Delta T_n$ (°C)[a]	$t_{final\ step}$ (h)	$t_{cooling}$ (h)	Phases	Global image				Segmentation			
								φ_v	N_A (μm^{-2})	S_N (μm)	N_V (μm^{-3})	$l_{max,avg}$[c] (μm)	$w_{max,avg}$[c] (μm)	l_{mean}[d] (μm)	w_{mean}[d] (μm)
Test 1	No	ISO	1175	0	24		gl, Plg	-	-	-	-	-	-	-	-
Test 2	No	ISO	1180	-5	24		gl, P.c, Plg	-	-	-	-	-	-	-	-
Test 3	No	ISO	1185	-10	24		gl, P.c, Plg ?	-	-	-	-	-	-	-	-
G 0	No	ISO	1190	-15	24		gl, P.c[b]	<< 0,01	2.23E-05	12	1.98E-06	36	22	16	11
Test 5	No	ISO	1200	-25	24		gl	-	-	-	-	-	-	-	
Test 6	1450 °C for 2 hours	ISO	1170	5	24		gl, Plg								
Test 7	1451 °C for 2 hours	ISO	1180	-5	24		gl	-	-	-	-	-	-	-	
Test 8	1452 °C for 2 hours	ISO	1190	-15	24		gl	-	-	-	-	-	-	-	
Test 9	1453 °C for 2 hours	ISO	1200	-25	24		gl	-	-	-	-	-	-	-	
G 1-0		1	1175	0	0	15.00	gl. Plg	0.01	4.14E-05	16	2.59E-06	52	27	22	11
G 1-1a1		1	1165	10	0	25.00	gl. Plg	0.06	2.55E-04	15	1.69E-05	87	41	21	10
No crystal corona		1	-	-	-	25.00	-	0.01	9.03E-05	11	8.58E-06	25	17	12	7
G 1-1a2		1	1165	10	0	25.00	gl, Plg	0.03	1.62E-04	13	1.21E-05	68	34	21	10
G 1-2		1	1137	38	0	53.00	gl, Plg	0.12	4.31E-04	17	2.54E-05	114	43	20	10
G 1-3		1	1120	55	0	70.00	gl, Plg, Ox	0.21	4.99E-04	20	2.65E-05	130	42	23	9
No crystal corona		1	-	-	-	-	-	0.1	5.08E-04	14	3.62E-05	-	-	-	-
G 1-4		1	1100	75	0	90.00	gl, Plg, Ox	0.21	5.63E-04	20	2.88E-05	183	56	26	11
G 2-0		3	1175	0	0	5.00	gl, Plg	0.01	4.58E-05	13	3.61E-06	41	27	16	10
G 2-1a		3	1165	10	0	8.33	gl, Plg	0.03	1.61E-04	14	1.16E-05	60	23	17	7
G 2-1b		3	1165	10	0	8.33	gl, Plg	<< 0,01	1.21E-05	15	7.95E-07	35	19	23	12
G 2-2		3	1140	35	0	16.67	gl, Plg	0.11	3.73E-04	17	2.15E-05	135	40	24	9

G 2-3	3	1120	55	0	23.33	gl, Plg	0.15	5.07E-04	17	2.97E-05	127	43	23	9
G 2-4	3	1100	75	0	30.00	gl, Plg, Ox	0.2	5.30E-04	20	2.70E-05	156	45	27	10
G 3-0	9	1175	0	0	1.67	gl, Plg	0.001	4.47E-06	16	2.87E-07	26	15	20	12
G 3-1	9	1165	10	0	2.78	gl, Plg	0.01	1.63E-04	8	1.92E-05	31	20	10	5
G 3-2a1 (Seg1)	9	1140	35	0	5.56	gl, Plg	0.14	7.05E-04	14	5.00E-05	123	35	18	7
G 3-2a1 (Seg2)	9	1140	35	0	5.56	gl, Plg	0.14	7.05E-04	14	5.00E-05	103	33	18	7
G 3-2a2	9	1140	35	0	5.56	gl, Plg	0.09	6.77E-04	12	5.75E-05	113	37	15	7
G 3-3a	9	1120	55	0	7.78	gl, Plg	0.14	3.30E-04	21	1.58E-05	187	40	30	9
G 3-3b	9	1120	55	0	7.78	gl, Plg	0.15	4.01E-04	19	2.11E-05	140	36	24	8
G 3-4	9	1100	75	0	10.00	gl, Plg, Ox	0.24	8.81E-04	17	5.30E-05	126	42	21	8
G 3-5	9	1050	125	0	15.56	gl, Plg, Ox, Cpx	0.39	5.69E-04	26	2.17E-05	133	46	35	13
G 3-6	9	1000	175	0	21.11	gl, Plg, Ox, Cpx	0.48	-	-	-	103	39	35	14

[a]: $-\Delta T_n$ = difference between the liquidus temperature and the final temperature

[b]: P.c : Pre-existing crystals.

[c]: Average value on the 10 longest (*l*) and widest (*w*) crystals.

[d]: Average 2D long (*l*) and small (*w*) axis measured on the various zooms.

Table III-3*: Textural characteristics and image segmentation data. Phase abbreviations: P.c., pre-existing plagioclase fragments; Plg, plagioclase; Cpx, clinopyroxene; Ox, Fe-Ti oxides; gl, glass.*

Cooling experiments

Experiments were first heated to 1190 °C, i.e. 15 °C above the plagioclase saturation temperature (T_{sat} = 1175 °C), for 24 h. This step ensured that no new plagioclase grains formed during the initial heating stage, while retaining a small fraction of pre-existing crystals to initiate nucleation (*Pichavant et al. 2007*) (**Figure III-2a**, ***Supplementary file III-2***). Experiments were then cooled to various final temperatures (1175, 1165, 1140, 1120, or 1100 °C) at one of three cooling rates (1, 3, or 9 °C/h; **Figure III-1**) and quenched in water. The fastest cooling experiments were also extended to quenching temperatures of 1050 °C and 1000 °C (**Figure III-1**, **Table III-3**). To test experimental reproducibility, experiments G 2-1 (3 °C/h, 1165 °C), and G 3-3 (9 °C/h, 1120 °C) were repeated twice.

Following *Kirkpatrick (1981)*, *Faure et al. (2003)*, and *Faure and Tissandier (2014)*, we refer to the nominal degree of undercooling, $-\Delta T_n$, defined as the difference between the plagioclase saturation temperature in the starting composition (OS36) and the quench temperature ($-\Delta T_n = T_{sat,\,OS36}$[2] $- T_f$). Accordingly, in our study, $-\Delta T_n$ ranged from 0 °C at the liquidus to 175 °C. However, *Faure and Tissandier (2014)* explained that this definition, particularly in the case of a slow cooling, corresponds to an oversimplification of the real undercooling ($-\Delta T$) which changes during cooling due to the progressive evolution of the melt composition.

[2] $T_{sat,\,OS36}$ corresponds to the saturation temperature of plagioclase in OS36, determined using MELTS and verified experimentally)

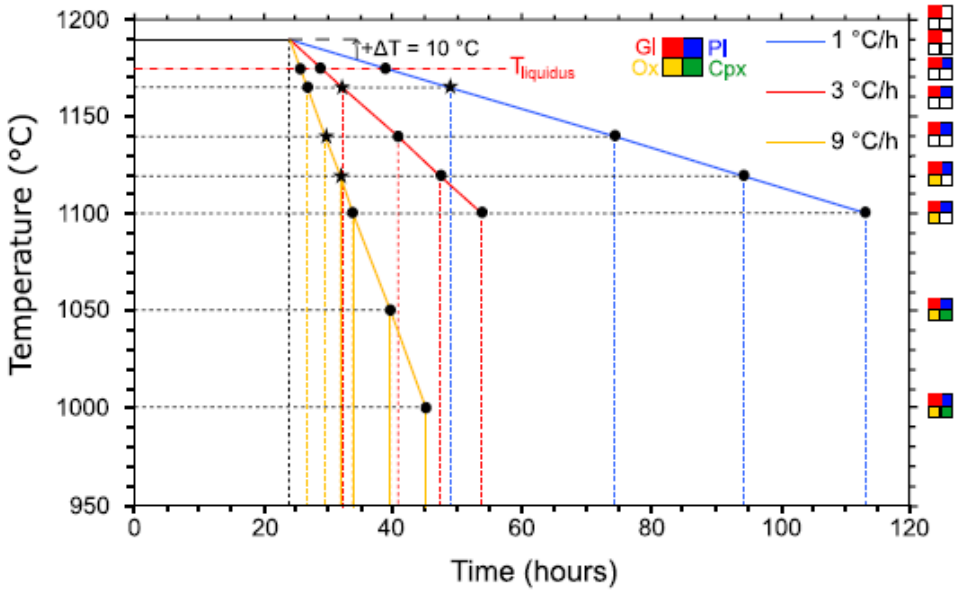

Figure III-1*: The thermal paths of experiments in this study. The order in which phases appeared during cooling is indicated by the color code to the right of the diagram. Each experiment began with a 24-h isothermal heating step at 10 °C above the liquidus 24 h (run GERO 0) before cooling at 1, 3, or 9 °C/h and quenching at 1175 °C, 1165 °C, 1140 °C, 1120 °C, or 1100 °C; additional experiments cooled at 9 °C/h were also quenched at 1050 °C and 1000 °C. Stars indicate replicate experiments, either performed twice or with two samples during the same run.*

Chemical analysis

Experimental runs were embedded in epoxy, polished, and examined with a scanning electron microscope (SEM) equipped with a field-emission gun source using backscattered electron imaging (BSE) at KU Leuven (TESCAN Mira4) and RWTH Aachen (FEI QEMSCAN 650F). SEM imaging was performed at a working distance of 10–15 mm, with a dwell time of 10 µs and a voltage of 15 KV (20 KV for EDS analyses, with a beam current of 6–9 nA). Chemical analyses of glasses (using a defocused beam), Fe-Ti oxides and plagioclase crystals were performed by energy dispersive X-ray analysis (EDS) and wavelength dispersive X-ray spectroscopy (WDS). Calibration details for WDS analyses are provided below. Up to 10–15 plagioclase crystals and 6–9 Fe-Ti oxides per sample were analyzed by WDS.

The CAMECA SX Five Tactics (Clermont-Ferrand) calibration standards were the same as those of *Bechon et al. (2022)*: wollastonite (Ca, Si), $TiMnO_3$ (Ti, Mn), Al_2O_3 (Al), fayalite (Fe), forsterite (Mg), albite (Na,), Cr_2O_3 (Cr), orthose (K), and NiO (Ni). Experimental charges analyzed with this calibration were G 1-2 and G 1-4 (1 °C/h, 1140 °C and 1100 °C,

respectively), G 2-1 and G 2-2 (3 °C/h, 1165 °C and 1140 °C, respectively), and G 3-1, G 3-2 (samples 1 and 2), G 3-3, and G 3-4 (9 °C/h, from 1165 °C to 1100 °C, respectively).

For the JEOL JXA-8530F (KULeuven), the standards were:

- Obsidian (SiO_2, Al_2O_3, K_2O), apatite (P_2O_5), diopside (CaO), hematite (FeO), jadeite (Na_2O), olivine (MgO), rutile (TiO_2), rhodonite (MnO), chromium oxide (Cr_2O_3), and nickel (NiO) for glasses.
- Albite (Al_2O_3), diopside (SiO_2), apatite (P_2O_5), hematite (FeO), jadeite (Na_2O), olivine (MgO), obsidian (K_2O), diopside (CaO), rutile (TiO_2), chromium oxide (Cr_2O_3), and rhodonite (MnO) for plagioclase.

The experimental charges analyzed with this calibration were G 0 (1190 °C during 24 h) and G 2-1 (3 °C/h, 1165 °C).

The standards for the JEOL JXA-ISP 100 (Aachen University) were:

- Glass (SiO_2, Al_2O_3, K_2O), jadeite (Na_2O), olivine (MgO), apatite (P_2O_5), diopside (CaO), rutile (TiO_2), hematite (FeO), Mn oxide (MnO), and chromite (Cr_2O_3) for glasses.
- Plagioclase (SiO_2, Al_2O_3, CaO), jadeite (Na_2O), olivine (MgO), apatite (P_2O_5), orthoclase (K_2O), rutile (TiO_2), hematite (FeO), Mn oxide (MnO), and chromite (Cr_2O_3) for plagioclase.
- Plagioclase (Al_2O_3), olivine (SiO_2, MgO), rutile (TiO_2), magnetite (FeO), Mn oxide (MnO), chromite (Cr_2O_3), and Ni oxide (NiO) for Fe-Ti oxides.

The experimental charges analyzed with this calibration were G 0 (1190 °C during 24 h), series G 1 (cooled at 1 °C/h), G 2-2, G 2-3, and G 2-4 (3 °C/h, 1140 °C, 1120 °C, and 1100 °C, respectively), and G 3-1, G 3-3b, G 3-5, and G 3-6 (9 °C/h, 1165 °C, 1120 °C, 1050 °C, and 1000 °C, respectively).

WDS analyses of plagioclase confirmed homogeneous anorthite contents (excluding cores of crystals corresponding to pre-existing crystals)) for each sample, with 1σ errors between 0.01 and 0.04 An mol.%. EDS analyses were more scattered, with 1σ errors between 0.01 and 0.08 wt.%. Crystals analyzed by both EDS and WDS exhibited differences in anorthite content ranging from 1% to 13% (see ***Supplementary file III-3***). Glasses (quenched melt) were measured by WDS in some samples (up to eight analyses per sample) (***Supplementary file III-3***).

Image processing

Data acquisition

BSE images of entire sections were used to determine the number of crystals in each section (between 100 and 3000 plagioclase crystals per section, ranging from >2 µm to 333 µm, depending on crystallinity). For textural measurements, we outlined crystals in the BSE images. For better precision, especially for the smallest crystals (<5 µm), the full images were subdivided into four to ten subsections (magnified by 160–750×) depending on the crystal density and sample heterogeneity of the sample. Because the BSE pixel size was about 0.5 µm on a side, we could only accurately measure crystals larger than 2 µm.

We first used the Weka Segmentation plugin of Fiji (ImageJ) to automate the outlining of the plagioclase crystals and their potential relic cores after adjusting the image contrast. Subsequently, the crystal outlines were verified, and each crystal was manually extracted from the images using GIMP software. The long (l) and short axes (w) of the outlined crystals were measured using the best-fit ellipse method in Fiji (*see* ***Supplementary file III-4***).

Textural parameters

We determined plagioclase proportions (φ_V), shape (see next subsection), sizes ($l_{max,avg}$ and $w_{max,avg}$ being the average dimensions respectively on the 10 longest and widest crystals; and l_{mean} and w_{mean} being the corresponding mean values of the entire crystal population in the section), and crystal number densities per unit area (N_A = number of crystals/surface area of the entire section) (**Table III-1**, **Table III-3**). Using φ_V and N_A, we calculated the global mean crystal size (S_N) and volumetric crystal density (N_V) as (*Hammer et al. 1999*; *Shea and Hammer 2013*):

$$S_N = \sqrt{\frac{\varphi_V}{N_A}} \quad (1)$$

$$N_V = \frac{N_A}{S_N} \quad (2)$$

Plagioclase proportions and areal and volumetric number densities were measured from the global images of each section. Except for the experiments quenched at the beginning of

crystallization at 1175 and 1165 °C, the crystal size parameters (l_{max}/w_{max}, $l_{max,avg}/w_{max,avg}$, and l_{mean}) were measured from the various subsectional images, and the results were then combined to derive the final data for the overall sample.

3D crystal shape

Crystal shapes imaged by SEM are 2D cross-sections of 3D objects, generally cut randomly. We used the algorithm ShapeCalc (*Mangler et al. 2022*) to estimate the 3D crystal shape (*S*:*I*:*L*; with *S*, *I*, and *L* being the 3D short, intermediate and long axes of elongation, respectively) based on the 2D width/length (*w*/*l*) distribution. Details on the algorithm are provided in *Mangler et al. (2022)*.

Phase proportions

We used two methods to obtain phase proportions: 2D image processing (φ_V) reported in **Table III-3**, and mass balance (φ_{WDS}) based on the WDS data (plagioclase and glass). The first method assumes that calculated phase proportions correspond to volume proportions (*Delesse 1847*; *Brugger and Hammer 2010b*). For the second method, we used densities as estimated by MELTS at the temperature of quenching (see ***Supplementary file III-4***). As highlighted by *Vetere et al. (2024)*, the two methods gave similar results (absolute differences ranging between 1% and 4%, averaging around 1% and 2%). In the following, we use only the phase proportions obtained with 2D images processing (φ_V).

Crystal Size Distribution

Crystal Size Distribution (CSD) represents the total number of crystals *N*(*L*) as a function of their size (*L*):

$$N(L) = \int_0^L n(L)\, d(L) \quad (3)$$

where *n(L)* corresponds to the number of crystals in each size range (*L*) per unit volume. In many magmatic systems, the plot of *N*(*L*) vs. log(*L*) is a straight line with a negative slope (*Cashman and Marsh 1988*; *Marsh 1988, 1998*):

$$\ln\big(N(L)\big) = -L \times \frac{1}{G \times t} + \ln(N_0) \quad (4)$$

where N_0 is the number of crystal nuclei (crystals of zero length) and t is the duration below the saturation temperature of plagioclase (T_{sat} = 1175 °C). Assuming constant G (*Armienti 2008*; *Marsh 1988, 1998*), characteristic crystal size l_c, J, and G are determined as (with analogous equations for their 3D counterparts based on L_c):

$$l_c = G \times t \quad (5)$$

$$G_{CSD} = \frac{1}{\text{slope} \times t} \quad (6)$$

$$J_{CSD} = n_0 \times G_{CSD} \quad (7)$$

Additional details on the theory, methodology used and CSD data are provided in ***Supplementary files III-1 and 4***, respectively. The objective of this comparison was to observe the evolution of the CSD curves during progressive cooling, and also to extract the nucleation ($J_{CSD,2D}$ and $J_{CSD,3D}$) and growth ($G_{CSD,2D}$, $G_{CSD,3D}$) by linear regression.

Nucleation and growth rates

Nucleation and growth rates were calculated using different methods: the batch method (*Brugger and Hammer 2010a, b*), CSDs (2D and 3D; *Burkhard 2002*; *Pupier et al. 2008*), and the l_{mean} and l_{max} method (*Shea and Hammer 2013*). Rates derived from the log-linear segments of the CSDs are defined above (**Eqs. 6 and 7**). Maximum growth rates were derived from the average 2D length (l) and width (w) of the 10 longest crystals and 10 widest crystals ($G_{max,l}$, $G_{max,w}$) respectively:

$$G_{max,l} = \frac{l_{max,avg}}{2t} \text{ and } G_{max,w} = \frac{w_{max,avg}}{2t} \quad (8)$$

Because many crystals displayed relic cores (**Figure III-2b**), we also calculated a growth rate based only on the overgrowth rim (G_{rim}; *Shea and Hammer 2013*) by subtracting the l and w axes of the ellipses fit to the relic cores from those of the total crystals. Seeds displaying resorbed textures, G_{rim} values refer only to the l axis.

We obtained mean growth rates using the batch, l_{mean}, and CSD methods. $G_{mean,w}$ and $G_{mean,l}$ were calculated considering the average minor (w_{mean}) and major axis lengths (l_{mean}) lengths among the entire plagioclase population, respectively, as:

$$G_{\text{mean},l} = \frac{l_{\text{mean}}}{2t} \text{ and } G_{\text{mean},w} = \frac{w_{\text{mean}}}{2t} \quad (9)$$

For comparison, G_{batch} was calculated using S_N and J_{batch} using N_V:

$$G_{\text{batch}} = \frac{S_N}{2t} \quad (10)$$

$$J_{\text{batch}} = \frac{N_V}{t} \quad (11)$$

For all methods, we assumed that crystallization occurred symmetrically on a given crystal face, and thus used the major and minor radii (respectively $\frac{l}{2}$ and $\frac{w}{2}$) of the best-fit ellipses.

Results

Phase assemblages and proportions

At 1190 °C (i.e. 15 °C above the liquidus), the experimental charges contained only resorbed anorthite-rich plagioclase grains, representing remnants of the initial starting powder (**Figure III-2a**). At lower temperatures, these remnant grains were observed to be enclosed within larger plagioclase crystals (**Figure III-2b**, **e**). Plagioclase was the only crystalline phase down to 60 °C below the liquidus, followed by Fe-Ti oxides (titanomagnetite) appearing between 1120 and 1100 °C, and clinopyroxene (Cpx) below 1050 °C (**Figure III-2h**). More broadly, below 1140 °C, sample textures are considered porphyritic (**Figure III-2e-h**; ***Supplementary file III-2***). Pt wire (Fig. 2b) and gas bubbles, resulting from intergrain free volume that can trap CO-CO_2 gas, served as preferred nucleation sites for plagioclase crystals. Clustering increased with decreasing temperature (increasing $-\Delta T_n$), ranging from pairs of sintered crystals to well-developed plagioclase clusters containing many grains, suggesting agglomeration (*Pupier et al. 2008*). Although the distribution of plagioclase tends to gradually homogenize during cooling (with a more even distribution of individual crystals and clusters), it remains strongly heterogeneous above 1050 °C, with portions of the experiments dominated either by residual liquid or by crystals (individual crystals, clusters, or groups surrounding bubbles; e.g., at 1140 °C, ***Supplementary file III-2***). Finally, a "fully" homogeneous crystal distribution was only attained at advanced stages of crystallization at 1050 and 1000 °C.

The proportion of plagioclase increased with increasing $-\Delta T_n$, from 1–3% at T_f = 1165 °C ($-\Delta T_n$ = 10 °C) to 20–24% at 1100 °C ($-\Delta T_n$ = 75 °C) and 48% at 1000 °C ($-\Delta T_n$ = 175 °C; **Table III-3**). Observed plagioclase proportions were within 1–4% of those predicted by Rhyolite-MELTS (***Supplementary file III-4***). The proportion of plagioclase does not appear to have been influenced by cooling rate. Pyroxene proportions increased from 0% at T_f = 1100 °C to 15% and 31% at 1050 and 1000 °C, respectively, much higher than that predicted by Rhyolite-MELTS (8%). Fe-Ti oxides comprised a constant proportion of 1–2% from 1120 °C to 1000 °C.

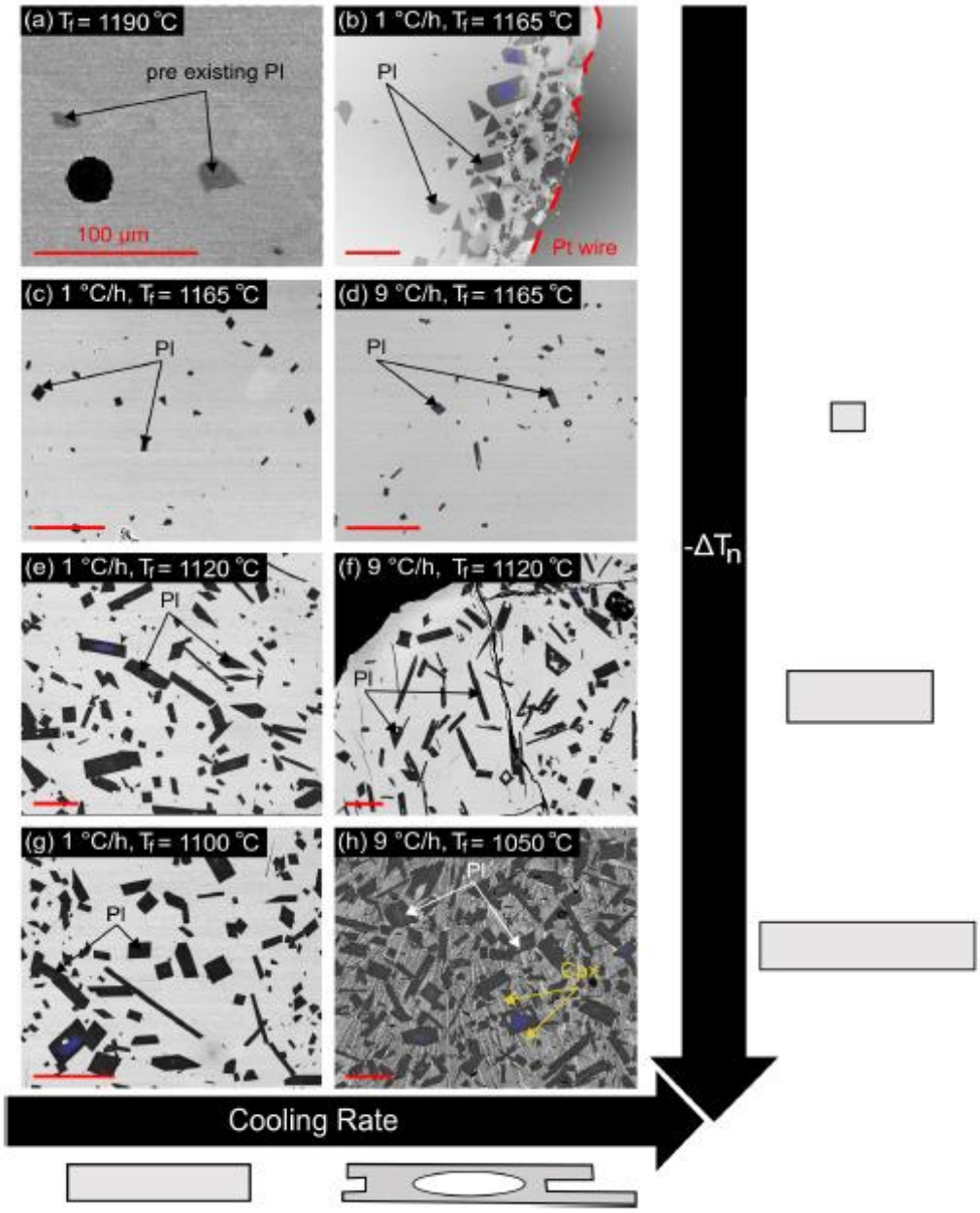

Figure III-2*: Backscattered electron images documenting the textural evolution of plagioclase. (a) Primitive plagioclase relic cores observed at 1190 °C (ΔT = 10 °C), displaying a rounded texture*

indicative of resorption. (b, c, e, g) Textural evolution during cooling at 1 °C/h, showing a transition from small, equant crystals at 1165 °C (c) to larger, more tabular crystals at lower temperatures (e and g). Panel (b) illustrates preferential nucleation, with larger plagioclase crystals forming near the Pt wire (marked by the red dashed line, later removed during polishing). (d, f, h) Textural evolution during cooling at 9 °C/h. Skeletal crystals appear at an intermediate stage (f: 1120 °C), coinciding with the increased cooling rate. At the most advanced stage of cooling (h), dendritic clinopyroxenes and oxides are observed. The blue shading in panels (e, g, and h) highlights the seed portions in some of the larger crystals.

Phase compositions

Mineral compositions

The composition of plagioclase as a function of temperature is presented in **Figure III-3a**. Resorbed plagioclase crystals were anorthite-rich, with compositions ranging from An_{70} to An_{89} (An = 100 × molar Ca/(Ca+Na)). We interpret these anorthite-rich cores as relics from the starting material because their compositions overlap those of resorbed crystals at 1190 °C and plagioclase cores ($An_{80–88}$) in the original sample OS36 (*Bechon et al. 2022*). During cooling, the anorthite contents of plagioclase overgrowths decreased from An_{62} at 1165 °C to An_{55} at 1100 °C (**Figure III-3a**). No significant compositional difference was observed between rims formed under different cooling rates, except at 1120 °C, where plagioclases crystallized at 9 °C/h had lower anorthite contents ($An_{55–57}$ vs. $An_{60–61}$ at 1 and 3 °C/h).

Oxide compositions were within the ranges 4–7 wt.% TiO_2 and 71–75 wt.% $FeO_{(t)}$. Some samples showed zoned distributions of Fe-Ti oxide compositions (e.g., sample G 1-3, 1 °C/h, 1120 °C; ***Supplementary file III-2***) suggesting a potential redox gradient within the charges (**Figure III-3b**). In sample G 1-4 (1 °C/h, 1100 °C), oxide compositions ranged from 7.13 ± 0.23 TiO_2 near the Pt wire, to 6.27 ± 0.04 in the inner part of the sample. However, these variations appear to depend on the sample. For instance, oxide compositions in sample G 1-3 ranged from 4.36 ± 0.16 wt.% TiO_2 and 74.40 ± 0.43 wt.% $FeO_{(t)}$ at the edge, to 4.70 ± 0.13 wt.% TiO_2 and 75.32 ± 0.41 wt.% $FeO_{(t)}$ at the core.

Melt composition

The melt composition ranged from andesitic (57–59 wt.% SiO_2, ~5 wt.% $Na_2O + K_2O$) at the liquidus to dacitic (67–71 wt.% SiO_2, ~4.5–5 wt.% $Na_2O + K_2O$) at 1000 °C (**Table III-**

2). Cooling led to a slight decrease in CaO and Al_2O_3 contents due to plagioclase crystallization (**Figure III-3c**). Aside from slightly lower Al_2O_3 and CaO contents near the sample edge and the Pt-wire (where plagioclase crystals were most abundant), the melt composition was homogeneous (***Supplementary file III-3***). The concentration of other elements remained generally constant during crystallization. At 1050 °C and 1000 °C, pyroxene crystallization induced a slight decrease of FeO and MgO contents in the melt. We did not observe clear trends in liquid composition as a function of cooling rate (**Figure III-3c**).

Figure III-3 (see below)*: The evolving chemical compositions of (a) plagioclase, (b) Fe-Ti oxides, and (c) the residual melt. (a) An content in plagioclase rims and cores vs. temperature (open symbols, WDS data; filled symbols, EDS data). Error bars correspond to the minimum and maximum values obtained for each sample. Rim An contents slightly decreased with decreasing temperature. (b)* $FeO_{(t)}$ *vs.* TiO_2 *in Fe-Ti oxides. Results are shown for crystals in the sample center and for those near the sample edge. Filled symbols indicate average values calculated from the individual point measurements (unfilled symbols). Error bars are 1σ errors. (c) CaO,* Al_2O_3*, MgO, and FeO contents vs.* SiO_2 *content in the experimental melts. The red vertical line indicates the appearance of Cpx in the experiments.*

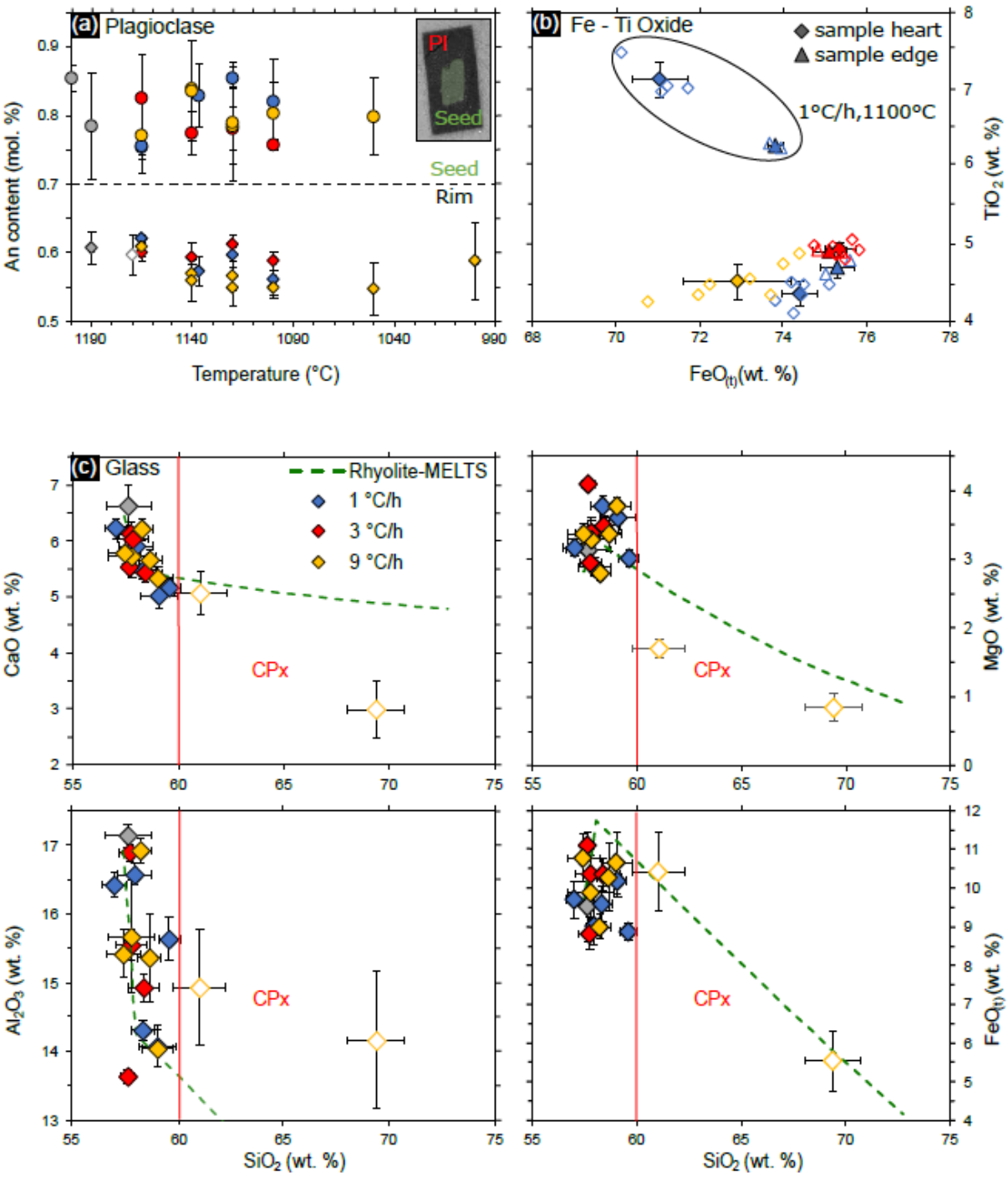

Microstructural variations

Plagioclase grain shapes ranged from anhedral and resorbed relic crystals near the liquidus to euhedral during cooling (**Figure III-2**). Most experiments displayed well-faceted crystals with well-defined prismatic/tabular shapes, corresponding to interface-controlled growth at low degrees of undercooling (**Figure III-2c, e, g**). However, experiments cooled at 9 °C/h, especially those quenched at 1120 °C, contained hollow/skeletal plagioclase crystals

(**Figure III-2d, f**; ***Supplementary file III-2)***. Fe-Ti oxides and clinopyroxenes in those experiments also exhibited skeletal/dendritic textures, indicating diffusion-limited growth consistent with rapid growth at high degrees of undercooling (**Figure III-2h**, ***Supplementary file III-2***).

Crystal density and size parameters

The volumetric proportion (φ_V) and sizes of crystals (l_{max}), as well as their number densities (N_A), increased with increasing $-\Delta T_n$ (**Figure III-4a–d**) down to 1050 °C. The apparent decrease in crystal size (Fig. 4d) between 1050 and 1000 °C can be explained by (i) a higher crystal content, leading to the formation of more equant crystals, or (ii) excessively high crystallinity, making segmentation more difficult and uncertain. The relatively high values of S_N and l_{max} at 1175 °C (G 1-0, G 2-0, G 3-0) are explained by an initial stage involving growth on pre-existing crystal seeds, forming larger crystals than those that newly nucleated (**Table III-3**). Experiments cooled at 1 °C/h and 3 °C/h showed a more rapid and linear increase in size and number density at low to moderate $-\Delta T_n$ (10–35 °C), with a break in slope below 1140 - 1120 °C ($\varphi_V = 0.11 – 0.15$). Despite a more scattered evolution of the number density at 9 °C/h, a similar trend was observed, with the highest N_A values exceeding 4×10^{-4} µm^{-2} at 1140 °C (**Figure III-4c**). The anomalously low N_A values ($3–4 \times 10^{-4}$ µm^{-2}) in the experiments quenched at 1120 °C were related to the presence of skeletal crystals. Contrary to the observations of *Conte et al. (2006)*, we found no clear relationship between crystal size and cooling rate, except in experiments quenched at 1100 °C, in which l_{max} decreased with increasing cooling rate (**Table III-3**).

2D morphology

Crystal sizes and shapes (quantified as the aspect ratio *w/l*) varied significantly within each experimental charge. Although we observed no distinct mode of 2D aspect ratio (*w/l*) between 1140 and 1100 °C, the ratio generally decreased with increasing $-\Delta T_n$, as illustrated by an increasing proportion of crystals with $w/l < 0.3–0.4$ at lower quenching temperatures (**Figure III-4f**). This global evolution from equant to tabular shapes was associated with increased crystal size **(Figure III-4e, *Supplementary file III-4*)**. Crystals larger than 100 µm were characterized by $w/l < 0.25$. Despite some variations, at a given temperature the 2D aspect ratio tended to decrease with increasing cooling rate (**Figure III-4g**); for example, at 1100 °C

the proportion of crystals with w/l = 0.6–1.0 was lower in experiments cooled at 3 °C/h and 9 °C/h than in those cooled at 1 °C/h, whereas the proportion of crystals with w/l = 0.1–0.4 was higher.

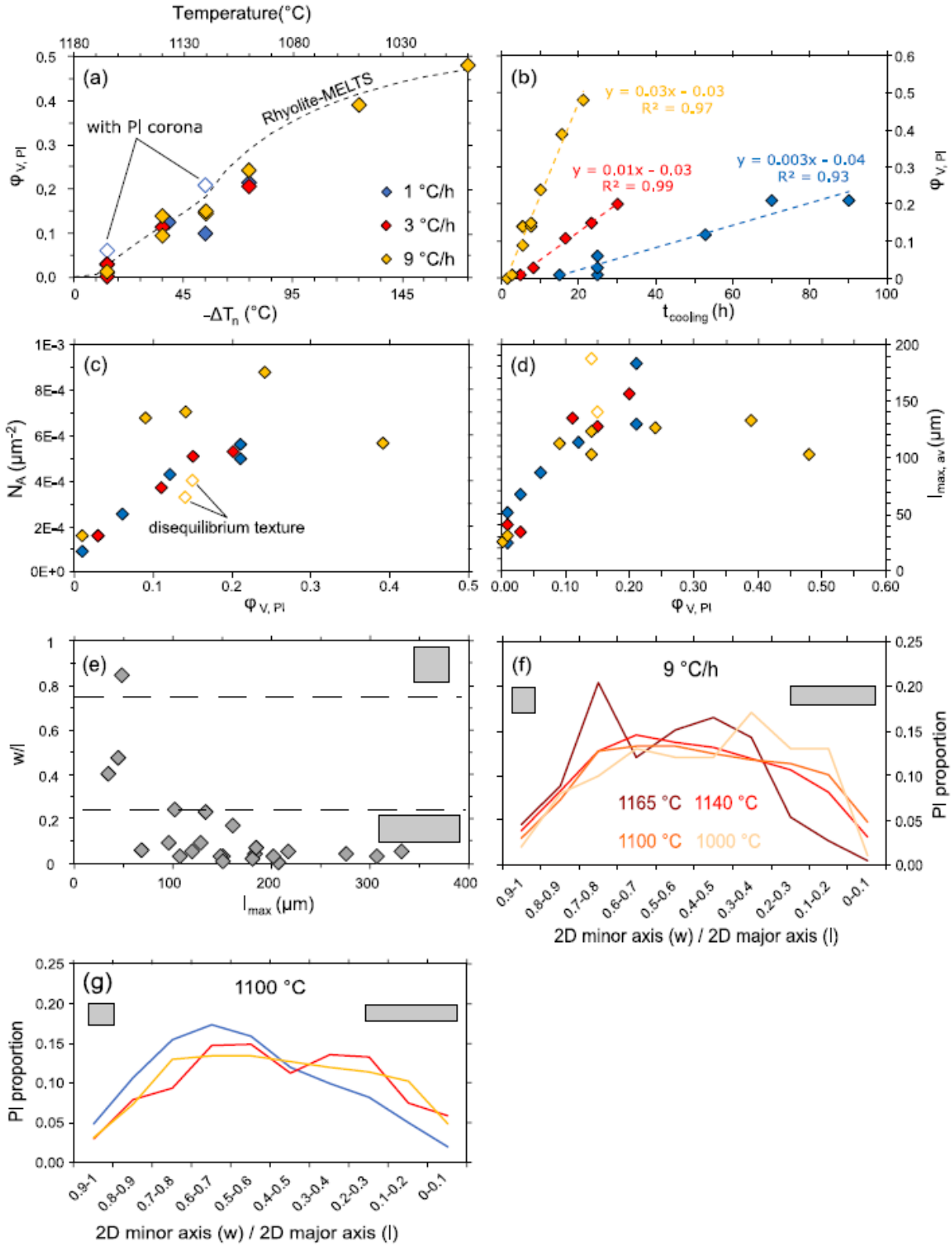

***Figure III-4**: Textural data from cooling experiments. (a, b) Volumetric proportion of plagioclase (ϕ_V) as functions of the (a) temperature and (b) cooling time ($t_{cooling}$). (c, d) Crystal number density per unit area (N_A) and the average maximum crystal sizes ($l_{max,avg}$, averaged from the 10 largest crystals), respectively, as functions of the plagioclase proportion (as a measure of crystallization progress). (e) 2D aspect ratio (w/l) vs. maximum (longest) crystal size (l_{max}). (f, g) Proportions of plagioclase crystals binned as a function of w/l for different (f) quench temperatures and (g) cooling rates. In (e–g), 2D crystal sketches illustrate w/l. Because the temperature and plagioclase proportion are directly linked, the x-axis in panels (c) and (d) is the plagioclase proportion, highlighting the linear relationship observed at 1 and 3 °C/h. Multiple symbols for the same run conditions (e.g. cooled at 9 °C/h and quenched at 1140 °C) correspond to replicate experiments. Symbol colors indicate cooling rate except in panel (e), where cooling rates are not indicated, and (f), where colors indicate quench temperature.*

3D shape

3D crystal shapes are classified as equant ($S = I = L$), elongated/oblong [3]($S = I < L$), prismatic/bladed ($S < I < L$), or tabular ($S < I = L$), and are presented in Zingg diagrams (I/L vs. S/I; *Zingg 1935*) (**Figure III-5**, ***Supplementary file III-4***). Except for experimental charges cooled at 9 °C/h, characterized by elongated skeletal crystals at 1120 °C, there is no clear variation in 3D shape with increasing $-\Delta T_n$ from 40 to 80 °C. Only a small decrease in S/I and increase in I/L was observed when considering the entire crystal population of each experiment (**Figure III-5a**). The 3D shape (S/I) decreased from 0.8 to 0.65 at 1 °C/h, and from 0.65 to 0.55 at 3 °C/h. The only exception to this trend is for experiments at 1190 °C, 1175 °C and 1165 °C, which were above or very near the liquidus, and at 1050 °C, corresponding to an advanced step of crystallization (S/I = 0.37, I/L = 0.48).

Considering distinct ranges of crystal sizes, crystal shapes were generally correlated with increasing crystal size (**Figure III-5b**): the smallest crystals were equant to elongated (i.e. w/l = 0.7–0.8 at 1165 °C). This evolution from equant to elongated shapes mainly occurred along the long axis, decreasing I/L. The main growth stage to larger tabular/bladed crystals (w/l = 0.4–0.5 at 1120 and 1100 °C) occurred along the intermediate axis (decreasing S/I). Finally, the largest crystals (>100 µm) had prismatic/tabular shapes (w/l = 0.3–0.1) and, at high $-\Delta T_n$ (1100 °C), were nearly equant to tabular, with $I = L$.

[3] Corresponds to the term "prismatic" in *Lindoo et al. (2025)*. The 3D shape estimation "S < I < L" refers to a bladed morphology

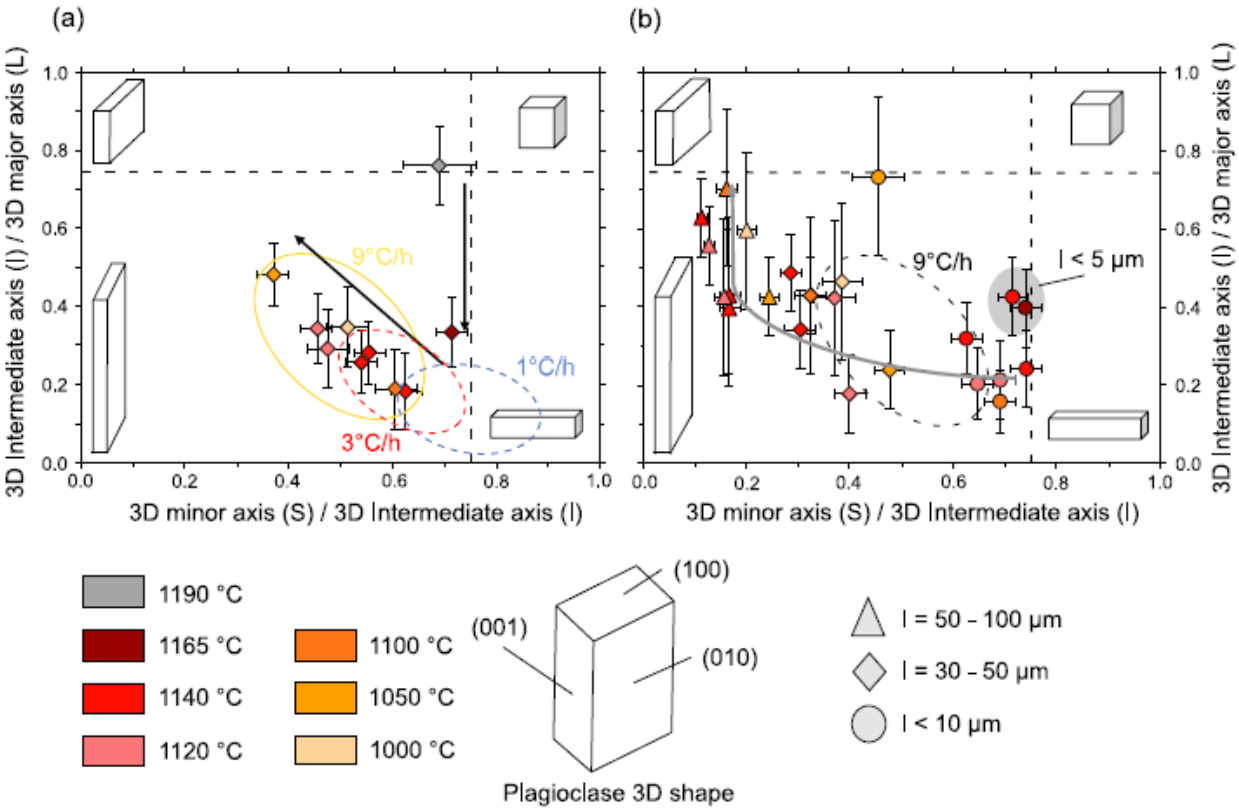

***Figure III-5**: Zingg diagrams of G-3 runs (cooling rate = 9 °C/h) using the 3D shapes (S:I:L) calculated with Shapecalc (Mangler et al. 2022). (a) 3D shape evolution considering all G-3 samples. Bue and red dashed ellipses indicate the ranges of values for runs cooled at 1 and 3 °C/h, respectively, but individual data points are not shown here. (b) 3D shapes of distinct crystal size populations. Similar results are shown for the other series of experiments in **Supplementary file III-3**.*

Crystal size distributions

CSDs plotted with and without 3D correction were quite similar; accordingly, we focus on CSDs without 3D correction (see ***Supplementary file III-4*** for the various CSD parameters). Although the nucleation number densities of the smallest crystals and the *y*-axis intercept changed by 10–25% when using CSDCorrections, all curves displayed the same overall shape commonly observed in most experimental (*Pupier et al. 2008*; *Brugger and Hammer 2010b*) and natural studies (*Cashman and Marsh 1988*; *Marsh 1998*): CSDs comprised a prominent log-linear, negatively sloped segment extending from 10–15 to 95 µm at 1165 °C and to 145 µm at 1100 °C, followed by a shallowly sloped segment corresponding to the largest crystals (**Figure III-6a**) that can be attributed to fewer measured crystals or variable growth rates. A

strong upward (convex) curvature, i.e. a positive slope at the smallest crystal sizes (≤5–10 µm), was observed in several runs.

The evolutions of the characteristic size (l_c) and intercept (ln (n_0) for l=0) presented **Figure III-6b** are globally consistent with microstructural evolutions (see section above). For the same cooling rate, the slope of the log-linear part of the CSDs flattened as T_f decreased, marking an increase of l_c (**Figure III-6a**). This increase in crystal size seems to be linked to the increased cooling time (**Figure III-6f**). Despite very small increases in the intercepts at cooling rates of 1 and 3 °C/h (by 8 and 3% respectively), the maximum crystal density was reached at 1140 °C (cooling at 9 °C/h) or 1120 °C (cooling at 1 and 3 °C/h), followed by a decrease with increasing cooling time (**Figure III-6b**). A stagnation of the initial crystal density with a relative difference of the intercept value ranging from 1 and 3 % is noted between 1140 and 1100 °C. As mentioned above, the decreased intercept at 1050 and 1000 °C (i.e. at advanced stages of crystallization) correlated with a sharp decrease in the proportion of crystals smaller than 10 µm.

Considering l_{max} and N_A, fluctuations of the CSD intercept value, especially at 9 °C/h and 1120 °C, reflect a change from tabular/prismatic to skeletal crystal shapes. More generally, runs cooled at 9 °C/h displayed lower l_c values and higher intercept values (**Figure III-6c-e**) This observation is linked to the instantaneous degree of undercooling, which increases with increasing cooling rate. The CSD parameters (l_c, ln(n_0)) obtained at 1 and 3 °C/h were similar, particularly the intercept values (**Figure III-6c** and **e**).

Figure III-6 (see below)*: CSDs obtained by image segmentation. (a) 2D CSD data illustrating the evolution of the CSD with decreasing quench temperature at a cooling rate of 9 °C/h. (b) Characteristic crystal size lc (−1/slope) and the intercept of the CSD (ln(n0)) as functions of temperature and cooling rate. (c) CSD plots as a function of the cooling rate in samples quenched near the liquidus. (d, c) lc and ln(n0), respectively, vs. cooling rate, and (f) lc vs. cooling time. In panel (f), filled and unfilled symbols are for CSD data obtained without and with 3D correction, respectively.*

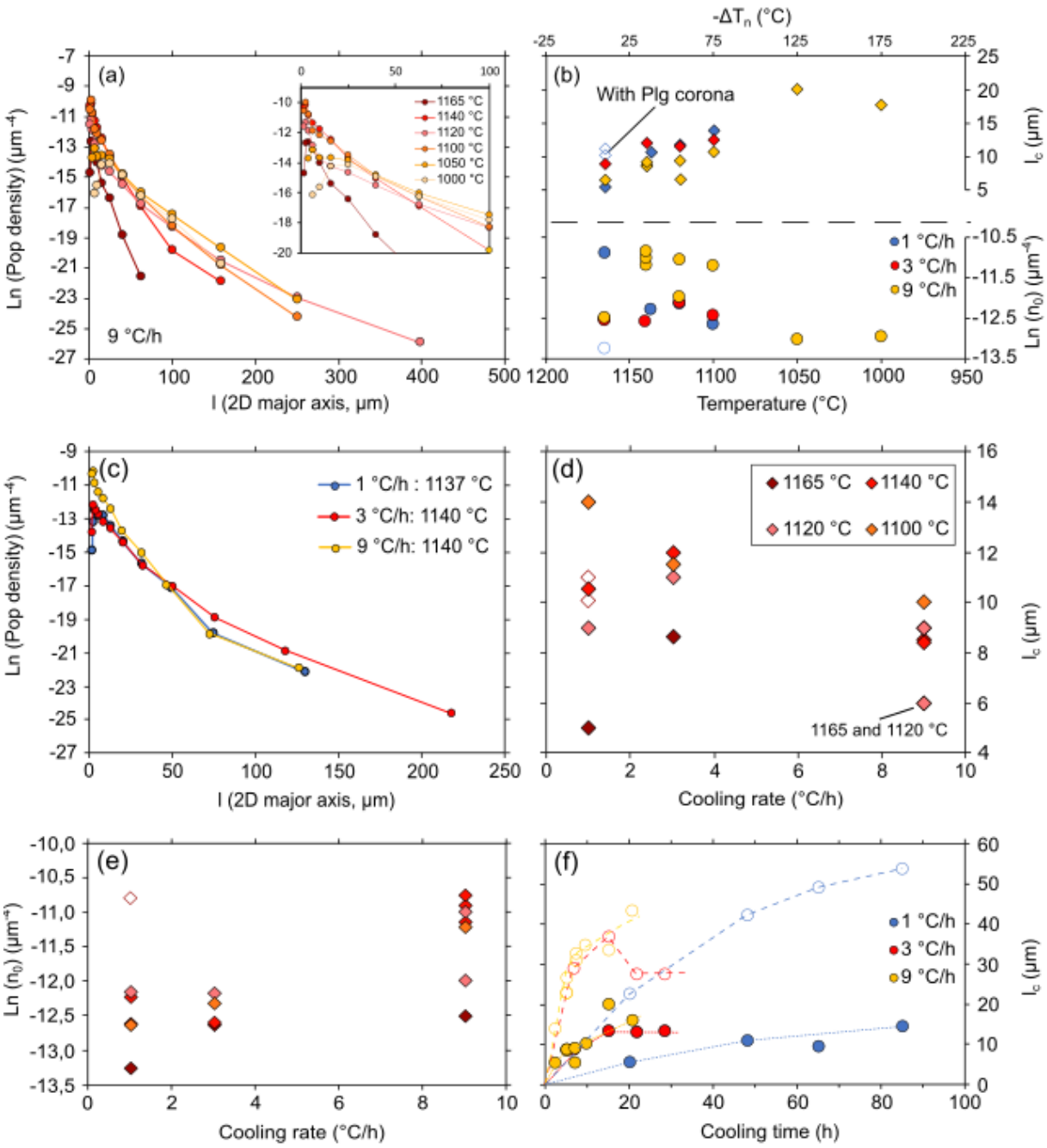

Nucleation and growth rates

Nucleation and growth rates ranged from 1.66×10^{1} to 6.33×10^{3} cm^{-3} s^{-1} and from 2.04×10^{-9} to 4.39×10^{-7} cm/s, respectively (**Table III-4**), similar to the rates obtained by *Pupier et al. (2008)* at comparable cooling rates. Both *J* and *G* followed similar trends (**Figure III-7a**), with an initial increase just below the liquidus to a maximum at 1165 °C (runs cooled at 1 or 3 °C/h) or 1140–1120 °C (9 °C/h), before gradually decreasing by nearly half an order of magnitude.

Between the series cooled at 1 and 9 °C/h, nucleation rates increased by more than 1 order of magnitude, and growth rates by a factor of 8 (***Supplementary file III-5***). However, the rates measured depend on the method used (**Table III-4**, **Figure III-7b**). Average growth rates ranged from 1.00×10^{-7} to 3.70×10^{-9} cm/s using the batch method, from 1.25×10^{-7} to 4.81×10^{-9} cm/s considering the entire, segmented population (l_{mean}), and from 4.39×10^{-7} to 3.28×10^{-8} cm/s based on l_{max}, the latter being 1 order of magnitude higher than the rates calculated using the batch and l_{mean} methods. Similarly, nucleation rates ranged from 4.80×10^{3} to 6.63×10^{1} cm^{-3} s^{-1} with the batch method and from 1.33×10^{3} to 1.66×10^{1} cm^{-3} s^{-1} with the 3D CSD method. All rates are reported in **Table III-4**. The growth rates obtained from G_{mean} and G_{max} along the 2D major axis (l) were respectively 2.22 ($R^2 = 0.97$) and 2.52 ($R^2 = 0.87$) times higher than those obtained from the 2D minor axis (w), suggesting axis-dependent growth (*Pupier et al. 2008*; *Mangler et al. 2022*).

			Growth rate ($cm.s^{-1}$)									Nucleation rate ($cm^{-3}.s^{-1}$)			
Sample	Cooling rate (°C/h)	T_f (°C)	G_{Batch}	$G_{mean, w}$	$G_{mean, l}$	$G_{CSD, 2D}$	$G_{CSD, 3D}$	$G_{max, l}$	$G_{max, w}$	G_{rim}	J_{Batch}	$J_{CSD, 2D}$	$J_{CSD, 3D}$	J_{mean}
G 1-1 (sample 1)	1	1165	2.08E-08	1.39E-08	2.92E-08	1.40E-08	4.57E-08	1.21E-07	5.69E-08	2.56E-08	4.69E+02	4.65E+02	9.57E+01	2.59E+02
No crystal corona	1	1165	1.53E-08	9.72E-09	1.67E-08	6.94E-09	3.13E-08	3.47E-08	2.36E-08	-	2.38E+02	1.43E+03	1.90E+02	4.66E+02
G 1-1 (sample 2)	1	1165	1.81E-08	1.39E-08	2.92E-08	1.53E-08	5.79E-08	9.44E-08	4.72E-08	-	3.36E+02	2.64E+02	4.84E+01	1.63E+02
G 1-2	1	1137	6.21E-09	3.65E-09	7.31E-09	3.85E-09	1.54E-08	4.17E-08	1.57E-08	8.61E-09	1.86E+02	1.87E+02	3.88E+01	1.04E+02
G 1-3	1	1120	5.05E-09	2.53E-09	5.81E-09	2.27E-09	1.25E-08	3.28E-08	1.06E-08	9.72E-09	1.34E+02	1.19E+02	2.49E+01	7.07E+01
G 1-4	1	1100	3.70E-09	2.04E-09	4.81E-09	2.59E-09	9.74E-09	3.39E-08	1.04E-08	6.67E-09	1.07E+02	8.40E+01	1.66E+01	5.30E+01
G 2-1 (sample 1)	3	1165	5.83E-08	2.92E-08	7.08E-08	3.61E-08	1.20E-07	2.50E-07	9.58E-08	8.42E-08	9.67E+02	1.17E+03	2.87E+02	6.09E+02
G 2-1 (sample bis)	3	1165	6.25E-08	5.00E-08	9.58E-08	-	-	1.46E-07	7.92E-08	-	6.63E+01			3.52E+01
G 2-2	3	1140	2.02E-08	1.07E-08	2.86E-08	1.43E-08	4.43E-08	1.61E-07	4.76E-08	3.33E-08	5.12E+02	4.77E+02	1.17E+02	2.78E+02
G 2-3	3	1120	1.29E-08	6.82E-09	1.74E-08	8.33E-09	2.12E-08	9.62E-08	3.26E-08	2.69E-08	4.50E+02	4.30E+02	1.34E+02	2.55E+02
G 2-4	3	1100	1.11E-08	5.56E-09	1.50E-08	6.39E-09	1.53E-08	8.67E-08	2.50E-08	2.31E-08	3.00E+02	2.81E+02	8.70E+01	1.68E+02
G 3-1	9	1165	1.00E-07	6.25E-08	1.25E-07	7.50E-08	1.73E-07	3.88E-07	2.50E-07	1.13E-07	4.80E+03	2.77E+03	9.83E+02	2.14E+03
G 3-2 (sample 1) Seg 1	9	1140	5.00E-08	2.50E-08	6.43E-08	3.04E-08	8.10E-08	4.39E-07	1.25E-07	-	3.57E+03	5.55E+03	1.25E+03	2.59E+03
G 3-2 (sample 2)	9	1140	4.29E-08	2.14E-08	5.36E-08	2.99E-08	9.49E-08	4.04E-07	1.32E-07	7.75E-08	4.11E+03	6.33E+03	1.19E+03	2.91E+03
G 3-2 (sample 1) Seg 2	9	1140	5.00E-08	2.50E-08	6.43E-08	3.21E-08	8.26E-08	3.68E-07	1.18E-07	-	3.57E+03	4.60E+03	1.33E+03	2.38E+03
G 3-3 (sample 1)	9	1120	4.77E-08	2.05E-08	6.82E-08	2.05E-08	7.04E-08	4.25E-07	9.09E-08	9.08E-08	7.18E+02	1.27E+03	2.38E+02	5.58E+02
G 3-3 (sample bis)	9	1120	4.32E-08	1.82E-08	5.45E-08	1.36E-08	7.44E-08	3.18E-07	8.18E-08	-	9.59E+02	2.27E+03	3.00E+02	8.83E+02
G 3-4	9	1100	2.83E-08	1.33E-08	3.50E-08	1.67E-08	5.76E-08	2.10E-07	7.00E-08	4.22E-08	1.77E+03	2.22E+03	4.84E+02	1.12E+03
G 3-5	9	1050	2.60E-08	1.30E-08	3.50E-08	2.00E-08	3.29E-08	1.33E-07	4.60E-08	-	4.34E+02	4.82E+02	2.14E+02	2.84E+02
G 3-6	9	1000		1.00E-08	2.50E-08	1.25E-08	3.09E-08	7.36E-08	2.79E-08	-		3.17E+02	1.18E+02	2.17E+02

***Table III-4**: Nucleation ($cm^{-3}.s^{-1}$) and growth ($cm.s^{-1}$) rates calculated by various methods.*

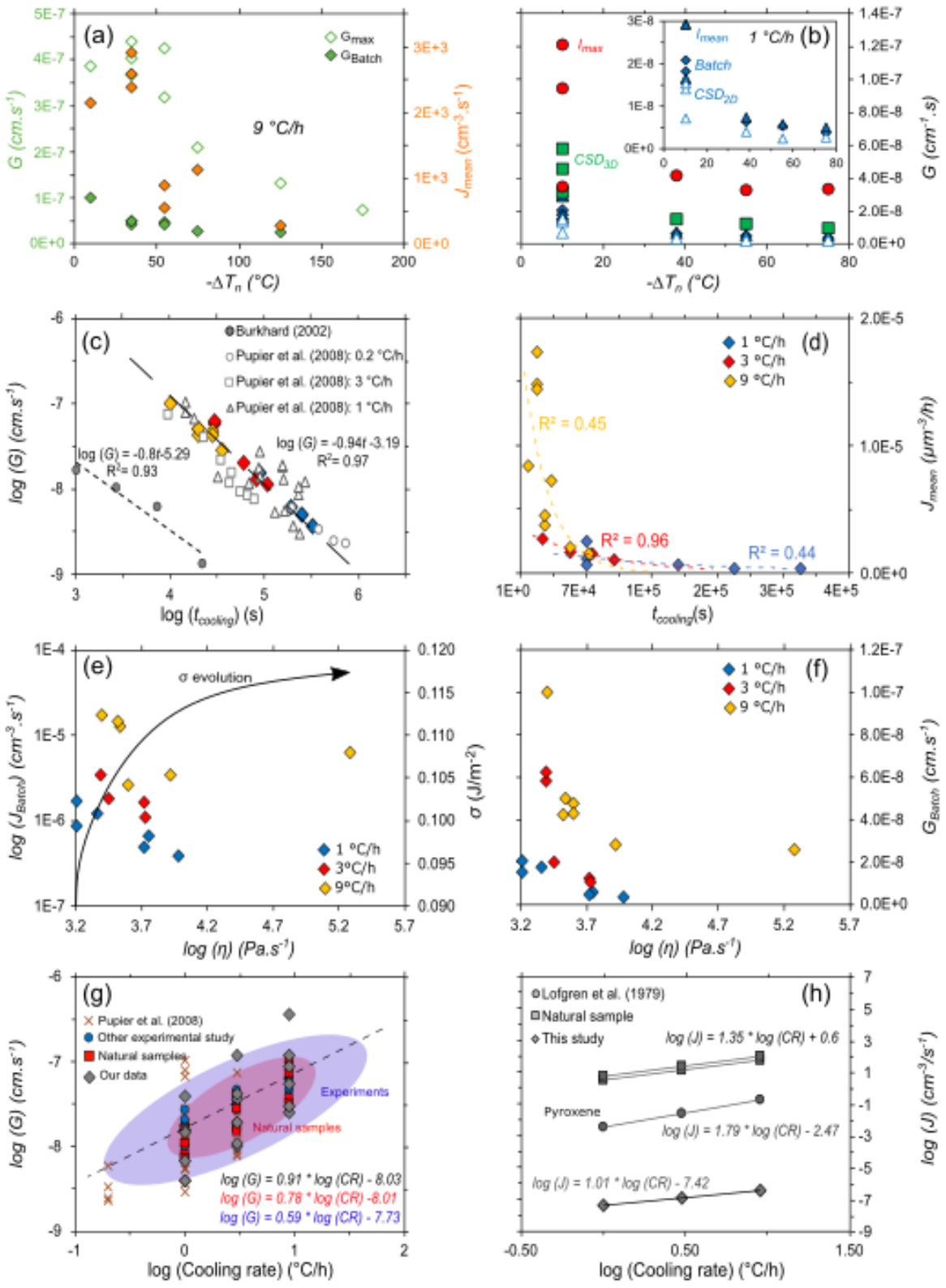

***Figure III-7**: Nucleation and growth rates determined from the cooling experiments. (a) The evolution of nucleation (J_{mean}, averaged from J_{batch}, $J_{CSD,3D}$, and $J_{CSD,2D}$) and growth rates (G_{batch} and $G_{max,l}$) in samples cooled at 9 °C/h. (b) G calculated by various methods ($G_{max,l}$, $G_{CSD,3D}$, $G_{CSD,2D}$, $G_{mean,l}$, and G_{batch}) for experiments cooled at 1 °C/h (G-1). (c) log (G) vs. log($t_{cooling}$); values from Pupier et al. (2008) and*

Burkhard (2002) concerning cooling and re-heating experiments on basaltic compositions are provided for comparison. (d) J_{mean} vs. cooling time. (e, f) J_{batch} and G_{batch}, respectively, vs. melt viscosity. The interfacial free energy (σ; calculated following Arzilli et al. 2015) is also indicated in (e). (g, h) G (obtained by l_{max}, Batch, l_{mean} and CSD methods) and J (obtained by Batch and CSD methods), respectively, vs. cooling rate. Except for data from Pupier et al. (2008), other experimental and natural data are from Cashman's (1993) compilation.

Experimental reproducibility

To confirm the reproducibility of our results, several experiments were replicated in separate runs (3 °C/h and 1165 °C, runs G 2-1a and b; 9 °C/h and 1120 °C, runs G 3-3a and b). In addition, in some cases, we included two separate samples in the same runs (1 °C/h and 1165 °C, runs G 1-1a1 and a2; 9 °C/h and 1140 °C, runs G 3-2a1 and a2). Except for experiments G 2-1a and b (1165 °C, 3 °C/h), the textural parameters (texture data, 2D aspect ratio, CSD parameters, and nucleation and growth rates) in replicated experiments were very similar (***Supplementary file 4***), demonstrating good reproducibility.

The overall crystal distributions, as well as the distributions of the 2D aspect ratio *w/l* were very similar, with relative differences of 1–36%. Similar reproducibility values were obtained for the textural data and CSD parameters. In contrast, G 2-1 replicates at 1165 °C showed relative differences of 92–93% for N_A/N_V and J_{batch}; this gap is attributed to semi-random nucleation near the liquidus, partly due to the random density and distribution of pre-existing crystal seeds. To assess uncertainties related to image segmentation, experiment G 3-2a1 (9 °C/h, 1140 °C) was segmented twice. The differences observed in this comparison were generally 2% for textural and CSD data and 14% for nucleation and growth rates. The largest deviations (28%) are attributed to segmentation of the smallest crystals and the associated determination of their aspect ratios.

Discussion

Crystallization kinetics

The small number of surviving seeds after 24 h at 1190 °C, and their resorbed textures, indicate that the crystal seeds were not in chemical equilibrium with the melt. The appearance of less calcic overgrowths on seeds suggests a rapid stabilization of plagioclase during the first 2 h of cooling (at 9 °C/h, T_f = 1175 °C).

Nucleation mechanisms

The higher proportion of plagioclase grains with cores corresponding to seeds from the initial crystal population compared to completely newly formed crystals at 1175 °C suggests that growth primarily occurs on pre-existing crystals rather than on newly formed nuclei at the lowest degrees of nominal undercooling ($-\Delta T_n$). This is consistent with the large activation energy required for plagioclase nucleation, as well as the decreasing critical size of the atom clusters needed to form stable nuclei with increasing degrees of undercooling (*Berkebile and Dowty 1982*; *Hammer 2008*; *Shea and Hammer 2013*). The slightly variable crystal densities observed in experiments quenched at low degrees of effective undercooling (e.g. samples cooled at 3 °C/h and quenched at 1165 °C) suggest erratic nucleation at the beginning of crystallization, potentially due to an inhomogeneous distribution of seeds in the starting material. Previous studies (*Gibb 1974*; *Sato 1995*; *Fokin et al. 2006*; *Hammer 2008*) argued that sufficiently fast cooling rates can cool the melt faster than the time necessary for the unrelaxed structure of the melt to 'rebalance' and enable nucleation. The resultant incubation period could explain the sharp decrease in newly formed crystals with increased cooling rate at 1175 °C.

The abundance of large crystals both around the platinum wire and at the surface of gas bubbles indicates that heterogeneous nucleation occurred (e.g. *Lofgren 1983*; *Nabelek et al. 1978*; *Pupier et al. 2008*; *Shea and Hammer 2013*). As noted by *Corrigan (1982a, b)*, the random configuration of the Pt wire within each sample can generate spatially variable heterogeneous nucleation, contributing to the inhomogeneous distribution of crystals often observed in our experiments. Such heterogeneous nucleation, which is particularly evident at low degrees of undercooling ($-\Delta T_n$ = 0–10 °C), was also present during crystallization at lower temperatures ($-\Delta T_n$ = 35–75 °C), with Fe-Ti oxide grains nucleating at the contact with Pt wire. However, the difficulty in obtaining material from the experimental charge in direct contact with the Pt wire prevents us from determining whether this trend continues through the most advanced stages of crystallization at 1050 and 1000 °C ($-\Delta T_n$ = 125–175 °C).

The absence of both crystal clusters and a preferential crystal spatial distribution in the sample center at 1165 °C ($-\Delta T_n$ = 15 °C) suggests that homogeneous nucleation also occurred, although this is difficult to verify because heterogeneous nucleation can occur even on sub-microscopic particles. The absence of an initial strong superheating step ($+\Delta T$ = 15 °C) in our experiments likely preserved nanometric plagioclase nuclei (as observed by *Burkhard (2005)*, which can act as substrates for nucleation. Accordingly, the pronounced curvature in our CSDs

between 1140 and 1100 °C (***Supplementary file III-4***) suggests that 70–98% of crystals nucleated via heterogeneous nucleation (*Špillar and Dolejš 2015*).

With decreasing temperature from 1140 to 1100 °C, the number of plagioclase clusters increased in our experiments. These were formed either by the relative movement of nearby but previously isolated crystals, or through secondary nucleation upon the breakage of pre-existing crystals when impinged by neighboring crystals as crystal density increased. The dendritic pyroxene crystals radiating from plagioclase grains ($-\Delta T_n$ = 125 and 175 °C) were most likely due to the heterogeneous nucleation of pyroxene on plagioclase (*Rusiecka et al. 2020*; *Walker et al. 1978*; *Shea and Hammer 2013*). Similarly, clinopyroxene acts as a nucleation substrate for Fe-Ti oxides, with many oxides crystallizing on clinopyroxene edges (*Griffiths et al. 2023*). Heterogeneous nucleation was thus a dominant process in our experiments, which therefore compare rather well to magma reservoirs (*Cashman and Marsh 1988*), in which xenocrysts and antecrysts are common (e.g. *Sunagawa 1981*; *Berkebile and Dowty 1982*; *Lofgren 1983*).

Plagioclase growth mechanisms

Interface-controlled growth (limited by reactions at the crystal-melt interface) typically produces euhedral crystals (*Watson and Liang 1995*), whereas diffusion-controlled growth (limited by the diffusion of components from the melt to the interface) results in skeletal to dendritic shapes (*Kirkpatrick 1975, 1981*; *Sunagawa 1981*; *Watson 1996*). Recently, *Mangler et al. (2023)* proposed an additional intermediate growth regime for euhedral crystals, in which melt-interface reactions and melt diffusivities compete. Here, the growth of the longest 2D dimension (with the faster interfacial reaction rate) is limited by the melt diffusion rate, resulting in reduced growth along the 2D major axis (l) compared to the 2D minor axis (w). Crystals growing in this regime become more compact (increasing w/l) and can develop hopper or swallowtail textures as diffusion becomes the limiting factor. As explained above, at low nominal undercooling ($-\Delta T_n$= 0–10 °C), slow nucleation favors overgrowth on pre-existing crystals. Indeed, at slow cooling rates of 1–3 °C/h, corresponding to low degrees of undercooling between 15 and 80 °C, euhedral/equant to prismatic or tabular plagioclases and Fe-Ti oxides were observed, suggesting interface-controlled growth.

At a faster cooling rate of 9 °C/h, corresponding to an increased degree of undercooling, the transition from euhedral crystals to hopper (1165 and 1140 °C) and swallowtail habits (particularly visible at 1120 °C) suggests predominantly diffusion-controlled growth (e.g.

Lofgren 1974; *Kirkpatrick 1975*; *Hammer and Rutherford 2002*; *Couch et al. 2003a*; *Shea and Hammer 2013*). The intermediate growth regime of *Mangler et al. (2023)* can explain the evolution from tabular to compact and, eventually, swallowtail habits when diffusion becomes the rate-limiting mechanism of growth along 2D longest axis. However, the significant shape variations observed in 2D sections, combined with sectioning effects, make it difficult to verify the transition from tabular/prismatic to compact crystals.

At advanced stages of crystallization (1050 °C and 1000 °C, $-\Delta T_n$ = 125–175 °C) and under fast cooling (9 °C/h), the absence of crystals smaller than 10 µm could result from suppressed nucleation and the dominance of growth because Ostwald ripening, a relatively slow process, is precluded at high degrees of undercooling (*Cabane et al. 2005*). Another explanation proposed by *Marsh (1998)* is the scarcity of the available liquid around 50 % crystallinity that could induce a strong decrease of the nucleation.

Increased cooling rates also affect clinopyroxene and Fe-Ti oxides, which develop skeletal textures rather than the euhedral shapes observed at slower cooling rates (1 and 3 °C/h). Clinopyroxene crystallization is particularly dependent on the cooling rate, with nucleation delayed by 60 °C (marked by crystallization mediated by plagioclase) under a fast cooling rate of 9 °C/h. In contrast, no delay was observed for Fe-Ti oxides or plagioclase. The textural differences observed during crystallization (corresponding to $-\Delta T_n$) and between the various cooling rates correspond to an increase of the true degree of undercooling ($-\Delta T$), demonstrating the complexity of making direct comparisons. Furthermore, despite a significant increase in cooling rate from 1 to 9 °C/h, similar to values used by *Pupier et al. (2008)* on synthetic basalt, the resulting textural variations observed herein remain generally small compared to those observed studies conducted at very fast cooling rates exceeding 100–900 °C/h (*Kohut and Nielsen 2004*; *Arzilli et al. 2019*).

Determination of activation energies for nucleation and growth

We used the following equations to constrain the T dependence of J and G, as well as the activation energies of nucleation and growth (E_J and E_G, respectively; *Burkhard 2005*):

$$\ln(G) = \ln(G_0) - \frac{E_G}{RT} \quad (12)$$

$$\ln(J) = \ln(J_0) - \frac{E_J}{RT} \quad (13)$$

For the different methods of calculation used herein (e.g. batch, CSD), the average values of E_J and E_G are 280–424 KJ/mol and 128–443 KJ/mol, respectively, in agreement with those determined in the isothermal crystallization experiments of *Burkhard (2005)*; around 300–350 KJ/mol). We observed a strong decrease (by more than 100 KJ/mol) when the cooling rate increases from 1 to 9 °C/h because increased cooling rates, and hence the degree of undercooling, favors crystal nucleation and growth. Indeed, crystallization time decreases as the cooling rate increases. Nucleation and growth rates are respectively more than 7 and 11 times faster during a cooling at 1 °C/h than 9 °C/h. *Lesher et al. (1999)* demonstrated that the solidification of a MORB basalt occurs 50 times faster in a magma cooled at 1000 °C/h than in one cooled at 10 °C/h. Similar E_J and E_G values are respectively observed between cooling at 3 and 9 °C/h, and between 1 and 3 °C/h.

Evolution of growth and nucleation rates during crystallization

Here, we focus our discussion on the evolution of growth and nucleation rates as a function of effective undercooling (which varies with temperature), as well as the true instantaneous degree of undercooling, which increases with increasing cooling rate. Because it is impossible to precisely determine the true instantaneous degree of undercooling, this discussion is necessarily qualitative.

Growth as a function of crystal axis

Marsh (1998) assumed that the log-linear part of a CSD in a closed system results from an exponential increase of nucleation at a constant growth rate, without modification over time or with crystal size. However, several lines of evidence show that this assumption is incorrect. *Pupier et al. (2008)* and *Mangler et al. (2023)* observed that as crystal size increases, crystal shape evolves from equant/prismatic (S/I = 0.7–0.8 for the smallest crystals, <5–10 µm) to more bladed/tabular (S/I = 0.2–0.3 for crystals of 30–50 µm) (**Figure III-5b**, **Figure III-6b)**. Furthermore, they observed that stable shapes are only attained once crystals reach 50 µm in size, marked by only slight variations of S/I from 0.1 to 0.2.

Our results obtained with G_{mean}, G_{max} (faster along the l axis than along the w axis), and G_{CSD} ($G_{CSD,3D} = 2.8 \times G_{CSD,2D}$; $R^2 = 0.94$) indicate that growth depends not only on crystal size,

but also on crystal axis[4], with significant growth occurring along the 3D intermediate axis (2D major axis). The correlation between the aspect ratio and crystal size, as well as the curved shape of the CSDs (with a flattened trend toward larger crystals), suggests a growth rate dependent on crystal size (*Eberl et al. 2002*; *Kyle and Eberl 2003*), in contrast to the conclusions of *Zieg and Lofgren (2006)*.

Some authors, such as *Pupier et al. (2008)* and *Nie et al. (2014)*, suggested that the downturn of the CSD at the smallest crystal sizes could be explained by late-stage maturation processes, such as Ostwald ripening (characterized by the preferential dissolution of smaller crystals in favor of the growth of larger ones) or crystal agglomeration (synneusis). Although agglomeration textures with crystal clusters are present, no evidence of coalescence has been observed. Moreover, because our grain size measurements separated the various crystals of the clusters for individual measurements, clustering cannot explain the flattening and kinked portions of the CSDs observed for the largest and smallest size ranges, respectively. Similarly, except for experiments quenched at 1050 and 1000 °C, in which the proportion of the smallest crystals (<10 µm) decreases sharply (***Supplementary file III-4***), Ostwald ripening cannot explain this phenomenon in the other experiments, where this proportion remains nearly constant. In our case, as suggested by *Cashman and Marsh (1988)*, resolution limits and sectioning effects, both of which reduce the probability of intersecting the smallest crystals, seem to better explain the obtained CSDs.

The role of temperature and cooling time

Nucleation and growth rates were calculated based on the duration of cooling below the liquidus (1175 °C). Because nuclei are likely formed at various steps during cooling, these rates represent minimum values. We obtained a linear correlation between log (J)/log (G) and log(t), with R^2 respectively of 0.88 and 0.90 **Figure III-7c**, ***Supplementary file III-5***). The slope of the log(G)-log(t) plot (−0.94) is somewhat steeper than the range of −0.5 to −0.8 suggested for mafic systems by *Grove (1978)* and *Kohut and Nielsen (2004)*. However, data from *Pupier et al. (2008)* are consistent with our results, with variations potentially due to the initial superliquidus pre-treatment. Variation of the nucleation rate near the liquidus induced a lower R^2 value in the log(J)-log(t) plot. The sharp decrease in nucleation rates at relatively small to

[4] See *Lindoo et al. (2025)*, who demonstrated the link between anisotropic plagioclase growth and instantaneous undercooling, thereby quantifying the influence of the 'real' undercooling experienced during continuous-cooling experiments on plagioclase shape.

moderate $-\Delta T_n$ (between 1165 °C and 1140 °C, depending on the cooling rate) indicates that nucleation slowed altogether shortly after cooling began (**Figure III-7d**). This evolution is consistent with the intercepts in our CSDs, which were stable between 1140 and 1100 °C (from −12.24 to −12.64 at 1 °C/h, and from −12.64 to −12.18 at 3 °C/h in the 2D CSDs; ***Supplementary file III-4***), before the strong decrease in the proportion of small plagioclase (<10 µm) from 0.36 at 1100 °C to 0.01 at 1000 °C (***Supplementary file III-4***). This sharp decrease could be due to (1) a potential decrease in the proportion of liquid and available space (*Špillar and Dolejš 2014*) or, more likely, (2) textural maturation suppressing further nucleation due to overgrowths on pre-existing crystals being energetically favorable. The absence of a systematic decrease in the CSD intercepts between 1140 °C and 1100 °C could be due to the nature of the initial material (synthetic powder vs. natural powder with pre-existing crystals), which, in our case might favor nucleation due to the initial presence of seeds. The high curvatures at the smallest crystal sizes due to heterogeneous nucleation may also have impacted the determined intercepts.

As for the nucleation rate, growth rate (*G)* decreased with increasing $-\Delta T_n$. The constant plagioclase sizes below 1100 °C in experiments cooled at 9 °C/h indicate a probable shutdown of growth at $-\Delta T_n$ > 100 °C. In comparison, a recent *in situ* study of progressive olivine crystallization (*Welsch et al. 2023*) also indicated a non-constant growth rate characterized by a first stage of accelerating growth followed by growth at a constant rate and a final stage of slowing growth. Our measured plagioclase growth rates are likely the sum of these three stages, and thus 'bulk' growth rates. The observed decrease of nucleation and growth with time contradicts *Marsh's (1988)* assumption that nucleation rates increase exponentially at a constant growth rate (increasing $\ln(n_0)$, but a constant slope during cooling).

The exponential decrease of *J* and *G* (***Supplementary file III-5***) with increasing run duration is correlated with a gradual increase in melt viscosity, from 1.62×10^3 Pa.s at 1165 °C to 9.55×10^3 Pa.s at 1100 °C. At an advanced crystallization stage, viscosity becomes significantly higher, reaching 10^5 Pa.s at 1050 °C and 10^7 Pa.s at 1000 °C (***Supplementary file III-5***). This increase probably causes a slower Ca-Al diffusion at lower temperatures (**Figure III-7e, f**; *Giordano et al. 2008*). We used the Eyring equation to quantify the "network diffusivity" reflecting chemical transport at the crystal-melt interface (*Mangler et al. 2023*):

$$D = \frac{k_B \times T}{\lambda \times \eta} \quad (14)$$

Where k_B is the Boltzman constant (J/K), T the final temperature (K), λ the diffusing element's diameter (0.14 nm for O^{2-}; *Watkins et al. 2009*; *Mangler et al. 2023*) and η the melt viscosity (Pa.s). As expected, Eyring diffusivity decreases as melt viscosity increases (***Supplementary file III-5***), dropping from 10^{-14} $m^2.s$ between 1165-1100 °C, to 10^{-16} – 10^{-18} $m^2.s$ at 1050 and 1000 °C. Except at 1050-1000 °C, where values are 3-4 orders of magnitude lower than those of *Mangler et al. (2023)*, values calculated between 1165 and 1100 °C under "dry" conditions are between those obtained in basalt and hydrous haplodacite.

The resulting J and G decrease is modest at slow cooling rates but more substantial at faster cooling rates (*Pupier et al. 2008*). Therefore, at the very slow cooling rates occurring in natural magma bodies, growth rates are likely to be nearly constant over time, as deduced by *Marsh (1998)* from natural data.

The impact of cooling rate

Plagioclase sizes, nucleation and growth rates are linearly correlated with cooling rate (**Figure III-7g**, **h;** l_c evolution with cooling rate in **Figure III-6d**), consistent with previous observations (*Walker et al. 1978*; *Cashman 1993*; *Pupier et al. 2008*). The linear correlation between $\log(l_{max,avg})$ and log(CR) (CR being the cooling rate) is clearly temperature-dependent, with some fluctuations (R^2 = 0.88–0.99) probably due to the similarity of the cooling rates used herein (1–9 °C/h) compared to the wider range explored in other studies (1–9000 °C/h; *Iezzi et al. 2008*; *Vetere et al. 2015*; *Giuliani et al. 2020*). Indeed, we observed a slight decrease in the characteristic crystal size (l_c = −1/slope) with increasing cooling rate (**Figure III-6d**; ***Supplementary file III-4***).

The correlations between log(J) and log(G) with log(CR) are given by (for further details, see ***Supplementary file III-5***):

$$\log(J_{mean}) = (-6.43 \pm 0.19) + [(1.25 \pm 0.22)\log(dT/dt)];\ R^2 > 0.9 \quad (14)$$

$$\log(G) = (-8.029 \pm 0.360) + [(0.914 \pm 0.074)\log(dT/dt)];\ R^2 > 0.9 \quad (15)$$

The slope of the linear correlation obtained for the growth rates (the average value of the different methods of calculation) falls barely within the 1σ error range of values summarized by *Cashman (1993)* from experimental and natural samples (slopes of 0.42–0.88); e note

relative differences of 12–29 % and 3–6 % for slope and intercept values, respectively. As observed by *Pupier et al. (2008)*, when considering each cooling rate series separately, trends in the J vs. $t_{cooling}$ plot are nearly linear (and even becomes rapidly "constant" at 1°C/h) and broadly overlap at slow cooling rates (1, 3 °C/h). However, they become exponential, with fluctuations, at higher cooling rates (here, 9 °C/h) (**Figure III-7d**). This exponential decrease in J_{mean} (averaged from J_{batch}, $J_{CSD,2D}$, and $J_{CSD,3D}$) at slow cooling rates is explained by the system evolving toward equilibrium over time, resulting in decreasing nucleation and growth rates that approach zero as the true degree of undercooling nears zero.

For the experimental series cooled at 1 and 3 °C/h, the range of J and G values remains within the same order of magnitude as the cooling rate variations (***Supplementary file III-5***). This fact, previously mentioned by *Pupier et al. (2008)* for cooling rates between 0.2 and 3 °C/h, is less visible in experiments cooled at 9 °C/h, in which some skeletal textures were observed. This suggests a near-thermodynamic equilibrium in the proportion of plagioclase, which remained consistent across each cooling rate.

Comparison of calculated growth and nucleation rates

Determining crystallization kinetics is a complex problem (*Zieg and Marsh 2002*) and the various methods used to quantify crystallization (e.g. here, batch, CSD, l_{mean}, l_{max}) tend to return different parameter values. In this section, we compare the results obtained using each method in an effort to determine which methods give the best results. No discussion will be presented here regarding the various assumptions concerning the CSD method (see next section for this).

	y = ax		
y = f(x)	a	1 sigma error	R^2
$G_{Batch} = f(G_{CSD, 2D})$	1.54	0.05	0.97
$G_{Batch} = f(G_{mean, l})$	0.76	0.05	0.99
$G_{Batch} = f(G_{mean, w})$	1.58	0.2	0.97
$G_{CSD, 2D} = f(G_{mean, l})$	0.5	0.01	0.98
$G_{Batch} = f(G_{max, l})$	0.19	0.04	0.88
$G_{CSD, 2D} = f(G_{max, l})$	0.11	0.02	0.88
$G_{mean, l} = f(G_{max, l})$	0.24	0.09	0.87
$G_{Batch} = f(G_{rim})$	0.73	0.06	0.97
$G_{max, l} = f(G_{rim})$	4.14	0.67	0.98
$G_{max, l} = f(G_{CSD, 3D})$	2.63	0.84	0.9
$J_{Bacth} = f(J_{CSD, 2D})$	0.85	0.12	0.88
$J_{Batch} = f(J_{CSD, 3D})$	3.47	0.19	0.95
$J_{CSD, 2D} = f(J_{CSD, 3D})$	4.4	1.66	0.94

***Table III-5**: Summary of the linear correlations between the various methods for calculating nucleation and growth rates.*

We obtained nucleation rates by the two methods generally used: the batch method (J_{batch}), referring to an average value estimated by point counting (N_V; Eq. 2), and the CSD method ($J_{CSD,2D}$ and $J_{CSD,3D}$; Eq. 9), linking the intercept and growth rate estimated from the same data. Although the results of these methods are well correlated ($R^2 > 0.88$), strong variations are present (**Figure III-8a** and **b; Table III-5**). Indeed, nucleation rates obtained by the batch method were 50–85% higher than those estimated from the 3D CSD, as observed by *Brugger and Hammer (2010a)*, but quite close to those estimated with from the 2D CSD ($J_{CSD,2D} = (0.94 \pm 0.13) \times J_{batch}$ for the series cooled at 1 and 3 °C/h). The greatest variations occurred near the liquidus (heterogeneous nucleation, few crystals), and for the series cooled at 9°C/h ($J_{CSD,2D} = (1.43 \pm 0.52) \times J_{batch}$), in which the microtextures were more variable. Uncertainties on J_{batch} result mainly from the impact of the image resolution of the smallest analyzable crystals (<5 µm) and from coarsening and agglomeration processes. In contrast, J_{CSD} depends mainly on the slope (G) and intercept of the log-linear part of the CSD, parameters that are strongly dependent on the selected bin width (***Supplementary file III-4***; *Higgins 2000*) and on the interpretation of the CSD shape. $J_{CSD,2D}$ values were 56–87% higher than $J_{CSD,3D}$ values, which

account for sectioning effects. Because J and G are directly linked, a relative difference of 10–50% on the slope (***Supplementary file III-4)*** will certainly impact the determined value of J.

We similarly employed various common methods to determine growth rates, including the batch (G_{batch}), CSD (G_{CSD}), and l_{max} ($G_{max,l}$) methods, as well as additional methods focused exclusively on the overgrowths around seed crystals (G_{rim}; *Shea and Hammer 2013*) and on the average size of the entire segmented plagioclase population segmented ($G_{mean,l}$). Growth rates obtained using these methods differed by 1–2 orders of magnitude (**Table III-4** and ***Supplementary file III-5***).

G_{batch}, $G_{CSD,2D}$, and $G_{mean,l}$ values were very well correlated ($R^2 > 0.95$; **Table III-5**), returning values of the same order of magnitude (less than factor of 2 difference; **Table III-4**). The differences are directly linked to the various estimations of the characteristic sizes (S_N, l_c, and $l_{mean;}$ **Figure III-8e**): $l_c = 0.61 \times S_N$, $R^2 = 0.95$; $l_{mean} = 1.31 \times S_N$, $R^2 = 0.99$. In the batch method, S_N depends only on crystal counts, with no consideration of axis and size variability among crystals, whereas l_{mean} corresponds to the average length of the l axis across the entire crystal population. Distinctly, l_c is directly obtained by linear regression of the CSDs and is subject to uncertainties, such as the number of crystals per size range, the interpreted boundaries of the steepest part of the curve, and the selected bin width.

$G_{max,l}$ (based on the 10 largest crystals) and $G_{CSD,3D}$ (measured on the 3D major axis L) gave the fasted growth rates. $G_{max,l}$, corresponding to the first crystals nucleated, was 2–15 times higher than the mean values estimated using $G_{batch}/G_{mean,1}$ or $G_{CSD,\ 2D}$, consistent with estimates of *Pupier et al. (2008)* at similar cooling rates. Because of the presence of seeds in the cores of some of the largest crystals, $G_{max,l}$ tends to overestimate the growth rate. Accordingly, considering only the overgrowths (G_{rim}) returned values closer to those estimated from G_{batch} and $G_{mean,l}$: G_{rim} values were 1.6 ± 0.32 and 1.3 ± 0.25 times higher than G_{batch} and $G_{mean,l}$, respectively.

Because G_{mean} and G_{CSD} are both based on the entire segmented crystal population, they probably give a better estimation of the mean growth rate. As for the l_{mean} method, the CSD method is the most time consuming, but can link the nucleation/growth parameters with the experimental conditions to provide additional qualitative information such as the type of nucleation and the temporal evolution of crystal abundance per size range. Because of the size- and axis-dependence of growth rates, a combination of the CSD method ($G_{CSD,2D}$ and $G_{CSD,3D}$, providing mean G values along l and L, respectively) with the l_{max} method (providing a maximum growth rate) would constrain the possible range of growth rates. Importantly, *Brugger and Hammer (2010b)* and *Cooper and Kent (2014)* noted that order of magnitude of

growth rate variation is directly reflected in determined magmatic timescales. However, these variations appear to result more from the duration of cooling/decompression (a factor of 8 difference between the series cooled at 1 and 9 °C/h) than from the calculation method.

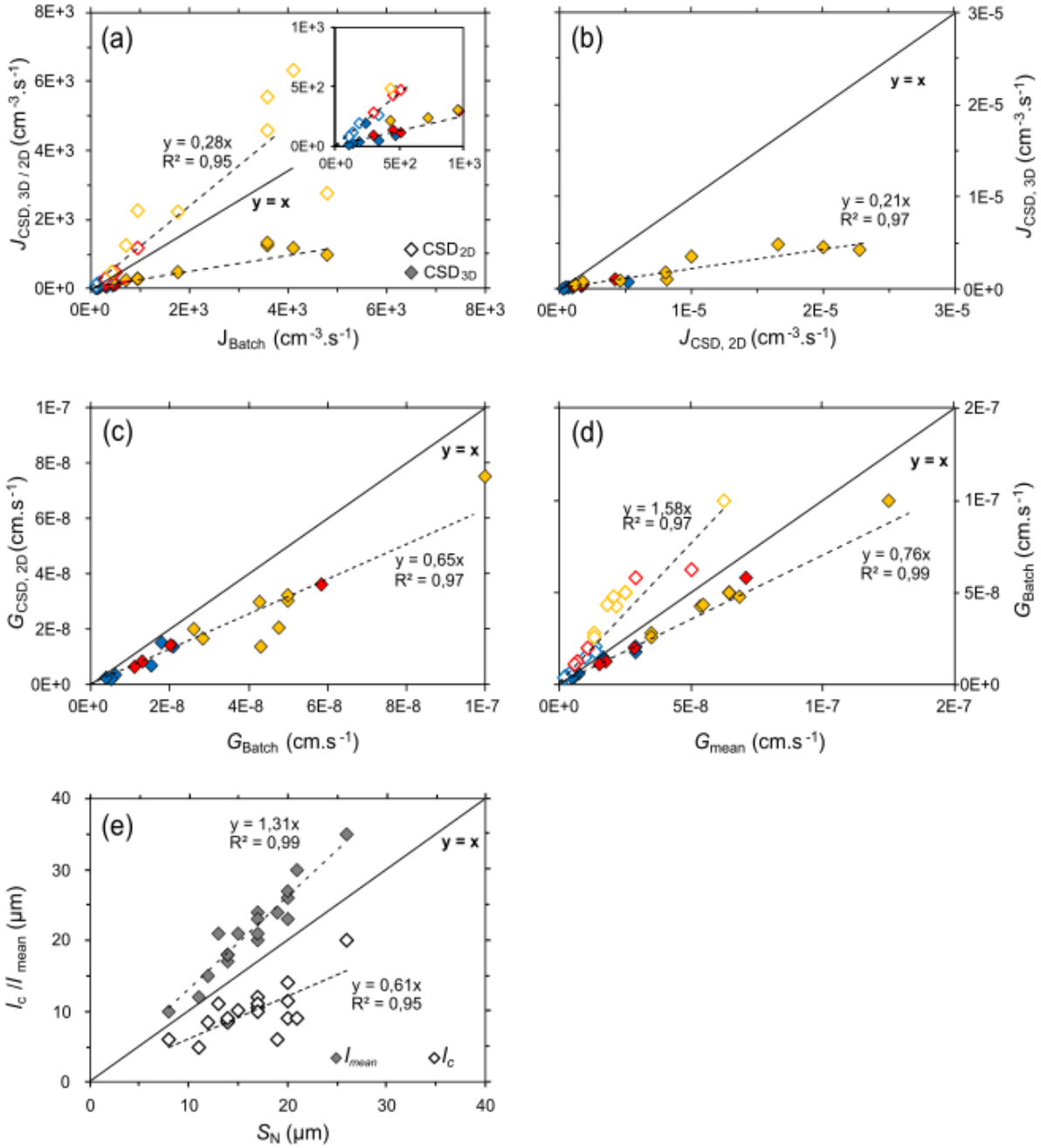

***Figure III-8**: Comparison of the various methods used to calculate (a, b) nucleation (J), (c, d) growth rates (G) and the crystal size (e). (a) $J_{CSD,2D}$ and $J_{CSD,3D}$ vs. J_{batch}. (b) $J_{CSD,3D}$ vs. $J_{CSD,2D}$. (c) $G_{CSD,2D}$ vs. G_{batch}. (d) $G_{mean,l}$ and $G_{mean,w}$ vs. G_{batch}. For each diagram, the x and y scales are the same, and the 1:1 correspondence line y = x is plotted to facilitate comparison.*

Discussion on the theory of CSD for experimental conditions

Despite the similar log-linear CSD plots between batch crystallization models and steady-state open systems (see theory in and ***Supplementary file III-1***[5]), the CSD slope in a non-steady batch system, with continuous crystallization, depends on both nucleation and growth rates (*Cashman and Marsh 1988, 1998*). In the case of a closed (batch) system, CSD theory generally assumes an exponential increase in the nucleation rate at a constant growth rate (independent of time and crystal size). However, as also noted by *Pupier et al. (2008)* and *Ni et al. (2014)*, several observations contradict this assumption. First, the non-permanent increase in the intercept value; stable between 1140 and 1100 °C (and with a significant decrease at 1050 and 1000 °C, when crystallinity reaches around 40–50%) do not support the hypothesis of an exponential increase in nucleation rate during the entire crystallization period. Second, the size-dependent crystal shape and the complex CSD curves observable after 1140 °C, characterized by a more flattened portion for the largest crystals (especially apparent at advanced stages of crystallization), highlight a size and time dependent crystal growth rate.

Moreover, since the crystal population in a closed system is never renewed, according to the theory established by *Marsh (1998, 1998)*, except during the earliest stages of crystallization, the total crystallization time can only be estimated using the growth rates of the largest crystals (G_{max} in our case). As proposed by *Pupier et al. (2008)*, the quantitative determination of nucleation (J) and growth (G) rates via CSD in a closed system (such as experimental samples) should be limited to the early stages of crystallization (between 1175 and 1165 °C in our case). During this period, CSD are effectively marked by an exponential increase total crystallinity remains below 5%, and the behavior of batch and open systems is comparable.

The role of experimental conditions on growth rates

We compared our determined growth rates with available literature data. We selected 20 experimental datasets, compiling >400 growth rate estimates (***Supplementary file III-6***). Selected studies cover a range of experimental parameters, including the type of experiments (static or dynamic, with an additional shear rate), the nature of the initial material (synthetic vs. natural samples), the composition of the starting material (especially SiO_2 and H_2O contents), the crystallization path (initial degree of superheating, cooling/decompression rate, the

[5] : More details in **Chapter II**

inclusion of a final isothermal step), and the method used to calculate G (l_{max}, batch, CSD). Experiments were performed under hydrous or anhydrous conditions, and crystallization was induced by decompression, cooling, or isothermally below the liquidus. The starting compositions range from basalt to rhyodacite; most studies were performed on basaltic compositions, with only a few on more evolved compositions such as andesite and dacite (e.g. *Conte et al. 2006*; *Shea and Hammer 2013*).

The nominal degree of undercooling ($-\Delta T_n$) does not account for the various rates of cooling/decompression and is therefore neither directly comparable with the true ($-\Delta T$) nor the effective degree of undercooling ($-\Delta T_{eff}$, caused by the change of the liquidus temperature due to degassing during decompression), the latter used in some decompression experiments under hydrous conditions (*Hammer and Rutherford 2002*; *Mollard et al. 2012*). We thus analyzed the growth rate variations as a function of the cooling/decompression time ($t_{cooling/decompression}$) or the cooling rate.

In **Figure III-9a**, growth rates calculated using different methods (l_{max}, batch, CSD) are plotted as a function of experimental duration. Our data plot within the range of other *ex situ* experimental data (10^{-11}–10^{-6} cm.s^{-1}) obtained on 2D sections. In all datasets, G decreases with increasing time and -ΔT_n. These results are usually lower than growth rates obtained with *in situ* analyses (10^{-4}–10^{-3} cm.s^{-1}; *Arzilli et al. 2019*; *Le Gall et al. 2021*), in which the beginning of nucleation and the end of growth are better constrained. Except for one set of points (*Mollard et al. 2012*), whose higher values may be due to the method of calculation, the method used does not seem have a large impact. Growth rates appear to be dependent on the cooling and decompression rates. Although it is difficult to directly compare the two, growth rate values (10^{-10}–10^{-5} cm.s^{-1}) obtained in decompression experiments are similar to those obtained from cooling experiments (10^{-9}–10^{-6} cm.s^{-1}), except at very high decompression rates. Recent studies by *Vona and Romano (2013)*, and *Vetere et al. (2021, 2024)* focusing on dynamic isothermal experiments have shown the impact of strain rates on crystallization, with growth rates ranging from 10^{-8} to 10^{-6} cm.s^{-1}. These values, which are from 1 to 2 orders of magnitude higher than those reported in other static studies such as *Orlando et al. (2008)* (10^{-9}–10^{-8} cm.s^{-1}; **Figure III-9a**, ***Supplementary file III-6***) under similar isothermal conditions and comparable growth rate determination methods, can be explained by more efficient transport near the liquid–crystal interface. Our growth rate values, ranging between 10^{-9} and 10^{-7} cm.s^{-1} in cooling experiments, confirm the lowest values obtained under "static" conditions.

Our growth rates (10^{-9}–10^{-7} cm.s^{-1}) are equivalent to those of *Pupier al. (2008*; 10^{-9}–10^{-8} cm.s^{-1}) obtained under similar cooling conditions in a basaltic starting material. Comparison of

rates determined for basalts (*Agostini et al. 2013*; *Moschini et al. 2023*) and dacites (*Hammer and Rutherford 2002*; *Brugger and Hammer 2010a, b*) in hydrous decompression experiments shows that the growth rates obtained for these distinct compositions partly overlap, with a trend towards lower *G* values in dacites (**Figure III-9b**). We note that data from *Shea and Hammer (2013)* for basaltic andesite overlap with results obtained using basaltic compositions, and are two orders of magnitude higher than those obtained using dacitic compositions (10^{-11}–10^{-9} cm.s^{-1}; *Hammer and Rutherford 2002*; *Couch et al. 2003b*). The significantly higher values of *Mollard et al. (2012)*, i.e. 3–5 orders of magnitude higher than those *Hammer and Rutherford (2002)* or *Brugger and Hammer (2010a, b)*, likely result from decompression rates 15 to >2000 times faster than those used by *Brugger and Hammer (2010a, b)*, and perhaps their use of a crystal-free starting material. As mentioned by *Brugger and Hammer (2010a)*, the cooling path strongly controls the growth rate (**Figure III-9c**) and can potentially hide the compositional influence.

Another potential important compositional parameter is H_2O, which substantially lowers melt viscosity. Comparison of our data on an anhydrous basaltic andesite with data from Shea and Hammer (2013) on a similar composition under hydrous conditions (**Figure III-9d**), as well as the few anhydrous data of Conte et al. (2006), demonstrates that plagioclase growth rates are less than an order of magnitude faster in hydrous conditions, perhaps because of the faster diffusion of plagioclase-forming elements in the liquid.

***Figure III-9 (see below)**: Comparison of our plagioclase growth rates with published data. Twenty studies (list provided in **Supplementary file III-5**) using different experimental setups (initial composition, water content, cooling/decompression path, final dwell time, etc.) were selected, comprising >400 growth rates. Abbreviations: DP, decompression experiments; CR, cooling rate experiments; ISO, isothermal experiments; B, basalt; BA, basaltic andesite; A, andesite; D: Dacite; T: Tonalite. (a) Global comparison between our results and literature experimental data without discrimination of the crystallization path. Isothermal experiments are separated in two groups, corresponding to "static" experiments (without shear rate), and "dynamic" experiments with a shear rate. The gray field corresponds to natural samples (Cashman 1993). The data are generally grouped with some scatter. (b) Hydrous decompression experiments performed using starting compositions ranging from basalt to dacite, highlighting a decrease of G with increasing SiO_2 content and experimental duration. Open and filled symbols denote results calculated using the batch and l_{max} methods, respectively. (c) Cooling experiments on basalt and basaltic andesite starting compositions as a function of cooling rate. All experiments are anhydrous, except those of Shea and Hammer (2013). Conte et al. (2006) used an instantaneous temperature drop. Our data fill a lack of data for basaltic*

andesite compositions. (d) log(G) vs. cooling time in experiments using intermediate compositions (basaltic andesite, andesite) as starting materials (open symbols, G_{batch}; filled symbols, $G_{max,l}$). The growth rates estimated by Shea and Hammer (2013) in hydrous conditions are slightly higher than ours obtained in anhydrous conditions. Logarithmic scales are used to facilitate comparison and to clarify the diagrams.

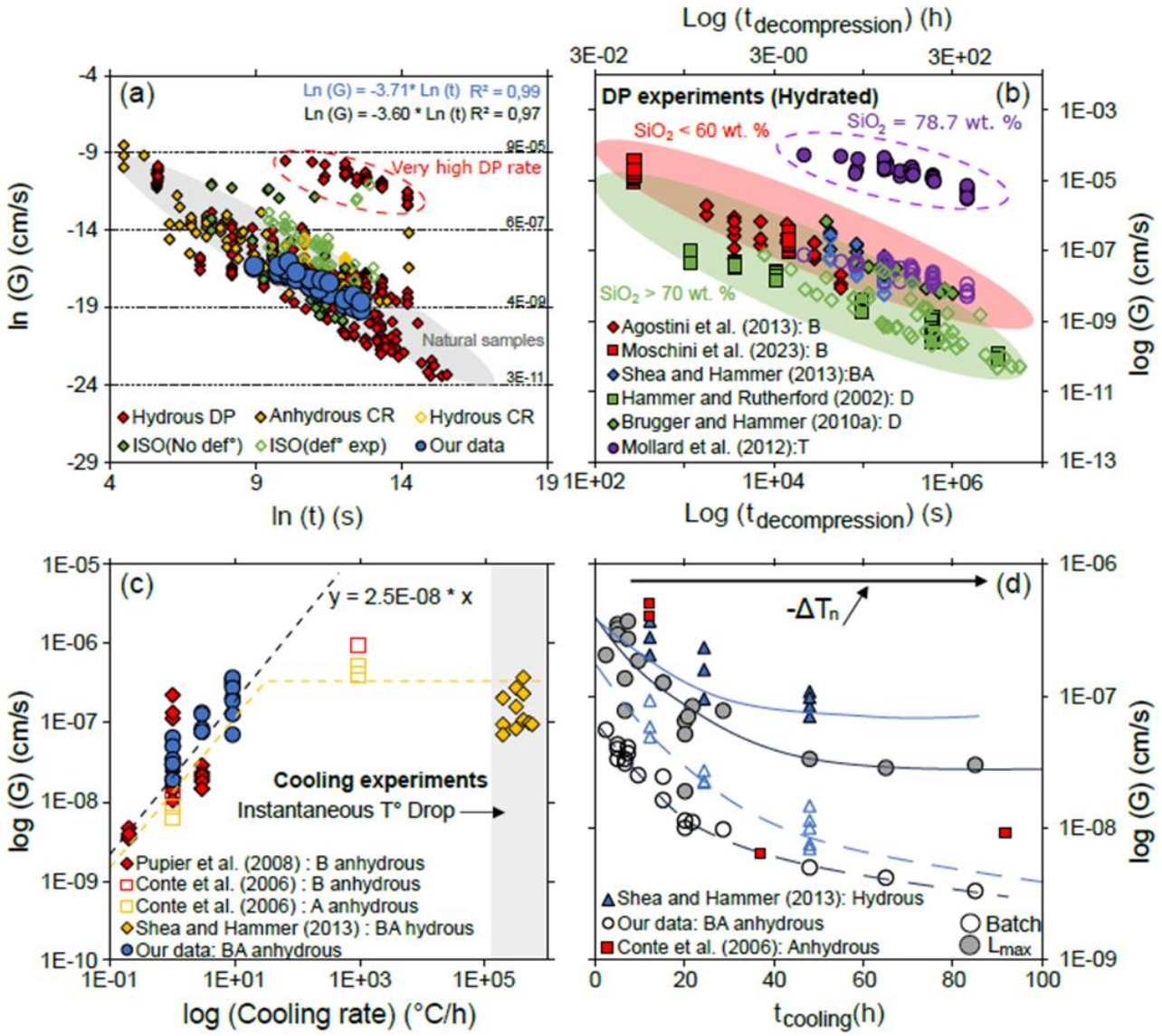

Conclusions

This study had three main objectives: (1) to examine the evolution of crystal size, density, and shape textural parameters during the slow cooling (<10 °C/h) of an anhydrous basaltic andesite; (2) to determine plagioclase nucleation (*J*) and growth rates (*G*) for those experiments; and (3) to compare the various methods of calculating *J* and *G*, with the goal of determining

the most appropriate method for deriving timescales from textural analyses of natural samples. Our results and their implications are as follows:

- During cooling, plagioclase crystal shape (2D aspect ratio) varied significantly, evolving from blocky and equant/elongate to tabular/bladed. Crystal sizes and number densities followed the same overall trend: increasing as cooling progressed down to $-\Delta T_n$ = 80 °C, then decreasing at the most advanced stages of crystallization.
- Crystal sizes and phase proportions were independent of the cooling rate. However, increased cooling rates favor increased crystal number densities and the formation of elongate crystals with skeletal/dendritic habits.
- Nucleation and growth rates similarly increased to a maximum at 1165 °C ($-\Delta T_n$ = 15 °C: 1 and 3 °C/h) or 1140 °C ($-\Delta T_n$ = 40 °C: 9 °C/h), before decreasing at more advanced stages of crystallization.
- J and G increased by an order of magnitude with increasing cooling rate from 1 to 9 °C/h. This increase was correlated with cooling time and was minimal at slower cooling rates (1 and 3 °C/h) where J and G remained nearly constant over time, but became exponential at 9 °C/h.
- Our growth rates (between 2.04×10^{-9} and 4.39×10^{-7} cm.s^{-1}) overlap with those of *Pupier et al. (2008)*, measured at similar cooling conditions in a basaltic composition, and of *Shea and Hammer (2013)*, acquired under instantaneous cooling conditions in a hydrous basaltic andesite.
- Comparison of the different methods to calculate G (l_{max}, batch, l_{mean} $G_{CSD,2D}$, $G_{CSD,3D}$) indicates that differences in experimental conditions lead to greater variability than the method of calculation. G_{batch} is the least time-consuming method but provides the least accurate values. In contrast, G_{mean} and G_{CSD} both based on the entire segmented crystal population, give better estimations of the mean growth rate. Although the CSD method requires the selection of certain parameters (e.g., bin width, and shape model), it gives the most accurate average estimations, whether considering 2D or 3D long axes. Because growth rates are size-dependent, coupling this method with the l_{max} method can constrain the full range of possible rates.

Our comparison with other experimental datasets indicated that plagioclase growth rates depend more on the thermal history and initial treatment of the starting material than on the composition of the starting material. This complicates the application of CSDs for the determination of the timescales of magmatic processes such as ascent rate and storage time. Furthermore, as discussed above, except during the earliest stages of crystallization, the various

assumptions underlying the closed-system CSD (as for *Cashman and Marsh 1988*; *Pupier et al. 2008*; and *Brugger and Hammer 2010b*) theory do not appear to hold true. Therefore, the quantitative determination of J and G should be conducted with caution, particularly in the case of experimental samples.

References

Agostini C, Fortunati A, Arzilli F, Landi P, Carroll MR (2013) Kinetics of crystal evolution as a probe to magmatism at Stromboli (Aeolian Archipelago, Italy). Geochimica et Cosmochimica Acta 110:135–151. https://doi.org/10.1016/j.gca.2013.02.027

Armienti P (2008) Decryption of Igneous Rock Textures: Crystal Size Distribution Tools. Reviews in Mineralogy and Geochemistry 69:623–649. https://doi.org/10.2138/rmg.2008.69.16

Armienti P, Pareschi MT, Innocenti F, Pompilio M (1994) Effects of magma storage and ascent on the kinetics of crystal growth: The case of the 1991-93 Mt. Etna eruption. Contributions to Mineralogy and Petrology 115:402–414. https://doi.org/10.1007/BF00320974

Armienti P, Perinelli C, Putirka KD (2013) A New Model to Estimate Deep-level Magma Ascent Rates, with Applications to Mt. Etna (Sicily, Italy). Journal of Petrology 54:795-813. doi:10.1093/petrology/egs085

Arzilli F, Mancini L, Voltolini M, et al. (2015) Near-liquidus growth of feldspar spherulites in trachytic melts: 3D morphologies and implications in crystallization mechanisms. Lithos 216-217, 93-105. https://doi.org/10.1016/j.lithos.2014.12.003

Arzilli F, La Spina G, Burton MR, Polacci M, Le Gall N, Hartley ME, Di Genova D, Cai B, Vo NT, Bamber EC, Nonni S, Atwood R, Llewellin EW, Brooker RA, Mader HM, Lee, P.D. (2019) Magma fragmentation in highly explosive basaltic eruptions induced by rapid crystallization. Nature Geoscience 12:1023–1028. https://doi.org/10.1038/s41561-019-0468-6

Bechon T, Billon M, Namur O, Bolle O, Fugmann P, Foucart H, Devidal J-L, Delmelle N, Vander Auwera J (2022) Petrology of the magmatic system beneath Osorno volcano (Central Southern Volcanic Zone, Chile). Lithos 426–427, 106777. https://doi.org/10.1016/j.lithos.2022.106777

Bennett EN, Lissenberg CJ, Cashman KV (2019) The significance of plagioclase textures in mid-ocean ridge basalt (Gakkel Ridge, Arctic Ocean). Contributions to Mineralogy and

Petrology 174:49. https://doi.org/10.1007/s00410-019-1587-1

Berkebile CA, Dowty E (1982) Nucleation in laboratory charges of basaltic composition. American Mineralogist 67:886-899.

Brugger CR, Hammer JE (2010a) Crystal size distribution analysis of plagioclase in experimentally decompressed hydrous rhyodacite magma. Earth and Planetary Science Letters 300:246–254. https://doi.org/10.1016/j.epsl.2010.09.046

Brugger CR, Hammer JE (2010b) Crystallization Kinetics in Continuous Decompression Experiments: Implications for Interpreting Natural Magma Ascent Processes. Journal of Petrology 51:1941–1965. https://doi.org/10.1093/petrology/egq044

Burkhard DJ (2002) Kinetics of crystallization: example of micro-crystallization in basalt lava. Contributions to Mineralogy and Petrology 142:724–737. https://doi.org/10.1007/s00410-001-0321-x

Burkhard DJ (2005) Nucleation and growth rates of pyroxene, plagioclase, and Fe-Ti oxides in basalt under atmospheric conditions. European Journal of Mineralogy 17:675-685. https://doi.org/10.1127/0935-1221/2005/0017-0675

Cabane H, Laporte D, Provost A (2005) An experimental study of Ostwald ripening of olivine and plagioclase in silicate melts: implications for the growth and size of crystals in magmas. Contributions to Mineralogy and Petrology 150:37–53. https://doi.org/10.1007/s00410-005-0002-2

Cashman KV (1990) Chapter 10. Textural constrains on the kinetics of crystallization of igneous rocks. In: Nicholls, J., Russel, J.K. (Eds.), Modern Methods of Igneous Petrology: Understanding Magmatic Processes. Rev. Mineral 24:259–314. https://doi.org/10.1515/9781501508769-014

Cashman KV (1993) Relationship between plagioclase crystallization and cooling rate in basaltic melts. Contributions to Mineralogy and Petrology 113:126–142. https://doi.org/10.1007/BF00320836

Cashman KV, Marsh BD (1988) Crystal size distribution (CSD) in rocks and the kinetics and dynamics of crystallization II: Makaopuhi lava lake. Contributions to Mineralogy and Petrology 99:292–305. https://doi.org/10.1007/BF00375363

Cassidy M, Castro JM, Helo C, Troll VR, Deegan FM, Muir D, Neave DA, Mueller SP (2016) Volatile dilution during magma injections and implications for volcano explosivity. Geology 44:1027–1030. https://doi.org/10.1130/G38411.1

Conte AM, Perinelli C, Trigila R (2006) Cooling kinetics experiments on different Stromboli lavas: Effects on crystal morphologies and phases composition. Journal of Volcanology

and Geothermal Research 155:179–200. https://doi.org/10.1016/j.jvolgeores.2006.03.025

Cooper K, Kent A (2014) Rapid remobilization of magmatic crystals kept in cold storage. Nature 506:480–483. https://doi.org/10.1038/nature12991

Corrigan GM (1982a) Supercooling and the crystallization of plagioclase, olivine, and clinopyroxene from basaltic magmas. Mineralogical Magazine 46:31-42. https://doi.org/10.1180/minmag.1982.046.338.06

Corrigan GM (1982b) The crystal morphology of plagioclase feldspar produced during isothermal supercooling and constant rate cooling experiments. Mineralogical Magazine 46:433-439. https://doi.org/10.1180/minmag.1982.046.341.04

Costa F, Dohmen R, Chakraborty S (2008) Time scales of magmatic processes from modeling the zoning patterns of crystals. Reviews in Mineralogy and Geochemistry 69:545–594. https://doi.org/10.2138/rmg.2008.69.14

Couch S, Harford CL, Sparks RSJ, Carroll MR (2003a) Experimental Constraints on the Conditions of Formation of Highly Calcic Plagioclase Microlites at the Soufrière Hills Volcano, Montserrat. Journal of Petrology 44:1455-1475. https://doi.org/10.1093/petrology/44.8.1455

Couch S, Sparks RSJ, Carroll MR (2003b) The Kinetics of Degassing-Induced Crystallization at Soufrière Hills Volcano, Montserrat. Journal of Petrology 44:1477-1502. https://doi.org/10.1093/petrology/44.8.1477

Delesse MA (1847) Procédé mécanique pour déterminer la composition des roches. Comptes rendus de l'Académie des Sciences (Paris), 25:544–545.

Del Gaudio P, Mollo S, Ventura G, Iezzi G, Taddeucci J, Cavallo A (2010) Cooling rate-induced differentiation in anhydrous and hydrous basalts at 500 MPa: Implications for the storage and transport of magmas in dikes. Chemical Geology 270:164–178. https://doi.org/10.1016/j.chemgeo.2009.11.014

Eberl DD, Kile DE, Drits VA (2002) On geological interpretations of crystal size distributions: Constant vs. proportionate growth. American Mineralogist 87:1235–1241. https://doi.org/10.2138/am-2002-8-923

Faure F, Trolliard G, Nicollet C, Montel JM (2003) A developmental model of olivine morphology as a function of the cooling rate and the degree of undercooling. Contributions to Mineralogy and Petrology 145:251–263. https://doi.org/10.1007/s00410-003-0449-y

Faure F, Tissandier L (2014) Contrasted Liquid Lines of Descent Revealed by Olivine-hosted

Melt Inclusions and the External Magma. Journal of Petrology 55:1779-1798. https://doi.org/10.1093/petrology/egu041

Fokin VM, Zanotto ED, Yuritsyn NS, Schmelzer JWP (2006) Homogeneous crystal nucleation in silicate glasses: A 40 years perspective. Journal of Non-Crystalline Solids 352:2681-2714. https://doi.org/10.1016/j.jnoncrysol.2006.02.074

Gibb FGF (1974) Supercooling and the crystallization of plagioclase from a basaltic magma. Mineralogical Magazine 39:641–653. https://doi.org/10.1180/minmag.1974.039.306.02

Giordano D, Russell JK, Dingwell DB (2008) Viscosity of magmatic liquids: a model. Earth and Planetary Science Letters 271:123-134. https://doi.org/10.1016/j.epsl.2008.03.038

Giuliani L, Iezzi G, Vetere F, Behrens H, Mollo S, Cauti F, Ventura G, Scarlato P (2020) Evolution of textures, crystal size distributions and growth rates of plagioclase, clinopyroxene and spinel crystallized at variable cooling rates from a mid-ocean ridge basaltic melt. Earth-Science Reviews 204:103165. https://doi.org/10.1016/j.earscirev.2020.103165

Griffiths, TA, Habler G, Ageeva O, Sutter C, Ferrière L, Abart R (2023) The Origin of Lattice Rotation during Dendritic Crystallization of Clinopyroxene. Journal of Petrology 64:1-19. https://doi.org/10.1093/petrology/egac125

Grove TL (1978) Cooling histories of Luna 24 very low Ti (VLT) Ferrobasalts: An experimental study. Lunar and Planetary Science Conference 9th, 565-584.

Grove TL (1981) Use of FePt Alloys to Eliminate the Iron Loss Problem in 1 Atmosphere Gas Mixing Experiments: Theoretical and Practical Considerations. Contributions to Mineralogy and Petrology 78: 298-304. https://doi.org/10.1007/BF00398924

Grove TL, Baker MB (1984) Phase equilibrium controls on the tholeiitic versus calc-alkaline differentiation trends. Journal of Geophysical Research 89:3253–3274. https://doi.org/10.1029/JB089iB05p03253

Gualda GAR, Ghiorso MS, Lemons RV, Carley TL (2012) Rhyolite-MELTS: a Modified Calibration of MELTS Optimized for Silica-rich, Fluid-bearing Magmatic Systems. Journal of Petrology 53:875–890. https://doi.org/10.1093/petrology/egr080

Hammer JE (2008) experimental Studies of the Kinetics and energetics of Magma Crystallization. Reviews in Mineralogy and Geochemistry 69:9-59. https://doi.org/10.2138/rmg.2008.69.2

Hammer JE, Cashman KV, Hoblitt RP, Newman S (1999) Degassing and microlite crystallization during pre-climactic events of the 1991 eruption of Mt. Pinatubo,

Philippines. Bulletin of Volcanology 60:355–380. https://doi.org/10.1007/s004450050238

Hammer JE, Rutherford MJ (2002) An experimental study of the kinetics of decompression-induced crystallization in silicic melt. Journal of Geophysical Research 107 (B1). https://doi.org/10.1029/2001JB000281

Higgins MD (2000) Measurement of crystal size distributions. American Mineralogist 85:1105–1116. https://doi.org/10.2138/am-2000-8-901

Honour VC, Holness MB, Charlier B, Piazolo SC, Namur O, Prosa TJ, Martin I, Helz RT, Maclennan J, Jean MM (2019) Compositional boundary layers trigger liquid unmixing in a basaltic crystal mush. Nature Communications 10:4821. https://doi.org/10.1038/s41467-019-12694-5

Humphreys M, Menand T, Blundy JD, Klimm K (2008) Magma ascent rates in explosive eruptions: Constraints from H2O diffusion in melt inclusions. Earth and Planetary Science Letters 270:25-40. https://doi.org/10.1016/j.epsl.2008.02.041

Iezzi G, Mollo S, Ventura G, Cavallo A, Romano C (2008) Experimental solidification of anhydrous latitic and trachytic melts at different cooling rates: The role of nucleation kinetics. Chemical Geology 253:91–101. https://doi.org/10.1016/j.chemgeo.2008.04.008

Kent AJR, Darr C, Koleszar AM, Salisbury MJ, Cooper KM (2010) Preferential eruption of andesitic magmas through recharge filtering. Nature Geoscience 3:631–636. https://doi.org/10.1038/ngeo924

Kirkpatrick RJ (1975) Crystal Growth from the Melt: A Review. American Mineralogist 60:798-814.

Kirkpatrick RJ (1977) Nucleation and growth of plagioclase, Makaopuhi and Alae lava lakes, Kilauea Volcano, Hawaii. Geological Society America Bulletin 88:78-84. https://doi.org/10.1130/0016-7606(1977)88<78:NAGOPM>2.0.CO;2

Kirkpatrick RJ (1981) Kinetics of Crystallization of Igneous Rocks. Reviews in Mineralogy and Geochemistry 8:321-398.

Kohut E, Nielsen RL (2004) Melt inclusion formation mechanisms and compositional effects in high-An feldspar and high-Fo olivine in anhydrous mafic silicate liquids. Contributions to Mineralogy and Petrology 147:684–704. https://doi.org/10.1007/s00410-004-0576-0

Kyle DE, Eberl DD (2003) On the origin of size-dependent and size-independent crystal growth: Influence of advection and diffusion. American Mineralogist 88:1514-1521.

https://doi.org/10.2138/am-2003-1014

Le Gall N, Arzilli F, La Spina G, Polacci M, Cai B, Hartley ME, Vo NT, Atwood RC, Di Genova D, Nonni S, Llewellin EW, Burton MR, Lee PD (2021) In situ quantification of crystallisation kinetics of plagioclase and clinopyroxene in basaltic magma: Implications for lava flow. Earth and Planetary Science Letters 568:117016. https://doi.org/10.1016/j.epsl.2021.117016

Lesher CE, Cashman KV, Mayfield JD (1999) Kinetic controls on crystallization of tertiary North Atlantic basalt and implications for the emplacement and cooling history of lava at site 989, Southeast Greenland rifted margin. Proceedings of the Ocean Drilling Program 163:138-145.

Lofgren GE (1974) An experimental study of plagioclase crystal morphology: Isothermal crystallization. American Journal of Science 274:243-273.

Lofgren, G.E. (1983) Effect of Heterogeneous Nucleation on Basaltic Textures: A Dynamic Crystallization Study. Journal of Petrology 24, 229–255. https://doi.org/10.1093/petrology/24.3.229

Mangler MF, Humphreys MCS, Wadsworth FB, Iveson AA, Higgins MD (2022) Variation of plagioclase shape with size in intermediate magmas: a window into incipient plagioclase crystallisation. Contributions to Mineralogy and Petrology 177:64. https://doi.org/10.1007/s00410-022-01922-9

Mangler MF, Humphreys MCS, Geifman E, Iveson AA, Wadsworth FB, Brooker RA, Lindoo A, Hammond K (2023) Melt Diffusion-Moderated Crystal Growth and its Effect on Euhedral Crystal Shapes. Journal of Petrology 64:egad054. https://doi.org/10.1093/petrology/egad054

Marsh, BD (1988) Crystal size distribution (CSD) in rocks and the kinetics and dynamics of crystallization. I. Theory. Journal of Petrology 99:277-291.

Marsh BD (1998) On the Interpretation of Crystal Size Distributions in Magmatic Systems. Journal of Petrology 39:553-599. https://doi.org/10.1093/petroj/39.4.553

Mollard E, Martel C, Bourdier JL (2012) Decompression-induced Crystallization in Hydrated Silica-rich Melts: Empirical models of Experimental Plagioclase Nucleation and Growth Kinetics. Journal of Petrology 53:1743-1766. https://doi.org/10.1093/petrology/egs031

Mollo S, Misiti V, Scarlato P, Soligo M (2012) The role of cooling rate in the origin of high temperature phases at the chilled margin of magmatic intrusions. Chemical Geology 322-323:28-46. https://doi.org/10.1016/j.chemgeo.2012.05.029

Morgado E, Parada MA, Contreras C, Castruccio A, Gutiérrez F, McGee LE (2015) Contrasting records from mantle to surface of Holocene lavas of two nearby arc volcanic complexes: Caburgua-Huelemolle Small Eruptive Centers and Villarrica Volcano, Southern Chile. Journal of Volcanology and Geothermal Research 306:1-16. https://doi.org/10.1016/j.jvolgeores.2015.09.023

Morse SA (2013) Experimental Equilibrium Tested by Plagioclase Loop Widths. Journal of Petrology 54:1793–1813. https://doi.org/10.1093/petrology/egt031

Moschini P, Mollo S, Pontesilli A, Nazzari M, Petrone CM, Fanara S, Vona A, Gaeta M, Romano C, Scarlato P (2023) A review of plagioclase growth rate and compositional evolution in mafic alkaline magmas: Guidelines for thermometry, hygrometry, and timescales of magma dynamics at Stromboli and Mt. Etna. Earth-Science Reviews 240:104399. https://doi.org/10.1016/j.earscirev.2023.104399

Nabelek PI, Taylor LA, Lofgren GE (1978) Nucleation and growth of plagioclase and the development of textures in a high-alumina basaltic melt. Lunar Planetary Science Conference 9th, 725-741.

Ni H, Keppler H, Walte N, Schiavi F, Chen Y, Masotta M, Li Z (2014) In situ observation of crystal growth in a basalt melt and the development of crystal size distribution in igneous rocks. Contributions to Mineralogy and Petrology 167:1003. https://doi.org/10.1007/s00410-014-1003-9

Orlando AD, Armienti P, Borrini D. (2008) Experimental determination of plagioclase and clinopyroxene crystal growth rates in an anhydrous trachybasalt from Mt Etna (Italy). European Journal of Mineralogy 20:653–664. https://doi.org/10.1127/0935-1221/2008/0020-1841

Pichavant M, Costa F, Burgisser A, Scaillet B, Martel C, Poussineau S (2007) Equilibration Scales in Silicic to Intermediate Magmas Implications for Experimental Studies. Journal of Petrology 48:1955–1972. https://doi.org/10.1093/petrology/egm045

Pupier E, Duchene S, Toplis MJ (2008) Experimental quantification of plagioclase crystal size distribution during cooling of a basaltic liquid. Contributions to Mineralogy and Petrology 155:555–570. https://doi.org/10.1007/s00410-007-0258-9

Reubi O, Blundy J (2009) A dearth of intermediate melts at subduction zone volcanoes and the petrogenesis of arc andesites. Nature 461:1269–1273. https://doi.org/10.1038/nature08510

Rusiecka MK, Bilodeau M, Baker DR (2020) Quantification of nucleation delay in magmatic systems: experimental and theoretical approach. Contributions to Mineralogy and

Petrology 175:47. https://doi.org/10.1007/s00410-020-01682-4

Rutherford MJ (2008) Magma ascent rates. Reviews in Mineralogy and Geochemistry 69:241-271. https://doi.org/10.2138/rmg.2008.69.7

Sato H (1995) Textural difference between pahoehoe and aa lavas of Izu-Oshima volcano, Japan - an experimental study on population density of plagioclase. Journal of Volcanology and Geothermal Research 66:101-113. https://doi.org/10.1016/0377-0273(94)00055-L

Schiavi F, Walte N, Keppler H (2009) First in situ observation of crystallization processes in a basaltic-andesitic melt with the moissanite cell. Geology 37:963–966. https://doi.org/10.1130/G30087A.1

Shea T, Hammer JE (2013) Kinetics of cooling- and decompression-induced crystallization in hydrous mafic-intermediate magmas. Journal of Volcanology and Geothermal Research 260:127–145. https://doi.org/10.1016/j.jvolgeores.2013.04.018

Špillar V, Dolejš D (2014) Kinetic model of nucleation and growth in silicate melts: implications for igneous textures and their quantitative description. Geochimica et Cosmochimica Acta 131:164–183. https://doi.org/10.1016/j.gca.2014.01.022

Špillar V, Dolejš D (2015) Heterogeneous nucleation as the predominant mode of crystallization in natural magmas: numerical model and implications for crystal–melt interaction. Contributions to Mineralogy and Petrology 169:4. https://doi.org/10.1007/s00410-014-1103-6

Sunagawa I (1977) Natural crystallization. Journal of Crystal Growth 45:3-12. https://doi.org/10.1016/0022-0248(77)90197-X

Sunagawa I (1981) Characteristics of crystal growth in nature as seen from the morphology of mineral crystals. Bulletin de Mineralogy 104:2-3. https://doi.org/10.3406/bulmi.1981.7438

Toplis MJ, Carroll MR (1995) An Experimental Study of the Influence of Oxygen Fugacity on Fe-Ti Oxide Stability, Phase Relations, and Mineral-Melt Equilibria in Ferro-Basaltic Systems. Journal of Petrology 36:1137–1170. https://doi.org/10.1093/petrology/36.5.1137

Vander Auwera J, Namur O, Dutrieux A, Wilkinson CM, Ganerod M, Coumont V, Bolle O (2019) Mantle Melting and Magmatic Processes Under La Picada Stratovolcano (CSVZ, Chile). 60:907-944. https://doi.org/10.1093/petrology/egz020

Vetere F, Iezzi G, Behrens H, Holtz F, Ventura G, Misiti V, Cavallo A, Mollo S, Dietrich M (2015) Glass forming ability and crystallisation behaviour of sub-alkaline silicate melts.

Earth-Science Reviews 150:25–44. https://doi.org/10.1016/j.earscirev.2015.07.001

Vetere F, Petrelli M, Perugini D, Haselbach S, Morgavi D, Pisello A, Iezzi G, Holtz F (2021) Rheological evolution of eruptible Basaltic-Andesite Magmas under dynamic conditions: The importance of plagioclase growth rates. Journal of Volcanology and Geothermal Research 420:107411. https://doi.org/10.1016/j.jvolgeores.2021.107411

Vetere F, Merseburger S, Pisello A, Perugini D, Viti C, Petrelli M, Musu A, Almeev R, Caricchi L, Iezzi G, Cassetta M, Holtz F (2024) The role of deformation on the early crystallization and rheology of basaltic liquids. Earth and Planetary Science Letters 644: 118934. https://doi.org/10.1016/j.epsl.2024.118934

Vona A, Romano C (2013) The effects of undercooling and deformation rates on the crystallization kinetics of Stromboli and Etna basalts. Contributions to Mineralogy and Petrology 166:491-509. https///doi.org/10.1007/s00410-013-0887-0

Walker D, Powell MA, Lofgren GE, Hays JF (1978) Dynamic crystallization of a eucrite basalt. Proc. Lunar Planetary Science Conference 9th, 1369-1391.

Watson EB (1996) Surface enrichment and trace-element uptake during crystal growth. Geochimica et Cosmochimica Acta 60:5013-5020. https://doi.org/10.1016/S0016-7037(96)00299-2

Watkins JM, DePaolo DJ, Huber C, Ryerson FJ (2009) Liquid composition-dependence of calcium isotope fractionation during diffusion in molten silicates. *Geochimica et Cosmochimica Acta* 73(24):7341–7359. https://doi.org/10.1016/j.gca.2009.09.004.

Watson EB, Liang Y (1995) A simple model for sector zoning in slowly grown crystals: Implications for growth rate and lattice diffusion, with emphasis on accessory minerals in crustal rocks. American Mineralogist 80:1179-1187. https://doi.org/10.2138/am-1995-11-1209

Welsch B, Faure F, First EC (2023) Reappraising Crystallization Kinetics with Overgrowth Chronometry: an in Situ Study of Olivine Growth Velocities. Journal of Petrology 64:egad055. https://doi.org/10.1093/petrology/egad055

Zieg MJ, Marsh BD (2002) Crystal Size Distributions and Scaling Laws in the Quantification of Igneous Textures. Journal of Petrology 43:85–101. https://doi.org/10.1093/petrology/43.1.85

Zieg MJ, Lofgren GE (2006) An experimental investigation of texture evolution during continuous cooling. Journal of Volcanology and Geothermal Research 154:74–88. https://doi.org/10.1016/j.jvolgeores.2005.09.020

Zingg T (1935) Beitrag zur schotteranalyse.Schweiz. Mineral.Petrogr. Mitt. 15:39–140.

Chapter IV

Dynamics of plagioclase textural evolution and the impact of thermal history on nucleation

Submitted in *Contribution to mineralogy and Petrology* (*CMP*)[6]

In revision process since the 12th of December

[6] In this Chapter, the mentions **Fig. IV-S…** refer to BSE images provided in the supplementary files

Abstract

The solidification history of silicate melts strongly controls melt composition and the textures and compositions of crystalline phases. In particular, increasing supersaturation markedly affects crystal nucleation and growth dynamics. Here, we investigate how different crystallization paths influence plagioclase nucleation and crystal habit. Three sets of solidification experiments were performed at atmospheric pressure using a crystal-poor anhydrous andesitic starting material containing plagioclase fragments: (1) isothermal experiments across super- and sub-liquidus conditions, (2) continuous cooling from super-liquidus conditions, and (3) cooling runs held at final temperature. To evaluate the effect of initial superheating, we repeated the isothermal and continuous cooling experiments with a crystal-free melt pre-heated to 1450 °C from a higher initial temperature. Isothermal runs produced numerous small, homogeneous crystals, reflecting spontaneous nucleation. Continuous cooling promoted both growth and nucleation, yielding euhedral to dendritic plagioclase habits with increasing cooling rate. Greater initial superheating or nucleation suppression led to fewer but larger dendritic crystals, similar to those in the fastest cooled seeded runs. These results demonstrate the strong control of thermal pre-treatment on crystal habit and clarify the relative roles of homogeneous and heterogeneous nucleation. Superheating suppresses nucleation by reducing sites for heterogeneous crystallization, favoring growth-dominated textures with limited morphological variability. Although sample edges and Pt wire promote early crystallization, most nucleation occurs on heterogeneities such as gas bubbles, seeds, or impurities, suggesting that homogeneous nucleation may be indistinguishable from heterogeneous nucleation on nano- to micrometric heterogeneities.

Keywords: plagioclase, cooling rate, isothermal, superheating, nucleation, heterogeneous nucleation

Introduction

The progressive crystallization of a silicate melt to form a fully solidified rock is controlled by thermodynamic disequilibrium, characterized by the degrees of supersaturation and undercooling ($-\Delta T = T_{\mathrm{liq}} - T$; with T_{liq} corresponding to the liquidus temperature). Crystallization involves both nucleation (controlled by supersaturation and undercooling) and growth (controlled by diffusion in the liquid and the rate of atomic attachment at the crystal surface). Of these, nucleation plays a primary role in controlling the final microtexture, including the crystal number, size, and habit (*Swanson 1977*; *Berkebile and Dowty 1982*; *Lofgren 1983*; *Fokin et al. 1999*; *Auxerre et al. 2022*). Theoretical insights into nucleation processes have been developed through classical nucleation theory (*CNT*; *Volmer and Weber 1926*; *Becker and Doring 1935*). According to *CNT*, nucleation invoves the continuous appearance and disappearance of clusters of atoms (embryo) due to diffusive fluctuations in the melt below the liquidus temperature. An embryo becomes a stable nucleus only if its radius r exceeds the critical radius r^* (m), beyond which the volumetric bulk free energy gain (ΔG_V) from the phase change overcomes the interfacial energy cost (σ; J.m^{-2}) associated with the crystal–melt boundary. The thermodynamic barrier (ΔG^*) that must be overcome to produce a macroscopic grain ($r > r^*$) is expressed as:

$$-\Delta G^* = \left(\frac{4}{3}\right)\pi(r^*)^3\Delta G_{\mathrm{V}} + 4\pi(r^*)^2\sigma \quad (1)$$

The steady state nucleation rate for the formation of spherical critical nuclei (J, m^{-3} s^{-1}) as a function of the temperature (T, in K) is expressed as:

$$J = J_0 \exp\left(\frac{-\Delta G^* + \Delta G_{\mathrm{D}}}{k_{\mathrm{B}}T}\right) \quad (2)$$

with J_0 the pre-exponential term, k_{B} the Boltzmann constant, and ΔG_{D} the kinetic barrier to the attachment of atoms to a cluster.

Because ΔG^* decreases with increasing undercooling, the critical nucleus size decreases as temperature decreases, increasing the nucleation rate. However, nucleation is not instantaneous, and a nucleation delay is commonly observed (*Kashchiev 1969*). Although CNT and its alternatives (*Schmelzer et al. 2019a, b*) reliably describe the behaviour of chemically simple Li- and Na-metasilicate melts (with congruent melting points; *Lasaga 1998*; *Fokin et al.*

2006), it does not accurately account for observations in natural multicomponent systems such as magmas (*Rusiecka et al. 2020*), especially in dynamic regimes involving temperature variations.

Accordingly, there remain many open questions concerning the influence on nucleation of factors such as thermal history (e.g., cooling rate, initial degree of superheating, final dwell time), liquid composition (with the critical cooling rate - defined as that required to produce a glass, i.e. cooling to the glass transition temperature over timescales shorter than the nucleation delay - increasing by more than three orders of magnitude, from 0.0167 °C/min in rhyolitic to 30 °C/min in basaltic compositions; *Vetere et al. 2013*), and the nature of nucleation (heterogeneous vs. homogeneous).

The simplest form of *CNT* concerns homogenous nucleation, which assumes an equal probability of nucleation throughout the liquid (*James 1974*; *Kirkpatrick 1976, 1977*). In contrast, heterogeneous nucleation occurs on substrates such as bubbles, container walls, or pre-existing crystals (*Davis and Ihinger 1998*; *Berkebile and Dowty 1982*; *Bonechi 2020*). However, the effects of the nature of the substrate and liquid composition on crystallization rate are only partly understood. The thermal history of a melt before crystallization can be important, with a high degree of superheating resulting in the dissolution of potential sites of heterogeneous nucleation and an increase in the degree of undercooling required to form stable nuclei (*Donaldson 1979*; *Berkebile and Dowty 1982*; *Vetere et al. 2013*). Nonetheless, the overall impact of the degree of superheating on the final rock texture remains debated. For example, *Tsuchiyama (1983)*, *Mollo et al. (2012)*, and *First et al. (2020)* observed that above a certain degree of superheating (either sufficiently high temperature or a sufficient duration above the liquidus), no further additional effect is observed.

The aim of this study is to investigate experimentally the influence of thermal history (isothermal; cooling, both with and without a final dwell time) on the final microstructure (crystallized vs. vitrified) in a natural andesitic composition. Particular attention is placed on characterizing the nucleation process and identifying which parameters most strongly influence it. To shed light on the ongoing debate between heterogeneous vs. homogeneous nucleation, we also evaluate the potential roles of different nucleation sites (e.g., Pt-wires, gas bubbles, pre-existing seeds) in our experimental runs. Plagioclase was chosen as the target phase due to its abundance in both terrestrial (e.g., basaltic to dacitic magmas) and extraterrestrial rocks (e.g., lunar basalts; *O'Hara et al. 1970*). Moreover, because plagioclase, due to its more complex crystallographic network, is more difficult to nucleate than pyroxene or olivine (*Fenn 1977*;

Donaldson 1979; *Lofgren 1983*), and its habit is particularly sensitive to cooling rate, melt composition, and superheating conditions (*Bennett et al. 2019*), this phase is an ideal probe for testing nucleation dynamics under controlled experimental conditions.

Methods

Starting materials and experimental methodology

Two starting materials were used: OS36 and OS36* (**Figure IV-1a**). OS36 is a finely ground powder (weighted mean grain diameter of 16 µm; maximum size = 90 µm) of a crystal-poor basaltic-andesite (analysed by *Bechon et al. 2022*; and used by *Billon et al. 2025*), and OS36* was obtained by heating a few grams of OS36 at 1450 °C for two hours in a muffle furnace to obtain a crystal-free glass (**Fig. IV-*S1c***). This glass was then ground into powder using an agate mortar and pestle. XRF analyses of the two starting materials showed a relative difference of only 1 to 7% for most elements (***Supplementary file IV-2***), except for $FeO_{(t)}$, which showed a relative difference of 15% (due to FeO contamination introduced during the 1450 °C heating of OS36* in a platinum crucible that may have retained residual iron from previous melting experiments). Surviving plagioclase fragments in seed-bearing runs had sizes ranging from 6 to 50 µm, with an average of ~16 µm (**Fig. IV-*S1a and b***).

For each experiment, a ~50 mg powder pellet was placed on a 0.2-mm-diameter Pt wire loop previously equilibrated for 24 hours at the final target temperature and oxygen fugacity, using the same sample composition, to minimize iron loss during the experiment (*Grove 1982*). Iron-saturated Pt loops were then mounted at the extremity of a ceramic rod positioned in the hot spot of a CARBOLITE GERO vertical furnace at University of Liege (Belgium). A subset of experiments were performed with the same methodology using a Nabertherm vertical furnace at KU Leuven (Belgium).

Following the approach of *Faure and Tissandier (2014)*, we refer to the nominal degree of undercooling ($-\Delta T_n$), defined as the difference between the plagioclase saturation temperature in the starting material (T_{sat}, marking the nucleation of new crystals), and the quench temperature (T_f). The theoretical saturation temperature of 1175 °C measured by *Billon et al. (2025)* using isothermal experiments, agrees with that estimated using Rhyolite-MELTS v. 1.2.0 (1170 – 1175 °C; *Gualda et al. 2012*). However, experimental conditions such as superheating, decompression, or cooling rate can shift the liquidus position (ΔT_{th}; **Table IV-1**) and delay nucleation (*Lofgren 1983*; *Conte et al. 2006*; *Iezzi et al. 2008*; *Vetere et al. 2013*).

Therefore, when necessary, the theoretical saturation temperature was adjusted from the theoretical degree of superheating (ΔT_{th} for T_{sat} = 1175 °C) to the experimental one (ΔT_{exp}; **Table IV-1**), based on the appearance of the first new crystals.

We performed a total of 56 experiments exploring four thermal paths at atmospheric pressure: one isothermal paths and three different cooling paths (**Figure IV-1**). The experiments were conducted under Ni-NiO equilibrium conditions (~97.5% CO_2 and 2.5% CO, adjusted for different temperatures) with a gas flow rate of 0.07 cm/s, and samples were finally quenched in water.

1. In isothermal experiments (using OS36 and OS36* as starting materials; **Figure IV-1a**), samples were held for 24 h at temperatures from 1200 °C to 1150 °C ($T_{sat, Plg}$ = 1175 ± 5 °C; see *Billon et al. 2025*). The goal was to investigate the impact of initial plagioclase fragments on the textures developed at temperatures around the plagioclase saturation temperature.
2. Cooling rates experiments (**Figure IV-1b**), conducted on both OS36 (natural powder with plagioclase fragments) and OS36* (fully glassy material; ***Fig. S1c, d***) to study the impact of initial crystal fragments. Samples were held at 1190 °C ($+\Delta T$ = 15 °C) for 24 hours, then cooled at constant rates of 1, 9, 25, or 125 °C/h. Each run was quenched between 1165 and 1000 °C ($-\Delta T_n$ = 10–175 °C) to investigate progressive crystallization. The results of experiments on OS36 cooled at 1 and 9 °C/h have been presented by *Billon et al. (2025)*.
3. High superheating cooling history (**Figure IV-1c**) performed only on OS36, which was held at higher super-liquidus temperatures (1210 or 1230 °C; $+\Delta T$ = 35–55 °C) for 24 hours, then cooled at 1 °C/h without the intermediate hold at 1190 °C, and finally quenched between 1165 and 1100 °C. This design aimed to study the influence of the magnitude of the initial superheating on crystallization behavior.
4. Cooling experiments with a final isothermal dwell were performed on OS36 in three steps (**Figure IV-1d**). After being held at 1190 °C for 24 h, charges were cooled at 1 or 9 °C/h to 1165 or 1120 °C, then finally quenched after dwell times

of 2 h, 5 h, 10 h, 24 h, 240 h (10 days), 264 h (11 days), 384 h (16 days), or 744 h (31 days).

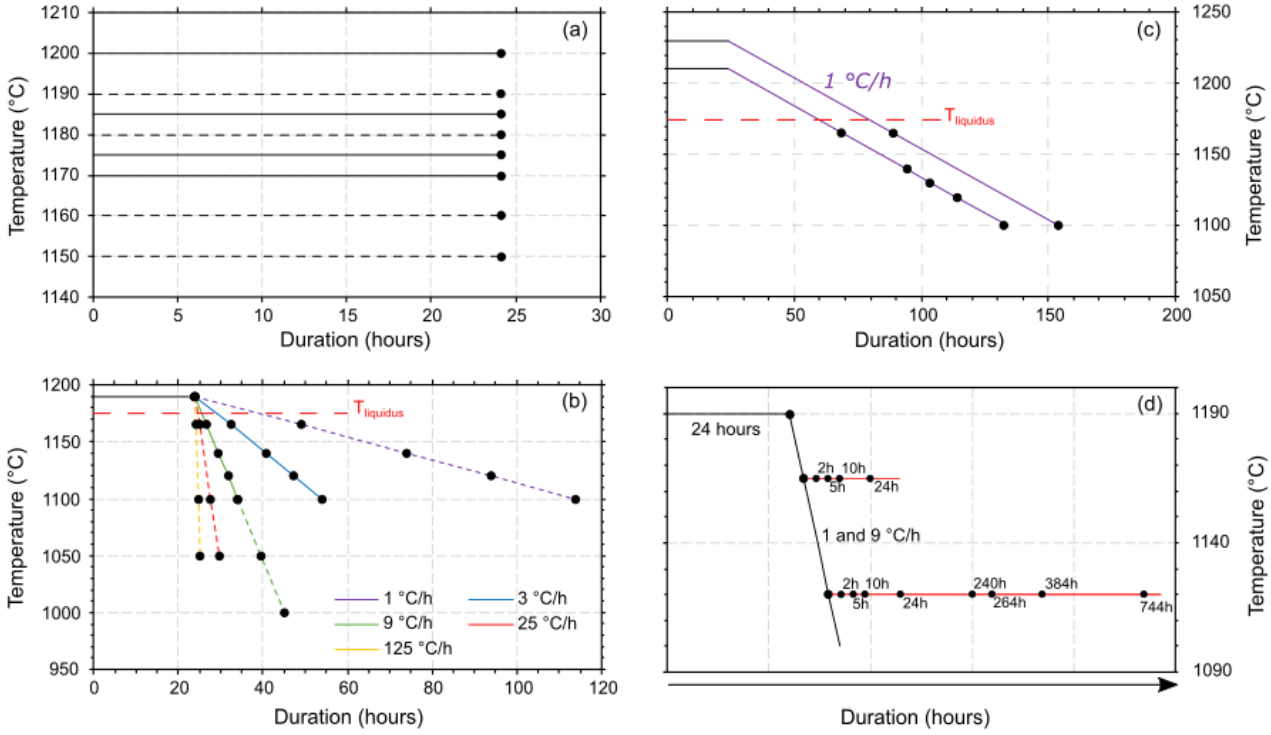

***Figure IV-1**: Overview of the four temperature-time paths used in this study. Solid lines indicate experiments with OS36 (crystal-bearing) as the starting material; dashed lines indicate those with both OS36* (crystal-free, pre-heated to 1450 °C for 2 h) and OS36 as the starting material. **a** 24-h isothermal experiments initially used to determine the liquidus temperature. **b** Experiments cooled at 1, 3, 9, 25, and 125 °C/h after an initial 24-h isothermal step at 1190 °C. Runs were quenched at 1165, 1140, 1120, 1100, 1050, or 1000 °C. Experiments using OS36 cooled at 1, 3, and 9 °C/h are from Billon et al. (2025). **c** Experiments cooled at 1 °C/h, after an initial 24-h isothermal step at 1210 °C (ΔT = 35 °C) or 1230 °C (ΔT = 55 °C). Runs were quenched at various temperatures between 1165 and 1100 °C. **d** Complex crystallization paths involving a cooling step similar to those in **(b)** at 1 and 9 °C/h, followed by final isothermal dwell times from 2 h to 31 days at 1165 or 1120 °C.*

Analytical techniques

Scanning electron microscopy (SEM)

The product of each experimental run was mounted in epoxy and prepared as a polished section. Whenever possible, samples were polished parallel to the platinum wire to maximize

the accessible surface area. Polished sections were examined by SEM with a field-emission gun and backscattered electron (BSE) imaging at KU Leuven (TESCAN Mira4), RWTH Aachen (FEI QEMSCAN 650F), and Cambridge University (FEI QEMSCAN 650F). Imaging was performed at a working distance of 10–15 mm, a dwell time of 10 µs, and an accelerating voltage of 15 kV (20 kV for energy-dispersive X-ray spectroscopy, EDS, with a beam current of 6–9 nA). Crystals and melt were analyzed using focused and defocused beam modes, respectively, with a beam current of 20 nA for plagioclase and 10 nA for the residual liquid. Analyses were conducted at 10 mm working distance and 15 kV accelerating voltage. Full analytical conditions, calibration standards, and chemical data are provided in ***Supplementary Files IV-1 and 2***. As chemical analyses were not the main focus of this study, and semi-quantitative data were sufficiently representative (see *Vetere et al. 2013*; *Billon et al. 2025*), EDS was often preferred as a practical alternative.

Image processing and textural analysis

We used the Weka Segmentation plugin of FIJI (ImageJ) to highlight relic cores and automate the quantification of plagioclase abundance (φ_V) from the BSE images (*Schneider et al. 2012*). Crystal outlines were drawn manually in Gimp, and 2D textural parameters (sectioned areas, roundness/circularity, length l and width w) were obtained using the best-fit ellipse method in FIJI. Full samples were typically imaged in several areas, away from the sample edges, at ~750× magnification to improve precision. Microstructural data from all sections from the same sample were then compiled. Phase proportions (φ_V) and 2D (N_A) and 3D crystal number densities (N_V) (based on manual point counting in FIJI), as well as the global mean crystal size (S_N) were determined from the full images of each sample (equations provided in ***Supplementary file IV-1***). Crystal size parameters (area, minor axis, and long axis of each crystal) were compiled into a single Excel spreadsheet. From this compilation, the $l_{max,\ av}$ (average size of the 10 largest crystals) and l_{mean} (mean size of the entire segmented crystal population) parameters were calculated

Nucleation and growth rates were calculated from the entire segmented crystal population of each experiment using the batch (G_{batch}), l_{mean} (G_{mean}), and l_{max} (G_{max}) methods. We calculated incremental nucleation (J_i) and growth rates (G_i) (*Couch 2003*) as the differences between two different dwell times at the same temperature; these rates were used to assess the evolution of crystallization during the final dwell periods of relevant experiments (equations provided in ***Supplementary file IV-1***). A complete summary of our microstructural dataset is

available in **Table IV-1** and ***Supplementary file IV-3***. Importantly, crystallization duration (*t*) needs to be well defined. Accordingly, because the presence of pre-existing crystals may promote early overgrowth before the onset of nucleation, growth rates were computed from the onset of visible overgrowths. Nucleation rates were calculated from the first appearance of new crystals.

Crystal Size Distributions (CSDs) and diffusion-limited growth

CSD analyses were performed on BSE images of experimental samples using the 2D long axis of more than 100 crystals. All CSD diagrams and data are available in ***Supplementary file IV-4***. The CSDCorrections method of *Higgins (2000)* was used to obtain the CSD curve by specifying the 3D crystal shape obtained using ShapeCalc (*Mangler et al. 2022*), the massive rock fabric, and roundness factor. Because dendritic plagioclase grains have more complex structures, potentially appearing as several fragments in 2D sections through the sample, their accurate segmentation is challenging. An incorrect determination of the contour of each crystal can have a strong impact on textural parameters (size, shape, and number of crystals), associated CSDs, and therefore resultant nucleation and growth rates. To solve this problem, we used the alignment and crystallographic orientation of each fragment, determined by electron backscatter diffraction (EBSD) using a MEB-FEG HITACHI SU5000 equipped with a Symmetry EBSD camera (Université de Lille, France), to guide image segmentation. Analyses were performed at an accelerating voltage of 20 kV, a beam current of a few nanoamperes, and a working distance of 15–20 mm. To ensure a good EBSD signal without carbon coating (detrimental for the EBSD signal), a partial vacuum of 30 Pa was applied. Details are provided in ***Supplementary File IV-1***. To assess the impact of observed complex morphologies (particularly swallowtail crystals) on the obtained textural data (2D aspect ratio, 3D shape), the **2**D aspect ratio distributions and 3D shape estimates were compared with those derived from a theoretical complete euhedral parallelepiped that was manually defined and segmented (***Supplementary file IV***-3).

											Global image				Segmentation	
Sample	Type	Pre-treatment	Pre-existing crystals	T_i (°C)	T_f (°C)	$+\Delta T_{th}$[a] (°C)	$+\Delta T_{exp}$[b] (°C)	$-\Delta T_n$[c] (°C)	$t_{final\ step}$ (h)	Phases	N_P (μm^{-2})	N_A (μm^{-2})	l_{mean} (μm)	$l_{max,\ av}$ (μm)	Diff (l_{mean}/l_{max}; %)
G 0-0a (Billon et al., 2025)	ISO	-	Yes	1190	1190	*15*	15	-	24	P.c, gl (100)	2.74E-06	2.2E-05	16	36	125
G 0-0b1	ISO	-	Yes	1190	1190	*15*	15	-	24	P.c, gl (100)	1.05E-06	3.6E-06	-	-	-
G 0-0b2	ISO	-	Yes	1190	1190	*15*	15	-	24	P.c, gl (100)	1.43E-06	8.3E-06	-	-	-
G 0-0b3	ISO	-	Yes	1190	1190	*15*	15	-	24	P.c, gl (100)	0.00E+00	4.5E-06	-	-	-
G 0-0b4	ISO	-	Yes	1190	1190	*15*	15	-	24	P.c, gl (100)	8.28E-07	1.0E-05	-	-	-
G 0-1 (Billon et al., 2025)	ISO	-	Yes	1185	1185	*10*	10	-	24	P.c (1), Plg? gl (99)	4.12E-06	1.3E-04	11	28	149
G 0-2 (Billon et al.,. 2025)	ISO	-	Yes	1180	1180	*5*	5	-	24	P.c, Plg (3), gl (97)	1.92E-05	2.4E-04	12	54	341
G 0-3 (Billon et al., 2025)	ISO	-	Yes	1175	1175	*0*	0	-	24	Plg (3), gl (97)	4.12E-06	1.3E-04	11	28	149
G 0-4	ISO	-	Yes	1160	1160	-	-	15	24	Plg (7), gl (93)	2.92E-05	5.5E-04	10	36	262
G 0-5	ISO	-	Yes	1150	1150	-	-	25	24	Plg (14), Ox (2) gl (84)	9.00E-05	2.4E-03	9	32	243
G 0-6	ISO	1450 °C, 2 h	No	1200	1200	*25*	25	-	24	gl (100)	-	-	-	-	-
G 0-7	ISO	1450 °C, 2 h	No	1190	1190	*15*	15	-	24	gl (100)	-	-	-	-	-
G 0-8	ISO	1450 °C, 2 h	No	1180	1180	*5*	5	-	24	gl (100)	-	-	-	-	-
G 0-9	ISO	1450 °C, 2 h	No	1170	1170	-	-	5	24	Plg (5), gl (95)	3.59E-05	4.1E-03	5	15	184
G 0-10	ISO	1450 °C, 2 h	No	1160	1160	-	-	15	24	Plg (5), gl (95)	5.90E-05	8.2E-03	6	17	198
G 0-11	ISO	1450 °C, 2 h	No	1150	1150	-	-	25	24	Plg (8), gl (92)	5.24E-05	1.4E-02	5	17	220
G 1-1a1 (Billon et al., 2025)	CR (1 °C/h)	-	Yes	1190	1165	*15*	15	10	-	Plg (6), gl (94)	9.44E-06	2.6E-04	21	87	308
No crystal corona	CR (1 °C/h)	-	Yes	1190	1165	*15*	15	10	-	Plg (1), gl (99)	9.44E-06	9.0E-05	12	25	113
G 1-1a2 (Billon et al., 2025)	CR (1 °C/h)	-	Yes	1190	1165	*15*	15	10	-	Plg (3), gl (97)	2.14E-06	1.6E-04	21	68	226
G 1-2 (Billon et al., 2025)	CR (1 °C/h)	-	Yes	1190	1137	*15*	15	38	-	Plg (12), gl (88)	4.26E-06	4.3E-04	20	114	472
G 1-3 (Billon et al., 2025)	CR (1 °C/h)	-	Yes	1190	1120	*15*	15	55	-	Plg (21), Ox (2), gl (77)	0.00E+00	5.0E-04	22	130	482
No crystal corona	CR (1 °C/h)	-	Yes	1190	1120	*15*	15	55	-	Plg (10), Ox (2), gl (90)	0.00E+00	5.1E-04	-	-	-
G 1-4 (Billon et al., 2025)	CR (1 °C/h)	-	Yes	1190	1100	*15*	15	75	-	Plg (21), Ox (<1), gl (79)	3.14E-06	5.6E-04	25	183	633
G 2-1a (Billon et al., 2025)	CR (3 °C/h)	-	Yes	1190	1165	*15*	15	10	-	Plg (3), gl (97)	1.44E-06	1.6E-04	16	60	278
G 2-1b (Billon et al., 2025)	CR (3 °C/h)	-	Yes	1190	1165	*15*	15	10	-	Plg (<1), gl (100)	0	1.2E-05	23	35	55
G 2-2 (Billon et al., 2025)	CR (3 °C/h)	-	Yes	1190	1140	*15*	15	35	-	Plg (11), gl (89)	3.0584E-06	3.7E-04	23	135	483
G 2-3 (Billon et al., 2025)	CR (3 °C/h)	-	Yes	1190	1120	*15*	15	55	-	Plg (15), gl (85)	2.6835E-06	5.1E-04	22	127	466

G 2-4 (Billon et al., 2025)	CR (3 °C/h)	-	Yes	1190	1100	*15*	15	75	-	Plg (20), gl (80)	1.6852E-06	5.3E-04	26	156	499
G 3-1 (Billon et al., 2025)	CR (9 °C/h)	-	Yes	1190	1165	*15*	15	10	-	Plg (1), gl (99)	1.73E-06	1.6E-04	9	31	236
G 3-2a1 (Billon et al., 2025)	CR (9 °C/h)	-	Yes	1190	1140	*15*	15	35	-	Plg (14), gl l (86)	3.56E-06	7.1E-04	14	113	683
G 3-2a2 (Billon et al., 2025)	CR (9 °C/h)	-	Yes	1190	1140	*15*	15	35	-	Plg (9), gl (91)	1.61E-06	6.8E-04	18	103	483
G 3-3a (Billon et al., 2025)	CR (9 °C/h)	-	Yes	1190	1120	*15*	15	55	-	Plg (14), gl l (86)	5.09E-07	3.3E-04	28	187	562
G 3-3b (Billon et al., 2025)	CR (9 °C/h)	-	Yes	1190	1120	*15*	15	55	-	Plg (15), gl (85)	1.99E-06	4.0E-04	24	140	491
G 3-4 (Billon et al., 2025)	CR (9 °C/h)	-	Yes	1190	1100	*15*	15	75	-	Plg (24), Ox (1), gl (75)	3.29E-06	8.8E-04	19	126	567
G 3-5 (Billon et al., 2025)	CR (9 °C/h)	-	Yes	1190	1050	*15*	15	125	-	Plg (39), Ox (1), Cpx (15), gl (45)	3.00E-06	5.7E-04	35	133	276
G 3-6 (Billon et al., 2025)	CR (9 °C/h)	-	Yes	1190	1000	*15*	15	175	-	Plg (48), Ox (1), Cpx (1), gl (20)	1.76E-06	-	35	103	191
G 4-1	CR (25 °C/h)	-	Yes	1190	1165	*15*	15	10	-	P.c, Plg (<1), gl (100)	3.36E-07	3.8E-05	13	31	135
G 4-2	CR (25 °C/h)	-	Yes	1190	1100	*15*	15	75	-	Plg (23), gl (77)	2.43E-06	6.7E-04	21	135	551
G 4-3	CR (25 °C/h)	-	Yes	1190	1050	*15*	15	125	-	Plg (32), Cpx (1), gl (67)	2.81E-06	4.8E-04	39	222	468
G 5-1	CR (125 °C/h)	-	Yes	1190	1165	*15*	15	-	-	P.c (<1), gl (100)	9.89E-07	3.0E-06	17	24	42
G 5-2a1	CR (125 °C/h)	-	Yes	1190	1100	*15*	53	37.5	-	Plg (4), gl (96)	1.62E-06	3.2E-04	16	83	422
G 5-2a2	CR (125 °C/h)	-	Yes	1190	1100	*15*	53	37.5	-	Plg (6), gl (94)	3.22E-06	3.0E-04	19	92	392
G 5-3	CR (125 °C/h)	-	Yes	1190	1050	*15*	53	87.5	-	Plg (36), gl (64)	4.19E-07	1.6E-03	25	203	711
G 6-1	CR (1 °C/h) + ISO	-	Yes	1190	1165	*15*	15	10	2	Plg (1), gl (99)	2.34E-07	2.5E-05	28	66	139
G 6-2a1	CR (1 °C/h) + ISO	-	Yes	1190	1165	*15*	15	10	5	Plg (5), gl (95)	0.00E+00	1.4E-04	27	83	204
G 6-2a2	CR (1 °C/h) + ISO	-	Yes	1190	1165	*15*	15	10	5	Plg (4), gl (96)	2.98E-07	1.3E-04	27	114	317
G 6-3	CR (1 °C/h) + ISO	-	Yes	1190	1165	*15*	15	10	10	Plg (3), gl (97)	0.00E+00	6.0E-05	34	96	185
G 6-4	CR (1 °C/h) + ISO	-	Yes	1190	1165	*15*	15	10	24	Plg (4), gl (96)	2.61E-07	4.3E-05	42	131	209
G 6-5	CR (1 °C/h) + ISO	-	Yes	1190	1120	*15*	15	55	2	Plg (15), gl (85)	0.00E+00	1.7E-04	49	195	296
G 6-6	CR (1 °C/h) + ISO	-	Yes	1190	1120	*15*	15	55	5	Plg (18), gl (82)	0.00E+00	1.3E-04	58	221	279
G 6-7	CR (1 °C/h) + ISO	-	Yes	1190	1120	*15*	15	55	10	Plg (19), Ox (<1), gl (81)	0.00E+00	9.5E-05	78	268	245
G 6-8	CR (1 °C/h) + ISO	-	Yes	1190	1120	*15*	15	55	24	Plg (18), gl (82)	0.00E+00	1.4E-04	68	297	337
G 6-9	CR (1 °C/h) + ISO	-	Yes	1190	1120	*15*	15	55	240	Plg (18), Ox (<1), gl (82)	0.00E+00	1.4E-04	59	254	332
G 6-10	CR (9 °C/h) + ISO	-	Yes	1190	1165	*15*	15	10	5	Plg (3), gl (97)	1.23E-06	1.3E-04	22	103	369
G 6-11	CR (9 °C/h) + ISO	-	Yes	1190	1165	*15*	15	10	24	Plg (4), gl (96)	0.00E+00	1.2E-04	31	114	267
G 6-12	CR (9 °C/h) + ISO	-	Yes	1190	1120	*15*	15	55	10	Plg (17), gl (83)	0.00E+00	2.1E-04	49	271	452

G 6-13	CR (9 °C/h) + ISO	-	Yes	1190	1120	*15*	15	55	24	Plg (20), gl (80)	1.02E-06	2.1E-04	58	271	364
G 6-14	CR (9 °C/h) + ISO	-	Yes	1190	1120	*15*	15	55	264	Plg (18), gl (82)	6.07E-07	2.9E-04	51	239	372
G 6-15	CR (9 °C/h) + ISO	-	Yes	1190	1120	*15*	15	55	384	Plg (19), gl (81)	1.23E-06	3.2E-04	45	236	428
G 6-16a	CR (9 °C/h) + ISO	-	Yes	1190	1120	*15*	15	55	744	Plg (21), gl l (79)	0.00E+00	3.5E-04	46	258	457
G 6-16b	CR (9 °C/h) + ISO	-	Yes	1190	1120	*15*	15	55	744	Plg (22), Cpx (<1), gl (78)	0.00E+00	2.9E-04	48	237	392
G 6-17	CR (1 °C/h) + ISO	-	No	1210	1120	*35*	65	25	24	Plg (14), gl (86)	0.00E+00	8.4E-06	371	1354	265
G 7-1	CR (1 °C/h)	1450 °C, 2 h	No	1190	1165	*15*	15	10	0	Plg (1), gl (99)	0.00E+00	1.7E-05	52	142	171
G 7-2	CR (1 °C/h)	1450 °C, 2 h	No	1190	1140	*15*	15	35	0	Plg (7), gl (93)	0.00E+00	1.6E-05	154	274	78
G 7-3	CR (1 °C/h)	1450 °C, 2 h	No	1190	1120	*15*	15	55	0	Plg (20), gl (80)	0.00E+00	6.4E-05	121	380	214
G 7-4	CR (1 °C/h)	1450 °C, 2 h	No	1190	1100	*15*	15	75	0	Plg (21), Ox (<1), gl (79)	0.00E+00	3.3E-05	116	372	221
G 8-1	CR (9 °C/h)	1450 °C, 2 h	No	1190	1050	*15*	15	125	0	Plg (33), Ox (1), Cpx (1), gl (65)	0.00E+00	5.6E-05	210	576	174
G 8-2	CR (9°C/h)	1450 °C, 2 h	No	1190	1000	*15*	15	175	0	Plg (37), Ox (<1), Cpx (18), gl (45)	0.00E+00	1.1E-04	141	404	186
G 9-1	CR (25°C/h)	1450 °C, 2 h	No	1190	1165	*15*	80	-	0	gl (100)	0.00E+00	0.0E+00	-	-	-
G 9-2	CR (25°C/h)	1450 °C, 2 h	No	1190	1100	*15*	80	10	0	Plg (5), gl (95)	0.00E+00	3.6E-05	128	294	130
G 9-3	CR (25°C/h)	1450 °C, 2 h	No	1190	1050	*15*	80	60	0	Plg (36), gl (64)	0.00E+00	5.4E-05	230	491	113
G 10-1	CR (125°C/h)	1450 °C, 2 h	No	1190	1165	*15*	-	-	0	gl (100)	0.00E+00	0.0E+00	-	-	-
G 10-2	CR (125°C/h)	1450 °C, 2 h	No	1190	1050	*15*	-	-	0	gl (100)	0.00E+00	0.0E+00	-	-	-
G 11-1	CR (1 °C/h)	-	No	1210	1165	*15*	20		0	gl (100)	0.00E+00	0.E+00	-	-	-
G 11-2	CR (1 °C/h)	-	No	1210	1140	*15*	-	5	0	Plg (1), gl (99)	0.00E+00	9.0E-07	445	644	45
G 11-3	CR (1 °C/h)	-	No	1210	1130	*15*	-	15	0	Plg (9), gl (91)	0.00E+00	3.3E-06	644	1116	73
G 11-4	CR (1 °C/h)	-	No	1210	1120	*15*	-	25	0	Plg (15), gl (85)	0.00E+00	1.0E-05	420	1099	162
G 11-5	CR (1 °C/h)	-	No	1210	1100	*15*	-	45	0	Plg (20), gl (80)	0.00E+00	8.1E-06	477	1124	136
G 11-6	CR (1 °C/h)	-	No	1230	1165	*15*	20	-	0	gl (100)	0.00E+00	0.0E+00	-	-	-
G 11-7	CR (1 °C/h)	-	No	1230	1100	*15*	-	45	0	Plg (21), gl (79)	0.00E+00	1.1E-05	387	1218	215

[a]: degree of superheating relative to the modelled plagioclase liquidus temperature (1175 °C)

[b]: degree of superheating, considering the shift in the onset of crystallization caused by the thermal path

[c]: nominal degree of undercooling, considering the modification of the onset of crystallization

***Table IV-1**: Microstructural characteristics determined from image segmentation. T_i, T_f refer to the initial and final temperatures of the runs. $+\Delta T_{th}$ and $+\Delta T_{exp}$ respectively represent the degree of superheating relative to the plagioclase saturation temperature determined from isothermal experiments (1175 °C) and that relative to the onset of nucleation when nucleation was delayed. $-\Delta T_n$ is the nominal degree of undercooling ($-\Delta T_n = T_{sat} - T_f$). The duration of the final experimental step is also provided in hours ($t_{final\ step}$). N_P and N_A refer to bubble and plagioclase number densities. l_{mean} is the mean plagioclase crystal size measured on the entire segmented population. $l_{max,\ av}$ is the maximum plagioclase size, calculated as the average of the ten largest plagioclase crystals. CR and ISO correspond, respectively, to cooling rate and isothermal runs. Phase abbreviations: P.c., pre-existing crystal seeds; Plg, plagioclase; Cpx, clinopyroxene; Ox, Fe-Ti oxides; gl, glass.*

Results

Isothermal experiments

Experiments performed without pre-existing crystal fragments (OS36*) produced a homogeneous population of small (l_{mean} = 5 µm) euhedral, and tabular (lath-shaped; **Figure IV-2a**, **b**) plagioclases (w/l = 0.2–0.4) surrounded by a visible compositional boundary layer in the melt at the extremities of the crystals' longest axes (**Figure IV-2a**, ***IV-S4***). The crystal population exhibits a narrow size distribution, with similar l_{mean} and $l_{max,\ av}$ values (**Table IV-1**). In comparison, seed-bearing runs using OS36 produced rounded (w/l = 0.6–0.8) and larger (l_{mean} = 9–13 µm) plagioclases (**Figure IV-2c**, **d**). The largest crystals ($l_{max,\ av}$ = 28–45 µm) preserve evidence of overgrowth of seeds (see *Billon et al. 2025*; **Figure IV-2c**). Below 1170 °C, isothermal experiments displayed higher crystal number densities ranging from 4.08×10^{-3} to 1.43×10^{-2} µm^{-2} in runs without pre-existing crystals, and from 2.41×10^{-4} to 2.37×10^{-3} µm^{-2} in runs containing pre-existing crystals. This difference is particularly evident in the CSDs, where the intercept increases from about −13 µm^{-4} at 1180–1175 °C in seed bearing runs, to between −10 and −9 µm^{-4} and reaches approximately −7 µm^{-4} at 1160–1150 °C, in runs with and without initial crystal fragments respectively (***Supplementary File IV-4***). Both the intercepts and slopes of the CSDs, which increase with progressive crystallization, are consistently higher in OS36* runs compared to OS36 runs.

All isothermal experiments contained abundant gas bubbles (**Figure IV-2a**, **d**) and are characterized by strongly heterogeneous crystal spatial distributions (especially in OS36* runs; **Figure IV-2a**). Small spherical and agglomerated particles (**Figure IV-2d**) particularly rich in

FeO (~83 wt. %, with traces, ~5-7 wt. % of Ti, Mg and Al; probably magnetite), were present at 1150 °C in seed-bearing runs.

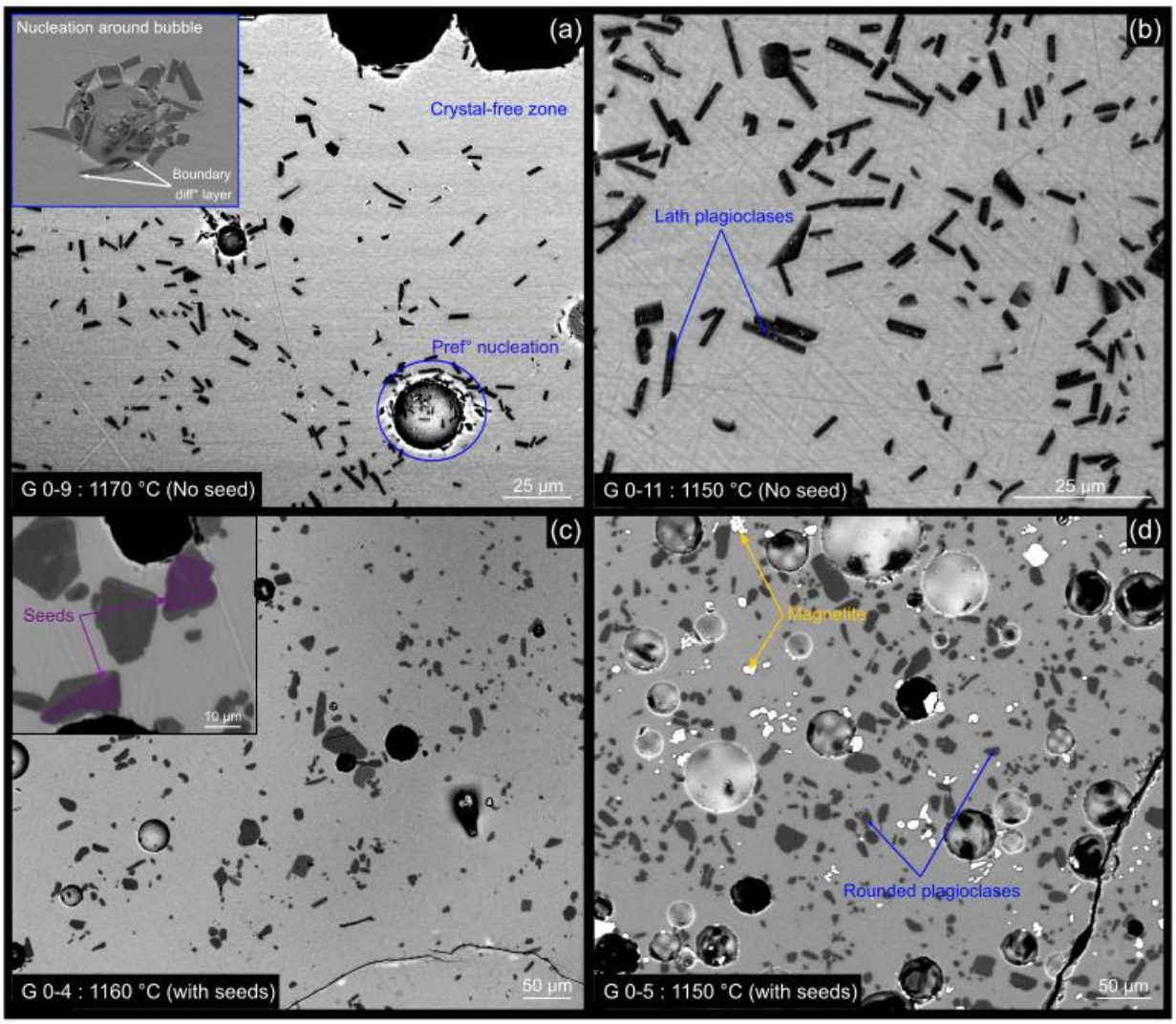

***Figure IV-2**: Backscattered electron images of the microstructural evolution of plagioclase in isothermal experiments. **a, b** Experiments conducted without any pre-existing crystal fragments (OS36*). Preferential nucleation at the surface of gas bubbles is visible in (**a**), and the crystal population is characterized by a lath-shaped morphology in (**b**). **c, d** Experiments conducted with pre-existing plagioclase crystal fragments (OS36). Plagioclases are more rounded, with greater variability in size and 2D aspect ratio.*

Cooling experiments

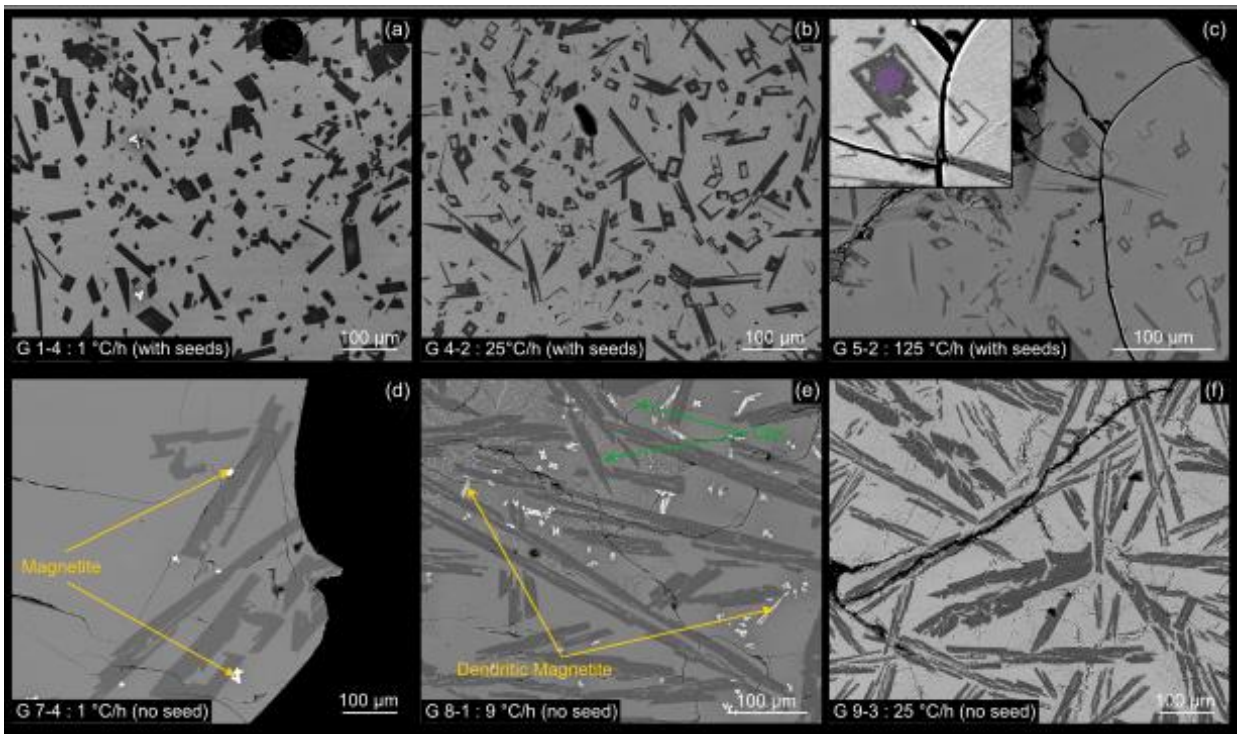

Figure IV-3*: Backscattered electron images of cooling experiments illustrating microstructural evolution.* ***a–c*** *Runs conducted with initial plagioclase crystal fragments (OS36) and quenched at 1100 °C after cooling at 1, 25 and 125 °C/h, respectively. Plagioclase habit evolves from euhedral at 1 °C/h (**a**) to skeletal at 25 and 125 °C/h (**b**, **c**), and samples cooled at 125 °C/h show dendritic extensions (**c, inset**). All OS36 cooling runs are characterized by highly variable crystal sizes.* ***d–f*** *Runs conducted with an initially fully glassy material (OS36*) and quenched at 1100 °C (**d**, cooling at 1 °C/h) and 1050 °C (**e, f**, cooling at 9 and 25 °C/h, respectively). All OS36* cooling runs exhibit dendritic plagioclases, with microstructural complexity increasing from 1 to 25 °C/h.*

Seed-bearing starting material

Experiments containing plagioclase seed crystals (**Figure IV-3a–c;** ***IV-S2***) showed a progressive microstructural evolution with increasing cooling rate, from equant/tabular (with sharp edges) at 1 °C/h, to skeletal/dendritic habits at 25 and 125 °C/h (**Figure IV-3b, c**). As discussed by *Billon et al. (2025)*, the internal morphology of the crystals often varied depending on crystal size (**Figure IV-3a–c**), as highlighted by the steepening of the CSD slopes from −0.02 at 1 °C/h to −0.07 at 125 °C/h (***Supplementary file IV-4***), indicating accelerated growth (see **Figure IV-9**). At the fastest cooling rates (>25 °C/h), particularly at 125 °C/h, plagioclase evolved from resorbed textures around relic cores when quenched at 1165 °C to

skeletal/dendritic (with principally hopper sections) at 1100 ($-\Delta T_n$ = 75 °C) and 1050 °C ($-\Delta T_n$ = 125 °C) (**Figure IV-3b, c**). The largest crystals grown around the initial plagioclase fragments display complex habits comprising tabular overgrowths, dendritic extensions, and embayments (**Figure IV-3c, inset**; **Fig. *IV-S2k***). Magnetite and clinopyroxene typically crystallized at 1120 and ~1050 °C, respectively, at slow to moderate cooling rates (1–9 °C/h), but were absent at 25 and 125 °C/h, respectively (**Table IV-1**). Aside from preferential nucleation around the Pt-wire, particularly during the beginning of crystallization, most nucleation appears to have occurred in the internal regions of each charge.

The plagioclase proportion (φ_V), density (N_A), and size (l_{mean}, $l_{max,\ av}$) at 25 remain comparable to those at 1 and 9 °C/h (**Table IV-1**, **Figure IV-4a, b**). In contrast, at 125 °C/h, a smaller plagioclase proportion is observed due to nucleation only beginning the predicted 1175 °C value (**Figure IV-4a**). For subsequent calculations concerning runs cooled at 125 °C/h, the liquidus temperature is adjusted to 1137.5 °C (the average between 1165 and 1110 °C). This delay explains the lower CSD intercept at 125 °C/h (compared to the increasing trend from 1 to 25 °C/h) in runs quenched at 1100 °C. This initial nucleation delay was compensated by a continuous increase in plagioclase number density between 1100 and 1050 °C.

The maximum crystal size ($l_{max,\ av}$) decreases with increasing cooling rate from 183 µm at 1 °C/h to 83–92 µm at 125 °C/h (**Figure IV-4c**). At tested cooling rates, plagioclase crystals larger than 100 µm were rare (<1%), whereas crystals smaller than 10 µm were abundant (~40–50%). The abundance of small crystals only declined below 1100 °C, temperatures at which the availability of liquid and interstitial space diminished. At 1100 °C, N_A vs. cooling rate forms a bell-shaped curve peaking at 9 °C/h, reflecting liquidus depression and delayed nucleation at 125 °C/h. Testing various liquidus temperatures for the runs cooled at 125 °C/h, and different nominal undercoolings shows that the relationship varies (***Supplementary file IV-3***). For $T_{liq} \approx$ 1125 °C, and a $-\Delta T_n$ = 75–85 °C), N_A increases with cooling rate (**Figure IV-4d**) when crystals are homogeneously distributed.

Crystal-free starting material

These experiments were performed on the glassy OS36* material (**Fig. *IV-S3a - f***). They were initially held at 1190 °C ($+\Delta T$ = 15 °C) for 24 h, then cooled at 1, 9, 25, or 125 °C/h. These runs displayed heterogeneous crystal distributions when quenched above 1100 °C ($-\Delta T_n$ = 75 °C) due to preferential plagioclase nucleation on the Pt-wires and charge margins (**Figure IV-3d; *IV-S4a***). At slow to moderate cooling rates (1 and 9 °C/h), plagioclases grains acted as

heterogeneous nucleation sites for skeletal Fe-Ti oxides (~1100 °C) and spherulitic clinopyroxene (~1050 °C), as in seeded runs (**Figure IV-3e**; ***IV-S4f***). At increased cooling rates, plagioclase nucleation was delayed (indicated by low φ_V values in **Figure IV-4a**): we obtained crystal-free glasses down to ~1100 °C at 25 °C/h and in all runs at 125 °C/h. Plagioclase habits evolved from elongated skeletal forms with a few tabular euhedral crystals at 1 °C/h to more complex, multi-branched dendritic structures with increasing degree of nominal undercooling and cooling rate (**Figure IV-3f**). Similar dendritic morphologies were observed at 1050 °C (9 °C/h) and 1100 °C (25 °C/h).

Regardless of cooling rate, experimental runs starting with crystal-free glasses contained 1 to 2 orders of magnitude fewer plagioclase crystals, but those crystals had mean sizes up to 1 order of magnitude larger (**Figure IV-3b**, **Table IV-1**; see CSDs in ***Supplementary file IV-4***); with a lower variability in size (<1% of crystals smaller than 10 μm) and shape ($w/l \leq 0.2$) (**Figure IV-3d**, **f**). This restricted range of 2D aspect ratios explains the accurate 3D shape estimations ($R^2 = 0.98–0.99$) obtained using *ShapeCalc*.

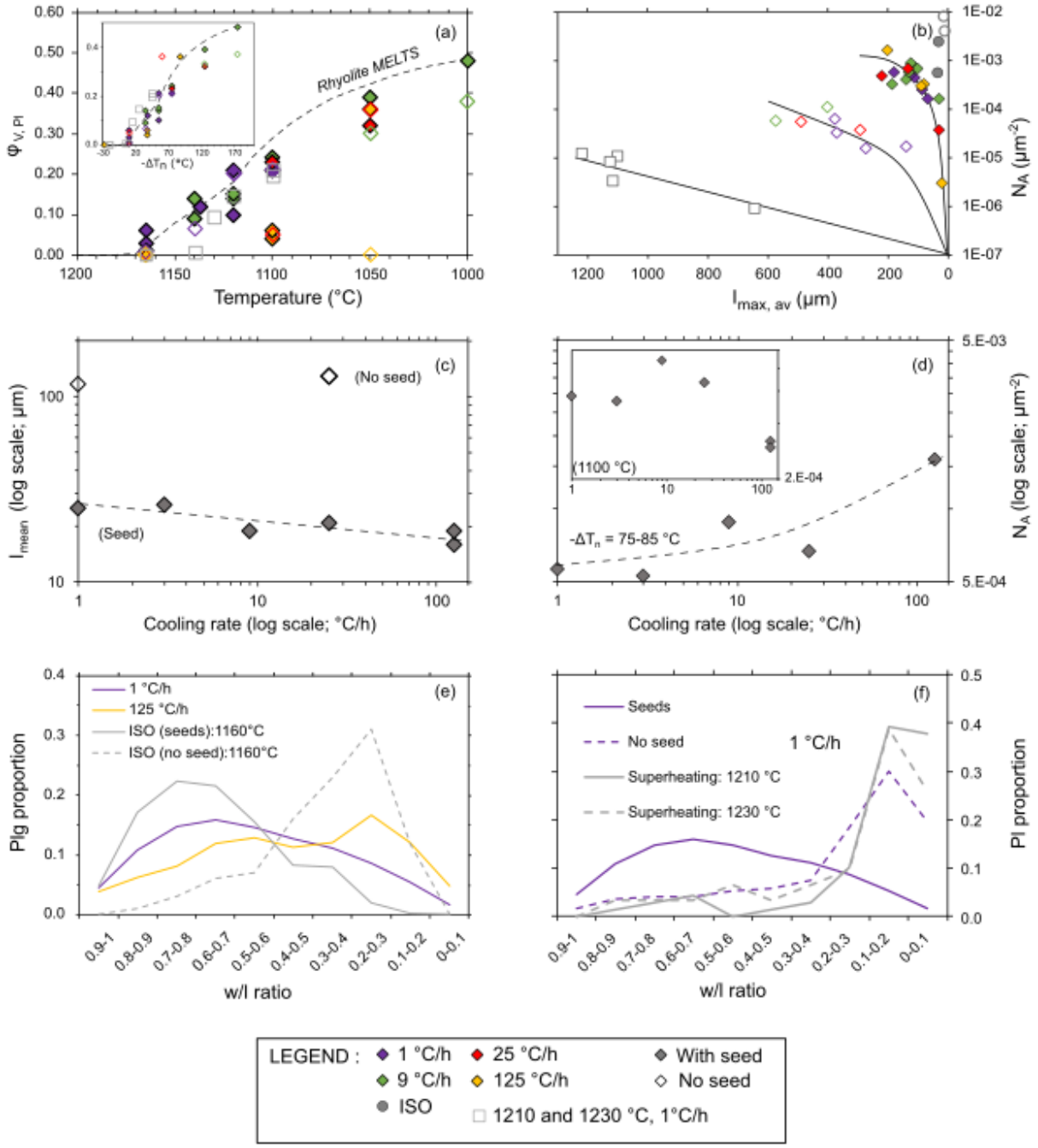

***Figure IV-4**: Plagioclase microstructural data from cooling experiments. **a** Volumetric plagioclase proportion ($\phi_{V, Pl}$) as functions of temperature (outset) and degree of effective undercooling $-\Delta T_n$ (inset; corrected for depression of the liquidus temperature). **b** Plagioclase crystal number density (N_A) vs. maximum crystal size ($l_{max, av}$). **c, d**: Average crystal size (l_{mean}) and crystal number density (N_A), respectively, as functions of the cooling rate. The inset in (**d**) shows how N_A evolved with cooling rate for the same quench temperature of 1100 °C. **e, f** Plagioclase aspect ratio (w/l) distributions (**e**) as a function of cooling rate and (**f**) variations associated with the initial pre-heating step.*

Slow cooling from higher degrees of superheating

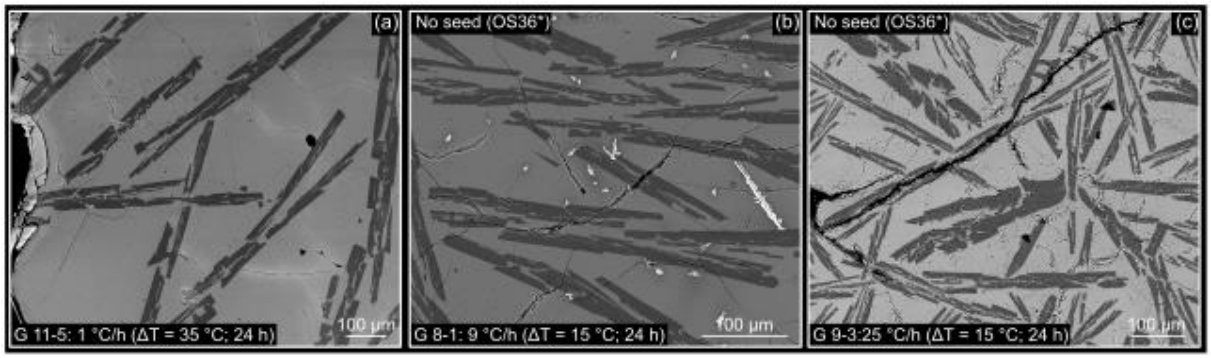

Figure IV-5*: Backscattered electron images of cooling experiments conducted from various initial degrees of superheating.* ***a*** *Run (starting material OS36) superheated to 35 °C for 24h above the liquidus, cooled at 1 °C/h, and quenched at 1100 °C.* ***b, c*** *Runs (starting material OS36*) cooled from 1190 °C (+ΔT = 15 °C) at 9 and 25 °C/h, respectively, and quenched at 1050 °C; shown here for comparison. Note the similar plagioclase habit in the three panels, particularly in (**a**) and (**b**).*

This series used the OS36 starting material superheated to 1210–1230 °C ($+\Delta T_{th}$ = 35–55 °C) for 24 hours and then cooled at 1 °C/h (**Fig. *IV-S3g–i***). In total, including the isothermal step and part of the cooling, these experiments lasted for a prolonged period of 59–79 hours above the theoretical liquidus temperature of 1175 °C (**Fig. IV-1c**). Similar to cooling experiments on OS36* cooled at 25 °C/h, nucleation was delayed by 30–35 °C (**Fig**. ***IV-S3g***), only beginning around 1145 °C instead of 1175 °C. Nucleation occurred exclusively on Pt-wires and charge margins, and the dendritic plagioclase habits (**Figure IV-5a**) are very similar to those observed in cooling experiments on OS36* at 9 and 25 °C/h (**Figure IV-5b**, **c**). In contrast to experiments containing initial plagioclase seeds that started at a low degree of superheating, all plagioclase crystals exhibited complex twinning patterns produced by rapid growth (*Brugger and Hammer 2015*; *Xu et al. 2016*; ***Supplementary File IV-1***). Fe-Ti oxides and clinopyroxenes were absent.

Plagioclase crystal number densities (N_V) ranged from 10^{-8} to 10^{-7} µm^{-3}, and average maximum lengths ($l_{max,\,av}$) reached 1100–1200 µm (**Figure IV-4b**, **Table IV-1**). As in the OS36 cooling experiments, the crystals again exhibited a very restricted range of sizes (**Table IV-1**) and aspect ratios (w/l = 0–0.2; **Figure IV-4f**), corresponding to bladed or tabular habits.

All series performed using a crystal-free initial material (either using OS36* or an initial strong degree of superheating between 35 and 55 °C) are characterized by a high proportion of large crystals (40–80% of crystals being larger than 100 µm), an almost complete absence of

small crystals (≤10 µm, ***Supplementary file IV-3***), and similar dendritic to bladed habits (**Figure IV-5a–c**).

Cooling experiments with a final isothermal dwell

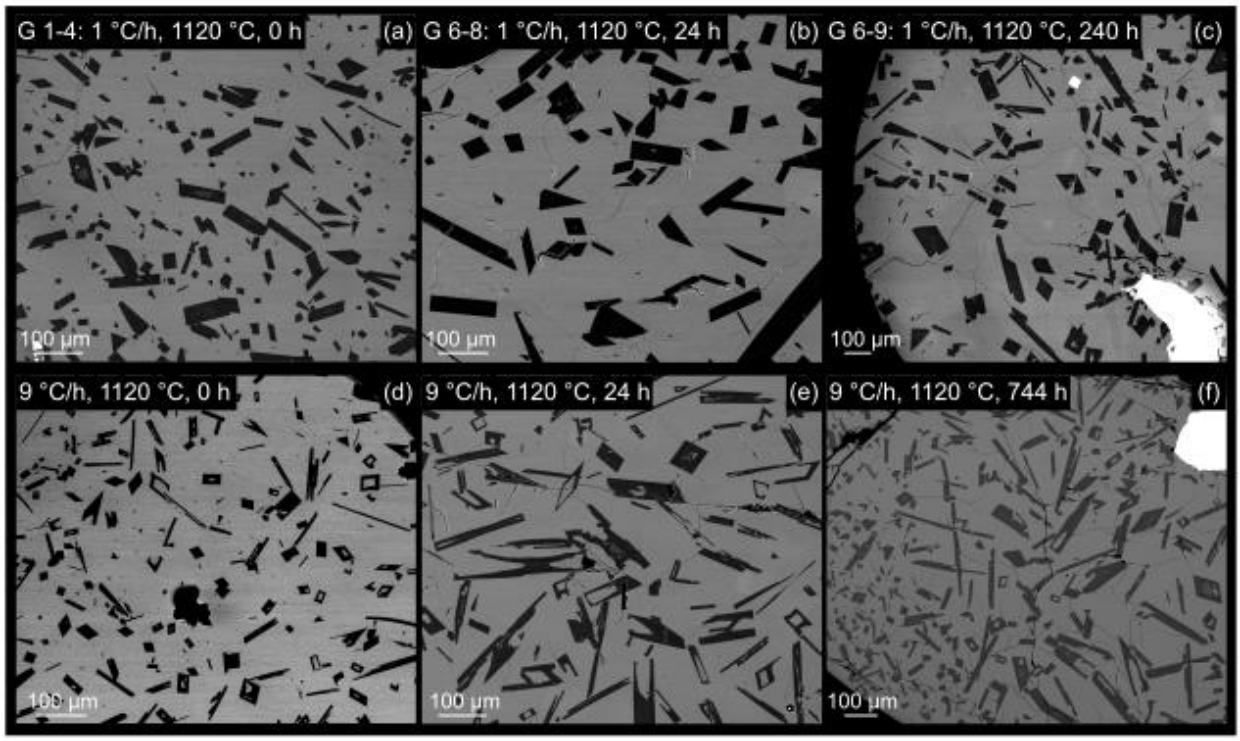

Figure IV-6*: BSE images of experiments held isothermally at 1120 °C after an initial cooling at* ***a–c*** *1 °C/h and* ***d–f*** *9 °C/h. Larger plagioclase crystals observed at longer dwell durations (****b****,* ***d****) are associated with a decrease in the abundance of smaller crystals (****b, c, e****). Except for a second nucleation and growth event that produced abundant tabular crystals in the charge margins, distinct from earlier skeletal habits after cooling at 9 °C/h and a 31-day dwell time (****f****), no significant textural modifications are observed.*

Microstructural observations

Figure IV-6 illustrates the microstructural evolution during the final isothermal step, from an immediate quench at the final temperature (0 h) to dwell durations of 31 days. For a given cooling rate and final temperature, both the overall microstructure and plagioclase modal abundance remained relatively stable at around 0.02 at 1165 °C and 0.18 at 1120 °C (as predicted by Rhyolite-MELTS; **Figure IV-6a–e**, **Figure IV-7a**). Both the occurrence of tabular crystals (**Figure IV-7d**), and crystal size (l_{mean}, l_{max}) increased with increasing dwell time, whereas the number density decreased (**Figure IV-7b**). Accordingly, the proportion of small

crystals (<10 μm) decreased from 30–68% initially to 2–10% depending on the cooling rate and final temperature, and the proportion of the largest crystals (>100 μm) increased steadily (**Figure IV-7e**; ***Supplementary file IV-3***). The proportion of crystals <10 μm dropped below 5% at 1120 °C ($-\Delta T_n$ = 55 °C), suggesting slowed or arrested nucleation. Crystal sizes stabilized after 24 h (**Figure IV-7c**).

In experiments held at 1165 °C, the most pronounced changes occurred during the first two hours of the dwell time, in which the proportion of small crystals fell from 40% to 10% at 1 °C/h, and from 70% to 28% at 9 °C/h (***Supplementary file IV-3***). At 9 °C/h, long-duration experiments (>11 days) showed a second episode of nucleation, with N_A increasing from 2 × 10^{-4} to 3–3.5 × 10^{-4} μm^{-2}, and smaller crystals formed around the sample edges (**Figure IV-6f**), with more tabular habits in contrast to the earliest elongated skeletal/dendritic forms. The first large euhedral pyroxene crystals were also observed in experiments quenched after 31 days.

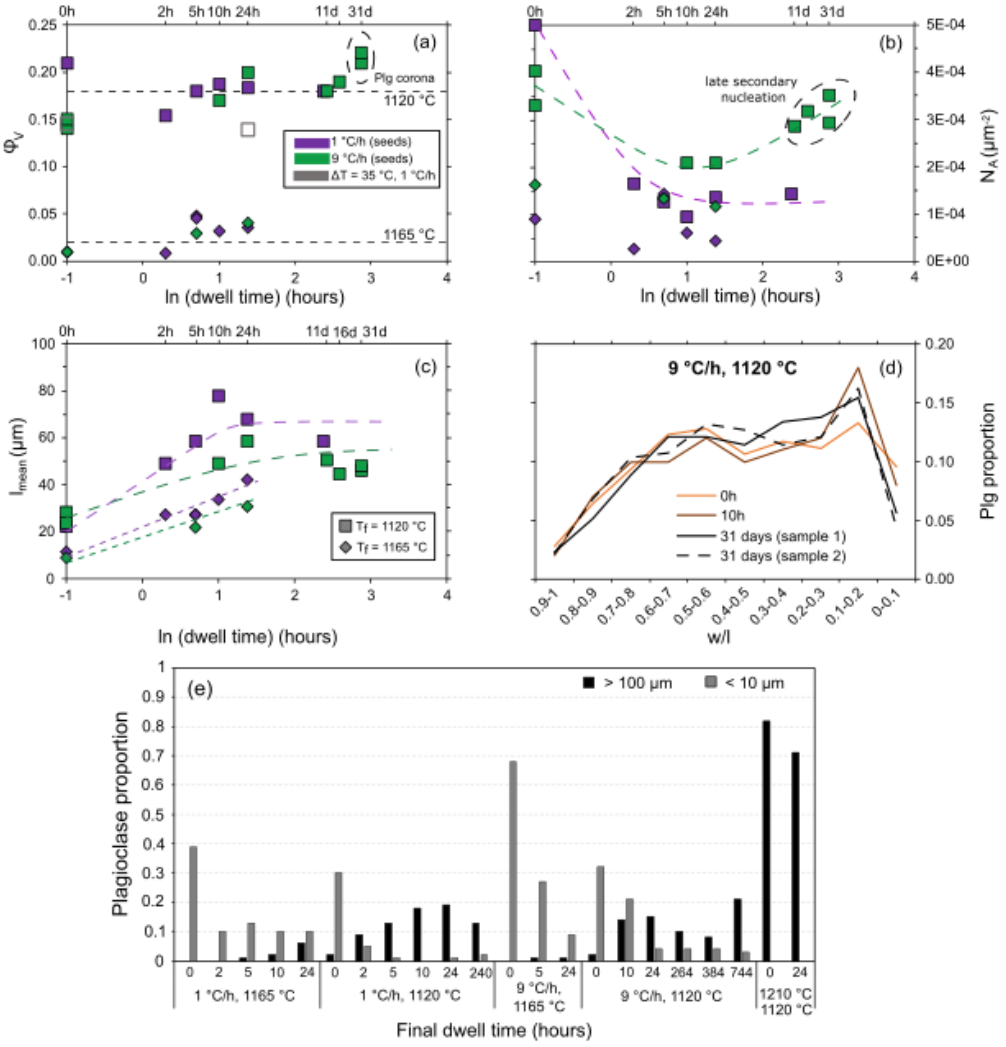

Figure IV-7*: Microstructural data from cooling experiments followed by a final isothermal dwell (relaxation) time.* ***a–c*** *Plagioclase volume proportion (φ_V), number density (N_A), and mean crystal size (l_{mean}) vs. final dwell duration.* ***d*** *Proportion of plagioclase crystals vs. their 2D aspect ratio (w/l) for the different relaxation times at 1120 °C following cooling at 9 °C/h.* ***e*** *Evolution of the abundance of the largest (>100 µm) and smallest (<10 µm) plagioclase crystals with final dwell time under various experimental conditions.*

CSD data

The CSDs obtained for these experiments (**Figure IV-8**) show a decrease in both slope and intercept (***Supplementary file 4***), supporting a reduced nucleation and growth with increasing dwell time. After 11 days at 1120 °C, the intercept increased again (**Figure IV-8b**), consistent with the observed second nucleation event. CSDs from 2 and 5 h runs are similar, whereas the 24 h experiment at 1165 °C shows upward curvature, likely due to low crystal counts.

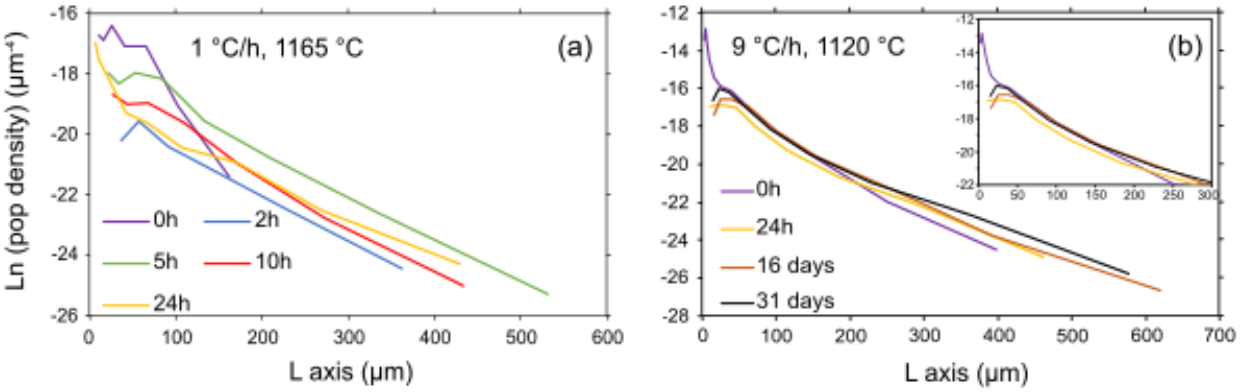

***Figure IV-8**: 3D plagioclase crystal size distributions (CSDs) after various relaxation durations ranging from 0 h (i.e., immediately after the cooling step) to 31 days. The inset plot in b corresponds to a zoom on the first part of the CSD.*

Summary of key results

Before moving onto the interpretation of our experimental results, we provide here a short summary of our key observations:

- Despite preferential nucleation near the Pt wire at the onset of crystallization and in superheated runs, seeded cooling runs showed significant nucleation in the interior of the charge.
- Isothermal experiments produced abundant small crystals of similar size, particularly when using crystal-free glass (OS36*) as the starting material (**Figure IV-9**).
- Cooling experiments displayed greater crystal size variation, reflecting continuous nucleation. With increasing cooling rate, these runs showed progressive microstructural evolution from euhedral to skeletal/dendritic habits.
- Increasing the degree of initial superheating in cooling runs promoted the growth of fewer but larger dendritic crystals (**Figure IV-9**), opposite to the trend observed in isothermal experiments.
- Experiments held at their final temperature displayed near-equilibrium crystal proportions after 2–5 h. Nonetheless, the crystal habits remained unchanged, even after 31 days.

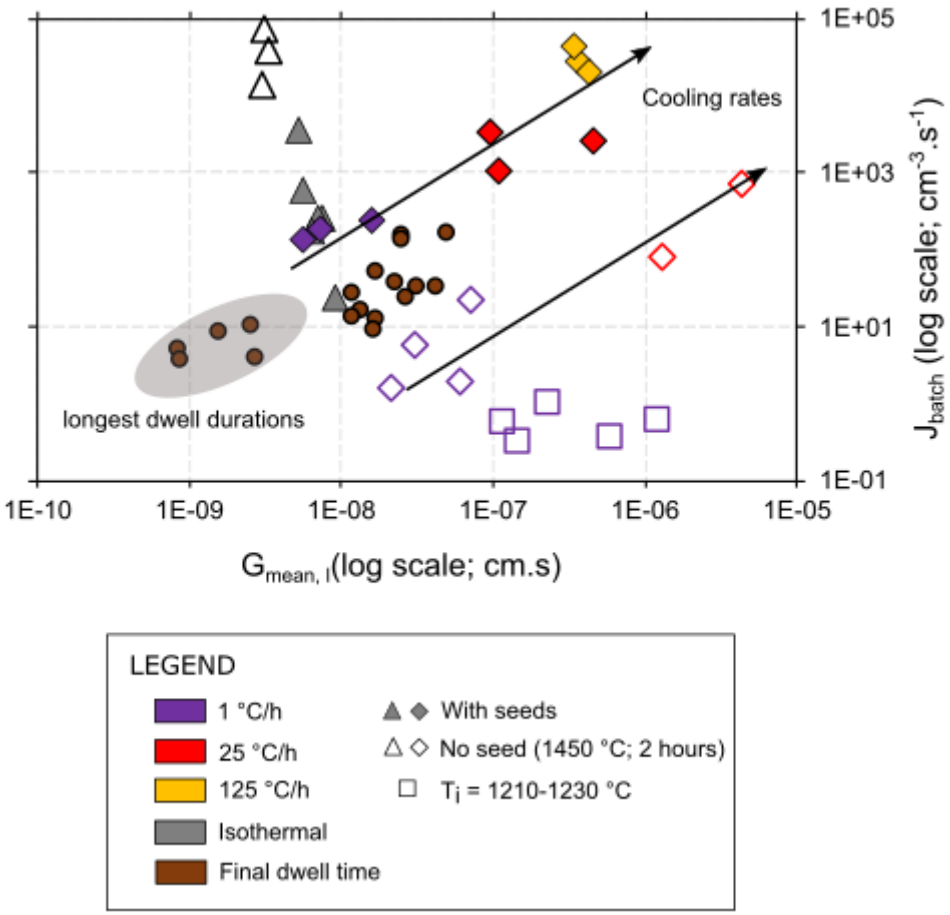

***Figure IV-9**: J vs. G diagram illustrating the competition between nucleation and growth during the various explored solidification paths. Note that values referring to final dwell durations do not represent incremental data, but the entire experimental duration.*

Discussion

The impact of thermal history on the experimental liquidus

The effective liquidus temperature was constrained to 1175 °C by *Billon et al. (2025)* using isothermal experiments. However, the temperature at which crystallization begins is sensitive to both the degree of superheating and the cooling rate. In superheated runs, nucleation was delayed, as previously noted by *Walker et al. (1978)*: from $+\Delta T = 35$ °C, plagioclase only began crystallizing at ~1145 °C, i.e., 30 °C below the theoretical liquidus. This depression of the liquidus is confirmed by the similar crystal abundances obtained at 1100 °C in samples preheated at either 1210 or 1230 °C. Crystal-free glasses (OS36*) also showed this effect at high cooling rates (25–125 °C/h), with crystallization completely suppressed at 125 °C/h in our runs. These results are consistent with *Donaldson (1979)* and define a critical cooling rate (R_c)

above which no crystals nucleate (*Fan et al. 2007*), permitting the system to attain the glass transition temperature with no nucleation (*Fokin et al. 2003, 2006*; *Iezzi et al. 2008, 2011*). Our R_c (between 25 and 125 °C/h) in a melt containing 56.50 wt.% SiO_2 is comparable to that of latitic melts (60 °C/h) with similar silica contents (57.72 wt.% SiO_2; *Iezzi et al. 2011*). Small variations in melt composition or initial crystal content can increase R_c by over an order of magnitude (R_c > 125 °C/h in seed-bearing runs).

The observed changes in the effective liquidus affect the calculation of nucleation (J) and growth (G) rates. As mentioned by *Rusiecka et al. (2020)*, durations are often measured from the start of experiments (*Swanson 1977*), which remains valid for superheated cooling runs in which nucleation occurs in a crystal-free melt. However, only a few studies, such as those of *Sirbescu et al. (2017)* and *Auxerre et al. (2022)*, consider the potential for delayed nucleation due to modifications of the thermal history. Experiments involving the presence of crystal seeds, for example, tend to promote primary growth above the effective liquidus in similar but unseeded runs, implying different onset times for nucleation and growth. For moderate cooling rates (1–9 °C/h), this shift has only a minor effect on G: accounting for the onset of growth at 1190 °C instead of 1175 °C increases growth rates by a factor of 1.1–2.5 (*Billon et al. 2025*), which is minor given their magnitude (10^{-7}–10^{-8} cm/s). However, at faster cooling rates (25 °C/h), growth and nucleation rates may be underestimated by up to one order of magnitude if the depression of the effective liquidus is not taken into account; growth rates can increase by a factor of 2–7, and nucleation rates by a factor of 3–15.

Evolution of nucleation and growth rates during cooling and isothermal experiments

The effect of cooling rate on growth and nucleation

The concept of textural equilibrium describes the microstructure for which the internal energies are at a minimum (*Higgins 2011*). For isolated crystals in a liquid, this entails the crystals attaining their equilibrium Wulff shape, for which the energy of the interfaces is minimized (*Herring 1951*; *Fonseca 1991*). Although the Wulff shape for plagioclase in silicate liquids is not known, textural equilibration must involve a decrease of the surface area-to-volume ratio (*First et al. 2020*); compact, inclusion-free polyhedral crystals are therefore closer to equilibrium than skeletal or dendritic forms. Regardless of the degree of initial superheating

or undercooling, rapid cooling drives phase compositions and crystal habit progressively away from both chemical and textural equilibrium (*Conte et al. 2006*; *Mollo et al. 2012*).

In our seeded experiments, the transition from euhedral to skeletal/dendritic habits occurred when cooling exceeds 9 °C/h: the appearance of skeletal plagioclase at 1120 °C indicates a shift from interface-controlled to diffusion-limited growth. This change in control of the growth habit is further evidenced by the observation of diffuse compositional boundary layers in experiments cooled at 125 °C/h, and a sharp increase in growth rates at 25–125 °C/h (***Supplementary file IV-3***). According to *Watson and Müller (2009)*, the compositional boundary layer observed at 9 and 25 °C/h reflects the low viscosity and high cation diffusivity of the melt. The transient skeletal habits observed at 1120 °C when cooling at 9 °C/h may therefore reflect an intermediate growth regime (*Mangler et al. 2023*) characterized by rapid transitions between rate-controlling processes. A similar trend was observed in initially crystal-free runs (OS36*), though over a narrower range of cooling rates, with skeletal habits observed at 1 °C/h and dendritic ones at 25 °C/h.

Despite the high cooling rates explored here (25–125 °C/h), the log(G) and log(J) vs. log(t) regressions from Billon et al. (2025) remain largely unaffected: slope/intercept values vary by only ~10% for growth and <5% for nucleation (**Figure IV-10a, b**). Crystal number density (N_A) peaks at 9 °C/h, then decreases with increasing cooling rate, likely due to liquidus depression caused by the large degree of effective undercooling ($-\Delta T_n$). After correcting for this effect, nucleation rates increase from 10^2 to 10^4 cm^{-3} s^{-1} with increasing cooling rate (**Figure IV-4d**).

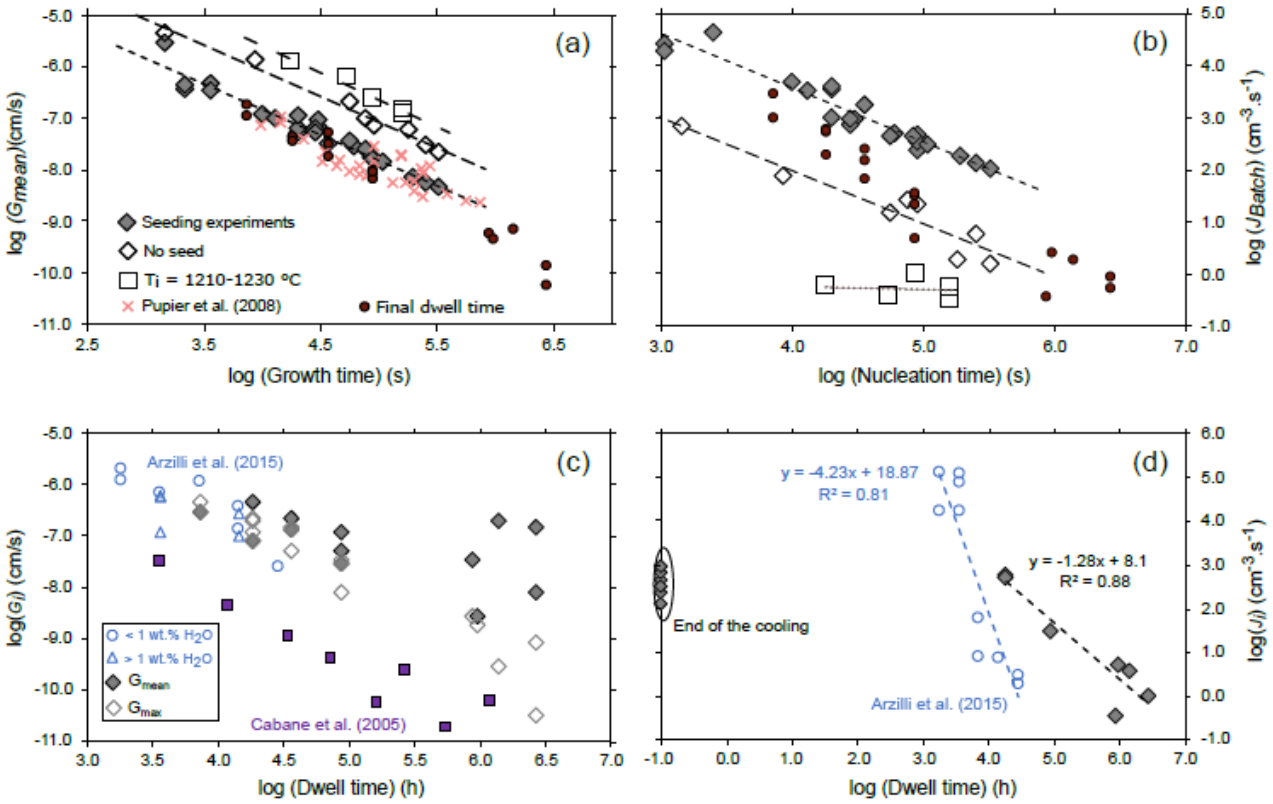

***Figure IV-10**: Evolution of **a, c** log(G) and **b, d** log(J) as functions of **a** growth and **b** nucleation time and **c, d** dwell time. Circles and triangles in (**c**) represent hydrated experiments containing less than and more than 1 wt.% H_2O, respectively.*

Comparison with isothermal experiments

Regardless of the initial thermal pre-treatment, the low mean growth rates in experiments conducted at $-\Delta T_n$ = 5-25 °C (3.02–5.74 × 10^{-9} cm/s) contrast with those in cooling experiments, in which increased degrees of undercooling enhanced the growth rate from 2.96 × 10^{-8} cm/s at 1 °C/h to 2.93 × 10^{-6} cm/s at 125 °C/h, particularly in seeded runs.

According to CNT, near-liquidus nucleation should be minimal. Yet, with or without initial superheating to 1450 °C, our isothermal runs systematically display the highest crystal number densities (5.45 × 10^{-4} to 1.43 × 10^{-2} µm^{-2}), up to two orders of magnitude higher than those during cooling experiments, even at high $-\Delta T_n$ values (**Table IV-1**). Because seeds of plagioclase were not abundant (<< 1 %), or were even absent, heterogeneous nucleation cannot account for these high values. Experiments on initially crystal-free glass showed a sudden

proliferation of similarly shaped crystals around 1170 °C, along with a diffuse compositional boundary layer indicative of diffusion-limited growth.

The strong correlation between high crystal densities and elevated porosity (**Table IV-1**) suggests that bubbles act as preferential nucleation sites (*Davis and Ihinger 1998*). Although high viscosity likely inhibits bubble formation, the initial thermal treatment plays a key role. In cooling experiments, extending heating at 1190 °C may have promoted volatile incorporation (e.g., CO_2) and subsequent bubble dissolution. *Du et al. (2003)* showed that small particles can stabilize emulsions by adhering to interfaces. By analogy, though hypothetical in silicate melts, growing microcrystals might locally stabilize gas bubbles. For example, *Dickinson et al. (2004)* showed that air bubbles larger than ~80 µm stabilized by silica nanoparticles remain indefinitely; a similar process may explain the rare but large bubbles formed in our cooling experiments.

Impact of final dwell time

The impact of dwell time on crystallization kinetics has been addressed in only a few studies, mainly those focused on relaxation following isothermal crystallization (*Cabane et al. 2001, 2005*) or after extremely rapid cooling/decompression events (>1000 °C/h; *Arzilli et al. 2015*; *Pontesilli et al., 2019*). In our experiments, initial cooling at 1 and 9 °C/h led to a stable modal proportion, with nucleation and growth predominantly occurring during the first two hours of the dwell time, consistent with *Arzilli et al. (2015)*. Incremental rates dropped sharply, growth rates from 10^{-7}–10^{-8} to 10^{-10}–10^{-11} cm/s and nucleation rates from 10^{3} to 10^{1}–10^{-1} cm^{-3} s^{-1}, with increasing dwell time (**Figure IV-10**, ***Supplementary File IV-3***), matching trends from both dry and hydrous isothermal studies (*Cabane et al. 2005*; *Pontesilli et al. 2019*). Additional experiments with short dwell times (<2 h) should be performed to test whether chemical equilibrium is reached immediately post-cooling. Despite rapid modal equilibration, plagioclase grains retained high surface area to volume ratios even after 31 days, with features like hopper cavities (**Figure IV-6f**; *Arzilli et al. 2015*), contrasting with the more rounded and compact pyroxenes of *Pontesilli et al. (2019)*. This suggests that plagioclase grains require much longer to achieve a low energy shape than does pyroxene.

To isolate the effect of the final dwell time, we performed regressions of $\log(J_i)$ and $\log(G_i)$ versus $\log(t_{dwell})$ (**Figure IV-10c, d**; **Table IV-2**):

- $\log(J_{Batch}) = -1.28 \times \log(t_{dwell}) + 8.1$; $R^2 = 0.88$ (3)

- $\log(G_{mean}) = -1.14\ (\pm 0.07) \times \log(t_{dwell}) - 2.42\ (\pm 0.30)$; $R^2 = 0.93$ (4)
- $\log(G_{max}) = -1.21\ (\pm 0.11) \times \log(t_{dwell}) - 1.67\ (\pm 0.49)$; $R^2 = 0.83$ (5)

The 1σ errors reflect the inclusion or exclusion of long dwell durations (>10 days), in which further nucleation might occur. Compared to cooling experiments, nucleation and growth rates considering dwell time differ only modestly (by 23% for nucleation and 14–15% for growth). The observed decrease in growth rate aligns with isothermal and isobaric trends reported by *Cabane et al. (2005)* and *Arzilli et al. (2015)*, whereas the decrease in nucleation rate is less steep (slope −1.28 vs. −4.23 in *Arzilli et al. 2015)*. Growth rate trends for various minerals (plagioclase, pyroxene, olivine) are similar, with slopes around −1.12 ± 0.14 (**Table IV-2**). Only 6 of 18 runs held at the final temperature yielded usable J values, due to N_V decreasing with increasing dwell time, producing negative J values. Applying the standard J_{Batch} equation is not appropriate here, as it neglects the two-step (cooling + dwell) experimental design. The sharp decrease in nucleation rate and the reduced abundance of small crystals (<10 µm; **Figure IV-7e**; **Table IV-2**) are suggestive of post-nucleation processes associated with textural maturation (or textural coarsening; *Cabane et al. 2005; Higgins 2011*), which is consistent with the downturn of the CSD curve at smallest sizes (**Figure IV-8**).

			$Log(G) = a \times Log(t_{dwell\ time}) + b$						$Log(J) = a \times Log(t_{dwell\ time}) + b$		
			G_{mean}			G_{max}			J_{Batch}		
Study	H_2O wt. %	Mineral	a	b	R^2	a	b	R^2	a	b	R^2
Our data	0	Pl	-1.14	-2.42	0.93	-1.21	-1.67	0.83	-1.28	8.1	0.88
Cabane et al. (2005)	0	Pl	-1.18	-3.54	0.89	-	-	-	-	-	-
Cabane et al. (2005)	0	Ol	-0.81	-4.57	0.93	-	-	-	-	-	-
Pontesilli et al. (2019)	0	Px	-	-	-	-1.14	-2.43	0.92	-	-	-
Pontesilli et al. (2019)	2	Px	-	-	-	-0.99	-3.07	0.59	-	-	-
Pontesilli et al. (2019)	0	Fe-Ti oxide	-1.29	-3.05	0.86	-1.13	-3.39	0.91	-	-	-
Pontesilli et al. (2019)	2	Fe-Ti oxide	-0.45	-6.25	0.19	-2.48	2.85	0.47	-	-	-
Arzilli et al. (2015)	< 1	Pl	-	-	-	-1.23	-1.69	0.77	-4.23	18.87	0.81

***Table IV-2**: Comparison of linear regression parameters for log(G_i) and log(J_i) versus log($t_{dwell\ time}$) obtained in this study and previous isothermal/isobaric experiments. Data correspond to different minerals (olivine, plagioclase, pyroxene, and Fe-Ti oxides) under dry and hydrous conditions.*

The impact of superheating on nucleation and growth rates

The initial temperature relative to the liquidus strongly influences crystal number density during cooling (**Table IV-1**). Compositions OS36 and OS36* differed only in the presence of visible pre-existing plagioclase fragments in OS36 (3.58×10^{-6} to 2.23×10^{-5} µm^{-2}, i.e., <1% of total crystals). However, even such low abundances significantly enhanced N_A by 1–2 orders of magnitude, as previously reported for olivine (*Lofgren 1989*; *Anwar et al. 2015*; *Auxerre et al. 2022*). *Dowty (1980)* attributed this to cavitation, where adding a single seed induces abundant nucleation through local undercooling enhanced by mechanical agitation or shock waves. At 1210 °C ($+\Delta T = 35$ °C), the N_A ratio between experiments initially maintained at 1190 and 1210 °C was 2.09×10^{-3} at the onset of crystallization, consistent with the suggestion of *Arzilli et al. (2015)* that a high degree of superheating followed by a low degree of undercooling is thermodynamically unfavorable to nucleation. As crystallization progressed, sustained nucleation in runs containing plagioclase fragments increased the ratio to 1.44×10^{-2} in runs without an intermediate isothermal step ($+\Delta T = 35$–275 °C), and to 1.40 in runs with such a step ($+\Delta T = 15$ °C; OS36*).

Nucleation and growth rates were similar for all experiments initially held 35–55 °C above the liquidus, and were respectively 1–2 orders of magnitude lower (J) and higher (G) than in seed-bearing runs (**Figure IV-7; *Supplementary file IV-3***). When an additional intermediate isothermal step ($+\Delta T = 15$ °C) was included, the magnitude of the difference was only approximately one order. Interestingly, in isothermal runs, this trend was reversed: nucleation rates were 1–2 orders of magnitude higher in unseeded runs. This opposite trend may reflect an episode of overgrowth favored in isothermal runs conducted with OS36, explaining both the rounded crystal shapes and the reduced nucleation. Combined with insufficient elemental supersaturation or an overly short dwell time, plagioclase crystals may thus display anhedral morphologies.

As shown previously (*Grove 1978*; *Kohut and Nielsen 2004*; *Billon et al. 2025*), the $\log(J)$ and $\log(G)$ versus $\log(t)$ trends follow linear regressions with R^2 values between 0.90 and 0.98 (**Figure IV-10a**, **b; *Supplementary file IV-4***). The slopes of the trends are also similar: −1.03 (±0.01) for J and −1.01 (±0.03) for G, reflecting consistent time dependence. These trends are comparable between the various experimental series conducted at various initial degrees of superheating. Nonetheless, the intercepts are higher for G and lower for J in strongly superheated runs, suggesting that superheating enhances skeletal/dendritic growth while inhibiting nucleation. Nucleation appears strongly controlled by the initial material, with higher

J intercepts in seed-bearing runs, even when cooling in highly superheated runs was preceded by a moderate superheating step. The log(*J*)–log(*t*) regression was poor for highly superheated runs (+Δ*T* = 35–55 °C) due to low nucleation and limited data (only 3–34 crystals).

The log(G)–log(t) trends align with growth rate measurements from *Pupier et al. (2008)*, who used synthetic crystal-free material and low degrees of superheating (+5–15 °C). However, their intercept (−4.11) is 41 % lower than in our seeded runs (and 105 % lower compared to our runs using OS36*), while their crystal shapes more closely resemble those in our seeded experiments.

Factors impacting the nucleation process

The role of the substrate

Although the starting temperature of the experiment exerts a fundamental control on nucleation, other parameters such as the initial liquid composition (*Iezzi et al. 2008*; *Vetere et al. 2013*) and the nature of substrates also influence nucleation. Heterogeneous nucleation has long been used in ceramic systems (*Norton 1937*; *Holand et al. 2003*; Deubener *and Höland 2017*) and is often used to trigger solidification near the liquidus (*Berkebile and Dowty 1982*). In the case of our initially highly superheated cooling runs (**Figure IV-1c**), most nucleation occurred at the sample edges (**Fig. *IV-S4d***) and on the Pt wire, especially at low effective degrees of undercooling in seed-bearing runs ($-\Delta T_n$ = 15 °C; **Fig. *S4a***; see also *Dowty 1980*; *Lofgren and Smith 1980*; *Pupier et al. 2007*). In contrast, *Iezzi et al. (2008)* and *Mollo et al. (2012)* did not report such effects at Pt substrates in their experiments. *Mollo et al. (2012)* attributed this to the use of a differentiated trachytic melt with low cation diffusivity, delaying nucleation. They also explained that the high oxidation temperature (~1300 °C) limited iron diffusion from the melt to the Pt substrate, preventing the formation of iron-rich particles to act as preferential nucleation sites for clinopyroxene. Although the Pt wire promotes early nucleation at low degrees of undercooling, it represents only a small fraction of the area examined (4 ± 2%) and cannot explain the overall high crystal abundances observed (**Fig. *IV-S4c***). However, when coupled with a heterogeneous distribution of nucleation sites within the melt (*Billon et al. 2025*), this could explain the lower experimental reproducibility observed at the onset of crystallization (G 2-1a and b, cooled at 3 °C/h and quenched at 1165 °C in *Billon et al. 2025*).

Substrate crystal structure is also known to affect nucleation. *Mollo et al. (2012)* found that nucleation was promoted for phases structurally similar to the seed mineral. *Holness et al. (2023)* argued that heterogeneous nucleation on a substrate of the same phase is thermodynamically disfavored, and that continuous growth is more likely. This aligns with our observations of plagioclase overgrowths around anorthite seeds (**Figure IV-2c**, **Figure IV-3c**; ***IV-S4b***) and the dendritic nucleation of oxides and pyroxene on plagioclases at 1050–1000 °C (**Figure IV-3e**; ***IV-S4f***).

The effect of thermal history on nucleation

Crystal number density and delayed nucleation depend on the critical radius (r^*), which must be exceeded for growth (>1 µm; *Davis 2001*). According to *Donaldson (1979)* and *Kirkpatrick (1981)* at, or slightly below, the liquidus r^* is large, inhibiting nucleation. At lower temperatures, r^* decreases, allowing significant nucleation with high N_A. This consideration of homogeneous nucleation contrasts with our experimental results, which show significant nucleation beginning at $-\Delta T_n$ = 5–15 °C, depending on the experimental path (cooling vs. isothermal). As noted by *Billon et al. (2025)*, in seed-bearing runs cooled at 1–9 °C/h, the maximum nucleation rate occurs early during crystallization ($-\Delta T_n \approx 15$ °C); this may be explained by several factors, including initial long relaxation times, slow cooling rates, or heterogeneous nucleation.

Donaldson (1979) suggested that higher cooling rates promote increased nucleation but at lower temperatures (*Walker et al. 1976*). The J_{Batch} vs. temperature plot (***Supplementary File IV-3***) reveals a clear shift in the temperature at which the maximum nucleation rate occurs, from 1165 °C at 1 °C/h to 1140 and 1100 °C at 9 and 25 °C/h, respectively. At 125 °C/h, nucleation occurred even later (1100 °C) and increased until 1050 °C (**Figure IV-4d**). A similar shift also appeared in fully molten samples (OS36*), where number densities increased significantly at 1050 °C (**Table IV-1**).

Other parameters such as the initial material composition (natural, synthetic, or fully molten) or the degree of superheating can indirectly affect r^*, dissolving potential nucleation sites (crystal seeds, glass fragments). Accordingly, an important outstanding question is: can nucleation truly be homogeneous, or does it mainly rely on heterogeneous nucleation on sites such micro-crystal fragments, trace dissolved elements, or bubble surfaces?

Nucleation style related to the initial thermal treatment

The use of seeds as sites for the nucleation of new crystals is common (*Mollo et al. 2012*; *Anwar et al. 2015*), sometimes referred to as "self-nucleation" for the growth of a similar crystalline structure around a seed (purple areas in **Figure IV-3c; Fig. S in *Supplementary file 1***; *Shea and Hammer 2013*; *Holness et al. 2023*; *Billon et al. 2025*). An example of true heterogeneous nucleation is plagioclase nucleation on the surface of gas bubbles (**Fig. *IV-S4e***), and the nucleation of clinopyroxene and Fe-Ti oxides on a plagioclase substrate (**Figure IV-3d and e**). In turn, newly formed crystals can themselves act as seeds, enabling further nucleation through various mechanisms, such as crystal motion, or inter-crystal contact (*Dowty 1980*; *Cui and Myerson 2014*; *Anwar et al. 2015*).

Studies using fully molten samples (*Lofgren 1974*; *Donaldson 1979*) interpreted the resulting microstructures as a product of internal homogeneous nucleation. However, the dendritic and skeletal plagioclase crystals in our unseeded cooling runs tended to appear first along the sample edges (**Figure IV-3d** and ***IV-S4d***; *Berkebile and Dowty 1982*). This, together with the limited increase in crystal number density (N_A), the absence of small crystals (≤10 µm), and the apparent consistency of crystal shape in initially highly superheated runs point to the occurrence of a single heterogeneous nucleation event. This behavior contrasts the continuous nucleation observed in seeded experiments, which are characterized by broad ranges of crystal sizes and shapes (**Figure IV-2c, d**, **Figure IV-3a–c**). Secondary nucleation, due perhaps to the formation of semi-ordered clusters at the interface of pre-existing crystals, or to micro-attrition processes (e.g., mechanical breakage or collision between crystals larger than 10 µm; *Cui and Myerson 2014*), may account for the observed continuous character of nucleation at high degrees of effective undercooling ($-\Delta T_n$ = 10–125 °C).

Although we cannot exclude the process of internal homogeneous nucleation in cooling or isothermal experiments using either seeded or crystal-free materials, super-liquidus survival of nanometric/micrometric residual substrates (crushing impurities, nanometric clusters, or gas bubbles) is sufficient to promote nucleation (*Lofgren et al. 1978*; *Berkebile and Dowty 1982*; *Davis and Ihinger 1998*), with perhaps 10^5 - 10^6 potential heterogeneities per centimeter that are too small to observe (<0.1 µm in size; *Turnbull 1956, 1969*). The presence of such nanometric/micrometric nucleation sites could therefore explain the continuous nucleation observed when a subliquidus isothermal step is added, even in initially crystal-free systems. A similar mechanism may account for the euhedral olivine shapes reported by *Pupier et al. (2008)*, despite their use of a nominally crystal-free synthetic material. Such synthetic compositions are

often prepared from mixed oxide powders, which can contain potential nucleation sites and may explain the differences compared to our experiments using fully molten natural glass. Finally, when nucleation sites are homogeneously distributed throughout the melt, heterogeneous nucleation can become indistinguishable from truly homogeneous nucleation, as observed in our rapidly cooled seeded experiments (e.g., 125 °C/h; T_f = 1100 °C).

This ambiguity between homogeneous and heterogeneous nucleation is also supported by the empirical relationship proposed by *Toramaru and Kichise (2023)* and *Toramaru (2025)*, linking crystal number density (N_A) to cooling or decompression rate as a function of the abundance of heterogeneous nucleation sites:

$$\log(N_A) = \xi \times \frac{dT}{dt} \quad (6)$$

where ξ reflects the nucleation type and is assigned values of 3/2 or −1 for purely homogeneous or heterogeneous nucleation, respectively. In our seeded experiments, ξ values ranged from 0.2 (1–9 °C/h) to −0.4 (9–125 °C/h), whereas those in initially crystal-free runs varied from 0.48 to −0.55. These values are consistent with those reported by *Toramaru and Kichise (2023)*, indicating a mixed regime combining both homogeneous and heterogeneous nucleation, with the relative contribution of each depending on undercooling intensity and substrate availability.

Nucleation mechanism link to the superheating effect

Although the degree and duration of superheating (*First et al. 2020*) impact the style and efficiency of nucleation, questions remain regarding the underlying mechanism. It may result either from incomplete structural rearrangement of the melt or from the removal of nanometric particles or bubbles. Some studies tend to support the second hypothesis (*Dingwell 2006*; *Vetere et al. 2013*), suggesting that structural reorganization occurs almost instantaneously at high temperatures.

We used the Maxwell relation (*Vetere et al. 2013*) to constrain the timescale of structural relaxation (τ) of the silicate melt in our experiments (***Supplementary file IV-3***):

$$\tau = \frac{\eta}{S_h} \quad (7)$$

with η being the melt viscosity (Pa s) calculated at 1190, 1200, and 1450 °C, and S_h the shear modulus (~10 GPa; *Richer 2002*; *Webb 2005*; *Vetere et al. 2013*). τ reflects the equilibration timescale for slow-diffusing Si cations. At 1190 °C, τ ranges from 10^{-3} to 10^{-4} minutes, increasing to ~30 minutes at 1000 °C ($\eta \approx 10^7$ Pa s). These values are consistent with the results of *Vetere et al. (2013)* (10^{-6}–10^{-9} minutes at 1300 °C for basaltic and rhyolitic melts) and remain negligible during our 24-hour isothermal experiments. Thus, structural relaxation in silicate melts is effectively instantaneous over the experimental durations at superliquidus temperatures and is largely independent of the crystallization path. This agrees with our observations that superheating to 1210–1230 °C ($+\Delta T$ = 35–55 °C) yields similar nucleation behavior. *Tsuchiyama (1983)* noted that when superheating exceeds 40 °C for more than 45 minutes, the magnitude of superheating has a comparable effect on nucleation.

The second hypothesis related to the timescale and minimum length required for melt re-homogenization (i.e., the suppression of microscopic gas bubbles, chemical inhomogeneities, or soluble surface impurities) was tested by calculating the diffusion length, x, (*Vetere et al. 2013*) of the main cations (Al, Ca, Mg, and Si) as:

$$x = \sqrt{2D \times t} \quad (8)$$

where D corresponds to the cation's diffusivity, and t is the experimental duration (5–168 hours). Cation diffusivities were estimated using the Eyring relation (D_η; *Chakraborty 1995*) for Si and empirical equations (35), (25), and (22) from *Zhang et al. (2010)* for Al, Ca, and Mg, respectively (see ***Supplementary File IV-3***). The resulting diffusion lengths (277 µm at 1200 °C to 58 µm at 1000 °C) suggest that only impurities larger than ~280 µm may persist after prolonged superliquidus heating. This explains the variable seed number density observed in our experiments, which was consistently far less than 1% of the total crystallinity. Importantly, this process concerns only soluble particles (*Vetere et al. 2013*). As observed by *Berkebile and Dowty (1982)*, the absence of internal nucleation in runs heated to 15 °C above the liquidus, but without a subliquidus isothermal step, supports two conclusions: (i) internal nucleation is likely controlled by residual soluble particles (e.g., nanometric gas bubbles, local chemical inhomogeneities, or contaminants introduced by the experimental setup); and (ii) maintaining the temperature close to the liquidus (here a $+\Delta T$ = 15 °C) is required to regenerate such particles. However, due to the size range involved and the absence of nanoscale observations, it remains impossible to distinguish conclusively between truly homogeneous nucleation and

heterogeneous nucleation initiated by submicroscopic impurities or gas bubbles distributed homogenously throughout the melt (*Davies and Ihinger 1998*).

Conclusions and implications for natural rocks

Rock microstructure result from a complex interplay between phase assemblage and crystal shape, size, number density, and spatial distribution. Among these, nucleation plays a key role in controlling the final number of crystals. Our experiments demonstrate that thermal history, especially the degree of initial superheating and the cooling or decompression rate, strongly influences the timing and efficiency of nucleation. A modest initial degree of superheating of just 35 °C is sufficient to significantly suppress nucleation (**Figure IV-11b**), reducing crystal number densities by as much as two orders of magnitude. In comparison, achieving a similar effect through cooling alone would require a 100-fold increase of the cooling rate, highlighting the dominant control of superheating on nucleation behavior.

Crystal growth mechanism correlate strongly with the nucleation regime. At low degrees of undercooling, large and euhedral phenocrysts form, whereas greater degrees of undercooling, often caused by prior superheating or rapid cooling, favor the development of numerous skeletal or dendritic microlites, whose size is limited by the available space within the residual melt (**Figure IV-11a**). At such high degrees of undercooling, fast growth produces disequilibrium features such as complex twinning. As noted by *Cabane et al. (2005)*, Ostwald ripening in plagioclase is sluggish, and likely ineffective on short timescales, explaining the absence of euhedral shapes.

The spatial distribution of crystals also reflects the type of nucleation and thermal path. In strongly superheated runs, nucleation is not only delayed, but is often restricted to a few sites permitting heterogeneous nucleation such as on the Pt wire or sample edges (**Figure IV-11b**). In the most extreme cases, nucleation is nearly suppressed or limited to a single event. Although true homogeneous nucleation remains rare due to the existence of microscopic substrates in the melt, intermediate conditions may cause continuous mixed nucleation with both internal and edge-related events, especially early during crystallization.

These experimental insights have important implications for natural systems: phenocrysts likely reflect subliquidus crystallization with limited nucleation, whereas microlite-rich textures suggest moderate superheating and more efficient nucleation. As shown in our isothermal experiments, gas bubbles, particularly during decompression, can act as

effective nucleation sites, promoting the formation of abundant, small plagioclase laths as magma rises prior to eruption.

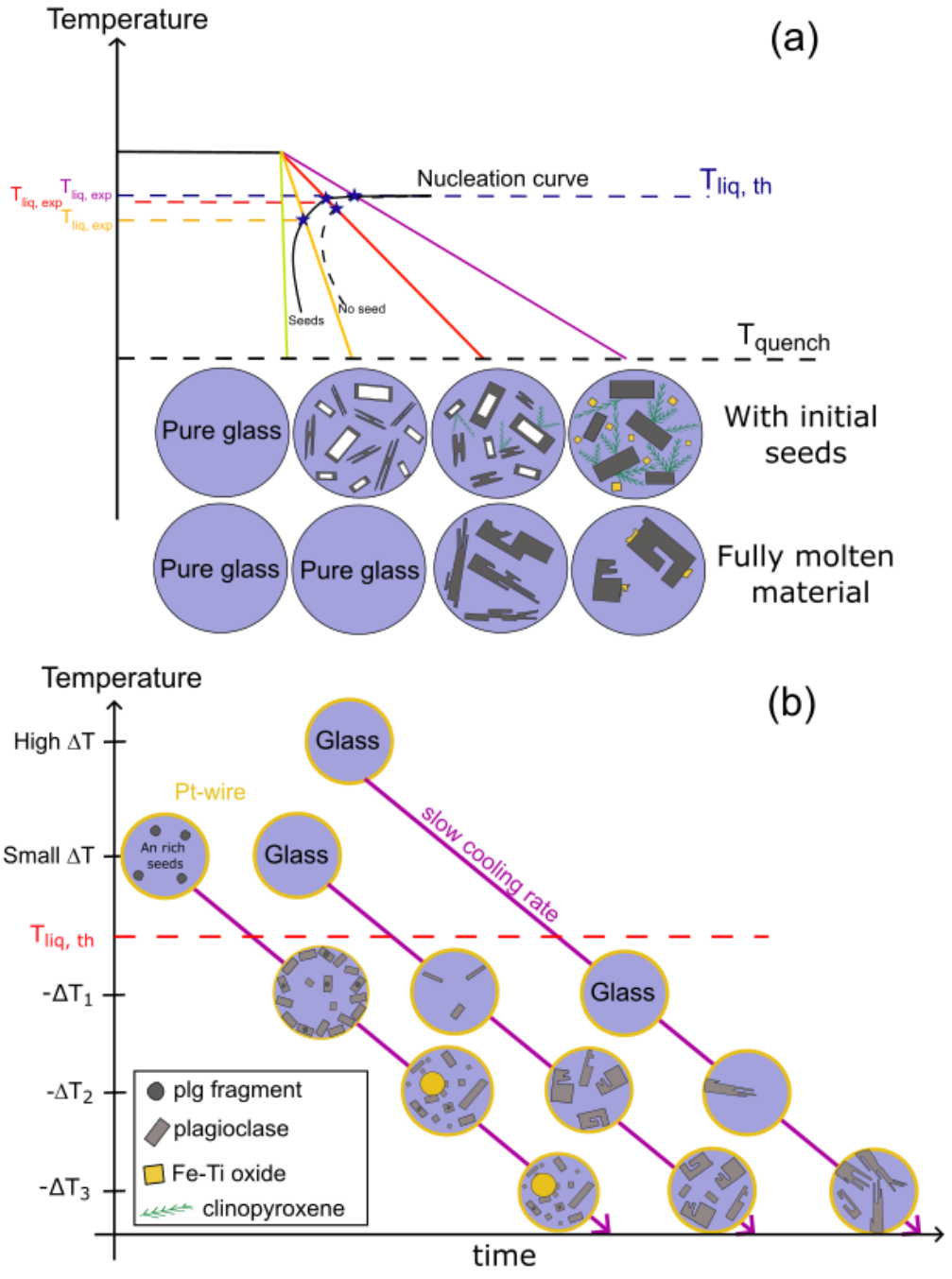

***Figure IV-11**: Schematic time–temperature–transformation diagrams illustrating microstructural evolution in terms of the degree of initial superheating and cooling rate. **a** Final microstructures resulting from different cooling rates. The progressive decrease of the liquidus temperature is also represented. **b** Microstructural evolution during slow cooling from different initial temperatures relative to the liquidus.*

References

Anwar J, Khan S, and Lindfors L (2015). Secondary Crystal Nucleation: Nuclei Breeding Factory Uncovered. Angewandte Chemie International Edition 54:14681–14684. https://doi.org/10.1002/anie.201501216

Arzilli F, Agostini C, Landi P, Fortunati A, Mancini L, Carroll MR (2015). Plagioclase nucleation and growth kinetics in a hydrous basaltic melt by decompression experiments. Contributions to Mineralogy and Petrology 170, 55. https://doi.org/10.1007/s00410-015-1205-9

Auxerre M, Faure F, Lequin D (2022). The effects of superheating and cooling rate on olivine growth in chondritic liquid. Meteoritics and Planetary Science 57:1474–1495. https://doi.org/10.1111/maps.13830

Bechon T, Billon M, Namur O, Bolle O, Fugmann P, Foucart H, Devidal J-L, Delmelle N, Vander Auwera J (2022). Petrology of the magmatic system beneath Osorno volcano (Central Southern Volcanic Zone, Chile). Lithos 426–427, 106777. https://doi.org/10.1016/j.lithos.2022.106777

Becker R, Doring W (1935). Kinetische behandlung der keim buildung in ubersattingten dampfen. Ann Physik 5 :719-752. https://doi.org/10.1002/andp.19354160806

Bennett EN, Lissenberg CJ, Cashman KV (2019). The significance of plagioclase textures in mid-ocean ridge basalt (Gakkel Ridge, Arctic Ocean). Contribution to Mineralogy and Petrology, 174:49. https://doi.org/10.1007/s00410-019-1587-1

Berkebile CA, Dowty E (1982). Nucleation in laboratory charges of basaltic composition. American Mineralogist 67:886-899.

Billon M, Vander Auwera J, Namur O, Faure F, Holness MB, Charlier B (2025). Plagioclase crystal size distributions, growth and nucleation rates in an anhydrous arc basaltic andesite. Contributions to Mineralogy and Petrology 180(26). https://doi.org/10.1007/s00410-025-02213-9

Bonechi B (2020). Influence of Pre-Existing Nuclei on the Crystallization Kinetics of Primitive Alkaline Magmas: Insights on the Deep Feeding System of the Campi Flegrei Volcanic District. Minerals 10(3), 234. https://doi.org/10.3390/min10030234

Brugger CR, Hammer JE (2015). Prevalence of growth twins among anhedral plagioclase microlites. American Mineralogist 100:385–395. https://doi.org/10.2138/am-2015-4809

Cabane H, Laporte D, Provost A (2001). Experimental investigation of the kinetics of Ostwald ripening of quartz in silicic melts. Contributions to Mineralogy and Petrology 142:361–373. https://doi.org/10.1007/s00410-005-0002-2

Cabane H, Laporte D, Provost A (2005). An experimental study of Ostwald ripening of olivine and plagioclase in silicate melts: implications for the growth and size of crystals in magmas. Contributions to Mineralogy and Petrology 150:37–53. https://doi.org/10.1007/s00410-005-0002-2

Chakraborty S (1995). Chapter 10. DIFFUSION IN SILICATE MELTS. In: Stebbins, J. F., McMillan, P. F. and Dingwell, D. B. (eds) Structure, Dynamics, and Properties of Silicate Melts. De Gruyter, 411–504.

Conte AM, Perinelli C, Trigila R (2006). Cooling kinetics experiments on different Stromboli lavas: Effects on crystal morphologies and phases composition. Journal of Volcanology and Geothermal Research 155(3-4): 179–200. https://doi.org/10.1016/j.jvolgeores.2006.03.025

Couch S, Sparks RSJ, Carroll MR (2003). The Kinetics of Degassing-Induced Crystallization at Soufriere Hills Volcano, Montserrat. 44(8):1477-1502. https://doi.org/10.1093/petrology/44.8.1477

Cui Y, Myerson AS (2014). Experimental Evaluation of Contact Secondary Nucleation Mechanisms. Crystal Growth and Design 10, 5152–5157. https://doi.org/10.1021/cg500861f

Davis MJ (2001). Effect of the Growth Treatment on Two-Stage Nucleation Experiments. Journal of the American Ceramic Society 84(3):492-496. https://doi.org/10.1111/j.1151-2916.2001.tb00688.x

Davis MJ, Ihinger PD (1998). Heterogeneous crystal nucleation on bubbles in silicate melt. American Mineralogist 83:1008–1015.

Deubener J, Höland W (2017). Editorial: Nucleation and Crystallization of Glasses and Glass-Ceramics. Frontiers in Materials 4. https://doi.org/10.3389/fmats.2017.00014

Dickinson E, Ettelaie R, Kostakis T, Murray BS (2004). Factors Controlling the Formation and Stability of Air Bubbles Stabilized by Partially Hydrophobic Silica Nanoparticles. Langmuir 20:8517–8525. https://pubs.acs.org/doi/10.1021/la048913k

Dingwell DB (2006). Transport Properties of Magmas: Diffusion and Rheology. Elements 2(5):281–286. https://doi.org/10.2113/gselements.2.5.281

Donaldson CH (1979). An experimental investigation of the delay in nucleation of olivine in Mafic Magmas. Contributions to Mineralogy and Petrology 69:21–32. https://doi.org/10.1007/BF00375191

Du Z, Bilbao-Montoya MP, Binks BP, et al. (2003). Outstanding Stability of Particle-Stabilized Bubbles. Langmuir 19:3106–3108. https://doi.org/10.1021/la034042n

Fan GJ, Choo H, Liaw PK (2007). A new criterion for the glass-forming ability of liquids. Journal of Non-Crystalline Solids 353(1):102–107. https://doi.org/10.1016/j.jnoncrysol.2006.08.049

Faure F, Tissandier L (2014). Contrasted Liquid Lines of Descent Revealed by Olivine-hosted Melt Inclusions and the External Magma. Journal of Petrology 55(9):1779–1798. https://doi.org/10.1093/petrology/egu041

Fenn PM (1977). The nucleation and growth of alkali feldspars from hydrous melts. Journal of the Mineralogical Association of Canada 15, 135-161.

First EC, Leonhardi TC, Hammer JE (2020). Effects of superheating magnitude on olivine growth. Contributions to Mineralogy and Petrology 175, 13. https://doi.org/10.1007/s00410-019-1638-7

Fokin VM, Potapov OV, Chinaglia CR, Zanotto ED (1999). The effect of pre-existing crystals on the crystallization kinetics of a soda-lime-silica glass. The courtyard phenomenon. Journal of Non-Crystalline Solids 258:180-186. https://doi.org/10.1016/S0022-3093(99)00417-2

Fokin V M, Zanotto ED, Schmelzer JWP (2003). Homogeneous nucleation versus glass transition temperature of silicate glasses. Journal of Non-Crystalline Solids 321:52–65. https://doi.org/10.1016/S0022-3093(03)00089-9

Fokin VM, Zanotto ED, Yuritsyn NS, Schmelzer JWP (2006). Homogeneous crystal nucleation in silicate glasses: A 40 years perspective. Journal of Non-Crystalline Solids 352:2681–2714. https://doi.org/10.1016/j.jnoncrysol.2006.02.074

Fonseca I (1991). The Wulff Theorem Revisited. Proceedings of the Royal Society A 432(1884). https://doi.org/10.1098/rspa.1991.0009

Gibb FGF (1974). Supercooling and the crystallization of plagioclase from a basaltic magma. Mineralogical Magazine 39, 641–653. https://doi.org/10.1180/MINMAG.1982.046.338.06

Grove TL (1978). Cooling history of Luna 24 very low Ti (VLT) ferrobasalts: An experimental study. Proc. Lunar Planet. Sci. Conf 9th, 565-584

Grove TL (1982). Use of FePt alloys to eliminate the iron loss problem in 1 atmosphere gas mixing experiments: Theoretical and practical considerations. Contributions to Mineralogy and Petrology 78:298–304. https://doi.org/10.1007/BF00398924

Gualda GAR, Ghiorso MS, Lemons RV, Carley TL (2012). Rhyolite-MELTS: a Modified Calibration of MELTS Optimized for Silica-rich, Fluid-bearing Magmatic Systems. Journal of Petrology 53(5):875–890. https://doi.org/10.1093/petrology/egr080

Herring C (1951). Some Theorems on the Free Energies of Crystal Surfaces. Physical Review 82:87–93. https://doi.org/10.1103/PhysRev.82.87

Higgins MD (2000). Measurement of crystal size distributions. American Mineralogist 85:1105–1116. https://doi.org/10.2138/am-2000-8-901

Higgins MD (2011). Textural coarsening in igneous rocks. International Geology Review, 53(3–4), 354–376. https://doi.org/10.1080/00206814.2010.496177

Höland W, Rheinberger V, Schweiger M (2003). Control of nucleation in glass ceramics. Philosophical Transactions of the Royal Society of London. Series A: Mathematical, Physical and Engineering Sciences 361:575–589. https://doi.org/10.1098/rsta.2002.1152

Holness MB, Vukmanovic Z, O'Driscoll B (2023). The Formation of Chromite Chains and Clusters in Igneous Rocks. Journal of Petrology 64(1):egac124. https://doi.org/10.1093/petrology/egac124

Iezzi G, Mollo S, Ventura G, Cavallo A, Romana C (2008). Experimental solidification of anhydrous latitic and trachytic melts at different cooling rates: The role of nucleation kinetics. Chemical Geology 253(3-4):91-101. https://doi.org/10.1016/j.chemgeo.2008.04.008

Iezzi G, Mollo S, Torresi G, et al. (2011). Experimental solidification of an andesitic melt by cooling. Chemical Geology 283(3-4):261–273. https://doi.org/10.1016/j.chemgeo.2011.01.024

James PF (1974) Kinetics of crystal nucleation in lithium silicate glasses. Physics and Chemistry of Glasses 15:95-105.

Kashchiev D (1969). Solution of the non-steady problem in nucleation kinetics. Surface Science. 14(1):209–220. https://doi.org/10.1016/0039-6028(69)90055-7

Kirkpatrick RJ (1976). Towards a Kinetic Model for the Crystallization of Magma Bodies. Journal Of Geophysical Research 81(14):2565-2571. https://doi.org/10.1029/JB081i014p02565

Kirkpatrick RJ (1977). Nucleation and growth of plagioclase, Makaopuhi and Alae lava lakes, Kilauea Volcano, Hawaii. Geological Society of America Bulletin 88(1):78-84. https://doi.org/10.1130/0016-7606%281977%2988%3C78%3ANAGOPM%3E2.0.CO%3B2

Kirkpatrick RJ (1981). Kinetics of crystallization of igneous rocks. Rev. Mineral 8.

Kohut E, Nielsen RL (2004). Melt inclusion formation mechanisms and compositional effects in high-An feldspar and high-Fo olivine in anhydrous mafic silicate liquids. Contributions to Mineralogy and Petrology 147:684–704. https://doi.org/10.1007/s00410-004-0576-0

Lasaga AC (1998). Kinetic Theory in the Earth Sciences. Princeton Series in Geochemistry. x+811 pp. Princeton, Chichester: Princeton University Press. Geological Magazine 137(5):593-598. https://doi.org/10.1017/S0016756800234614

Lofgren G (1974). An experimental study of plagioclase crystal morphology: Isothermal crystallization. American Journal of Science 274(3):243-273. https://doi.org/10.2475/ajs.274.3.243

Lofgren GE (1983). Effect of Heterogeneous Nucleation on Basaltic Textures: A Dynamic Crystallization Study. Journal of Petrology 24:229–255.

Lofgren GE (1989). Dynamic crystallization of chondrule melts of porphyritic olivine composition: Textures experimental and natural. Geochimica et Cosmochimica Acta 53, 461-470. https://doi.org/10.1016/0016-7037(89)90397-9

Lofgren GE, Smith DP, Brown RW (1978). Dynamic crystallization and kinetic melting of the lunar soil. Proc. Lunar Planet Sci. Conf. 9th, 959-975.

Mangler MF, Humphreys MCS, Wadsworth FB, et al. (2022). Variation of plagioclase shape with size in intermediate magmas: a window into incipient plagioclase crystallisation. Contributions to Mineralogy and Petrology 177(64). https://doi.org/10.1007/s00410-022-01922-9

Mangler MF, Humphreys MCS, Geifman E, et al. (2023). Melt Diffusion-Moderated Crystal Growth and its Effect on Euhedral Crystal Shapes. Journal of Petrology 64(8):egad054. https://doi.org/10.1093/petrology/egad054

Mollo S, Iezzi G, Ventura G, et al. (2012). Heterogeneous nucleation mechanisms and formation of metastable phase assemblages induced by different crystalline seeds in a rapidly cooled andesitic melt. Journal of Non-Crystalline Solids 358 (12-13):1624–1628. https://doi.org/10.1016/j.jnoncrysol.2012.04.010

Norton BFH (1937). The control of crystalline glazes. Journal of the American Ceramic Society 20:217–224.

O'Hara M, Biggar G, Richardson S, et al. (1970). The nature of mascons, seas, and the lunar interior in the light of experimental studies, Proc Apollo 11 Lunar Science Conference 1, 695.

Pontesilli A, Masotta M, Nazzari M, et al. (2019). Crystallization kinetics of clinopyroxene and titanomagnetite growing from a trachybasaltic melt: New insights from isothermal time-series experiments. Chemical Geology 510:113–129. https://doi.org/10.1016/j.chemgeo.2019.02.015

Pupier E, Duchene S, Toplis MJ (2008). Experimental quantification of plagioclase crystal size distribution during cooling of a basaltic liquid. Contributions to Mineralogy and Petrology 155, 555–570. https://doi.org/10.1007/s00410-007-0258-9

Richet P (2002). Enthalpy, volume and structural relaxation in glass-forming silicate melts. Journal of Thermal Analysis and Calorimetry 69:739–750. https://doi.org/10.1023/a:1020635401536

Rusiecka MK, Bilodeau M, Baker DR (2020). Quantification of nucleation delay in magmatic systems: experimental and theoretical approach. Contributions to Mineralogy and Petrology 175(5), 47. https://doi.org/10.1007/s00410-020-01682-4

Schmelzer JWP., Abyzov AS, Ferreira EB, et al. (2019a). Curvature dependence of the surface tension and crystal nucleation in liquids. International Journal of Applied Glass Science 10(1):57–60. https://doi.org/10.1111/ijag.12900

Schmelzer JWP, Abyzov AS, Baidakov VG (2019b). Entropy and the Tolman parameter in nucleation theory. Entropy 21(7), 670. https://doi.org/10.3390/e21070670

Schneider CA, Rasband WS, Eliceiri KW (2012). NIH Image to ImageJ: 25 years of image analysis. Nature Methods 9:671–675. https://doi.org/10.1038/nmeth.2089

Shea T, Hammer JE (2013). Kinetics of cooling- and decompression-induced crystallization in hydrous mafic-intermediate magmas. Journal of Volcanology and Geothermal Research 260:127–145. https://doi.org/10.1016/j.jvolgeores.2013.04.018

Sirbescu M-LC, Schmidt C, Veksler IV, et al. (2017). Experimental crystallization of undercooled felsic liquids: generation of pegmatitic texture. Journal of Petrology 58:539–568. https://doi.org/10.1093/petrology/egx027

Swanson SE (1977). Relation of crystal-growth rate to the granitic textures. American Mineralogist 62:966–978.

Toramaru A (2025). The theoretical basis for textural indices of eruption dynamics: review and new conceptual models. Earth Planets Space 77, 27. https://doi.org/10.1186/s40623-025-02146-4

Toramaru A, Kichise T (2023). A new model of crystallization in magmas: impact of pre-exponential factor of crystal nucleation rate on cooling rate exponent and log-linear crystal size distribution. Journal of Geophysical Research: Solid Earth, 128:e2023JB026481. https://doi.org/10.1029/2023JB026481

Tsuchiyama A (1983). Crystallization kinetics in the system $CaMgSi_2O_6$-$CaAl_2Si_2O_8$: the delay in nucleation of diopside and anorthite. American Mineralogist 68(7-8):687-698

Turnbull D (1956). Phase Changes. Solid State Physics 3:225–306. https://doi.org/10.1016/S0081-1947(08)60134-4

Turnbull D (1969). Under what conditions can a glass be formed? Contemporary Physics 10:473–488. https://doi.org/10.1080/00107516908204405

Vetere F, Iezzi G, Behrens H, et al. (2013). Intrinsic solidification behaviour of basaltic to rhyolitic melts: A cooling rate experimental study. Chemical Geology 354:233–242. https://doi.org/10.1016/j.chemgeo.2013.06.007

Volmer M, Weber A (1926). Kimbildung in ubersattingten gebilden. Zeitschrift für Physikalische Chemie 119:277-301. https://doi.org/10.1515/zpch-1926-11927

Walker D, Kirkpatrick RJ, Longhi J, et al. (1976). Crystallization history of lunar picritic basalt sample 12002: Phase-equilibria and cooling-rate studies. Geological Society of America Bulletin 87(5):646-656. https://doi.org/10.1130/0016-7606(1976)87%3C646:CHOLPB%3E2.0.CO;2

Walker D (1978). Dynamic crystallization of a eucrite basalt. Lunar and Planetary Science Conference, 9th, 1369-1391.

Watson EB, Müller T (2009). Non-equilibrium isotopic and elemental fractionation during diffusion-controlled crystal growth under static and dynamic conditions. Chemical Geology 267(3-4):111–124. https://doi.org/10.1016/j.chemgeo.2008.10.036

Webb SL (2005). Silicate melts at extreme conditions. European Mineralogical Union 7. https://doi.org/10.1180/EMU-notes.7

Xu C, Zhao S-R, Li C, et al. (2016). Plagioclase twins in a basalt: an electron backscatter diffraction study. Journal of Applied Crystallography 49(Pt 6):2145–2154. https://doi.org/10.1107/S1600576716015739

Zhang Y, Ni H, Chen Y (2010). Diffusion Data in Silicate Melts. Reviews in Mineralogy and Geochemistry 72(1):311–408. https://doi.org/10.2138/rmg.2010.72.8

Chapter V

Textural Timescales in Arc Magmas: Insights from CSD Analyses

Submitted in *Journal of Volcanology and Geothermal Research*

Abstract

Crystallization timescales are commonly estimated using U-series dating and diffusion modeling, which provide absolute ages but require suitable accessory minerals such as zircon and well-preserved crystals. As an alternative, textural analyses based on crystal growth rates can yield complementary constraints on crystallization dynamics. Here, we determined crystallization timescales for three active Chilean volcanoes (Osorno, Calbuco, and Villarrica) using crystal size distribution (CSD) analysis. CSD-derived timescales range from a few days to about three years, depending on crystallization conditions and assumed growth rates (10^{-8}–10^{-12} cm/s). These durations are significantly shorter than those obtained from diffusion modeling (decades to centuries) or U-series disequilibria (tens of thousands of years), indicating that each method records distinct stages of magmatic evolution. Our results highlight the potential of CSD analysis to quantify short-lived crystallization episodes and to complement geochemical chronometers in reconstructing magmatic histories.

Key words: Timescales, CSD method, Growth rate, Phenocrysts

Introduction

Over the past 15 years, studies quantifying magmatic timescales have increased drastically, now exceeding 50 publications per year, largely driven by advances in experimental and analytical techniques (*Turner and Costa 2007*; *Petrelli and Zellmer 2021*). These timescales cover a variety of processes, ranging from magma transfer from depth to shallow reservoirs (*Turekian and Holland 2013*), to crustal magma storage (driven by mechanisms such as magma replenishment and mixing that promote magma stagnation and differentiation at a given depth; *Reid 2003*), and finally magma ascent toward the surface accompanied by decompression and volatile exsolution. Constraining such timescales is essential for understanding the dynamics of crustal magmatic systems and for improving volcanic hazard assessments. Petrological data can reveal key parameters such as the depth, thermal regime, and differentiation history of magmatic reservoirs (*Gudmundsson 2012*). However, estimating the duration of magmatic processes in shallow reservoirs immediately preceding eruptions remains particularly challenging (*Eppich et al. 2012*), and many questions persist regarding magma solidification and volcanic plumbing systems.

To quantify these different magmatic processes, a wide range of geochronological and petrological approaches has been developed, including thermal and mechanical modeling,

isotopic decay systems, diffusion chronometry, textural analyses, melt-inclusion studies, and the Microlite Number Density method (*MND*; *Toramaru et al. 2008*). The U-Th-Ra disequilibrium method for example, is used since more than 30 years to measure crystallization ages, and to provide absolute ages by analyzing isotopic ratios in bulk rocks, mineral separates, or individual crystals. Zircons and allanites for example are typically used to track long-term magma storage in large, silica-rich bodies, providing timescales of tens to hundreds of thousands of years (*Bourdon et al. 2003*; *Putirka 2008*), whereas Ra–Th disequilibria in feldspar aggregates capture shorter timescales, from hundreds to thousands of years. Concerning the diffusion chronometry, it is based on chemical re-equilibration, and allows to record much shorter events from hours to days for magma ascent and up to decades for storage and mixing (*Costa et al. 2020*). The wide range of reported timescales largely reflects the diversity of the dated processes (*Cooper et al. 2001*). Each chronometric method has its own advantages and limitations, and thus provides access to specific temporal windows. For instance, diffusion chronometry critically depends on well-constrained diffusion coefficients for the relevant element–mineral systems. Although recent experiments have refined several key diffusivities, the influence of important physico-chemical variables such as oxygen fugacity, water fugacity, and point-defect concentrations remains poorly quantified.

However, despite the rise of timescales studies, except those concerning the Mount Hood (*Cooper and Reid 2003*; *Eppich et al. 2012*; *Cooper and Kent 2014*) and Kīlauea (*Mangan 1990*; *Cooper et al. 2001*; *Rae et al. 2016*; *Lynn et al. 2017*), few have directly compared these techniques on a same volcano (*Cooper and Kent 2014*). Yet, the absence of suitable mineral phases or the presence of disequilibrium textures (e.g., melt inclusions, sieve textures) can limit the application of these methods. Chronometers based on bubbles/crystals textural analyses, such as nucleation and growth rates (*Kirkpatrick 1977*; *Dowty 1980*) correspond to an alternative approach to constrain magmatic durations without providing an absolute age for the rock or the event they record (*Cooper and Kent 2014*; *Costa et al. 2020*). The Crystal Size Distribution (CSD) method quantitatively links crystal population evolution to magmatic processes and remains one of the most robust tools for estimating crystallization timescales (*Marsh 1988, 1998*; *Cashman and Marsh 1988*; *Higgins 2006*).

The Southern Andes offers an exceptional natural laboratory, hosting more than 70 stratovolcanoes in an active subduction setting. Among them, Villarrica and Calbuco rank among the most active and hazardous volcanoes in the central Southern Volcanic Zone (CSVZ) of Chile, as shown by Calbuco's 2015 sub-Plinian eruption, which caused major economic and environmental impacts (*Hayes et al. 2019a and b*; *Namur et al. 2019*; *Vander Auwera et al.*

2021). Despite their activity, only two studies (*Morgado et al. 2019, 2022*) have attempted to constrain magmatic timescales in this region, both using diffusion chronometry. The main objective of this work is to assess how the CSD method can constrain magmatic timescales in active arc volcanoes. To achieve this, we analyze plagioclase crystal populations from three key volcanic centers of the central CSVZ: Osorno, Calbuco, and Villarrica, and compare the resulting timescales with those reported for similar systems worldwide.

CSD theory

The CSD theory, originally developed for steady-state crystallizers (*Randolph and Larson 1971*) and later adapted to less well-constrained magmatic systems (*Marsh 1988*; *Cashman and Marsh 1988*), describes the variation in crystal number as a function of size. The cumulative distribution is defined as:

$$N(L) = \int_0^L n(L)\ dL \quad (1)$$

where $n(L)$ corresponds to the population density. In an open magmatic system with size-independent growth rate G, the steady-state solution yields:

$$\ln\ n = \ln\ n_0 - \frac{L}{G\tau} \quad (2)$$

where $n_0$is the nucleation density at $L = 0$ and τ the crystal residence time. The slope of the linear CSD trend is therefore $-1/(G\tau)$. With known growth rates, residence times can be calculated, and the nucleation rate is given by $J = n_0 G$. CSD analysis thus provides quantitative constraints on nucleation, growth, and residence times in magmatic systems.

Geological context

The Andean Southern Volcanic Zone (SVZ) is a ~1400 km long (33 °S to 46 °S) volcanic chain of more than 70 Pleistocene and Holocene stratovolcanoes (closely averaging global arc composition; *Turner et al. 2016*) which correspond to the continental arc subduction of the oceanic Nazca plate below the South American continental plate (*Dewey and Lamb 1992*). It is accompanied by the NS regional Liquiñe-Ofqui Fault Zone (LOFZ), a 1200 km-

long transpressional NNE-trending dextral strikeslip structure, which affects much of the arc volcanism between ~38° and ~46°S (*Hickey-Vargas 2016*) (**Figure V-1a**). The Southern Volcanic Zone presents the particularity to be built on crust of variable thickness with a constant slab thermal parameter (*Turner et al. 2016*). It is subdivided into four segments on the basis of recent volcanic activity, including geochemical and petrologic considerations (*López-Escobar et al. 1995a*; *Stern 2004*; *Hickey-Vargas et al. 2016*) (**Figure V-1a**): the Northern (NSVZ, 33.3 to 34.4°S), Transitional (TSVZ, 34.4 to 37°S), Central (CSVZ, 37 to 42°S), and Southern (SSVZ, 42 to 46°S) zones. Crustal thickness in the SVZ decreases from 55 – 60km in the NSVZ to 35 – 55km in the TSVZ and <30 – 35km in the CSVZ and SSVZ (*Syracuse et al. 2010*; *Hickey- Vargas et al. 2016*).

The central part (CSVZ) includes several of the most active volcanoes in this segment, such as Calbuco (last eruption in 2015) and Villarrica, characterized by continuous degassing from a summit lava lake/vent punctuated by explosive events (*Gurioli et al. 2008*) (**Figure V-1a**). The CSVZ is bounded to the north (37°S) by the end of the Liquiñe–Ofqui Fault Zone (LOFZ), marking a change in basement composition from Meso-Cenozoic volcano-sedimentary rocks in the north to Meso-Cenozoic plutonic rocks of the Patagonian Batholith in the south (*Parada et al. 1987*). Quaternary volcanic rock compositions also evolve, dominated by andesitic to dacitic compositions in the north and basaltic to basaltic-andesitic in the south (*Hickey-Vargas et al. 2016b*).

Osorno

Osorno is an active stratovolcano of the CSVZ (41.06 °S, 72.20CW), and lies ~13 km west of the main trace of the LOFZ (**Figure V-1b**). It constitutes the southern and westernmost member of a NW alignment together with La Picada, Puntiagudo, and Cordón Cenizos (*Vander Auwera et al. 2019*). Its maximum height is 2661 m above sea level (m.a.s.l.), and its base level between 50 and 250 (m.a.s.l.). Its volume is estimated between 130 and 160 km^3, covering an area of 250 km^2 (*Moreno et al. 2010*; *Völker et al. 2011*). Its ice-capped summit has the potential to produce lahars, threatening the surrounding communities in a region that is rapidly growing economically, partly owing to increased tourism. Osorno is sixth on the Chilean volcanic risk ranking.

Its earliest activity dates from the Middle Pleistocene (~200 ka; *Moreno et al. 2010*). Its postglacial activity has been reported as summit crater eruptions, fissure-fed lava flows, and flank dacitic domes. The volcano has a record of around 15 effusive and explosive eruptions,

with a VEI between 1 and 3 (*Petit-Breuilh 1999*; *Smithsonian website*). The last major event occurred between January and December 1835 (VEI = 3), and since then activity has been limited to fumarolic episodes.

The Osorno volcano products vary from basalts to basaltic andesites with a few dacitic flows limited to domes (~50 – 70% SiO2; e.g. *Moreno et al. 2010*; *Bechon et al. 2022*), classified into four units (1, 2, 3, and 4) depending on the age of the deposits. A striking contrast with Calbuco, its neighboring volcano only 26 km away, is the absence of andesitic rocks (the 'Daily gap'), and the quasi absence of amphibole (*Lopez-Escobar et al. 1992*; *Moreno et al. 2010*; *Bechon et al. 2022*), supporting the idea of a low water content (~1 – 1.5 wt% H_2O; *Morgado 2019*; *Bechon et al. 2022*). Osorno magmas derive from the fractional crystallization of a low-H_2O tholeiitic basalt parent (~1 wt% H_2O; well below the ≈4 wt% arc average; *Plank et al. 2013*). *Diaz et al. (2020)* and *Bechon et al. (2022)* provided evidence for a general magma reservoir beneath Osorno divided into two parts: an upper crustal reservoir (~ 4 - 8 km; 2 ± 0.5 kbar; T = 820 – 920 °C) where most of the magma resides, and a deeper crustal reservoir extending the storage area vertically to depths of 10–15 km (T = 1000 – 1100 °C).

Calbuco

Calbuco is a Late Pleistocene truncated-cone stratovolcano covering ~150 km² and reaching 2,003 m a.s.l. (*Morgado et al. 2019a*), located on the southern shore of Lake Llanquihue, ~30 km west of the Liquiñe–Ofqui Fault Zone (41.20°S, 72.37°W; **Fig. V-2c**). The edifice, active for the past ~300 kyr, has produced twelve historical eruptions since 1792, the most recent occurring in April 2015 (*Morgado et al. 2019a and b*; *Namur et al. 2020*; *Mixon et al. 2021*).

Calbuco eruptive products range from basalts, basaltic andesites to dacites, basaltic andesites being dominant, including lava flows, pyroclastic deposits, block-and-ash flows, and lahars (*Lopez-Escobar et al. 1992, 1995*). Based on stratigraphy and geochemistry, four main units have been distinguished (*Sellés and Moreno 2011*; **Figure V-2c**). Using new $^{40}Ar/^{39}Ar$ dating performed on 65 samples (spanning the Pleistocene to Holocene eruptive evolution), *Mixon et al. (2021)* redefined the ages of these units. *Unit 1* (Plc1: 100–55 ka) is generally observed below 1200–1000 m in elevation and is dominated by basaltic andesitic lavas interlayered with volcaniclastic deposits. Plc1 lavas are characterized by a relative enrichment in ortho- and clinopyroxene, in contrast to their lower overall crystal content (~35%) compared to the other units (~45–50%). *Unit 2* (Plc2, Plav2 and Hap: 30–7 ka) consists mainly of

andesitic lavas interbedded with pyroclastic material and forms most of the upper edifice. Plc2 lavas, mineralogically similar to Plc1, exhibit glaciovolcanic features such as fine-scale curving joints. This unit is linked to a major post-LGM sector collapse (Plav2, 9.5–6.5 ka) and the subsequent emplacement of the Alerce Ignimbrite (Hap, ~7.7–7.1 ka), produced by an extensive postglacial eruption and previously attributed to *Unit 3* (*Selles and Moreno 2011*), west of the summit. *Unit 3* (Hc3, Hlp; post-glacial events after ~4 ka) includes basaltic andesite lavas (Hc3) and pyroclastic deposits (Hlp) that constructed the modern cone. The lavas are characterized by a composition similar to, but slightly more mafic than, the older outcrops (SiO_2 ~55 wt.%). *Unit 4* (post-1893) encompasses the most recent historical eruptions, which were mainly explosive. It includes andesitic lava flows, numerous lahar and pyroclastic deposits produced between 1893 and 1895 (the last ash-flow eruption occurred in 1912; *Petit-Breuilh 1999*), as well as the growth of an endogenous dome within the summit crater. The last major historical eruption, characterized by two Sub-Plinian events on April 22 and 23, 2015, generated >15 km-high ash plumes and pyroclastic density currents (PDCs), with no associated lava flow.

Compared to neighboring Osorno and La Picada (<20 km), which erupt mostly basalts and basaltic andesites, Calbuco is mineralogically distinct due to its amphibole-rich andesitic compositions (*Lopez-Escobar et al. 1992, 1995*; *Hickey-Vargas et al. 2016b*; *Vander Auwera et al. 2021*). It represents a hydrous end-member of the CSVZ, with unusually high H_2O contents (3–3.5 wt.% in basalts at ~50 wt.% SiO_2, and 3.5–4.5 wt.% in basaltic andesites; *Namur et al. 2020*; *Vander Auwera et al. 2021*), initially attributed to the assimilation of metasediments and later considered as inherited from the mantle source (*Sellés et al. 2004*; *Vander Auwera et al. 2021*). Fractional crystallization of gabbronoritic cumulates from basaltic andesite parents has also been proposed as a major differentiation process (*Lopez-Escobar et al. 1995*; *Vander Auwera et al. 2021*). Based on the April 2015 eruption, timescales data (*Morgado et al. 2019b*) suggest a prior heating event only affecting only the bottom crystal-mush section of the magmatic reservoir; situated at 5 – 11km depth (*Delgado et al. 2017*; *Morgado et al. 2019a*).

Villarrica

Villarrica, located at 39.42°S and 71.93°W near the city of Pucón (**Figure V-1d**), is one of the most active stratovolcanoes of the Southern Volcanic Zone (SVZ), with over 60 eruptions of various styles (violent Strombolian activity, lava fountains, lava flows, and lahars) recorded

since 1558 (*Petit-Breuilh and Jobato 1994*), generally reaching VEI > 2 (*Simkin and Siebert 1994*; *Petit-Breuilh 2004*; *Global Volcanism Programme 2023*).

Volcanism at Villarrica is commonly divided into three main stages (*Clavero 1996*) (**Figure V-2d**). The first stage, during the Middle Pleistocene (>90–14 ka), corresponds to the construction of a large stratocone that ended with the caldera-forming Lican Ignimbrite eruption, emplacing ~10 km³ of basaltic-andesite deposits across the eastern and southeastern flanks (*Cortés et al. 2024*). The second stage (4 to 3.7 ka) saw the growth of a new stratocone on the northwestern margin of the first caldera and the emplacement of the 3.3–5.0 km³ basaltic-andesite Pucón Ignimbrite (*Silva-Parejas et al. 2010*). The third and current stage corresponds to the active cone, built on the northwestern margins of the earlier edifices, characterized by successive andesitic lava flows and pyroclastic deposits ranging from Strombolian to sub-Plinian fallout and surges (*Costantini et al. 2011*).

The most recent eruptive cycle includes violent Strombolian eruptions in 2015 and 2021, punctuated by milder Strombolian activity between 2018 and 2019 (*Cortés et al. 2024*). At the summit, a 200 m-wide crater has hosted a persistently degassing lava lake (30–40 m in diameter) since at least 1985 (*Witter et al. 2004*; *Moussallam et al. 2016*), reflecting continuous recharge of a shallow magma reservoir and frequent Strombolian activity (last paroxysm in 2015).

Villarrica's plumbing system comprises both shallow (~3 km) and deeper (~9–12.7 km) magma reservoirs, sustained by volatile-rich recharge that promotes magma mixing and degassing (*Cortés et al. 2024*). Exsolved volatiles enhance heat transfer between reservoirs, maintaining the lava lake during background activity. The erupted products are consistently basaltic to basaltic-andesitic in composition (*Hickey-Vargas et al. 1989*; *Witter et al. 2004*; *Constantini et al. 2011*). Major eruptions are not triggered directly by recharge, but by subtle variations in recharge rates or volatile exsolution, which destabilize and remobilize the resident crystal mush, leading to paroxysmal activity (*Cortés et al. 2024*). Such rapid transitions from background to explosive activity, on timescales of days to months, make Villarrica one of the most hazardous volcanoes in the SVZ.

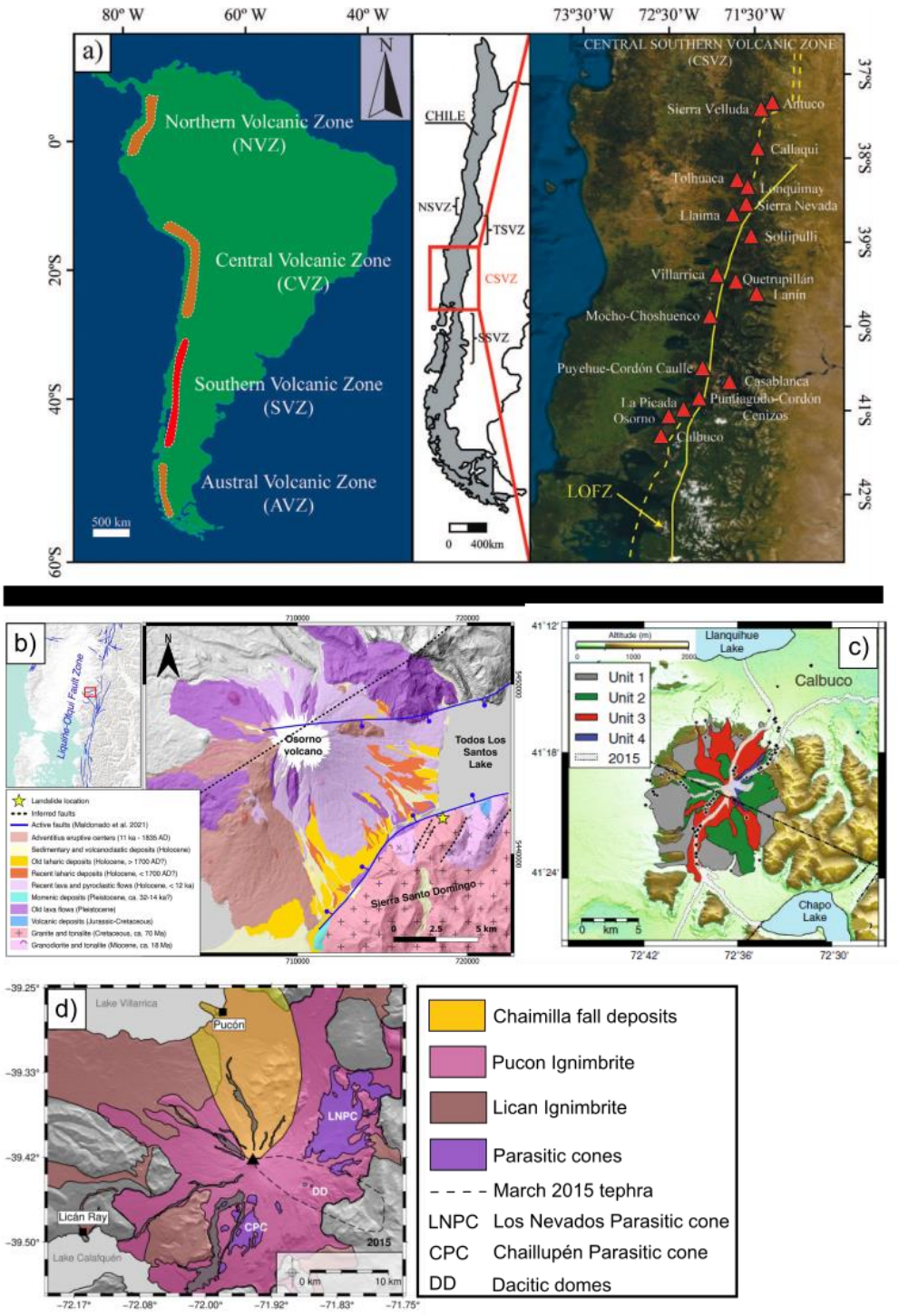

Figure V-1: *(a) Location of the main volcanic subdivisions in the Andes, with a zoom on the central part of the SVZ (in red) (modified after Moragado et al. 2022). A satellite view showing the alignment of the main stratovolcanoes is also provided, with the location of the LOFZ indicated in yellow. Maps illustrating the different eruptive units of Osorno (from Moreno et al. 2010), Calbuco (from Vander Auwera et al. 2021), and Villarrica (from Boschetty et al. 2022) are also shown.*

Methodology

							Plagioclase phenocrysts			Plagioclase	
Sample	volcano	Unit (Age)	Type	SiO_2 wt. (%)	Latitude (°)	Longitude (°)	Crystal number	N_A (μm^{-2})	Plg proportion	Single crystals	clusters
OS23	Osorno	Plo1a (2580 - 126 ka)	Basalt (lava)	50,93	-41,14111952	-72,58800907	1063	2,15E-06	0,18	0,91	0,09
OS127	Osorno	no data	Basalt (lava)	53,33	-41,12534429	-72,48139573	-	-	0,15	-	-
OS30	Osorno	Ho4 (126 -11,7 ka)	Basaltic-Andesite (lava)	53,94	-41,08552938	-72,47913197	609	1,38E-06	0,24	0,65	0,35
OS114	Osorno	Plo2 (126 - 11,7 ka)	Basaltic-Andesite (lava)	52,40	-41,12747917	-72,50623356	698	1,80E-06	0,22	0,76	0,24
OS42	Osorno	H1790 (< 4 ka)	Dacite (lava)	67,86	-41,09863495	-72,4545913	481	5,01E-07	0,05	0,81	0,19
OS128	Osorno	Hds (< 1 ka)	Dacite (lava)	68,85	-41,12568072	-72,4827765	525	7,98E-07	0,06	0,76	0,24
OS130	Osorno	Hds (< 1 ka)	Dacite (lava)	69,00	-41,12582913	-72,48297332	422	5,89E-07	0,07	0,85	0,15
OS136	Osorno	Hdw (< 1 ka)	Dacite (lava)	66,50	-41,1024555	-72,52196986	238	3,47E-07	0,02	0,65	0,35
CL119	Calbuco	Plc1 (340 - 110 ka)	Basalt (lava)	50,34	-41,3337898	-72,68740603	458	3,79E-06	0,24	0,86	0,14
CL22	Calbuco	Hc3 (< 126 ka)	Basaltic-Andesite (lava)	54,83	-41,29172342	-72,56750397	360	6,27E-07	0,10	0,90	0,10
CL88	Calbuco	3 (< 126 ka)	Andesite (Bomb)	57,81	-41,31784751	-72,68202048	539	6,41E-06	0,20	0,74	0,26
CL94	Calbuco	2 (126 - 20 ka)	Andesite (lava)	59,18	-41,34057146	-72,63073417	131	1,91E-06	0,21	0,48	0,52
CL108	Calbuco	4 (< 4 ka)	Andesite (Bomb)	60,16	-41,2953913	-72,56079927	1045	1,65E-06	0,19	0,79	0,21
VR1	Villarrica	Hv3 (<11.7 ka)	Basaltic-Andesite (lava)	52,48	-39,37800033	-71,94387061	-	-	0,14	-	-
VR25e	Villarrica	Hvch1 (<11.7 ka)	Basaltic-Andesite (lava)	56,34	-39,44425257	-71,86401761	551	3,63E-06	0,14	0,86	0,14
VR27	Villarrica	Dacitic dome (<11.7 ka)	Basaltic-Andesite (lava)	54,53	-39,31439659	-71,98010851	293	1,35E-06	0,04	0,92	0,08
VR36	Villarrica	H3v (<11.7 ka)	Basaltic-Andesite (lava)	52,36	-39,32052585	-71,88274888	522	1,65E-06	0,15	0,84	0,16
VR40	Villarrica	H3v (<11.7 ka)	Basaltic-Andesite (lava)	52,17	-39,4032961	-71,96936558	349	1,52E-06	0,10	0,85	0,15
VR26a	Villarrica	Hv3 (<11.7 ka)	Dacite (lava)	64,89	-39,44252345	-71,87056919	386	3,21E-07	0,03	0,73	0,27

***Table V-1**: Summary of the various segmented samples (type of rock, unit, and GPS coordinates). Textural parameters (plagioclase number, number density N_A, and proportion) are also indicated.*

Sampling and segmentation method

Samples, mostly lavas, ranging from basalts to dacites were collected from Osorno (OS), Calbuco (CL), and Villarrica (VR) (**Table V-1** and **Figure V-2**) to cover a large part of the eruptive history of these volcanoes. In the case of OS and CL, samples correspond to those previously studied by *Vander Auwera et al. (2021)* and *Bechon et al. (2022)*. GPS coordinates, as well as the eruption units are provided in **Table V-1**. Several CL products, principally basaltic andesites and andesites correspond to bombs (CL 88, and 108) or blocks. Given the time-consuming nature of the CSD method, 5–8 samples per volcano were analyzed.

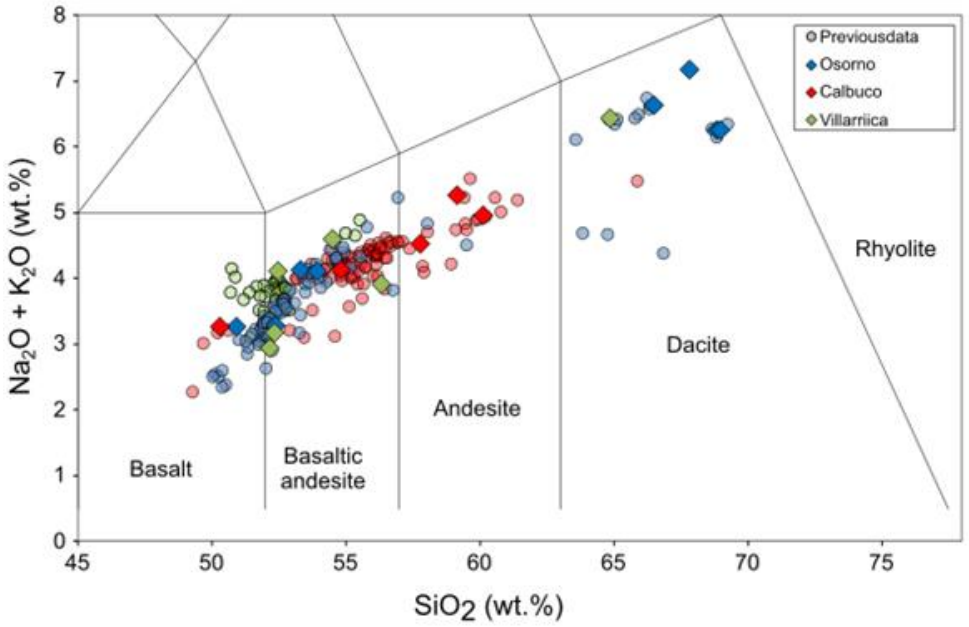

***Figure V-2**: Total alkali versus SiO_2 diagram for the selected samples (left). Previously published data (colored circles) from Bechon et al. (2022) (Osorno), Vander Auwera et al. (2021) (Calbuco), Hickey-Vargas et al. (1989), Witter et al. (2004), and Cortés et al. (2024) (Villarrica) are also shown for comparison.*

Because volcanic plumbing systems are highly complex, linking crystal textures to growth rates and timescales, particularly through the CSD method, requires a reliable segmentation process, which remains a challenging task. To obtain plagioclase CSDs, thin-section were scanned, and crystals were manually outlined and separated using *GIMP* freeware. 2D textural parameters (area, minor axis *w*, major axis *l*, roundness) of each crystal were extracted using *Fiji/ImageJ* (***Supplementary file V-1***). As samples were generally homogeneous, segmentation was sometimes limited to part of the thin section, depending on texture and crystal number density. Dacites, with <10% crystals, were usually segmented entirely. Manual outlines were verified with a polarizing optical microscope. The segmentation size limit is estimated to be around 10 µm to obtain robust results. However, because microlites are extremely abundant, it remains very difficult to segment them reliably using only an optical microscope. The microlitic populations of two Villarrica samples (VR1 and VR27) were therefore segmented using the TESCAN Mira4 scanning electron microscope (SEM) at KU Leuven. SEM imaging was performed at a working distance of 10–15 mm, with a dwell time of 10 µs and an accelerating voltage of 15 kV (20 kV for EDS analyses, with a beam current of 6–9 nA).

Due to the high fraction of clusters, and their potential impact on the CSD shape, the crystal population was estimated in 3 ways: only single (isolated) crystals, isolated crystals with also the clusters (as observable in the thin section), and isolated crystals with separation of crystals within the clusters (**Figure V-3**). To estimate residence times, the crystal cargo was classified by origin (*Toramaru 2022*) and apparent 2D size (limit around 100 – 150 µm; *Vernon 2018*). Microlites (<150 µm) were interpreted as formed during final ascent in the conduit, and phenocrysts (>150 µm), the focus of this study, as crystallized slowly in the main storage region.

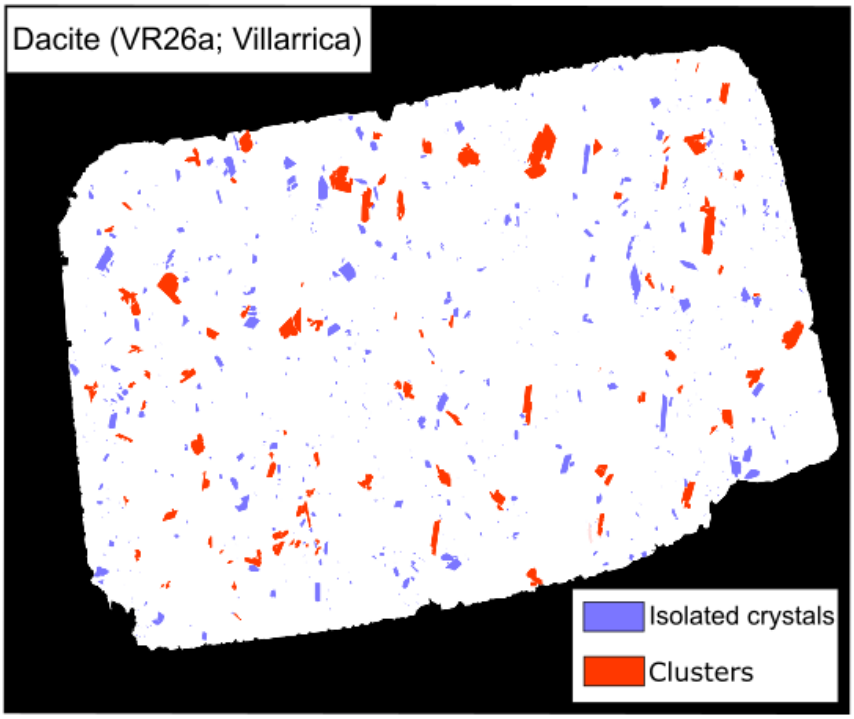

***Figure V-3**: Example of segmentation performed on a dacite thin section from Villarrica, illustrating the distinction between isolated plagioclase crystals (in blue) and clusters (in red).*

CSD measurements

All the CSD measurements were based on the 2D major axis (l), using the *CSDcorrection* program of *Higgins (2000)*. A massive fabric without lineation or foliation was assumed for our samples. For improved accuracy, porosity was corrected from the total sample area when necessary. Crystal 3D shapes (S:I:L, corresponding to the minor, intermediate, and major axes) were estimated using the *ShapeCalc* Excel spreadsheet of *Mangler (2022)*. The plagioclase fraction and the average roundness factor of the phenocryst cargo (0 = blocky,

1 = ellipsoidal; 0–0.6 in our samples) were also input. All input parameters for each sample are provided in the ***Supplementary file V-2***.

CSD plots of ln(population density) versus plagioclase 3D length (*L*) (*Marsh 1988*) were constructed with a log10 length interval. No gaps were observed. Following Higgins' recommendations, size bins containing only 1–2 intersections, generally the first and last bins, were excluded (marked in red in our CSD data) due to their imprecision (*Higgins and Roberge 2003*). All CSD plots presented in the following section concern macrocrysts (> 150 μm). Due to the high number of glomerocrysts (from 22 to 222; ranging from a simple contact between 2 crystals, to a more complex structure), 3 types of CSD plots were traced: (1) using only isolated crystals, (2) using isolated plagioclase crystals together with clusters, and (3) using isolated plagioclase crystals with each crystal within aggregates separated (*Mangan 1990*); to assess the impact of these clusters on the CSD parameters. The groundmass population of two VR samples (VR19-1 and VR19-27) was imaged by BSE to compare the CSD profiles obtained with those of phenocrysts.

Petrology

The petrology of these volcanoes' products has been the subject of several studies (*Lopez-Escobar et al. 1995*; *Namur et al. 2020*; *Vander Auwera et al. 2021; Bechon et al. 2022*; *Morgado et al. 2019, 2022*). A petrological variability can be observed both within the products of a single volcano and between the different volcanoes. For instance, at OS and VR andesites are almost absent (*Bechon et al. 2022*), whereas at CL, they mainly occur as bombs and blocks in pyroclasts (*Vander Auwera et al. 2021*). Basaltic andesites and andesites (Calbuco) constitute the predominant rock types.

The overall crystallinity ranges from <10 to >50 vol.% (*Namur et al. 2020*; *Vander Auwera et al. 2021*; *Bechon et al. 2022*; *Cortés et al. 2024*), approaching the critical crystallinity threshold. Lower values are generally observed in dacites, whereas basaltic andesites exhibit the largest variability (*Bechon et al. 2022*); from phyric (fine-grained groundmass) to hyalopilitic (plagioclase-rich groundmass, with crystals in varied orientations) (**Figure V-4a - i**). The phenocryst assemblage consists of plagioclase, clinopyroxene, orthopyroxene, spinel, and olivine (forsterite) in the most mafic and primitive samples. A major difference between OS and CL concerns the occurrence of amphibole; restricted to trace amounts in Osorno (*Bechon et al. 2022*; *Morgado et al. 2022*) but preserved as subhedral crystals in many andesitic bombs from CL (Lopez Escobar et al., 1995; *Vander Auwera et al. 2021*). Amphibole,

commonly mantled by magnetite, points to a tholeiitic basalt–basaltic andesite parental magma at Calbuco that was relatively water-rich (3–4.5 wt.% H_2O; *Namur et al. 2020*; *Vander Auwera et al. 2021*). This contrasts with nearby volcanoes, where tholeiitic parental magmas are significantly poorer in volatiles (~1 wt.% H_2O in Osorno; *Bechon et al. 2022*).

Plagioclase

Plagioclase is the dominant phase, representing 70–80 vol.% or more of the crystalline fraction (*Vander Auwera et al. 2021*; *Bechon et al. 2022*; *Cortés et al. 2024*), and is the main source of the strong textural variability observed during differentiation. In our samples, plagioclase phenocrysts constitute 3–24 vol.% of the rock volume (**Table V-1**), consistent with previous studies. Most samples display glomerophyric textures (**Figure V-4**; *Morgado et al. 2019*; *Bechon et al. 2022*; *Cortés et al. 2024*), with clusters (mainly monomineralic plagioclase aggregates), accounting for 8–52% of the total plagioclase population (average 0.21 ± 0.11; **Table V-1**). Some textural variations also occur within the basaltic and basaltic andesite samples (**Figure V-4a, b** and **e**), particularly in the proportion of clusters (syneusis or simple agglomeration features). Despite this variability, the highest cluster proportions are generally observed in andesitic and dacitic samples. Dacitic samples appear to display less pronounced textural variability, notably showing simpler clustering features in which plagioclase crystals exhibit well-defined edges within the clusters.

Textural parameters

The phenocryst plagioclase number density (N_A) ranges from 10^{-6} to 10^{-7} µm^{-2} (**Table V-1**). However, the segmentation (due to the magnification) tends to largely underestimate the smallest macrocryst fraction, whose grain sizes approach those of the groundmass. N_A values broadly scales with plagioclase abundance, with dacites showing the lowest values. Phenocryst size is highly variable, ranging from 150 µm to >2 mm for isolated crystals (up to 3.7 mm in sample VR19-36 from VR), and 4–4.6 mm for crystal clusters. Size distributions of isolated crystals are similar across all samples and volcanoes, with numerous small phenocrysts (150–350 µm) and progressively fewer large crystals (***Supplementary file V-2***). A minor excess in the largest size fraction (>950 µm) is commonly observed, possibly reflecting crystals that were detached from glomerocrysts due to collision or convection processes.

As reported by *Namur et al. (2020)*, plagioclase exhibits a wide 2D morphological variability, from euhedral blocky to prismatic/tabular, with possible partial dissolution texture

(Sieve cores, partially resorbed textures, and patchy zoning; **Figure V-4g**) (*Morgado et al. 2019*; *Vander Auwera et al. 2021*; *Bechon et al. 2022*). Some hypotheses such as a fluid-absent rapid decompression (*Annen et al. 2006*) or post-crystallization heating related to magma mixing (*Lohmar et al. 2012*) are often mentioned to explain this destabilization.

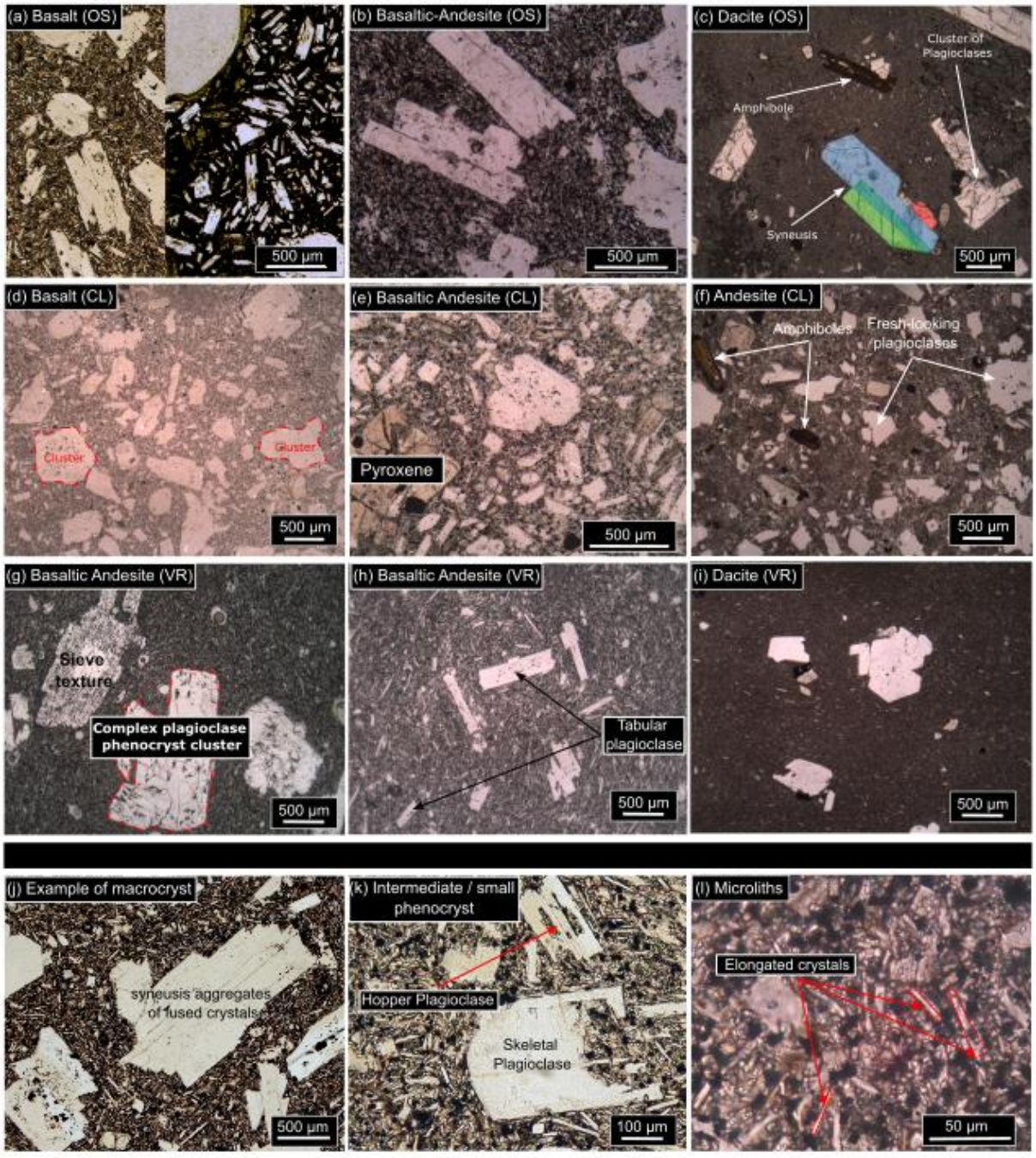

Figure V-4[7]*: Plane light microphotographs showing textures of basalts to dacites (a–c: OS; d–f: CL; g–i: VR). As shown in panel (a), textures in basalts, as well as in the basaltic andesites (b and e), are*

[7] Due to the effect of the thin-section resin on the camera, some images may appear yellowish or pinkish. Post-processing correction was applied to reproduce the colors as accurately as possible.

quite variable, in contrast to those observed in the dacites (c and i). Phenocryst arrangements are mainly governed by clustering patterns (c, d, g and j; individual crystals are shown in different colours). Numerous "disequilibrium" features, such as sieve textures, are commonly observed (g). Panels (j–l) show plagioclase texture from macrocrysts to micro-phenocrysts and microliths No significant textural differences are observed between the three volcanoes.

Some isolated phenocrysts exhibit well-defined prismatic or tabular shapes (**Figure V-4e** and **h**). The decrease in crystal size is characterized by a transition from large euhedral plagioclases to more hopper/skeletal microtextures (**Figure V-4j** and **k**). Microliths (<150 µm) are typically elongate and skeletal (**Figure V-4j - l**). Crystals smaller than 10 µm are considered to be quench products. Most separated crystals have a quite variable 2D aspect ratio (*w/l*) mode between 0.5 and 0.1, corresponding from elongate to tabular shapes (***Supplementary file V-2***), whereas clusters raise the average aspect ratios to 0.5–0.7, producing more equant morphologies (***Supplementary file V-2***). Consistently, microliths exhibit a w/l mode below 0.3, in agreement with their elongated habit. Subdividing phenocrysts into three size classes (150–350, 350–750, >750 µm) reveals no systematic differences in 3D shape estimates between the various size ranges (*S/I* = 0.21–0.65; *I/L* = 0.18–0.70; ***Supplementary file V-2***).

Chemical data

Plagioclase compositions from OS and CL volcanoes have been described by *Vander Auwera et al. (2021)* and *Bechon et al. (2022)*. Crystal textures range from homogeneous to oscillatory or patchy zoned, and include both normal and reverse zoning (*Namur et al. 2020*; *Bechon et al. 2022*). The anorthite content (molar Ca/[Ca + Na]) typically spans $An_{35–90}$, with systematic variations depending on bulk-rock composition: $An_{69–92}$ in basalts, $An_{34–92}$ in basaltic andesites, and $An_{40–60}$ in dacites, with rims generally more albitic than cores (*Bechon et al. 2022*). At CL, plagioclases generally show $An_{65->90}$ (*Vander Auwera et al. 2021*) and is also mainly characterized by normal zoning. In agreement with *Arzilli et al. (2019)* and *Morgado et al. (2019a)*, *Namur et al. (2020)* reported average rim compositions of 69.8 ± 7.0 mol.% An and core compositions of 86.8 ± 5.1 mol.% An.

At VR, plagioclase phenocrysts display two main compositional populations and zoning types (*Cortés et al. 2024*): reversely zoned bytownitic cores ($An_{77–86}$) and unzoned labradoritic crystals ($An_{58–69}$). Similar labradoritic compositions ($An_{58–68}$) have been reported for the 1971 eruption and the Pucón ignimbrite, whereas background tephra shows cores ranging from bytownitic to labradoritic, with rims consistently labradoritic. In our samples, anorthite contents

range from An_{36-92}, with strong variations depending on bulk-rock composition: $An_{62–88}$ in basalts, $An_{49–92}$ in basaltic andesites, and $An_{36–61}$ in dacites. Various zoning patterns are observed, including normal (**Figure V-5b**), reverse (for dacitic samples; **Figure V-5c**), and oscillatory types (**Fig. V-5a**). Most samples show complex oscillatory. Homogeneous compositions ($An_{66±3}$) dominate crystals smaller than 1 mm (**Figure V-5d**), whereas larger phenocrysts commonly display normal zoning, with cores around $An_{84±6}$ and rims around $An_{66±4}$. Notably, these rim compositions are similar to the homogeneous compositions of the smaller (<1 mm) phenocrysts. All chemical data are provided in ***Supplementary file V-3***.

Figure V-5 (see below)*: Examples of plagioclase BSE images showing Al_2O_3 and CaO chemical compositions (wt.%) and anorthite (An; mol.%) content variations, illustrating zoning patterns in plagioclase crystals from Villarrica: oscillatory (a, alternating high- and low-An bands), normal (b, decreasing An from core to rim), reverse (c, increasing An from core to rim), and homogeneous (d, nearly constant An throughout the crystal).*

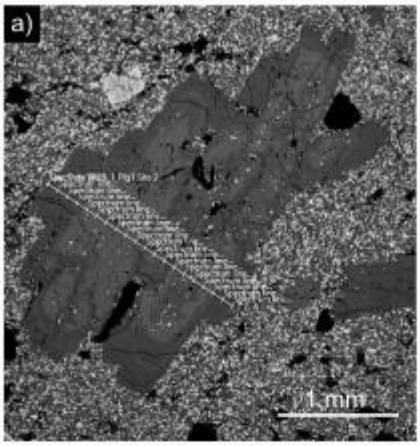
a)
1 mm

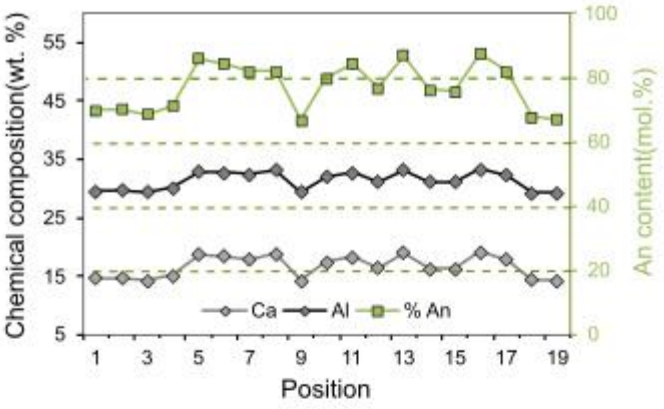
Chemical composition(wt. %)
An content(mol.%)
Ca
Al
% An
Position

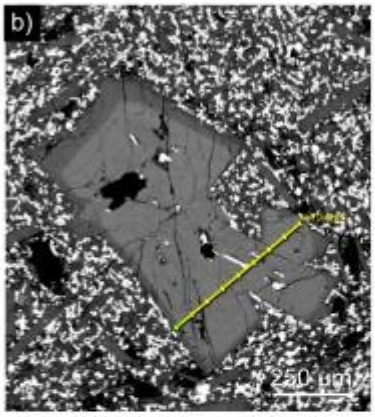
b)
250 µm

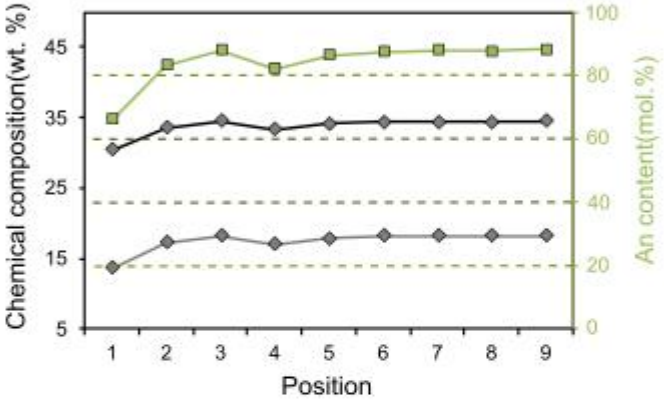
Chemical composition(wt. %)
An content(mol.%)
Position

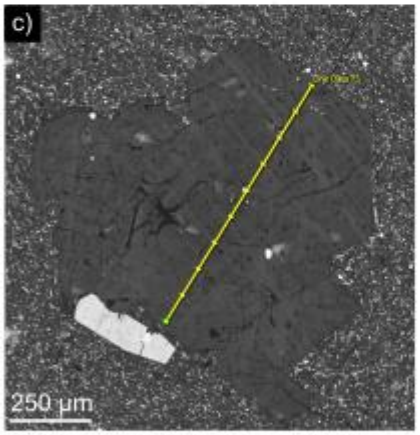
c)
250 µm

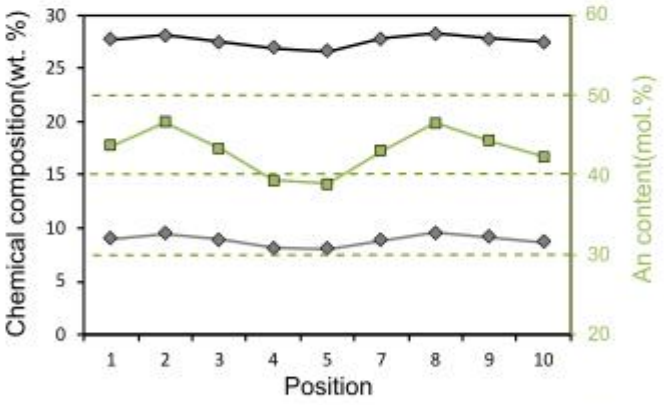
Chemical composition(wt. %)
An content(mol.%)
Position

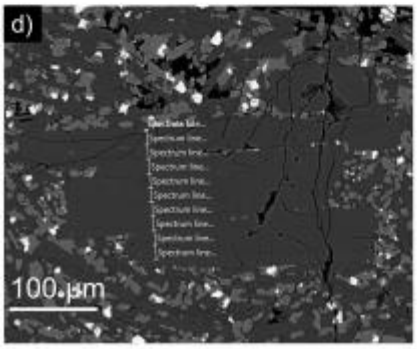
d)
100 µm

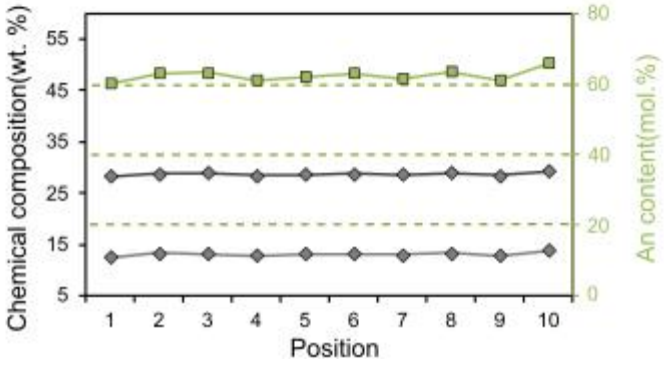
Chemical composition(wt. %)
An content(mol.%)
Position

Crystal size Distribution

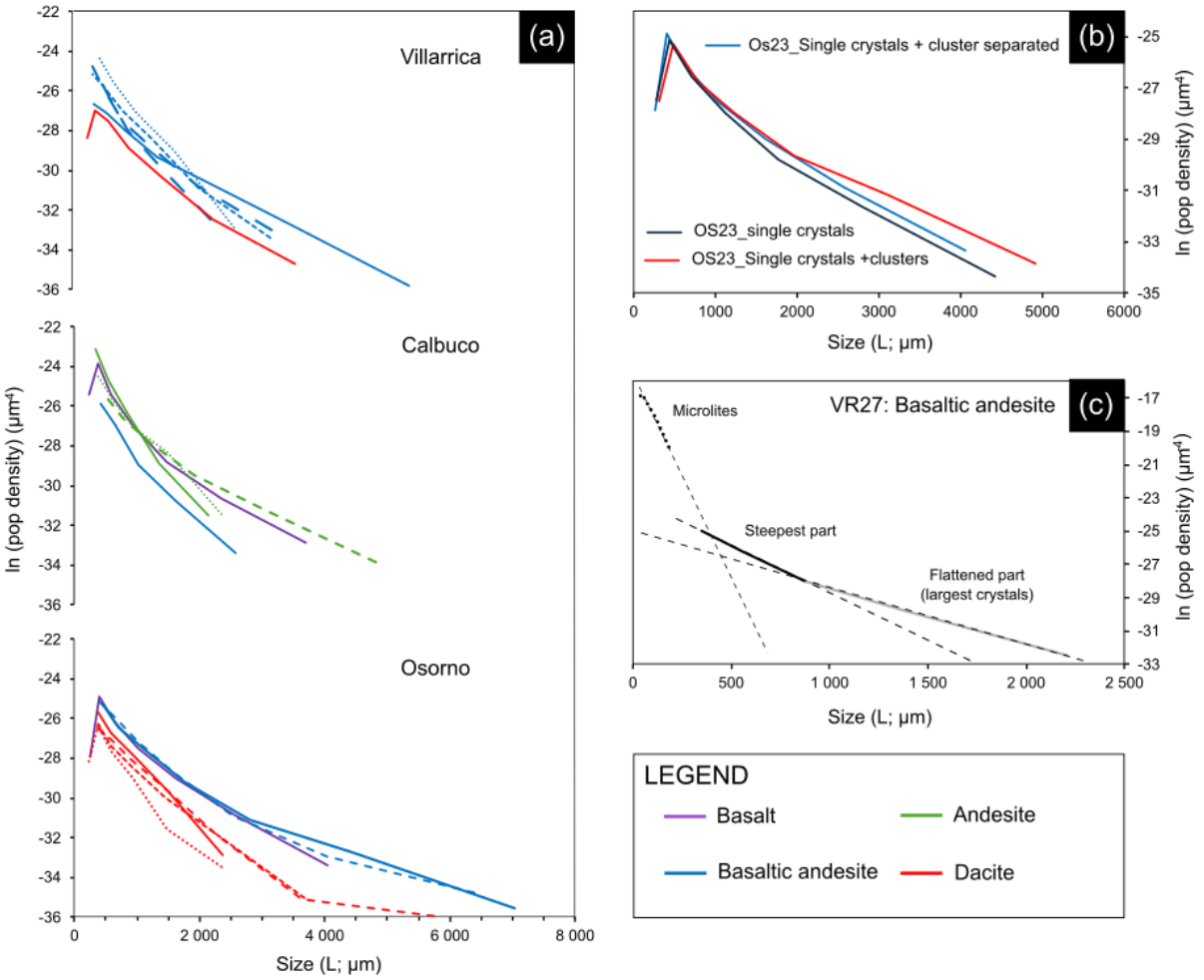

***Figure V-6**: (a) CSD diagrams for samples from the different volcanoes. Similar trends are observed among the various volcanoes, although some variations occur between samples of the same type (basalt, basaltic andesite, etc.). CSDs from dacites show lower plagioclase number densities. (b) Effect of crystal clustering on CSD patterns. (c) CSD slopes corresponding to the different crystal populations.*

Groundmass

Plagioclase groundmass population (<150 µm) can be divided into ascent-related crystals (10–150 µm, used for CSDs) and quenched crystals (<10 µm) formed by contact with water or air during the final eruption. CSDs for the groundmass (samples VR19-1 and VR19-27) display the steepest slopes (–0.02 to –0.05 μm^{-1}) and highest intercepts (–12 to –15.6 μm^{-4}) (**Figure V-6c**), indicating populations dominated by small microlites (L_c = 20–43 µm; **Table V-2**); typically formed during a final rapid magma ascent to the surface under high undercooling

conditions, as indicated by the acicular and skeletal habits (**Figure V-3j–l**), which reflect growth under disequilibrium conditions.

Groundmass crystallinity ranges from 38 to 49 % of the total measured area. Microlites in VR basaltic andesites exhibit acicular morphologies, comparable to those described by *Cashman (1988)* in dacite domes and pyroclastic blasts. In contrast to the microlites measured by *Schiavon et al. (2023)* in scoria clasts, the abundance of skeletal and dendritic textures seems less important, and no bright diffuse glass layer is observed around them. The relatively high crystallinity hampered crystal delineation and separation. Nevertheless, the presence of a distinct 2D aspect ratio mode (~0.1–0.3) is consistent with the elongated shapes observed and supports interpretation of a single nucleation episode (***Supplementary file V-2***).

Phenocrysts

CSDs obtained are summarized in **Figure V-6a**, with additional details provided in ***Supplementary File 1***. Most CSDs display a similar characteristic three-part shape (**Figure V-6a and b**): (i) an initial upward curvature for the smallest sizes, (ii) a steeper linear segment corresponding to the majority of phenocrysts ($L_{c,\,pop1}$ = 279 ± 82 µm; intercept = –23.90 ± 1.30), and (iii) a shallower segment corresponding to the macro-phenocrysts ($L_{c,\,pop2}$ = 552 ± 227 µm; intercept = –26.64 ± 1.44) which generally correspond to the phenocrysts forming the largest clusters. The slope break between the populations 1 and 2 occurs around 1149–1358 µm (mean around 1244 ± 387 µm). Dacite samples differ from this pattern, being mostly characterized by the absence of the secondary population associated with the shallower tail, and by lower intercept values (–25.29 ± 0.69 compared to –23.40 ± 1.09). Population 2 shows a greater size variability, mainly due to the strongly sample-dependent number of clusters, and to the difficulty of identifying and separating isolated crystals within these clusters. The upward curvature at the smallest sizes, commonly attributed to Ostwald ripening, may alternatively reflect resolution limitations (also linked to the magnification) and stereological uncertainty associated with a conversion artefact (e.g., *Higgins 2006*).

The main difference between CSD plots including or excluding clusters is in the shallow segment corresponding to the largest phenocrysts (**Figure V-6b**). When only isolated phenocrysts are considered, the second population is often absent, resulting sometimes in an apparent decrease in the maximum 3D crystal size. This highlights the strong influence of clustering on specific section of CSD plots. Except for a few extreme values (***Supplementary file V-2***), the mean relative differences between the three types of CSDs are 13 ± 8% for the slope (with highest values corresponding to the flattened section: 14 ± 9%) data and 3 - 5% for

the intercept values. The steeper slopes and higher intercepts in the smallest micro-phenocrysts are consistent with rapid magma ascent, which typically promotes high nucleation rates and the development of abundant small crystals at higher degrees of undercooling. An intermediate population is observed in VR40 (isolated crystals and clusters; ***Supplementary file V-2***), probably resulting from a progressive increase in undercooling, indicating a gradual rise in the decompression and cooling rates during magma ascent (*Armienti 2008*).

Table V-2*: Summary of the CSD parameters corresponding to the segmentation of isolated plagioclase crystals and the separation of the different plagioclase crystals forming clusters. Phenocrytic populations 1 and 2 refer to the steepest and flattened segments of the CSD diagrams, respectively.*

			Groundmass (< 150 µm)		Population 1		Population 2	
Sample	Volcano	Type	slope (cm^{-1})	Intercept (cm^{-4})	slope (cm^{-1})	Intercept (cm^{-4})	slope (cm^{-1})	Intercept (cm^{-4})
OS23	Osorno	Basalt			-41,72	13,51	-17,76	10,63
OS127	Osorno	Basalt			-23,06	13,77	-	-
OS30	Osorno	Basaltic-Andesite			-29,21	12,67	-10,54	8,71
OS114	Osorno	Basaltic-Andesite			-30,05	12,84	-9.76	8.16
OS42	Osorno	Dacite			-24,50	10,67	-	-
OS128	Osorno	Dacite			-35,64	12,38	-	-
OS130	Osorno	Dacite			-28,27	11,40	-	-
OS136	Osorno	Dacite			-46,34	12,11	-22,13	8,54
Mean					**-32,35**	**12,42**	**-15.05**	**9,01**
1 sigma					***8,23***	***0,96***	***5,94***	***1,10***
CL119	Calbuco	Basalt			-54,44	14,84	-17,94	10,57
CL22	Calbuco	Basaltic-Andesite			-49,81	13,04	-28,72	10,81
CL88	Calbuco	Andesite			-62,88	15,74	-38,83	13,54
CL94	Calbuco	Andesite			-33,94	13,35	-	-
CL108	Calbuco	Andesite			-32,51	12,89	-14,88	10,17
Mean					**-46,72**	**13,97**	**-25,09**	**11,27**
1 sigma					***13,18***	***1,26***	***10,91***	***1,54***
VR1	Villarrica	Basaltic-Andesite	-497,65	24,86	-26,54	11,08	-16,15	9,72
VR25e	Villarrica	Basaltic-Andesite			-38,58	13,91	-	-
VR27	Villarrica	Basaltic-Andesite	-235,01	21,25	-57,21	13,86	-33,43	11,74
VR36	Villarrica	Basaltic-Andesite			-33,86	12,70	-21,68	10,32
VR40	Villarrica	Basaltic-Andesite			-57,95	13,89	-21,36	10,51
VR26a	Villarrica	Dacite			-35,83	11,22	-20,03	9,16
Mean					**-41,66**	**12,78**	**-22,53**	**10,29**
1 sigma					***12,96***	***1,34***	***6,48***	***0,87***

Timescales determination

As outlined in the CSD theory section, the CSD intercept and slope, when combined with constraints on either the timescale of crystallization or on crystallization parameters (nucleation rate *J* and growth rate *G*), allow these variables to be derived from one another. This approach has been applied by several authors, such as *Kirkpatrick (1997)* to the Makaopuhi lava lake, *Cashman (1993)* to dacites from Mount St. Helens, and by *Cortés et al. (2024)* to estimate crystal residence times in the VR plumbing system. Following *Cashman (1988)*, who obtained timescales corresponding to eruption intervals, we used eruption dates reported by the *Smithsonian Institution* to define eruption intervals, which were then used to calculate nucleation and growth rates. These results were compared with estimates derived from laboratory experiments (*Pupier et al. 2008*; *Billon et al. 2025*). A comparable analysis was performed for the groundmass microlite, using the shallowest reservoir depth beneath VR (~3 km; *Cortés et al. 2024*) and ascent rates between 0.001 and 0.015 $m \cdot s^{-1}$ (*Rutherford 2008*).

The interval between eruptions varies strongly between volcanoes: from 3 ± 2 years at VR (the most active volcanic system) to 17 ± 28 years at CL and 29 ± 26 years at OS (***Supplementary file 2***; *Smithsonian Institution*). Using slope values obtained from phenocryst populations across several thin sections and adopting average eruption intervals, we estimate crystal growth rates of ~10^{-11} $cm \cdot s^{-1}$ at OS and CL, and ~10^{-10} $cm \cdot s^{-1}$ at VR (**Table V-3**). Corresponding nucleation rates range between 10^{-5} and 10^{-7} $cm^{-3} \cdot s^{-1}$.

Using experimental growth rates constrained in some studies (10^{-9} to 10^{-6} cm/s; e.g. *Pupier et al. 2008*; *Shea and Hammer 2013*; *Billon et al. 2025*), we calculate crystal residence times ranging from <1 day (≈7 h) to several weeks for rates of 10^{-7}–10^{-6} $cm \cdot s^{-1}$, and up to ~3 years for rates of 10^{-9}–10^{-8} $cm \cdot s^{-1}$ (**Table V-3**; ***Supplementary file V-2***). For a crystal of a given size, residence time decreases linearly with growth rate. Two distinct crystal populations are distinguished (**Table V-2**). Population 2, corresponding to the flattened segment of the CSD, consists of the largest intratelluric crystals and records the longest storage times. In contrast, Population 1 (microphenocrysts) appears to have formed during various magma ascent episodes.

At VR, segmentation of microlite populations combined with assumed ascent rates of 0.001 to 10 $m \cdot s^{-1}$ (*Rutherford 2008*; *Moschini et al. 2023*) yields growth rates of 10^{-10}–10^{-6} $cm \cdot s^{-1}$ (***Supplementary file V-2***). The corresponding nucleation rates are estimated at ~1–10^{4} $cm^{-3} \cdot s^{-1}$.

			Res time (Pop 1; month)		Res time (Pop 2; month)		*G* estimation (eruption intervals)		L_{max} method (month)	
Sample	Volcano	Type	1E-06	1E-09	1E-06	1E-09	Pop 1	Pop 2	1,00E-06	1,00E-09
OS23	Osorno	Ba	0,009	9,11	0,021	21,40	2,58E-11	6,07E-11	0,09	88,14
OS127	Osorno	Ba	0,016	16,48	-	-	4,68E-11	-	0,06	58,40
OS30	Osorno	Ba - And	0,013	13,01	0,036	36,07	3,69E-11	1,02E-10	0,11	108,63
OS114	Osorno	Ba - And	0,013	12,64	0,039	38,92	3,59E-11	6,33E-11	0,12	116,88
OS42	Osorno	Da	0,016	15,51	-	-	4,40E-11	-	0,10	104,64
OS128	Osorno	Da	0,011	10,66	-	-	3,03E-11	-	0,07	73,65
OS130	Osorno	Da	0,013	13,44	-	-	3,81E-11	-	0,09	85,06
OS136	Osorno	Da	0,08	8,20	0,017	17,17	2,33E-11	4,87E-11	0,04	44,33
Mean			**0,012**	**12,38**	**0,028**	**28,39**	**3,51E-11**	**6,88E-11**	**0,08**	**84,97**
1 sigma			***0,002***	***2,91***	***0,011***	***10,72***	***8,26E-12***	***2,33E-11***	***0,03***	***25,24***
CL119	Calbuco	Ba	0,007	6,98	0,021	21,18	3,40E-11	1,03E-10	0,09	88,63
CL22	Calbuco	Ba - And	0,008	7,63	0,013	13,23	3,71E-11	6,44E-11	0,04	40,99
CL88	Calbuco	And	0,006	6,04	0,010	9,79	2,94E-11	4,76E-11	0,04	41,10
CL94	Calbuco	And	0,011	11,20	-	-	5,45E-11	-	0,06	61,67
CL108	Calbuco	And	0,012	11,69	0,026	25,54	5,69E-11	1,24E-10	0,10	95,59
Mean			**0,09**	**8,71**	**0,017**	**17,44**	**4,24E-11**	**8,48E-11**	**0,07**	**65,60**
1 sigma			***0,003***	***2,56***	***0,007***	***7,21***	***1,25E-11***	***3,51E-11***	***0,03***	***25,74***
VR1	Villarrica	Ba - And	0,014	14,32	0,024	23,53	3,87E-10	6,35E-10	0,15	148,48
VR25e	Villarrica	Ba - And	0,010	9,85	-	-	2,66E-10	-	0,05	54,52
VR27	Villarrica	Ba - And	0,007	6,64	0,011	11,37	1,79E-10	3,07E-10	0,05	47,83
VR36	Villarrica	Ba - And	0,011	11,22	0,018	17,53	3,03E-10	4,73E-10	0,17	165,25
VR40	Villarrica	Ba - And	0,007	6,56	0,018	17,79	1,77E-10	4,80E-10	0,17	174,87
VR26a	Villarrica	Da	0,013	10,60	0,019	18,97	2,86E-10	5,12E-10	0,10	96,58
Mean			**0,010**	**9,87**	**0,018**	**17,84**	**2,66E-10**	**4,82E-10**	**0,11**	**114,59**
1 sigma			***0,003***	***2,95***	***0,004***	***4,35***	***7,97E-11***	***1,17E-10***	***0,06***	***56,10***
Mean Tot			**0,011**	**10,62**	**0,021**	**20,96**	**1,10E-10**	**2,32E-10**	**0,09**	**89,22**
1 sigma Tot			***0,003***	***3,12***	***0,009***	***8,64***	***1,17E-10***	***2,17E-10***	***0,06***	***56,10***

Table V-3*: Summary of crystal residence times obtained using different methods: CSD diagrams, eruption interval estimates, and the L_{max} method. For the CSD approach (population 1: steepest segment; population 2: flattened segment), the table reports the residence times calculated using the two extreme experimental growth rates considered (10^{-9} to 10^{-6} cm·s^{-1}). Ba : Basalt, Ba – And: Basaltic-andesite, And: Andesite, Da: Dacite.*

Discussion

Crystallization processes

Nucleation

The different types of nucleation (homogeneous vs. heterogeneous) have been widely investigated. According to the Classical Nucleation Theory (*CNT*), preferential sites lower the activation barrier, so nucleation should predominantly be heterogeneous (*Dowty 1980*; *Kirkpatrick 1983*). Yet uncertainties remain regarding the actual nucleation mode and the nature of preferential substrates.

Spillar and Dolejš (2014) attributed the upward curvature of some natural CSDs to heterogeneous nucleation, in addition to processes such as discontinuous nucleation or magma mixing. They argued that >70–80 % of heterogeneous nuclei are required to noticeably modify textures, although nearly linear CSDs, such as in some of our samples, may be explained by ~65–70 % heterogeneous nucleation.

Grain relationships in low-crystallinity samples (dacites, in our case) were examined by *Kirkpatrick (1977)*, who reported clusters of plagioclase and pyroxene (and occasionally olivine) as well as monomineralic plagioclase clusters (**Figure V-3**). Similar clusters in our samples likely reflect preferential nucleation and radial growth (*Kirkpatrick 1977*; *Hammer et al. 2010*). Experiments also show that nucleation tends to occur on structurally similar substrates (*Lofgren 1983*), such as olivine nucleating around Mg-oxide particles. Yet nucleation on identical minerals is thermodynamically unfavorable (*Holness et al. 2023*), and overgrowth rims frequently observed in experiments and often interpreted as heterogeneous nucleation, are more commonly expected (*Shea and Hammer 2013*; *Billon et al. 2025*).

Although some isolated crystals occur in the melt, the dominance of plagioclase-only clusters suggests aggregation of initially separate grains. Possible mechanisms include impingement or overlapping boundary layers (*Finnigan et al. 2008*), nucleation on microscopic particles (true heterogeneous nucleation), liquid-mediated aggregation or syneusis (*Vance 1969*; *Schwindinger 1999*), and convection-driven clustering (*Rice and Von Gruenewaldt 1995*). *Spillar and Dolejš (2014)* further emphasized that heterogeneous nucleation may combine with late-stage processes, such as mush movement, melt extraction, or agglomeration, to alter the cluster index and the CSD record.

Interpretations remain limited by the invisibility of nanometric particles, the 2D constraints of thin sections (*Kirkpatrick 1977*), and late-stage differentiation. Still, since natural

magmas are likely to host abundant heterogeneities (microporosity, crystal surfaces, dislocations) that favor heterogeneous nucleation (*Philpotts and Ague 2009*; *Spillar and Dolejš 2014*), hence nucleation in natural systems is best regarded as predominantly heterogeneous.

Crystal growth

Experimental studies show that crystal habit is highly sensitive to both undercooling and the solidification path, with shapes evolving from tabular or prismatic to skeletal or dendritic as undercooling increases. *Lindoo et al. (2025)* distinguished nominal undercooling ($-\Delta T_n$ = $T_{sat,\ bulk} - T_{quench}$) controlled by the final temperature, from instantaneous undercooling ($-\Delta T_I$), which depends on the cooling/decompression path. *Lofgren (1974)* reported that undercooling must remain below ~30 °C to produce euhedral tabular plagioclase. At constant final temperature, *Lindoo et al. (2025)* observed a shift from equant crystals at low $-\Delta T_I$ to increasingly tabular forms at higher $-\Delta T_I$ and cooling rates. Based on these results, a 3D equant habit is expected after a long crystallization period at very low cooling rates.

Our 2D aspect ratio measurements (*w/l*) highlight a clear distinction between the groundmass and phenocryst populations (***Supplementary file V-2***). Groundmass plagioclase (≤150 µm) is dominated by elongated (modal *w/l* ≈ 0.2) and skeletal habits, consistent with diffusion-controlled growth at high undercooling and with rapid terminal magma ascent (> 0.2–0.5 m/s; *Rutherford 2008*). In contrast, phenocrysts (≥150 µm) display more variable euhedral tabular to prismatic morphologies (modal *w/l* ≤ 0.4–0.5; **Figure V-4**; ***Supplementary files V-2 and 4***), suggesting crystallization under lower and more stable undercooling conditions.

To evaluate whether the largest crystals recording low $-\Delta T_I$ exhibit more equant morphologies, as predicted by *Lindoo et al. (2025)*, we estimated 3D crystal shapes for our largest isolated plagioclases (>900 µm) using the ShapeCalc spreadsheet (*Mangler et al. 2022*). Although crystals >2000 µm show typical *w/l* values around 0.2–0.3 (**Figure V-7a**), aspect ratios span a wide range (0.2–0.6) with no systematic trend. The corresponding 3D *S/I* (0.36–0.53) and *I/L* (0.13–0.35) ratios indicate prismatic to bladed morphologies (**Figure V-7b**), rather than equant shapes. Our results therefore do not support the prediction of *Lindoo et al. (2025)* that the largest plagioclase crystals should approach equant morphologies. While this discrepancy may partly reflect sectioning effects and the limited number of measured crystals, it may also suggest that natural crystallization conditions differ from those achieved experimentally (e.g., maturation stages, magma reinjection episodes).

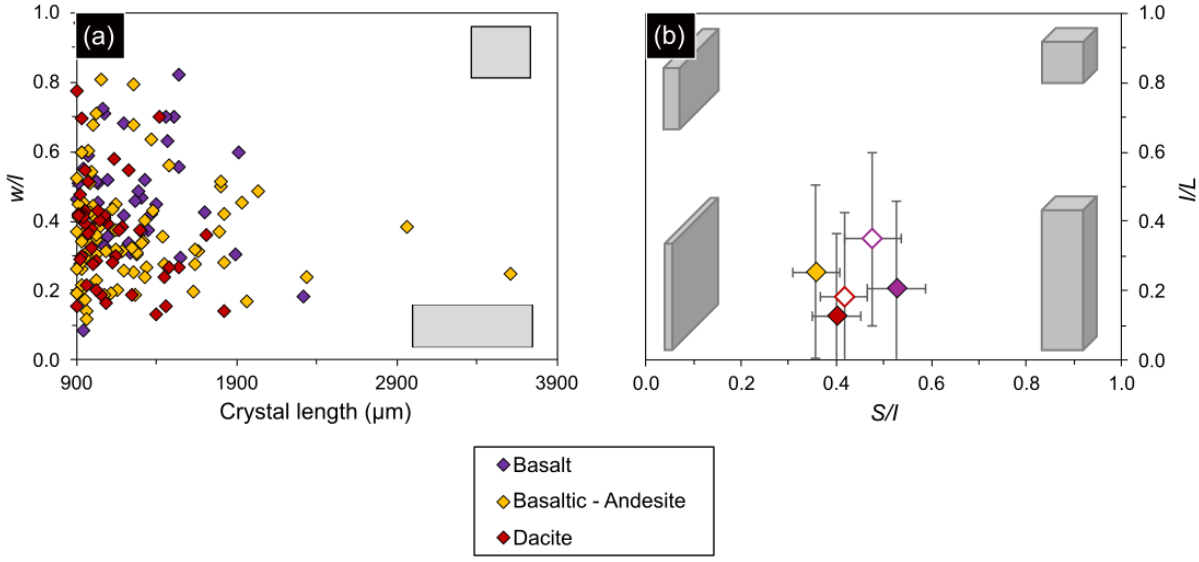

***Figure V-7**: **(a)** Evolution of the 2D aspect ratio (w/l) for the largest plagioclase phenocrysts (> 900 µm). **(b)** 3D shape estimates obtained using the Mangler et al. (2022) spreadsheet. Open and filled symbols correspond to estimates made on plagioclase crystals > 700 µm and > 900 µm, respectively.*

Despite the abundance of sieve texture and partial resorbed textures (**Figure V-4h**), most phenocrysts display well-defined euhedral shapes similar to those obtained experimentally at relatively slow cooling rates and low or absent superheating. The absence of skeletal crystals suggests an interface-controlled growth process, which involves a planar interface associated with a lateral growth mechanism (surface nucleation or screw dislocation/spiral growth), occurring through the spreading of one-molecule-high steps across the surface (*Kirkpatrick 1975*).

Following *Kirkpatrick (1977)*, and using the experimental growth rate compilation of *Billon et al. (2025)* ($G = 10^{-7} – 10^{-9}$ cm/s) as well as the maximum crystal size (0.4 cm), it is possible to estimate a lower limit for the diffusion coefficient (D) in the melt using the following relation:

$$D = x \times \frac{G}{C} \quad (8)$$

where x is the spacing (mm^{-1}) and C is a constant depending on the concentration gradient within the melt (≤ 1; *Kirkpatrick 1972*). Depending on the values of C and G, the diffusion coefficient ranges from 4.00×10−7 cm²/s ($C = 1$, $G = 10^{-7}$ cm/s) to 4.00×10−10 cm²/s (C = 0.1, $G = 10^{-9}$ cm/s). For growth rates below 10^{-9} cm/s, the estimated D values are consistent with those reported by *Donaldson (1975)* and *Kirkpatrick (1977)* for natural systems, as well as with the values estimated by *Billon et al. (2025)* for dry experiments at small to moderate

undercooling ($-\Delta T_n$ = 10–75 °C). Since the diffusion coefficient depends on the element of interest, this equation provides only a general average estimate.

Discussion on the CSD theory

According to *Marsh (1988, 1998)* and *Cashman and Marsh (1988)*, crystallization in open systems (at a constant volume) should produce linear CSDs. However, several of our CSDs show curved profiles, consistent with both natural observations (*Mangan 1990*; *Higgins and Roberge 2003*; *Cortés et al. 2024*) and experimental results (*Pupier et al. 2008*; *Billon et al. 2025*). Such curvatures have been attributed to size-dependent growth rates (*Marsh 1988*), successive nucleation and growth episodes (*Armienti et al. 1994*), changes in crystallizing phases (*Cashman 1993*), mixing of distinct crystal populations originally from different regions of the reservoir (*Higgins 1996*; *Ruprecht et al. 2008*), or textural maturation processes such as Ostwald ripening (DeHoff 1991; *Voorhees 1992*; *Higgins 2011*) and agglomeration/syneusis (*Vance 1969*; *Burkhard 1980*). These mechanisms generally steepen the slopes at small crystal sizes and flatten them at larger sizes.

Concerning the microlite population (VR19_1 and 27), the eruption of magma leads to a strong increase in the undercooling; promoting a strong nucleation of small crystals (**Figure V-6c**; ***Supplementary file V-2***) (*Higgins and Roberge 2003*). Because plagioclase dominates all stages of differentiation, and minor phases are insufficient to modify the slopes, the *Cashman (1993)* hypothesis of a change in the crystallizing phase can be excluded for phenocryst populations. Sequential nucleation and growth (*Armienti et al. 1994*) better explains the observed curvature. The scarcity of reverse zoning at OS and CL (*Vander Auwera et al. 2021*; *Bechon et al. 2022*) does not support a magma mixing process (*Higgins 1996*). In contrast to *Cortés et al. (2024)* observations, who reported bytownitic plagioclase with reverse zoning ($An_{77–86}$) in VR reverse zoning in our samples occur only in dacitic sample (VR19-26a; $An_{36–61}$), while VR basaltic andesites show predominantly oscillatory or normal zoning.

Clustering may also contribute to slope breaks (***Supplementary file V-2***). CSDs constructed from clustered crystals often show slope modifications, particularly in the larger size fraction, consistent with agglomeration effects. However, clusters span a wide size range and exhibit strong variability, indicating that clustering alone cannot, by itself, explain the observed curvatures. Therefore, a combination of sequential nucleation and growth (*Armienti et al. 1994*) with clustering effects provides the most plausible explanation. The deficit in

number density at the smallest sizes likely reflects resolution limits, which underestimate the smallest phenocrysts, around 150 µm, comprised in the groundmass.

Discussion on timescale estimations

Signification and limitation of textural approaches

One of the most fundamental aspects of the CSD approach is that it does not provide absolute ages, but only crystallization durations, similar to diffusion chronometry (*Turner and Costa 2007*). Because it relies solely on crystal size, CSD constrains the time elapsed between the saturation temperature of the studied phase and the temperature at which this phase reaches its equilibrium proportion. Plagioclase, the dominant phenocryst in many volcanic systems, constitutes a robust indicator of the overall thermal history: in the Osorno plumbing system, its saturation and solidus temperatures are estimated at ~1190 °C and <1000 °C, respectively (*Bechon et al. 2022*; *Morgado et al. 2022*), allowing the use of CSDs to estimate magma residence times; supposing a residence time equivalent to the crystallization duration.

The method, providing average residence time, can be compared with the L_{max} approach, an easier and faster textural technique, which estimates maximum growth durations from the largest observed crystal size (*Cooper and Kent 2014*) that probably nucleated first. In our case, both techniques yield consistent results, with an average difference of 383 % (ranging from 158 to 883 %; ***Supplementary file V-2***), partly explained by the fact that the L_{max} method refers to the maximum 2D size, whereas the CSD technique estimates the true 3D size. While the L_{max} method is primarily sensitive to image segmentation quality and to the difficulty of confidently identifying the largest crystal in the magma (*Kirkpatrick 1977*), CSD estimates additionally depend on factors such as the accuracy of 3D size reconstructions, corrections for sectioning effects, and the distinction between different crystal populations.

As a purely textural method, CSD is not directly affected by chemical contamination or temperature dependencies and can be used to constrain magmatic timescales from segmented crystals. Moreover, this method allows discrimination of various crystal populations. This is a significant advantage over other techniques, such as Uranium series dating (except on zircons) and diffusion modeling, which are temperature dependent (*Costa et al. 2020*) and do not provide indication on the different crystal populations.

Two main limitations, however, must be emphasized. (1) The thermal and eruptive history of plumbing systems is often difficult to reconstruct. Multiple reservoirs may coexist at

different depths, and crystal cargo can be redistributed by magma mixing (*Ruprecht et al. 2008*), juxtaposing crystals that record distinct thermal histories (*Bechon et al. 2022*; *Cortés et al. 2024*). (2) In addition to its dependence on the CSD slope, this method is inherently governed by crystal growth processes and is therefore sensitive to growth interruptions such as episodes of reheating; inducing dissolution and partially reset the textural record (*Ruprecht et al. 2008*; *Cooper and Kent 2014*).

Contributions on the storage history

The resulting timescales (ranging from <1 month to >3 years, and up to ~100 years when considering eruption intervals) are consistent with the data compilation reported by *Cooper and Kent (2014)*, who used a similar range of growth rates. However, except for VR, where eruption intervals are around 3 years, such timescales do not appear to be directly linked to any specific observable magmatic process.

Large intratelluric crystals (Population 2).

The largest crystals, characterized by flattened CSD slopes, assumed to represent long-time crystallization at a slow cooling rate, record residence durations on the order of 20 ± 7 months (minimum ~10 months, maximum ~3 years), for a growth rate of ~10^{-9} cm·s^{-1}. These values correspond to the lowest experimentally explored cooling rates (0.2–1 °C·h^{-1}; *Pupier et al. 2008*; *Billon et al. 2025*), and under isobaric/isothermal conditions. Similar results were also obtained in natural systems. *Wright and Fiske (1971)* and *Mangan (1990)* applying the CSD method to olivines from Kīlauea, inferred shallow storage times of 5–35 years, with growth rates of ~10^{-9}–10^{-10} cm·s^{-1}. For Mt. Etna, *Moschini et al. (2023)* estimated crystal residence times of 3–9 years, using an experimentally derived growth rate of ~10^{-8} cm·s^{-1} and cooling rates around 0.16 °C·h^{-1} (undercooling <30 °C; *Cashman 1993*). Using the L_{max} method and a similar growth rate of 10^{-9} cm/s on our samples, it is possible to estimate a maximum crystallization time of 7 (+/- 5) years.

In contrast, much longer crystallization times (tens to hundreds of years, at growth rates of 10^{-10}–10^{-11} cm·s^{-1}) inferred from eruption recurrence intervals broadly agree with those of Villarrica, but remain faster when considering Osorno and Calbuco. This hypothesis would imply a complete renewal of the magma chamber between eruptions, which represents an unrealistic scenario. Contrary to Osorno and Calbuco, Villarrica remains persistently active,

hosting a permanent lava lake. The observed agreement between crystal residence times and eruption recurrence intervals may reflect both a higher local permeability of the country rock and a larger ratio of eruptive products to crystallized plutons. Considering longer timescales derived from U–Th disequilibria, *Cashman (1988)* and *Turner et al (2003)* estimated growth rates from 10^{-13} to 10^{-11} cm/s; between 2 and 4 orders of magnitude lower than the minimum values determined experimentally.

Smaller phenocrysts (Population 1).

Smaller phenocrysts, corresponding to the steepest CSD slopes, are often difficult to clearly distinguish from the flattened section. Their sizes suggest residence times shorter than those of macrophenocrysts but longer than those of microlites, implying late crystallization episodes in the shallow upper-crustal reservoir where magma is stored prior to eruption. These late nucleation episodes could result from different magma remobilization processes, including magma mixing accompanied by episodic reheating, internal heat transfer, volatile exsolution, or a gradual increase in undercooling during magma cooling (*Higgins and Roberge 2003*). Such processes can generate microtextures ranging from euhedral to skeletal. This population likely represents a distinct and later nucleation event (*Armienti et al. 1994*), producing abundant, well-formed crystals, under undercooling values higher than 30 °C (*Lofgren 1974*), yet still relatively modest (< 60 °C). A growth rate between 10^{-9} and 10^{-8} cm·s^{-1} appears reasonable, corresponding to timescales of weeks to several months, consistent with the predictions of *Cortés et al. (2024)*, as well as with seismic activity generally recorded at depths where magma is stored prior to eruption. For instance, before the April 2015 eruption of Calbuco, *Valderrama et al. (2015)* reported more than 147 seismic events between February and April 2015.

Microlites

Microlites record the shortest crystallization timescales and provide sensitive markers of the final stages of magma ascent. *Cortés et al. (2024)* estimated residence times of only a few days for VR, corresponding to ascent rates of 0.005–0.01 m·s^{-1} (*Rutherford 2008*) and growth rates of ~10^{-9} cm·s^{-1}. Faster ascent (>0.1 m·s^{-1}; *Hammer and Rutherford 2002*; *Couch et al. 2003a and b*) increases growth rates to 10^{-8}–10^{-7} cm·s^{-1}, producing crystallization durations of less than 1 hour (e.g., ~50 minutes at 1 m·s^{-1}). Based on previous estimates for Stromboli, Etna, and Kīlauea (*La Spina et al. 2016, 2021*; *Polacci et al. 2019*; *Moschini et al. 2021, 2023*), final ascent rates in the last 2 km (Villarrica's shallow reservoir at ~3 km depth)

may reach 23–50 m·s^{-1}, corresponding to growth rates of ~10^{-5} cm·s^{-1} and ascent/crystallization times of less than 2 minutes. Using a diffusion model of H zoning in olivines, *Barth et al. (2019)* estimated ascent rates between 2 and 19 m·s^{-1}, corresponding to decompression rates of 0.05 to 0.5 MPa·s^{-1} at Pali-Aike, Cerro Negro, and Kīlauea volcanoes.

Based on our previous expectations, ascent rates >10 m·s^{-1}, corresponding to growth rates of ~10^{-5}–10^{-6} cm·s^{-1}, are likely. Because the final ascent is rapid relative to reservoir crystallization, microlites generally form syn-eruptively under high undercooling (60–140 °C; *Arzilli et al. 2019*; *Moschini et al. 2023*), producing skeletal or elongated morphologies with homogeneous textures. In-situ experiments confirm this behavior, reporting growth rates of 10^{-4}–10^{-5} cm·s^{-1} during highly explosive basaltic eruptions (*Arzilli et al. 2019*). Lower ascent rates (<0.1 m·s^{-1}), consistent with expected growth rates for population 1, could instead reflect magma transfer between crustal reservoirs.

Sources of uncertainties

According to equation (**6**), the crystallization time (τ) is directly proportional to (1/G), with a slope coefficient defined as (a = –1 / CSD slope):

$$\tau = a \times \frac{1}{G} \quad (9)$$

Timescales depend on both growth rates and CSD slopes. Variations in CSD slopes only account for minor differences (~7–17% between populations), whereas growth rates span five orders of magnitude (10^{-6}–10^{-11} cm·s^{-1}) and therefore represent the dominant source of uncertainty.

Experimental studies show that the highest growth rates (10^{-6}–10^{-7} cm·s^{-1}), corresponding to timescales of weeks to months, occur under rapid crystallization conditions such as decompression-induced degassing (*Hammer and Rutherford 2002*; *Couch et al. 2003*), or fast cooling (up to 900 °C·h^{-1}; *Conte et al. 2006*). By contrast, slowest cooling rates (0.2–1 °C·h^{-1}; *Conte et al. 2006*; *Pupier et al. 2008*) and isothermal conditions (*Nabelek et al. 1978*; *Moschini et al. 2023*) yield lower growth rates around 10^{-8}–10^{-9} cm·s^{-1}. Importantly, experiments also indicate that growth is not constant, but decreases rapidly after an initial burst (*Welsh et al. 2023*; *Billon et al. 2025*), implying that crystal growth may decline or even cease during magma storage.

These experimental values remain systematically higher than those inferred from natural systems. Eruption intervals, strongly influenced by local permeability and large-scale structural controls, suggest rates of 10^{-10}–10^{-11} cm·s^{-1} (*Kirkpatrick 1977*; *Cashman 1988*); thermal models yield values around 10^{-11} cm·s^{-1} (*Moore and Evans 1967*), and U-series data indicate even lower rates (10^{-12}–10^{-13} cm·s^{-1}; *Turner et al. 2003*). U-series analyses from Kīlauea, for instance, constrain long-term cooling rates of 10^{-6}–10^{-5} °C/h (*Cooper et al. 2001*), which are 10^{5}–10^{6} times lower than those achievable under experimental conditions. Such discrepancies underscore the marked contrast between laboratory timescales, governed by short-term kinetic processes, and natural records that integrate magmatic evolution over thousands of years.

In natural systems, additional processes such as overheating or partial resorption may also occur, potentially reducing crystal size. Experimental dissolution rates range from 10^{-5} to 10^{-7} cm·s^{-1}; similar to growth rates (*Ruprecht et al. 2008*; *Cooper and Kent 2014*), with dominant mechanisms yielding ~10^{-7} cm·s^{-1} (*Zhang et al. 1989*; *Liang 2003*). However, such high rates persist only for minutes before dropping by over an order of magnitude (~$10^{1.5}$; *Ruprecht et al. 2008*). Consequently, as observed, most phenocrysts remain euhedral, with resorption textures limited to crystal edges. As noted by *Cooper and Kent (2014)*, it is therefore unlikely that crystals experienced a thermal history long enough to develop pervasive resorption textures followed by skeletal crystal growth.

Comparison with other dating methods

Only a limited number of timescale studies have been conducted on the volcanoes of interest (*Morgado et al. 2019, 2022*). Nevertheless, textural methods based on crystal growth, still rarely applied, offer a useful complement to classical chronometers such as U-series disequilibria and diffusion modeling. U–Th–Ra disequilibria, particularly in accessory phases such as zircon, typically yield residence times of 10,000 to >100,000 years (*Charlier and Zellmer 2000*; *Eppich et al. 2012*), probably reflecting multiple magma influxes into the reservoir. In contrast, diffusion modeling applied to feldspars, olivine, or pyroxene generally records much shorter intervals, from years to a few hundred years and rarely up to ~1,000 years (*Druitt et al. 2012*; *Rubin et al. 2017*; *Cooper and Kent 2014*). Such discrepancies, even when both methods are applied to the same mineral (*Rubin et al. 2017*), highlight that different chronometers capture distinct parts of a crystal's history.

Our textural estimates fall within the same order of magnitude as diffusion timescales but remain offset by more than two orders of magnitude. This discrepancy suggests that reconciling both approaches would require significantly slower crystal growth rates, on the order of ~10^{-10}–10^{-11} cm/s. In this context, experimentally derived growth rates (10^{-8}–10^{-9} cm/s) and those inferred from U-series disequilibria (10^{-12}–10^{-13} cm/s) can be viewed as the upper and lower bounds of the plausible range, respectively. These timescale differences are best interpreted as reflecting the thermal sensitivity of each method: U-series record long-term storage and integrated histories, whereas diffusion and textural methods are more sensitive to short-term processes. The diffusion methods, very sensitive to temperature (in addition to crystal orientation or also pressure and fO_2) only measures the time spent above a specific temperature; while, textural techniques will measure the crystallization time (quite fast and non continuous process). In addition to constraining crystallization durations, the latter also capture timescales of magma transfer and ascent between reservoirs, as well as final pre-eruptive ascent (*Costa et al. 2020*; *Druitt et al. 2012*).

Taken together, these approaches suggest that long-term storage of magmas over thousands of years is punctuated by rapid remobilization and transfer between reservoirs, with the final pre-eruptive ascent occurring on timescales of decades at most.

Conclusion

CSD-derived timescales typically range from a few days to about three years, depending on the crystallization context. Longer timescales are generally associated with crystallization in shallow reservoirs, whereas shorter ones reflect late-stage processes before eruption, such as reheating by magma mixing, internal heat transfer, or increasing undercooling during cooling. These estimates are highly sensitive to the assumed growth rates (10^{-8}–10^{-12} cm/s). In contrast, U-series and diffusion modeling record much longer durations, on the order of tens of thousands of years and decades to centuries, respectively; highlighting that each method captures distinct segments of a crystal's history. While U-series disequilibria provide absolute ages that reflect the entire residence time in the plumbing system and recording multiple magma influx, CSD analyses capture only short crystallization episodes, typically representing less than 1% U-series–derived timescales. However, because undercooling, crystal shape, and crystallization parameters (J and G) are clearly correlated, the use of textural methods such as the CSD approach offers valuable advantages by linking relative timescales (and possibly absolute ones if the eruption date is known) to specific magmatic processes.

References

Annen C, Blundy JD, Sparks RSJ (2006). The Genesis of Intermediate and Silicic Magmas in Deep Crustal Hot Zones. Journal of Petrology 47:505–539. https://doi.org/10.1093/petrology/egi084

Armienti P (2008). Decryption of Igneous rock textures: Crystal Size distribution tools. Reviews in Mineralogy & Geochemistry, 69(1):623-649. https://doi.org/10.2138/rmg.2008.69.16

Armienti P, Pareschi MT, Innocenti F, et al. (1994) Effects of magma storage and ascent on the kinetics of crystal growth: The case of the 1991?93 Mt. Etna eruption. Contributions to Mineralogy and Petrology 115:402–414. https://doi.org/10.1007/BF00320974

Arzilli F, La Spina G, Burton MR, et al. (2019). Magma fragmentation in highly explosive basaltic eruptions induced by rapid crystallization. Nature Geoscience 12:1023–1028. https://doi.org/10.1038/s41561-019-0468-6

Barth A, Newcombe M, Plank T, et al (2019). Magma decompression rate correlates with explosivity at basaltic volcanoes — Constraints from water diffusion in olivine. Journal of Volcanology and Geothermal Research 387:106664. https://doi.org/10.1016/j.jvolgeores.2019.106664

Bechon T, Billon M, Namur O, et al (2022) Petrology of the magmatic system beneath Osorno volcano (Central Southern Volcanic Zone, Chile). Lithos 426–427:106777. https://doi.org/10.1016/j.lithos.2022.106777

Billon M, Vander Auwera J, Namur O, et al (2025) Plagioclase crystal size distributions, growth and nucleation rates in an anhydrous arc basaltic andesite. Contributions to Mineralogy and Petrology 180:26. https://doi.org/10.1007/s00410-025-02213-9

Bourdon B, Henderson GM, Lundstrom CC, et al. (2003) Introduction to U-series geochemistry. Reviews in Mineralogy and Geochemistry 52(1):1–21. https://doi.org/10.2113/0520001

Cashman KV (1990) Textural constraints on the kinetics of crystallization of igneous rocks. Reviews in Mineralogy and Geochemistry 24(1): 259-314.

Cashman KV (1993) Relationship between plagioclase crystallization and cooling rate in basaltic melts. Contributions to Mineralogy and Petrology 113:126–142. https://doi.org/10.1007/BF00320836

Cashman KV, Marsh BD (1988) Crystal size distribution (CSD) in rocks and the kinetics and dynamics of crystallization II: Makaopuhi lava lake. Contr Mineral and Petrol 99:292–

305. https://doi.org/10.1007/BF00375363

Charlier B, Zellmer G (2000) Some remarks on U–Th mineral ages from igneous rocks with prolonged crystallisation histories. Earth and Planetary Science Letters 183:457–469. https://doi.org/10.1016/S0012-821X(00)00298-3

Clavero J (1996) Ignimbritas andesítico-basálticas postglaciales del Volcán Villarrica, Andes del Sur (39°25′S). M.S.c Thesis, Universidada de Chile.

Conte AM, Perinelli C, Trigila R (2006) Cooling kinetics experiments on different Stromboli lavas: Effects on crystal morphologies and phases composition. Journal of Volcanology and Geothermal Research 155:179–200. https://doi.org/10.1016/j.jvolgeores.2006.03.025

Cooper KM, Kent AJR (2014) Rapid remobilization of magmatic crystals kept in cold storage. Nature 506:480–483. https://doi.org/10.1038/nature12991

Cooper KM, Reid MR (2003) Re-examination of crystal ages in recent Mount St. Helens lavas: implications for magma reservoir processes. Earth and Planetary Science Letters 213:149–167. https://doi.org/10.1016/S0012-821X(03)00262-0

Cooper KM, Reid MR, Murrell MT, Clague DA (2001) Crystal and magma residence at Kilauea Volcano, Hawaii: 230Th–226Ra dating of the 1955 east rift eruption. Earth and Planetary Science Letters 184:703–718. https://doi.org/10.1016/S0012-821X(00)00341-1

Cortés JA, Gertisser R, Calder ES (2024) Magma recharge in persistently active basaltic–andesite systems and its geohazards implications: the case of Villarrica volcano, Chile. Int J Earth Sci (Geol Rundsch) 113:1145–1163. https://doi.org/10.1007/s00531-024-02414-w

Costa F, Shea T, Ubide T (2020) Diffusion chronometry and the timescales of magmatic processes. Nature Reviews Earth Environment 1:201–214. https://doi.org/10.1038/s43017-020-0038-x

Costantini L, Pioli L, Bonadonna C, et al (2011) A Late Holocene explosive mafic eruption of Villarrica volcano, Southern Andes: The Chaimilla deposit. Journal of Volcanology and Geothermal Research 200:143–158. https://doi.org/10.1016/j.jvolgeores.2010.12.010

Couch S, Harford CL, Sparks RSJ, et al. (2003a) Experimental Constraints on the Conditions of Formation of Highly Calcic Plagioclase Microlites at the SoufrieÁ re Hills Volcano, Montserrat. 44(8):1455-1475. https://doi.org/10.1093/petrology/44.8.1455

Couch S, Sparks RSJ, Carroll MR (2003b) The Kinetics of Degassing-Induced Crystallization at Soufrière Hills Volcano, Montserrat. Journal of Petrology 44(8): 1477-1502.

https://doi.org/10.1093/petrology/44.8.1477

Delgado F, Pritchard ME, Ebmeier S, et al (2017) Recent unrest (2002–2015) imaged by space geodesy at the highest risk Chilean volcanoes: Villarrica, Llaima, and Calbuco (Southern Andes). Journal of Volcanology and Geothermal Research 344:270–288. https://doi.org/10.1016/j.jvolgeores.2017.05.020

Dewey JF, Lamb SH (1992) Active tectonics of the Andes. Tectonophysics 205:79–95. https://doi.org/10.1016/0040-1951(92)90419-7

Díaz D, Zúñiga F, Castruccio A (2020) The interaction between active crustal faults and volcanism: A case study of the Liquiñe-Ofqui Fault Zone and Osorno volcano, Southern Andes, using magnetotellurics. Journal of Volcanology and Geothermal Research 393:106806. https://doi.org/10.1016/j.jvolgeores.2020.106806

Donaldson CH, Williams RJ, Lofgren G (1975) A sample holding technique for study of crystal growth in silicate melts. American Mineralogist 60 (3-4): 324-326

Dowty E (1980) Chapter 10. Crystal Growth and Nucleation Theory and the Numerical Simulation of Igneous Crystallization. In: Physics of Magmatic Processes. Princeton University Press, pp 419–486

Eppich GR, Cooper KM, Kent AJR, Koleszar A (2012) Constraints on crystal storage timescales in mixed magmas: Uranium-series disequilibria in plagioclase from Holocene magmas at Mount Hood, Oregon. Earth and Planetary Science Letters 317–318:319–330. https://doi.org/10.1016/j.epsl.2011.11.019

Finnigan CS, Brenan JM, Mungall JE, McDonough WF (2008) Experiments and Models Bearing on the Role of Chromite as a Collector of Platinum Group Minerals by Local Reduction. Journal of Petrology 49:1647–1665. https://doi.org/10.1093/petrology/egn041

Gudmundsson A (2012) Magma chambers: Formation, local stresses, excess pressures, and compartments. Journal of Volcanology and Geothermal Research 237–238:19–41. https://doi.org/10.1016/j.jvolgeores.2012.05.015

Gurioli L, Harris AJL, Houghton BF, et al (2008) Textural and geophysical characterization of explosive basaltic activity at Villarrica volcano. Journal of Geophysical Research 113:2007JB005328. https://doi.org/10.1029/2007JB005328

Hammer JE, Rutherford MJ (2002) An experimental study of the kinetics of decompression-induced crystallization in silicic melt. Journal of Geophysical Research 107. https://doi.org/10.1029/2001JB000281

Hammer JE, Sharp TG, Wessel P (2010) Heterogeneous nucleation and epitaxial crystal growth

of magmatic minerals. Geology 38:367–370. https://doi.org/10.1130/G30601.1

Hayes JL, Calderón B R, Deligne NI, et al (2019a) Timber-framed building damage from tephra fall and lahar: 2015 Calbuco eruption, Chile. Journal of Volcanology and Geothermal Research 374:142–159. https://doi.org/10.1016/j.jvolgeores.2019.02.017

Hayes JL, Wilson TM, Stewart C, et al (2019b) Tephra clean-up after the 2015 eruption of Calbuco volcano, Chile: a quantitative geospatial assessment in four communities. J Appl Volcanol 8:7. https://doi.org/10.1186/s13617-019-0087-3

Hickey -Vargas R, Roa HM, Escobar LL, Frey FA (1989) Geochemical variations in Andean basaltic and silicic lavas from the Villarrica-Lanin volcanic chain (39.5 °S): an evaluation of source heterogeneity, fractional crystallization and crustal assimilation. Contributions to Mineralogy and Petrology 103: 361–386. https://doi.org/10.1007/BF00402922

Hickey-Vargas R, Abdollahi MJ, Parada MA, et al. (1995) Crustal xenoliths from Calbuco Volcano, Andean Southern Volcanic Zone: implications for crustal composition and magma-crust interaction. Contributions to Mineralogy and Petrology 119: 331-344.

Hickey-Vargas R, Holbik S, Tormey D, et al (2016) Basaltic rocks from the Andean Southern Volcanic Zone: Insights from the comparison of along-strike and small-scale geochemical variations and their sources. Lithos 258–259:115–132. https://doi.org/10.1016/j.lithos.2016.04.014

Higgins MD (2000) Measurement of crystal size distributions. American Mineralogist 85:1105–1116. https://doi.org/10.2138/am-2000-8-901

Higgins MD (2006). Quantitative textural measurements in igneous and metamorphic petrology. Cambridge university press.

Higgins MD (2011) Textural coarsening in igneous rocks. International Geology Review 53(3-4):354-376 doi:10.1080/00206814.2010.496177

Higgins MD, Roberge J (2003) Crystal Size Distribution of Plagioclase and Amphibole from Soufrière Hills Volcano, Montserrat: Evidence for Dynamic Crystallization-Textural Coarsening Cycles. Journal of Petrology 44(8): 1401-1411. https://doi.org/10.1093/petrology/44.8.1401

Kirkpatrick RJ (1977) Nucleation and growth of plagioclase, Makaopuhi and Alae lava lakes, Kilauea Volcano, Hawaii. Geological Socoety of America Bulletins 88:78. https://doi.org/10.1130/0016-7606(1977)88<78:NAGOPM>2.0.CO;2

Kirkpatrick RJ (1972) The kinetics of crystal growth in the system diopside-cats and the

application of crystal growth theory to some geologic problems. PhD Thesis, Univ. Illinois

Kirkpatrick RJ (1975) Crystal Growth from the Melt: A Review. American Mineralogist 60: 798-814.

Kirkpatrick RJ (1983) Theory of nucleation in silicate melts. American Mineralogist 68: 66-77.

La Spina G, Arzilli F, Llewellin EW, et al (2021) Explosivity of basaltic lava fountains is controlled by magma rheology, ascent rate and outgassing. Earth and Planetary Science Letters 553:116658. https://doi.org/10.1016/j.epsl.2020.116658

La Spina G, Burton M, Vitturi M, et al. (2016) Role of syn-eruptive plagioclase disequilibrium crystallization in basaltic magma ascent dynamics. Nature Communications 1–10. https://doi.org/10.1038/ncomms13402

Liang Y, Guo Y (2003) Reactive dissolution instability driven by chemical diffusion with applications to harzburgite reactive dissolution. Geophysical Research Letters 30:1–4. https://doi.org/10.1029/2003GL017687

Lindoo A, Humphreys MCS, Gordon C et al. (2025). Linking crystal shape and dynamic undercooling: a new framework for inferring magmatic crystallization histories. Contributions to Mineralogy and Petrology 180:92. https://doi.org/10.1007/s00410-025-02278-6

Lofgren GE (1983) Effect of Heterogeneous Nucleation on Basaltic Textures: A Dynamic Crystallization Study. Journal of Petrology 24:229–255. https://doi.org/10.1093/petrology/24.3.229

Lohmar S, Parada M, Gutiérrez F, et al (2012) Mineralogical and numerical approaches to establish the pre-eruptive conditions of the mafic Licán Ignimbrite, Villarrica Volcano (Chilean Southern Andes). Journal of Volcanology and Geothermal Research 235–236:55–69. https://doi.org/10.1016/j.jvolgeores.2012.05.006

López-Escobar L, Cembrano J, Moreno H (1995) Geochemistry and tectonics of the Chilean Southern Andes basaltic Quaternary volcanism (37-46°8). Revista Geologica de Chile 22(2):219-234.

Lopez-Escobar L, Parada MA, Hickey-Vargas R, et al (1995) Calbuco Volcano and minor eruptive centers distributed along the Liquiñe-Ofqui Fault Zone, Chile (41°–42° S): contrasting origin of andesitic and basaltic magma in the Southern Volcanic Zone of the Andes. Contributions to Mineralogy and Petrology 119:345–361. https://doi.org/10.1007/BF00286934.

López-Escobar L, Parada MA, Moreno H, et al A contribution to the petrogenesis of Osomo

and Calbuco volcanoes, Southern Andes (41 °00'-41 °30'S): comparative study. Revista Geologica de Chile 19(2): 211-226.

Mangan MT (1990) Crystal size distribution systematics and the determination of magma storage times: The 1959 eruption of Kilauea volcano, Hawaii. Journal of Volcanology and Geothermal Research 44:295–302. https://doi.org/10.1016/0377-0273(90)90023-9

Mangler MF, Humphreys MCS, Wadsworth FB, et al (2022) Variation of plagioclase shape with size in intermediate magmas: a window into incipient plagioclase crystallisation. Contributions to Mineralogy and Petrology 177:64. https://doi.org/10.1007/s00410-022-01922-9

Marsh BD (1998) On the Interpretation of Crystal Size Distributions in Magmatic Systems. Journal of Petrology 39(4): 553-599. https://doi.org/10.1093/petroj/39.4.553

Mixon EE, Singer BS, Jicha BR, Ramirez A (2021). Calbuco, a monotonous andesitic high-flux volcano in the Southern Andes, Chile. Journal of Volcanology and Geothermal Research 216: 107279.

Moore JG, Evans BW (1967) The role of olivine in the crystallization of the prehistoric Makaopuhi tholeiitic lava lake, Hawaii. Contributions to Mineralogy and Petrology 15:202–223. https://doi.org/10.1007/BF01185342

Moreno R, Hugo L, Lara E, Orozco G (2010) Carta Geologia del volcan Osorno. El Servicio Nacional de Geología y Minería

Morgado E, Morgan DJ, Castruccio A, et al (2019a) Old magma and a new, intrusive trigger: using diffusion chronometry to understand the rapid-onset Calbuco eruption, April 2015 (Southern Chile). Contributions to Mineralogy and Petrology 174:61. https://doi.org/10.1007/s00410-019-1596-0

Morgado E, Morgan DJ, Harvey J, et al (2019b) Localised heating and intensive magmatic conditions prior to the 22–23 April 2015 Calbuco volcano eruption (Southern Chile). Bull Volcanol 81:24. https://doi.org/10.1007/s00445-019-1280-2

Morgado E, Morgan DJ, Harvey J, et al (2019c) Localised heating and intensive magmatic conditions prior to the 22–23 April 2015 Calbuco volcano eruption (Southern Chile). Bull Volcanol 81:24. https://doi.org/10.1007/s00445-019-1280-2

Morgado E, Morgan DJ, Harvey J, et al (2022a) The Magmatic Evolution and the Regional Context of the 1835 AD Osorno Volcano Products (41°06'S, Southern Chile). Journal of Petrology 63:egac105. https://doi.org/10.1093/petrology/egac105

Morgado E, Morgan DJ, Harvey J, et al (2022b) The Magmatic Evolution and the Regional Context of the 1835 AD Osorno Volcano Products (41°06'S, Southern Chile). Journal

of Petrology 63:egac105. https://doi.org/10.1093/petrology/egac105

Morgado E, Parada MA, Morgan DJ, et al (2017) Transient shallow reservoirs beneath small eruptive centres: Constraints from Mg-Fe interdiffusion in olivine. Journal of Volcanology and Geothermal Research 347:327–336. https://doi.org/10.1016/j.jvolgeores.2017.10.002

Moschini P, Mollo S, Gaeta M, et al (2021) Parameterization of clinopyroxene growth kinetics via crystal size distribution (CSD) analysis: Insights into the temporal scales of magma dynamics at Mt. Etna volcano. Lithos 396–397:106225. https://doi.org/10.1016/j.lithos.2021.106225

Moschini P, Mollo S, Pontesilli A, et al (2023) A review of plagioclase growth rate and compositional evolution in mafic alkaline magmas: Guidelines for thermometry, hygrometry, and timescales of magma dynamics at Stromboli and Mt. Etna. Earth-Science Reviews 240:104399. https://doi.org/10.1016/j.earscirev.2023.104399

Moussallam Y, Bani P, Curtis A, et al (2016) Sustaining persistent lava lakes: Observations from high-resolution gas measurements at Villarrica volcano, Chile. Earth and Planetary Science Letters 454:237–247. https://doi.org/10.1016/j.epsl.2016.09.012

Namur O, Montalbano S, Bolle O, Vander Auwera J (2020) Petrology of the April 2015 Eruption of Calbuco Volcano, Southern Chile. Journal of Petrology 61:egaa084. https://doi.org/10.1093/petrology/egaa084

Parada MA, Godoy E, Herve F, Thiele R (1987) Miocene calc-alkaline pluton in the chilean southern Andes. Revista Brasileira de Geociencias 17(4):450-455.

Petit-Breuilh Sepulveda ME (1999) Cronología eruptiva histórica de los volcanes Osorno y Calbuco, Andes del Sur. Sernageomin

Petit-Breuilh Sepulveda ME (2004). La historia eruptiva de los volcanes hispanoamericanos (siglos XVI al XX): el modelo chileno. isbn: 978- 84-95938-32-9. url: https://dialnet.unirioja.es/servlet/libro?codigo=249104.

Petit-Breuilh Sepulveda ME, Jobato J (1994) Analísis comparativo de la cronología eruptiva histórica de los volcanes Llaima y Villarrica, 38°-39° LS. Sernageomin p.366-370.

Petrelli M, Zellmer GF (2020) Rates and Timescales of Magma Transfer, Storage, Emplacement, and Eruption. In: Vetere F (ed) Geophysical Monograph Series, 1st edn. Wiley, pp 1–41

Philpotts AR, Ague JJ (2009) Principles of igneous and metamorphic petrology. Cambridge University Press.

Plank T, Kelley KA, Zimmer MM, et al (2013) Why do mafic arc magmas contain ~4wt%

water on average? Earth and Planetary Science Letters 364:168–179. https://doi.org/10.1016/j.epsl.2012.11.044

Polacci M, Andronico D, De' Michieli Vitturi M, et al (2019) Mechanisms of Ash Generation at Basaltic Volcanoes: The Case of Mount Etna, Italy. Frontiers Earth Sciences 7:193. https://doi.org/10.3389/feart.2019.00193

Pupier E, Duchene S, Toplis MJ (2008) Experimental quantification of plagioclase crystal size distribution during cooling of a basaltic liquid. Contributions to Mineralogy and Petrology 155:555–570. https://doi.org/10.1007/s00410-007-0258-9

Putirka KD (2008) Introduction to Minerals, Inclusions and Volcanic Processes. Reviews in Mineralogy and Geochemistry 69:1–8. https://doi.org/10.2138/rmg.2008.69.1

Randolph AD, Larson MA (1971) Theory of Particulate Processes: Analysis and Techniques of Continuous Crystallization. 2nd edition, academic press., New York. https://doi.org/10.1016/B978-0-12-579650-7.X5001-5

Rice A, Von Gruenewaldt G (1995) Shear aggregation (convective scavenging) and cascade enrichment of PGEs and chromite in mineralized layers of large layered intrusions. Mineralogy and Petrology 54:105–117

Ruprecht P, Bergantz GW, Dufek J (2008) Modeling of gas-driven magmatic overturn: Tracking of phenocryst dispersal and gathering during magma mixing. Geochem Geophys Geosyst 9:2008GC002022. https://doi.org/10.1029/2008GC002022

Rutherford MJ (2008) Magma Ascent Rates. Reviews in Mineralogy and Geochemistry 69:241–271. https://doi.org/10.2138/rmg.2008.69.7

Schiavon B, Mollo S, Pontesilli A, et al (2023) Plagioclase crystal size distribution parameterization: A tool for tracking magma dynamics at Stromboli. Lithos 446–447:107143. https://doi.org/10.1016/j.lithos.2023.107143

Schwindinger KR (1999) Particle dynamics and aggregation of crystals in a magma chamber with application to Kilauea Iki olivines. Journal of Volcanology and Geothermal Research 88:209–238. https://doi.org/10.1016/S0377-0273(99)00009-8

Sellés D, Moreno HR (2011). Geología del volcán Calbuco, Región de los Lagos. Carta geológica de Chile serie geología básica, Sernageomin. N° 130. ISBN: ISSN 0717-7283.

Sellés S, Rodrigués AC, Dungan MA, et al (2004) Geochemistry of Nevado de Longaví Volcano (36.2°S): a compositionally atypical arc volcano in the Southern Volcanic Zone of the Andes. Revista Geologica de Chile 31:293–315

Shea T, Hammer JE (2013) Kinetics of cooling- and decompression-induced crystallization in

hydrous mafic-intermediate magmas. Journal of Volcanology and Geothermal Research 260:127–145. https://doi.org/10.1016/j.jvolgeores.2013.04.018

Silva Parejas C, Druitt TH, Robin C, et al (2010) The Holocene Pucón eruption of Volcán Villarrica, Chile: deposit architecture and eruption chronology. Bull Volcanol 72:677–692. https://doi.org/10.1007/s00445-010-0348-9

Simkin T, Siebert L (1994) Volcanoes of the World, xi+ 349 pp. Tucson: Geoscience Press for the Smithsonian Institution. Geological Magazine 134:121–142

Špillar V, Dolejš D (2014) Kinetic model of nucleation and growth in silicate melts: Implications for igneous textures and their quantitative description. Geochimica et Cosmochimica Acta 131:164–183. https://doi.org/10.1016/j.gca.2014.01.022

Stern CR (2004) Active Andean volcanism: its geologic and tectonic setting. Revista geológica de Chile 31:161–206. http://dx.doi.org/10.4067/S0716-02082004000200001

Syracuse EM, Van Keken PE, Abers GA (2010) The global range of subduction zone thermal models. Physics of the Earth and Planetary Interiors 183:73–90. https://doi.org/10.1016/j.pepi.2010.02.004

Toramaru A (2022) Vesiculation and Crystallization of Magma. In Advances in Volcanology, Springer Singapore. https://doi.org/10.1007/978-981-16-4209-8

Toramaru A, Noguchi S, Oyoshihara S, Tsune A (2008) MND(microlite number density) water exsolution rate meter. Journal of Volcanology and Geothermal Research 175:156–167. https://doi.org/10.1016/j.jvolgeores.2008.03.035

Turner S, Costa F (2007) Measuring Timescales of Magmatic Evolution. Elements 3:267–272. https://doi.org/10.2113/gselements.3.4.267

Turner SJ, Langmuir CH, Katz RF, et al (2016a) Parental arc magma compositions dominantly controlled by mantle-wedge thermal structure. Nature Geosci 9:772–776. https://doi.org/10.1038/ngeo2788

Turner SJ, Langmuir CH, Katz RF, et al (2016b) Parental arc magma compositions dominantly controlled by mantle-wedge thermal structure. Nature Geosciences 9:772–776. https://doi.org/10.1038/ngeo2788

Valderrama, Ó, Franco, L, Gil-Cruz, F (2015) Erupción intempestiva del volcán Calbuco, Abril 2015, XIV Congreso Geológico Chileno, III, p. 91–93

Vance JA (1969) On synneusis. Contributions to Mineralogy and Petrology 24:7–29

Vander Auwera J, Montalbano S, Namur O, et al (2021) The petrology of a hazardous volcano: Calbuco (Central Southern Volcanic Zone, Chile). Contributions to Mineralogy and Petrology 176:46. https://doi.org/10.1007/s00410-021-01803-7

Vander Auwera J, Namur O, Dutrieux A, et al (2019) Mantle Melting and Magmatic Processes Under La Picada Stratovolcano (CSVZ, Chile). Journal of Petrology 60:907–944. https://doi.org/10.1093/petrology/egz020

Vernon RH (2018) A Practical Guide to Rock Microstructure. Cambridge University press

Völker D, Kutterolf S, Wehrmann H (2011) Comparative mass balance of volcanic edifices at the southern volcanic zone of the Andes between 33°S and 46°S. Journal of Volcanology and Geothermal Research 205:114–129. https://doi.org/10.1016/j.jvolgeores.2011.03.011

Voorhees PW (1992) Ostwald ripening of two-phase mixtures. Annual Review of Materials Science 22:197–215

Witter JB, Kress VC, Delmelle P, Stix J (2004) Volatile degassing, petrology, and magma dynamics of the Villarrica Lava Lake, Southern Chile. Journal of Volcanology and Geothermal Research 134:303–337. https://doi.org/10.1016/j.jvolgeores.2004.03.002

Wright TL, Fiske RS (1971) Origin of the differentiated and hybrid lavas of Kilauea Volcano, Hawaii. Journal of Petrology 12:1–65. https://doi.org/10.1093/petrology/12.1.1

Zhang Y, Walker D, Lesher CE (1989) Diffusive crystal dissolution. Contributions to Mineralogy and Petrology 102:492–513.

Chapter VI

Conclusions

This thesis set out to constrain the timescales of magmatic processes taking place within the main magma reservoirs using the Crystal Size Distribution (CSD) method, by combining experimentally determined plagioclase growth rates with a textural study of 19 thin sections from three active Chilean volcanoes (Osorno, Calbuco, and Villarrica). This work thus integrated experimental and natural approaches to provide quantitative constraints on plagioclase crystallization kinetics and to improve the interpretation of textural records in arc magmas.

Two additional experimental objectives guided this research: (1) to determine plagioclase nucleation and growth rates under slow cooling conditions using an intermediate basaltic-andesite composition representative of subduction-related magmas, and (2) to evaluate the influence of thermal crystallization paths, particularly preheating conditions on crystallization mechanisms, nucleation regime and plagioclase microtextures.

Our experimental results showed that nucleation and growth follow a broadly similar evolution during cooling, reaching their maximum values at the onset of crystallization under the lowest cooling rates, before rapidly decreasing during the main crystallization stage. Linear relationships were observed between log(J), log(G), and both log(CR) and log(t), consistent with previous studies (e.g., *Grove 1978*; *Kohut and Nielson 2004*). Increasing the cooling rate, which enhances undercooling and shifts the temperature of maximum nucleation and growth toward lower values, promotes higher nucleation and growth rates and drives a pronounced evolution in crystal morphology from euhedral to hopper and dendritic habits, marking the transition from interface-controlled to diffusion-limited growth. The addition of a final relaxation time at the end of the cooling demonstrates that plagioclase crystals are characterized by a markedly slower textural equilibration than other minerals such as pyroxenes (P*ontesilli et al. 2019*). The persistence of high surface area–to–volume ratios and hopper morphologies, even after prolonged relaxation (>31 days), underlines the long timescales required for plagioclase to attain a low-energy equilibrium shape. This explains the preservation of certain disequilibrium microtextures during the final stages of magma ascent up to eruption.

Across more than 400 literature data points covering a wide range of compositions (SiO_2 = 50–75 wt%) and experimental conditions, our study confirms that the crystallization path exerts the primary control on kinetic parameters and the nucleation regime. At a low initial superheating (ΔT around 15 °C) under isothermal conditions, our nucleation and growth rate values (J and G) typically range from 10^0 to 10^4 $cm^{-3} \cdot s^{-1}$ and from 10^{-8} to 10^{-9} $cm \cdot s^{-1}$, respectively, with a single main nucleation episode. In cooling experiments (1–125 °C/h), the nucleation regime remains roughly continuous, and both rates increase with cooling rate, from 10^{-4} to 10^{-1} $cm^{-3} \cdot s^{-1}$

for nucleation and from 10^{-9} to 10^{-6} cm·s^{-1} for growth. The highest rates correspond to the most rapid cooling, consistent with previous ex situ studies (10^{-6}–10^{-11} cm·s^{-1}), but remain two to three orders of magnitude lower than in situ measurements (10^{-3}–10^{-4} cm·s^{-1}; *Arzilli et al. 2019*; *Le Gall et al. 2021*).

Increasing the duration of the initial superheating does not significantly alter the linear relationships of J and G with cooling rate or crystallization time but produces a pronounced decrease in the nucleation rate (down to 10^{-1} cm^{-3}·s^{-1} for ΔT = 35–55 °C) and, in some cases, a complete suppression of nucleation at the highest cooling rates (125 °C/h). This reduction in nucleation is counterbalanced by a marked increase in growth rate from 10^{-8}–10^{-7} to 10^{-6} cm·s^{-1} between 1 and 25 °C/h, accompanied by the development of dendritic, disequilibrium microtextures. Similar microtextures and J/G ratios are observed in experiments performed under high initial superheating and those conducted at the fastest cooling rates, emphasizing the comparable effects of these two thermal conditions on plagioclase crystallization dynamics. Thermal results also provided new insights into the nucleation regime. Our experiments highlight the coexistence of several mechanisms depending on the thermal path: "self-nucleation" processes occurring in seed-bearing runs (*Holness et al. 2023*), heterogeneous nucleation of clinopyroxene and Fe–Ti oxides on plagioclase substrates, and the formation of the first plagioclase crystals on Pt wire or sample walls during early cooling. At more advanced crystallization stages, although internal homogeneous nucleation (*Lofgren 1974*; *Donaldson 1979*) in cooling or isothermal experiments using either seeded or crystal-free materials cannot be excluded, the super-liquidus survival of nanometric or micrometric residual substrates may be sufficient to promote nucleation (*Lofgren et al. 1978*; *Berkebile and Dowty 1982*; *Davis and Ihinger 1998*), explaining the continuous nucleation phenomenon observed when a subliquidus isothermal step is added, even in initially crystal-free systems.

These results highlight that thermal conditions, particularly cooling and preheating exert a dominant control on crystallization kinetics and textures, while the influence of secondary factors such as calculation methods (L_{max}, Batch, or segmentation/CSD approach) or starting composition remains limited. Indeed, growth rates from basaltic and dacitic melts largely overlap, and the addition of water increases growth rates by less than one order of magnitude (*Shea and Hammer 2013*).

The application of experimentally constrained growth rates to natural plagioclase populations provides realistic estimates of magmatic crystallization timescales. CSD-derived timescales from the 19 natural samples range from a few days for microphenocrysts to about three years for macrophenocrysts. Longer timescales are associated with crystallization in shallow magma

reservoirs, whereas shorter ones correspond to late-stage processes preceding eruption, such as reheating, magma mixing, or increased undercooling. These short durations represent less than 1% of the total timescales inferred from isotopic dating (10–100 kyr; Cooper and Kent, 2014) and suggest that crystallization proceeds rapidly during transient thermal events.

Altogether, this work refines our understanding of plagioclase crystallization kinetics and demonstrates the strong potential of the CSD approach for quantifying short-lived magmatic processes when combined with experimentally derived constraints. This thesis thus makes a significant contribution to the quantitative interpretation of crystal records in magmatic systems and establishes a robust methodological framework for future investigations of dynamic magmatic processes. Building on these results, future studies could explore hydrous systems through dynamic experiments including the influence of shear and extend this approach to multi-mineral crystallization contexts, thereby providing a more comprehensive view of the complexity of natural magmatic systems. Overall, by bridging experimental kinetics and volcanic textures, this work contributes to a more quantitative and dynamic understanding of magmatic evolution in subduction-related environments.

References

Arzilli F, La Spina G, Burton MR, et al. (2019) Magma fragmentation in highly explosive basaltic eruptions induced by rapid crystallization. Nature Geosciences 12:1023–1028. https://doi.org/10.1038/s41561-019-0468-6

Berkebile CA, Dowty E (1982). Nucleation in laboratory charges of basaltic composition. American Mineralogist 67, 886-899.

Cooper KM, Kent AJR (2014) Rapid remobilization of magmatic crystals kept in cold storage. Nature 506:480–483. https://doi.org/10.1038/nature12991

Davis MJ, Ihinger PD (1998) Heterogeneous crystal nucleation on bubbles in silicate melt. American Mineralogist 83:1008–1015. https://doi.org/10.2138/am-1998-9-1008

Donaldson CH (1979) An experimental investigation of the delay in nucleation of olivine in Mafic Magmas. Contributions to Mineralogy and Petrology 69:21–32. https://doi.org/10.1007/BF00375191

Grove TL (1978). Cooling history of Luna 24 very low Ti (VLT) ferrobasalts: An experimental study. Proc. Lunar Planet. Sci. Conf 9th, 565-584

Le Gall N, Arzilli F, La Spina G, et al. (2021) In situ quantification of crystallisation kinetics of plagioclase and clinopyroxene in basaltic magma: Implications for lava flow. Earth and Planetary Science Letters 568:117016. https://doi.org/10.1016/j.epsl.2021.117016

Lofgren GE (1974). An experimental study of plagioclase crystal morphology: Isothermal crystallization. American Journal of Science 274, 243-273.

Lofgren GE, Smith DP, Brown RW (1978). Dynamic crystallization and kinetic melting of the lunar soil. *Proc. Lunar Planet. Sci. Conf. 9th*, 959-975.

Holness MB, Vukmanovic Z, O'Driscoll B (2023) The Formation of Chromite Chains and Clusters in Igneous Rocks. Journal of Petrology 64:egac124. https://doi.org/10.1093/petrology/egac124

Kohut E, Nielsen RL (2004) Melt inclusion formation mechanisms and compositional effects in high-An feldspar and high-Fo olivine in anhydrous mafic silicate liquids. Contrib Mineral Petrol 147:684–704. https://doi.org/10.1007/s00410-004-0576-0

Pontesilli A, Masotta M, Nazzari M, et al (2019) Crystallization kinetics of clinopyroxene and titanomagnetite growing from a trachybasaltic melt: New insights from isothermal time-series experiments. Chemical Geology 510:113–129. https://doi.org/10.1016/j.chemgeo.2019.02.015

Shea T, Hammer JE (2013) Kinetics of cooling- and decompression-induced crystallization in hydrous mafic-intermediate magmas. Journal of Volcanology and Geothermal Research 260:127–145. https://doi.org/10.1016/j.jvolgeores.2013.04.018

Supplementary File II-1: BSE images of the experimental loads

The objective of this supplementary file is to show the sample textures obtained in our experimental runs (BSE images of the whole sample, with additional zooms highlighting various textures or zones of interest). Additional data are available in the accompanying folder, including images of crystal clusters and the experimental formation of melt inclusions.

To remember, experiments were conducted using two different starting materials from the same natural basaltic – andesite (OS36) sample. In the first case, OS36 is a finely ground powder of a crystal poor basaltic-andesite (*Bechon et al. 2022*, *Billon et al. 2025*). Because some experiments generally start with an initial step at 1190 °C (ΔT = 15 °C), a few surviving plagioclase fragments can be found. These fragments range in size from 6 to 50 µm, with an average of approximately 16 µm. Runs initially conducted with this type of starting material correspond to our seed-bearing experiments. The second type of starting material (OS36*) was obtained by heating OS36 at 1450 °C for two hours in a muffle furnace to produce a crystal-free glass. As explained in the **Chapter IV**, three thermal paths were conducted at atmospheric pressure, at Ni-NiO condition, with a CO – CO2 operating flow rate of 0.07 cm/second:

1. Isothermal experiments (using OS36 and OS36* as starting materials; **Fig. SII-1a**) where samples were held during 24 hours at temperatures from 1200 °C to 1150 °C ($T_{sat, Plg}$ = 1175 °C ± 5 °C; see Billon et al. 2025).

2. Cooling experiments on OS36 (natural powder with plagioclase fragments, likely present in eruptive lavas; Lofgren 1983) and OS36* (fully glassy material reduced in powder). In the first series, samples were firstly held at 1190 °C (ΔT = 15 °C) and then cooled at constant rates of 1, 3, 9, 25 and 125 °C/h (**Fig. SII-1b**). Cooling experiments at 1, 3 and 9 °C/h on OS36 are presented in Billon et al. (2025). Each run was quenched at final temperatures (T_f) between 1165 and 1000 °C ($-\Delta T_n$ comprised between 10 and 175 °C) to study the progressive crystallization. In the second series, slow cooling experiments at 1 °C/h with an initially higher superheating degree (**Fig. SII-1c**) were performed on OS36. Experimental charges were initially maintained at super-liquidus

temperatures (1210 and 1230 °C; ΔT = 35 - 55 °C) for 24 hours, and then cooled at 1 °C/h before quenching at temperatures from 1165 to 1100 °C.

3. Cooling experiments with isothermal dwell (**Fig. SII-1d**) were led on OS36 using three steps. After 24 h at 1190°C, charges were cooled at 1 and 9 °C/h, down to 1165 and 1120 °C; and finally quenched after dwells of 2, 5, 10, 24, 240 (10 days), 264 (11 days), 384 (16 days) and 744 hours (31 days).

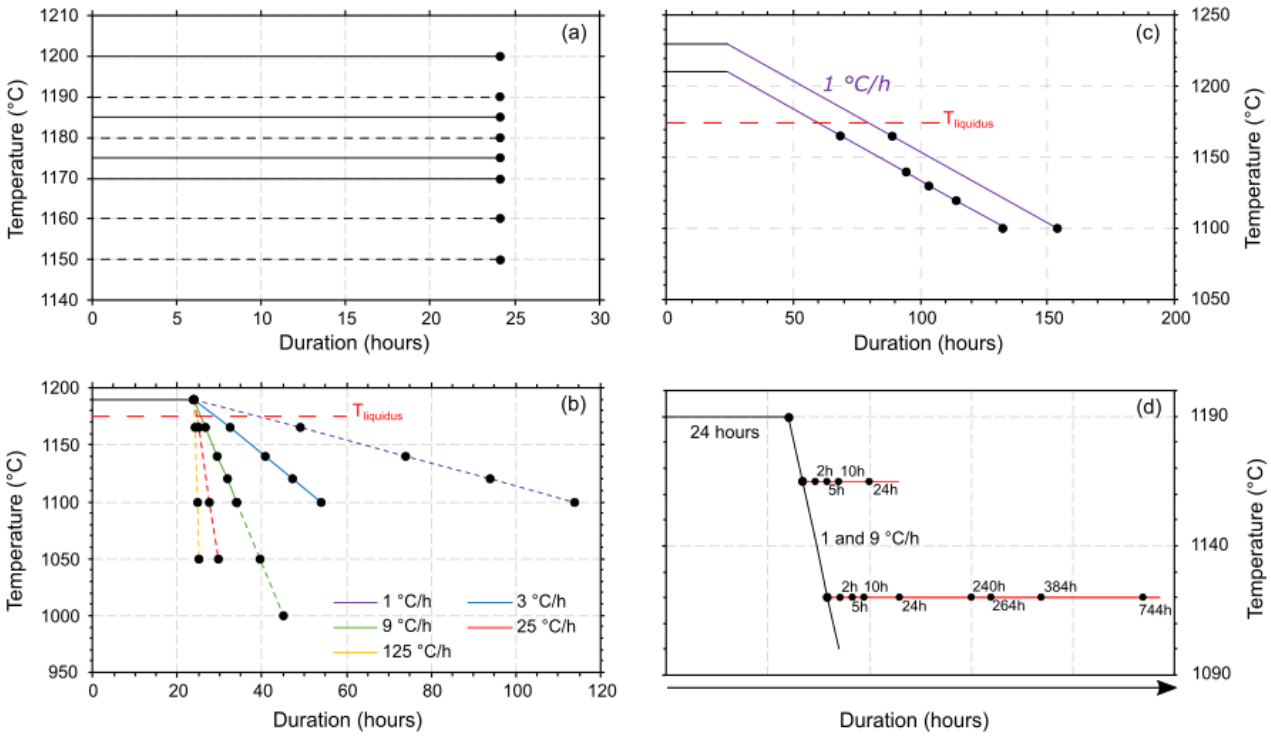

Figure SII-1 (Taken from the Figure IV-1): *Overview of the temperature-time paths used in this study. Solid lines indicate experiments with OS36 (crystal-bearing) as the starting material; dashed lines indicate those with both OS36* (crystal-free, pre-heated to 1450 °C for 2 h) and OS36 as the starting material.* ***a*** *24-h isothermal experiments initially used to determine the liquidus temperature.* ***b*** *Experiments cooled at 1, 3, 9, 25, and 125 °C/h after an initial 24-h isothermal step at 1190 °C. Runs were quenched at 1165, 1140, 1120, 1100, 1050, or 1000 °C. Experiments using OS36 cooled at 1, 3, and 9 °C/h are from Billon et al. (2025).* ***c*** *Experiments cooled at 1 °C/h, after an initial 24-h isothermal step at 1210 °C (ΔT = 35 °C) or 1230 °C (ΔT = 55 °C). Runs were quenched at various temperatures between 1165 and 1100 °C.* ***d*** *Complex crystallization paths involving a cooling step similar to those in* ***(b)*** *at 1 and 9 °C/h, followed by final isothermal dwell times from 2 h to 31 days at 1165 or 1120 °C.*

								Global image	Segmentation					
Chapter	Sample	Type (ISO, CR)	Pre-treatment	Pre-existing crystals	T_i (°C)	T_f (°C)	$t_{final\ step}$ (h)	Phases (prop; %)	N_A (µm^{-2})	l_{mean} (µm)	$l_{max,\ av}$ (µm)	2D aspect ratio mode	2D aspect ratio median (mean)	Plg 2D habit
Chapter 3[a]	G 0-0a	ISO	-	Yes	1190	1190	24	P.c, gl (100)	2.23E-05	16	36	0,6 - 0,7	0,6 (0,65)	Resorbed
	G 0-0b1	ISO	-	Yes	1190	1190	24	P.c, gl (100)	3.58E-06	-	-	-	-	Resorbed
	G 0-0b2	ISO	-	Yes	1190	1190	24	P.c, gl (100)	8.30E-06	-	-	-	-	Resorbed
	G 0-0b3	ISO	-	Yes	1190	1190	24	P.c, gl (100)	4.50E-06	-	-	-	-	Resorbed
	G 0-0b4	ISO	-	Yes	1190	1190	24	P.c, gl (100)	1.02E-05	-	-	-	-	Resorbed
Chapter 3[a]	G 0-1	ISO	-	Yes	1185	1185	24	P.c (1), Plg? gl (99)	1.28E-04	11	28	0,6 - 0,8	0,6 (0,64)	Rounded
Chapter 3[a]	G 0-2	ISO	-	Yes	1180	1180	24	P.c, Plg (3), gl (97)	2.41E-04	12	54	0,6 - 0,7	0,61 (0,66)	Rounded
Chapter 3[a]	G 0-3	ISO	-	Yes	1175	1175	24	Plg (3), gl (97)	1.28E-04	11	28	0,6 - 0,7	0,59 (0,63)	Rounded
	G 0-4	ISO	-	Yes	1160	1160	24	Plg (7), gl (93)	5.45E-04	10	36	0,6 - 0,8	0,62 (0,65)	Rounded
	G 0-5	ISO	-	Yes	1150	1150	24	Plg (14), Ox (2) gl (84)	2.37E-03	9	32	0,6 - 0,8	0,61 (0,65)	Rounded
	G 0-6	ISO	1450 °C, 2 h	No	1200	1200	24	gl (100)	-	-	-	-	-	-
	G 0-7	ISO	1450 °C, 2 h	No	1190	1190	24	gl (100)	-	-	-	-	-	-
	G 0-8	ISO	1450 °C, 2 h	No	1180	1180	24	gl (100)	-	-	-	-	-	-
	G 0-9	ISO	1450 °C, 2 h	No	1170	1170	24	Plg (5), gl (95)	4.08E-03	5	15	0,3 - 0,4	0,29 (0,37)	Lamellar
	G 0-10	ISO	1450 °C, 2 h	No	1160	1160	24	Plg (5), gl (95), Ox (<<1)	8.23E-03	6	17	0,2 - 0,3	0,28 (0,36)	Lamellar
	G 0-11	ISO	1450 °C, 2 h	No	1150	1150	24	Plg (8), gl (92)	1.43E-02	5	17	0,2 - 0,3	0,28 (0,36)	Lamellar
Chapter 3[a]	G 1-0	CR (1 °C/h)	-	Yes	1190	1175	0	P.c, gl (99), Plg (1)	4.14E-05	22	52	-	-	Equant/Tabular
Chapter 3[a]	G 1-1a1	CR (1 °C/h)	-	Yes	1190	1165	0	Plg (6), gl (94)	2.55E-04	21	87	0,7 - 0,8	0,51 (0,55)	Equant/Tabular
Chapter 3[a]	G 1-1a2	CR (1 °C/h)	-	Yes	1190	1165	0	Plg (3), gl (97)	1.62E-04	21	68	0,6 - 0,7	0,52 (0,57)	Equant/Tabular
Chapter 3[a]	G 1-2	CR (1 °C/h)	-	Yes	1190	1137	0	Plg (12), gl (88)	4.31E-04	20	114	0,5 - 0,7	0,52 (0,56)	Equant/Tabular

Chapter 3[a]	G 1-3	CR (1 °C/h)	-	Yes	1190	1120	0	Plg (21), Ox (2), gl (77)	4.99E-04	22	130	0,6 - 0,7	0,48 (0,52)	Equant/Tabular
Chapter 3[a]	G 1-4	CR (1 °C/h)	-	Yes	1190	1100	0	Plg (21), Ox (<1), gl (79)	5.63E-04	25	183	0,6 - 0,7	0,54 (0,56)	Equant/Tabular
Chapter 3[a]	G 2-0	CR (3 °C/h)	-	Yes	1190	1175	0	P.c, gl (99), Plg (1)	3,61E-06	16	41	-	-	Resorbed/Equant
Chapter 3[a]	G 2-1a	CR (3 °C/h)	-	Yes	1190	1165	0	Plg (3), gl (97)	1.61E-04	16	60	0,6 - 0,7	0,47 (0,52)	Equant/Tabular
Chapter 3[a]	G 2-1b	CR (3 °C/h)	-	Yes	1190	1165	0	Plg (<1), gl (100)	1.21E-05	23	35	-	-	Equant/Tabular
Chapter 3[a]	G 2-2	CR (3 °C/h)	-	Yes	1190	1140	0	Plg (11), gl (89)	3.73E-04	23	135	0,6 - 0,7	0,46 (0,48)	Tabular/Elongated
Chapter 3[a]	G 2-3	CR (3 °C/h)	-	Yes	1190	1120	0	Plg (15), gl (85)	5.07E-04	22	127	0,5 - 0,6	0,45 (0,5)	Tabular/Elongated
Chapter 3[a]	G 2-4	CR (3 °C/h)	-	Yes	1190	1100	0	Plg (20), gl (80)	5.30E-04	26	156	0,5 - 0,6	0,44 (0,48)	Tabular/Elongated
Chapter 3[a]	G 3-0	CR (9 °C/h)	-	Yes	1190	1175	0	P.c, gl (100), Plg (<<1)	4.47E-06	20	26	-	-	Resorbed
Chapter 3[a]	G 3-1	CR (9 °C/h)	-	Yes	1190	1165	0	Plg (1), gl (99)	1.63E-04	9	31	0,7 - 0,8	0,52 (0,57)	Equant/Tabular
Chapter 3[a]	G 3-2a1	CR (9 °C/h)	-	Yes	1190	1140	0	Plg (14), gl 1 (86)	7.05E-04	14	113	0,6 - 0,7	0,43 (0,49)	Tabular/Elongated
Chapter 3[a]	G 3-2a2	CR (9 °C/h)	-	Yes	1190	1140	0	Plg (9), gl (91)	6.77E-04	18	103	0,6 - 0,7	0,47 (0,51)	Tabular/Elongated
Chapter 3[a]	G 3-3a	CR (9 °C/h)	-	Yes	1190	1120	0	Plg (14), gl 1 (86)	3.30E-04	28	187	0,5 - 0,6	0,39 (0,44)	Skeletal
Chapter 3[a]	G 3-3b	CR (9 °C/h)	-	Yes	1190	1120	0	Plg (15), gl (85)	4.01E-04	24	140	0,4 - 0,5	0,39 (0,44)	Skeletal
Chapter 3[a]	G 3-4	CR (9 °C/h)	-	Yes	1190	1100	0	Plg (24), Ox (1), gl (75)	8.81E-04	19	126	0,5 - 0,7	0,45 (0,49)	Tabular/Elongated
Chapter 3[a]	G 3-5	CR (9 °C/h)	-	Yes	1190	1050	0	Plg (39), Ox (1), Cpx (15), gl (45)	5.69E-04	35	133	0,1 - 0,2	0,36 (0,42)	Tabular
Chapter 3[a]	G 3-6	CR (9 °C/h)	-	Yes	1190	1000	0	Plg (48), Ox (1), Cpx (1), gl (20)	-	35	103	0,3 - 0,4	0,4 (0,48)	Tabular
Chapter 4[b]	G 4-1	CR (25 °C/h)	-	Yes	1190	1165	-	P.c, Plg (<1), gl (100)	3.76E-05	13	31	0,6 - 0,7	0,58 (0,6)	Resorbed/Tabular
Chapter 4[b]	G 4-2	CR (25 °C/h)	-	Yes	1190	1100	-	Plg (23), gl (77)	6.67E-04	21	135	0,4 - 0,5	0,39 (0,44)	Skeletal
Chapter 4[b]	G 4-3	CR (25 °C/h)	-	Yes	1190	1050	-	Plg (32), Cpx (1), gl (67)	4.80E-04	39	222	0,1 - 0,2	0,32 (0,41)	Skeletal/Dendritic
Chapter 4[b]	G 5-1	CR (125 °C/h)	-	Yes	1190	1165	-	P.c (<1), gl (100)	2.97E-06	17	24	-	-	Resorbed
Chapter 4[b]	G 5-2a1	CR (125 °C/h)	-	Yes	1190	1100	-	Plg (4), gl (96)	3.20E-04	16	83	0,2 - 0,3	0,39 (0,45)	Skeletal/Dendritic
Chapter 4[b]	G 5-2a2	CR (125 °C/h)	-	Yes	1190	1100	-	Plg (6), gl (94)	2.96E-04	19	92	0,3 - 0,4	0,37 (0,44)	Skeletal/Dendritic

Chapter 4[b]	G 5-3	CR (125 °C/h)	-	Yes	1190	1050	-	Plg (36), gl (64)	1.61E-03	25	203	0,2 - 0,3	0,34 (0,42)	Skeletal/Dendritic
Chapter 4[b]	G 6-1	CR (1 °C/h) + ISO	-	Yes	1190	1165	2	Plg (1), gl (99)	2.52E-05	28	66	0,6 - 0,7	0,52 (0,58)	Equant/Tabular
Chapter 4[b]	G 6-2a1	CR (1 °C/h) + ISO	-	Yes	1190	1165	5	Plg (5), gl (95)	1.43E-04	27	83	0,7 - 0,8	0,51 (0,54)	Tabular
Chapter 4[b]	G 6-2a2	CR (1 °C/h) + ISO	-	Yes	1190	1165	5	Plg (4), gl (96)	1.33E-04	27	114	0,6 - 0,7	0,54 (0,57)	Tabular
Chapter 4[b]	G 6-3	CR (1 °C/h) + ISO	-	Yes	1190	1165	10	Plg (3), gl (97)	6.00E-05	34	96	0,6 - 0,7	0,51 (0,53)	Tabular
Chapter 4[b]	G 6-4	CR (1 °C/h) + ISO	-	Yes	1190	1165	24	Plg (4), gl (96)	4.31E-05	42	131	0,6 - 0,7	0,53 (0,57)	Tabular/Elongated
Chapter 4[b]	G 6-5	CR (1 °C/h) + ISO	-	Yes	1190	1120	2	Plg (15), gl (85)	1.66E-04	49	195	0,6 - 0,7	0,46 (0,5)	Tabular/Equant/Elongated
Chapter 4[b]	G 6-6	CR (1 °C/h) + ISO	-	Yes	1190	1120	5	Plg (18), gl (82)	1.26E-04	58	221	0,6 - 0,7	0,48 (0,51)	Tabular/Equant
Chapter 4[b]	G 6-7	CR (1 °C/h) + ISO	-	Yes	1190	1120	10	Plg (19), Ox (<1), gl (81)	9.45E-05	78	268	0,6 - 0,7	0,44 (0,48)	Tabular/Equant
Chapter 4[b]	G 6-8	CR (1 °C/h) + ISO	-	Yes	1190	1120	24	Plg (18), gl (82)	1.36E-04	68	297	0,4 - 0,5	0,4 (0,46)	Tabular
Chapter 4[b]	G 6-9	CR (1 °C/h) + ISO	-	Yes	1190	1120	240	Plg (18), Ox (<1), gl (82)	1.43E-04	59	254	0,5 - 0,6	0,47 (0,48)	Tabular/Elongated
Chapter 4[b]	G 6-10	CR (9 °C/h) + ISO	-	Yes	1190	1165	5	Plg (3), gl (97)	1.32E-04	22	103	0,6 - 0,7	0,4 (0,49)	Tabular/Elongated
Chapter 4[b]	G 6-11	CR (9 °C/h) + ISO	-	Yes	1190	1165	24	Plg (4), gl (96)	1.16E-04	31	114	0,3 - 0,4	0,44 (0,49)	Tabular/Elongated
Chapter 4[b]	G 6-12	CR (9 °C/h) + ISO	-	Yes	1190	1120	10	Plg (17), gl (83)	2.07E-04	49	271	0,1 - 0,2	0,36 (0,43)	Skeletal
Chapter 4[b]	G 6-13	CR (9 °C/h) + ISO	-	Yes	1190	1120	24	Plg (20), gl (80)	2.09E-04	58	271	0,1 - 0,2	0,34 (0,42)	Skeletal
Chapter 4[b]	G 6-14	CR (9 °C/h) + ISO	-	Yes	1190	1120	264	Plg (18), gl (82)	2.85E-04	51	239	0,1 - 0,3	0,36 (0,43)	Skeletal/Tabular
Chapter 4[b]	G 6-15	CR (9 °C/h) + ISO	-	Yes	1190	1120	384	Plg (19), gl (81)	3.18E-04	45	236	0,1 - 0,2	0,39 (0,45)	Skeletal/Tabular
Chapter 4[b]	G 6-16a	CR (9 °C/h) + ISO	-	Yes	1190	1120	744	Plg (21), gl 1 (79)	3.52E-04	46	258	0,1 - 0,2	0,37 (0,44)	Skeletal/Tabular
Chapter 4[b]	G 6-16b	CR (9 °C/h) + ISO	-	Yes	1190	1120	744	Plg (22), Cpx (<1), gl (78)	2.93E-04	48	237	0,1 - 0,2	0,4 (0,45)	Skeletal/Tabular
Chapter 4[b]	G 6-17	CR (1 °C/h) + ISO	-	No	1210	1120	24	Plg (14), gl (86)	8.35E-06	371	1354	-	-	Dendritic
Chapter 4[b]	G 7-1	CR (1 °C/h)	1450 °C, 2 h	No	1190	1165	0	Plg (1), gl (99)	1.69E-05	52	142	-	-	Equant/Elongated
Chapter 4[b]	G 7-2	CR (1 °C/h)	1450 °C, 2 h	No	1190	1140	0	Plg (7), gl (93)	1.55E-05	154	274	-	-	Skeletal
Chapter 4[b]	G 7-3	CR (1 °C/h)	1450 °C, 2 h	No	1190	1120	0	Plg (20), gl (80)	6.37E-05	121	380	0,1 - 0,2	0,15 (0,32)	Skeletal

Chapter 4[b]	G 7-4	CR (1 °C/h)	1450 °C, 2 h	No	1190	1100	0	Plg (21), Ox (<1), gl (79)	3.29E-05	116	372	0- 0,1	0,23 (0,34)	Skeletal (Dendritic extensions)
Chapter 4[b]	G 8-1	CR (9 °C/h)	1450 °C, 2 h	No	1190	1050	0	Plg (33), Ox (1), Cpx (1), gl (65)	5.62E-05	210	576	0,1 - 0,2	0,12 (0,24)	Dendritic
Chapter 4[b]	G 8-2	CR (9°C/h)	1450 °C, 2 h	No	1190	1000	0	Plg (37), Ox (<1), Cpx (18), gl (45)	1.08E-04	141	404	0,1 - 0,2	0,14 (0,24)	Dendritic
Chapter 4[b]	G 9-1	CR (25°C/h)	1450 °C, 2 h	No	1190	1165	0	gl (100)	0.00E+00	-	-	-	-	-
Chapter 4[b]	G 9-2	CR (25°C/h)	1450 °C, 2 h	No	1190	1100	0	Plg (5), gl (95)	3.63E-05	128	294	0 - 0,2	0,08 (0,19)	Dendritic
Chapter 4[b]	G 9-3	CR (25°C/h)	1450 °C, 2 h	No	1190	1050	0	Plg (36), gl (64)	5.40E-05	230	491	0,1 - 0,2	0,10 (0,17)	Dendritic
Chapter 4[b]	G 10-1	CR (125°C/h)	1450 °C, 2 h	No	1190	1165	0	gl (100)	0.00E+00	-	-	-	-	-
Chapter 4[b]	G 10-2	CR (125°C/h)	1450 °C, 2 h	No	1190	1050	0	gl (100)	0.00E+00	-	-	-	-	-
Chapter 4[b]	G 11-1	CR (1 °C/h)	-	No	1210	1165	0	gl (100)	0.00E+00	-	-	-	-	-
Chapter 4[b]	G 11-2	CR (1 °C/h)	-	No	1210	1140	0	Plg (1), gl (99)	8.99E-07	445	644	-	-	Dendritic
Chapter 4[b]	G 11-3	CR (1 °C/h)	-	No	1210	1130	0	Plg (9), gl (91)	3.28E-06	644	1116	-	-	Dendritic
Chapter 4[b]	G 11-4	CR (1 °C/h)	-	No	1210	1120	0	Plg (15), gl (85)	1.04E-05	420	1099	-	-	Dendritic
Chapter 4[b]	G 11-5	CR (1 °C/h)	-	No	1210	1100	0	Plg (20), gl (80)	8.10E-06	477	1124	-	-	Dendritic
Chapter 4[b]	G 11-6	CR (1 °C/h)	-	No	1230	1165	0	gl (100)	0.00E+00	-	-	-	-	-
Chapter 4[b]	G 11-7	CR (1 °C/h)	-	No	1230	1100	0	Plg (21), gl (79)	1.19E-05	387	1218	0 - 0,1	0,07 (0,2)	Dendritic

Table S2-1: *Summary of the main textural parameters (phases with proportions in parentheses, plagioclase number density N_A, mean crystal size l_{mean}, maximum crystal size l_{max}, and 2D aspect ratio). P.c: Pre-existing plagioclase fragments; Plg: plagioclase; Gl: glass; Ox: Fe–Ti oxide; Cpx: clinopyroxene*

ISOTHERMAL EXPERIMENTS

Isothermal conditions: 1190 °C for 24 hours

Starting material: OS36 (G0-0a and b1 to b4), OS36* (G 0-7)

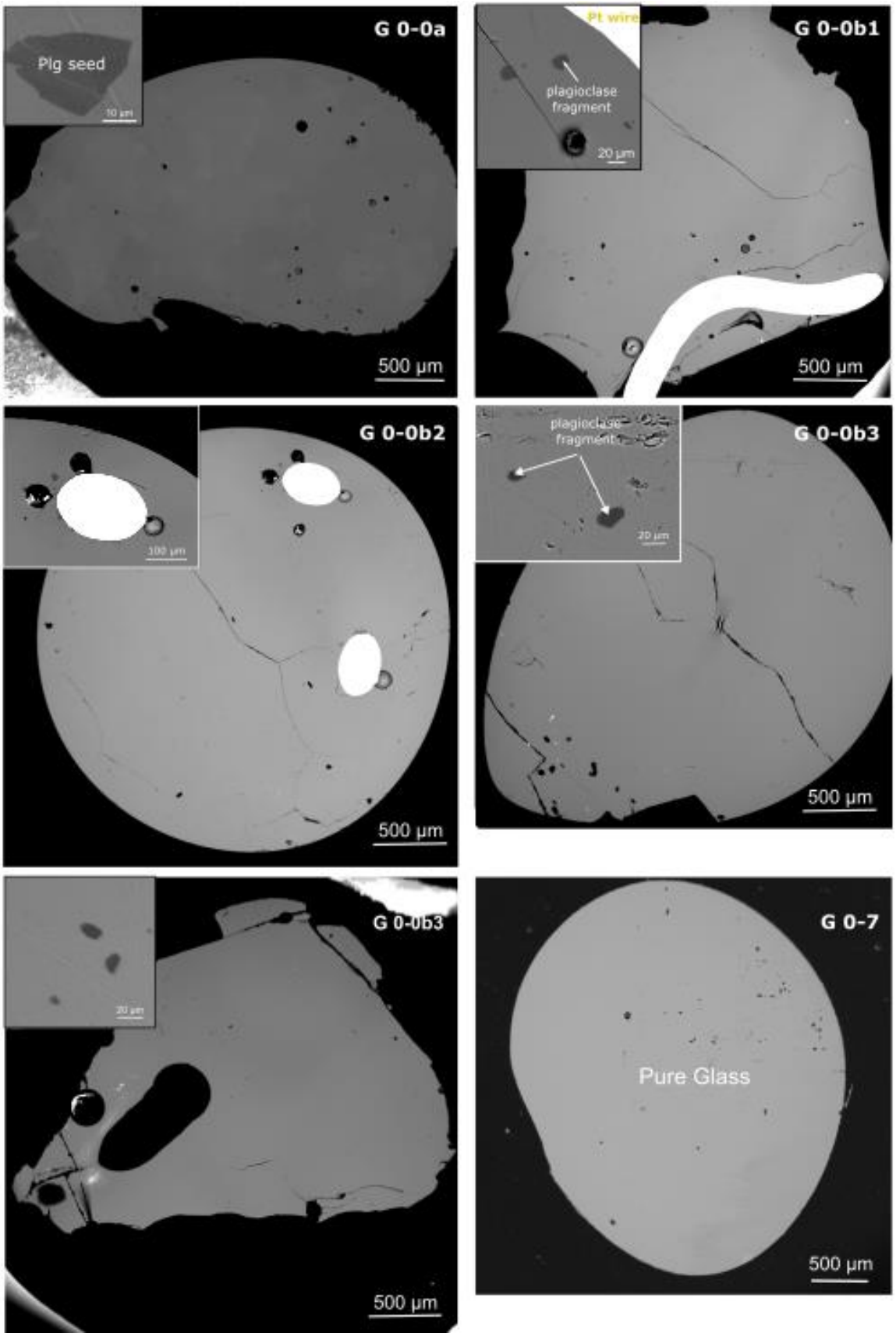

Isothermal conditions: 1180 °C for 24 hours

Starting material: OS36 (G0-2), OS36* (G 0-8)

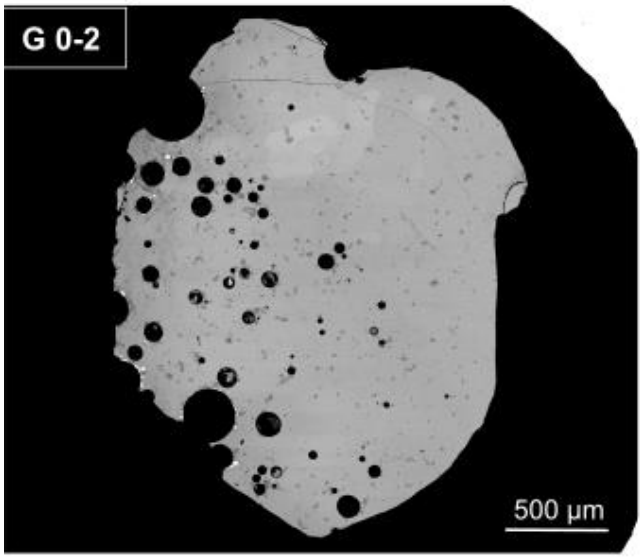

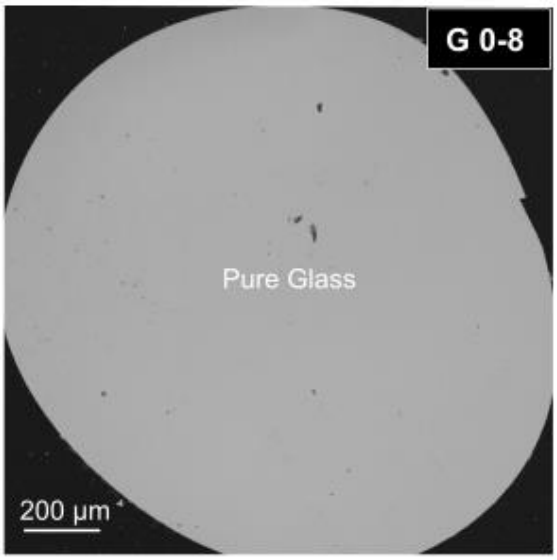

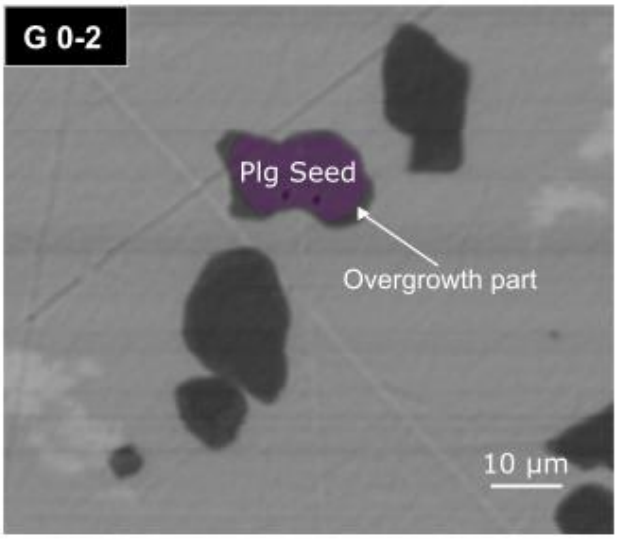

Isothermal conditions: 1175 - 1170 °C for 24 hours

Starting material: OS36 (G0-3), OS36* (G 0-9)

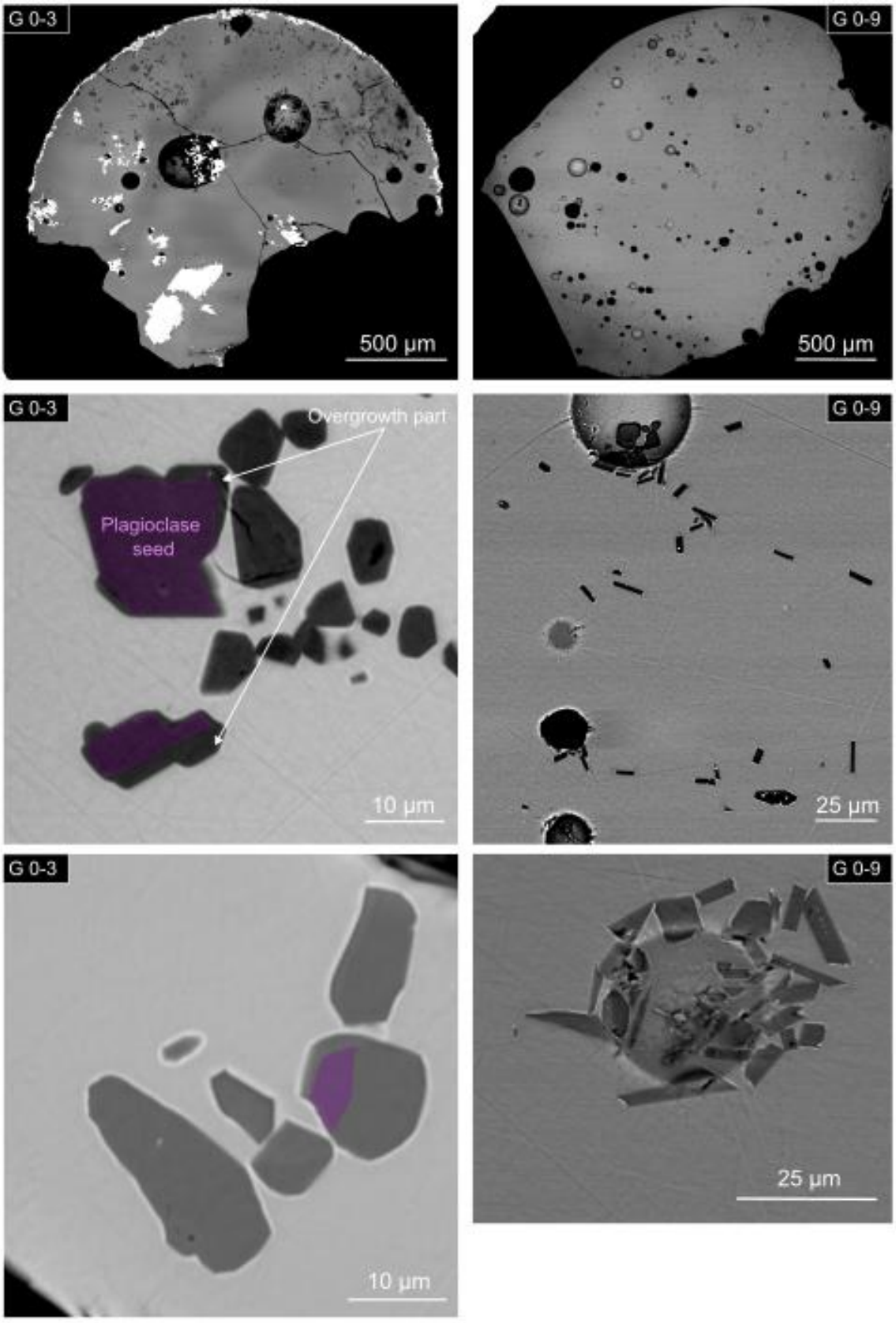

Isothermal conditions: 1160 and 1150 °C for 24 hours

Starting material: OS36 (G 0-4 and G 0-5), OS36* (G 0-10 and G 0-11)

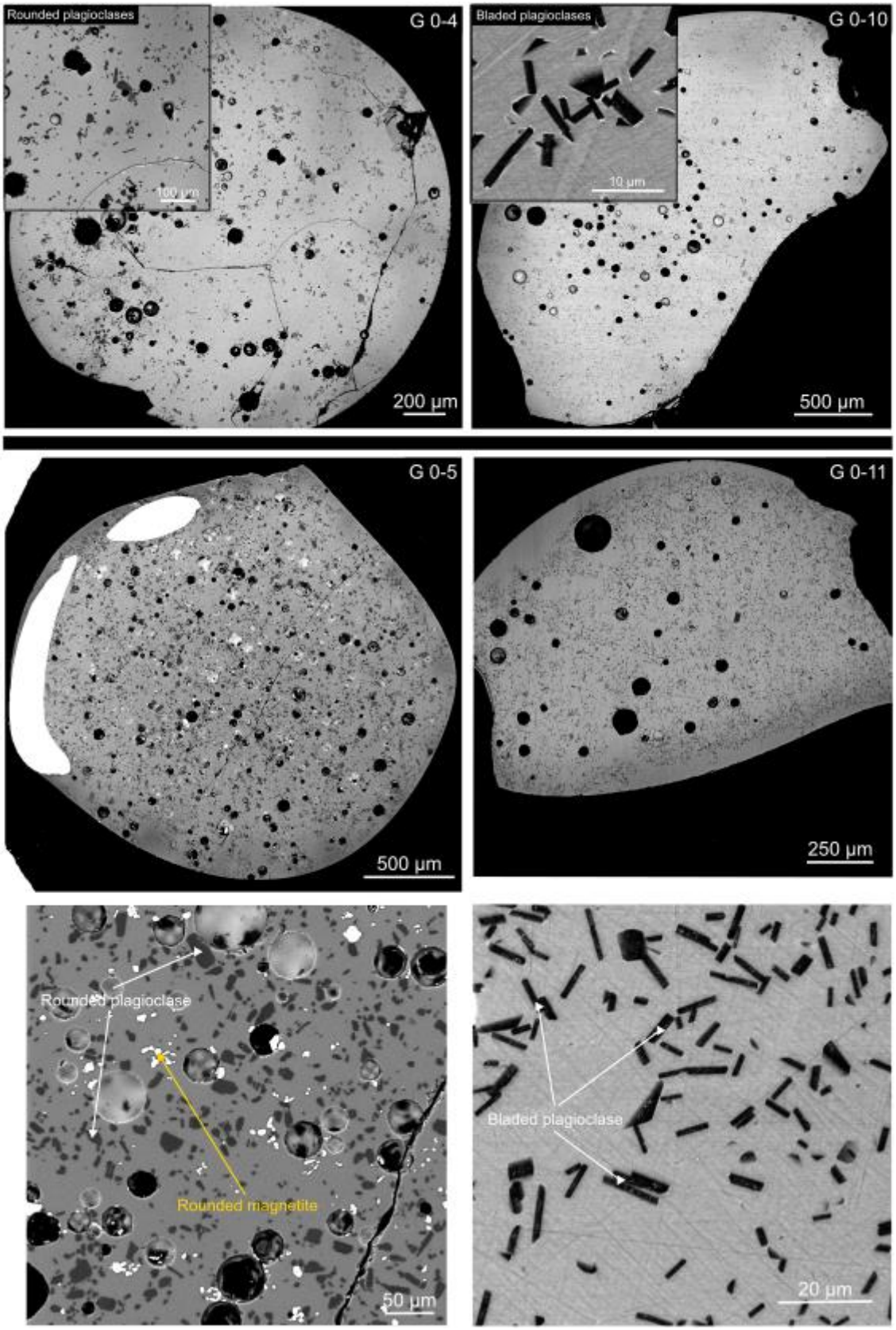

COOLING RUNS

Cooling conditions: 1 °C/h (with seeds)

Starting material: OS36 (from G 1-0 to G 1-4)

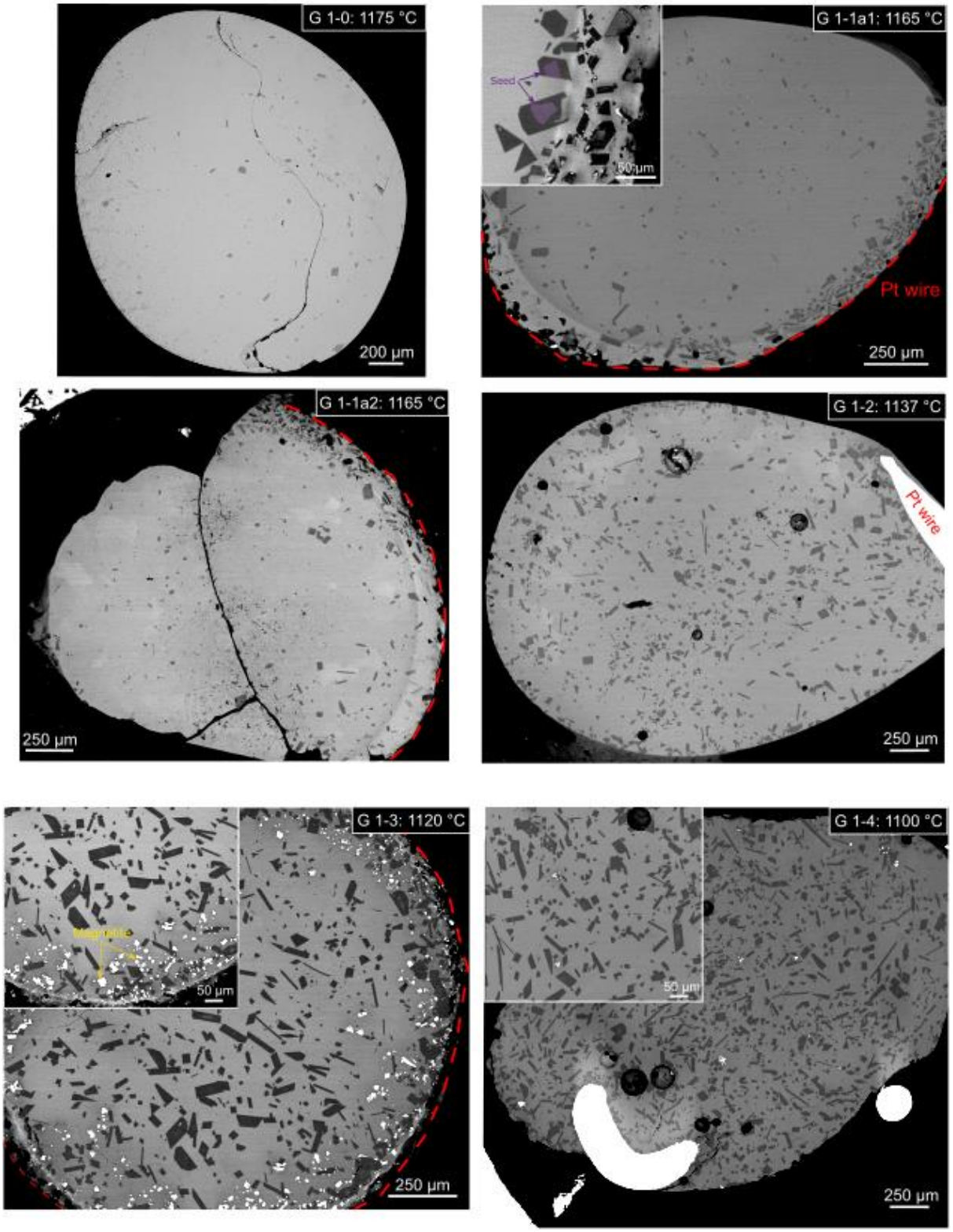

Cooling conditions: 3 °C/h (with seeds)

Starting material: OS36 (from G 2-0 to G 2-4)

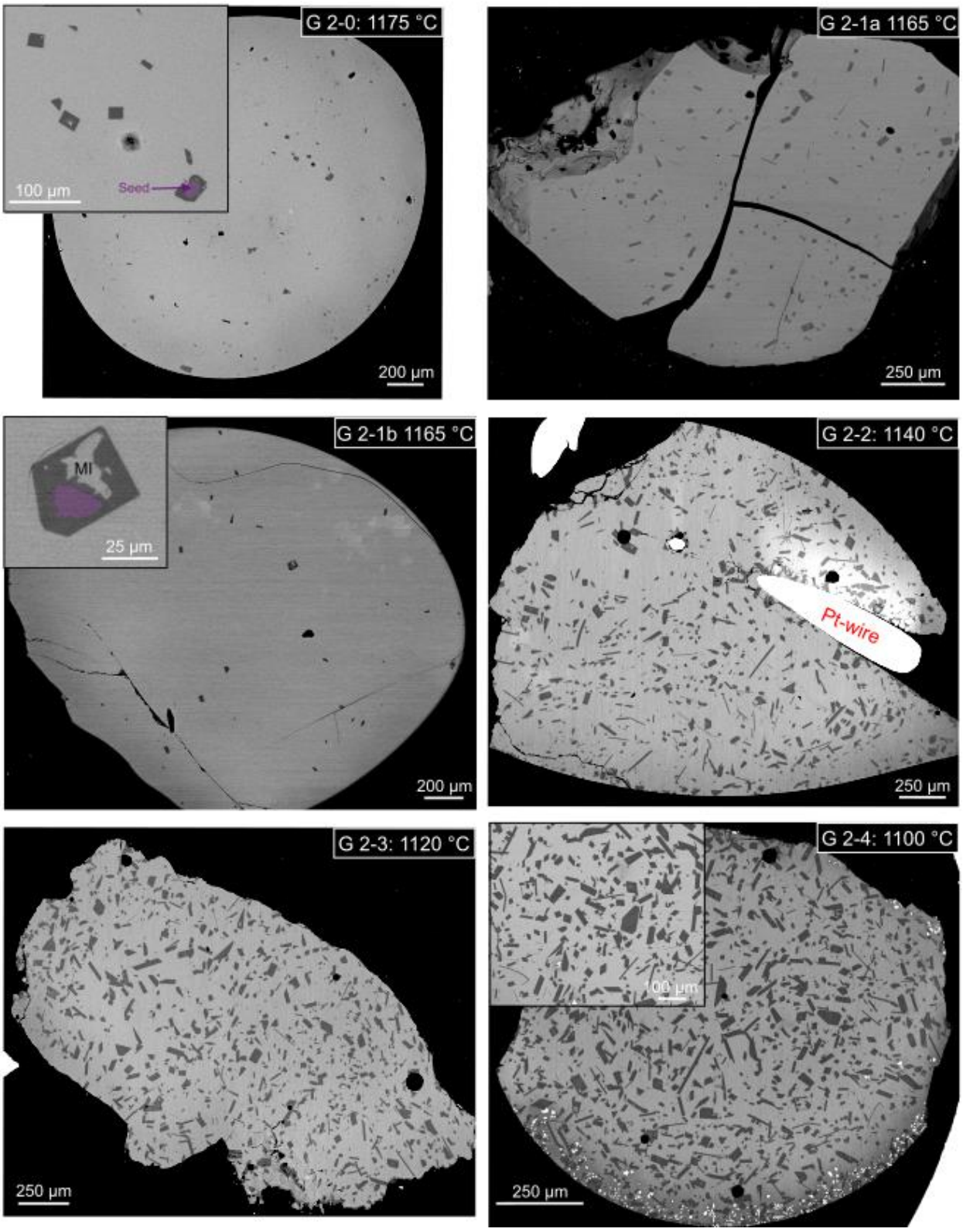

Cooling conditions: 9 °C/h (with seeds)

Starting material: OS36 (from G 3-1 to G 3-6)

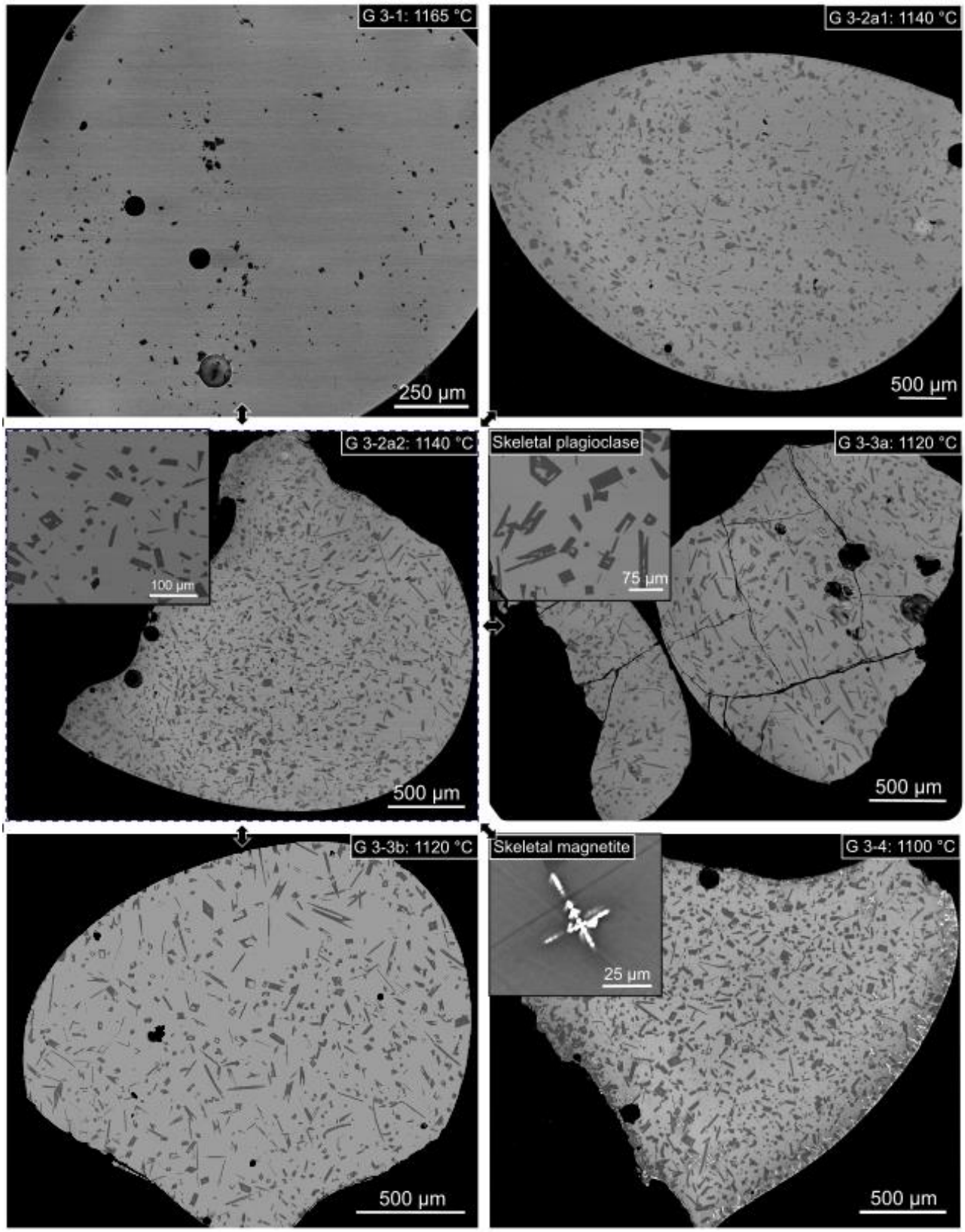

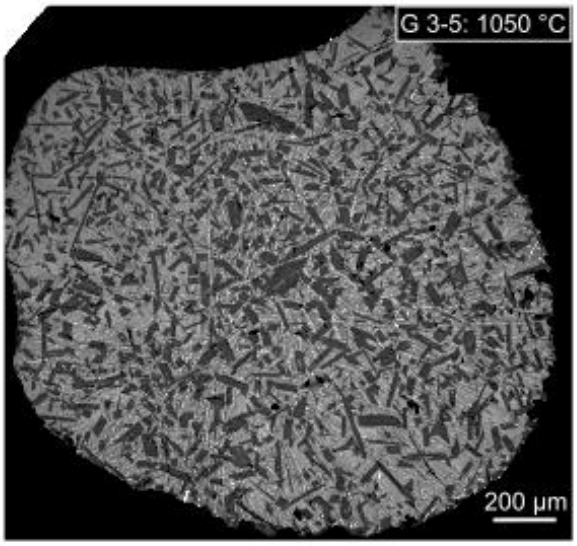
G 3-5: 1050 °C
200 µm

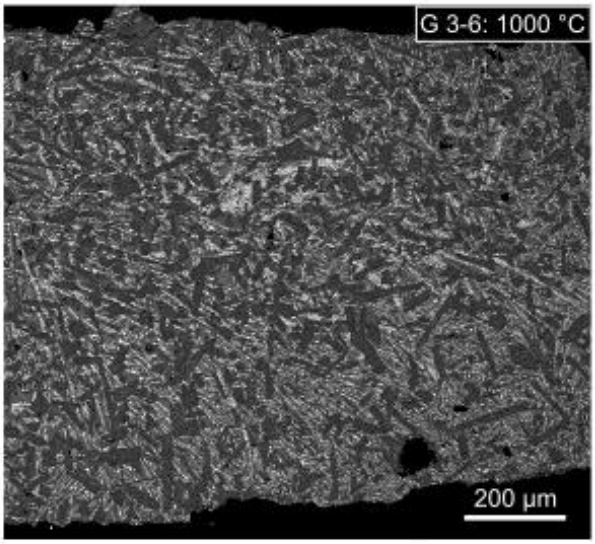
G 3-6: 1000 °C
200 µm

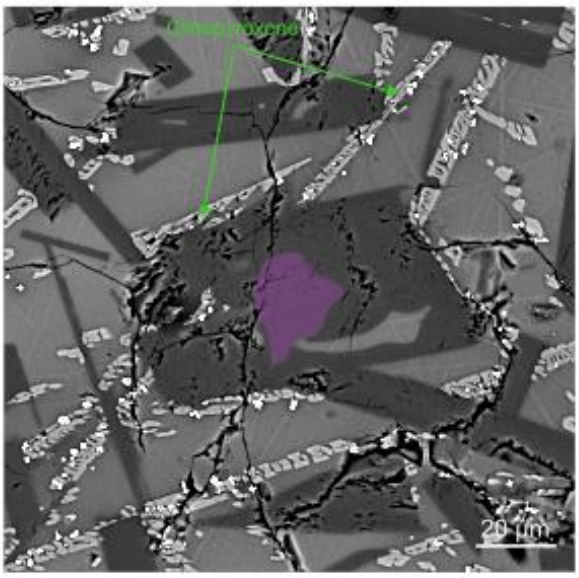
Clinopyroxene
20 µm

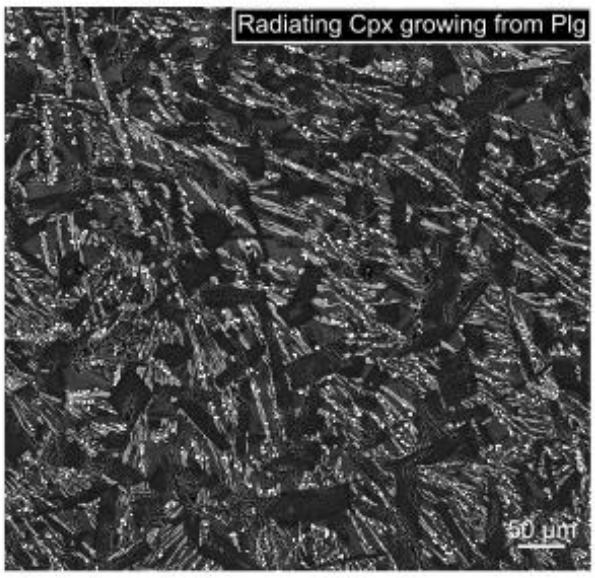
Radiating Cpx growing from Plg
50 µm

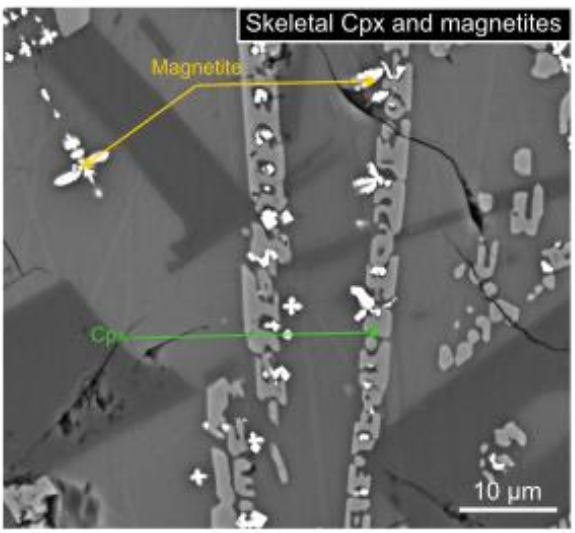
Skeletal Cpx and magnetites
Magnetite
Cpx
10 µm

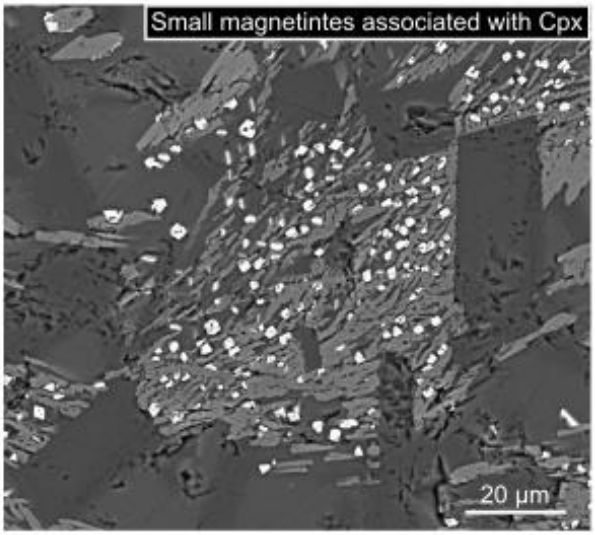
Small magnetintes associated with Cpx
20 µm

Cooling conditions: 25 °C/h (with seeds)

Starting material: OS36 (from G 4-1 to G 4-3)

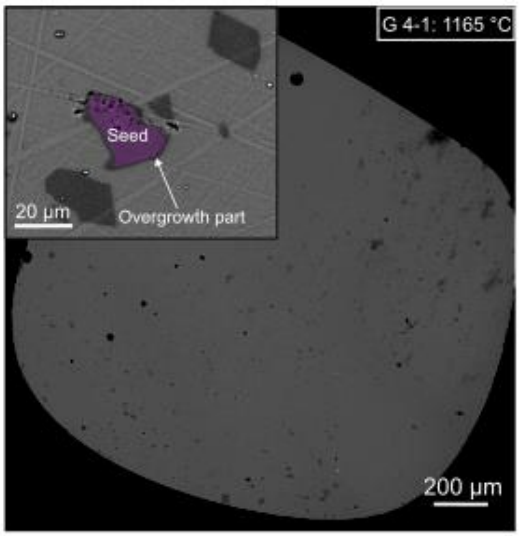

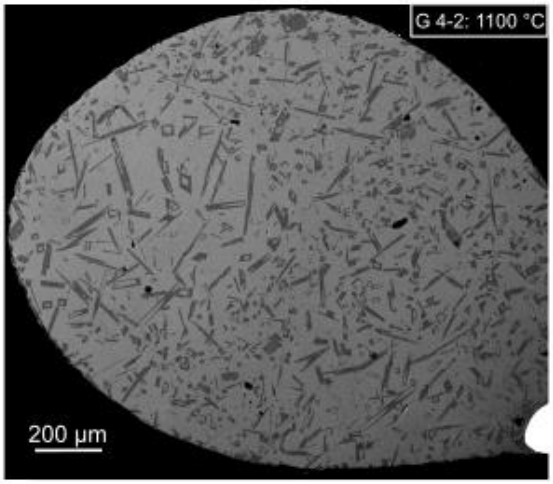

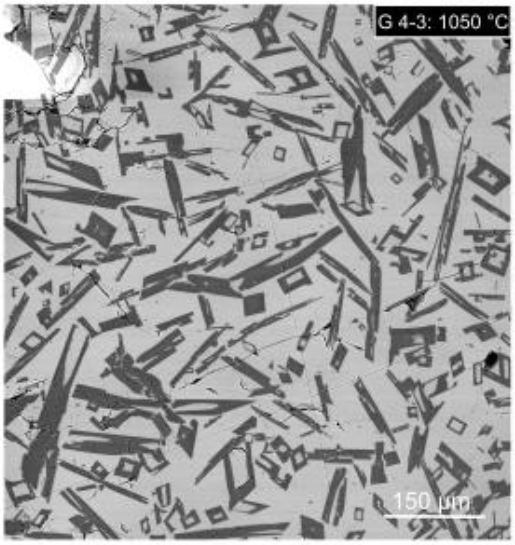

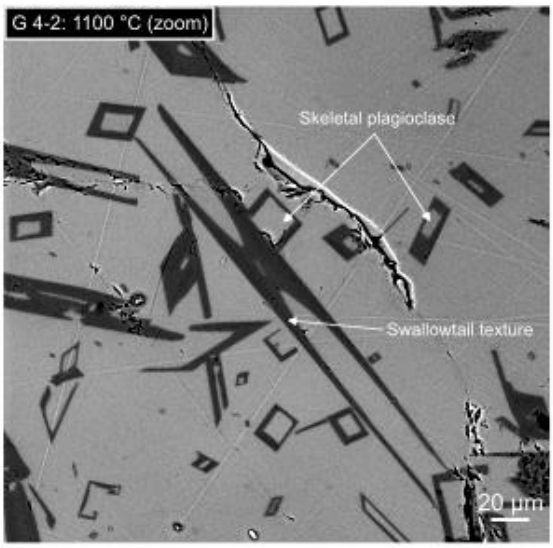

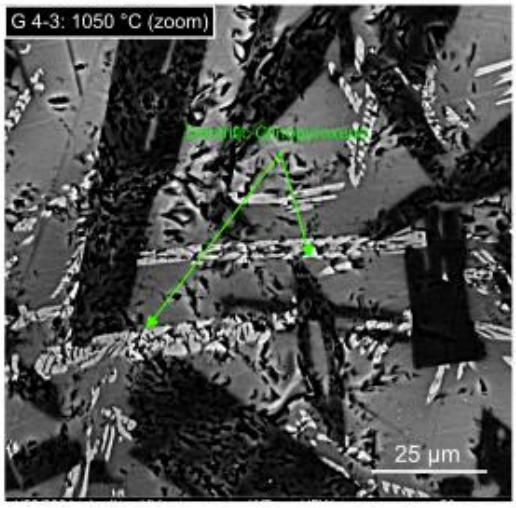

Cooling conditions: 125 °C/h (with seeds)

Starting material: OS36 (from G 5-1 to G 5-3)

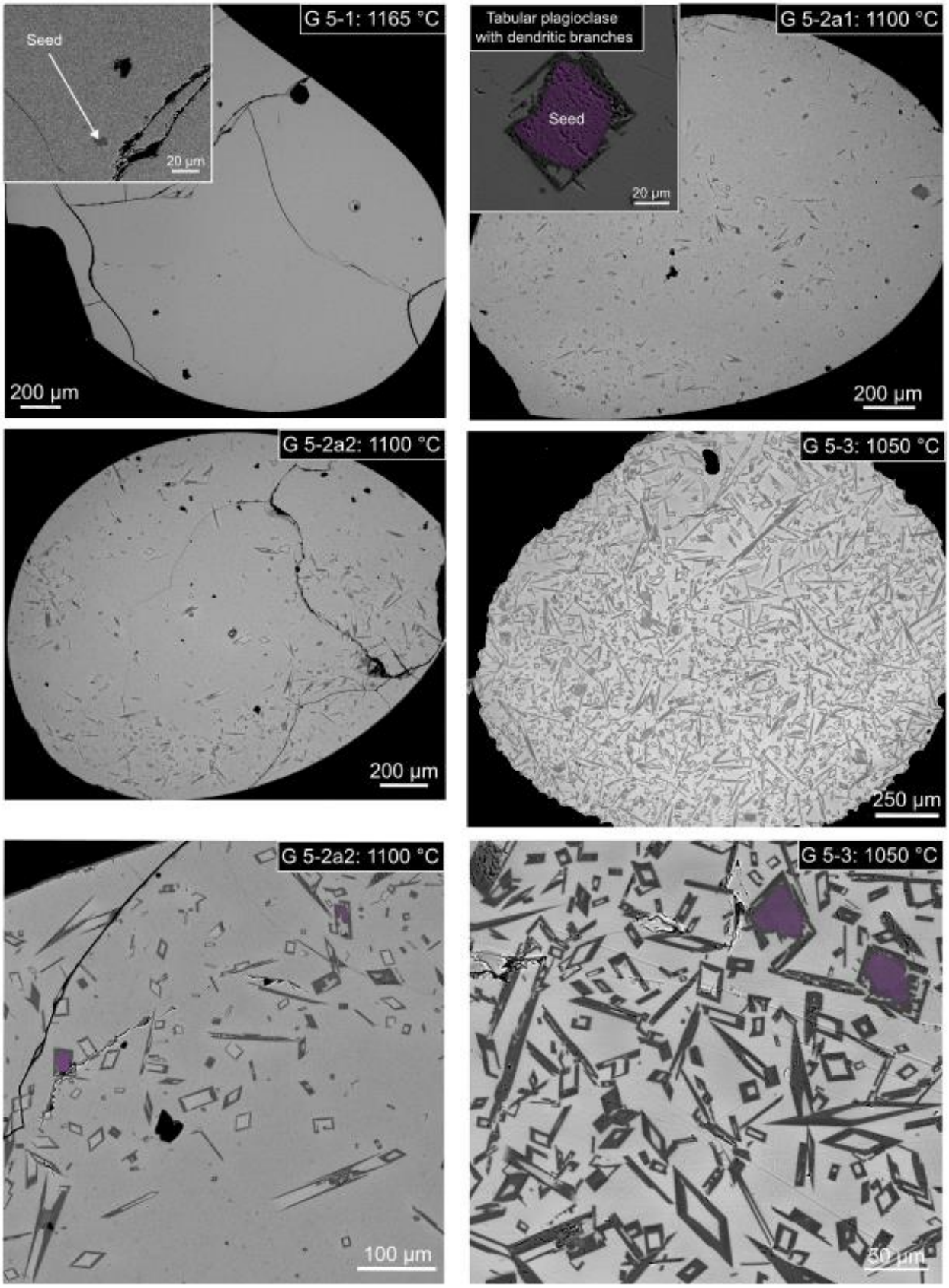

Cooling conditions: 1 °C/h (No seed)

Starting material: OS36* (from G 7-1 to G 7-4)

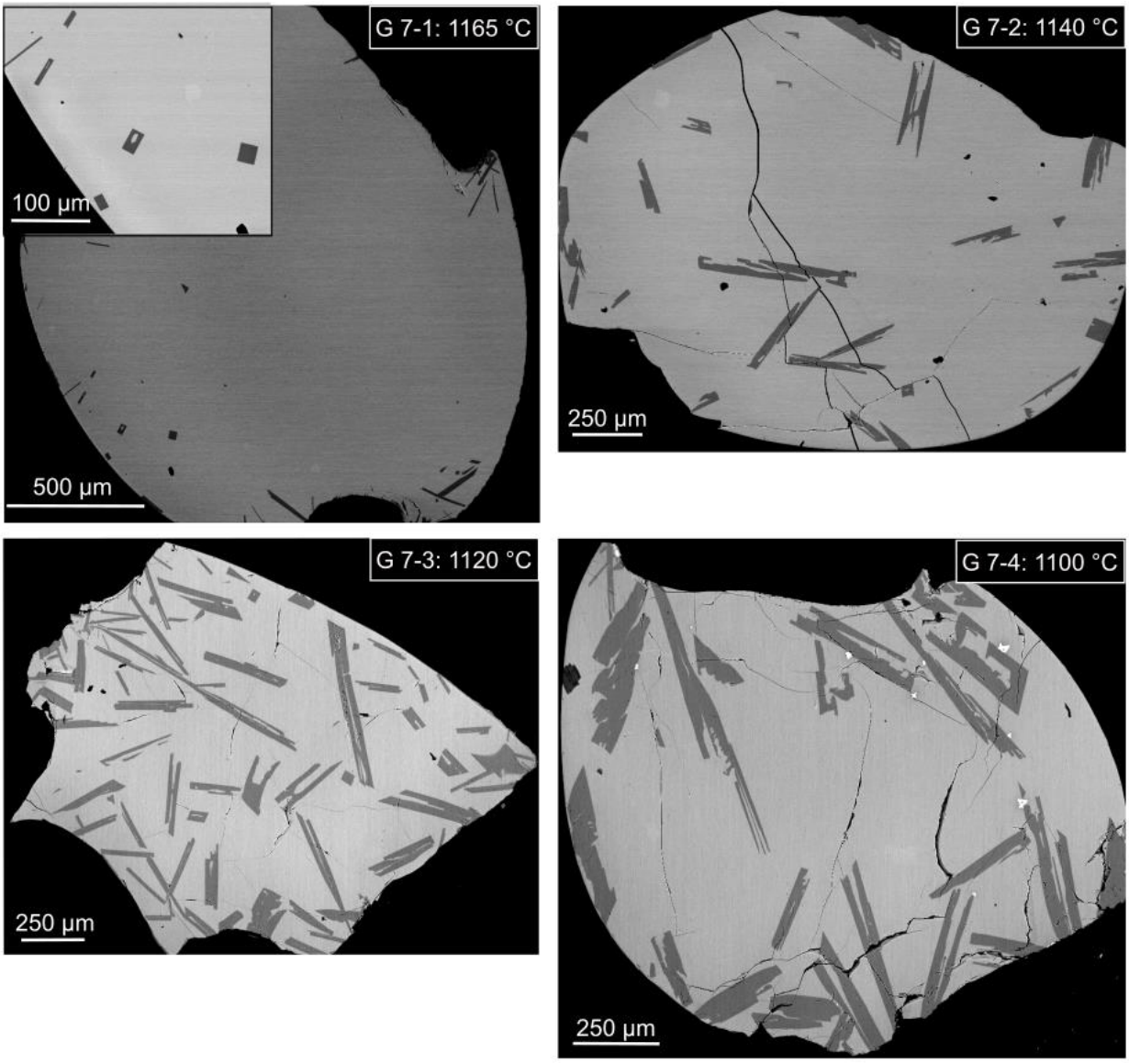

Cooling conditions: 9 °C/h (No seed)

Starting material: OS36* (from G 8-1 to G 8-2)

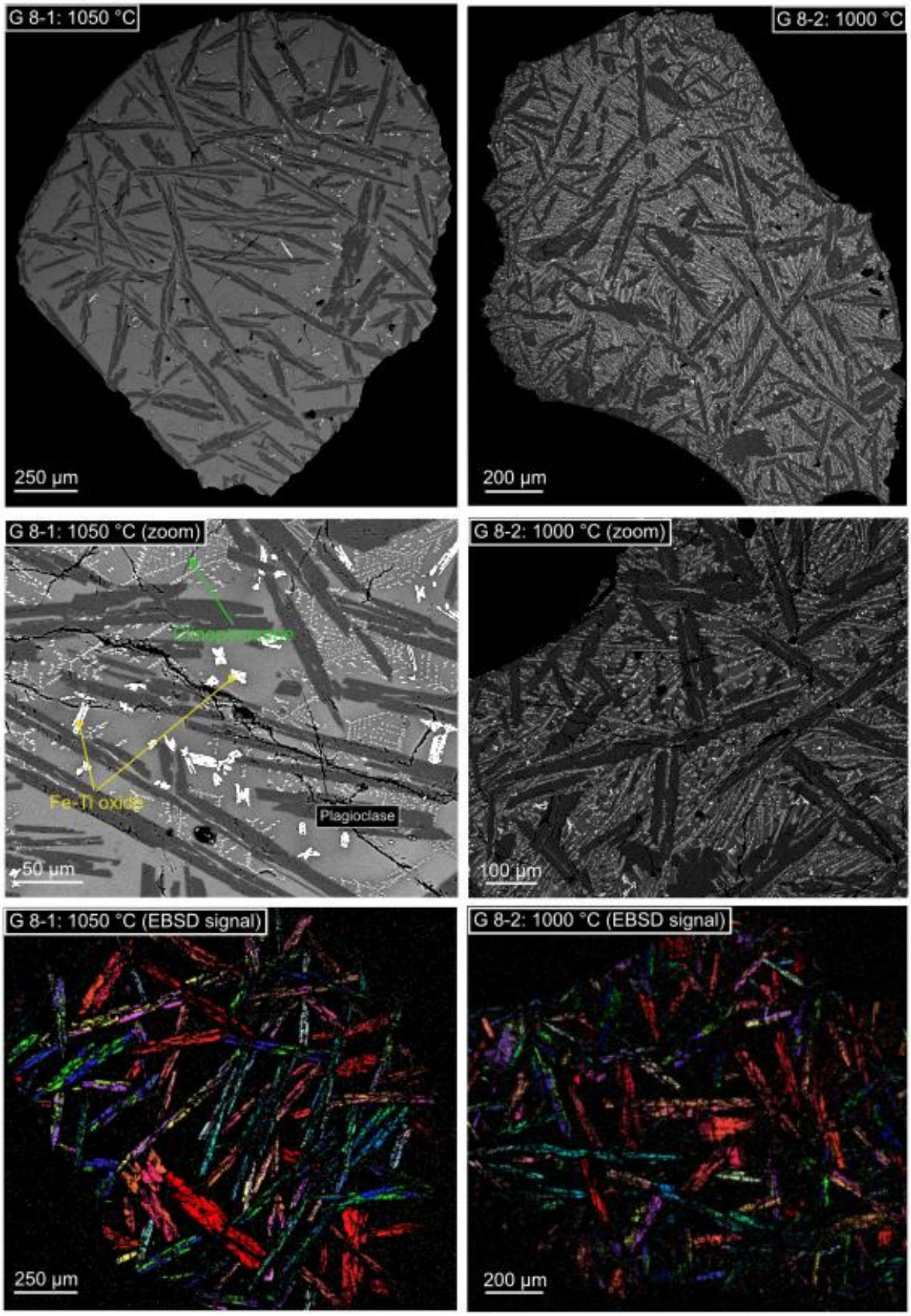

Cooling conditions: 25 °C/h (No seed)

Starting material: OS36* (from G 9-1 to G 9-3)

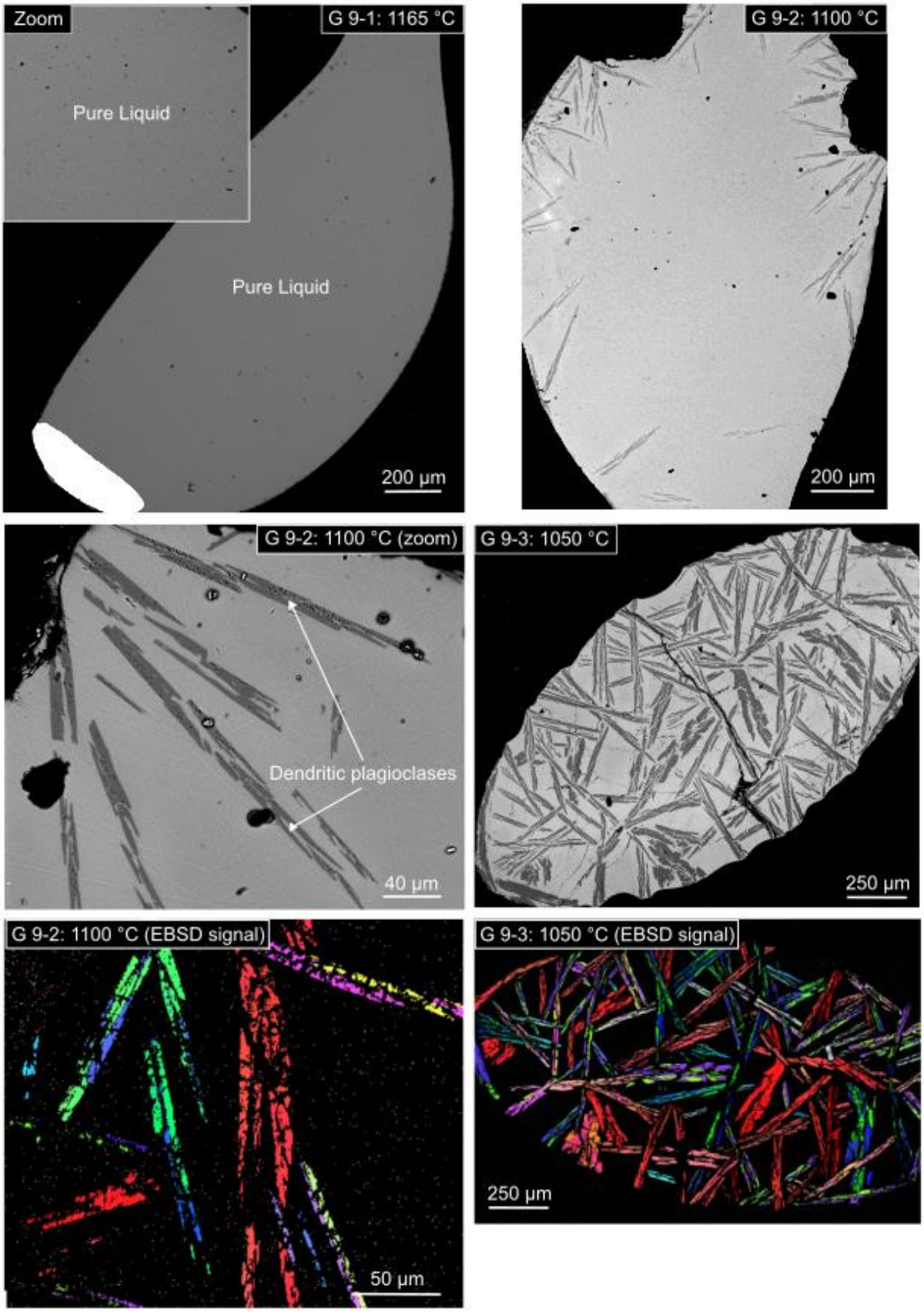

Cooling conditions: 125 °C/h (No seed)

Starting material: OS36* (from G 10-1 to G 10-2)

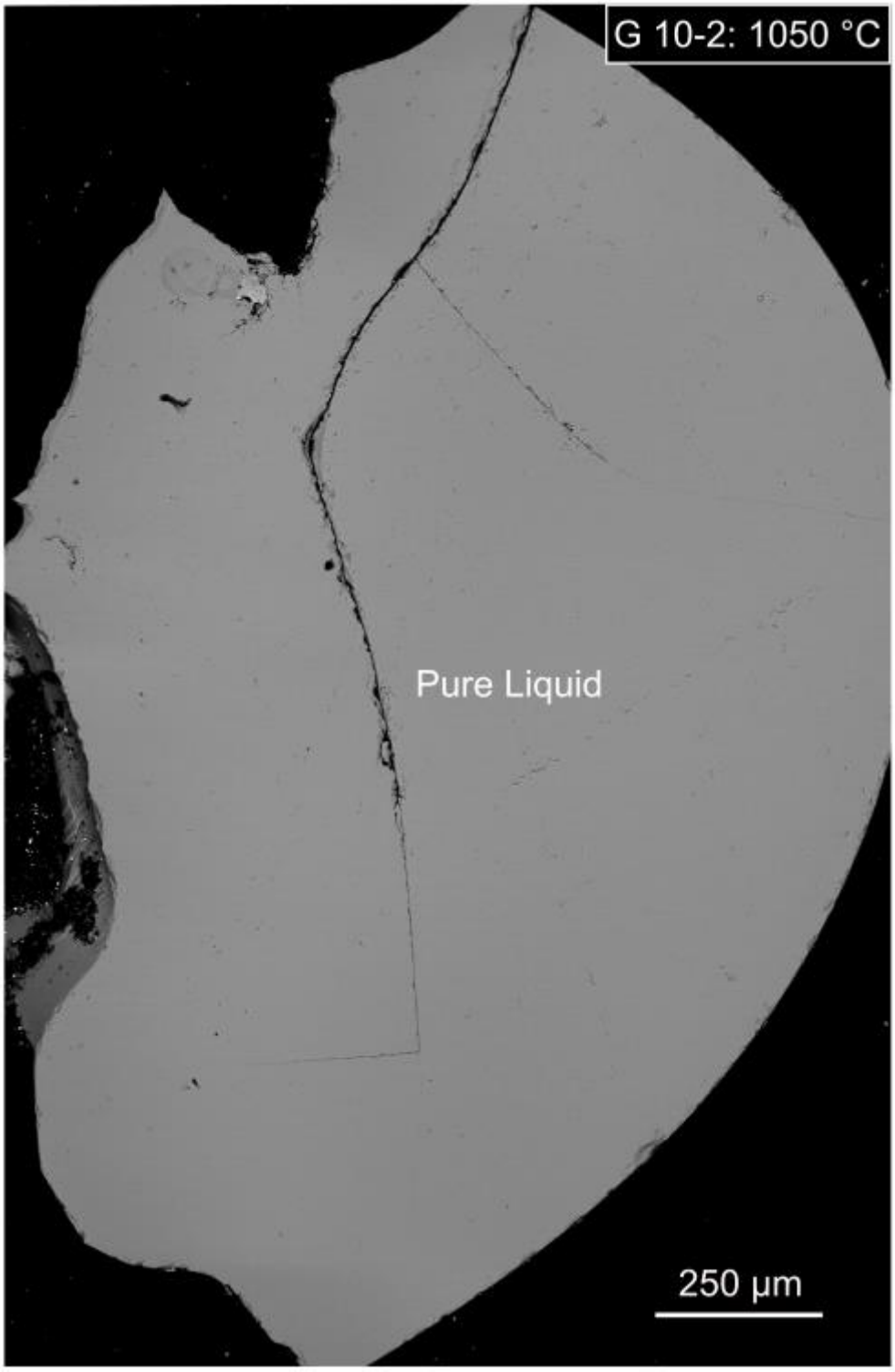

Cooling conditions: 125 °C/h (No seed)

Starting material: OS36* (from G 10-1 to G 10-2)

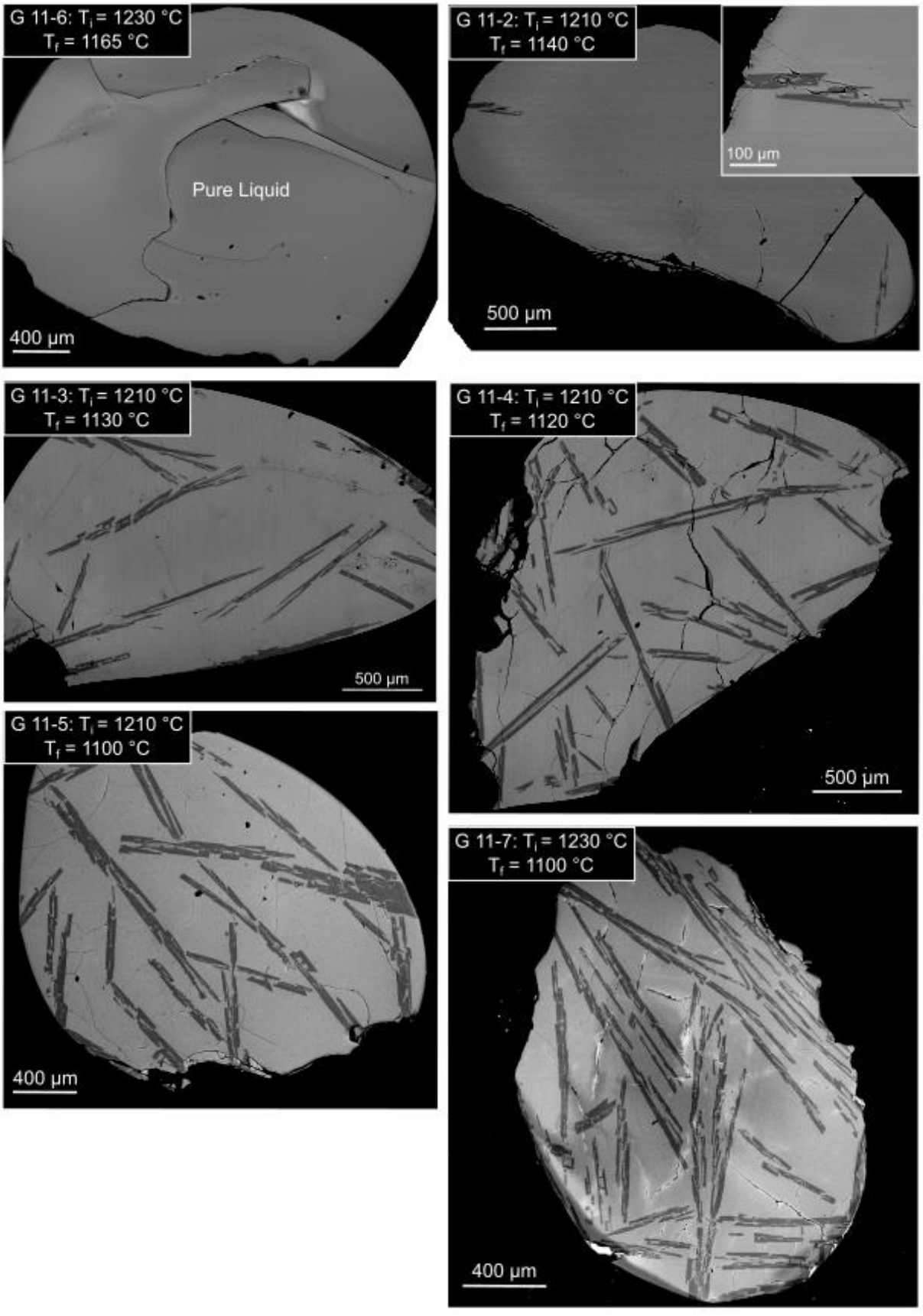

COOLING RUNS + FINAL DWELL DURATION

Cooling conditions: 1 °C/h, T_f = 1165 °C

Starting material: OS36 (from G 6-1 to G 6-2)

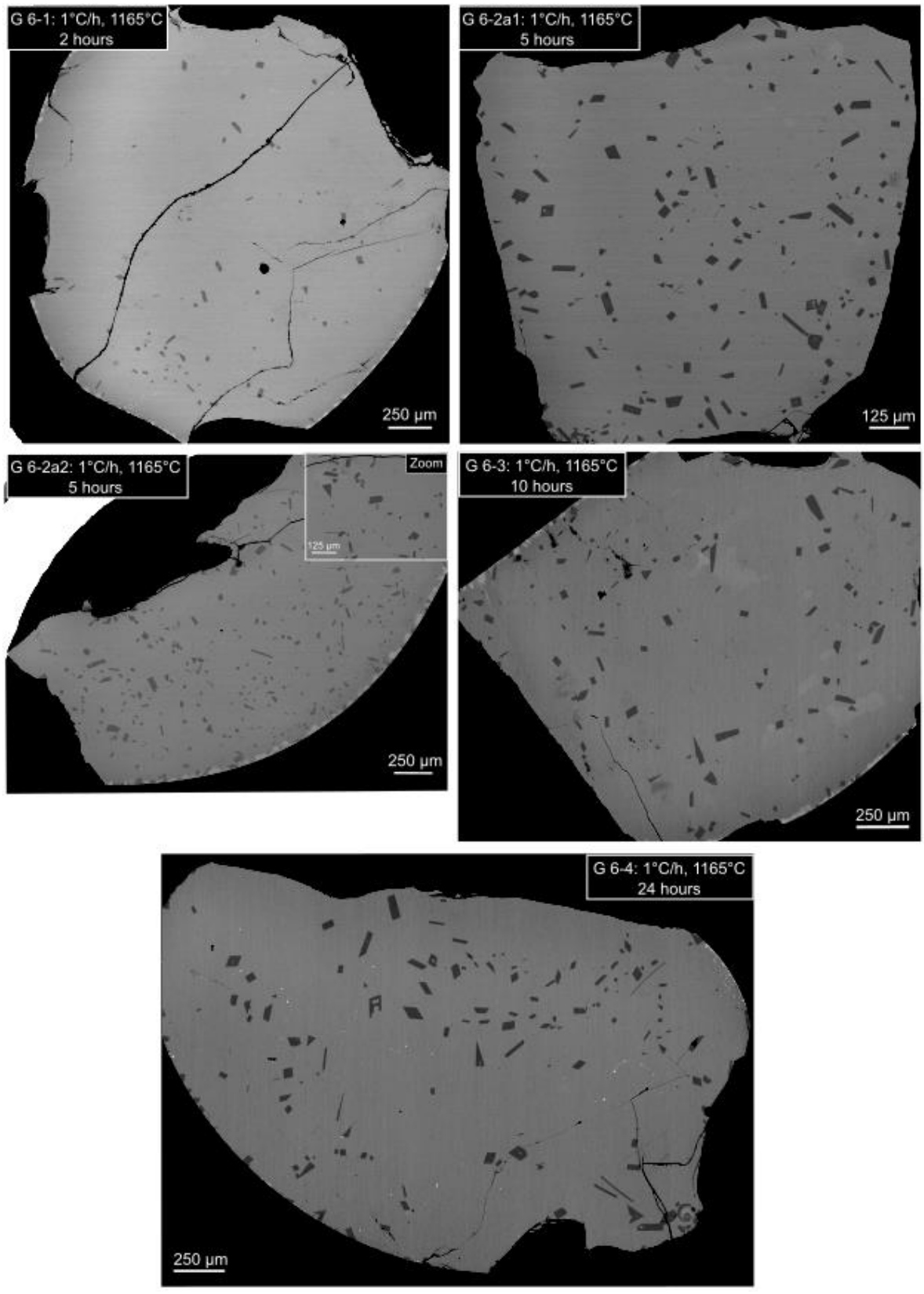

Cooling conditions: 1 °C/h, T_f = 1120 °C

Starting material: OS36 (from G 6-5 to G 6-9)

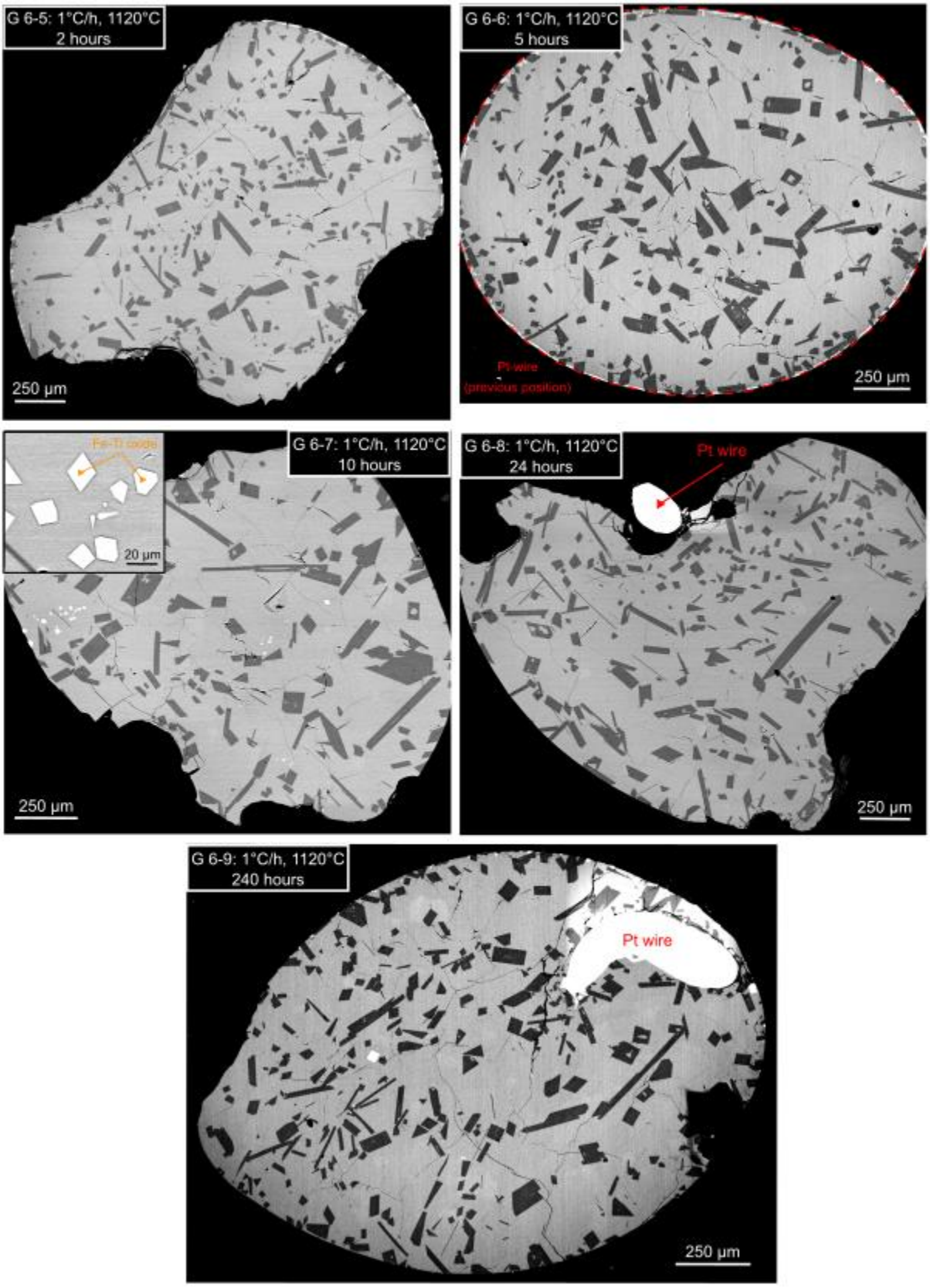

Cooling conditions: 1=9 °C/h, T_f = 1165 °C

Starting material: OS36 (from G 6-10 to G 6-11)

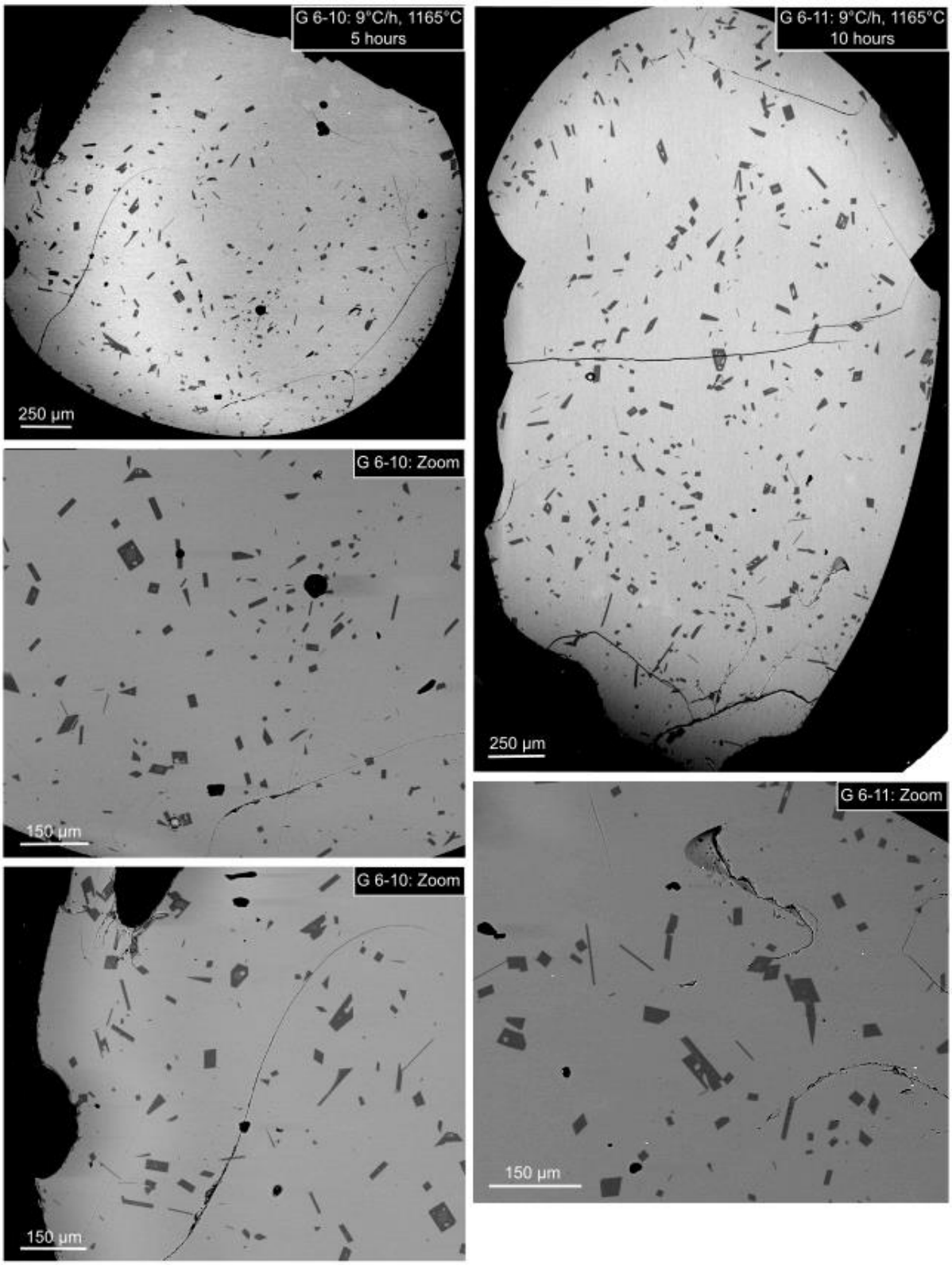

Cooling conditions: 1=9 °C/h, T_f = 1120 °C

Starting material: OS36 (from G 6-12 to G 6-15)

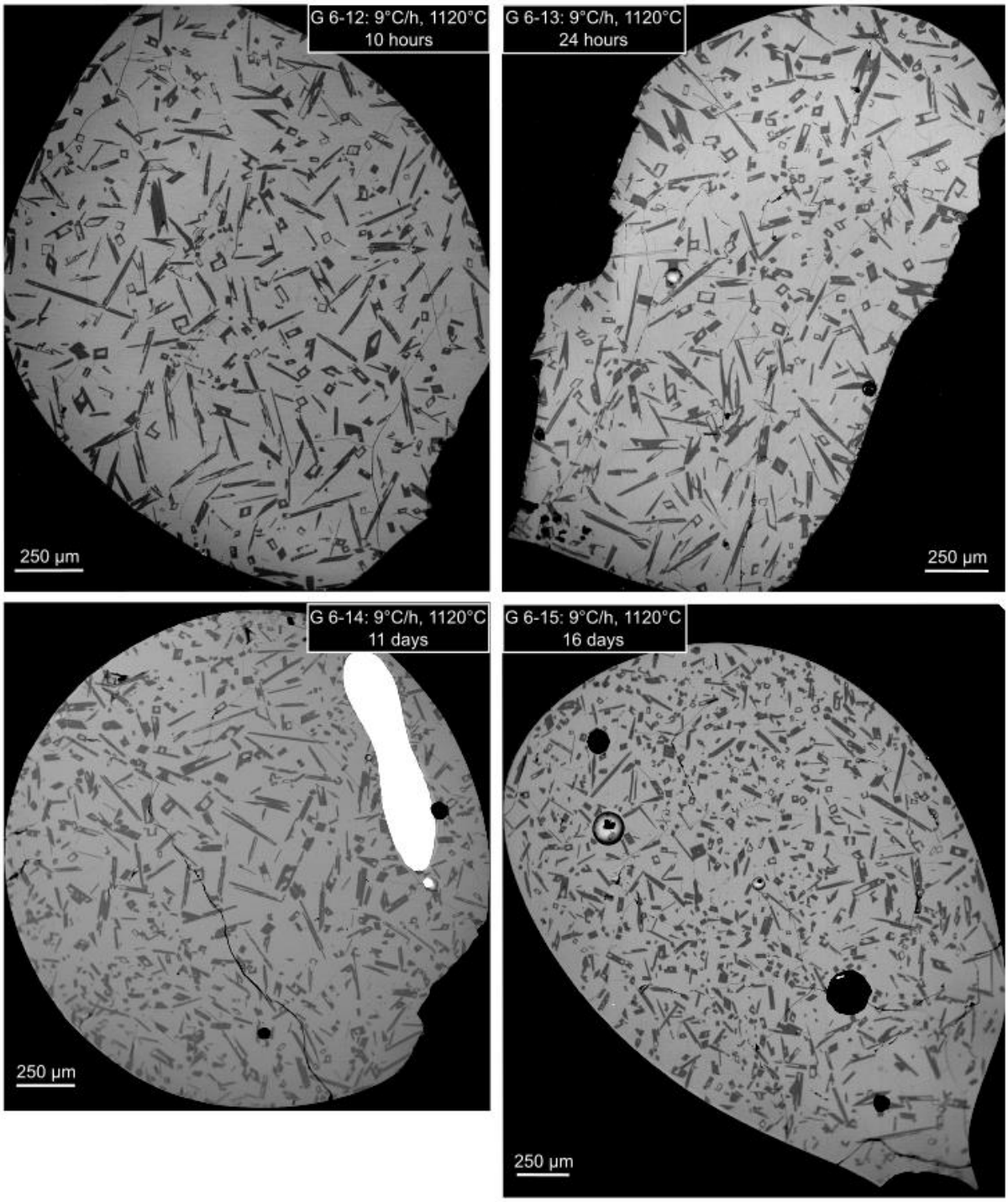

Cooling conditions: 1=9 °C/h, T_f = 1120 °C

Starting material: OS36 (from G 6-16 sample 1 and 2)